J. Astrophys. Astr. (2000) **21,** 1–17

A Measurement of the Cosmic Microwave Background Temperature at 1280 MHz

A. Raghunathan & Ravi Subrahmanyan*, *Raman Research Institute, C. V. Raman Avenue, Bangalore – 560 080, India*
**Present address: Australia Telescope National Facility, CSIRO, Locked bag 194, Narrabri, NSW, Australia.*

Received 2000 April 18; accepted 2000 May 11

Abstract. The absolute temperature of the cosmic microwave background (CMB) has been measured at a frequency of 1280 MHz. The observation was made with a modified version of the L-band receiver used in the Giant Metre wavelength Radio Telescope (GMRT): the feed horn was replaced by a corrugated plate and the receiver was placed on the ground, directed at zenith, and shielded from ground radiation by an aluminium screen with corrugated edges. Novel techniques have been adopted for

- reducing and cancelling unwanted contributions to the system temperature of the receiver and
- calibrating the contributions from the feed assembly and receiver.

The thermodynamic temperature of the CMB is estimated to be 3.45 ± 0.78 K.

Key words. Cosmic microwave background — cosmology: observations.

1. Introduction

The spectrum of the cosmic microwave background (CMB) has been measured by the *COBE-FIRAS* experiment (Fixen *et al.* 1996) to be very closely Plankian in form over the frequency range 70–640 GHz; the best-fit thermodynamic temperature of the radiation was determined to be 2.728 ± 0.004 K over this frequency range. This is consistent with the expectation – within the Standard big-bang cosmology – that the relict radiation was thermalized via free-free and radiative Compton scattering at redshifts $z > z_{\rm th} \sim 7.5 \times 10^6$ (Burigana, Danese & De Zotti 1991).

The damping of small wavelength (large *k-mode)* sub-horizon scale baryon adiabatic perturbations – as a result of photon diffusion – may be viewed as a mixing of radiation with different thermodynamic temperatures. As a consequence, the Plankian radiation spectrum undergoes a y-type distortion: it may be characterized by a Compton-y parameter. Damping of perturbations that 'enter' the horizon at epochs $z < z_{\rm th}$ when thermalization processes had ceased to be effective, but at epochs $z > z_c \sim 1.6 \times 10^5$ when Compton scattering was capable of driving the radiation spectrum to kinetic equilibrium, resulted in a transformation of the y distortions to μ-type distortions characterised by a chemical potential (Daly R.A. 1991; Hu, Scott & Silk 1994). These μ distortions are *inevitable* in 'standard' theories of structure formation; the magnitude of the distortion is a probe of the amplitude of the primordial perturbation spectrum at large k modes or – combined with the COBE normalization for small k modes – may be viewed as a probe of the index n of a power-law form spectrum.

Besides the inevitable distortions from structure formation, any processes that release radiant energy in the redshift interval $z_{th} > z > z_c$ would result in a μ distortion in the CMB today. For example, the decay of particles with half lives in this range of cosmic epochs could be probed via the expected μ distortions in the relict CMB (Silk & Stebbins 1983).

A simple μ distortion in a Plankian spectrum manifests as a divergence in the thermodynamic temperature with increasing wavelength. However, because the thermal bremsstrahlung, which is one of the processes responsible for the thermalization of the radiation at redshifts $z > z_{th}$, has a frequency dependence and is more effective at longer wavelengths, distortions at long wavelengths are thermalized and consequently the thermodynamic temperature of the radiation may be expected to have an extermum in its deviation. Maximum distortion occurs at about a wavelength $\lambda_m \sim 30$ cm (Burigana, Danese & De Zotti 1991).

μ distortions in the CMB that arise as a consequence of processes at epochs $z_{th} > z > z_c$ may, therefore, be best constrained by measurements of the absolute temperature of the CMB at frequencies about 1 GHz. We have attempted to make a measurement of the thermodynamic temperature of the CMB at 1280 MHz.

2. The receiver system

The receiver used for the measurement described in this work is a modified form of the L-band front-end package built for the Giant Metrewave Radio Telescope (GMRT; Swarup *et al.* 1991, 1997). This receiver was designed to be a package mounted at the prime focus of the GMRT antennae and its feed horn was designed to illuminate the parabolic dish aperture. For our experiment, the receiver package was placed on the ground and pointed at zenith. A schematic of the receiver configuration is shown in Fig. 1.

The corrugated feed-horn used in the GMRT receiver was replaced by a flat plate with concentric corrugations; this is directly connected to the top of the quadridged orthomode transducer (OMT) and serves as the interface between free space and the transducer. The OMT is a circular cylindrical waveguide and at the bottom end the

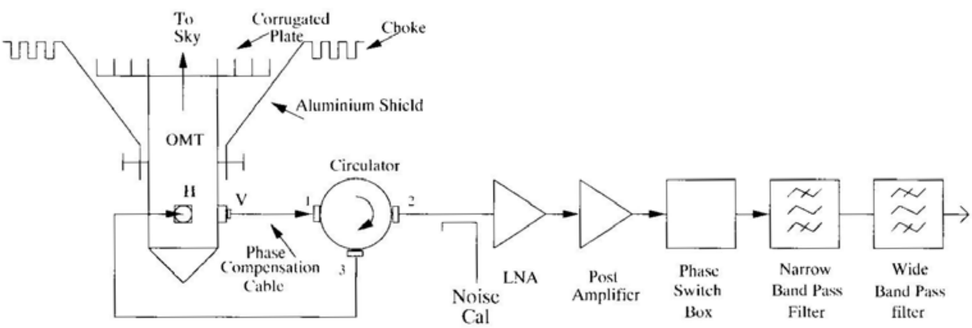

Figure 1. Schematic diagram of the 1280 MHz receiver.

signal is transduced onto coaxial cables. Although the OMT provides dual orthogonal polarizations, only a single linearly polarized signal ('V' port signal) has been used for the background measurement. This coaxial signal is fed to a low-noise amplifier (LNA) through a circulator. In section 3, we elaborate on issues related to the introduction of this circulator. The LNA output is connected to a chain of band-pass filters and is effectively limited to a 120 MHz band centred at 1280 MHz. The receiver package is at ambient temperature and no part is cooled.

The receiver output is connected to a spectrum analyser through a commercial Miteq amplifier. The noise figure of the spectrum analyser is so high that in the absence of the Miteq amplifier, the spectrum analyser's noise contribution degrades the signal-to-noise by contributing significantly to the overall system temperature. The power spectrum is measured by reading the trace of the spectrum analyser using a general purpose interface board (GPIB) and the spectral data are acquired through a personal computer.

The receiver and feed assembly are surrounded by an aluminium shield to minimize ground radiation leakage into the feed. The design of the shield and measurements of the ground contribution are detailed respectively in sections 4 and 12.

The cosmic microwave background temperature (T_{CMB}) has been measured using the above receiver at 1280 MHz over a bandwidth of 100 MHz. The signal power incident at the corrugated plate (feed) will be an additive combination of contributions from the cosmic microwave background, emission from the Milky Way Galaxy, atmospheric emission and ground contribution through sidelobes of the feed assembly. Therefore, the noise temperature entering the feed plate will be the sum of the Galactic temperature T_{Gal}, atmospheric temperature T_{atm}, ground temperature T_{gnd} and cosmic microwave background temperature T_{CMB} For an accurate determination of T_{CMB}, it is necessary to know the values of T_{Gal}, T_{atm}, and T_{gnd} so that these may be subtracted from the measurement of power at the feed plate. In sections below, these contributions are separately estimated.

The noise power entering the feed propagates via the OMT and circulator before amplification in the LNA. Beyond this point, the high gain in the LNA and the negligible signal-to-noise-ratio degradation in successive stages ensure that any additive noise contributions are insignificant. Following the calibration scheme discussed below in section 7, the power measured by the spectrum analyser is calibrated to represent the equivalent noise power referred to in the input port (port 1) of the circulator. Expressed in Kelvin, this noise power represents the total system temperature T_{sys} In order to estimate the noise power entering the feed and isolate this component in a measurement of the total system temperature, it is necessary to separately measure system parameters like the receiver temperature (T_{R}) and the reflection coefficient (Γ) and the absorption coefficient (α) of the feed assembly (corrugated plate + OMT).

We now present a formulation of the measurement problem. Let T_{α}'' represent the total external signal incident on the corrugated plate (feed):

$$T_a'' = T_{\text{Gal}} + T_{\text{atm}} + T_{\text{gnd}} + T_{\text{CMB}}. \tag{1}$$

The total (external + internally generated) power at the input terminal (port 1) of the circulator is given by

$$T_a = T_a''(1 - \Gamma^2)(1 - \alpha) + \alpha T_{\text{amb}}, \tag{2}$$

where the antenna temperature T_a is represented as an additive sum of the external power – corrected for attenuations and reflections in the feed assembly – and the internal noise generated as a consequence of the loss in the feed assembly. The feed assembly is at ambient temperature T_{amb}. The system temperature T_{sys}, as referred to the input of the circulator (port 1), is given by

$$T_{sys} = T_a''(1 - \Gamma^2)(1 - \alpha) + \alpha T_{amb} + T_R. \quad (3)$$

In this equation, the first term on the right represents the net external signal present at the input of the circulator, the second term represents the thermal noise contribution from the feed assembly and the third term is the receiver temperature as referred to the circulator input. Measurements of the various parameters in the above equations are necessary for an estimation of the absolute value of T_{CMB} from a measurement of the calibrated system temperature at the input of the circulator.

Photographs of the system, as used for the CMB measurement, are shown in Figs. 2 and 3. The receiver electronics is inside a (40 cm × 60 cm × 100 cm) rectangular box. Fig. 3 shows the system with the shield lowered: visible at the top of the receiver box is the corrugated plate – which serves as the feed – and this is connected to the OMT housed inside the box. As seen in the figure, the shields are constructed from trapezoidal aluminium plates and when the shield is mounted as shown in Fig. 2, the top of the receiver box, including the feed plate, is shielded on all four sides and the shield minimizes ground radiation entering the system. The receiver output is accessible below the shield and is connected to the spectrum analyser, mounted separately on a trolley, via an RF co-axial cable. The trace data obtained in the spectrum analyser are recorded via a GPIB interface in a Computer.

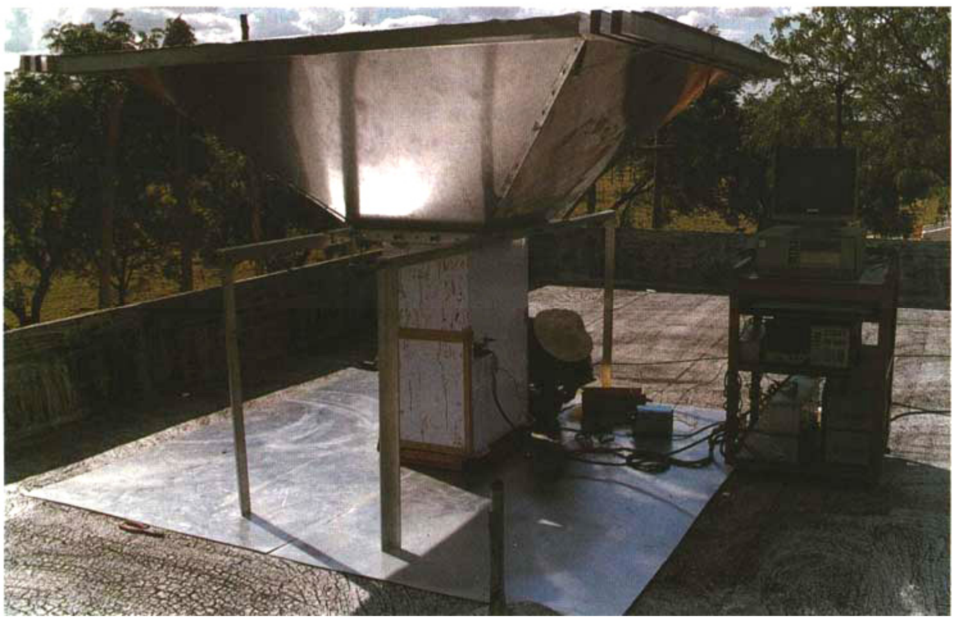

Figure 2. Photograph of the 1280 MHz receiver with the aluminium shield in place.

Figure 3. Photograph of the 1280 MHz receiver with the aluminium shield lowered to the ground.

3. Noise reduction techniques

The circulator has been introduced at the input of the LNA in order to isolate the LNA from reflections in the corrugated plate-OMT assembly while observing the sky. Multiple reflections, if allowed, may cause the LNA noise temperature to be significantly dependent on the input matching and, consequently, the LNA temperature as measured under test conditions in the laboratory (section 7) may be different from the LNA temperature when the receiver is configured to observe the CMB sky temperature.

As shown in Fig. 1, the V-channel output from the OMT, which represents the sky signal T_a that is to be measured, is connected to port 1 of the circulator and propagates, with a small loss, on to the LNA via port 2 of the circulator. The 'cold load' at port 3 of the circulator is derived from the 'H' port sky signal of the OMT. In addition, the 'H' port also serves as a conduit for radiating the LNA noise power – which propagates from the LNA into port 2 of the circulator – to the sky. We have verified that the isolation between the 'V' and 'H' ports exceeds 30 dB.

Any noise power (sky signal or reflected LNA noise) that enters port 3 of the circulator from the 'H' port of the OMT would propagate to the LNA as a spurious additive power via two paths:

- leakage directly from port 3 to port 2 and
- by being reflected from the 'V' port of the OMT.

We have selected the length of the cable connecting the 'V' port of the OMT to port 1 of the circulator so that the two signal paths would have a difference of half-integral wavelengths. Consequently, the ‘phase-compensation’ cable (Fig. 1) causes a partial cancellation of the spurious signal power and enhances the isolation, by an additional 5 dB, of the LNA from spurious signals entering via port 3.

4. Ground shields

The OMT in the receiver is a uniform circular waveguide. Usually, the free-space impedance is matched to the OMT impedance via a feed; in the case of the GMRT, a wide-flare-angle corrugated scalar horn is used. Derivation of the sky temperature from system temperature measurements requires a characterization of the losses in the feed assembly. The losses in the OMT are measured, as discussed below, by taking advantage of the fact that the OMT is uniform; however, the losses in any tapered horn are difficult to measure. Therefore, we omitted the feed horn from our receiver system. As a consequence:

- on the positive side we do not have to measure any losses in any feed system,
- the negative aspect is that the OMT is now poorly matched to free space.

The mismatch is measured, as described below, by taking advantage of reciprocity in the passive OMT.

Steps are taken to minimise the ground contribution as much as possible. We have chosen to have a simple corrugated plate on the top of the OMT to reduce the far-off sidelobes in the instrument response. The plate reactively, rather than resistively, attenuates any incoming power from directions at large angles to the OMT axis. Because this interface between the OMT and free space, which replaces the feed horn, acts only on signals incident at large off-axis angles where the OMT response is low, and because the corrugated plate is a reactive block, we do not expect any significant contribution from the plate to the system temperature.

We have also constructed a solid aluminium ground shield to further reduce the ground contribution. In order to reduce diffractive leakage of ground emission around the edges of the shield, chokes are placed all along the periphery of the shield around the receiver. In addition, as shown in Figs. 2 and 3, an aluminium sheet covers the ground directly below the system.

4.1 *Design of the corrugated plate*

A circular aluminium plate of 6 mm thickness and with outside diameter equal to 508 mm and inner diameter equal to 200 mm is used as a base for the choke slots. Three concentric corrugations are formed on this plate using 6 mm thick and 60 mm wide aluminium strips bent in the form of rings of different diameters as shown in Fig 4. The width of the circular strips are chosen to be $\lambda/4$ at the centre frequency (1280 MHz); this makes the corrugations $\lambda/4$ deep. The rings are spaced at approximately 0.125λ (30 mm) apart and this dimension will be the width of the concentric corrugation slots. These circular rings are fastened onto the metal plate using screws. For good electrical continuity, tinned copper braid is introduced between the circular rings and the base plate before fastening. The corrugated plate is attached to the OMT via an interface plate. The radiation pattern of the OMT with the

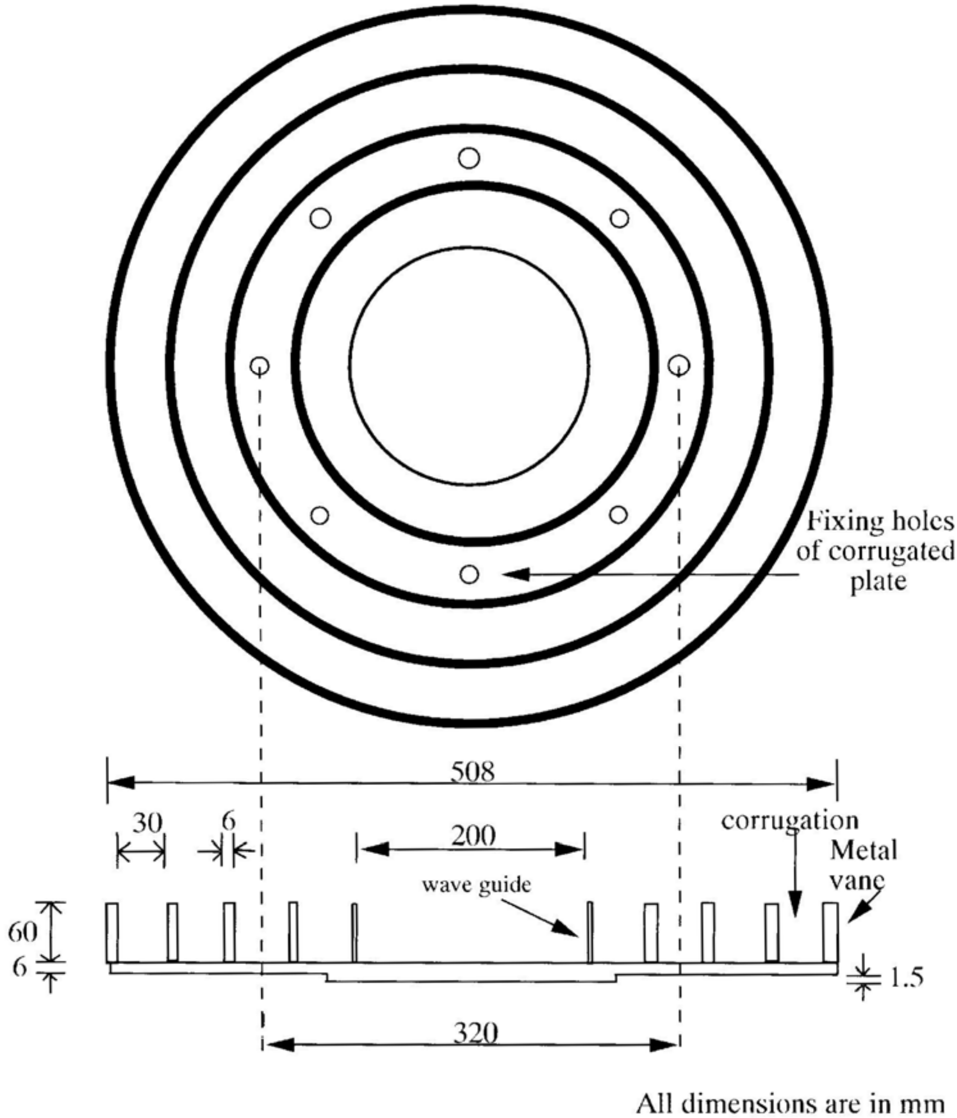

Figure 4. Schematic diagram of the corrugated plate.

corrugated plate is shown in Fig. 5. It is clear from the figure that the radiation patterns in both V and H planes are symmetrical and have a 3 dB beam width of ≈ 60°. The introduction of the plate marginally reduces the 3 dB width of the main lobe; as compared to the radiation pattern of the OMT (without the corrugated plate), the feed assembly has significantly (> 10 dB) reduced sidelobes.

4.2 *Design of the ground shield*

An aluminium shield is used to reduce the ground contribution to the system temperature of the receiver. The shield is made of four trapezoidal parts of similar

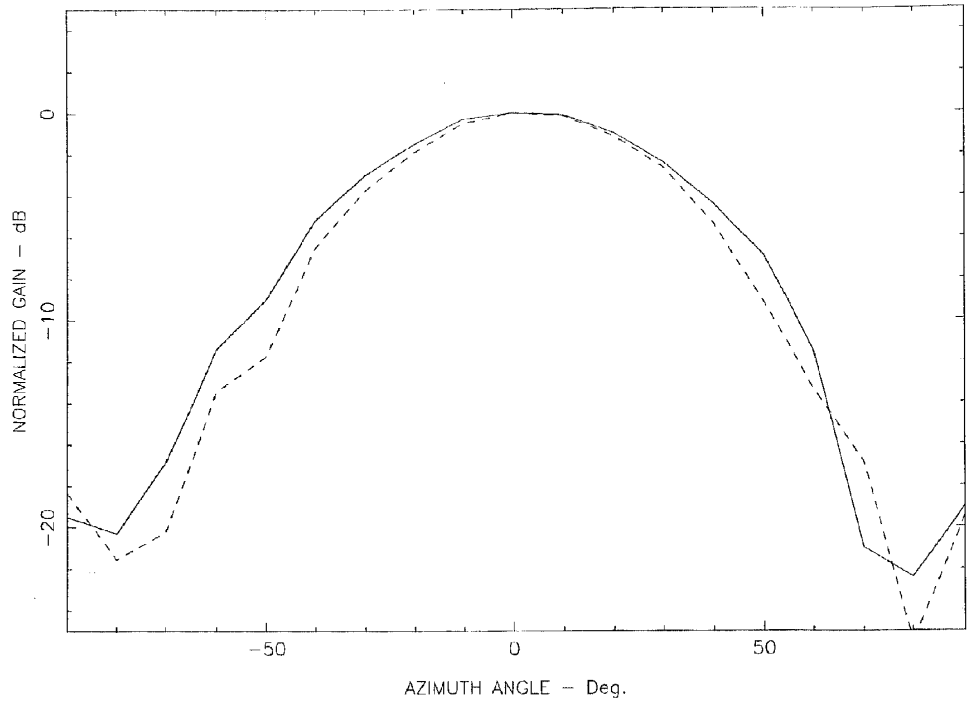

Figure 5. The radiation pattern of the modified feed assembly in the E (solid line) and H (dashed line) planes at 1280 MHz.

dimensions: they all have a short vertical straight section of about 10 cm height followed by a 1 m long section bent at an angle of 45° to the vertical axis. At the top of the 45° section is attached a choke formed of thin aluminium sheet. The purpose of the choke is to reduce the ground noise entering into the system over the top of the shield through edge diffraction. A schematic of the shield, along with the dimensions, is in Fig. 6. The shield is fixed to an aluminium square base frame made using 1.5-inch 'L' sections. The frame may be fixed to the receiver at any height. Too high a position disturbs the radiation pattern – as measured by a change in the return-loss of the feed assembly – whereas too low a position allows ground pick-up; the final position was found not to be critical as long as the location was not extreme.

5. The absolute temperature calibration

The absolute temperature calibration of the receiver was performed using resistances immersed in liquid baths whose physical temperature was measured using a platinum-wire resistance thermometer. In the laboratory, the reference baths were used to determine the noise temperature of the calibration signals injected at the LNA input. In the field, the noise diodes provided the secondary reference.

The platinum resistance thermometer was built using a Pt-100 sensor and a constant current source. This thermometer was calibrated by immersing it in the bath of a commercial temperature controlled chiller (Ultra Temp 2000) and examining the

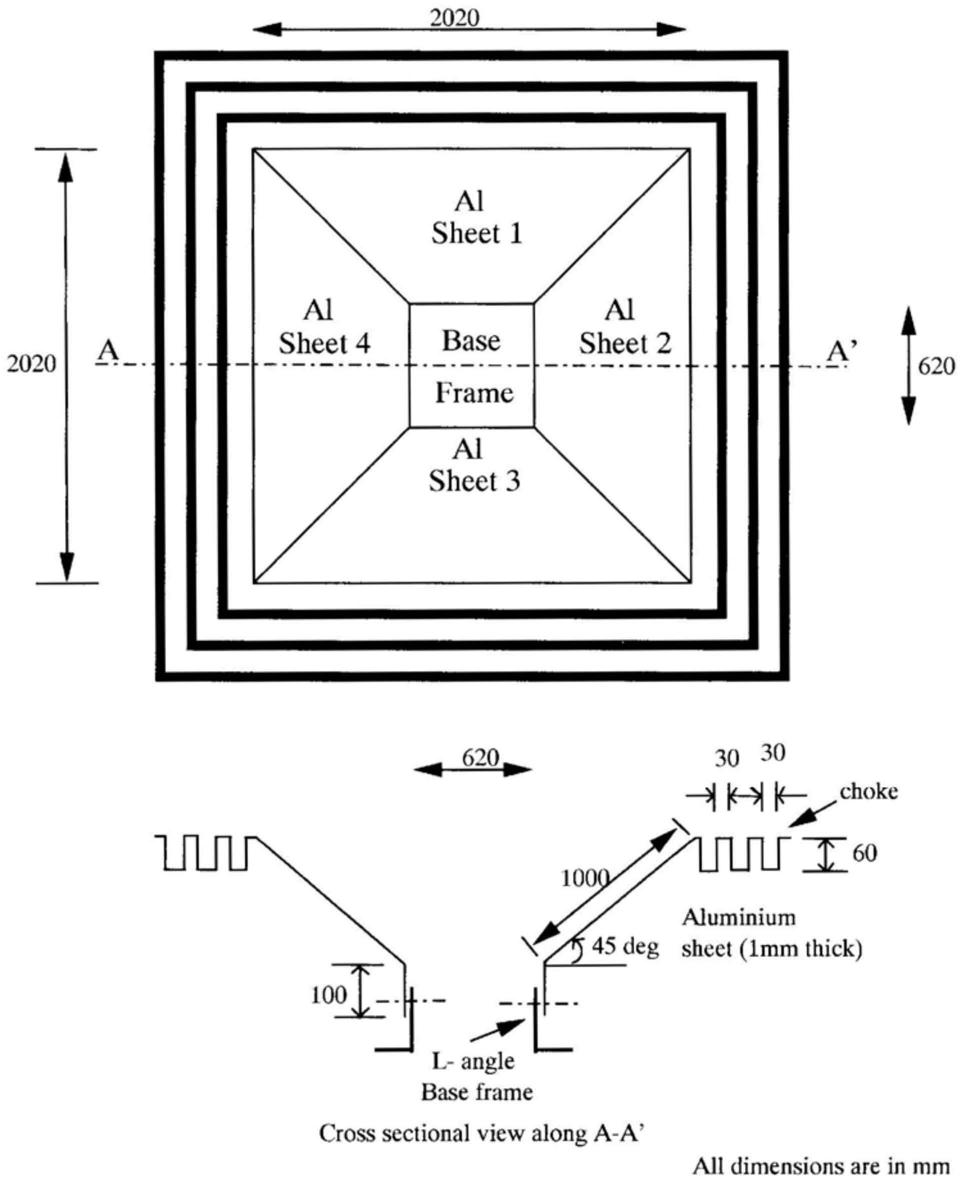

Figure 6. Schematic diagram of the aluminium shield.

variation in the voltage across the platinum resistance with the bath temperature. A precision mercury thermometer was placed in the bath in close proximity to the platinum resistor to measure the bath temperature and a calibration relationship was determined for the platinum resistance. The Pt-100 sensor was also calibrated at liquid nitrogen temperatures by placing it in a liquid nitrogen bath whose temperature was measured using (a) a calibrated cryogenic thermometer in the Indian Space Research Organization (ISRO) at Bangalore, India and (b) a Pt-l k commercial calibrated sensor from Rosemount Corporation. The relations obtained from the calibration measurements for the determination of temperature using the measured voltages were

$$V = 195.531799 + 0.757149(T + 273.15), \quad \text{and} \tag{4}$$
$$V = 0.83T - 25.88, \tag{5}$$

where T is the temperature of the sensor in Kelvin and V is the voltage measured across the sensor in volts. Equation 4 is used while measuring the temperature in the range 0–100°C and equation 5 is used in the temperature range 50–100 K. The calibrated platinum resistance thermometer is estimated to give the temperature of liquid nitrogen baths accurate to within 0.2 K and the temperature of water in the range 0–100°C to within 0.1 K.

6. The data acquisition system

The setup for the measurement of the cosmic microwave background temperature is shown in Fig. 7. The sky radiation collected by the corrugated plate-OMT is amplified and band limited within the receiver. The V-channel output of the receiver is connected to the spectrum analyser to measure the power received. Using a personal computer (PC) interfaced to the spectrum analyser, the instrument is initialized and trace data are acquired from the spectrum analyser. The spectrum analyser is configured to cover a 100-MHz span around 1280-MHz center frequency with a 1-MHz resolution bandwidth. The video-averaging function in the spectrum analyser is disabled.

A stable noise may be additively injected into the signal path close to the input of the LNA. This noise CAL is periodically switched ON and OFF during the acquisition and serves as a reference power for calibrating the receiver: the CAL remains ON for a second and OFF for a second. The appropriate CAL power level and filter selections are manually set prior to data acquisition.

The spectrum analyser is interfaced to the PC via a GPIB and the recording of the power spectrum is made by acquiring the trace data, as displayed by the spectrum analyser, into the PC. During each readout, a 401-point frequency spectrum is read

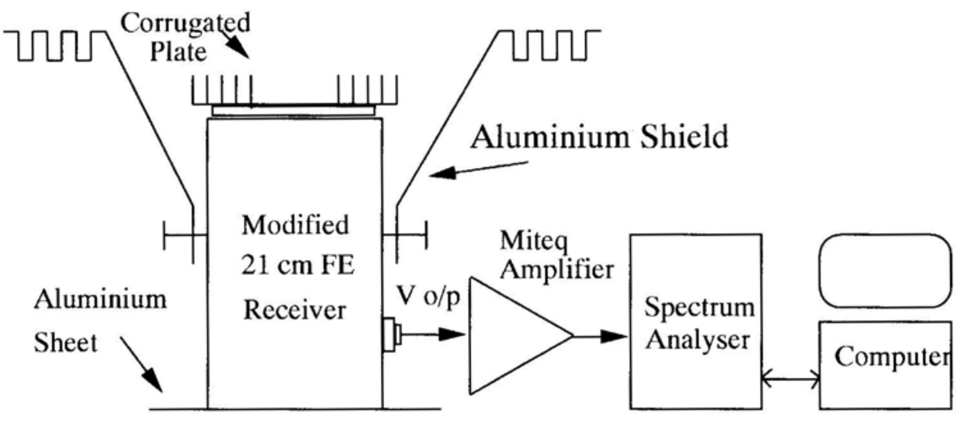

Figure 7. The experimental setup for the acquisition of the data

from the spectrum analyser. In each 2-sec period, 120 × 2 traces are read (120 with CAL in ON state and 120 with CAL OFF) and the traces are averaged separately for the CAL ON and CAL OFF states over the 100 MHz band. The laboratory determination of the CAL noise temperature (T_{cal}) — this procedure is described in section 7 – is used to calibrate the temperature scale of the acquired trace data. It may be noted here that the internal calibration of the spectrum analyser is not used for determining the temperature scale.

This acquisition system was used not only for making measurements of the CMB sky power but also in all the calibration measurements described below for determining T_R, T_{cal} and α. This ensured that all calibration measurements were made over the same frequency band and with the same spectral weighting.

Because we use the spectrum analyser to acquire the data, which effectively sweeps a narrow filter with 1 MHz width across the 100 MHz band in order to measure the spectrum, the effective integration time is only about 1 per cent of the observing duration. With our system, spectra are measured with a fractional accuracy of about 0.13 per cent if data are acquired for a period of one hour.

7. Laboratory measurement of T_R and T_{cal}

T_R and T_{cal} are the receiver noise temperature and calibration noise temperature referred to the input port of the circulator (port 1). The measurements of T_R and T_{cal} were made by comparing their noise powers with those from resistor termiations placed in standard temperature baths containing liquid nitrogen and ambient-temperature water separately.

For this measurement, as shown in Fig. 8, port 1 and port 3 of the circulator are terminated in 50Ω loads. Port 2 is connected to the LNA input and the signal

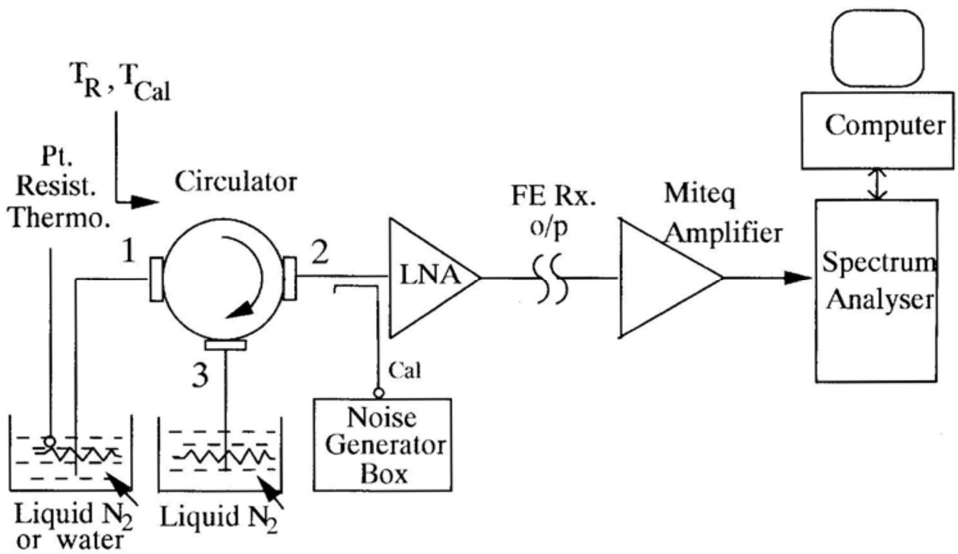

Figure 8. The experimental setup for the measurement of receiver temperature T_R and cal temperature T_{cal}.

continues through to the rest of the receiver and acquisition system. The termination at port 3 is kept immersed in liquid nitrogen, while the termination at port 1 is separately immersed in liquid nitrogen and then ambient temperature water for the process of calibration. The calibrated platinum resistance thermometer is used to measure the temperature of the 50 Ω load at port 1. The calibration signal (T_{cal}) is injected in alternate seconds of time as would be done during the sky temperature measurement.

The measured uncalibrated noise powers P_{on} and P_{off} , corresponding to the states when the CAL is ON and OFF, are used to compute *y-f*actors: $(P_{on} - P_{off})/P_{off}$. The *y*-factors x and y corresponding to the measurements with the port 1 load at ambient temperature T_{amb} and at liquid nitrogen temperature T_{N2} are used to estimate the LNA noise temperature

$$T_R = \frac{(xT_{amb} - yT_{N2})}{(y - x)} \tag{6}$$

and the CAL noise temperature

$$T_{cal} = x(T_R + T_{amb}). \tag{7}$$

The l-σ errors in the T_R and T_{cal} estimates owing to measurement noise (corresponding to the finite bandwidth and averaging time of the measurement) are 0.38 K and 0.20 K respectively. The errors due to the uncertainty in the temperatures of the liquid nitrogen and ambient temperature water baths are 0.34 K for T_R and 0.08 K for T_{cal}. The measured values of T_R and T_{cal} are

$$T_R = 52.12 \pm 0.51 \text{ K and} \tag{8}$$
$$T_{cal} = 70.166 \pm 0.215 \text{ K}, \tag{9}$$

where the uncertainties quoted represent the net l-σ errors.

8. The measurement of the reflection coefficient Γ

Due to the impedance mismatch between the feed assembly and the sky, part of the incident sky power is reflected back to the sky. The fractional power reflected is characterized by the voltage reflection coefficient (Γ) of the feed assembly. Because the feed system is passive and hence reciprocal, the system may be operated as a radiator in order to measure the reflection coefficient. The setup (Fig. 9) consists of a scalar network analyser connected to the V-channel of the feed assembly; the H-port of the OMT is terminated at a 50 Ω load for this measurement. The instrument injects power into the OMT port and measures the return loss: the fraction that returns as a reflected power.

The reflection coefficient of the feed assembly, as computed from the return loss measurement, is

$$\Gamma = 0.1265 \pm 0.01. \tag{10}$$

The uncertainty in this estimate has been assumed to be the measurement accuracy of the scalar network analyser.

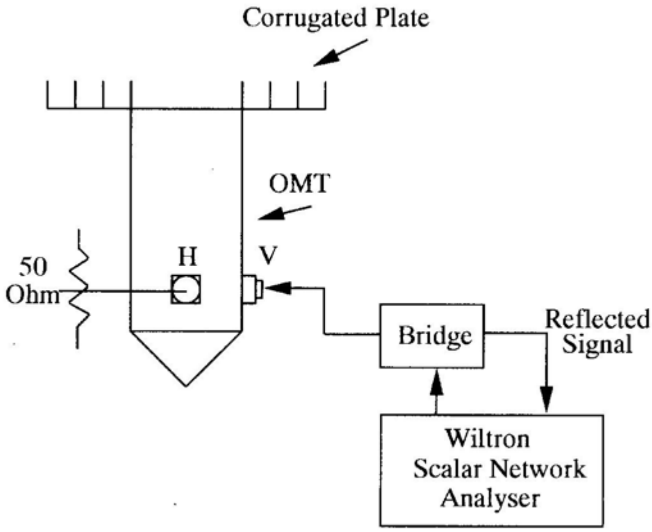

Figure 9. The experimental setup for the measurement of the reflection co-efficient of the feed assembly.

9. The measurement of the absorption coefficient α

The absorption coefficient α includes contributions from the OMT and the phase-compensation cable (and the associated connector). For reasons stated above, it has been assumed that the ohmic loss in the corrugated plate is negligible.

Advantage is taken of the cylindrical shape of the OMT: α for a single OMT along with its phase compensation cable is determined by combining an identical pair back-to-back and measuring the ohmic loss in the combined system. The apertures of the two OMTs are bolted together, the H-channel ports are terminated in 50 Ω loads and the V-channel ports are connected to identical-length phase-compensation cables. The procedure described in section 7 for the measurement of the receiver temperature T_R and the calibration noise temperature T_{cal} is repeated with the back-to-back OMT pair introduced between the port 1 of the circulator and the load termination that is separately placed in liquid nitrogen and ambient water baths. The measurement configuration is shown in Fig. 10.

In this configuration, the measured receiver and calibration noise temperatures are, respectively;

$$T_R{}' = \left[\frac{\alpha_p T_{\text{amb}}}{(1-\alpha_p)(1-\frac{\Gamma_a^2}{4})} + \frac{T_R + T_L}{(1-\alpha_p)(1-\frac{\Gamma_a^2}{4})^2}\right] \tag{11}$$

and

$$T_{\text{cal}}{}' = \left[\frac{T_{\text{cal}}}{(1-\alpha_p)(1-\frac{\Gamma_a^2}{4})^2}\right] \tag{12}$$

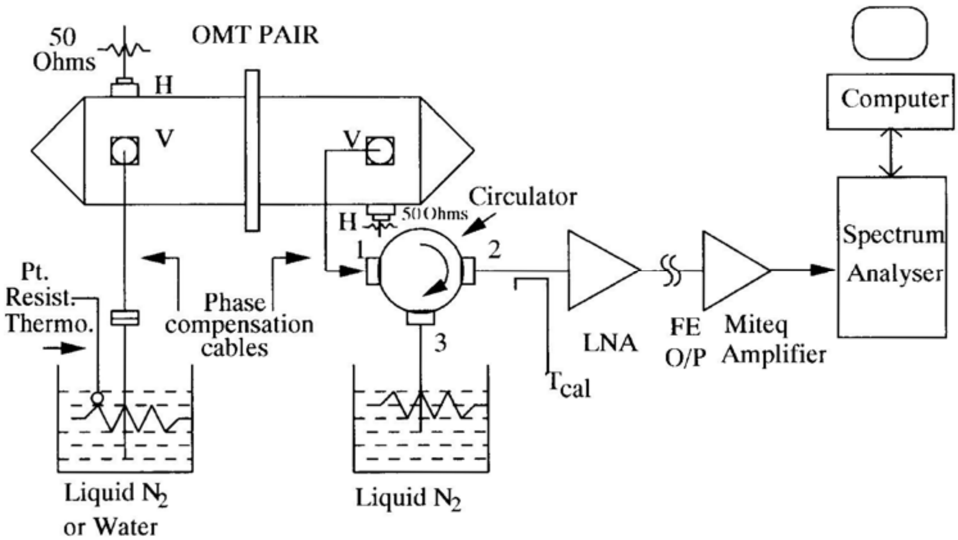

Figure 10. The experimental setup for the measurement of the absorption co-efficient of an OMT pair.

in terms of the T_R and T_{cal} values determined in section 7. In these equations, α_p is the absorption coefficient of the OMT pair along with the two phase compensation cables, Γ_o is the voltage reflection coefficient of the OMT pair and T_L is the small leakage signal at port 2 due to the load at port 3 of the circulator.

From the measurements, we find that the reflection coefficient of each OMT in this configuration is $\Gamma_0/2 = 0.0912$ and the absorption coefficient was determined to be

$$\alpha_p/2 = 0.031059 \pm 0.0016. \tag{13}$$

10. The galactic contribution T_{Gal}

We estimate the galactic contribution to the sky signal from a 408 MHz all sky map (Haslam *et al.* 1982). The sky image is smoothed to the resolution of the feed assembly and the brightness temperature at 1280 MHz is computed assuming a spectral index of –2.7 for the temperature spectrum.

The sky background observations were made at zenith from the radio observatory site at Gauribidanur which is at a latitude of +13°.5. The observations were made at night to avoid the sun. The sky region observed was away from the galactic plane and was at approximately RA:10–12$^{\mathrm{h}}$ and DEC:+13°.5. The value of the sky brightness T_{408} towards this region is 18 ± 2 K in the 408 MHz all sky map. Assuming that the CMB temperature at 408 MHz is 2.7 K, the galactic background temperature at 408 MHz may be 15.3 ± 2K. The galactic contribution at 1280 MHz is estimated to be

$$T_{\mathrm{Gal}} = 0.9 \pm 0.3\mathrm{K}. \tag{14}$$

The sources of uncertainty in this estimate are the uncertainty in the 408-MHz absolute temperature scale and the uncertainty in the spectral index of the galactic background.

11. The atmospheric contribution T_{atm}

A multiple slab model for the atmosphere (developed by J. Cernicharo and M. Bremer at IRAM) has been used to estimate the contribution of the atmosphere to the total system temperature. The model relates the physical parameters of the atmosphere slabs to be consistent with the altitude and latitude of the site and the local temperature, pressure, and zenith column density of water vapour. A prediction is made for the atmospheric emission brightness temperature. The Gauribidanur observatory is at 13°36′ 16" North latitude and at an elevation of 686 m; the ground temperature of the atmosphere was 25°C, pressure 931 mB and the zenith column density of water vapour was ≤ 10 mm during the sky temperature observations. Using the model, the atmospheric contribution T_{atm} at zenith is estimated to be

$$T = 1.55 \pm 0.2 \text{ K}. \tag{15}$$

12. The ground contribution T_{gnd}

The ground contribution is measured by radiating a 1280 MHz signal out through the OMT pointed at zenith (with the shield in place) and measuring the radiated signal with a dipole. This measurement of radiated power towards the ground yields the isolation between the ground and receiver and, invoking reciprocity, it is estimated that less than about 0.1% of the ground noise temperature enters the OMT. To avoid the leakage via gaps between the bottom of the shield and the receiver box, the ground close to the receiver was covered with aluminium sheets (see Fig. 2). With these ground sheets, ground shield and the corrugated plate all in place, and assuming the temperature of the ground to be 30°C, the ground contribution is estimated to be

$$T_{gnd} = 0.3 \pm 0.3\text{K}. \tag{16}$$

13. The measurement of the CMB brightness temperature

The measurement of the sky brightness temperature was done from the Gauribidanur observatory site towards zenith. The observations were made at a time when the galactic plane was far from the primary beam of the 'telescope' and at night to avoid the Sun: the observations were carried out between 10^h and 12^h LST (i.e. 10 pm and 12 pm local time) during which the zenith sky was at RA:10-12^h and DEC: +13°.5.

In Table 1 we have gathered all the calibration measurements from which we have derived the the sky temperature T_α'' to be 6.2 ± 0.68 K. From equation (1), the brightness temperature of the cosmic microwave background T_{CMB} was estimated to be

$$T_{CMB} = 3.5 \pm 0.78\text{K}. \tag{17}$$

14. A comparison with some earlier measurements

Our measurement is consistent, within the errors, with the *COBE-FIRAS* measurement.

Table 1. Values of various noise temperatures measured.

Measurement parameter	Absolute value	Uncertainty in the measurement $\pm$ K
T_R	52.12 K	0.51
T_{cal}	70.166 K	0.215
T_{gal}	0.9 K	0.3
T_{atm}	1.55 K	0.2
T_{gnd}	0.3 K	0.3
αT_{amb}	10.0 K	0.5
Γ	0.13	0.01
T''_a	6.2 K	0.68
T_{cmb}	3.45 K	0.78

Table 2. Some earlier measurements of T_{cmb} at frequencies below 1.5 GHz

Sl. no.	Frequency MHz	$T_{CMB} K$	Authors
1.	408 & 610	3.7 ± 1.2	Howell, T. F. & Shakeshaft, J. R., (1967)
2.	411 & 640	3.0 ± 0.5	Stankevich *et al.* (1970)
3.	600	3.0 ± 1.2	Sironi *et al.* (1990)
4.	1400	2.65 ± 0.3	Staggs *et al.* (1996)
5.	1470	2.26 ± 0.19	Bensadoun *et al.* (1993)

Previous measurements of the absolute temperature of the CMB at frequencies below 1.5 GHz are listed in Table 2. Below our frequency of 1280 MHz, the closest recent measurement is that of Sironi *et al.* (1990) at 600 MHz: their measurement is consistent – within their 1-σ error – with the *COBE-FIRAS* value; however, it may be noted that our measurements have a greater precision. At frequencies above 1280 MHz, the measurement by Staggs *et al* (1996) at 1400 MHz has a precision exceeding our measurement and is also consistent (within the 1-σ errors) with the *COBE-FIRAS* value. Our measurement at 1280 MHz, as well as these measurements at 600 and 1400 MHz, do not indicate any distortions in the CMB spectrum and are consistent with $\mu = 0$.

It may be noted, however, that the measurements of Levin *et al.* (1988) at 1410 MHz and those of Bensadoun *et al.* (1993) at 1470 MHz both imply lower thermodynamic temperatures for the CMB at these frequencies: their measurements of 2.11 ± 0.38 K and 2.27 ± 0.25 K are about 1.6-1.8-σ below the *COBE-FIRAS* value. Our measurement at 1280 MHz is inconsistent with such a low value for T_{CMB} at the 1.6-σ level.

15. Acknowledgements

We thank V. Radhakrishnan, A. A. Deshpande and N. Udaya Shankar for stimulating discussions during the course of this work.

References

Bensadoun, M., Bersanelli, M., De Amici, G., Kogut, A., Levin, S. M., Limon, M., Smoot, G. F., Witebsky, C. 1993, *Astrophys, J.,* **409,** 1.

Burigana, C., Danese, L., De Zotti, G. 1991, *Astr. Astrophys,* **246,** 49.

Daly, R. A. 1991, *Astrophys, J* **371,** 14.

Fixsen, D.J., Cheng E.S., Gales, J.M., Mather, J.C., Shafer, R.A., Wright, E.L. 1996, *Astrophys, J* **486,** 623.

Haslam, C.G.T., Salter, C.J., Stoffel, H., Wilson, W.E. 1982, *Asir. Astrophys Suppl.* No.47.

Howell, T.F., Shakeshaft, J.R. 1967, *Nature,* **216,**

Hu, W., Scott, D., Silk, J. 1994, *Astrophys, J.,* **430,** L5.

Levin, S. M., Witebsky, C., Bensadoun, M., Bersanelli, M., De Amici, G., Kogut, A., Smoot, G. 1988, *Astrophys J.,* **334,** 14.

Silk, J., Stebbins, A., 1983, *Astrophys, J.,* **269,** 1

Sironi, G., Limon, M., Marcellino, G., Bonelli, G., Bersanelli, M., Conti, G., Reif, K. *Astrophys., J.* **357,** 301.

Staggs, S. T., Jarosik, N.C., Wilkinson, D. T., Wollack, E.J. 1996, *Astrophys. J.,* **458,** 407.

Stankevich, K.S., Wielebinski, R., Wilson, W.E. 1970, *Aust. J. Phys.,* **23,** 529.

Swarup, G., Ananthakrishnan, S., Kapahi V. K., Rao, A. P., Subrahmanya, C. R., Kulkarni V. K. 1991, *Curr. Sci.,* **60,** 95.

Swarup, G., Ananthakrishnan, S., Subrahmanya, C.R., Rao, A.P., Kulkarni V.K. Kapahi V.K., 1997, in *High-sensitivity Radio Astronomy.* (eds.) N Jackson., R. J., Davis (Cambridge: Cambridge Univ. press).

J. Astrophys. Astr. (2000) **21,** 19–27

Nature of the Background Ultraviolet Radiation Field at High Redshifts

Archana Samantaray & Pushpa Khare, *Physics Department, Utkal University, Bhubaneswar, 751 004, India.*

Received 1999 September 20; accepted 2000 February 9

Abstract. We have tried to determine the flux of the ultraviolet background radiation field from the column density ratios of various ions in several absorption systems observed in the spectra of QSOs. We find that in most cases the flux is considerably higher than what has been estimated to be contributed by the AGNs. The excess flux could originate locally in hot stars. In a few cases we have been able to show that such galactic flux can only contribute a part of the total required flux. The results suggest that the background gets a significant contribution from an unseen QSO population.

Key words. Quasars: absorption lines—diffuse radiation.

1. Introduction

The shape and the intensity of the intergalactic UV background radiation are crucial factors in determining the ionization balance of the intergalactic medium and therefore influence the structure formation in the universe. Knowledge of this radiation field is thus necessary for the understanding of the early universe. AGNs are believed to be the major contributors to this background, though a significant contribution from star forming galaxies can not be ruled out. Detailed calculations of the propagation of AGN like ionizing radiation through intergalactic space, taking into account the absorption and reradiation by the galactic and intergalactic material, have been carried out by Haardt and Madau (1996, hereafter HM96). They have determined the frequency and redshift dependence of the background. Observationally, the intensity of the radiation has been determined in recent years, by studying the proximity effect in the Lyman alpha forest of the absorption lines in the spectra of QSOs (Bajtlik, Duncan & Ostriker 1988). This analysis is insensitive to the shape of the radiation (Bechtold 1994 and Das & Khare 1997). Values of the intensity of the background at the Lyman limit, J_{VLL}, obtained by Bechtold (1994) and Cooke *et al.* (1996) are considerably higher than the value expected from the distribution of visible QSOs. Several sources of uncertainty in the value of the flux obtained by the proximity effect analysis have been considered by various authors (Bechtold 1994, 1995; Srianand and Khare 1995; Das and Khare 1997). It has also been suggested (Fall & Pei 1993) that the actual number of QSOs may be larger than their observed number and that several QSOs may be rendered invisible due to dust extinction in the intervening absorbers. It is possible that the background radiation gets a significant contribution from star forming galaxies (Madau & Shull 1996; Giroux & Shapiro 1996; Khare &

Ikeuchi 1998). Here we try to obtain an independent estimate of the background flux by studying the ionization state of the QSO absorption systems for which an estimate of the particle density is available from the observations of the fine structure excited lines of C II. Where ever possible, we also try to estimate the contribution of the galactic flux to the total ionizing flux for the systems. In section 2 we present our analysis, the results are discussed in section 3.

2. Data and analysis

Several absorption systems reported in the literature, have the absorption lines of C II, C II*, C IV, H I, Si II, Si IV etc. Particle density in the absorber can be obtained from the column densities of C II and C II*. The column density ratio of C II to C IV is a good indicator of the ionization parameter as it changes rapidly with change in the ionization parameter, $\Gamma = \Phi/c\ n_H$, where Φ is the flux of the ionizing radiation i.e. the number of photons cm $^{-2}$ s^{-1}, n_H is the particle density and c is the velocity of light. This ratio is insensitive to the particle density and the abundance of carbon, but is very sensitive to the neutral hydrogen column density, $N_{H\ I}$, in the absorber, specially for $N_{H\ I} > 10^{17}$ cm^{-2} (Bergeron & Stasinska 1986). This particular column density ratio is also very sensitive to the shape of the ionizing radiation. This is shown in Fig. 1 which shows the ratios for neutral hydrogen column densities of 10^{17}cm^{-2} and 10^{19} cm^{-2} for **(i)** spectral shape as given by HM96 for a redshift of 2.5, **(ii)** galactic spectra as taken from Bruzal (1983) and **(iii)** a combination of both the above with the AGN flux taken to be same as the actual value given by HM96 for z = 2.5. These results have been obtained from the code 'CLOUDY', kindly supplied to us by Prof. Ferland. The galactic spectra produces much smaller values of the ratio compared to the AGN or power law spectra. This is due to the fact that the galactic spectra has a much smaller number of photons having sufficient energy to produce C IV. Thus it is necessary to know the shape of the ionizing radiation to determine the ionization parameter from the C II to C IV ratio. In order to get information about the intensity and the shape of the radiation field we can make use of the column density ratio of other ions. Si II to Si IV ratio is a useful ratio for this purpose. In Fig. 2 we have plotted the ratio of column densities of Si II to Si IV for the three cases listed above. This ratio is not very sensitive to the shape and can be used with the C II to C IV ratio to constrain the shape as well as the intensity of the ionizing radiation. Fe II to Fe III and Al II to Al III ratios can also be used for this purpose. These ratios are also plotted in Fig. 2. We have, therefore, selected from the literature, absorption systems for which the column densities of H I, C II and C II*, or limits on their values, have been determined and for which additional ions like the C IV, Si II, Si IV, Fe II, Fe III etc are also available. The details are given in Table 1.

The fine structure excited level of C II is primarily populated by collisions with electrons for the absorption systems considered here, which are either the Lyman limit or the damped Lyman alpha systems, while the collisions with H I and also the collisional deexcitations by electrons can be ignored (Bahcall & Wolfe 1968; Morris *et al*. 1986). As we are considering the absorption systems at high redshifts, the excitation of the fine-structure level by the absorption of the cosmic microwave background photons may be important. In order to check this we calculated the excitation

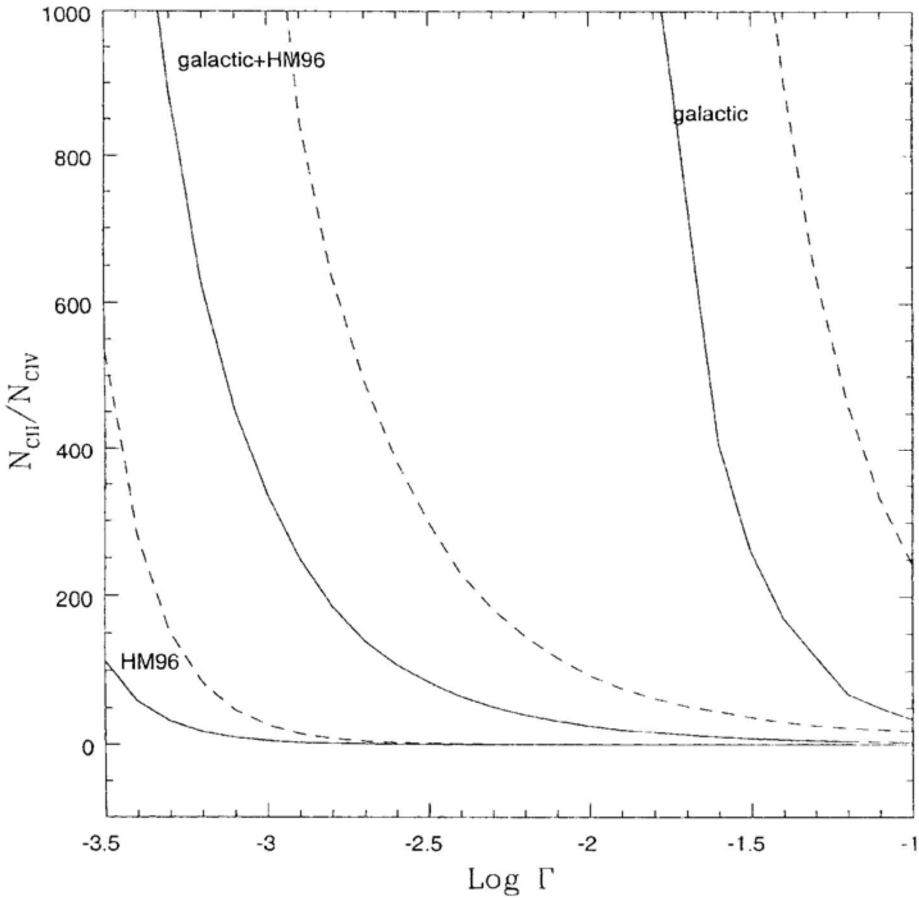

Figure 1. Column density ratios of C II to C IV as a function of the ionization parameter, for different shapes of the background radiation spectrum as explained in the text. The solid lines are for $N_{H\,I} = 10^{17}$ cm^{-2} and dashed lines are for $N_{H\,I} = 10^{19}$ cm^{-2}.

temperatures of C II* from the observed column densities. These are much higher than the corresponding temperatures of the microwave background at the redshifts of the absorbers as can be seen from Table. 2. We have therefore, ignored the excitation by the microwave background photons and have assumed the electron densities (assumed to be equal to the proton density) to be given by $n_e = 21\ [Nc_{\,\mathrm{II}*}/Nc_{\,\mathrm{II}}]$ (Morris *et al.* 1986). The hydrogen density obtained by adding the neutral hydrogen density to the electron density, corrected for the electrons coming from He II and He III, for each system is also given in Table 2. For a few of the systems, only an upper limit on C II*/C II was available. For these systems only an upper limit on the particle density could be obtained. For these systems we have assumed a lower limit on particle density to be 0.045 cm^{-2}, which is smaller than all the lower limits to the particle densities obtained for the systems considered here and is also considerably lower than the mean interstellar particle density. For each absorption system we have constructed a number of photoionization models for the observed neutral hydrogen column density and different spectral shapes. The AGN spectral shape at the redshift of the

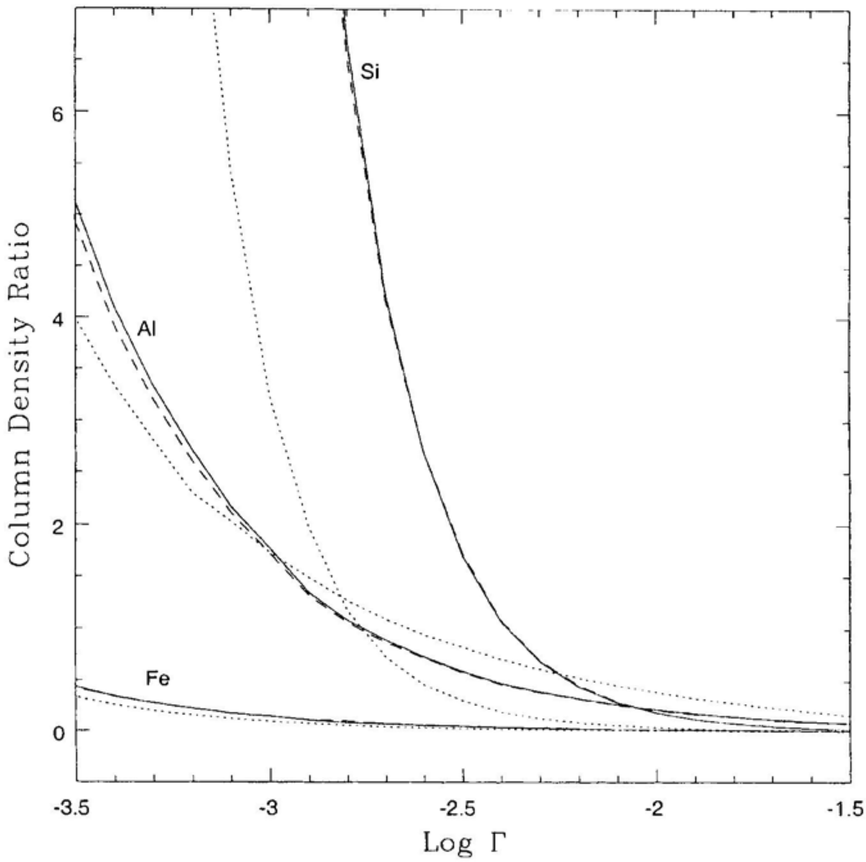

Figure 2. Column density ratios of Si II to Si IV, Al II to Al III and Fe II to Fe III for the three shapes of the background radiation spectrum as explained in the text, for $N_{H\ 1} = 10^{18} cm^{-2}$. Solid, dotted and dashed lines are for galactic spectra, AGN (HM96) spectra and AGN together with the galactic spectra respectively.

Table 1. Observational data for the absorption systems.

QSO	z_{abs}	$N_{HI}\ cm^{-2}$	$\frac{C\ II}{C\ IV}$	$\frac{Si\ II}{Si\ IV}$	$\frac{C\ II^*}{C\ II}$
Q1331 + 170	1.7765	20.92a	—	7.71 – 18	0.035 – 0.060
Q2348 – 14b	2.279	20.56 ± 0.075	—	< 1.458	0.002 – 0.046
PKS 2126 – 158	2.6364	16.401a	0.97 – 2.34	—	0.077 – 0.489
PKS 2126 – 158c	2.6376	17.92a	0.48 – 58.8	> 6.6d	0.005 – 0.20
Q2231 – 00e	2.652	19.12	—	< 1.2	0.002 – 0.003
HS 1946 + 7658	2.8443	20.23 ± 0.41	2.95 – 25.7	0.32 – 7.07	0.012 – 2.570
Q0347 – 38	3.025	20.80 ± 0.1	> 14.79	10.59 – 18.5	0.002 – 0.028
Q2212 – 1626	3.6617	20.20 ± 0.08	> 6.45	1.99 – 2.51	0.002 – 0.046
Q2237 – 0608	4.0803	20.52	> 10.984	6.025 – 7.585	0.003 – 0.002

(a) $N_{H\ I}$ in the components taken to be in the same ratio as $N_{Si\ II}$.
(b) $\frac{Al\ II}{Al\ III}$ is 0.812 ± 0.88 for this system.
(c) $\frac{Al\ II}{Al\ III}$ is 6.918 ± 41.68 for this system.
(d) Taking 3σ upper limit to Si IV for this system.
(e) $\frac{Fe\ II}{Fe\ III}$ is 0.338 ± 0.461 for this system.

Table 2. Results of photoionization models.

z_{abs}	$\frac{T_{ex}}{T_{CMB}}$	n_H cm^{-3}	Φ/Φ_{HM96}	$\Phi^{min}_{HM96}/\Phi_{HM96}$	Φ^a_G	$d(pc)^b$
1.7765	7.0 − 8.1	0.42 − 1.16	49.2 − 215.3	1.0c	15.2 − 69.0	41.7 − 89.0
2.279	3.5 − 6.3	0.045d − 0.82	62.3 − 1411	1.0c	41.0 − 976.2	11 − 43.1
2.6364	6.6 − 15.3	0.07 − 11.66	1.23 − 811	1.0c	>12000	<0.316
2.6376	3.7 − 9.5	0.11 − 6.28	1.88 − 176.1	1.1	1.6 − 236	22.5 − 273.9
2.652	3.3 − 3.3	0.047 − 0.072	4.58 − 10.0	3.8	0.67 − 5.2	151.0 − 423.0
2.8443	4.0 − 881.8	2.59 − 10.36	157.6 − 1997	98.8	194 − 3911	5.5 − 24.8
3.025	2.8 − 4.6	0.045d − 1.31	2.73 − 126.4	1.0c	1.9 − 122.0	31.1 − 110.1
3.6617	2.5 − 4.5	0.045d − 1.23	6.78 − 234.4	1.0c	3.76 − 145.6	25.4 − 120.2
4.0803	2.25 − 2.8	0.045d − 0.28	13.45 − 106.5	1.0c	4.06 − 33.87	59.54 − 108.4

(a) In units of 10^6 cm^{-2} s^{-1}.
(b) Distance from O star.
(c) Φ^{min}_{HM96} is taken to be the actual value of Φ_{HM96} at the redshift of the absorber in absence of necessary column densities.
(d) Lower limit assumed to be 0.045 cm^{-3}.

absorption system is taken from HM96. For some of the systems only the total neutral hydrogen column density is available, while C II* has been observed in some particular velocity component of the absorption line. For such systems we have assumed the neutral hydrogen column density in individual components to be in the same ratio as the Si II column densities, as the ionization potential of Si II is close to that of H I. Details of the models and comparison of their predictions with the observations are discussed below for individual absorption systems. The results are given in Table 2. Note that all the absorption systems are sufficiently far away from the respective QSOs (relative velocity is greater than 15000 km s^{-1}) and can be considered to be intervening (however, see Richards *et al.* 1999) so that the radiation of the parent QSO can be ignored. In the following analysis we have only used the ratios of the column densities of different ions of the same element. Our conclusions are, therefore, independent of the assumed values of chemical abundances.

2.1 *z = 1.7765 system towards Ql331+170*

This QSO has been observed by Kulkarni *et al.* (1996). However, for this system C IV column density has not been reported and so we could not constrain the spectral shape. Errors on column densities have not been reported by the authors and we assumed errors of 25% in the column densities. Neutral hydrogen column density in the component showing C II* has been obtained from the total H I column density (Green *et al.* 1995) by assuming the H I column densities to be in the same ratio as the Si II column densities. Analysis of the Si lines assuming HM96 spectral shape for z = 2 yields $-2.4 > \Gamma > -2.6$ giving $3.2\times10^7 \leq \Phi \leq 1.4 \times 10^8$. This is considerably higher than the value of HM96 flux at the redshift of the absorption system. It is, however, possible that the excess flux comes from the galaxies. We explored this possibility by constructing photoionization models with the shape as well as the intensity of the background as given by HM96 at the redshift of the absorber, the rest coming from the galaxies. For these models the limits become $-2.7 > \Gamma > -2.9$ giving $1.5 \times 10^7 \leq \Phi_G \leq 6.9 \times 10^7$, Φ_G being the galactic flux in cm^{-2} s^{-1}.

2.2 $z = 2.279$ *system towards Q2348–14*

This QSO has been observed by Pettini *et al.* (1994). An upper limit on the column density ratio of Si II to Si IV gives, for HM96 spectral shape for $z = 2.5$, a lower limit of –2.2 for log Γ. However, as only an upper limit on the particle density could be obtained, this can not be converted to a limit on the flux. Assuming the minimum value of the particle density to be 0.045 cm^{-3}, which is smaller than the observed upper limit by 1.2 dex, requires the flux to be larger than 8.5×10^6. The column density ratio of Al II to Al III gives $-1.3 > \log \Gamma > -1.4$, giving $5.3 \times 10^7 < \Phi < 1.2 \times 10^9$. Taking the actual value of the HM96 flux and assuming the rest of the contribution from the galactic sources requires $-1.4 > \log \Gamma > -1.5$, giving the galactic flux to be between 4.1×10^7 and 9.7×10^8.

2.3 $z = 2.638$ *system towards PKS 2126 –158*

This system has been observed by Giallongo *et al.* (1993) and has seven components spread over a velocity width of 270 km s^{-1} . A neutral hydrogen column density for the whole system has been obtained by Young *et al.* (1979) to be 1.1×10^{19} cm^{-2}. We have assumed the neutral hydrogen column density in individual components to be in the same ratio as the Si II column densities. C II* is observed in two of the components. These are considered below.

(i) $z = 2.6376$: We obtain log N_{HI} = 17.92. As Si IV lines are not observed we take a 3σ upper limit on equivalent width, which translates to an upper limit of $10^{13\ 23}$ cm^{-2} on the column density of Si IV, assuming a velocity dispersion parameter of 24.2 km s^{-1}, same as that for C IV. Assuming AGN shape, we get $-3.1 > \log \Gamma > -3.3$, giving $1.6 \times 10^6 \leq \Phi \leq 1.4 \times 10^8$. Taking the AGN flux to be that given by HM96 for $z = 2.5$, and additional flux from the galaxies, the observed column density ratios can not be explained and a minimum flux of 9.4×10^5 from the AGN is required, needing a total of $-2.9 > \log \Gamma > -3.1$, giving $1.6 \times 10^6 \leq \Phi_G \leq 2.3 \times 10^8$. Note that the Al II to Al IΠ ratio can not, however be explained by the same range of Γ for any shape and requires log $\Gamma \leq -3.3$.

(ii) $z = 2.6364$. We obtain log N_{HI} = 16.4. As Si II and Si IV lines have not been detected for this system, we could not obtain any constraints on the relative contribution from galaxy to the radiation flux. Taking all of the radiation to be AGN type, we obtained limits on the ionization parameter to be $-2.7 \geq \log \Gamma \geq -3.3$ so that the flux lies between 1.05×10^6 and 6.97×10^8. Taking the actual value of the AGN flux (HM96 value at $z = 2.5$), the rest coming from galaxy, requires $\log \Gamma \geq -1.0$, giving $\Phi_G \geq 1.2 \times 10^{10}$.

2.4 $z = 2.6522$ *system towards Q2231–00*

This Lyman limit system has been analysed in detail by Prochaska (1999). We have reanalysed this system taking the shape of the background to be that given by HM96 for $z = 2.5$. We determined the column density ratios for various ions for log N_{HI} of 19.12. The Fe II to Fe III and Si II to Si IV column density ratios constrain the ionization parameter to between –2.4 to –2.55 resulting in a background flux between 3.9×10^6 and 8.5×10^6. This is considerably higher than the value of 8.59×10^5 for HM96 for $z = 2.5$. Models with the shape as well as the intensity of the background as given by HM96 for $z = 2.5$, the rest of the flux coming from galaxy fail to yield a result as the column density ratios of Si and Fe can not simultaneously be produced by a single value (range) of ionization parameter. By gradually increasing the value of the flux contributed by the AGN background above the HM96 value, we find that a minimum AGN flux of 3.3×10^6 was needed to explain the ion ratios, for which we get $-2.4 > \log \Gamma > -2.6$, requiring Φ_G to be between 6.7×10^5 and 5.2×10^6. Thus the minimum of AGN type flux required is more than a factor of 3.8 larger than that obtained by HM96.

2.5 $z = 2.844$ *system towards HS1946+7658*

This system has been observed and analysed by Fan & Tytler (1994). Cloudy models with HM96 spectral shape at $z = 3$ give $-2.3 > \log \Gamma > -2.8$, giving $10^8 \leq \Phi \leq 10^9$. A minimum flux of 8.4×10^7 of the HM96 type is needed, with $-1.9 \geq \log \Gamma \geq -2.6$, giving $1.9 \times 10^8 \leq \Phi_G \leq 3.9 \times 10^9$. Thus almost all of the flux is being contributed by galaxy. Note that the flux for $z = 3$ of HM96 is 7.8×10^5.

2.6 $z = 3.025$ *system towards Q0347–38*

This QSO has been observed by Prochaska & Wolfe (1999). Only a lower limit is available for the C II to C IV ratio, so that the galactic fraction of the flux could not be constrained. AGN shape for $z = 3.0$ for the radiation gives $-2.6 > \log \Gamma > -2.8$, giving $2.1 \times 10^6 \leq \Phi \leq 9.8 \times 10^7$, for the assumed minimum value of the particle density. Taking the actual value of the HM96 flux for $z = 3$ and assuming the rest of the contribution from the galactic sources requires $-2.5 \geq \log \Gamma \geq -2.7$, giving $1.9 \times 10^6 \leq \Phi_G \leq 1.2 \times 10^8$, for the assumed minimum value of n_H.

2.7 $z = 3.6617$ *system towards Q2212–1626*

This QSO has been observed by Lu *et al.* (1996). Only a lower limit is available for the C II to C IV ratio, so that the galactic fraction of the flux could not be constrained. AGN shape for $z = 3.5$ for the radiation gives $-2.5 > \log \Gamma > -2.6$, giving $3.4 \times 10^6 \leq \Phi \leq 1.1 \times 10^8$, for the assumed minimum value of n_H. Taking the actual value of the HM96 flux at $z = 3.5$ and assuming the rest of the contribution from the galactic sources requires $-2.4 > \log \Gamma > -2.5$, giving $3.8 \times 10^6 \leq \Phi_G \leq 1.4 \times 10^8$, for the assumed minimum value of n_H. Note that the value of flux for HM96 for $z = 3.5$ is 5.0×10^5.

2.8 $z = 4.0803$ *system towards Q2237–0608*

This QSO has been observed by Lu *et al.* (1996). Only a lower limit is available for the C II to C IV ratio, so that the galactic fraction of the flux could not be constrained.

AGN shape for $z = 4$ for the radiation gives $-2.6 > \log \Gamma > -2.7$, giving $2.6 \times 10^6 \leq \Phi \leq 2.1 \times 10^7$ for the assumed minimum value of n_{H}. Taking the actual value of the HM96 flux at $z = 4$ and assuming the rest of the contribution from the galactic sources requires $-2.4 \geq \log \Gamma > -2.5$, giving $4.0 \times 10^6 \leq \Phi_{\mathrm{G}} \leq 3.3 \times 10^7$, for the assumed minimum value of n_{H}. .Note that the value of flux for HM96 for $z = 4$ is 2×10^5.

3. Discussion

For five of the systems we could derive the range of flux values assuming the radiation to be the AGN type. All of these are higher than the corresponding HM96 values by minimum factors ranging from 1.2 to 158. Note that we have taken into account the uncertainties in the column densities of all the ions which is the reason for obtaining large ranges for the flux values. For three of these systems we could obtain a minimum value for the flux of the AGN background. These values are 1.1, 3.8 and 98.8 times higher than the HM96 values at the appropriate redshifts. For these systems a large flux is needed from galaxies. For four other systems a lower limit to the flux could only be obtained with an assumption of the lower limit on the particle density to be 0.045 cm^{-3}, which is about half of the mean interstellar value of the particle density and which indicates that the actual C II column densities are higher than the observed lower limits by 0.64 to 1.37 dex. This is a reasonable lower limit as the systems being considered are Lyman limit or damped Lyman alpha systems and also as this value is considerably lower than the range of density values for systems for which the values could be obtained from the observations. For these systems, the required values of flux are higher than the HM96 values by minimum factors of 2.7 to 62. On the other hand, assuming the AGN flux to be that given by HM96, and assuming the rest of the required flux to be of local, galactic origin, very high galactic flux is required. For most of the systems, this high flux requires the absorption systems to be present within 100 parsecs of typical O stars. The typical radius of the Stromgren spheres of these stars is of the same order, indicating that the absorption systems are inside the H II regions. Such conclusions have earlier been rejected on the basis of statistical arguments about the properties of the absorption systems (Srianand & Khare 1994). The flux could come from QSOs which happen to lie close to the lines of sight at redshifts similar to the redshifts of the absorption systems. We have searched the catalogues for presence of any such QSOs near the line of sight to Q2231–00. However, no QSO is found to lie closer than 1000 Mpc to the line of sight within the required redshift range. The high values of the flux indicated by our analysis for almost all the systems, may be interpreted to indicate the presence of an unseen population of dust extinct QSOs.

Note that in all our analysis we have assumed that all the ions producing absorption in a given velocity range in an absorption system are physically located in the same region (cloud). This may not be always valid. Kirkman & Tytler (1999) and Churchill & Charlton (1999) have found evidence for ions with the same velocity structure in their absorption lines belonging to a given redshift system, arising in physically different gaseous components. If C IV ions are from a more widely distributed component, then, the C II/C IV column density ratio in the region of interest will be smaller and may require lower values of the flux.

Acknowledgement

This work was partially supported by a grant (No. SP/S2/013/93) by the Department of Science and Technology, Government of India. A. S. is supported by a C.S.I.R. fellowship.

References

Bahcall, J. N., Wolf, R. A. 1968, *Astrophys. J.,* **152,** 701.

Bajtlik, S., Duncan, R. C, Ostriker, J. P. 1988, *Astrophys. J.,* **327,** 570.

Bechtold, J. 1994, *Astrophys. J. SuppL,* **91,** 1.

Bechtold, J. 1995 in *QSO absorption lines* (ed) G. Meylan (Springer), p. 253.

Bergeron, J., Stasinska, G. 1986, *Astr. Astrophys.,* **169,** 1.

Bruzal, G. 1983, *Astrophys. J. Suppl,* **53,** 497.

Churchill, C. W., Charlton, J. C. 1999, *Astr. J.,* **118,** 59.

Cooke, A. J., Espey, B., Carswell, R. F. 1996, *Mon. Not. R. astr. Soc,* **284,** 552.

Das, S., Khare, P. 1997, *J. Astr. Astrophys.,* **18,** 133.

Fall, S. M., Pei, Y. C. 1993, *Astrophys. J.,* **402,** 479.

Fan, F. X., Tytler, D. 1994, *Astrophys. J. Suppl,* **94,** 17.

Giroux, M. L., Shapiro, P. R. 1996, *Astrophys. J. Suppl.,* **102,** 191.

Giallongo, E., Cristiani, S., Fontana, A., Travese, D. 1993, *Astrophys. J.,* **416,** 137.

Green, R. F., York, D. G., Huang, K., Bechtold, J., Welty, D., Carlson, M., Khare, P., Kulkarni, V. 1995, in *QSO absorption lines,* (ed) G. Meylan (Springer), p. 85.

Haardt, F., Madau, P. 1996, **461,** 20.

Khare, P., Ikeuchi, S. 1998, *PASJ,* **50,** 13.

Kirkman, D., Tytler, D. 1999, *Astrophys. J.,* **512,** L5.

Kulkarni, V. P., Huang, K., Green, R. F., Bechtold, J., Welty, D. E., York, D. G. 1996, *Mon. Not. R. astr. Soc,* **279,** 297.

Lu, L., Sargent, W. L. W., Barlow, T. A., Churchill, C. W., Vogt, S. S. 1996, *Astrophys. J. Suppl,* **107,** 475.

Madau, P., Shull, J. M. 1996, *Astrophys. J.,* **457,** 551.

Morris, S. L., Weymann, R. J., Foltz, C. B., Turnshek, D. A., Shectrnan, S., Price, S., Bonson, J. A. 1986, *Astrophys. J.,* **310,** 40.

Pettini, M., Smith, L. J., Hunstead, R. W., King, D. L. 1994, *Astrophys. J.,* **426,** 79.

Prochaska, J. X. 1999, *Astrophys. J.,* **511,** L71.

Prochaska, J. X., Wolfe, A. M. 1999, *Astrophys. J. Suppl,* **121,** 369.

Richards, G. T., York, D. G., Yanny, B., Kollgaard, R. I., Laurent-Muehleisen Vanden Berk D. E. 1999, *Astrophys. J.,* **513,** 576.

Srianand, R., Khare, P. 1994, *Mon. Not. R. astr. Soc,* **271,** 81.

Srianand, R., Khare, P. 1995, *Astrophys. J.,* **444,** 643.

Young, P. J., Sargent, W. L. W, Boksenberg, A., Carswell, R. F., Whelan, J. A. 1979, *Astrophys. J.,* **229,** 891.

J. Astrophys. Astr. (2000) **21**, 29–38

X-ray Observation of XTE J2012+381 during the 1998 Outburst

S. Naik[1], P. C. Agrawal[1], B. Paul[1,2], A. R. Rao[1], S. Seetha[3] & K. Kasturirangan[3]

[1]*Tata Institute of Fundamental Research, Homi Bhabha Road, Mumbai, 400005, India.*
[2]*Present Address: Institute of Space and Astronautical Science, 3-1-1 Yoshinodai, Sagamihara, Kanagawa 229-8510, Japan.*
[3]*ISRO Satellite Center, Airport Road, Vimanapura P.O., Bangalore 560017, India.*

Received 1999 October 22; accepted 2000 February 9

Abstract. The outburst of X-ray transient source XTE J2012+381 was detected by the RXTE All-Sky Monitor on 1998 May 24th. Following the outburst, X-ray observations of the source were made in the 2–18 keV energy band with the Pointed Proportional Counters of the Indian X-ray Astronomy Experiment (IXAE) on-board the Indian satellite IRS-P3 during 1998 June 2nd–10th. The X-ray flux of the source in the main outburst decreased exponentially during the period of observation. No large amplitude short-term variability in the intensity is detected from the source. The power density spectrum obtained from the timing analysis of the data shows no indication of any quasi-periodic oscillations in 0.002–0.5 Hz band. The hardness ratio i.e. the ratio of counts in 6–18 keV to 2–6 keV band, indicates that the X-ray spectrum is soft with spectral index >2. From the similarities of the X-ray properties with those of other black hole transients, we conclude that the X-ray transient XTE J2012+381 is likely to be a black hole.

Key words. Accretion, accretion disks—black hole physics—Xrays: stars—stars: individual—XTE J2012+381.

1. Introduction

The soft X-ray transients (SXT) are low-mass X-ray binaries, where the accretion of matter takes place from the Roche lobe filling companion onto a stellar mass black hole or neutron star. The source remains in a quiescent state for a long period as the mass accretion rate is low. Outburst occurs when the mass accretion rate reaches a limit to create instability in the accretion disk, resulting in increase in luminosity of the source by many orders of magnitude in a few days. At the peak of the outburst, the X-ray luminosity of the transient sources increases from 10^{33} erg s^{-1} to $10^{38} - 10^{39}$ erg s^{-1} (Tanaka & Lewin 1995). The luminosity of the source declines roughly either exponentially or linearly after the outburst. Some of the soft X-ray transients show secondary outbursts during the declining phase. During the secondary outburst, the luminosity increases sharply by a factor of up to 3, followed by an exponential or linear decay (Ertan & Alpar 1998). The soft X-ray transients (SXT) possess the characteristics of fast rise in flux in a few days and a slow decay with time scale of the order of one month. Some of the SXTs are recurrent with time scale of a few tens of years.

The X-ray transient source XTE J2012+381 was discovered by Remillard *et al.* (1998) from the observations with RXTE All Sky Monitor (ASM) on 1998 May 24th. The X-ray flux of the source was 23 mCrab in 2–12 keV energy band when detected and increased to 88 mCrab on 1998 May 27.3 (Remillard *et al.* 1998). The source spectrum became softer as the brightness increased. Following its discovery, the transient XTE J2012+381 was observed with ASCA X-ray observatory from May 29.30 UT to 30.19 UT (White *et al.* 1998). The position of the source was found to be RA(2000) = $20^h\ 12^m\ 39.1^s$ and Dec(2000) = 38° 10' 50" with an accuracy of 0.5'. Hjellming, Rupen & Mioduszewski (1998) observed the radio counterpart of the source with VLA with flux densities of 2 and 1.5 mJy at 1.4 and 4.9 GHz respectively on 1998 May 31.25 (Hjellming *et al.* 1998). The radio source was well inside the error region for the RXTE ASM position. The variability of the radio source at 15 GHz was reported by Pooley & Mullard (1998) with Ryle Telescope observation. From the optical and infrared observations, Hynes *et al.* (1999) identified the optical counterpart of the source XTE J2012+381 to be a faint red star which coincides with the radio counterpart and emits weak Halpha line.

Following the discovery of the source by RXTE ASM, X-ray observations were made with Pointed Proportional Counters (PPCs) of the Indian X-ray Astronomy Experiment (IXAE) during 1998 June 2nd–10th. The X-ray light curves of the source do not show any large amplitude variability on short time scales. The power density spectrum obtained from the timing analysis of the data does not show any indication of quasi-periodic oscillation in the source in the frequency range of 0.002 to 0.5 Hz. The results of the analysis are described in this paper.

2. Instrument and observations

The observations of the soft X-ray transient XTE J2012+381 were made using Pointed Proportional Counters (PPCs) on IXAE. The IXAE includes three identical, co-aligned, multi-wire, multi-layer PPCs with effective collecting area of 1200 cm^2. A gas mixture of 90% argon and 10% methane at a pressure of 800 torr is used as filling gas. A honeycomb type of collimator is used in each PPC which restricts the field of view to 2°.3 × 2°.3. All the three detectors operate in the energy range of 2–18 keV with an energy resolution of 22% at 6 keV. The gain stability of the detectors is monitored by the irradiation of X-rays from a radioactive Cd^{109} source to the Veto cells. The event processing time for the detectors is about 50 μs in the processing electronics. For a detailed description of the PPCs, refer to Agrawal (1998) and Rao *et al.* (1998).

The IRS–P3 satellite launched on 1996 March 21st, from India, is in a circular orbit at an altitude of 830 km and inclination angle of 98°. Pointing of the detectors towards any given source is done by inertial pointing using a star tracker with an accuracy of about ≤ 0°.l. The useful observation period is limited to the latitude range from –30° S to +50° N as the high inclination and high altitude region is very background prone. The large extent of the South Atlantic Anomaly (SAA) region restricts the observation to about 5 of the 14 orbits per day. In the non-operating regions, the high voltage to the detectors is reduced and data acquisition is stopped.

Table 1. X-ray observations of XTE J2012+381 with the IXAE for 1 sec time resolution mode.

Observation day, 1998 June	M.J.D.	From (UT)	To (UT)	Counts per sec
02	50966	11:03:00	11:17:00	284
		12:38:00	12:57:00	311
		14:20:00	14:36:00	310
		16:03:00	16:20:00	290
04	50968	15:17:00	15:37:00	271
05	50969	11:32:00	11:58:00	161
		13:14:00	13:38:00	208
		14:56:00	15:19:00	192
		16:38:00	16:58:00	180
		18:19:00	18:40:00	220
06	50970	11:13:00	11:33:00	166
		12:53:00	13:15:00	171
		14:35:00	14:55:40	170
		16:16:00	16:37:52	163
		17:58:00	18:19:40	169
07	50971	12:31:00	12:53:00	173
		14:13:00	14:35:00	175
		15:55:00	16:15:00	166
		17:36:00	17:57:00	180
08	50972	12:10:00	12:32:00	165
		13:53:00	14:13:00	150
		15:34:00	15:54:00	167
09	50973	11:49:00	12:11:00	155
		13:32:00	13:52:00	175
		15:13:00	15:33:00	155
10	50974	11:28:00	11:50:00	141
		13:11:00	13:31:00	146

The soft X-ray transient XTE J2012+381 was observed by IXAE from 1998 June 2nd-10th with 1 second integration time. The log of observation is given in Table 1 with background subtracted summed count rate for the three PPCs. The total useful period of observation of the X-ray source is about 37,100 seconds.

3. Analysis and results

3.1 *The X-ray light curve*

The light curve of the source XTE J2012+381 with average count rates per orbit, for the total period of observation by the PPCs is shown in Fig. 1. The inset in Fig. 1 represents the ASM light curve for the source with one day average data for the total outburst period. The IXAE observations, made just after the peak of the outburst, are marked by two vertical lines in the inset. The intensity of the source was maximum on 1998 May 31st with about 16 ASM counts s^{-1} (Crab = 74 ASM counts s^{-1}). The flux of the source again increased to a maximum of about 12 ASM counts s^{-1} after 24 days of the first peak, followed by a linear decay.

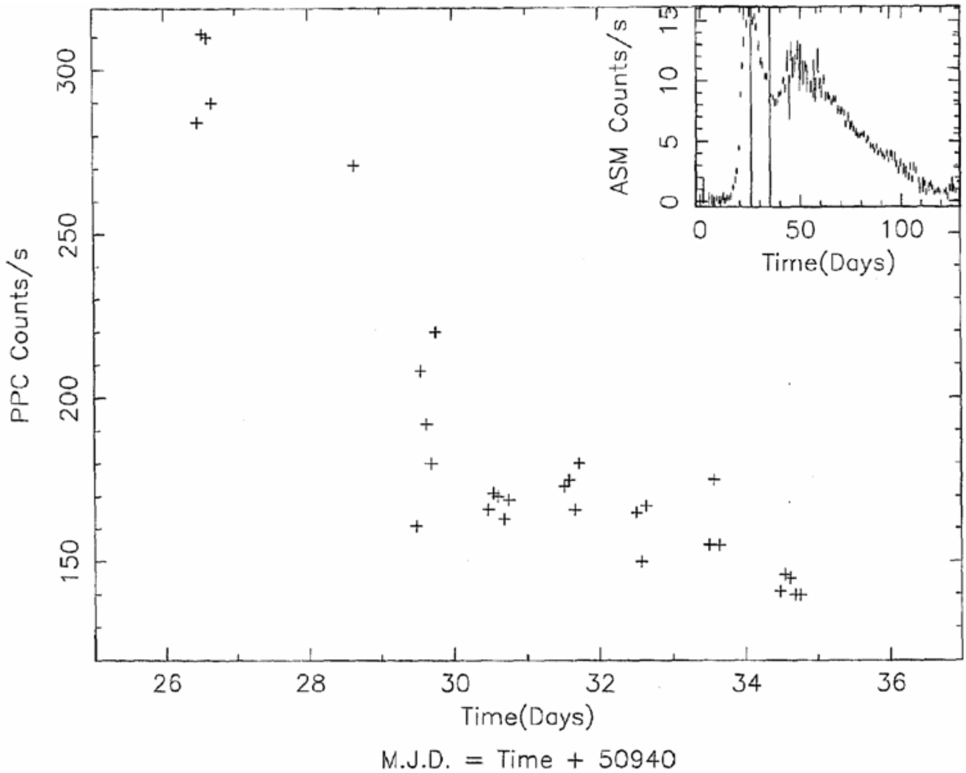

Figure 1. The count rate for XTE J2012+381 obtained from PPC observations. ASM light curve for 1-day average data is shown in the inset. The region between two vertical lines is the period of observation of the source with the PPCs.

The X-ray data for 2–18 keV and 2–6 keV energy bands are corrected for background and offset pointing. Dead time correction, which is less than 1% even at the maximum count rate of about 110 counts s^{-1} per PPC, has been neglected. The light curves were generated using the corrected data for the two different energy bands. The light curve for one of the observations on 1998 June 2nd for 1 s integration time is shown in Fig. 2. A constant intensity fit to the data gives an average count rate of 323 with reduced χ^2 of 1.4 for 498 degrees of freedom. From the light curve of Fig. 2, there is no indication of any large amplitude rapid variability or flaring of the kind seen in Cyg X–1 and some other black hole binaries. However there may be low amplitude variations which results in the large value of the reduced χ^2. Bining the same data in 5 s time bins yields a reduced χ^2 of 1.67 for 99 dof consistent with the presence of low amplitude intensity variations.

The hardness ratio i.e. the 6–18 keV counts divided by 2–6 keV counts, was computed for all the observations. A typical plot of hardness ratio for one of the observations on 1998 June 2nd is shown in Fig. 3. The ratio is found to be about 0.76 ± 0.01 with reduced χ^2 of 0.8 (260 degrees of freedom). There is no significant change in the hardness ratio during any individual observations. The hardness ratio of $0.76 + 0.01$ indicates that the X-ray flux, emitted by the source, is soft. The corresponding hardness ratio for Crab from the PPC observations is 0.85 (Mukerjee 1999), hence we conclude that the X-ray spectrum of XTE J2012+381, if represented as a

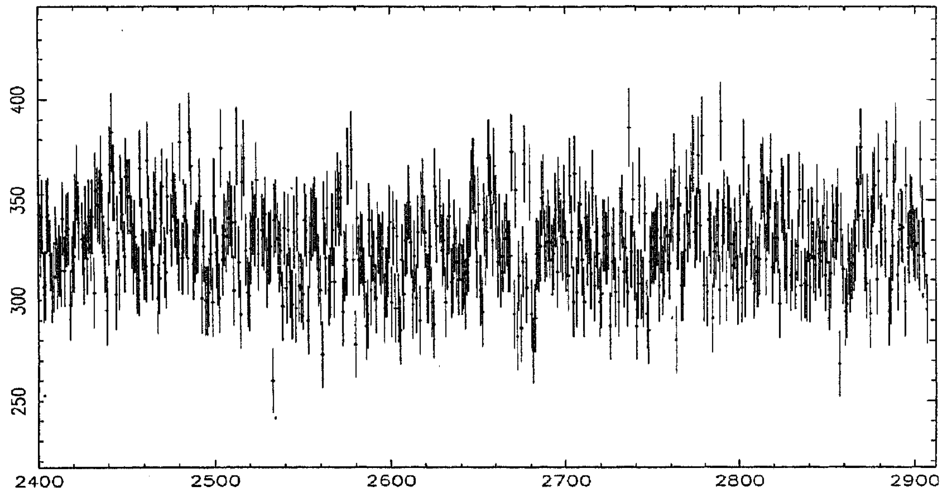

Figure 2. The light curve obtained from one of the observations of XTE J2012+381 on 1998 June 2nd for 1 s time resolution mode for all the PPCs.

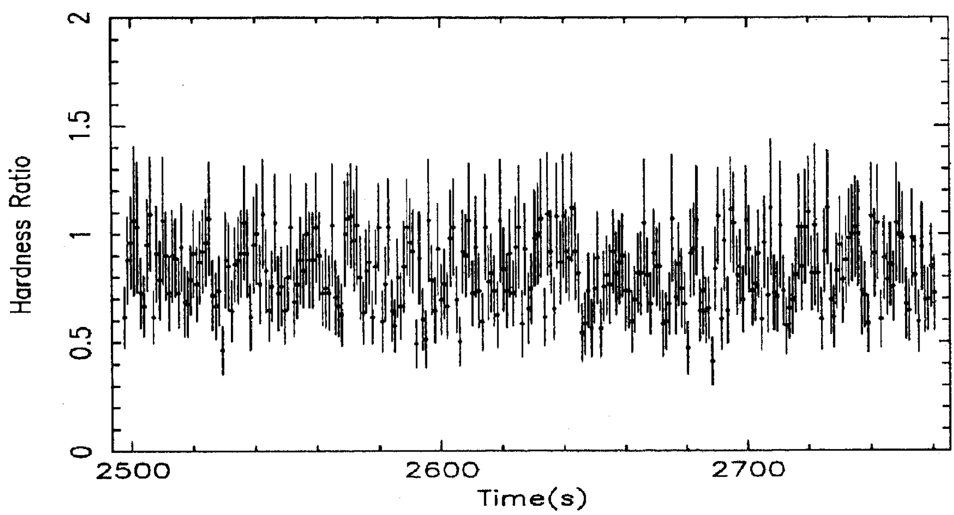

Figure 3. The hardness ratio i.e. count rate in 6–18 keV band divided by that in 2–6 keV interval, for one of the observations on 1998 June 2nd for XTE J2012+381.

power law, should have a photon index of > 2. This suggests that XTE J2012+381 is most likely to be a soft X-ray transient.

3.2 *The power density spectrum*

To study the timing behaviour of XTE J2012+381, power density spectra were generated by taking the Fourier transform of 1 s time resolution data. The light curves for 2–18 keV and 2–6 keV energy bands, generated from the data corrected for

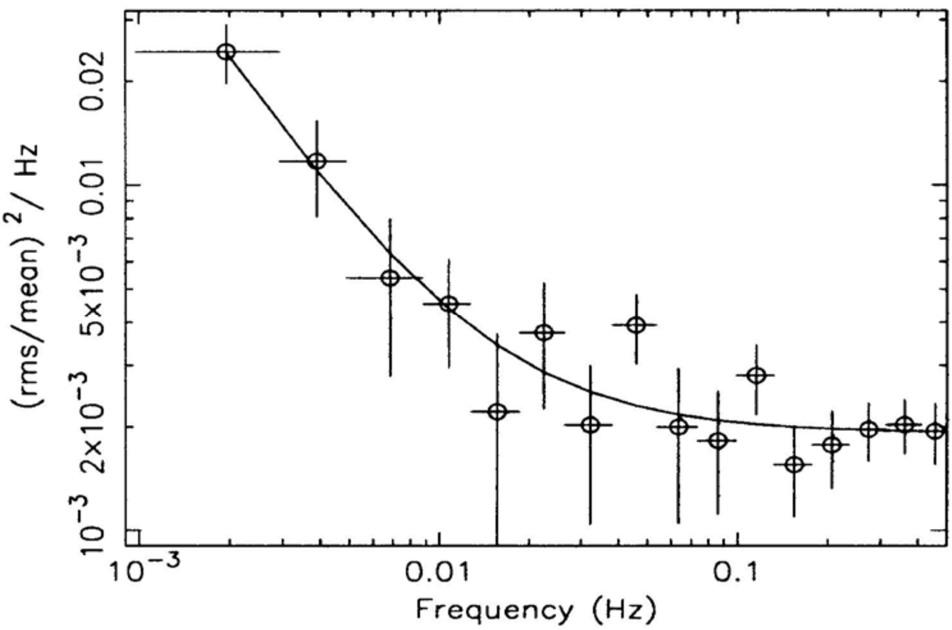

Figure 4. The co-added power density spectrum for XTE J2012+381 for the observations from 1998 June 2nd to 1998 June 10th in 2–18 keV energy band and 1 sec time resolution mode.

background and vignetting, were broken into segments of 512 seconds. The power density spectrum (PDS) was obtained for each data segment and then co-added to get the final PDS. The PDS are normalised to squared fractional rms per hertz. XRONOS software package is used for the data analysis.

Figure 4 shows the added PDS for all the observations for 1 s time resolution for 2–18 keV energy range. From the figure, it is clear that there is no indication of any QPO feature in the frequency range of 0.002 Hz to 0.5 Hz. The PDS is fitted well by a power law from 0.002 Hz to 0.02 Hz with index –1.29 and a constant in the higher frequency range with reduced χ^2 of 0.58 for 13 degrees of freedom. The rms variation of the PDS is calculated to be 2%. In the PDS, the power law represents the low-frequency noise component. The variation in the hardness ratio and percentage of rms variation for each day average data is shown in Fig. 5. The average count rate is found to be correlated with the hardness ratio of the source with a linear-correlation coefficient of 0.7 (7 degrees of freedom) corresponding to 95% of significance level. There is indication of a weak correlation between count rate and rms variation of power and hardness ratio and rms variation as indicated by correlation coefficients of 0.514 and 0.51 respectively.

4. Discussion

Many of the SXTs which contain a black hole as the compact object, show secondary outbursts. The decay time and the time scale of occurrence of the secondary maximum (t_s) in the various black hole X-ray transients are summarised in Table 2. The outburst profiles are classified as fast rise and slow decay (frsd), irregular (irr)

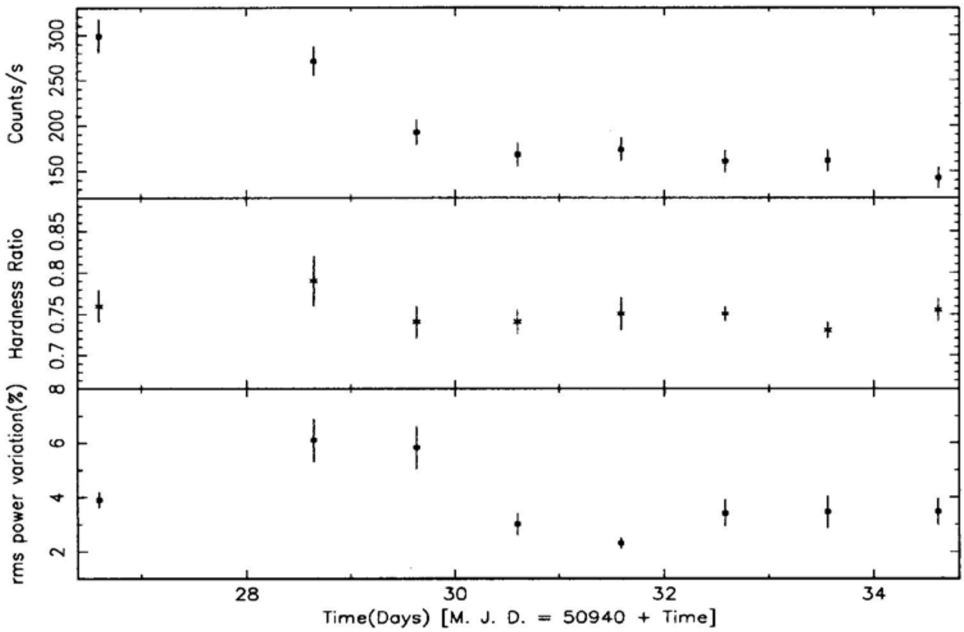

Figure 5. The observed PPC count rates for the source XTE J2012+381 averaged over one day are shown along with the corresponding variation in hardness ratio and rms variation(%) in the PDS.

Table 2. Summary of the outburst characteristics of black hole X-ray transient sources.

Source name	Overall light curve profile	t_s (days)	Decay time of primary outburst(days)	Reference
GRO J0422+32	frsd	38	40.1	Shahbaz *et al.* (1998)
A0620−00	frsd	54	26.3	Shahbaz *et al.* (1998)
GS/GRS1124−68	frsd	80	–	Ertan *et al.* (1998)
4U 1543−47	frsd	15	42.7	Shahbaz *et al.* (1998)
X1630−472	irr	–	–	Remillard (1998)
GRO J1655−40	irr	40	30.0	Remillard (1998)
GRS 1737−310	qp	–	–	Remillard (1998)
GRS 1739−278	frsd	83	34.0	Remillard (1998)
XTE J1739−302	qp	–	–	Remillard (1998)
XTE J1748−288	frsd	–	15.0	Revnivtsev *et al.* (1999)
XTE J1755−324	fsrd	–	30.2	Remillard (1998)
XTE J1856+053	fsrd	–	40.2	Remillard (1998)
GRS 1915+105	irr	–	–	Remillard (1998)
GS 2000+25	frsd	75	30.1	Shahbaz *et al.* (1998)
XTE J2012+381	fsrd	24	16.2 & 36.0	Present work
GS 2023+338	frsd	–	30–40	Zycki *et al.* (1999)

Note: frsd = fast rise and slow decay, **irr** = irregular, **qp** = quasi persistence, t_s = time of occurrence of secondary maximum from the maximum of the primary outburst.

and quasi persistent (qp) as given by Remillard (1998). For XTE J2012+381, we have determined the decay times of both the primary and the secondary outbursts by fitting an exponential to the decay profile obtained from the XTE ASM data and these values are given in the table. We have also determined the decay time for the primary outburst from the PPC data as 18.1 days using exponential fit which agrees with the value of 16.2 days obtained from the ASM light curve.

The soft X-ray transients A0620–00, GS 2000+25, GS/GRS 1124–68 and GRO J0422+32 (Ertan *et al.* 1998) show many similarities with the SXT J2012+381. The primary outburst profiles for these transients are characterised by a fast rise and slow decay. The typical exponential decay time is around one month. During decline, all the above five transients exhibit secondary outbursts. For GS 2000+25 and GS/GRS 1124–68, the secondary maxima are observed about 80 days after the main outburst while in A0620–00, it is observed 50 days after the main outburst. However for XTE J2012+381, the secondary maximum was observed 24 days after the main outburst.

The power density spectrum of XTE J2012+381 is similar to that of the black hole transient GS 2023+338 (Zycki *et al.* 1999) and XTE J1748–288 (Revnivtsev *et al.* 1999) in the frequency range 0.003 Hz to 0.5 Hz. Though the absolute value of the power for XTE J2012+381 is not exactly the same as that of XTE Jl748–288 in the high state, the fitted power law indices for the PDS are identical. The power law index for XTE J1748–288 in high state varies between 1.0 and 1.5 with 1% of fractional variability in the amplitude (Revnivtsev *et al.* 1999), which is similar to that of XTE J2012+381. There is no indication of large amplitude flux variation in XTE J1748–288 on shorter time scales ($\leq$ 5s) like the one found in Cyg X–l or GX 339–4. Though the QPOs are absent in XTE J2012+381, its PDS is similar to that of XTE J1748–288 in the high state of the 1998 outburst. Considering these similarities and the soft spectrum of the source, it is likely that the source may be in a high state during our observations. From the similarity of the decay time, the occurrence of the secondary maximum and also the similarity of the PDS with those of GS 2023+338 and XTE J1748–288, it can be infered that the soft Xray transient XTE J2012+381 is most likely a black hole.

The outburst of X-ray transients can be explained by the thermal accretion disk instability model or by instability in the accretion disk created by the enhanced mass transfer from the companion. Chen & Taam (1994) have investigated the time-dependant evolution of the thermal viscous instabilities in geometrically thin, optically thick accretion disks around black holes and neutron stars. Since the mass accretion rate for a black hole stellar source is expected to be large, the inner region of the disk is expected to be dominated by the radiation pressure. For such a disk in which the viscous stress (τ), is proportional to the total pressure (p) i.e. $\tau = -\alpha p$ where α is a constant, the disk becomes globally unstable due to the thermal and viscous instabilities (Lightman & Eardley 1974; Shakura & Sunyaev 1976). This results in burst like fluctuations of large amplitude in the disk luminosity.

It has been shown that at a given radius of the accretion disk, the stability of the disk traces a characteristic ‘S’ curve in the $\sum - T_{\text{eff}}$ plane, where $\sum$ is the surface density and T_{eff} is the effective temperature at that radius (Lasota, Hameury & Hure 1995). In the middle branch of the curve, the disk is thermally unstable. No stable physical states are accessible in this region (Lasota, Narayan & Yi 1996). When the mass accretion rate falls in the range corresponding to the above unstable branch in $\sum - T_{\text{eff}}$ curve, the disk becomes unstable and forced to a “limit cycle” behaviour. According to this model, the outburst in the soft X-ray transients occurs when the accretion disk makes a transition from the lower cold state to the upper hot state in the characteristic ‘S’ curve. The disk outburst begins when the surface mass density exceeds a critical value. For a constant mass accretion rate, the type of outburst depends on the time required for the deposition of matter on the disk to create the surface density larger than the critical value and the viscous time required for the matter to diffuse inward and cross the critical mass density region.

The main difference between the outburst light curves of SXTs and the dwarf novae is the longer decay time scale for the SXTs In the SXTs, the bolometric luminosity due to the infall of accreted matter towards the compact object is mainly emitted in X-rays. King & Ritter (1998) have explained the light curves of SXTs by the disk instability model, taking into account the irradiation by the X-ray source during the outburst. Irradiation from the X-ray source prevents the disc from coming to its cool state till the accretion rate is reduced sharply. King & Ritter (1998) have shown that the X-ray light curve of the source is roughly exponential if the irradiation is strong enough to ionize all of the disk to the edge. If the emitted X-rays from the central X-ray source are too weak to ionize the disc, the light curve should decline linearly. The X-ray light curve of the various SXTs, which are thought to contain a black hole as the compact object, are interrupted by a secondary maximum during which the X-ray flux increases by a factor of 2 or more, followed by a linear or exponential decay. According to King & Ritter (1998), when irradiation begins, the increase in viscosity is more in the outer regions compared to the inner region of the disk, causing a block of extra mass to move inwards and resulting in a secondary outburst. Chen, Livio & Gehrels (1993) have suggested that the secondary maxima (glitch) in the light curves result due to the extra mass loss from the companion when illuminated by the X-rays from the bursting primary object. Augusteijn *et al.* (1993) interpreted the secondary maximum (glitch) arising due to the enhanced mass transfer from the companion resulting from the heating by X-rays from the primary source, after the outburst. Time delay of a few months or so occurs in the similar linear flow of matter from the companion to the X-ray emitting inner disk.

More detailed studies of the characteristics of the light curves of SXTs will provide valuable insight into the mechanism of the occurrence of the outbursts in these sources.

Acknowledgements

We acknowledge the contributions of the scientific and technical staff of TIFR, ISAC and ISTRAC for the successful fabrication, launch and operation of the IXAE. It is a pleasure to acknowledge constant support of Shri K. Thyagarajan, Project Director IRS–P3 satellite, Shri R. N. Tyagi, Manager, PMO and Directors of ISAC and ISTRAC. Finally, we express our grateful thanks to Shri J. D. Rao and Shri T.V.S.R.K. Prasad and their colleagues at ISTRAC who have been principally responsible for the successful operation of the IXAE instrument in the stellar pointing mode.

References

Agrawal, P. C. 1998, in *Perspective in High Energy Astronomy and Astrophysics;* Proceedings of the International Colloquium, Aug. 12–17, 1996 at TIFR, Mumbai, (eds:) P. C. Agrawal & P. R. Viswanath (Universities Press) p 408.

Augusteijn, T., Kuulkers, E., Shaham, J. 1993, *Astr. Astrophys.* **279,** L13.

Chen, X., Taam, R. E. 1994, Astrophys. J. **431,** 732.
Chen, W., Livio, M., Gehrels, N. 1993, Astrophys. J. **408,** L5.
Ertan, U., Alpar, M. Ali 1998, Astr. Astrophys. **336,** 220E.
Hjellming, R. M., Rupen, M. P., Mioduszewski, A. J. 1998, IAU Circ No. 6932.
Hynes, R. I., Roche, P., Charles, P. A., Coe, M. J. 1999, Mon. Not. R. astr. Soc. **305,** L49.
King, A. R., Ritter, H. 1998, Mon. Not. R. astr. Soc. **293,** 42.
Lasota, J. P., Hameury, J. M., Hure, J. M. 1995, Astr. Astrophys. **302L,** 29.
Lasota, J. P., Narayan R., Yi, I. 1996, Astr. Astrophys. **314,** 813.
Lightman, A. P., Eardley, D. N. 1974, Astrophys. J. **187,** L1.
Mukerjee, K. (e-mail: kmukerji@tifr res.in), 1999, Private communication.
Pooley, G. G., Mullard 1998, IAU Circ No. 6926.
Rao, A. R., Agrawal, P. C, Paul, B., Vahia, M. N. et al. 1998, Astr. Astrophys. **330,** 181.
Revnivtsev, M. G., Trudolyubov, S. P., Borozdin, K. N. 2000, Mon. Not. R. astr. Soc. **312,** 151.
Remillard, R. A. 1998, astro-ph No. 9805224.
Remillard, R., Levine, A., Wood, A. et al. 1998, IAU Circ No. 6920.
Shahbaz, X, Charles, P. A., King, A. R. 1998, Mon. Not. R. astr. Soc. **301,** 382.
Shakura, N. I., Sunyaev, R. A. 1976, Mon. Not. R. astr. Soc. **175,** 613.
Tanaka, Y., Lewin, W. H. G., in X-Ray Binaries, (ed.) W. H. G. Lewin, jan van Paradijs & E. P. J. van den Heuvel (Cambridge University Press) 1995, 126.
White, N. E., Ueda, Y., Dotani, T., Nagase, F. 1998, IAU Circ No. 6926.
Zycki, P. T., Done, C, Smith, D. A. 1999, Mon. Not. R. astr. Soc. **305,** 231.

J. Astrophys. Astr. (2000) **21,** 39–52

X-ray Measurements of Black Hole X-ray Binary Source GRS 1915+105 and the Evolution of Hard X-ray Spectrum

R. K. Manchanda, *Tata Institute of Fundamental Research, Mumbai 400005, India.*

Received 1999 December 28; accepted 2000 February 9

Abstract. We report the spectral measurement of GRS 1915+105 in the hard X-ray energy band of 20–140keV. The observations were made on March 30th, 1997 during a quiescent phase of the source. We discuss the mechanism of emission of hard X-ray photons and the evolution of the spectrum by comparing the data with earlier measurements and an axiomatic model for the X-ray source.

Key words. Accretion, accretion disks—X-rays: stars—Black hole candidates, binary sources: individual—GRS 1915+105.

1. Introduction

Since its discovery in 1992 (Castro-Tirado *et al.* 1992), the Galactic X-ray transient source GRS 1915+105 has exhibted pronounced active phases during 1994, 1996 and 1997. A long term temporal behaviour of the source suggests an abundant mixture of outbursts and low luminosity episodes. The variety of other short term temporal features in the X-ray light curve include flickering, strong quasi-periodic oscillations, irregular X-ray bursts, pronounced dips and rapid high-low transitions both in soft and hard X-ray bands (Greiner *et al.* 1996; Morgan *et al.* 1997; Yadav *et al.* 1999).

Among the main dynamical features of the source are the emission of two symmetric radio jets with superluminal motion (Mirabel & Rodriguez 1994), super Eddington X-ray luminosity of 6.5×10^{39} erg/sec in the 6–120 keV band (Greiner *et al.* 1998) on various occasions and the presence of strong 0.5–10 Hz QPOs apart from the two spectral states signifying the 'High' and 'Low' state (Trudolyubov *et al.* 1998). GRS 1915+105 is one of the two known Galactic sources that exhibit superluminal radio jets (Mirabel & Rodriguez 1994). From the radio measurements in the H_I band and the relativistic constraints on the superluminal motion, the distance of the source is estimated to be 12.5±1.5 kpc. A probable counterpart with 23.4 mag in I band has been claimed to be detected by Mirabel *et al.* (1994) and recently a 52^d orbital period has been proposed from the analysis of the RXTE and BATSE light curves (Manchanda 1999). In the absence of a definite optical identification of the primary component, the true nature of the source is still unresolved.

Simultaneous observations of the source in radio, IR and X-ray band indicate a synchrotron origin of the low energy photons instead of thermal reprocessing of the X-rays (Foster *et al.* 1996; Fender *et al.* 1997). While the X-ray and Infrared photons show a one-to-one correlation, the time offset and the shape comparison suggest the decoupling between the two during the later stage (Eikenberry *et al.* 1998).

The X-ray luminosity from the source is observed to rise to super Eddington limit on several occasions, thereby suggesting the black-hole nature of the underlying object. Furthermore, on the basis of phenomenological arguments of similarity of two X-ray spectral states 'high soft' and 'low hard' to the well known BH candidates, absence of pulsation, correlation of the QPO power with the high spectral state, GRS 1915+105 is believed to be a black hole candidate. In addition, the temporal profile of the X-ray burst of slow rise and rapid decay and the hardening of the X-ray spectrum within the burst is taken to be the evidence of disappearance of the inner accretion disk into black-hole horizon (Belloni *et al.* 1997a). A variety of theoretical models involving bulk-motion, advection driven accretion and multi-colour black body emission have been invoked to explain the spectral and temporal features of the source. The periods of weaker emission, outburst and rapid flaring are believed to be due to rapid removal and replenishment of the inner part of the accretion disk (Belloni *et al.* 1997b), the X-ray spectrum is believed to originate by Compton upgradation of the keV photons (Titarchuk & Zannias 1998).

The evolution of the hard X-ray spectrum of GRS 1915+105 and its relation to the 1–10 keV flux does not indicate any well defined correlation. However, in general the low energy data below 30keV on the transient galactic black hole candidates suggest the presence of at least two main spectral states apart from the quiescent emission during which $L_x < 10^{-4} L_{\mathrm{Edd}}$ which are distinguished by the amount of soft 1–10 keV and ultra soft X-ray photons while the hard X-ray spectrum above 30 keV, in the two states are characterized by a power law tail with spectral index $\alpha \sim 2$ — 3 during high state and the $\alpha \sim 1.5 - 2$ during the low state.

In this paper we present the spectral measurement of GRS 1915+105 in the hard X-ray region made during the post-burst quiescent state. We discuss the spectral evolution using the RXTE measurements of the source made before and after our observations.

2. Instrument and observation

The observations were made with a Large Area Scintillation counter Experiment (LASE) which is designed to study fast variations in the flux of X-ray sources in the hard X-ray energy region up to 200 keV. The payload consists of three large area X-ray detector modules mounted on a servo-controlled platform. The detectors are a specially designed combination of thin and thick large area NaI(Tl) scintillation counters configured in back-to-back geometry. Each of the detector modules has a geometrical area of 400 cm^2 and the thickness of the prime detector is 3 mm. The active anti-coincidence shield is provided by a 30 mm thick crystal. The field of view of each module is 4.5°×4.5° and is defined by demountable mechanical slat collimator specially designed with a sandwiched material of lead, tin and copper. Each module along with the collimator is further encased with a passive shield. Each detector is designed as a stand-alone unit with independent on-board subsystems for HV power and data processing. The payload platform is servo-stabilized and the target X-ray source and the corresponding background region are tracked using an on-board micro-processor controlled tracker.

The detectors have almost 100% detection efficiency in the operative energy range and the back-to-back configuration gives 80% reduction in the detector background, most of which is produced due to partial energy loss by the Compton scattering of high energy photons in the main detector. The preflight calibration of the X-ray detectors is done at different energies using radioactive sources, Cd^{109} (22.1, 87.5 keV), Am^{241} (24.7 and 59.6keV) and Ba^{133} (32.4 and 81keV). In addition, an Am^{241} source is mounted on the pay load for the calibration of the detectors during the flight using ground command. The accepted events are pulse-height analyzed, time tagged with a 25μ sec resolution and transmitted to ground on a 40 Kbit PCM/FM link. The details of the detector design, associated electronics, control sub-systems and in-flight behaviour of the instrument are presented elsewhere (D'Silva *et al.* 1998). A 3σ sensitivity of the LASE telescope in the entire energy range up to 180keV is $\sim 1.5\times 10^{-6}\mathrm{cm}^{-2}\mathrm{s}^{-1}\ \mathrm{keV}^{-1}$ for a source observation of 10^4 sec.

The balloon flight was launched on March 30th, 1997 from Hyderabad, India (cut-off rigidity 16.8 GV) and reached the ceiling altitude of 3.3 mbars. A number of X-ray sources in the right ascension band of 16^h to 22^h were observed during the experiment. GRS 1915+105 was in the field of view of two detectors for a total period of 60 min (two sightings of 30 min each) between 0235 UT and 0350 UT and the background was measured for 20 min each before and after the source observation and for 10 min midway the source pointings. The off-source pointing location was carefully selected blank field from the known X-ray source catalog. The X-ray light curve from the all sky monitor on-board RXTE, suggests that at the time of our observation the source was in a post burst quiescent phase with source luminosity twice the lowest value.

3. Results and discussion

A total excess of 10300 counts due to GRS 1915+105 were recorded in the two detectors. This corresponds to a combined statistical significance of 20σ. The positive excess was seen up to 140 keV. The source contribution was divided in 10 energy bins and corrected for atmospheric absorption, window transmission, detector efficiency and energy resolution for each detector and co-added. The combined spectrum of the source is shown in Fig. 1. The errors on the data points correspond to 1 σ statistical errors. A systematic error of ~ 10% is estimated for the lowest energy channel and included in the plot. For comparison, we have also plotted the hard X-ray spectrum of the well known BH candidate Cyg X-1 during the 'low hard' X-ray state, shown with dotted line in the figure.

A single power law fit of the form $dN/dE = KE^{-\alpha}$ photons $\mathrm{cm}^{-2}\ \mathrm{s}^{-1}\ \mathrm{keV}^{-1}$ to the spectral data gives the best fit model parameters of $K = 36.8 \pm 2.6$ and $\alpha = 3.34 \pm 0.25$ for a χ^2 value of 0.31 per dof. The solid line in the figure shows the fitted spectrum. A simple comparison with the earlier data is not possible because the only composite model fits for the soft and hard X-ray band are used and the best fit parameters are quoted for the individual components. The spectral fits in the low energy domain are more complex as even in the simplest models, multi-colour temperature, equivalent hydrogen column density and contribution due to iron-line features are the free parameters. During the systematic spectral investigation of PCA and HEXTE data for about 50 of the 250 sightings of the source by RXTE, Greiner *et al.* (1998) have noted that even though the composite spectrum consists of 5 different components, the hard component up to 200 keV is best described by a power

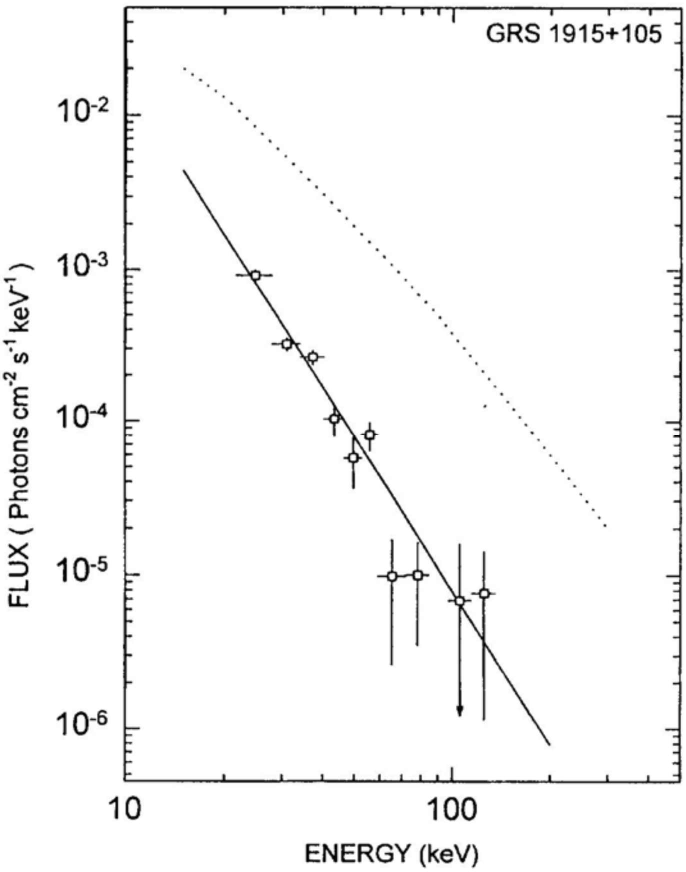

Figure 1. Hard X-ray spectrum of GRS 1915+105. The X-ray spectrum of Cyg X-l during 'low hard' state is shown in dotted line for comparison.

law model. The contribution is always present and is highly varying both in intensity and power index –2.0 and –4.8.

Surprisingly, the spectral index of 3.34 ±0.25 measured in the quiescent state compares very well with the spectral measurement from OSSE detector in the 50–300 keV energy band who report an average spectral index of 3.08 ±0.06 from 3 observations during the peak intensity of 1996 flare (Grove *et al.* 1998). Similarly, Greiner *et al.* (1998) have also reported the best fit power law index α ~3.2 in the 1–200 keV band for the Oct. 1997 flare.

For the analysis of timing properties of GRS 1915+105, we have searched our data for quasi-periodic oscillations in the 20–140 keV band. The detector counts in two separate sightings were first binned in 0.032 sec intervals and power spectrum analysis was performed using FTOOLS. The summed power density spectrum in the 0.0005–18 Hz are is shown in Fig. 2. It is clearly seen from the figure that data above 0.01 Hz are completely flat. The broad QPO peak visible between 0.025 and 0.045 Hz has a confidence level of only 90%. A low level QPO at 3.4 Hz in the PCA data on March 27th is reported by Trudolyubov *et al.* (1998) however, their data search is restricted to lower time scales. GRS 1915+105 is a peculiar source in which the QPO

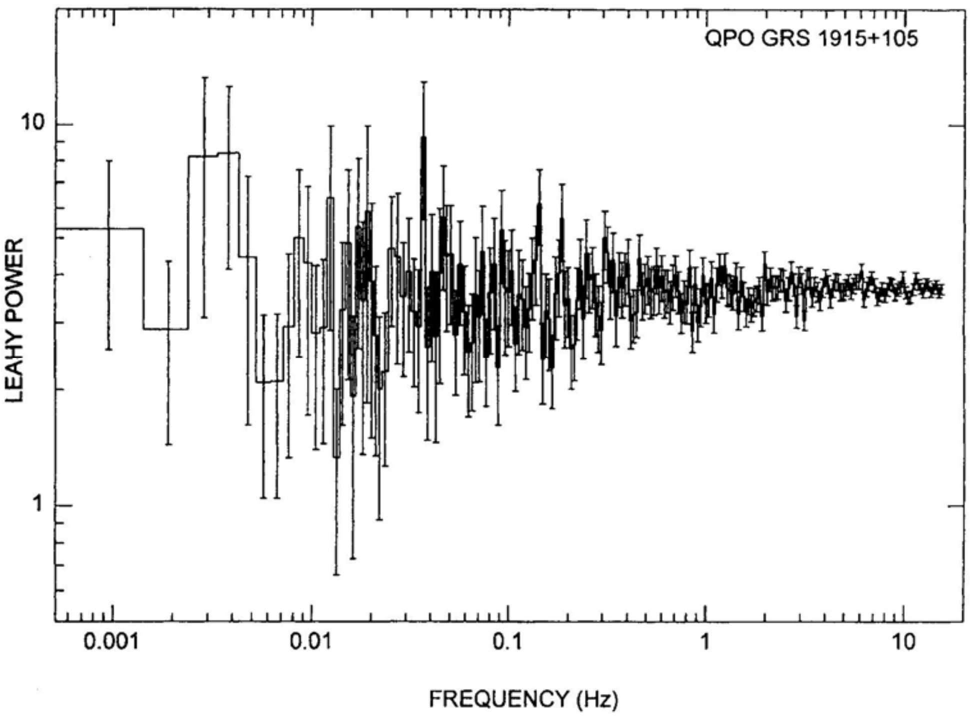

Figure 2. Power density spectrum in the 20-140 keV energy band.

frequency varies continuously in a random fashion. For example, a centroid frequency of 0.003 Hz for QPO was observed on June 16th, 1996 (Morgan *et al.* 1997) while the source was in the flaring mode rather than the featureless low intensity state during the time of present observation. However, from the analysis of the PCA and HEXTE data, Munno *etal.* (1999) find that frequency of the QPO is best correlated to the temperature of the inner accretion region. The presence of very low frequency QPO during the steady quasi-low state is quite probable. The low power for the feature is due to the fact that a correlation between the spectral and temporal states suggest that for power law index $\alpha > 3.05$ source behaves QPO quiet (Markwardt *et al.* 1999).

3.1 *Spectral evolution*

GRS 1915+105 was in the post-burst low intensity state during the present observations. In figure 3 we have plotted the X-ray light curve of the source taken from the BATSE data. The lowest intensity state corresponding to 0.02 ph.cm^{-2} s^{-1} keV^{-1} is shown by the dotted line in the figure and the date for our observations is marked by an arrow. It is seen from the figure that our observation followed a month after the high hard X-ray flux of 0.2 photons recorded by the BATSE detectors and average daily flux on the day was a factor of ~ 3 higher than the lowest flux. The ASM light curve during this period showed a steady behaviour at ~300mCrab (20c/s) and is shown in the upper panel in figure 3. It is also seen in the figure that light curves in the soft and hard X-ray band may not be one-to-one correlated at all times.

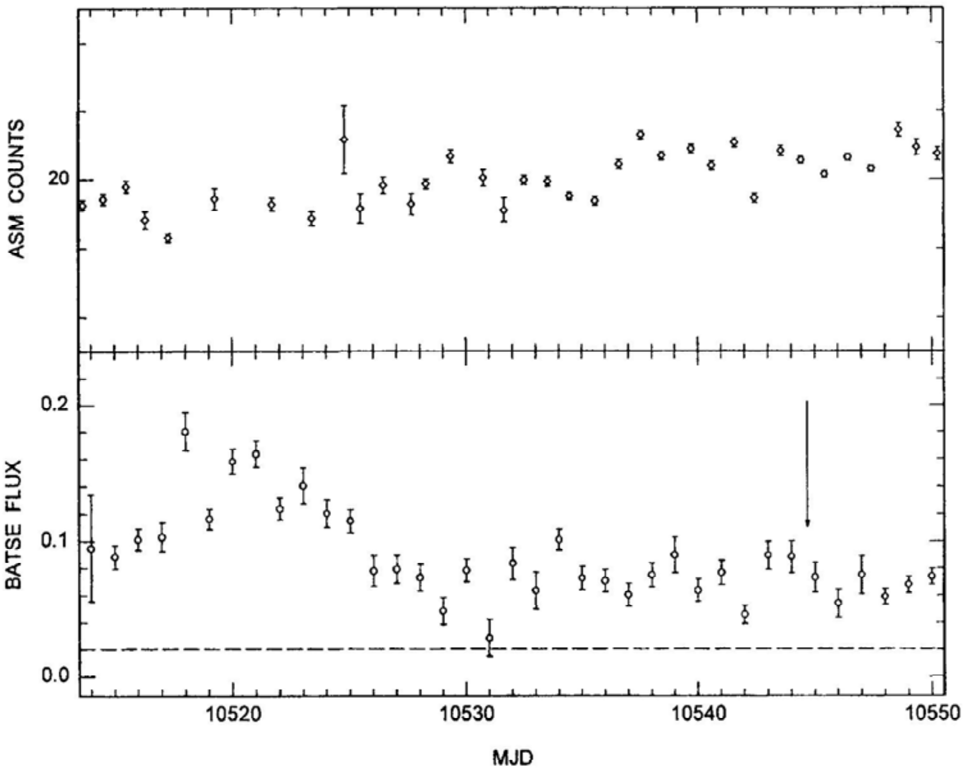

Figure 3. X-ray light curve of GRS 1915+105 in the 20120 keV band from BATSE data. The minimum intensity level is marked by the dotted line and the source intensity level corresponding to present observations is shown by an arrow.

In order to observe the change in the hard X-ray spectrum on a day-to-day basis in the high-to-low transit phase during the post-burst state, we have used the spectral data from PCA and HEXTE before and after our observations. The data are shown in figure 4. The dotted and dashed lines in the figure represent the PCA and HEXTE composite observed flux of the source on February 26th, 1997 and April 2nd, 1997 (Borozdin *et al.* 1999). OSSE data during the 1996 flare (Grove *etal.* 1998) is shown by the solid line in the figure. In terms of integral comparison of low state data shown in figure 4. the measured BATSE flux for the three dates are 0.10, 0.101 and 0.094 ph.cm^{-2}s $^{-1}$ keV^{-1} respectively and the corresponding best fit parameters on hard component from the PCA data give the flux levels to be comparable at 10.12, 10.0 and 11.14 nano-ergs c m^{-2} s^{-1} for the three observations.

Three points can be noted from the figure:

(i) Both the flux levels and the spectral shape on April 2nd (dotted line) observation is in good agreement with our measurements of March 30th.

(ii) For energies above 20 keV the data for February 26th is higher by a factor about 2 and the corresponding increase during maxima of the flare in 1996 is by a factor ~ 10.

(iii) The low energy data below l0 ke V does show a crossover.

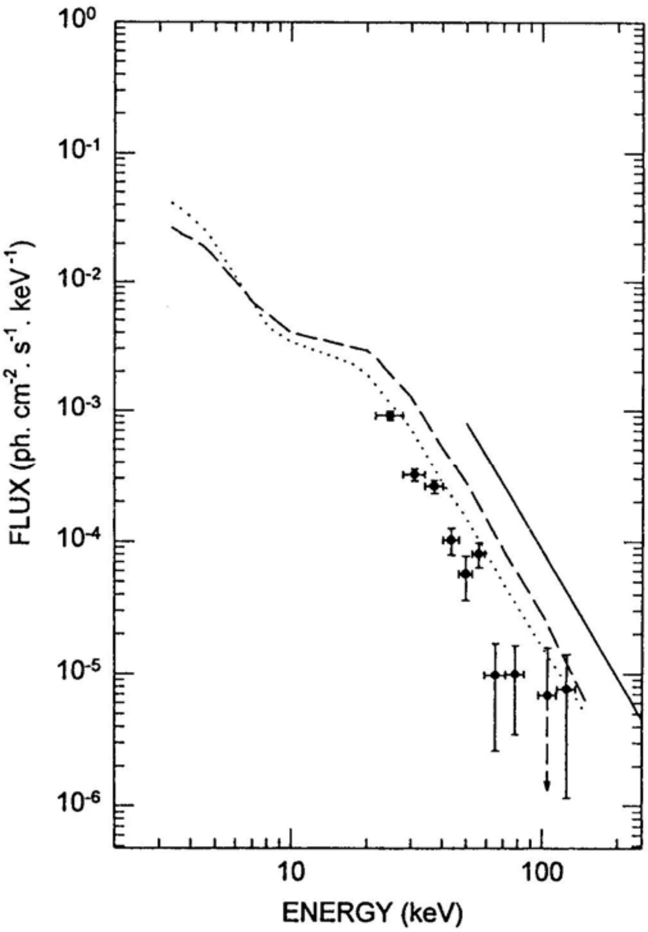

Figure 4. A comparison of the GRS 1915+105 spectra: • present data, dashed and dotted lines: PCA+HEXTE data on February 9th, 1997 and April 2nd, 1997 and solid line: OSSE data at peak during high state.

In the disk accretion models with advection dominated flow near to the stellar surface, a two temperature plasma is formed at the boundary layer (Narayan, Kato & Honna 1997; Chen, Abramowicz & Lasota 1997) and the hard X-ray and gamma ray emission is believed to originate in the inner region by comptonization of the soft X-ray photons most of which are supplied by the cool outer disk. Considering the comptonization due to bulk motion near to the stellar surface during the high state in black hole binary X-ray source, Ebisawa *et al.* (1996) have proposed, that two distinct spectral indices in the hard X-ray band corresponding to 'high soft' and 'low hard' state of the source. However, taking by itself the comparison of high energy spectral data above 20 keV during various phases of the source activity as seen in figure 4, clearly suggests that except for increase in the integral emission from the source, the spectral shape does not show any perceptible variation. This is a most significant inference which directly relates to the physical characteristics of the emission mechanism for the non-thermal component. Since the emitted power of

~2.3 $\times 10^{-7}$ erg cm^{-2} s^{-1} from the source in hard X-ray band is substantially higher than the bolometric flux of disk black body component in the low energy band (Greiner *et al.* 1998), the absence of spectral variation during the quiescence and the outburst should be the true indicator of the source properties. Therefore, it follows that during the composite spectral fitting, except for scaling the flux contribution above 20 keV, non-thermal power index should not be made a free parameter. As a result, the spectral properties of the thermal component should be inferred by computing the low energy residuals.

During comptonization, only if 4kT_e > hv the seed photons will be upgraded in energy and the increase in photon energy on average during each scattering is given by $\frac{\nu'}{\nu} \sim 1 + \frac{4}{3}[\gamma^2 - 1]$, even for a Maxwellian distribution of electrons with k$T_e \ll m_e c^2$. Therefore, multiple scattering even by a Maxwellian gas can lead to very high photon energies. In a non-relativistic plasma where k$T_e \ll m_e c^2$ and 1, the average number of scattering for the seed photon $n_s \sim \tau^2$ and the probability density for multiple scattering is given as; $P(n_s)$ α exp $[\frac{n_s \pi^2}{3(\tau + \frac{2}{3})^2}]$ The emergent spectrum therefore, develops into a unified power law from the ensemble of spectra produced by photons scattered by differing number of times. The emergent spectrum however, will be radically modified in the presence of the seed input spectrum and if the scattering electron cloud has a temperature gradient. Since the high energy photons arise after a large number of scatterings, the direction vector and the origin of the seed photons are completely forgotten. Furthermore, the reflected to transmitted ratio for photons above 15 keV is ~ 1, the spectral index of the emergent photons is almost independent of the source geometry i.e. whether the seed photons are distributed uniformly in the disk or located on one side of the disk (Pozdnyakov *et al.* 1983). In the limiting case spectral index should become —1.5 for monoenergetic seed photons and Maxwellian distribution of the electron scatterers (Titarchuk *et al,* 1998). The expected power will be however, reduced in the later case due to integration over limited solid angle.

We can therefore, conclude that the hard X-ray and gamma ray emission in GRS 1915+105, results mainly from the comptonization of soft X-ray photons from the outer disk in the hot boundary layers of the inner disk and thereby giving rise to a power law spectrum independent of the changes in the luminosity level of the source, which in turn is coupled to the level of mass accretion. In the alternate assumption of seed photons coming from the inner disk will lead to changes in the spectrum directly relating to the level of accretion. A single power law fit up to 300 keV for the GRS 1915+105 (Grove *et al.* 1998) is in contrast to the classical BH candidate Cyg X-l, in which the observed spectral index shows steepening above 100keV (Tanaka and Lewin 1995).

3.2 *Axiomatic model*

The phenomenological arguments about the physical characteristics of GRS 1915+ 105 suggest the compact object to be a black hole. The X-ray luminosity of the source is measured to be > $10^{39} \times (D/12.5\text{kpc})^2$ during the violent outburst of the source. Similarly, the presence of dominant QPO during high state resembles the nature of well known BH candidate Cyg X-l. The mass estimates of the black hole however varies between $10M_\odot$ and $33M_\odot$ Assuming that 67 Hz QPO represents the innermost stable orbit of non rotating black hole, the estimated mass of the X-ray source is

$33M_\odot$ and if the QPO arises in the g-mode oscillations in the inner disk, the derived mass limit is $10M_\odot$ (Nowak *et al.* 1997; Morgan *et al.* 1997). Also, following Manchanda (1999), if the 52_d period seen in the X-ray light curve represents the orbital period of the binary system, the primary star should have a mass of $\sim 8M_\odot$.

Therefore, as a working hypothesis one can assume that the X-ray emission in GRS 1915+105 is due to the compact object accreting mass from its binary companion. However, any scheme proposed for the observed dynamical properties must account for the three well know features:

(i) Long term temporal nature of random variation between quiescent and flaring episodes,
(ii) the generation of QPO and their relation with the geometrical variables, and
(iii) a Power-law hard X-ray spectrum and its non-evolution.

From the detailed analysis of these parameters observed from the PCA and HEXTE data since 1996, a variety of geometrical configurations and the corresponding best fit parameters have been discussed in literature (Belloni *et al.* 1997b; Titarchuck *et al.* 1998a; Titarchuk & Zannias 1998; Laurent & Titarchuk 1998; Narayan *et al* 1997; Yadav *et al.* 1999). These models mainly consider the accretion on to the black hole as the starting point and the dynamical and thermodynamical details differ in the inner region of the accretion disk.

In the standard model for mass accretion in a binary system the matter falling on to the compact object releases the gravitation potential energy which heats the gas and emits radiation while the transfer of the mass from the primary to the compact object takes place either through the Roche lobe overflow or by the stellar wind (Shakura & Sunyaev 1973; King 1995). Since the accreting gas will have intrinsic angular momentum, a Keplarian disk will be formed around the compact object. The exact spectral behaviour of the emergent photons will be determined by the accretion geometry, dominant heating and cooling mechanism, optical thickness of the gas in the emission region, net heating and cooling rates, radiation pressure, magnetic fields and the boundary conditions at large distance as well as stellar surface. Detailed description of various idealized cases has been discussed in literature (Shapiro & Teukolsky 1983; Abramowicz & Percival 1997; and references therein). In the specific case of accretion on to a black hole compact object, the ultrasoft and the soft X-ray excess in the 2–10 keV energy region is mainly due to the fact that the main cooling mechanism near to the surface of black hole is almost 100% advection (Chen *et al.* 1997a; Narayan & Yi, 1995a, 1995b) and the electron temperature does not rise to very high kT value. The hard X-ray spectrum is believed to originate in the inverse Compton scattering of the low energy photons (Sunyaev & Titarchuck 1985) which further gets modified at lower energies due to the bulk motion of the material close to the black hole (Chakrabarti & Titarchuk 1995). In a hot tenuous plasma bremsstrahlung and recombination losses are small and the energy exchange between electrons and photons is controlled by the multiple scattering. For $4kT_e > h\nu$, the seed photons are upgraded in energy and a composite power law spectrum therefore emerges due to the superposition of the photons scattering by differing number of times. The long term variability and the spectral evolution in such models are coupled to the rate of accretion and the changes in the physical characteristics of emission region.

Even in an oversimplified model, the accreted material must finally rest at the stellar surface at $R_0 = R_{NS}$ or R_{BH} $(= 3R_g)$, where R_{NS} , R_{BH} represent the radii of a neutron star and a black hole and R_g, is the Schwarzschild radius. The gas flowing from the Keplarian disk to the surface therefore, must adjust to the new boundary condition thus effecting the thermodynamical properties of the medium. The inner-most orbit at which the gas is in Keplarian motion is termed as the centrifugal barrier at $R = R_{CB}$ by Titarchuk *et al.* (1998a) who suggest that super Keplarian flow may occur at this boundary and give rise to the QPO in GRS 1915+105. This hot boundary layer can also generate the hard X-ray photons. It has been also proposed that the flow inside this boundary may be advection driven accretion leading to lower effective heating and low kT value (~ 1–2 keV) thereby leading to the enhanced soft X-ray emission as seen in the BH candidates (Narayan & Yi 1995a; and references therein).

While these models can explain the instantaneous nature of the source, the long term variability of the source from quiescent to outburst phases requires major modification to the accretion flow. The estimated accretion rate for the observed luminosity variation corresponds to $M > 2 - 10 \times 10^{-8} M_\odot$ for the quiescent phase and a variable enhancement by a factor of ~2 during the active phase. Belloni *et al* (1997a) have proposed the existence of the unstable disk to account for the transient high intensity episodes from the source.

In order to derive new constraints on the mass accretion in GRS 1915+105 we have performed rank analysis of the BATSE daily average source intensity in the 20–100 keV energy band. In our view the hard X-ray flux is the best indicator as it is not affected by the model dependent emission parameters as well as various correction factors due to intervening matter density and the uncertainties of detector response matrix. The data is shown in figure 5. Apart from considerable flaring

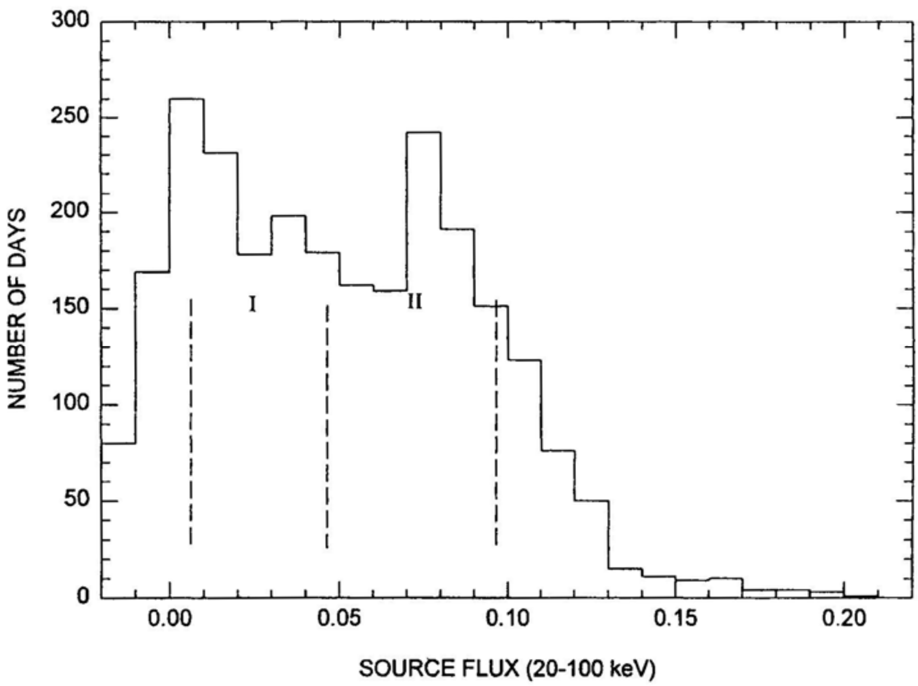

Figure 5. Rank distribution of the measured daily averaged X-ray intensity of GRS 1915+105 in the 20–100 keV band from BATSE data.

activity even above the flux level above 0.12 ph.cm^{-2} s^{-1} keV^{-1}, two distinct intensity levels marked by the peaks are clearly visible in the figure and are labeled as I and II. An empirical fit with two Gaussian shapes corresponding to the intensity level of 0.015 ph.cm^{-2} s^{-1} keV^{-1} and 0.8 ph.cm^{-2} s^{-1} keV^{-1} can fairly represent the data. This clearly points to two quasi-steady levels of mass accretion during different phases of source activity. We term the region I as corresponding to the quiescent state during which the source has low luminosity and region II defines the active phase with high luminosity state and caused by an enhanced accretion signifying the change in accretion geometry and during which the flaring activity gets amplified.

In summary, GRS 1915+105 has two quasi-steady luminosity levels signifying different levels of mass accretion and any geometrical model must provide for this change over. It is also seen from the figure that the source spends almost equal amount of time in the two stages of X-ray activity and therefore, the models ascribing this feature to be a simple statistical behaviour of change in accretion, are not tenable. The Gaussian distributions around the mean flux levels may however, arise due to statistical variations in the accreted mass. A two level steady accretion modes of GRS 1915+105 have also been inferred by Munno *et al.* (1999) from the correlation of QPO and the spectral states of the source during the detailed analysis of PCA data. It is found that 0.5–10 Hz QPO serves as a marker for the two modes. In the presence of the QPO, the source spectrum is primarily power-law while the disk emission giving rise to dominant soft X-ray flux is observed when the QPO is absent. Changing levels of accretion in a disk geometry have built in constraints. For example, in the unified model of Belloni *et al.* (1997b), rapid removal and replenishment of the inner parts of the optically thick accretion disk can only take place at viscous time scales. While a detailed look at the X-ray light curve suggests that large changes in luminosity can occur within 2 to 3 minutes. In the following, we outline a new geometrical structure for the inner accretion disk, which can provide the two accretion modes in a natural way.

We hypothesize that inner accretion disks may have a multiple ring structure with the first node touching the stellar surface through which actual mass is accreted on to the compact object. The schematic for the geometrical structure is shown in figure 6.

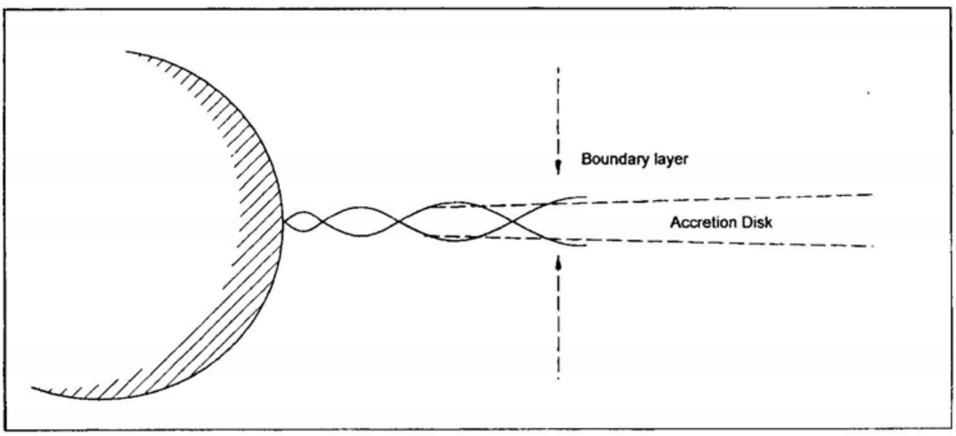

Figure 6. Geometrical structure of the inner accretion disk of GRS 1915+105.

An apparent correlation between the quiescent time and the burst duration during the fast flickering phase of the source does suggest a discrete annular behaviour of the inner disk accretion. Similarly, Titarchuck *et al.* (1998a) have also argued that QPO may arise due to non radial oscillations caused by the formation of kinks and shocks in the super Keplarian flow. Existence of the acoustic waves in the hot plasma have also been proposed as the possible source for QPO emission (Chen *et al.* 1997a).

The global solutions of the ADAF flow for various models of disk parameters ($\alpha, \dot{M}$, Pressure, Mack number) suggest that a transonic region is set up in the boundary layer of inner and outer disk at $r \sim 10^3 r_s$ (Chen *et al.* 1997b). We therefore, propose that during the dynamical adjustment from the boundary of the Keplarian disk to the stellar surface, transverse oscillations are excited at the boundary and propagate inward with decreasing amplitude. Added to this the existence of inherent p and g mode oscillation of the disk (Nowak & Wagner 1993), and progressively decreasing micro turbulence from the boundary layers to the stellar surface, a ring structure may be formed in the inner part. The reflected shock generated by the land-fall on to the stellar boundary, should further help stabilize the ring geometry. In the equilibrium conditions during the quiescent phase the mass accretion on to the surface in this geometry is controlled by the nodal cross-section. A bi-modal mass accretion as inferred earlier and consequent increased luminosity in our model arises when above a specific accretion rate, the node is pushed into the stellar boundary, and the available cross-section for mass transfer is increased. This can be triggered by a change in the accretion rate from the companion star into the boundary layers giving rise to enhanced turbulence. Such a change over appears natural as the Reynolds number of the accretion flow is proportional to the accretion rate and is believed to be the determining factor for the QPO frequency in the source. Fluctuations in the mean accretion rate may arise due to geometrical changes leading to oscillations of the inner most ring caused by the difference in the incoming and outgoing material. We believe that such ordered structure is much more likely than the formation of discontinuities which are hypothesized to remove the angular momentum from the accreted material and a continuously varying size of vacuum ring around the source hypothesized by Belloni *et al.* (1997b) to explain the observation of burst duration-to quiescent time correlation.

This simple empirical model predicts two observable features. First, the high-low transitions can take place much faster than the viscous time scale t_{vis} given by; $t_{vis} = 30\left(\frac{\alpha}{0.01}\right)^{-1} R_7^{7/2} \dot{M}_{18}^{-2} \geq 3000$ sec, for best fit parameters of the accretion disk up to the transonic boundary. Second, for an equivalent luminosity level, the spectral parameters are independent of rapidity at which the high-low transition takes place.

The difference between the emission behaviour of GRS 1915+105 and the classical black hole Cyg X-l can be understood in terms of its transient nature. In the currently accepted models, the transient sources are high mass X-ray binaries (HMXB) with generally a Be star companion, which provides the accretion material through mass ejection episodes. In fact all the 17 transient sources discovered so far, are associated with such systems (Paradisj van 1995). Even though in most of the transient sources, the compact object is a pulsating neutron star, the occurrence of Be star black hole binary system is not excluded by any selection rule. Since the mass ejection rate from Be star can be not only large but highly variable and thus can account for the luminosity transitions seen in GRS 1915+105. In comparison, the optical companion of Cyg X-1 is a O type star, which as a class can give large winds but do not show large changes in the mass-loss rate. It is surmised that large variations in the mass transfer rate from the Be star above the Eddigton limit results in the different geometrical structures for the inner accretion disk in GRS 1915+105 as discussed earlier.

Acknowledgement

I wish to thank Prof. A. R. Rao and Dr. J. S. Yadav for their comments on the manuscript and the RXTE and the BATSE teams for making the data available on public archives.

References

Abramowicz, M. A., Percival, M. J. 1997, *Class. Quantum Grav.,* **14,** 2003.
Belloni, T., Mendez, M., King, A. R., Van der Kliss M., van Paradisj, J. 1997a, *Astrophys. J.,* **479**, L 145.
Belloni, T., Mendez, M., King, A. R., Van der Kliss, M., van Paradisj, J. 1997b, *Astrophys. J.,* **488,** L 109.
Borozdin *et al.* 1999, *Astrophys. J.,* **517,** 367.
Castro-Tirado, A. J., Brandt, S., Lund, N. 1992, **IAU Circ. 5590.**
Chakrabarti, S., Titarchuck, L. 1995, *Astrophys. J.,* **455,** 623.
Chen, X., Swank, J. H., Tamm, R. E. 1997, *Astrophys. J.,* **477,** L41.
Chen, X., Abramowicz, M. A., Lasota, J. 1997, *Astrophys. J.,* **485,** L75.
D' Silva, J. A. R., Madhwani, P. P., Tembhurne, N., Manchanda, R. K. 1998, *Nucl Instr. And Meth.,* **A412,** 342.
Ebisawa, K., Titarchuck, L., Chakrabarti, S. 1996, *PAS J,* **48,** 59.
Eikenberry, S. S. *et al.* 1998, *Astrophys. J.,* **494,** L 61.
Fender, R. P. *et al.* 1997, *Mon. Not. R. astr. Soc,* **286,** 629.
Foster R. S. *et al.* 1996, *Astrophys. J.,* **467,** L81.
Greiner, J., Morgan, E. H., Remillard, R. 1996, *Astrophys. J.,* **473,** L107.
Greiner, J., Morgan, E. H., Remillard, R. 1998, preprint, Astro-ph/9806323.
Grove, J. E., Johnson, W. N., Kroeger, R. A., McNaron-Brown, K., Skibo, J. G.: 1998, *Astrophys. J.,* **500,** 898.
King, A. 1995 in *X-ray Binaries,* (ed.) Lewin, Paradisj & van den Heuvel (Cambridge. Univ. Press), 410.
Laurent, P., Titarchuck, L. 1998, Preprint astro-ph/9808015.
Manchanda, R. K. 1999, Preprint.
Markwardt, C. B., Swank, J. H., Taam, R. E. 1999, *Astrophys. J.,* **513,** L37.
Mirabel, I. F., Rodriguez, L. F. 1994, *Nature,* **46.**
Mirabel, I F. *etal.* 1994, *Astr. Astrophys.,* **282,** L17.
Morgan, E. H., Remillard, R. A., Greiner, J. 1997, *Astrophys. J.,* **482,** 993.
Munno, M. P., Morgan, E. H., Remillard, R. A. 1999, Preprint, Astro-Ph 9904087.
Narayan, R., Kato, S., Honma, F. 1997, *Astrophys. J.,* **476,** 49.
Narayan, R, Yi, I. 1995a, *Astrophys. J.,* **444,** 213.
Narayan, R, Yi, I. 1995b, *Astrophys. J.,* **452,** 710.
Nowak, M. A. *et al.* 1997, *Astrophys. J.*, **477,** L91.
Nowak, M. A., Wagner, R. V. 1993, *Astrophys. J.,* **418,** 187.
Pozdnyakov, L. A., Sobol, I. M., Sunyaev, R. A. 1983, *Sp. Sci. Rev.,* **2,** 189.
Paradisj Jan, V. 1995, in *X-ray Binaries,* (ed.) Lewin, Paradisj & van den Heuvel (Cambridge Univ. Press), 537.
Shakura, N. I., Sunyaev, R. A. 1973, *Astr. Astrophys.,* 24, 337.

Shapiro,.S. L., Teukolsky, 1983, in *Black holes, white dwarfs and Neutron stars,* (John Wiley & Sons Publ.)

Sunyaev, R. A., Titarchuck, L. G. 1985, *Astr. Astrophys.,* **143,** 374.

Tanaka, Y., Lewin, W. H. G. 1995, in *X-ray Binaries,* (ed.) Lewin, Paradisj & van den Heuvel (Cambridge. Univ. Press), 126.

Trudolyubov, S., Churazov, E., Gilfanov, M. 1998, preprint ASTR-Oph/9811449.

Titarchuck, L., Lapidus, I., Muslimov, A. 1998, *Astrophys. J.*, **499,** 315.

Titarchuck, L., Zannias, T. 1998, *Astrophys. J.,* **493,** 863.

Yadav, J. S. *et al.* 1999, *Astrophys. J.,* (in press).

J. Astrophys. Astr. (2000) **21**, 53–59

Scale Length of the Galactic Thin Disk

D. K. Ojha, *Tata Institute of Fundamental Research, Dr. Homi Bhabha Road, Mumbai 400 005, India*

Received 1999 September 14; accepted 2000 February 9

Abstract. This paper presents an analysis of the first 2MASS (The Two Micron All Sky Survey) sampler data as observed at lower Galactic latitude in our Galaxy. These new near-infrared data provide insight into the structure of the thin disk of our Galaxy, The interpretation of star counts and color distributions of stars in the near-infrared with the synthetic stellar population model, gives strong evidence that the Galactic thin disk density scale length, h_R, is rather short (2.7 ± 0.1 kpc).

Key words. Galaxy: stellar content—Galaxy: structure.

1. Introduction

Within the plane of the Galactic thin disk, the radial density function can be expressed in terms of the distance from the Galactic center, the Solar distance from the center, and the Galactic disk scale length. The latter parameter is poorly known at present but can be a major discriminant of theories of thin disk formation. The scale length of thin disk varies as a function of Galactic morphological type (Freeman 1970). For the Milky Way, published values of the scale length of thin disk range from 1.8 to 6 kpc (McCuskey 1969; De Vaucouleurs & Pence 1978; Knapp *et al.* 1978; Robin *et al.* 1992; Ruphy *et al.* 1996). It should also be noted that one way of constraining the value of the Hubble constant involves comparing the radial scale lengths of external disk galaxies, which are dependent on distance and hence the Hubble constant, with that of the Milky Way; thus the radial structure of the disk is also relevant for large-scale structure. Therefore it is of great interest to know the radial structure of the Galactic disk.

The 2MASS near-infrared data provide, for the first time, deep star counts on a large scale, in the J, H, K_s photometric bands. These surveys offer new inputs to determine the radial structural parameters in our Galaxy. Apart from the benefit of a lower interstellar extinction, the near-infrared data present another advantage on optical ones: they trace more reliably the total mass distribution, and therefore should be preferred to investigate the stellar distribution, specially at large distances from the Sun.

In this paper, we present the first analysis of star counts in the J and K_s bands in one of the 2MASS fields at lower Galactic latitude of our Galaxy. The counts are compared to the results of the model of stellar population synthesis of the Galaxy, in order to derive some constraints on the radial structure of the Galactic thin disk.

2. Observational data

We have used the first 2MASS sampler data, public release of point source catalogue, in J (1.25 μm), H (1.65 μm) and K_S-band (2.17 μm) for our analysis. The sampler data are drawn from observations obtained at the Northern 2MASS facility on the night of November 16th, 1997. 2MASS uses two new, highly-automated 1.3 m telescopes, one at Mt. Hopkins, AZ, and one at CTIO, Chile. Approximately 63 deg^2 of northern sky were covered by these observations. The data are complete to 16.0 in J, 15.5 in H and 15.0 in K_S. The 2MASS sampler point source catalog contains position and brightness information for 227,197 objects. We have used one of the 2MASS fields at lower Galactic latitude, which covers approximately 5.958 deg^2 area for our analysis. The positions of the field covered by the observations are: $\alpha_{2000} = 07^h05^m36^S$; = δ_{2000} = $+20^o49'30''$; $l = 196°$; $b = +12°$.

3. Analysis

3.1 *Stellar population synthesis model*

The Besançon model of stellar population synthesis was used to interpret the 2MASS near-infrared counts. Robin & Crézé (1986) started to build a self-consistent Galaxy model using an evolutionary model from Rocca-Volmerange *et al.* (1981), then they introduced the dynamical constraints (Boltzmann and Poisson equations) allowing the determination of the scale heights of the disk according to the potential (Bienaymé *et al.* 1987). The kinematical parameters of Galactic thin and thick disk were described in Robin & Oblak (1987); Robin *et al.* (1996) and Ojha *et al:* (1996). In order to check the Initial Mass Function (IMF) and the Star Formation Rate (SFR) history in the Galaxy, recently Haywood (1994, 1997ab) redesigned the evolution scheme from Rocca-Volmerange to a more detailed one using the most recent evolutionary tracks and gave strong constraints on the slope of the IMF, the history of the SFR in the past and on the age-velocity dispersion relation for the disk stars.

In the model, the Galactic thin disk in the *z*-direction is represented by a sum of 7 components with different scale heights, the 6 oldest components of which are isothermal. This model employs a constant SFR, a three-slope IMF, and a 21 km/s maximum velocity dispersion. The model also gives the thin disk a vertical metallicity gradient according to age-metallicity and age-scale height relations. In the model, the key parameter is the density law of the Galactic thin disk, which is an Einasto density law (Einasto 1979) for $R \leq R_{max}$ (radial cutoff), and is equal to 0 beyond R_{max}. The Einasto law is close to a $sech^2$ law in the vertical direction (see Bienaymé *et al.* 1987, for details), and close to an exponential law in the radial direction, in such a way that the parameter h_R is similar to a radial exponential scale length.

Since we are dealing with the field at lower Galactic latitude, the effect of extinction along the line of sight must be investigated. The effect of extinction on K_S star counts is limited, however J-K_S color distributions are significantly sensitive to the extinction. The fit of the position of the observed and model predicted distribution peaks allows to adjust the spatial extinction law in the model. This fit gives a value of

0.2 mag/kpc for the coefficient of the local diffuse visual absorption for the lower Galactic latitude field.

While examining the various parameters of the Galactic disk, we have started with the best fit Besançon model (as in Robin *et al.* 1996; Ojha *et al.* 1996).

3.2 *Scale length of Galactic thin disk*

In order to constrain the scale length of the Galactic thin disk, h_R, we produced a grid of models, with different values of the disk scale length. For each disk model, we simulate catalogues of data similar to the observed data set, including photometric errors. To avoid too large Poisson noise in the Monte Carlo simulations, we computed at least five simulations of 30 square degrees for each of the models tested in our analysis. The data are binned with a step of 1 mag in K_S, and 0.1 in J-K_S We determine the best value of the density scale length using a maximum likelihood technique, applied on a set of bins of K_s and J-K_S to the whole set of data, for stars brighter than 15 in K_S. The likelihood of each model is computed as described in Bienaymé *et al.* (1987):

Let q_i be the number of stars predicted by the model in bin i and f_i be the observed number. In case the deviations of f_i's with respect to q_i just reflect random fluctuations in counts, each f_i would be a Poisson variate with mean q_i. Then the probability that f_i be observed is:

$$\mathrm{d}P_i = \frac{q_i^{f_i}}{f_i!} \exp(-q_i).$$

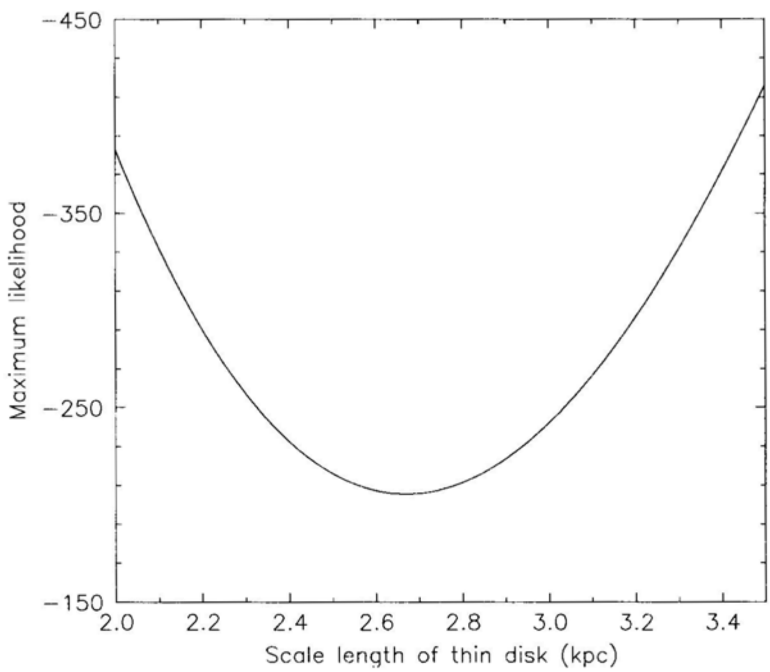

Figure 1. Maximum-likelihood curve for the density scale length, h_R, of the thin disk.

Then the likelihood of a set of q_i's given the relevant f_i is:

$$L = \ln \sum \mathrm{d}P_i = \sum_i (-q_i + f_i \ln q_i - \ln f_i!).$$

In search of the models that maximise L, it is convenient to use the reduced form:

$$L - L_0 = \sum_i f_i \left(1 - \frac{q_i}{f_i} + \ln \frac{q_i}{f_i}\right)$$

where L_0 is constant and $L - L_0 = 0$ for a model which would exactly predict all fi's.

Fig. 1 shows the maximum likelihood curve for different values of h_R for our data set. The maximum likelihood is obtained with a scale length, h_R, of 2.7 kpc.

3.3 *Confidence interval*

The confidence interval of our fit comes from the estimation of the variation of the likelihood due to the Poisson noise on the data. The likelihood of two realizations of the same model, differing just by the Poisson statistics, gives the value to add to the maximum likelihood to get the confidence level. We thus obtained an uncertainty of ±0.1 kpc for h_R. These uncertainties account only for Poisson errors, but do not account for other sources of errors that are very difficult to quantify, such as the uncertainties on the extinction model or on the luminosity function.

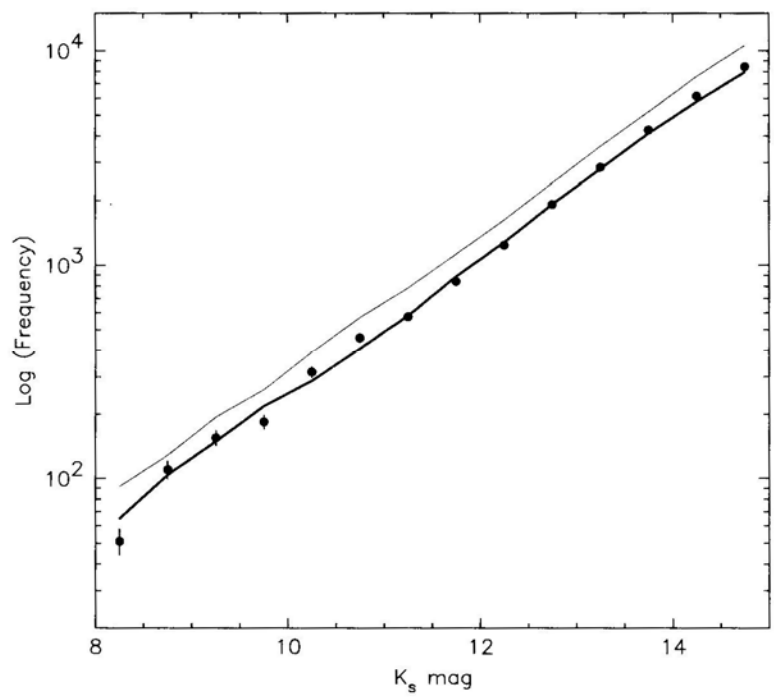

Figure 2. K_S star counts in 2MASS field. **Filled circle:** Observed counts with 1σ error bars (Poisson noise only). **Thick line:** Predicted counts assuming a density scale length, h_R, of 2.7kpc. **Thin line**: Predicted counts with h_R of 3.5 kpc.

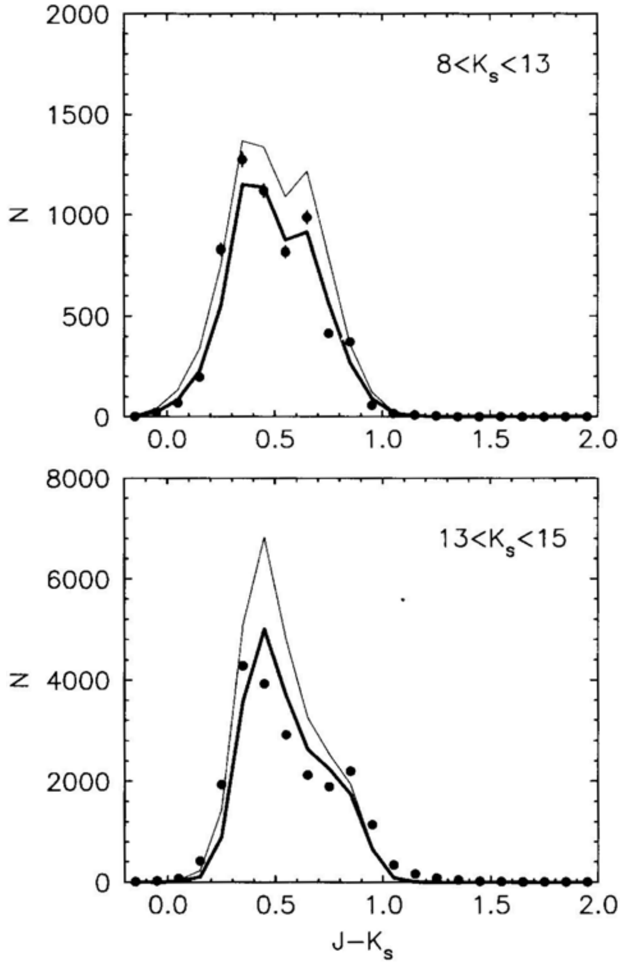

Figure 3. J-K$_S$ distributions of sources brighter than K$_S$ = 15 in 2MASS field. The symbols are as in figure 2.

3.4 *Comparison with observed data*

In Fig. 2, the observed apparent K$_S$ magnitude distribution is compared with the model predictions with thin disk scale lengths of 2.7 and 3.5 kpc. The total observed counts are in good agreement with the model predictions assuming the thin disk scale length, h_R, of 2.7 kpc. Fig. 3 shows J-K$_S$ distributions alongwith model predict-tions for two different thin disk scale lengths, h_R = 2.7kpc and h_R = 3.5 kpc. The excess of stars seen on Figs. 2 and 3 for h_R = 3.5 kpc, is significantly reduced with the new value of h_R. The model fit with data is not, however, completely satisfactory in J-K$_S$, which might be improved by a slight change of SFR history in the model. One expects that the Galactic evolution parameters will be better known after the analysis of the Hipparcos and Tycho catalogues. The Besançon model is in a further improvement phase by using the data from Hipparcos and Tycho (Robin *et al.* 1999).

4. Discussion and conclusion

There have been several determinations of the radial scale length in the thin disk of the Milky Way either from photometric or kinematic approach. The many different determinations based on photometry or star counts give possible values in a large range (Kent *et al.* 1991 give a recent review; see also Robin *et al.* 1992). To add to this apparent confusion, many published density scale lengths are deduced from kinematic data using the asymmetric drift relation, but generally the expressions used for the asymmetric drift are simplified without any strong theoretical support. For example, it is frequently assumed that the kinematic and density scale lengths are equal. Only in a recent contribution (Fux & Martinet 1994), the term including the shape (spherical, cylindrical...) of the potential is adjusted.

Here, we have presented a direct measurement of density scale length of thin disk by analysing the data using a synthetic model, reproducing observable quantities (magnitude and color counts). This method is expected to avoid systematic bias that can be encountered in inversing the process. The resulting density scale length of 2.7 ± 0.1 kpc has to be compared to some recent works: the value of 2.3 ± 0.1 kpc obtained by Ruphy *et al.* (1996) by analysing the DENIS near-infrared data towards anticenter direction; Robin *et al.* 1992: 2.5 ±0.3 kpc, from optical star counts towards the Galactic anticenter; Fux & Martinet 1994: $h_R = 2.5^{+0.8}_{-0.6}$ kpc, based on a rigorous analysis of the asymmetric drift relation; Porcel *et al.* 1998: 2.1 ± 0.3 kpc, from the near-infrared K-band counts from the TMSG (Two Micron Galactic Survey); Bienaymé (1999) finds out that the scale density length of the Galactic disk is 1.8 ± 0.2 kpc, using the neighbouring stars in Hipparcos catalogue. This quite short scale length is also fully compatible with star counts at median latitude regions of the Galaxy (Ojha *et al.* 1996).

We also notice that an increase of h_R (~ 0.8 kpc) predicts a significant excess of stars (in Figs. 2 and 3). It follows that the present 2MASS data are clearly incompatible with the larger values of h_R for thin disk, such as those found by van der Kruit (1986) (h_R = 5.5 ± 1 kpc); Lewis & Freeman (1989) (h_R = 4.4 ± 0.3 kpc, based on kinematics of disk K giants).

We conclude that the scale length of the Galactic thin disk is rather short (2.7 ± 0.1 kpc). Additional information will be gained when other 2MASS surveys in different directions of the Galaxy will be analyzed globally by using the Besançon model.

Acknowledgements

This publication makes use of data products from the Two Micron All Sky Survey, which is a joint project of the University of Massachusetts and the Infrared Processing and Analysis Center, funded by the National Aeronautics and Space Administration and the National Science Foundation. We thank Dr. Annie Robin for letting us use their model of stellar population synthesis. This research has made use of the DEC-ALPHA system of the Optical CCD astronomy programme of TIFR.

References

Bienaymé, O., Robin, A. C., Crézé, M. 1987, *Astr. Astrophys.,* **180,** 94.
Bienaymé, O. 1999, *Astr Astrophys.,* **341,** 86.
De Vaucouleurs, G., Pence, W. D. 1978, *Astr. J.,* **83,** 1163.
Einasto, J. 1979, *The large scale characteristics of the Galaxy,* IAU Symp. **84,** p. 451.
Freeman, K. C. 1970, *Astrophys. J.,* **160,** 811.
Fux, R., Martinet, L. 1994, *Astr. Astrophys.,* **287,** L21.
Haywood M. 1994, *Astr. Astrophys.,* **282,** 444.
Haywood, M., Robin, A. C., Crézé, M. 1997a, *Astr. Astrophys.,* **320,** 428.
Haywood, M., Robin, A. C., Crézé, M. 1997b, *Astrophys.,* **320,** 440.
Kent, S. M., Dame, T. M., Fazio, G. 1991, *Astrophys.* ***J.,*** **378,** 131.
Knapp, G. R., Tremaine, S. D. Gunn, J. E. 1978, *Astr.* ***J.,*** **83,** 1585.
Lewis, J. R., Freeman, K. C. 1989, *Astrophys.* ***J.,*** **97,** 139.
McCuskey, S. W. 1969, *Astr. J.,* **74,** 807.
Ojha, D. K., Bienaymé, O., Robin, A. C., Crézé, M., Mohan, V. 1996, *Astr. Astrophys.,* **311,** 456.
Porcel, C., Garzón, F., Jiménez-Vicente, J., Battaner, E. 1998, *Astr. Astrophys.,* **300,** 136.
Robin, A. C., Crézé, M. 1986, *Astr. Astrophys.,* **157,** 71.
Robin, A. C., Oblak E. 1987, *Publ. Astron. Inst. Czech. Acad. Sci.,* **69,** 323.
Robin, A. C., Crézé, M., Mohan, V. 1992, *Astrophys. J.,* **400,** L25.
Robin, A. C., Haywood, M., Crézé, M., Ojha, D. K., Bienaymé, 0. 1996, *Astr. Astrophys.* **305, 125.**
Robin, A. C., *et al.* 1999 (in preparation).
Rocca-Volmerange, B., Lequeux, J., Maucherat-Joubert, M. 1981, *Asti: Astrophys.,* **104,** 177.
Ruphy, S., Robin, A. C., Epchtein, N., Copet, E., Bertin, E., Fouque, P., Guglielmo, F. 1996, *Astr. Astrophys.,* **313,** L21.
van der Kruit, P. C. 1986, *Astr. Astrophys.,* **157,** 230.

J. Astrophys. Astr. (2000) **21**, 61–76

A New Scheme of Radiation Transfer in HII Regions including Transient Heating of Grains

S. K. Ghosh & R. P. Verma, *Tata Institute of Fundamental Research, Homi Bhabha Road, Mumbai 400005, India.*

Received 2000 April 15; accepted 2000 May 10

Abstract. A new scheme of radiation transfer for understanding the infrared spectra of HII regions, has been developed. This scheme considers non-equilibrium processes (e.g. transient heating of the very small grains, VSG; and the polycyclic aromatic hydrocarbon, PAH) also, in addition to the equilibrium thermal emission from normal dust grains (BG). The spherically symmetric interstellar dust cloud is segmented into a large number of "onion skin" shells in order to implement the non-equilibrium processes. The scheme attempts to fit the observed SED originating from the dust component, by exploring the following parameters: (i) geometrical details of the dust cloud, (ii) PAH size and abundance, (iii) composition of normal grains (BG), (iv) radial distribution of all dust (BG, VSG & PAH).

The scheme has been applied to a set of five compact H II regions (IRAS 18116 – 1646, 18162 – 2048, 19442 + 2427, 22308 + 5812, and 18434 – 0242) whose spectra are available with adequate spectral resolution. The best fit models and inferences about the parameters for these sources are presented.

Key words. HII regions—radiative transfer—PAH—VSG.

1. Introduction

Till recently, the mid to far infrared spectral energy distribution (SED) of Galactic star forming regions in general was available only in the four IRAS bands (12, 25, 60 and 100 μm). In some relatively rare cases, spectroscopy in the 10 μm band through the atmospheric window, was also available. However, the situation has changed drastically recently, due to the advent of the Infrared Space Observatory (ISO). The ISOPHOT photometer along with ISO-SWS and ISO-LWS spectrometers together has revolutionized the availability of information about SED of the astrophysical sources in general.

In the literature, several radiation transfer schemes have been used for interstellar dust clouds with embedded YSOs in spherical (e.g. Scoville & Kwan 1976; Leung 1976; Churchwell, Wolfire, & Wood 1990) as well as cylindrical (Ghosh & Tandon 1985, Dent 1988, Karnik & Ghosh 1999) geometries. All of these considered the dust grains to be in thermal equilibrium. The role of non-equilibrium processes (resulting in transient heating/excitation of grains, particularly in the vicinity of a source of UV radiation) has become evident from significant near and mid infrared continuum emission detected in Galactic star forming regions (Sellgren 1984; Puget, Leger & Boulanger 1985, Boulanger, Baud & van Albada 1985) as well as spectral features (Leger & Puget 1984; Allamandola *et al.* 1985; Puget & Leger 1989). The importance of these processes has also been demonstrated in extragalactic nuclei/star forming regions (Moorwood *et al.* 1996; Metcalfe *et al.* 1996, Ghosh, Drapatz, & Peppel 1986). A comparison of the observed mid-IR spectral features with laboratory data, has led to the identification of a new constituent of the interstellar medium-polycyclic aromatic hydrocarbons (PAH). The enhanced continuum emission in the near and mid IR has been mainly attributed to the very small grains (VSG) of radii 10–100 Å. Hence, it is obviously important to include the non-equilibrium processes in attempting to model the observed SED of star forming regions in general. Basically, grains of very small size or a large organic molecule, with effective heat capacity comparable to the energy of a single UV photon get excited (for a short time) to an energy state well above its thermal equilibrium state corresponding to the local radiation field. The photons emitted during the de-excitation process contribute to the near/mid IR part of the SED, which shows continuum excess and emission features which are unexplained by radiative transfer models considering the emission from large grains in thermal equilibrium alone. Recently, Siebenmorgen & Krugel (1992) have attempted to quantify the properties of the dust components relevant for non-equilibrium processes (VSG & PAH), from the infrared data of sources in different astronomical environments in our Galaxy. The role of VSG on the infrared emission from externally heated dust clouds has been studied by Lis & Leung (1991). Krugel & Siebenmorgen (1994) have presented a method to model the transfer of radiation in dusty galactic nuclei, which includes the presence of VSG and PAH.

Here we present a scheme of radiative transfer developed by us which is applicable in spherical geometry. This includes, in addition to the dust grains in thermal equilibrium (of normal size, hereafter big grains or BG), the transient heating of very small grains (VSG) as well as the PAH molecules. An attempt has been made to model five compact HII regions: IRAS 18116 – 1646, 18162 – 2048, 19442 + 2427, 22308 + 5812 and 18434 – 0242 using the above scheme.

In section 2, the radiative transfer modelling scheme is briefly described. The results of modelling the five compact HII regions are presented in section 3. The last section (4) consists of discussion.

2. The modelling scheme

2.1 *Dust components and their properties*

The normal grains (BG) consist of two components: astronomical silicate and graphite. Their size distribution is taken as per Mathis, Rumpl & Nordsieck (1977) to be a power law, $n(a) \propto a^{\gamma}$, with —3.5 as the exponent. The lower and upper limits of the grain radii are taken to be 0.01 μm and 0.25 μm respectively as recommended by Mathis *et al.* (1983), for both astronomical silicate as well as graphite grains. The scattering and absorption coefficients, and anisotropic scattering factors have been taken from Draine & Lee (1984) and Laor & Draine (1993).

The VSG component is taken to be graphite grains of a single size : either 10 Å or 50 Å in radius. Their optical properties have also been taken from Draine & Lee

(1984). Abundance of VSG is connected to that of the normal grains through a scaling factor Y_{VSG}, which gives the fraction of dust mass in VSG form to the normal BG form. The value of Y_{VSG}, was taken from Desert *et al.* (1990), which is needed to account for the 2200 Å bump in the average interstellar medium in the Galaxy, and it has been held fixed for all models considered here.

The PAH component is assumed to be either a single molecule with about 15–30 atoms, or a large complex consisting of 10–20 of these molecules as used by Siebenmorgen (1993). Their optical properties, feature centres, feature shape and widths have been taken from Leger & d'Hendecourt (1987). The abundance of PAH component is also connected through a scaling factor Y_{PAH} to the normal grains (BG). There are two additional parameters explored in the modelling of the observed PAH spectral features : (i) the radius of the PAH molecule / complex, α_{PAH}; and (ii) the de-hydrogenation factor, f_{de-H}. The value of f_{de-H} lies between 0 and 1 (f_{de-H} = 0 refers to completely hydrogenated PAH). Whereas α_{PAH} has implications of heat capacity and hence the efficiency of transient heating for a given radiation field, the f_{de-H} affects the ratios of PAH features resulting from the C–H versus C=C stretch modes.

2.2 *Geometry*

The star forming region is considered as a spherical dust cloud immersed in an isotropic interstellar radiation field, with an embedded source of energy (e.g. a ZAMS star) at its centre. A central cavity in this cloud represents sublimation/destruction of grains in the intense radiation field of the central source. A schematic of the dust cloud is presented in Fig. 1. This spherically symmetric dust cloud, is divided into a large number of concentric contiguous spherical shells (say $Sh_1, Sh_2, \ldots, Sh_N$) like "onion skins". Each shell, Sh_i, is identified by its inner and outer radii (R_i^{min} and R_i^{max}; see Fig. 1). These shells can be of different selectable thicknesses, depending on the optical depth at the shortest relevant wavelength. In order to incorporate the presence of both – normal grains (BG, responsible for emission at thermal equili-

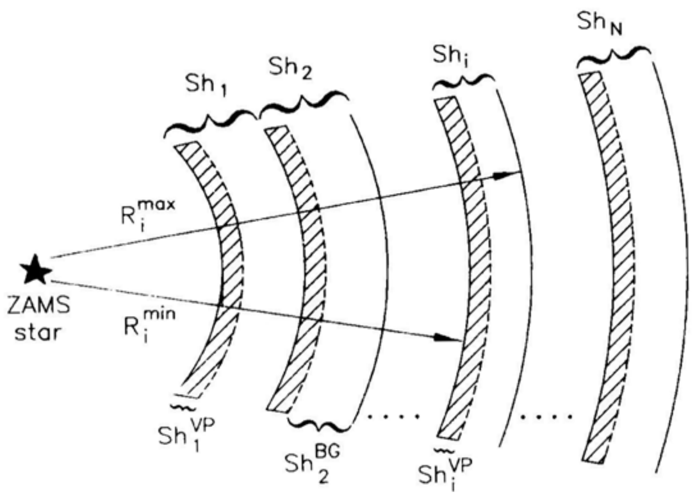

Figure 1. Schematic diagram of the shell structure of the cloud.

brium), as well as the grains responsible for non-equilibrium emission (VSG and PAH), each shell is subdivided into a pair of sub-shells, Sh_i^{BG} and Sh_i^{VP} corresponding to these two components respectively. Whereas the former consists of only BG, the latter consists of only the VSG and PAH.

The full detailed radiative transfer calculations assuming the normal grains to be in thermal equilibrium, are performed in each of the sub-shells Sh_i^{BG}, for i =1, 2, ... , N. The subshells Sh_i^{VP}, go through a statistical mechanical treatment describing the non-equilibrium emission processes for the VSGs and the PAHs. For simplicity of computations, the sub-shells Sh_i^{VP} are considered to be very thin compared to the total thickness of the shell Sh_i, and this sub-shell is assumed to be placed at the inner edge of the shell Sh_i (see Fig. 1). The final results are expected to be insensitive to the above simplification since individual shells are optically thin.

Radiative transport at each of the two sub-shells is carried out as a two point boundary value problem, the two boundary conditions being the incident radiation fields at the two surfaces. The calculations begin with the given spectrum emitted by the embedded energy source (in general, an Initial Mass Function weighted synthetic stellar spectrum ensemble) incident at the inner boundary of the first shell Sh_1. The outer surface of the last (outermost) shell, Sh_N, has the interstellar radiation field (ISRF) incident on it from the outside. Starting from the "core" side of the first shell, the radiation is transported through the sub-shell Sh_1^{VP} first and the emergent processed spectrum is considered to be incident on the other sub-shell $\mathrm{Sh}_1^{\mathrm{BG}}$. The emergent spectrum from the latter is the processed output of the entire shell Sh_1 and is used as input boundary condition for the next shell Sh_2. In this manner, the radiation field is transported outward from shell Sh_1 to Sh_2 ... till the last shell, viz., Sh_N is reached. This entire processing from shell 1, 2, ... to N, constitutes one iteration. Several such iterations (typically 5–10) are carried out until a set of predetermined convergence criteria are satisfied. The emerging spectrum from the last shell, Sh_N, is the desired output of the full model. The number of shells used for a specific source is determined by the criterion that the shell is optically thin in the shortest relevant wavelength.

2.3 *Processing of transient heating of the VSG and the PAH*

As described above, the dust components in a shell for which the non-equilibrium emission processes are important, are segregated into a separate sub-shell (Sh_k^{VP}) consisting only of the VSG and the PAH. The interaction of the total incident radiation field from both the surfaces of this sub-shell, (I^{ν}_{in}), with the VSG component, is considered using a code developed by us based on the statistical mechanical treatment prescribed by Desert *et al.* (1986). The incident radiation, partly extinguished by the VSGs ($I^{\nu}_{\mathrm{VP}}=I^{\nu}_{\mathrm{in}})\times e^{-T^{\nu}_{\mathrm{VSG}}}$), is considered incident on the PAH component and a similar computation is repeated. The final emerging spectrum consists of three components:

- the originally incident radiation extinguished by *both* VSG as well as PAH, ($I^{\nu}_{\mathrm{out}} = \mathrm{I}^{\nu}_{\mathrm{in}}\times e^{-(T^{\nu}_{\mathrm{VSG}}+T^{\nu}_{\mathrm{VSG}})}$),
- the emission from the VSG component, and
- the emission from the PAH component.

Whereas the first component is direction sensitive (the two surfaces get different contributions depending on the original spectrum incident at the other surfaces), the latter two contribute equally to the two surfaces.

The VSG and PAH components of grains have fluctuating temperature, mainly because their enthalpy (internal energy) is comparable to the energy of UV or visual photons. This means, the multiphoton absorption processes can become important (depending on the exact radiation field and the details of thermal and optical properties of these grains) as they can lead to a modified temperature distribution. An iterative method has been used here to consider these multiphoton processes for VSGs and PAHs separately. The method assumes a single grain in an isotropic radiation field, and follows the evolution of the grain temperature by solving the relevant stochastic differential equation.

A scheme of between 100 to 400 levels of internal energy (covering 0.5 eV to 200 eV) for considering discrete heating/cooling processes; and 400 energy levels (for energies 1.25×10^{-3} eV to 0.5 eV) for considering the continuum processes, has been incorporated. A total of 97 frequency grid points covering 0.0944 μm to 5000μm have been used. Several grid points are densely packed around the five PAH features at 3.3, 6.2, 7.7, 8.6 and 11.3 μm.

2.4 *Radiation transport through normal grains (BG)*

Each of the sub-shells consisting of the normal grains, (Sh_k^{BG}, k = 1, 2, ... N), separately undergoes full radiative transport calculation using the code CSDUST3 developed by Egan *et al.* (1988) (see also Leung 1975). In CSDUST3, the moment equation of radiation transport and the equation of energy balance are solved simultaneously as a two-point boundary value problem. The effects of multiple scattering, absorption and re-emission of photons on the temperature of dust grains and the internal radiation field have been considered self-consistently. In addition, multi grain components, radiation field anisotropy and linear anisotropic scattering are also incorporated.

The same frequency grid of 97 points, as used for VSG and PAH, has been used here. In order to avoid non-convergence problems due to sharp changes in optical depth at any of the frequency grids, logarithmically increasing radial grid spacings have been used at the inner shell boundary. Similarly smoothly decreasing grid spacings have been used near the outer shell boundary.

2.5 *The modelling scheme*

The scheme aims to construct a model constrained by the observed SED covering the entire infrared and the sub-mm/mm region. Based on comparisons of the model predicted SEDs with the observed SED, various model parameters are fine tuned till the best fit model is identified. The following model parameters are explored:

- the total radial optical depth (represented at a fiducial wavelength of 100 μm);
- exponent of the dust density distribution power law;
- the ratio of graphite component to the astronomical silicate component for BGs;
- size of VSGs, a_{VSG}: either 50 Å or 10 Å:

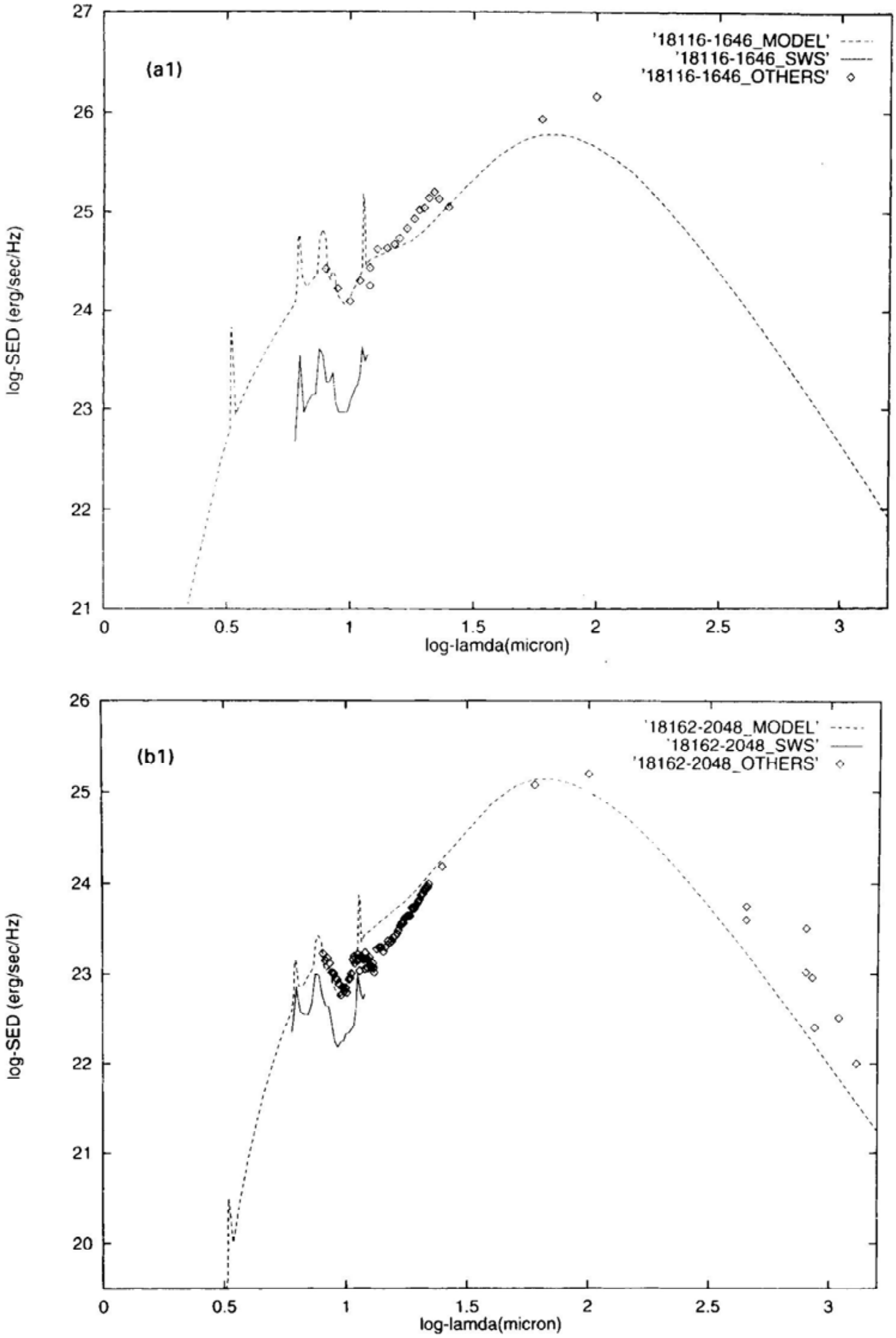

Figure 2. (*Continued*)

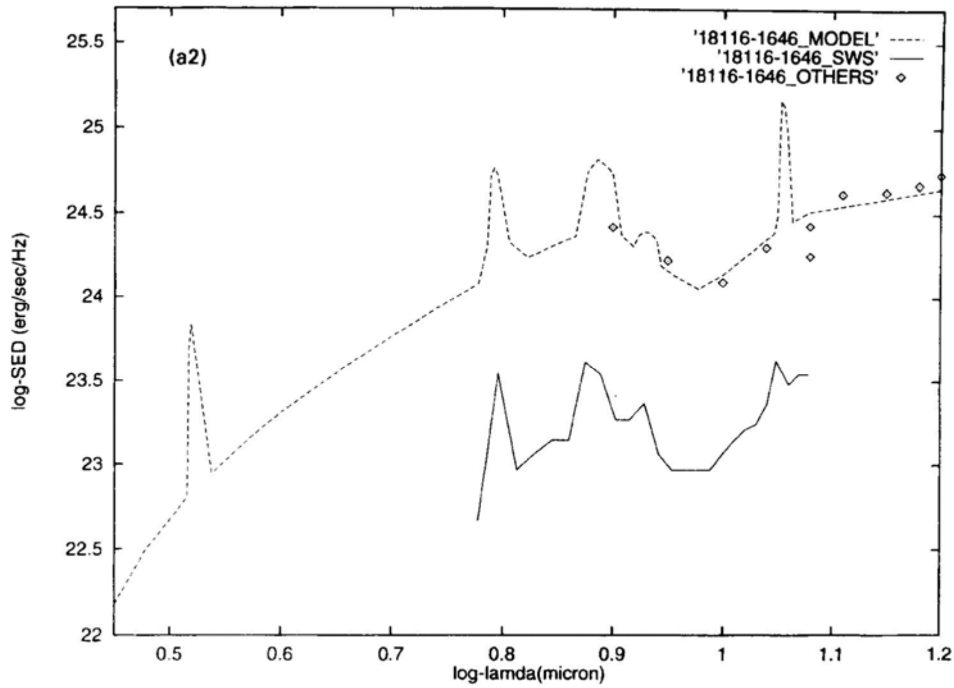

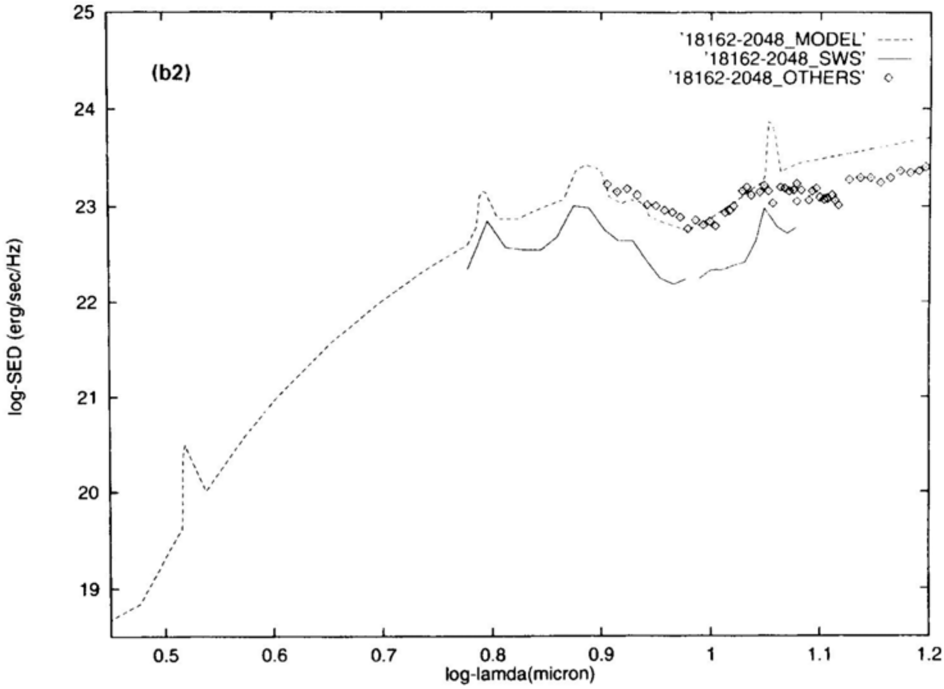

Figure 2. (*Continued*)

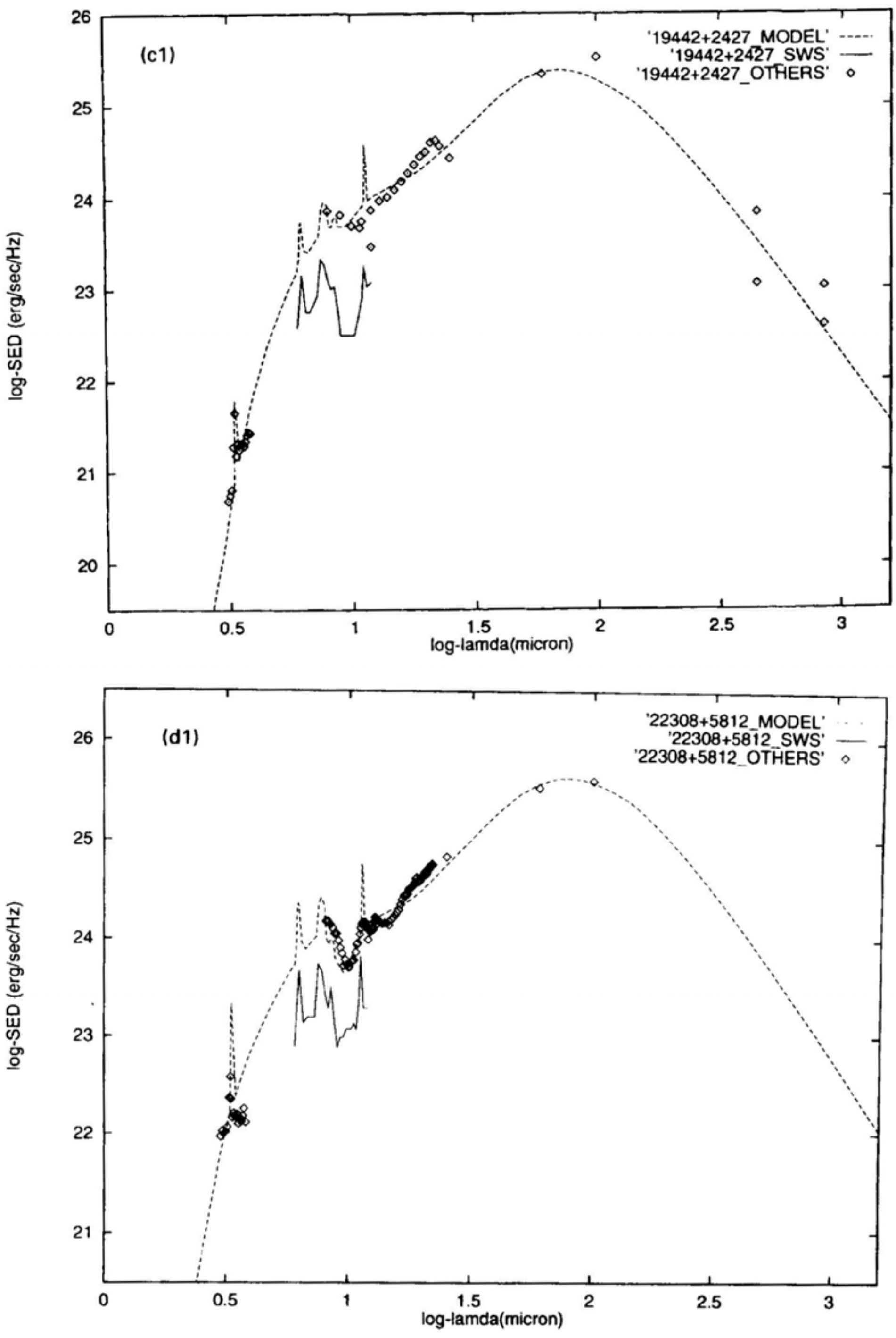

Figure 2. (*Continued*)

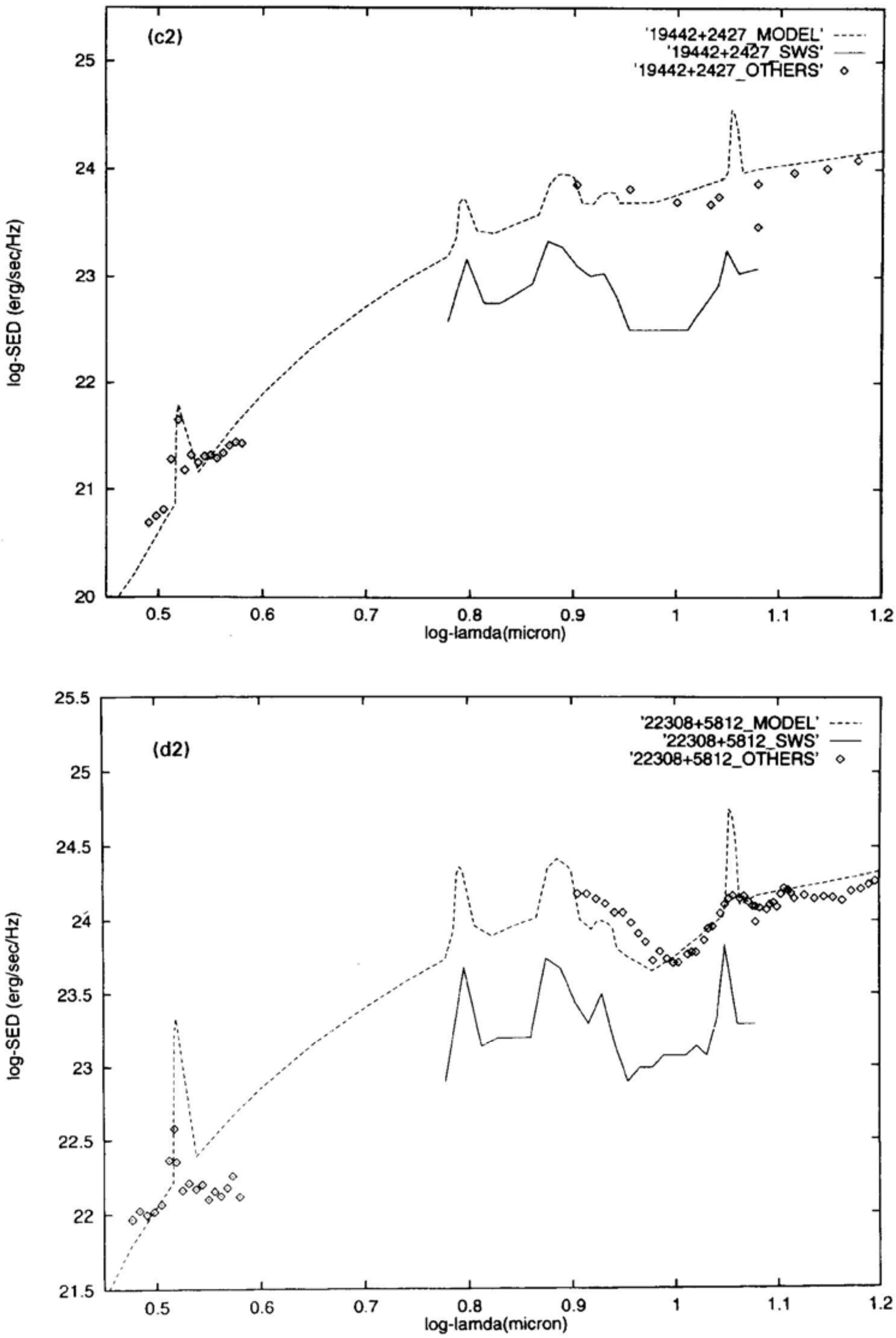

Figure 2. *(Continued)*

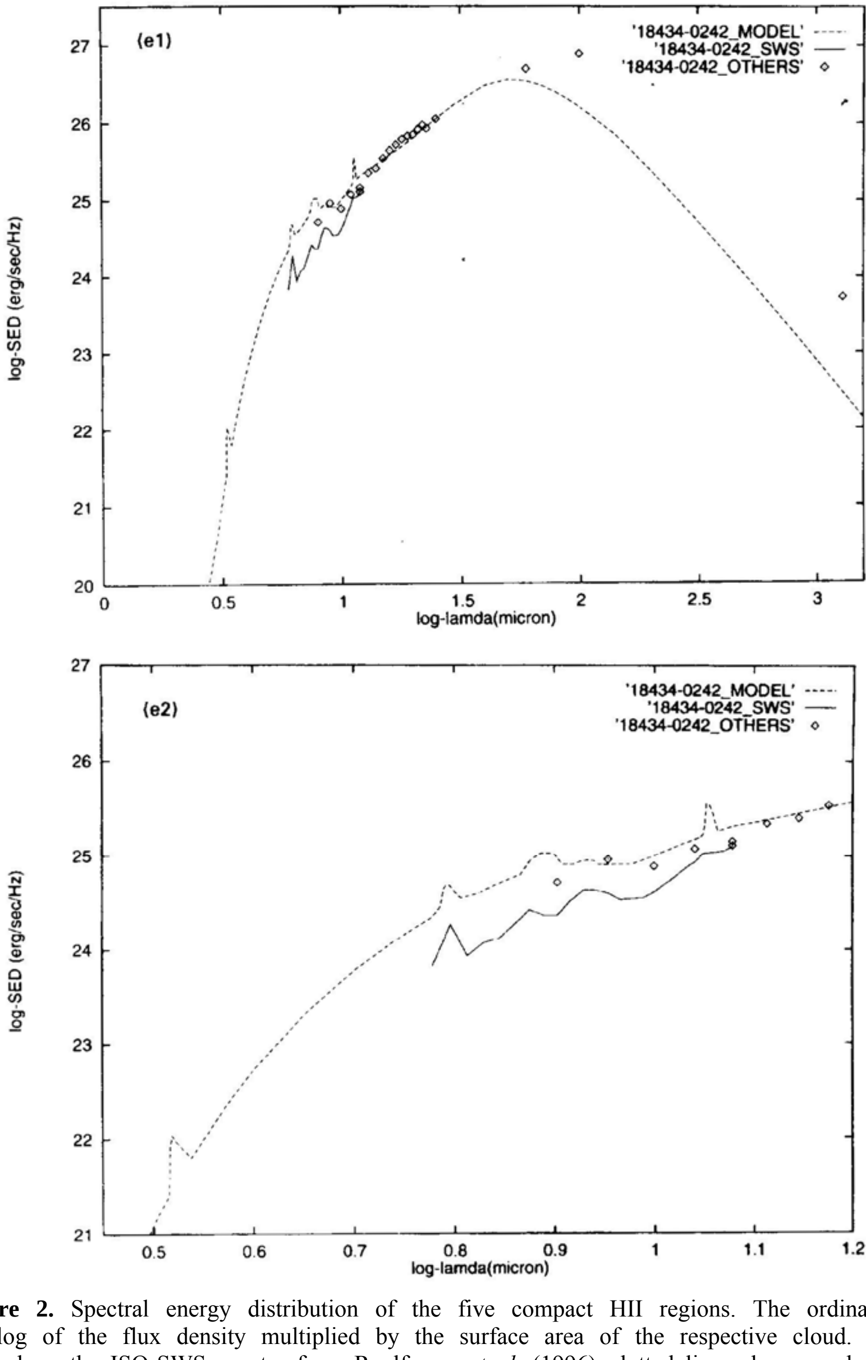

Figure 2. Spectral energy distribution of the five compact HII regions. The ordinate is the log of the flux density multiplied by the surface area of the respective cloud. Solid lines show the ISO-SWS spectra from Roelfsema *et al.* (1996); dotted lines show our best fit model spectra; diamonds show other observations. Other observations include — 3 μm observations from de Muizon *et al* (1990), IRAS LRS spectra from Olnon & Raimond (1986) or from Volk & Cohen (1989), IRAS PSC flux densities, sub-mm observations from McCutcheon *et al.* (1995), Jenness et al. (1995) or Barsony (1989), and 1.3 mm observation of Chini *et al* (1986). In order to show the PAH features clearly, mid IR region of the SEDs are shown separately.

- size of PAH molecule / cluster, a_{PAH}: 4.6 Å or 8 Å or 13.6 Å;
- relative abundance of PAH compared to BGs, Y_{PAH} (a constant or varying with the radial distance) ; and
- the de-hydrogenation factor, f_{de-H}

The inner radius (R_{in}), for each model of the spherical cloud, has been determined using the constraint that the temperature of the BG is equal to 1500 K, the sublimation temperature of the normal big grains (graphite and astronomical silicate). The radial dust density distribution law has been assumed to be a power law $n_d(r) \propto r^{-\alpha}$, and the values of α that have been explored are 0, 1 and 2.

3. Application of the modelling scheme

In order to demonstrate the usefulness of the scheme described above, an attempt has been made to apply the same to a few HII regions. The question is : in spite of rather simplistic treatment, can we get any insight into physical details of these sources?

3.1 *The sample of compact KII regions*

With the advent of Infrared Space Observatory (ISO), it has become now possible to have precise spectroscopic information in the entire infrared band encompassing near to far infrared region. The spectroscopic results for a sample of six Galactic compact HII regions, covering four of the five major PAH features have been published by Roelfsema *et al.* (1996). We have chosen five out of their six sources for our detailed study. The sixth source IRAS 21190+5140, identified with M1-78 and variously considered as HII region and planetary nebula (Puche *et al.* 1988; Acker *et al.* 1992), has not been considered here. Although the published spectral results from ISO is rather limited (6-12 μm), if the IRAS Point Source Catalog (IRAS PSC) measurements (at 12, 25, 60 and 100 μm), IRAS Low Resolution Spectra (IRAS LRS; between 8 and 22μm) and ground based spectroscopy around the 3.3 μm PAH feature, are included (whenever available), then sufficient observational constraints can be placed on the radiative transfer models. All these measurements have been compiled to construct the SEDs for the five compact HII regions, which are displayed in Fig. 2.

The total luminosity, L_{tot} has been taken from Roelfsema *et al.* (1996) for all the sources except for IRAS 18434–0242. The luminosity for IRAS 18434 — 0242 listed by them is too low compared to that estimated from the IRAS data. The latter has been used here for modelling. Assuming the embedded source to be a single ZAMS star of luminosity L_{tot}, a Planckian spectral shape with corresponding temperature taken from Thompson (1984), has been assumed and listed in Table 1. Since distance estimates are available for all these sources, angular sizes are required to fix the outer radii of the clouds. The mid infrared angular sizes are estimated by comparing the flux densities at 12 μm as measured by IRAS-LRS and the ISO-SWS and the solid angle covered by the ISO-SWS. It is assumed that the source size is smaller than the IRAS-LRS beam and has constant brightness per unit solid angle. The entire size of the cloud has been estimated from the 12μm size by using empirical relation between angular size and the wavelength for compact HII regions (Mookerjea & Ghosh 1999).

3.2 *Results of modelling*

It has been possible to get reasonable fits to the observed SEDs of all the five compact HII regions by varying parameters of our modelling scheme. The predicted spectra and the observations are compared in Fig. 2.

The following comments are valid for all the five compact HII regions studied here. It was found that the models with uniform density distribution i.e. $n(r) \propto r^0$ (as opposed to $n(r) \propto r^{-1}$ or r^{-2}) gave much better fits to the SEDs. The VSGs with a_{VSG} = 50 Å and the PAHs with intermediate size (i.e.a_{PAH} = 8 Å) give better fits to the respective spectra. The de-hydrogenation factor, f_{de-H}, needs to be zero (corresponding to $N_H = \sqrt{6 \times N_C}$) in order to fit the relative strengths of the PAH features for all the five sources. This value of f_{de-H}, is typical for the types of PAH which have been strongly proposed in the literature, viz., Coronene & Ovalene (Leger & Puget 1984). In addition, this f_{de-H}, is consistent with the value of a_{PAH} (8 Å) inferred from our modelling, since such PAHs are expected to be completely hydrogenated in the emission zones (Allamandola *et al* 1989). Table 2 lists those best fit parameters related to the various dust components, which are valid for the entire sample of compact HII regions.

It has been found that, whereas the BG and VSG components should exist throughout the cloud, it is absolutely necessary that the PAH component must be confined to a thin inner region ($R_{out}^{PAH} \ll R_{out}$), in order to reproduce the PAH features. The size of this region is quantified by a parameter η_{PAH}, which is defined as: η_{PAH} = $((R_{out}^{PAH} - R_{in})/(R_{out} - R_{in}))$. This parameter had to be varied for each source, till a good fit to the spectrum was obtained. In addition, the abundance of PAH relative to BGs, Y_{PAH}, needed to be increased by a factor 10 relative to the normal value

Table1. Input parameters of the compact HII regions.

IRAS Source	L ($L_\odot$)	T_* (K)	D_{sun} (kpc)	θ_{dia} (″)	R_{out} (pc)
18116 − 1646	1.6×10^5	40,000	4.4	105	1.12
18162 − 2048	2.8×10^4	30,900	1.9	63	0.29
19442 + 2427	5.4×10^4	35,500	2.3	93	0.52
22308 + 5812	8.8×10^4	37,500	5.7	95	1.31
18434 − 0242	1.0×10^6	48,000	7.4	38	0.69

Table. 2. Dust parameters valid for the entire sample of compact HII regions.

Dust component	Parameter (unit)	Value
BG	a_{min} (μm)	0.01
	a_{max} (μm)	0.25
	γ	−3.5
VSG	a_{VSG} (Å)	50.0
	Y_{VSG}	4.70×10^{-4}
PAH	a_{PAH} (Å)	8.0
	Y_{PAH}	4.30×10^{-3}
	f_{de-H}	0.0

Table 3. Best fit parameters of the compact HII regions as determined by modelling.

IRAS source name	R_{in} (pc)	R_{out} (pc)	n_H (cm^{-3})	M_{Tot} ($M_\odot$)	τ_{100}^{tot}	Graphite : Silicate (% : %)	η_{PAH}
18116 − 1646	1.4×10^{-3}	1.12	1.32×10^4	1.9×10^3	0.056	75 : 25	2.1×10^{-2}
18162 − 2048	5.3×10^{-4}	0.29	1.32×10^5	3.3×10^2	0.14	88 : 12	2.7×10^{-2}
19442 + 2427	7.5×10^{-4}	0.52	5.30×10^4	7.7×10^2	0.10	95 : 5	1.5×10^{-2}
22308 + 5812	1.5×10^{-3}	1.31	1.38×10^4	3.2×10^3	0.068	77 : 23	1.3×10^{-2}
18434 − 0242	2.2×10^{-3}	0.69	5.30×10^4	1.8×10^3	0.14	95 : 5	5.5×10^{-2}

obtained by Desert *et al.* (1990). However this does not lead to any conflict with the available carbon, since $\eta_{PAH} \ll 1$. The values of the best fit parameters specific to each source, are presented in Table 3.

4. Discussion

The following inferences can be drawn about the sources modelled here, provided the basic assumptions (e.g. spherical symmetry; sources of energy located only at the centre of the cloud; etc.) are not at great variance from the reality.

The most favoured radial dust density distribution law, *for all five sources,* turns out to be of uniform density. This can perhaps be understood in terms of the far infrared constraints (IRAS-PSC 60 and 100 μm data). If the dust density is falling with radial distance, then in order to fit the FIR part of the SED, so high a dust density is required at the vicinity of the embedded ZAMS star, that the mid infrared emission becomes invisible. This problem can perhaps be avoided in a non-spherically symmetric geometry. We have explored the effects of relaxing the assumption that $R_{in} = R_0$, where R_0 is the radial distance at which (BG) grain temperature becomes equal to the sublimation temperature (1500 K). The most important effect of making $R_{in} > R_0$ is to drastically modify the near and mid infrared continuum level of the predicted spectrum. In addition, the role of non-equilibrium processes vis-a-vis thermal equilibrium emission of the PAH features, as well as the continuum due to VSG, changes significantly.

A quick perusal of Figure 2 and Tables 2 and 3 brings out the following facts:

- All the compact HII regions considered here, are deeply embedded stars; total optical depth at 100 μm in the range of 0.056-0.14. This is necessary to explain the far IR spectra observed by IRAS.
- PAH is confined only to a thin central shell; the thickness of this shell being just a few per cent (1.3 — 5.5%) of the total thickness of the dust cloud. As these sources are optically thick at mid IR, if the PAH is distributed throughout the cloud, its emission which occurs in the inner hot region where high energy photons responsible for non-equilibrium processes are present, will be absorbed by the outer cooler shells, and PAH features will not be detectable.
- The BGs are dominated by graphites, with silicates contributing less than 25%. The latter has been tied down rather precisely by the 10 μm silicate feature.
- ISO-SWS fluxes are generally much smaller than IRAS fluxes at similar wavelengths, indicating that SWS is not sampling full emission at mid IR and the source sizes at these wavelengths are much larger than the SWS beam size (14″ x 20″). With this in mind, we have not tried to fit the absolute fluxes of the SWS but only used its shape as indicative of the importance of PAH molecules.

The following comments can be made about the individual sources:

IRAS 18116-1646: It has relatively lower optical depth. The fit to the IR data is quite reasonable, except at 100 μm where IRAS flux is higher; no sub-mm observation exists for this source.

IRAS 18162-2048: This source (GGD27) was originally thought to be a HH object. However now it has been established as a star forming region with reflection nebulosity as well as outflow (see for example Stecklum *et al.* 1997). The region has several near IR and mid IR sources; the source of energy being close to IRS2. The size of this source at sub-mm wavelengths is ~ 1' (McCutcheon *et al.* 1995), consistent with the size for the best fit model. The mass of the envelope estimated by our model is not far from the estimate of Yamashita *et al.* (1987), viz., $200M_{\odot}$. They have proposed a disk geometry for this source. This source has very high optical depth. The fit to the IR data is quite reasonable but at the sub-mm wavelengths the calculated flux densities are lower than the observed ones.

IRAS 19442+2427: This source lies in the HII region S87. The size of this source at sub-mm wavelengths is ~1′ (Jenness *et al.* 1995), consistent with the size for the best fit model. This source has medium optical depth. The fit to all the observations from 3 μm to 850 μm is quite reasonable.

IRAS 22308+5812: It has relatively lower optical depth. The fit to the IR data is quite reasonable; no sub-mm observation exists for this source.

IRAS 18434–0242 : This source is the most luminous source with high optical depth. There are no IR observations for this source other than those from IRAS and ISO. IRAS PSC 100 μm as well as 1.3 mm observations are higher than calculated.

From the above, we conclude that our new scheme of radiative transfer which includes non-equilibrium processes (transient heating of the grains /PAH/ VSG) in addition to the emission in thermal equilibrium, can give important physical insight into Galactic star forming regions. If the simplifying geometrical assumptions of our scheme are valid, then several important inferences can be made about the five compact HII regions considered for modelling here.

Acknowledgements

It is a pleasure to thank Bhaswati Mookerjea for her help in preparing some input parameters.

References

Acker, A., Marcout, J., Ochsenbein, F., Stenholrn, B., Tylenda, R. 1992, *Strasbourg-ESO Catalogue of Galactic Planetary Nebulae* (Munchen, ESO).
Allamandola, L. J., Tielens, A. G. G. M., Barker, J. R. 1985, *Astrophys. J. (Lett),* **290**, L25.
Allamandola, L. J., Tielens, A. G. G. M., Barker, J. R. 1989, *Astrophys. J. (Suppl.),* **71,** 733.
Barsony, M. 1989, *Astrophys. J.,* **345,** 268.
Boulanger, F., Baud, B., van Albada, G. D. 1985, *Astr. Astrophys.,* **144,** L9.
Chini, R., Krugel, E., Kreysa, E. 1.986, *Astr: Astrophys.,* **167,** 315.
Churchwell, E., Wolfire, M. G., Wood, D. O. S. 1990, *Astrophys. J.,* **354,** 247.
de Muizon, M. J., d'Hendecourt, L. B., Geballe, T. R. 1990, *Astr. Astrophys.,* **227,** 526.
Dent, W. R. F. 1988, *Astrophys. J.,* **325,** 252.
Desert, F. X., Boulanger, F., Puget, J. L. 1990, *Astr. Astrophys.,* **237,** 215.
Desert, F. X., Boulanger, F., Shore, S. N. 1986, *Asti: Astrophys.,* **160,** 295.
Draine, B. T., Lee, H. M. 1984, *Astrophys. J.,* **285,** 89.
Egan, M. P., Leung, C. M., Spagna, G. F. 1988, *Computer Physics Communications,* **48,** 271.

Ghosh, S. K., Drapatz, S., Peppel, U. C. 1986, *Astr, Astrophys.,* **167**, 341.
Ghosh, S. K., Tandon, S. N. 1985, *Mon. Not. R. Astr Soc.,* **215**, 315.
Jenness, T., Scott, P. F., Padman, R. 1995, *Mon. Not. R. Astr. Soc.,* **276,** 1024.
Karnik, A. D., Ghosh, S. K. 1999, *J. Astrophys. Astr.,* **20,** 23.
Krugel, E., Siebenmorgen, R. 1994, *Astr. Astrophys.,* **282,** 407.
Laor, A., Draine, B.T. 1993, *Astrophys. J.,* **402,** 441.
Leger, A., d'Hendecourt, L. 1987, *PAH and Astrophysics* (eds.) A. Leger, L. d'Hendecourt & N. Boccara, p 223.
Leger, A., Puget, J. L. 1984, *Astr. Astrophys.,* **137,** L5.
Leung, C. M. 1975, *Astrophys. J.,* **199,** 340.
Leung, C. M. 1976, *Astrophys. J.,* **209,** 75.
Lis, D. C., Leung, C. M. 1991, *Icarus,* **91,** 7.
Mathis, J. S., Mezger, P. G., Panagia, N. 1983, *Astr. Astrophys.,* **128,** 212.
Mathis, J. S., Rumpl, W., Nordsieck, K. H. 1977, *Astrophys. J.,* **217,** 425.
McCutcheon, W. H., Sato, T., Purton, C. R., Matthews, H. E., Dewdney, P. E. 1995, *Astr. J.,* **110,** 1762.
Metcalfe, L., Steel, S. J., Barr, P., *et al.* 1996, *Astr. Astrophys.,* **315,** L105.
Mookerjea, B., Ghosh, S. K. 1999, *Bull. Astr Soc. India,* **27,** 567.
Moorwood, A. F. M., Lutz, D., Oliva, E., *et al.* 1996, *Astr. Astrophys.,* **315,** L109.
Olnon E M., Raimond, E. (IRAS Science Team) 1986, *Astr: Astrophys. (Suppl.),* **65,** 607.
Puche, D., Zijistra, A. A., Boettcher, C., *et al.* 1988, *Astr Astrophys.,* **206,** 89.
Puget, J. L., Leger, A. 1989, *Annu. Rev. Astron. Astrophys.,* **27,** 161.
Puget, J. L., Leger, A., Boulanger, F. 1985, *Astr. Astrophys.,* **142,** L19.
Roelfsema, P. R., Cox, P., Tielens, A. G. G. M., *et al.* 1996, *Astr. Astrophys.,* **315,** L289.
Scoville, N. Z., Kwan, J. 1976, *Astrophys. J.,* **206,** 718.
Sellgren, K. 1984, *Astrophys. J.,* **277,** 623.
Siebenmorgen, R. 1993, *Astrophys. J.,* **408,** 218.
Siebenmorgen, R., Krugel, E. 1992, *Astr. Astrophys.,* **259,** 614.
Stecklum, B., Feldt, M., Richichi, A., Calamai, G., Lagage, P.O. 1997, *Astrophys. J.,* **479,** 339.
Thompson, R. I. 1984, *Astrophys. J.,* **283,** 165.
Volk, K., Cohen, M. 1989, *Astr. J.,* **98,** 931.
Yamashita, T., Sato, S., Nagata, T., Suzuki, H., Hough, J. H., McLean, I. S., Garden, R., Gatley, I. 1987, *Astr Astrophys.,* 177, 258.

J. Astrophys. Astr. (2000) **21**, 77–90

Stellar Sources in the ISOGAL Inner Galactic Bulge Field (l = 0°, b = –1°)

D. K. Ojha[1], A. Omont[2], S. Ganesh[3], G. Simon[4] & M. Schultheis[2],
[1]*Tata Institute of Fundamental Research, Homi Bhabha Road, Mumbai 400 005, India.*
[2]*Institut d' Astrophysique de Paris, CNRS, 98 bis, Bd Arago, F-75014, Paris, France.*
[3]*Physical Research Laboratory, Navrangpura, Ahmedabad 380 009, India.*
[4]*DASGAL, CNRS UMR 8633, Observatoire de Paris, France.*

Received 2000 March 27; accepted 2000 May 11

Abstract. ISOGAL is a survey at 7 and 15 μm with ISOCAM of the inner galactic disk and bulge of our Galaxy. The survey covers ~ 22 deg^2 in selected areas of the central l = ±30 degree of the inner Galaxy. In this paper, we report the study of a small ISOGAL field in the inner galactic bulge (l = 0°,b = –1°, area = 0.033deg^2). Using the multicolor near-infrared data (IJK$_s$) of DENIS (DEep Near Infrared Southern Sky Survey) and mid-infrared ISOGAL data, we discuss the nature of the ISOGAL sources. The various color-color and color-magnitude diagrams are discussed in the paper. While most of the detected sources are red giants (RGB tip stars), a few of them show an excess in J-K$_s$ and K$_s$-[15] colors with respect to the red giant sequence. Most of them are probably AGB stars with large mass-loss rates.

Keywords. Stars: AGB and post-AGB — stars: circumstellar matter— stars: mass- loss - dust - infrared: stars — Galaxy: bulge.

1. Introduction

ISOGAL is the first detailed mid-infrared imaging survey of the inner Galaxy, tracing the Galactic structure and stellar populations. It combines 7 and 15 μm ISOCAM data with IJK$_S$ DENIS survey available for all ISOGAL fields. The main goals of the ISOGAL survey are:

- to trace the large scale disk structure using primarily red giants (gM) old stars;
- to determine the number of (dusty) young stars;
- to map the star formation regions through diffuse ISM emission and extinction;
- to study the stellar populations and the structure of the bulge.

Multicolor mid-infrared data are essential to analyse these features. ISOGAL quantifies the distribution of the stellar populations, especially of AGB and other bright red giants, and young dusty stars mostly of intermediate mass, as well as both diffuse and dense interstellar material.

The scientific results of the analysis of the first ISOGAL field are detailed in Perault *et al.* (1996). The analysis of a small field in the inner bulge (l = 0°, b = +1^0) (Omont *et al.* 1999) confirms the importance of combining 7 and 15 μm data. It shows the remarkable capability of ISOGAL to detect and characterize

Table 1. Log of ISOCAM and DENIS observations in the l = 0.0° , b = –1.0° field.

Identification	Filter	Pixel size	Date of observations	Julian date	Remarks
13600430[b]	LW3	6″	01/04/96	24501755	12–18 μm
32500354[b]	LW2	6″	06/10/96	24503635	5.5–8.5 μm
84100927[a]	LW3	6″	05/03/98	24508785	
84100926[a]	LW2	6″	05/03/98	24508785	
DENIS[a]	I, J, K_s	1″, 3″, 3″	10/09/96	24503375	

[a]Data used in the present paper.
[b]These observations have been used for variability calculation.

mass-losing AGB and RGB tip stars. Glass *et al.* (1999) analysed the ISOGAL fields near Baade's Windows of low obscuration towards the inner parts of the bulge. Most of the detected objects towards Baade's Windows are late-type M stars, with a cut-off for those earlier than about M3-M4. The ISOGAL results are also summarized in Omont *et al* (2000).

In this paper, we present the ISOGAL/DENIS data of a small inner bulge field (area = 0.033 deg^2), centered at l = 0°, b= —1°. We have combined the 15 μm and 7 μm ISOCAM observations with DENIS IJK_s data to determine the nature of a source and the interstellar extinction. Analysis of the sources at five near- and mid-infrared wavelengths shows that the majority of the sources are red giants with luminosities just above or close to the RGB tip. The various color-color and magnitude-color diagrams are discussed in the paper.

The outline of the paper is as follows : in section 2, we discuss the ISOGAL and DENIS observations. Section 3 describes the cross-identification of ISOGAL and DENIS sources. In section 4, we present the color-magnitude diagram of DENIS sources detected in ISOGAL. The interstellar extinction in the line of sight of the inner bulge field is described in this section. In section 5, we discuss the nature of ISOGAL sources based on multicolor near and mid infrared data. Section 6 shows the comparison of the two inner bulge fields.

2. ISOGAL and DENIS observations

The 6″ ISOCAM* observations for the bulge field (l = 0°,b = –1°), mainly used in this paper, were performed in revolution 841 (5th March 1998) at 15 μm (filter LW3, 12 – 18 μm) and at 7 μm (filter LW2, 5.5 – 8.5 μm). We have repeated ISOGAL observations for this field with a gap of 2 years (Table 1), which were used to check the photometry, the reliability of detected sources and to identify the suspected variables in the field. A special reduction pipeline was applied to the ISOCAM data which is more sophisticated than the standard treatment and devised by Alard *et al.* (in preparation).

The histograms of the 7 and 15 μm source counts derived from the 6″ ISOGAL observations are displayed in Fig. 1. In order to ensure a reasonable level of reliability, completeness and photometric accuracy, we presently limit the discussion of ISOGAL data to sources brighter than 8.5 mag (8mJy) for LW3 sources and 9.75 mag (11 mJy) for LW2 sources (the fluxes and magnitudes used are defined in

*See Cesarsky *et al.* (1996) for a general reference to ISOCAM operation and performances. Table 1 shows the available ISOGAL and DENIS observations in detail.

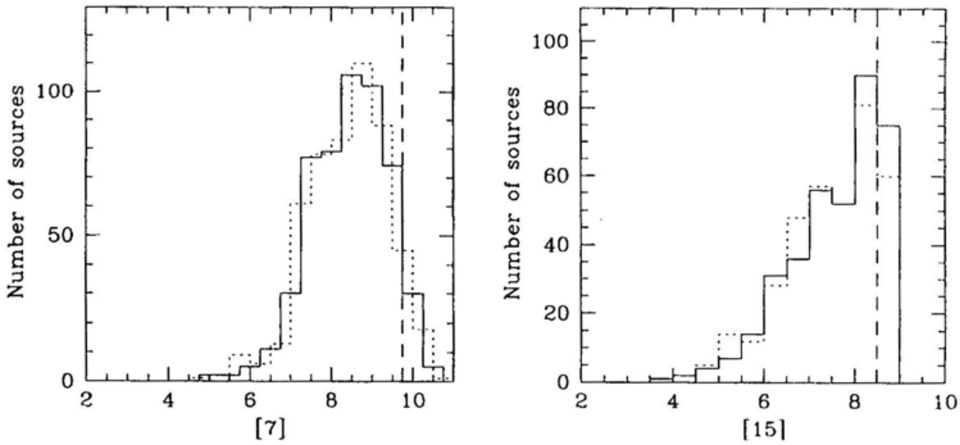

Figure 1. LW2 and LW3 source distributions in half magnitude bins. Solid lines indicate the number of detected sources in 1998 observations. Dotted lines indicate the number of detected sources in 1996 observations. Dashed lines show the limits ([7] = 9.75 and [15] = 8.5) of the sources discussed in the paper.

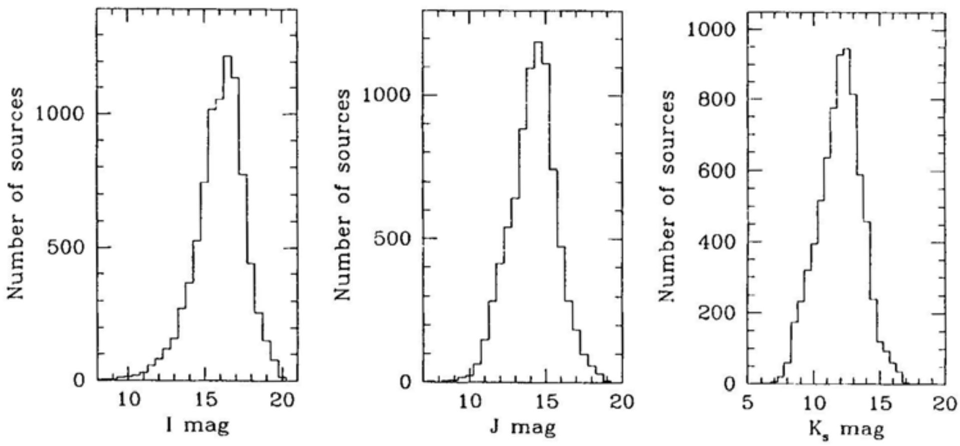

Figure 2. DENIS source counts in I, J, K_s bands in half magnitude bins.

Omont *et al.* 1999). The source counts in this field are thus 488 and 291, respectively in LW2 ([7] < 9.75) and LW3 ([15]) < 8.5). This is close to the confusion limit of 25 pixels [6″ × 6″] per source for LW2, The source densities are 1.5 10^4 deg^{-2} and 8.8 10^{-3} deg^{-2} for LW2 and LW3, respectively.

The near-infrared data used in this paper were acquired in the framework of the DENIS survey, in a dedicated observation of a large bulge field (Simon *et al.* in preparation), simultaneously in the three usual DENIS bands, Gunn-I (0.8 μm), J (1.25 μm) and K_s (2.15 μm). The region of the bulge field, which covers the ISOGAL field presented in this paper, was observed in September 1996. The histograms of the DENIS K_s, J, I sources are shown in Fig. 2. The completeness limit (due to confusion) is close to 11.5 in the K_s band and 14 in the J band.

Table 2. Catalog of bright ISOGAL + DENIS sources in the $l = 0°, b = -1°$ field ([7]) < 7.0).

No.	Name	I	J	K_s	[7]	[15]	Cross-id and comments
29	ISOGAL-DENIS-P J174906.9-293312	14.43	10.10	7.36	6.19	4.86	V
44	ISOGAL-DENIS-P J174909.1-292933	14.50	10.73	8.05	6.35	5.38	
51	ISOGAL-DENIS-P J174910.2-293441	S	S	S	6.41	6.23	F,M2 near raster edge
54	ISOGAL-DENIS-P J174910.7-293307	15.44	9.94	6.73	5.85	4.62	
87	ISOGAL-DENIS-P J174915.4-293255		11.01	7.82	6.89	5.36	
91	ISOGAL-DENIS-P J174915.9-293115	16.77	11.13	7.90	5.70	4.41	
120	ISOGAL-DENIS-P J174919.1-293325		10.49	7.53	6.39	5.40	V
132	ISOGAL-DENIS-P J174920.8-292602		10.50	7.61	5.55	4.33	
145	ISOGAL-DENIS-P J174921.8-292801		10.80	7.91	5.84	5.30	
147	ISOGAL-DENIS-P J174921.8-292523		10.95	7.82	6.92	5.95	
218	ISOGAL-DENIS-P J174926.6-293457	9.44	8.46	6.87	6.90	6.95	F,M2
314	ISOGAL-DENIS-P J174934.0-293026	15.31	10.83	8.22	6.81	5.95	
321	ISOGAL-DENIS-P J174934.4-292637	S	S	S	4.86	5.01	M4
328	ISOGAL-DENIS-P J174934.8-293041		11.35	8.66	6.98	5.37	
333	ISOGAL-DENIS-P J174935.0-292724	17.10	11.10	8.40	6.52	5.59	V
363	ISOGAL-DENIS-P J174937.1-292230		10.33	7.75	6.90	5.89	
402	ISOGAL-DENIS-P J174939.6-292722				6.66	4.64	IRAS 17464-2926
421	ISOGAL-DENIS-P J174941.2-291829			8.87	6.50	5.55	V
437	ISOGAL-DENIS-P J174942.2-292043		10.59	7.41	6.56	5.38	V
450	ISOGAL-DENIS-P J174943.3-291947		11.99	8.18	5.24	3.92	V
482	ISOGAL-DENIS-P J174946.0-292559	10.09	10.10	7.81	6.20	4.84	F,V
486	ISOGAL-DENIS-P J174946.4-292005		11.19	8.19	6.99	5.88	
488	ISOGAL-DENIS-P J174946.5-291933		10.48	7.63	6.54	5.51	
516	ISOGAL-DENIS-P J174948.8-292557	S	S	S	6.13	6.13	F
554	ISOGAL-DENIS-P J174953.8-291925	15.09	10.89	8.25	6.46	5.50	V near raster edge
562	ISOGAL-DENIS-P J174954.9-292017	13.11	9.62	7.11	6.34	5.67	V
568	ISOGAL-DENIS-P J174956.2-292530	15.27	11.32	8.53	6.68	5.56	

Note. F = Foreground star; V = Variable or suspected variable star; S = Saturated source.

3. Cross-identification of ISOGAL and DENIS sources

The cross-correlation between ISOGAL and DENIS sources has been made, which provides the multicolor data. This allows us to discuss the nature and properties of individual sources. Firstly, we have cross-correlated the ISOGAL LW2/LW3 sources. The search radius was fixed at a large value, 3.6″, for LW3/LW2 associations in order not to miss associations. The chance of spurious association with an LW2 source is then ~ 4%. Secondly, because of the very high density of DENIS sources, the search radius was reduced to 3.2″ for the DENIS/ISOGAL associations. Nevertheless, the density of the DENIS sources is so high that the chance of spurious associations remains ~ 7% for K_s sources with K_s < 10. The rms of the offsets

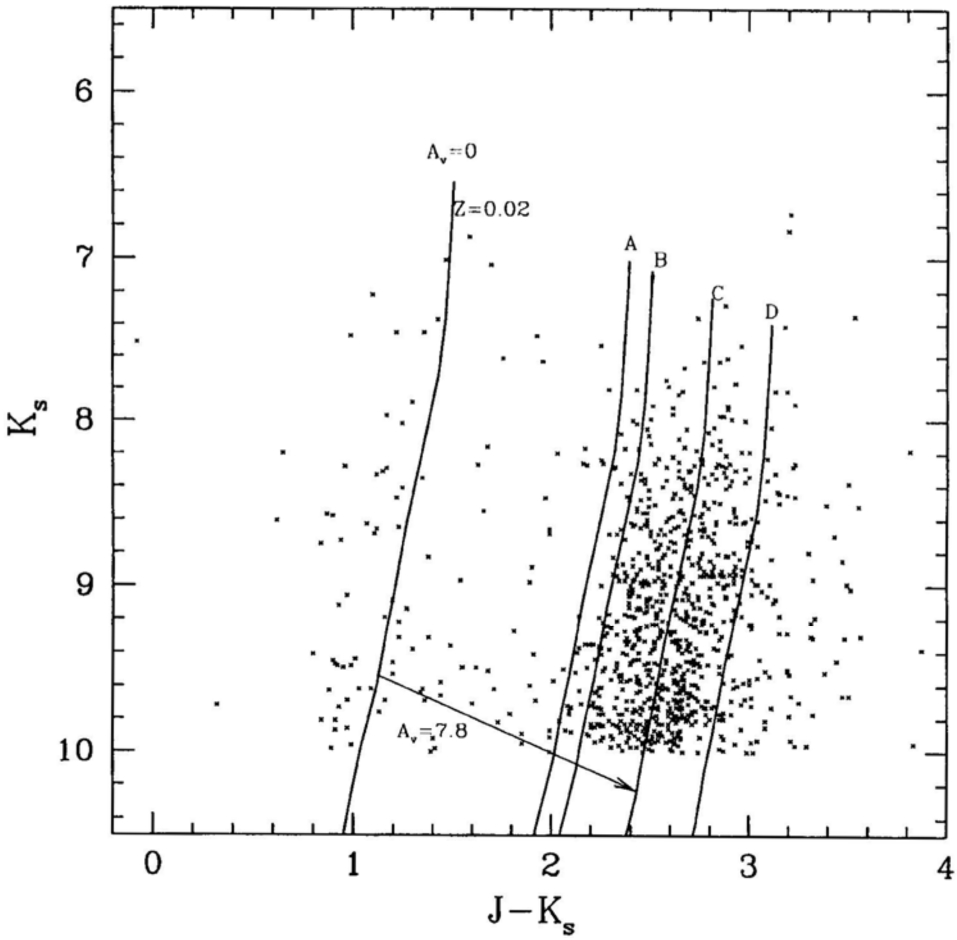

Figure 3. Color-magnitude diagram (J-K_s)/K_s for all DENIS sources in the field. An isochrone (Bertelli et al. 1994), placed at 8 kpc distance, is shown for a 10 Gyr population with Z = 0.02. The near-infrared colors of this isochrone have been computed with an empirical T_{eff} - $(J\text{-}K)_0$ color relation built by making a fit through measurements (see Schultheis et al., 1998, 1999) and Ng et al. (in preparation). The labels A, B, C, D identify the isochrones shifted by Av of 5.3, 6.0, 7.8 and 9.6, respectively.

of matched sources are ~ 1.7" and ~ 1.5" for LW3/LW2 and ISOGAL/DENIS, respectively.

Thus, a substantial fraction of the ISO sources have been identified with DENIS sources. Out of a total number of 488 LW2 sources, 359 (74%) are matched with a K_s < 10 source, 353 with a JK_s source and 221 with an IJK_s source. Out of 291 LW3 sources ([15] < 8.5), 251(86%) are matched with an LW2 source, 219 (75%) with a K_s(< l0)/LW2 source, 215 with a JK_s/LW2, and 133 with an IJK_s/W2 source. The number of LW2/LW3 sources without K_s or LW3/K_s sources without LW2 is small, 32 and 24, respectively.

Table 2 gives a catalogue of bright ISOGAL sources ([7] < 7.0), with three-band DENIS associations and identification of foreground sources and of candidate

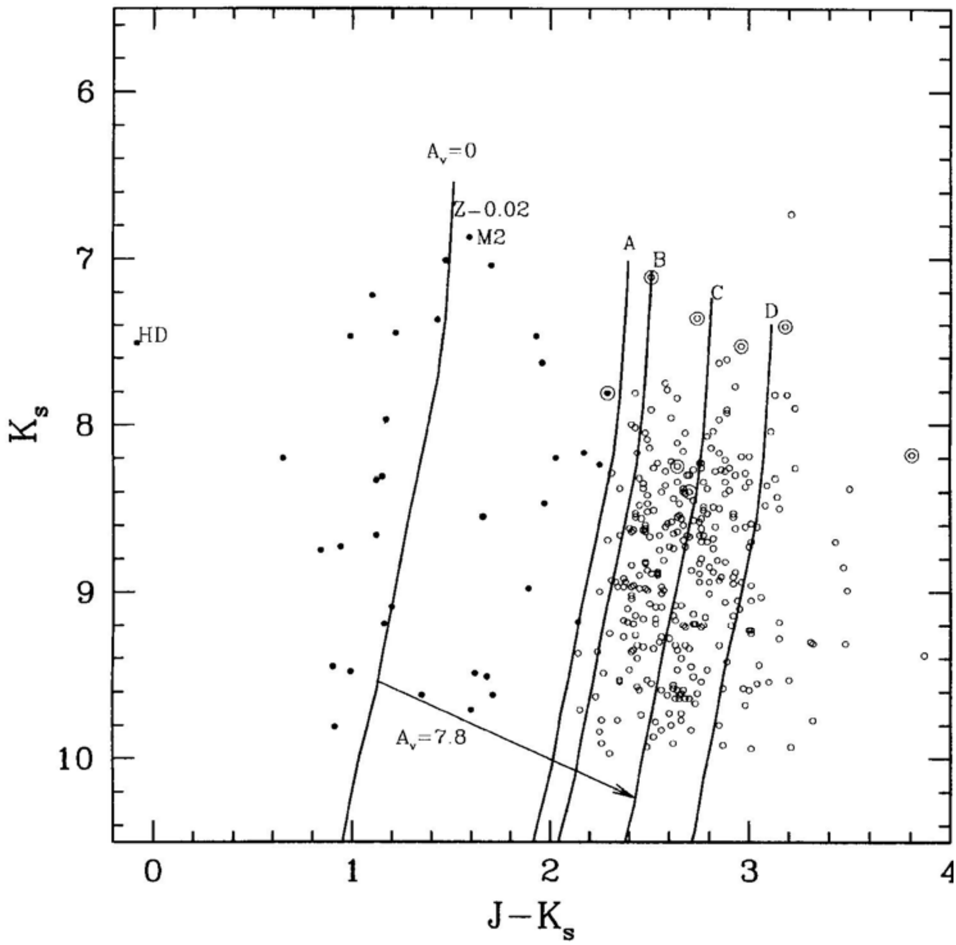

Figure 4. Color-magnitude diagram (J-K_s)/K_s for DENIS sources with [71] or [15] counterparts in the field. Filled circles represent the foreground sources with consistent data in the other diagrams. Suspected variables are indicated additionally by large open circles. The labels A, B, C, D and isochrones are as described in Fig. 3. The main sequence dwarf (HD 161908 : A9V) is denoted by HD. The M-type star in the catalog of Riharto et al. (1984) is denoted by M.

variable stars. We consider that DENIS values are saturated when K, < 7, J <8 and I < 9. The corresponding values are shown by *S* in Table 2. The cross-identified sources with SIMBAD are also shown with spectral type and IRAS name. The complete catalogue will be available at CDS, Strasbourg, within a few months.

4. Interstellar extinction

The adjunction of DENIS near-infrared data adds much to ISOGAL data, by providing different and more sensitive color indices, as well as estimates of the interstellar reddening. The K_s/J-K_s magnitude-color diagram of all DENIS sources in our field (Fig. 3) shows a bulge red giant sequence shifted and broadened by a non-uniform extinction of Av = 7.8 ± 2 magnitude with respect to the reference K_{s0} vs $(J\text{-}K_s)_0$ of Bertelli *et al.* (1994) with Z = 0.02 and a distance modulus of 14.5

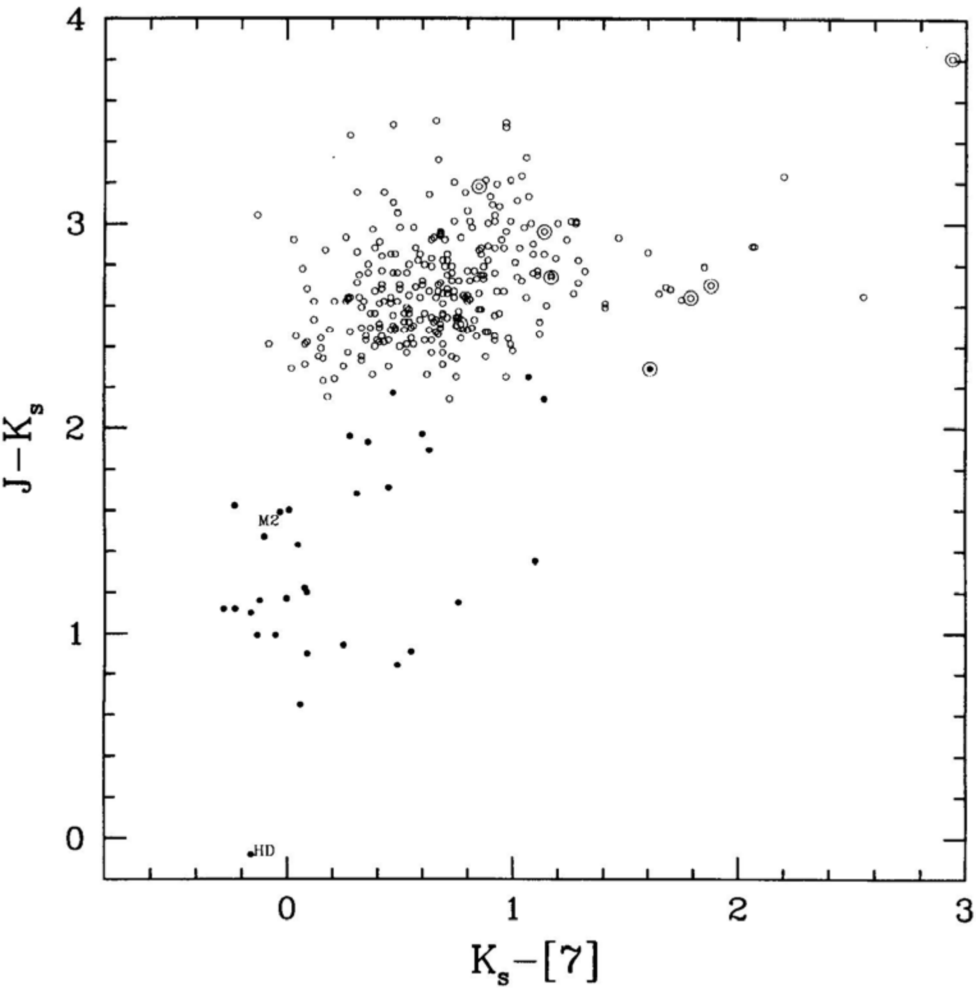

Figure 5. J-K_s/K_s-[7] color-color diagram of LW2 sources with DENIS counterparts. All symbols are as in Fig. 4.

(distance to Galactic Centre 8 kpc). We have assumed that $Aj / Av = 0.256$; $A_{Ks}/Av = 0.089$; $A_{[7]}/Av = 0.027$; $A_{[15]}/Av = 0.014$ (Glass *et al.* 1999). Most of the extinction should thus be associated with interstellar matter outside of the bulge.

The ISOGAL sources with anomalously low values of *Av* are probably foreground. They are visible in Fig. 4, which shows the subset of the K_s/J-K_s sources of Fig. 3, which were also detected at longer wavelengths. The sources located left of line *A*(Av < 5.3) are almost certainly foreground, while those to right of line *B*(Av > 6.0) are very probably in the "bulge", and the case is uncertain for those between lines *A* and *B*. The J-K_s excess of the sources much redder than line D is probably most related to larger extinction rather than to exceptionally large intrinsic J-K_s excess. This is demonstrated by the values of K_s-[7] and IC-[15], which remain characteristic of low mass-loss rates (except for the exceptional case of # 450, Table 2, there is also a group of bright stars (K_s< 8) close to line D [# 54, 87, 91,147, 137] with a moderate intrinsic J-K_s excess and a relatively strong excess at 15 μm, with the

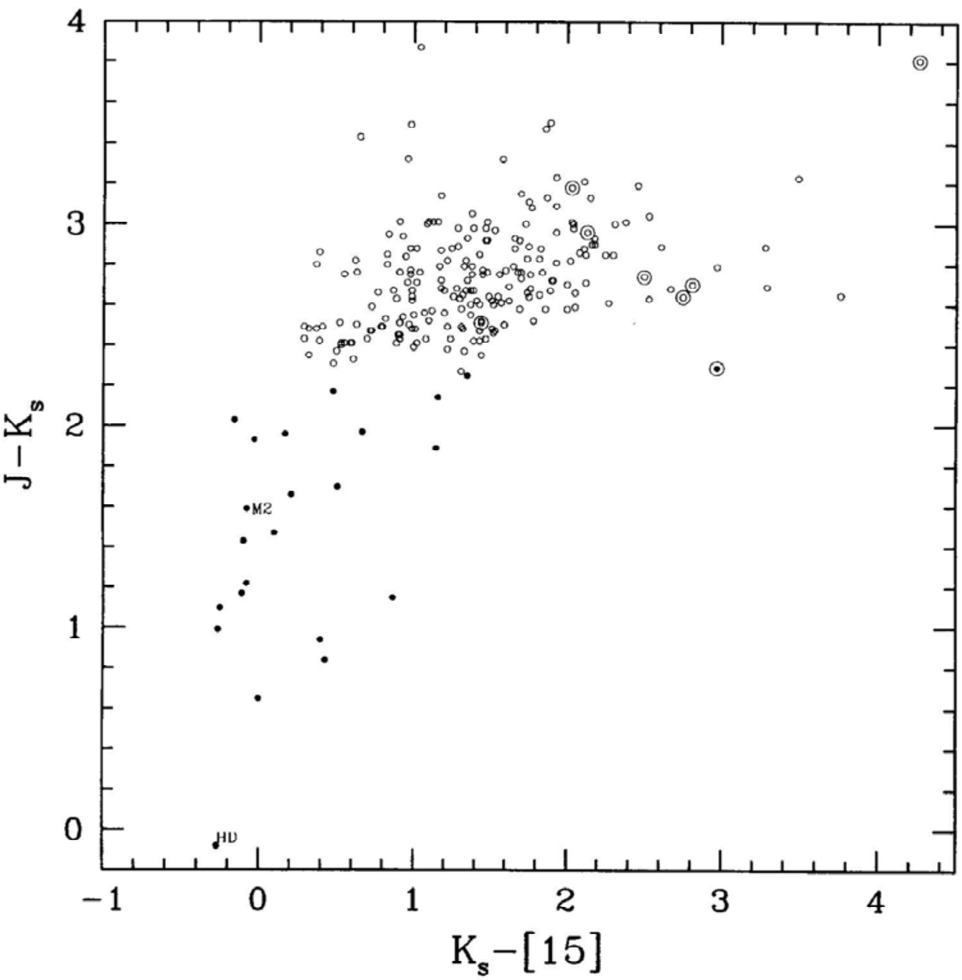

Figure 6. J-K_s/ K_s-[15] color-color diagram of LW3 sources with DENIS counterparts. All symbols are as in Fig. 4.

characteristics of relatively large mass-loss similar to miras). Such a large extinction could correspond either to parchy dust within the bulge or to background stars.

5. The nature of the ISOGAL sources

About 35 stars (~ 10% of the ISOGAL sources with DENIS counterparts: LW2/JK$_s$), which lie to the left of the line *A* (*Av* ~ 5.3) in Fig. 4 are probably foreground stars, in front of the main line of sight extinction. About half of the foreground stars are probably red giants with practically no extinction and that their number is much larger in this field (*b* = –1°) compared to the other bulge field (*b*=+1°, Omont *et al.* 1999). This may be because of the dust layers which are relatively far away in *b* = –1° direction. The other foreground stars with intermediate extinction look rather similar to the situation of *b* = +1° (Omont *et al.* 1999) and are perhaps at distances comparable to that of the dust layers.

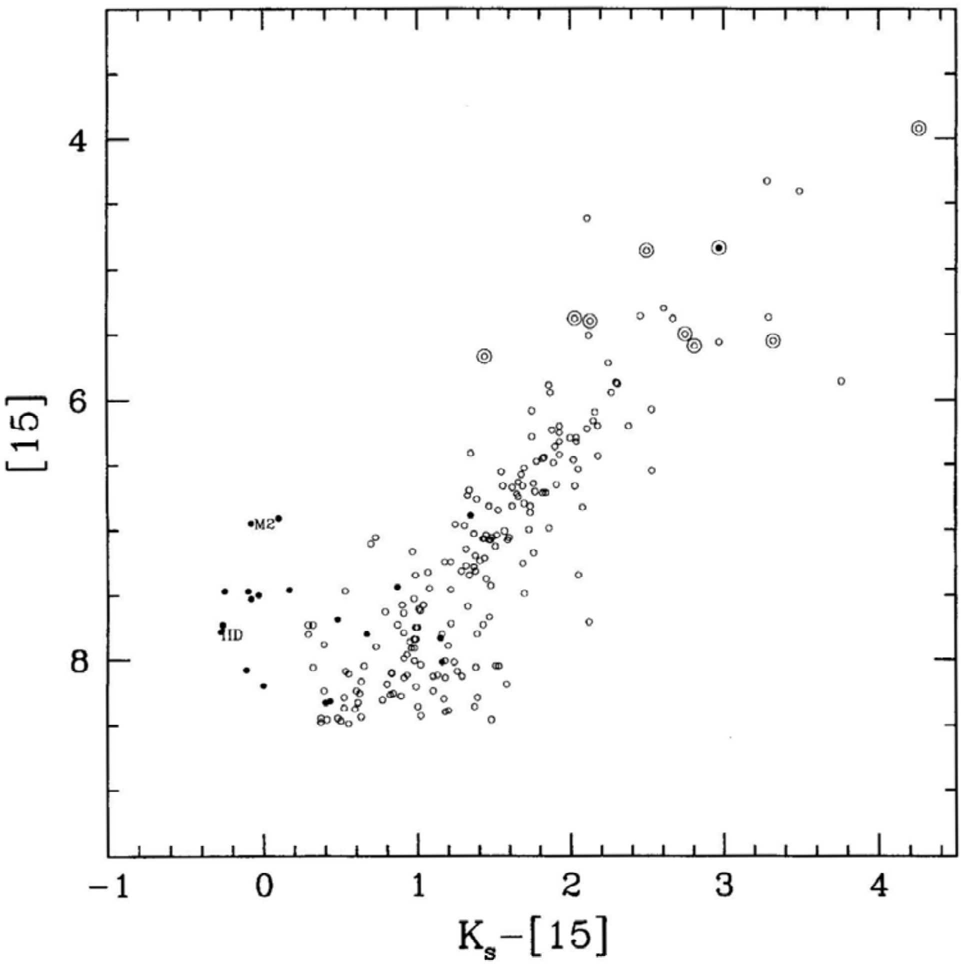

Figure 7. [15]/K$_s$ –[15] magnitude-color diagram of ISOGAL sources with DENIS counterparts. Symbols are as in Fig. 4.

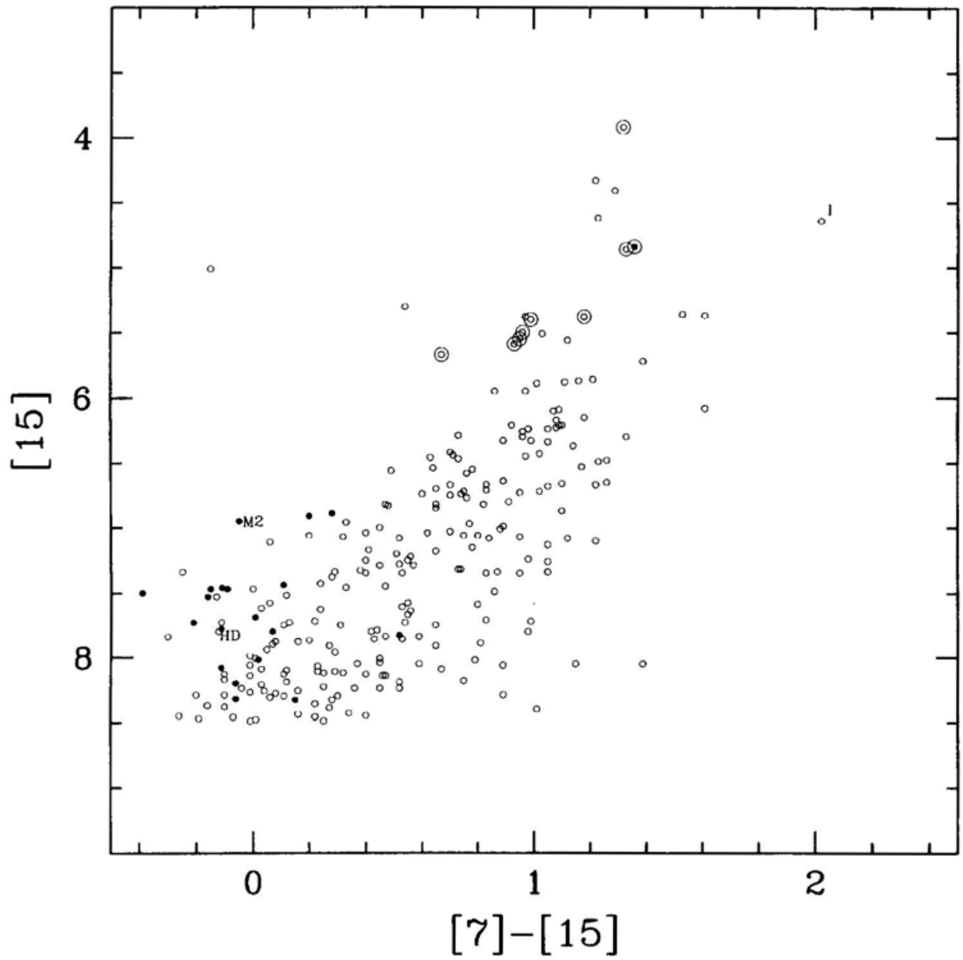

Figure 8. [15]/ [7]-[15] magnitude-color diagram of ISOGAL sources. Symbols are as in Fig. 4. The IRAS source is shown by I.

The J-K_s/K_s-[7] and J-K_s/K_s-[15] color-color diagrams are shown in Figs. 5 and 6. While the range of J-K_s values is restricted to ~ 0.5 mag for most of the sources, K_s-[15] ranges from 0.3 to 2.5 for the bulk of the sources (with an extension up to 4 magnitudes for a few sources). The colors [7]–[15] and K_s-[7] (Figs. 8 and 10) also display large ranges of excess, although somewhat smaller than for K_s-[15]. More than half of the sources under discussion have observed K_s-[15] colors redder than ~ 1, and very red [7]–[15] colors. Only the presence of the circumstellar dust can explain such a large excess. These data suggest that these are intermediate AGB stars or RGB tip stars with low and high mass-loss rates as discussed below.

The magnitude-color diagrams [15]/K_s-[15] and [15]/[7]–[15] are shown in Figs. 7 and 8, respectively. Characteristic values of the colors and magnitudes corresponding to the two ends of the intermediate AGB sequence are given in Table 3. The magnitude of the lower end of the sequence coincides with the ISOGAL sensitivity at 15μm, which is almost exactly that of the tip of the bulge ROB (K_0 ~ 8.2,

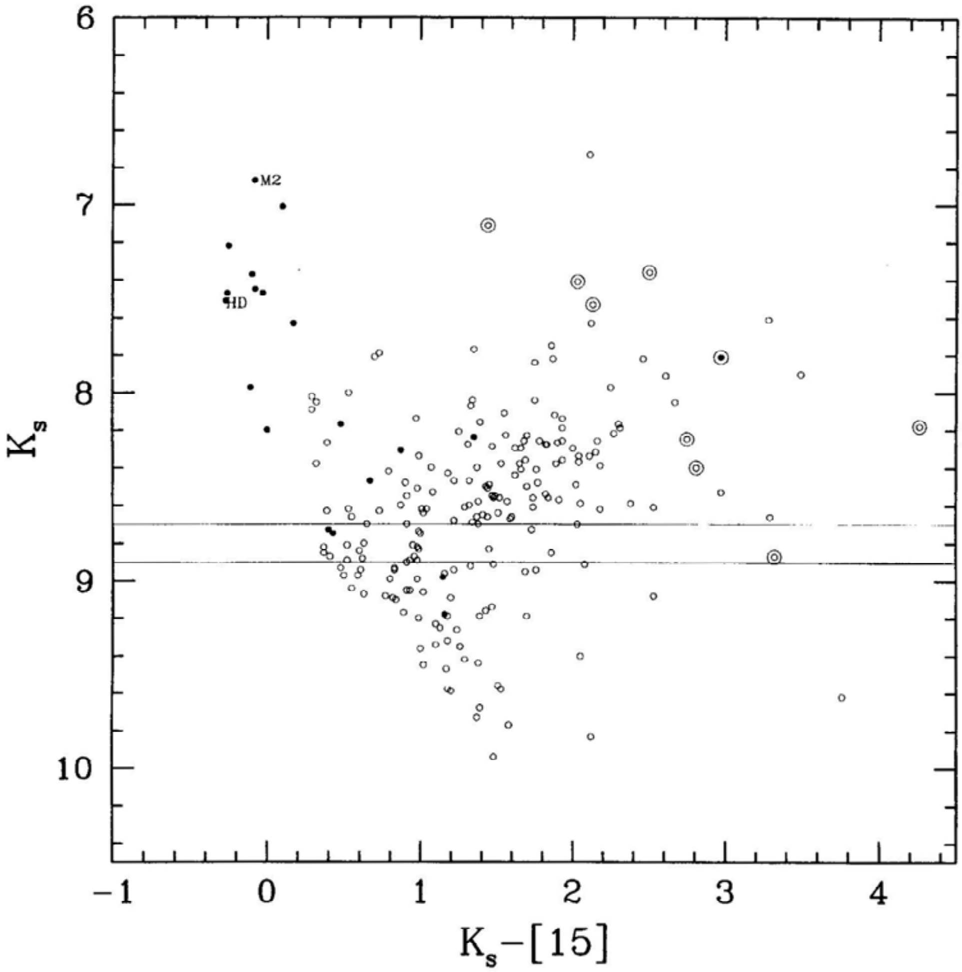

Figure 9. K_s/K_s-[15] magnitude-color diagram of ISOGAL sources detected both in LW2 and LW3, with DENIS counterparts. The approximate position of the RGB tip (taking into account the interstellar extinction in this field) is shown by the solid lines at K_s = 8.9 (K_0 ~ 8.2, Tiede *et al.* 1996) and K_s = 8.7(K_0 ~ 8.0, Frogel *et al.* 1999). All symbols are as in Fig. 4.

Tiede *et al.* 1996; K_0 ~ 8.0, Frogel *et al.* 1999). This K_{s0} magnitude range, 7.6 – 8.3 (Table 3), corresponds to M spectral types from M6 to M9 (Frogel & Whitford 1987 & Glass *et al.* 1999). This sequence of stars is described as "intermediate-AGB mass-loss sequence" (Omont *et al.* 1999).

From the SIMBAD data base, we have identified five sources in this field. [RHI84] 10–714 (M2), [RHI84] 10–733 (M2) and [RHI84] 10–745 (M4) are M-type stars in the catalogue by Riharto *et al.* (1984). These sources are denoted by "M" in Fig. 4. HD 161908 is an early main-sequence star with spectral type A9V. It is denoted by "A" in the figures. IRAS 17464–2926 with $S_{25\mu m}$ $S_{12\mu m}$ = 0.77 and [7]–[15] = 2.13 is denoted by "I" in Fig. 8.

In order to investigate the variability in this field, we have compared the repeated observations performed with 6" pixels, at two different dates (a gap of 2 years) with

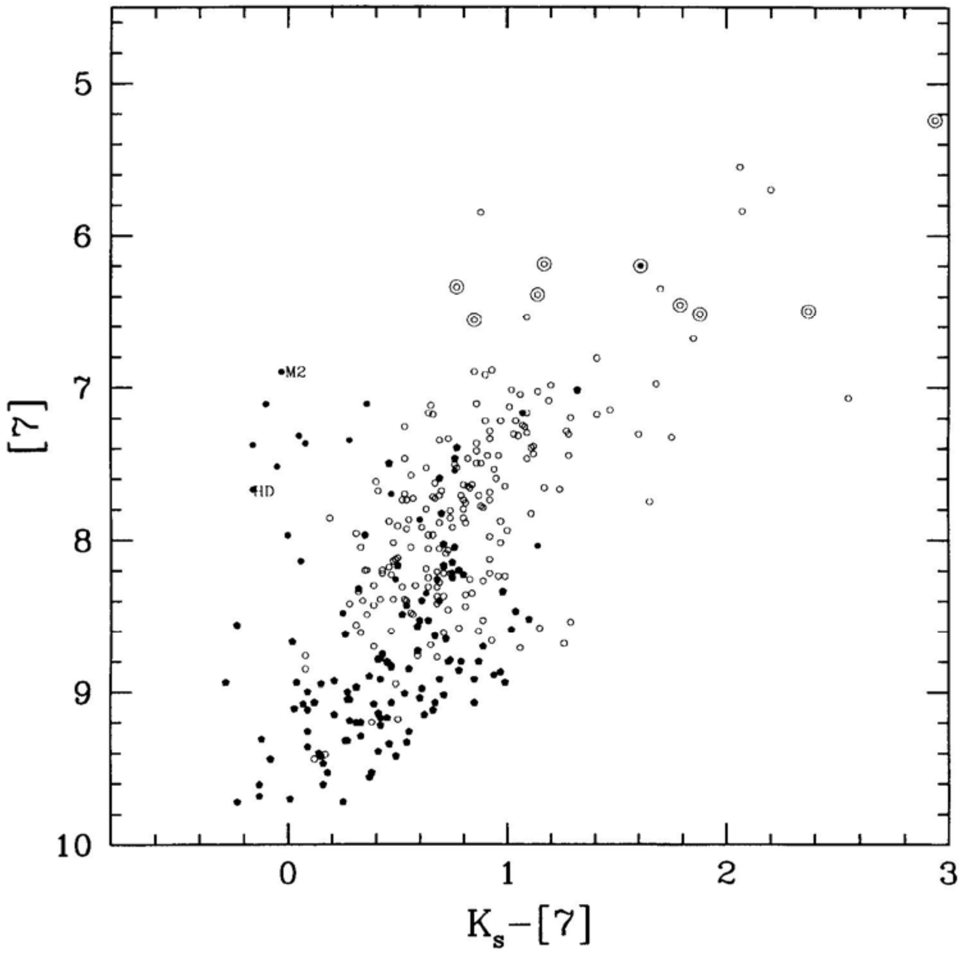

Figure 10. [7]/K_s-[47] magnitude-color diagram of all LW3 sources with DENIS counterparts. Filled asterisks represent sources without a detection at LW3. All other symbols are as in Fig. 4.

Table 3. Values of colors and magnitudes for the base and the tip of the mass-loss AGB sequence in the magnitude-colors diagrams in Figs 7, 8 and 9

	K_s–[15]	[7]–[15]	[15]	K_s	$(K_s-[15])_0$	K_{s0}	$M_K^{(a)}$	$M_{\rm bol}^{(b)}$	$L(L_\odot)$
Tip	2.3	1.3	6.0	8.3	1.7	7.6	−6.9	−3.9	2884
Base	0.5	0.0	8.5	9.0	−0.1	8.3	−6.2	−3.2	1514

[a] With a distance modulus of 14.5 (D = 8 kpc).
[b] With the K bolometric correction $M_{bol} - M_{Ks} = 3.0$ (Groenewegen 1997), which yields $M_{bol} \sim K_s - 12.2$ in this field.

both LW2 and LW3 filters (Table 1). Only a bright source has been considered for the variability, where there is a 3σ difference in one band. The sources selected in this way are displayed with special symbols in various figures. The repeated DENIS observations will also be used to look for the variable stars in all the inner bulge fields (Schultheis *et al.,* in preparation).

6. Comparison with bulge (*l* = 0°,*b* +1°) field

We have compared the results of the bulge field (present paper) with another ISOGAL bulge field at $l = 0°$, $b = +1°$, area = 0.033 deg^2. This field was analysed in detail and the results published in the paper by Omont *et al.* (1999). 3" ISOCAM observations are mainly used in this paper. However, the same field was also observed with ISOCAM in revolution 836 with 6" pixel size at LW3 and LW2, respectively (see Table 1 by Omont et al. 1999). To make a direct comparison between the two ($b = -1°$ & $b = +1°$) inner bulge fields, we have also analysed the 6" data of $b = +1°$ field. A detailed evaluation of 6" ISOCAM data of a few inner bulge fields including the $b = +1°$ will be presented elsewhere (Ojha *et al.,* in preparation).

The bulge field at $b = -1°$ seems to suffer more extinction (by ~ 2 magnitudes) and is more patchy compared to $b = +1°$ field. The source density in both LW2 and LW3 filters is higher (by a factor of ~ 1.2) in $b = -1°$ than in $b = +1°$ field. The density of foreground stars is larger in $b = -1°$ field by a factor of 1.5 compared to $b = +1°$ field. The density of foreground ISOGAL sources with DENIS JK_s counterparts is 1061 per deg^2 in $b = -1°$ field, while it is 697 per deg^2 in $b = +1°$ field. The origin of such differences is not entirely clear.

7. Conclusion

We have shown that the combination of near-infrared (DENIS) and mid-infrared (7 and 15 μm ISOGAL data allows reliable detection AGB and RGB tip stars. We conclude that most of the ISOGAL sources detected both at 7 and 15 um in the inner bulge field are intermediate AGB stars or RGB tip stars with low and high mass-loss rates. The sequence in various color-magnitude diagrams is well coincident with the late M AGB sequence, from M6 to M9, just above the RGB tip.

Acknowledgements

This publication makes use of data based on observations with ISO, an ESA project with instruments funded by ESA Member States (especially the PI countries: France, Germany, the Netherlands and the United Kingdom) and with the participation of ISAS and NASA. DENIS data are based on observations collected at the European Southern Observatory, La Silla, Chile. The DENIS project is partially funded by European Commission through SCIENCE and Human Capital and Mobility plan grants. It is also supported, in France by the Institut National des Sciences de 1'Univers; the Education Ministry and the Centre National de la Recherche Scientifique; in Germany by the State of Baden-Wiirtemberg; in Spain by the DG1CYT; in Italy by the Consiglio Nazionale delle Ricerche; in Austria by the Fonds zur Förderung der wissenschaftlichen Forschung und Bundesministerium für Wissenshaft und Forschung; in Brazil by the Foundation for the development of Scientific Research of the State of Sao Paulo (FAPESP); and in Hungary by an OTKA grant and an ESOC&EE grant. This research has made use of the DEC-ALPHA system of the Optical CCD astronomy programme of TIFR.

References

Bertelli, G., Bressan, A., Chiosi, C., Fagotto, F., Nasi, E. 1994, *Astr. Astrophys,* **106,** 275.
Cesarsky, C. *et al.* 1996, *Astr. Astrophys,* **315L**, 32.
Frogel, J. A., Whitford, A. E. 1987, *Astrophys J.,* **320,** 199.
Frogel, J. A., Tiede, G. P., Kuchinski, L. E. 1999, *Astrophys* **J., 117,** 2296.
Glass, I. S., Ganesh, S., Alard, C., Blommaert, J. A. D. L., Gilmore, G., Lloyd Evans, T., Omont, A., Schultheis, S., Simon, G. 1999, *Mon. Not. R. astr. Soc.,* **308,** 127.
Groenewegen, M.A.T. 1997, in *The Impact of Large Scale Near-IR Sky Surveys,* (eds). F. Garzon *et al.* (Kluwer) page 165.
Omont, A., Ganesh, S., Alard, C., Blommaert, J. A. D. L., Caillaud, B., Copet, E., Fouqué P., Gilmore, G., Ojha, D. *et al.* 1999, *Astr Astrophys,* **348,** 755.
Omont, A. and The ISOGAL Collaboration 2000, In Springer Lecture Notes of Physics Series, as part of the proceeding for "ISO Surveys of a Dusty Universe", a workshop held at Ringberg Castle, Germany, November 8-12, 1999.
Pérault, M., Omont, A., Simon, G., Séguin, P., Ojha, D. *et al.* 1996, *Astr. Astrophys*, **315,** L165.
Riharto, M., Hamajima, K., Ichikawa, T., Ishida, K., Hidayat, B 1984, *Ann. Tokyo Astron. Obs.,* 2nd Series, Vol. 19, No. 4, page 469.
Schultheis, M., Ng, Y. K., Hron, J., Kerschbaum, F. 1998, *Astr. Astrophys,* **338,** 581.
Schultheis, M., Ganesh, S., Simon, G., Omont, A., Alard, C., Borsenberger, J., Copet, E., Epchtein, N., Fouqué, P. Habing, H. 1999, *Astr. Astrophys,* **349,** L69.
Tiede, G.P., Frogel, J.A., Terndrup, D.M. 1996, *Astr. J.*, **110,** 2788.

J. Astrophys. Astr. (2000) **21**, 91–99

Porous and Fluffy Grains in the Regions of Anomalous Extinction

D. B. Vaidya, *Gujarat College, Ahmedabad 380006, India.*
B. G. Anandarao & J. N. Desai, *Physical Research Laboratory, Ahmedabad 380009, India.*
R. Gupta, *Inter-University Centre for Astronomy & Astrophysics, Pune 411007, India.*

Received 1997 December 24; accepted 2000 January 29

Abstract. It has long been established that the ratio of total to selective extinction is anomalously large (≥ 5) in certain regions of the interstellar medium. In these regions of anomalous extinction the dust grains are likely to be irregular in shape and fluffy in structure. Using discrete dipole approximation (DDA) we calculate the extinction for porous and fluffy grains. We apply DDA first to solid spheroidal particles assumed to be made of a certain (large) number of dipoles. Then we systematically reduce the number of dipoles to model the porous grains. The aggregates of these particles are suggested to form the fluffy grains. We study the extinction for these particles as a function of grain size, porosity and wavelength. We apply these calculations to interpret the observed extinct-tion data in the regions of star formation (e.g. the Orion complex).

Key words. Interstellar dust—extinction—porous grains—anomalous extinction.

1. Introduction

The ratio (R) of the total to the selective extinction (= $A_V/E(B–V)$) depends upon the environment along the line of sight. A direction through a low density interstellar medium (diffuse ISM) usually has a value of R ~ 3.1. However, a line of sight penetrating into a dense cloud, such as the Ophiuchus or the Taurus molecular clouds has $4 \leq R \leq 6$(Mathis 1990). Also several studies of visual and infrared colors of the Orion stars have found large value of R ~ 5.2 (Breger *et al.* 1981; Cardelli & Clayton 1988). These large values of R have been attributed to large grain sizes (≥ 0.2 μm) in these regions. These grains could have grown larger than normal size through either accretion or coagulation (Mathis 1990). If the grains have grown large due to accretion of the material, then the core mantle grain models would be appropriate in these regions, as suggested earlier (Leger *et al.* 1983; Vaidya & Anandarao 1993). The other possibility is that the grains have grown large due to coagulation as shown by Jura (1980) to interpret the observations of extinction toward ρ Oph. In the case of coagulation a single grain consists of an assembly of small particles stuck together loosely; i.e., the particles are porous and fluffy. Hence, there is a need for models of electromagnetic scattering by porous and fluffy grains. Exact solutions to Maxwell's equations are known to calculate absorption, scattering and extinction of electro-magnetic waves by homogeneous spheres (Van de Hulst 1981), spheroids (Asano &

Yamamoto 1975) and infinite cylinders (Greenberg 1960). However, in order to calculate the scattering, absorption and extinction of irregularly shaped and inhomogeneous (i.e. porous and fluffy) particles approximate methods are required. The discrete dipole approximation (DDA) is one such method. We apply DDA first to the spheroidal solid grains assumed to be made of a large number of dipoles. Then we systematically reduce the number of dipoles (by decreasing the packing density) to model the porous grains (Vaidya & Gupta 1997). Recently, Lumme & Rahola (1994) have used DDA to study the light scattering properties (angular distribution of the scattered intensity and polarization) of porous dust particles. Wolff *et al.* (1994) have used DDA to model the porous and fluffy grains. They have studied the extinction properties of the astronomical silicate grains and have compared their results with those obtained using the effective medium theory (EMT). In EMT the inhomogeneous particle is replaced by a homogeneous one with some averaged 'effective' dielectric function, which is obtained by using the classical Bruggeman and Maxwell-Garnet mixing rules (for discussion on EMT see, e.g., Bohren & Huffman 1983). However, the effects related to the fluctuations of the dielectric function within the inhomogeneous structures such as surface roughness and special distributions of the components can not be treated by the averaging approach of the EMT's. The DDA is a direct finite element technique and it allows the consideration of irregular shape effects and special distributions of the components in the particles. In the present study we have chosen the DDA method to take into account the influence of the internal structures (porosity) of the grains (including the non-Rayleigh structures, i.e., structure size large compared to the wavelength), which may not be possible by using the other methods (Wolff *et al.* 1994). Henning & Stognienko (1993) have used the DDA to study the polarization by porous silicate grains. Vaidya & Desai (1996) have used the porous grain model with the code 'ddscat.4b. 1' (Draine & Flatau 1994a) to calculate the angular distribution of the scattered intensity and polarization for the astronomical silicate particles. They have used the porous grain model to explain the low density and low albedo observed in the dust coma of the comet Halley.

In this paper first we show how the porous particles are generated. Then we calculate the extinction efficiencies of porous silicate grains at several wavelengths between 0.30 μm and 3.4 μm. In section 2 we describe the DDA, the validity criteria for DDA and the porous models. We present the results in section 3 and apply these results to interpret the observed extinction towards the Orion region of star formation. In section 4 we give the conclusions of the present study.

2. The DDA and the porous grain

The DDA is a very useful technique to study the scattering and absorption properties of the particles of arbitrary shape. It was first used by Purcell & Pennypacker (1973) and later developed by Draine (1988). The DDA replaces a solid particle by a 3-dimensional array of N point dipoles. We use the DDA program 'ddscat.4b.l' developed by Draine & Flatau (1994a) to generate porous grains. There are two validity criteria for DDA (Draine & Flatau 1994b): viz., (i) $mkd \leq 1$, where m is the complex refractive index, $k = \pi / \lambda$, and d is the lattice dispersion spacing and (ii) d should be small enough (N should be large enough) to describe the shape of the target satisfactorily. In this program it is also assumed that the dipoles are located on a cubic lattice. Initially we assume the number of dipoles N_x, N_y, N_z along the axis *x,y,z* for the spheroidal target grain. This would result in a certain number *N* of dipoles in the spheroidal target grain, e.g., for $N_x = 24$, $N_y = 18$, $N_z = 18$; we get N ~4088 (Draine & Flatau 1994a). Then we reduce N_x, N_y, N_z to generate the porous grains (viz., 16,12, 12; 8, 6, 6 and so on). The assumed shape of the grain is a prolate spheroid with the axial ratio of 1.3. If the semi-major and semi-minor axes of the prolate spheroids are denoted by $x/^2$ and $y/^2$ respectively then we have $a^3 = (x/2) \times (y/2)^2$; where *a* is the radius of a sphere whose volume is the same as that of a spheroid. Hence, e.g., for a spheroid with $N_x = 16$, $N_y = 12$ and $N_z = 12$, the program 'ddscat.4b.1' (Draine & Flatau 1994a) will yield $N \sim 4/3\times\pi\times(x/2)\times(y/2)^2$; $\sim 4/3\times\pi\times8\times(6)^2 \sim 1184$ (Vaidya & Gupta 1997). Depending upon the number of dipoles *N* in the grain the porosity *P* varies between $0 \leq P \leq 1$ (Greenberg 1990). In the present work *P* varies between (close to) 0 (for very large *N,* e.g. 4088) and 0.75 (for *N* =152). We know that *N* = 4088 is not very large but it is sufficiently large for the grain sizes and the wavelength range considered in the present study. Fig. 1 shows the plots of the lattice dispersion *mkd* as a function of grain size *a* at two wavelengths, viz. 0.70 μm and 3.4 μm for the porous silicate grains. These curves indicate validity criteria for DDA (viz. *mkd* <1*)* at these two wavelengths for the porous (*N* = 152,

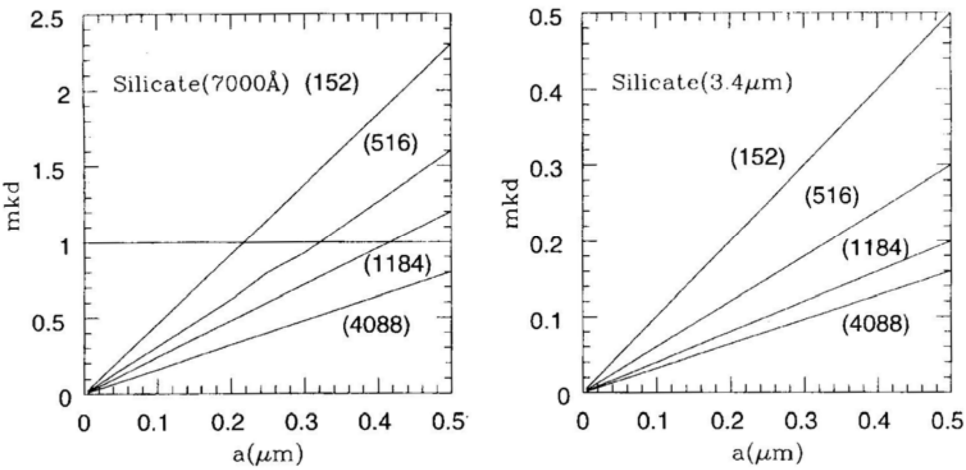

Figure 1. Lattice dispersion relation *mkd* as a function of grain size at two wavelengths for the porous silicate grains.

Table 1. Maximum grain size satisfying the DDA validity criteria.

Wavelength (μm)	$N = 152$ a(μm)	$N = 516$ a(μm)	$N = 1184$ a(μm)	$N = 4088$ a(μm)
0.3000	0.090	0.105	0.19	0.25
0.4400	0.134	0.195	0.27	0.40
0.5500	0.170	0.255	0.35	0.50
0.7000	0.215	0.305	0.42	0.63
1.0000	0.308	0.446	0.64	0.92
2.2000	0.678	1.050	1.34	2.03
3.4000	1.000	1.500	2.08	3.12

516, 1184 and 4088) silicate grains; similar curves at other wavelengths can be drawn from the *mkd* values obtained using the ‘ddscat.4b.1’ program (Draine & Flatau 1994a). Table 1 shows the maximum grain size satisfying the DDA validity criteria. It is seen from this table that as the wavelength increases the maximum grain size that satisfies the DDA validity criteria also increases. It varies between about 0.1 and 1.0 μm for N = 152 and from 0.25 to 3.0 μm for N = 4088.

3. Results and discussion

Using the ‘ddscat.4b.1’ program we have obtained the extinction efficiency factor Q_{ext}, the ratio of the cross section of the extinction to the geometrical cross section for the porous astronomical silicate grains (i.e., N = 152, 516, 1184 and 4088). These efficiencies are calculated using the optical constants given by Draine (1985, 1987). The prolate spheroidal grains are assumed to be randomly oriented and the

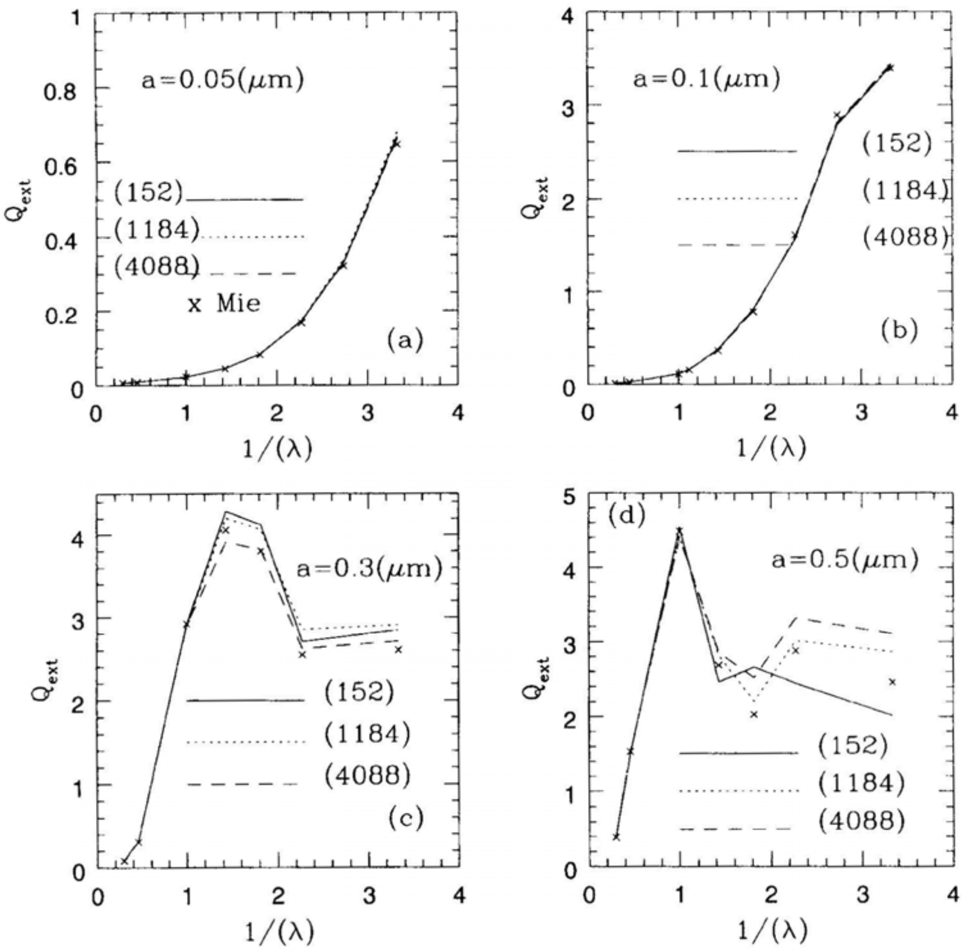

Figure 2. Extinction efficiencies Q_{ext} for porous silicate grains of four different sizes.

geometrical cross section of these prolate grains is taken to be $\pi \times (y/2)^2$, where y is the semi-major axis of the prolate spheroid. Fig. 2(a–d) show plots of the extinction efficiency Q_{ext} against $1/\lambda$ for the porous (N = 152, 1184 and 4088) silicate grains in the wavelength range of 0.30 μm-3.4 gm for the grain size a equal to (a) 0.05 (b) 0.10 (c) 0.30 and (d) 0.50 gm. For the solid grains the extinction efficiency factors Q_{ext} are obtained using Mie theory. The crosses in the figure show the extinction efficiency factors for the solid particles (Mie values). It is seen from these plots that for small grains (i.e., a = 0.05 μm and 0.10 μm) there is no significant variation in the extinction efficiencies for the porous grains. However, for grains with $a \geq 0.1$ μm the extinction is modified considerably (Fig. 2(c)). The extinction for the porous grains is enhanced (i.e., the extinction for the grains with N = 152 is more than that which is obtained for N = 1184, N = 4088 and solid grains (Mie values)). For grains with a = 0.5 μm (Fig. 2(d)) the extinction for the porous grains is enhanced; however, one notes that beyond 0.40 μm, the effect of porosity on the extinction is not very clear. This could be due to the number of dipoles N is not large enough for the grain size a = 0.5 μm in the wavelength range 0.40–0.30 μm, We use these results on the extinction by porous grains and the power law grain size distribution (Mathis, Rumpl & Nordsieck 1977), $n(a) \sim a^{-3\,5}$, with the size range of 0.005–0.300 μm, to reproduce the observed interstellar extinction curve, viz. $E(\lambda - V)/E(B - V)$ vs $1/\lambda$ for the star

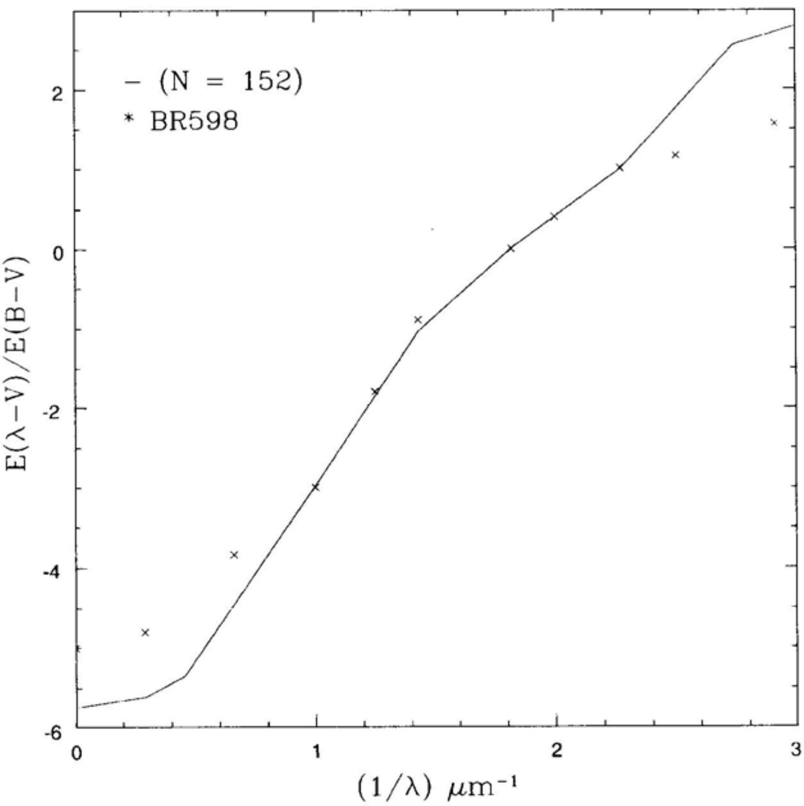

Figure 3. Comparison of the observed extinction curve with the porous silicate grains with N = 152.

BR598 (Breger *et al.* 1981) in the Orion. The ratio R of the total to the selective extinction is also evaluated for these porous grains. It is to be noted here that the maximum size for the porous grains required to obtain $R \sim 5.2$ is 0.30 μm whereas for the solid grains the maximum size required would be ≥ 0.500 (Leger *et al.* 1983; Vaidya & Anandarao 1993). Figs. 3, 4, 5 and 6 show the observed interstellar extinction curve with the model curve of porous silicate grains with N = 152, N = 516, N = 1184 and N = 4088 respectively. It is seen that models with N = 1184 and N = 4088 reproduce the observed extinction for this star reasonably well. A comparison of Figs. 3-6 shows that the model for N = 152 deviates considerably from the observed curve especially in the U band and in the IR. One also notes that the model N = 152 does not satisfy the validity criteria for DDA (Table 1, Fig. 1) for the large grain sizes (i.e., ≥ 0.1 μm). Grain models with N = 516 also do not fit well in the IR region. Among the other two possible models, however, one does not find much difference. This means that the porous grains with about 40% porosity (N = 1184) would fit the observed curve reasonably well and increasing the number of dipoles N (*e.g.,* 4088) would not improve the fit. The only possible criterion, therefore, to choose a particular model suitable for a given observation is by considering the total amount of matter locked up in grains (small for high porosity). Hence measurements in metallic abundances in the interstellar medium should be taken as a handle to select a particular model as the best fit for extinction observations

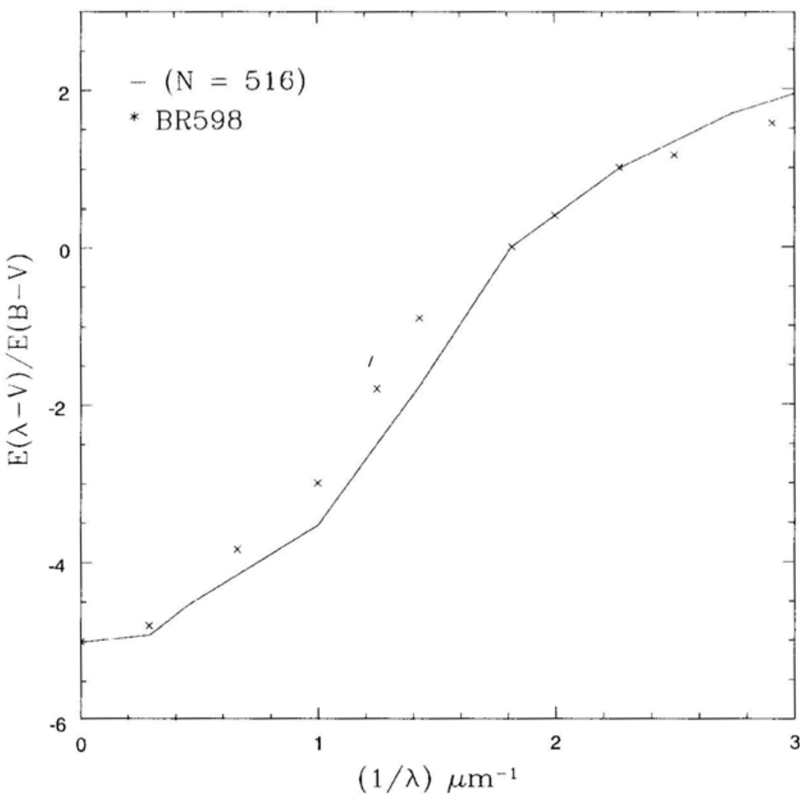

Figure 4. Same as Fig. 3 but with $N = 516$

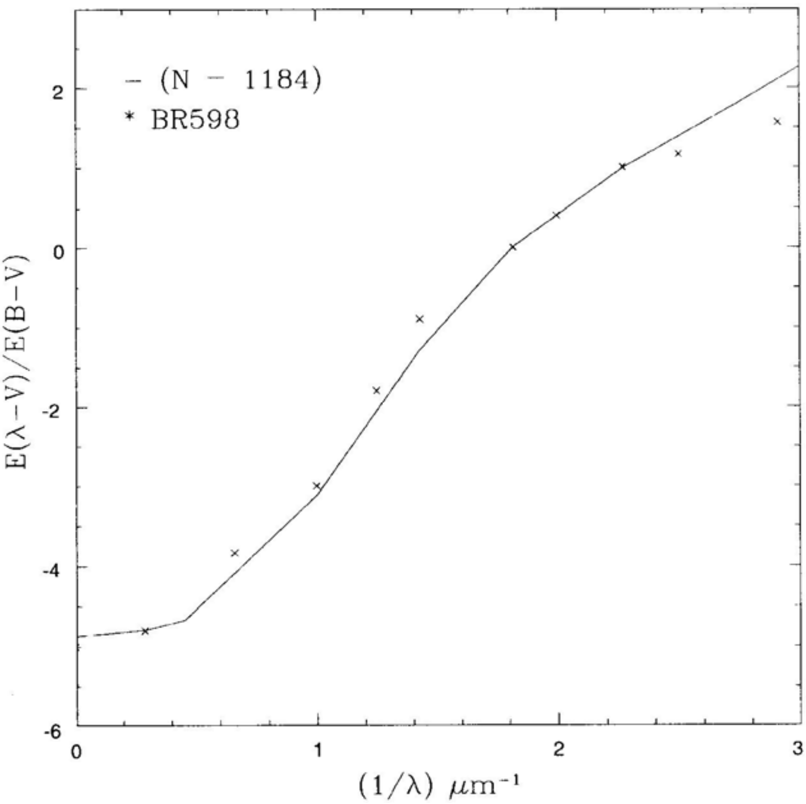

Figure 5. Same as Fig. 4 but with $N = 1184$.

(Mathis 1996; Dwek 1997). In order to quantify the material content from the model one needs to compare it with some spectral feature in the observed curve or one should assume that only one type of grain composition accounts for the infrared flux in the wavelength range considered. Earlier, Leger *et al.* (1983) have reported that large grains (1.2 μm) are required to fit the observed data in molecular clouds and in the high density interstellar medium. Our results indicate that the grains do not grow very large in the regions of anomalous extinction but they are porous. In these regions the grains can attach to each other by collisions in slow motion and coagulate. In case of accretion gas phase atoms and molecules are adsorbed on the surface of a core becoming a core-mantle grain. Further, it is shown (Jura 1980; Whittet 1992) that the time scale for grain-grain collision is

$$t_{\mathrm{col}} = \frac{n_d}{\pi a^2 v_d} \tag{1}$$

where n_d and v_d are the density and velocity of the grain and a its size. Jura (1980) finds for n_d 10^9 m^{-3} and $v_d = 0.1$ km/s, $t_{\mathrm{col}} \sim 3$ myr. This shows that the coagulation is possible within the life time of a cloud. Also, from the observations on the Ophiuchi sources Tanaka *et al.* (1990) have shown that stars having large R have moderate visual extinction ($1 \leq A_v \leq 10$) while the ice mantle particles are detected only towards the sources with $A_v \geq 10$. The value of A_v for BR598 is 1.68 (Breger

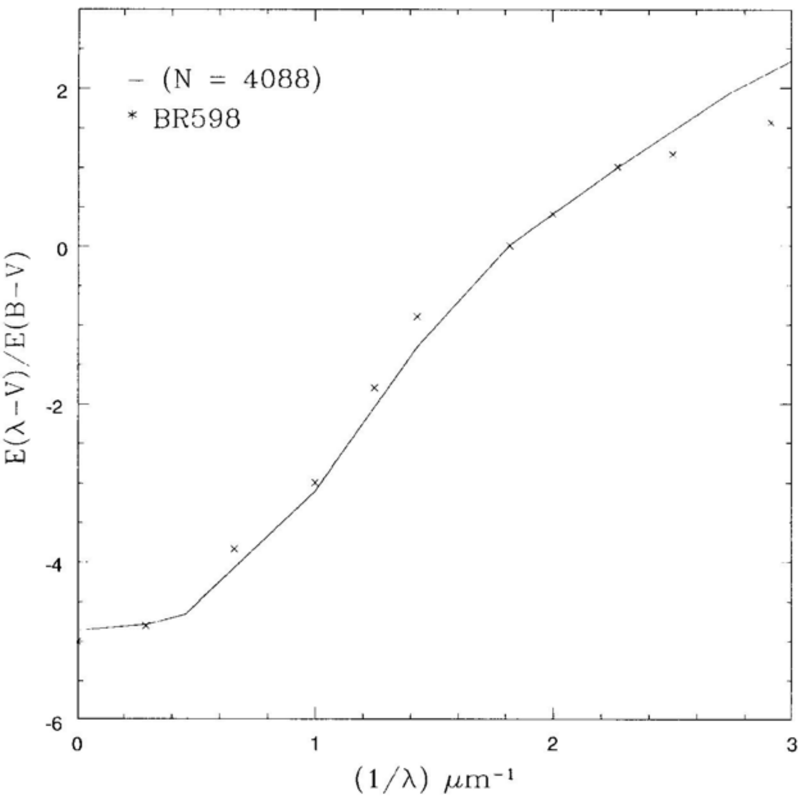

Figure 6. Same as Fig. 5 but with $N = 4088$

et al. 1981) hence in this region the dust grains are more likely to be porous rather than core-mantle.

4. Conclusions

Using discrete dipole approximation (DDA) we have obtained the extinction efficiencies of the porous astronomical silicate grains at several wavelengths between 0.30 μm and 3.4 μm. Our results show that the porosity affects the extinction efficiency of the particles. These porous grain models reproduce the observations of extinction toward Orion at wavelengths greater than 0.30 μm. These results indicate that grains do not grow very large in the regions of anomalous extinction but they might be porous and fluffy. These models are not unique but we only wish to illustrate how porous grains can reproduce the observations in the regions of anomalous extinction. The laboratory study using microwave analog technique has shown that the scattering properties of porous particles differ considerably from those of spheres (Giese *et al.* 1978; Greenberg & Gustafson 1981; Zerull *et al.* 1993). These laboratory data are used to interpret the observed data on zodiacal light and comets (Giese *et al.* 1978). Similarly, laboratory data on the extinction by porous particles are required to help interpret better the observed data in these regions of anomalous extinction.

Acknowledgements

We thank Prof. B. T. Draine for providing the ‘ddscat program. D. B. V. thanks the Physical Research Laboratory for providing computer and other facilities.

References

Asano, S., Yamamoto, G. 1975, *Appl. Optics,* **14,** 29.
Bohren, C. F., Huffman, D. R. 1983, *Absorption and Scattering of Light by Small Particles* (New York: J. Wiley).
Breger, M., Gehrz, R. D., Hackwell, J. A. 1981, *Astrophys. J.,* **248,** 963.
Cardelli, J. A., Clayton, G. C. 1988, *Astr. J.,* **95,** 516.
Draine, B. T. 1985, *Astrophys. J. Suppl.,* **57,** 587.
Draine, B. T. 1987, *Astrophys. J. Suppl.,* **64,** 595.
Draine, B. T. 1988, *Astrophys. J.,* **333,** 848.
Draine, B. T., Flatau, P. J. 1994a, User Notes for DDSCAT.4b.1.
Draine, B. T., Flatau, P. J. 1994b, *JOSAA*, **11,** 1491.
Dwek, E. 1997, *Astrophys. J.*, **484,** 779.
Giese, R. H. Weiss, K., Zerull, R. H., Ono, T. 1978, *Astr. Astrophys.,* **93,** 35.
Greenberg, J. M. 1960, *J. Appl. Phys.,* **31,** 82.
Henning, Th., Stognienko, R. 1993, *Astr Astrophys.,* **280,** 609.
Jura, M. 1980, *Astrophys. J.,* **235,** 63.
Leger, A., Gauthier, S., Defourneau, D., Rouan, D. 1983, *Astr. Astrophys.,* **117,** 164.
Lumme, K., Rahola, J. 1994, *Astrophys. J.,* **415,** 653.
Mathis, J. S. 1996, *Astrophys. J.,* **472,** 643.
Mathis, J. S, 1990, *ARAA,* **28,** 37.
Mathis, J. S., Rumpl, W., Nordsieck, K. H. 1977, *Astrophys. J.,* **217,** 425.
Purcell, E. M., Pennypacker, C. R. 1973, Astrophys. *J.,* **186,** 705.
Tanaka, M., Sato, S., Yamamoto, T. 1990, *Astrophys. J.,* **352,** 724.
Vaidya, D. B., Gupta, R. 1997, *Astr. Astrophys.,* **328,** 634.
Vaidya, D. B., Desai, J. N. 1996, *ASP Conf. Ser,* **104,** 433.
Vaidya, D. B., Anandarao, B. G. 1993, *Bull. Astr. Soc. India,* **21,** 591.
Van de Hulst, H. C. 1981, in *Light Scattering by Small Particles,* (N.Y.: Dover)
Whittet, D. C. B. 1992, in *Dust in the Galactic Environment,* p. 222.
Wolff, M. J., Clayton, G. C., Martin, P. G., Schulte-Ladbeck, R. E. 1994, *Astrophys.* J., **423**. 412.
Zerull, R. H., Gustafson, B. A. S., Schulz, K., Thiele-Corbach, E. 1993, *Appl. Opt.,* **32,** 4088.

J. Astrophys. Astr. (2000) **21,** 103–106

The Kodaikanal Observatory – A Historical Account

The East India Company having resolved to establish an observatory at Madras for promoting the knowledge of Astronomy, Geography and Navigation in India, Sir Charles Oakeley, then President of the Council had the building for the observatory completed by 1792. The Madras series of observations had commenced in 1787 through the efforts of a member of the Madras Government – William Petrie – who had in his possession two three-inch achromatic telescopes, two astronomical clocks with compound pendulums and an excellent transit instrument. This equipment formed the nucleus of instrumentation of the new observatory which soon embarked on a series of observations of the stars, the moon, and eclipses of Jupiter's satellites, with the accurate determination of longitude, as its first concern. The pier that carried the original small transit instrument on a massive granite pillar has on it an inscription in Latin, Tamil, Telugu and Hindustani, so that "Posterity may be informed a thousand years hence of the period when the mathematical sciences were first planted by British liberality in Asia". In any case this quotation from the first annual report of the observatory is at least a record of the fact that astronomical activity at the Madras Observatory was indeed the first among British efforts at scientific studies in India.

The longitude of the Madras Observatory has a most important role as a fundamental meridian from which observations for longitude in the Indian survey are reckoned. The accuracy with which a map of India fits into a map of the world depends solely on the accuracy of the longitude determination of the transit instrument pier at the Madras Observatory. The work of the Great Trigonometrical Survey of India commenced at Madras on April 10, 1802 when a baseline measurement, related to the Madras longitude, was made.

For over a century, the Madras Observatory continued to be the only astronomical observatory in India engaged in systematic measurement of star position and brightness. Goldingham, Taylor, Jacob and Pogson were the Government astronomers who dominated the activity at Madras. With a new five feet transit, Taylor completed in 1884 his catalogue of positions of over 11,000 stars. Double star catalogues, measures of their separation and the determination of their orbits were Jacob's principal interest. The observatory received a new meridian circle during his tenure and with it, besides observations for the determination of star position and evaluation of proper motions, a series of observations of the satellites of Jupiter and Saturn were commenced. From 1861 until his death in 1891, N. R. Pogson as Government astronomer, in keeping with progress in the science, entered into newer areas of observations. While the transit instrument and the meridian circle were both usefully utilized for a star catalogue of 3000 stars that included standard stars, large proper motion stars, variable stars and the like, it is with the new 8-inch Cooke equatorial that he made discoveries of asteroids and variable stars. The asteroids Asia, Sappho, Sylvia Camilla, Vera and the variable star Y Virginis, U Scorpii, T Sagittari, Z Virginis, X Capricorni and R Reticuli were all first discovered visually at Madras either with the transit instrument or by the equatorial instruments. The discovery in 1867 of the light variation of R. Reticuli by C. Raghunathachary is perhaps the first astronomical discovery by an Indian in recent history. Pogson also undertook the preparation of a catalogue and atlas of variable stars, complete with magnitude estimates made by him both of the comparison and the variable. These were edited by Turner after Pogson's death.

During this period the Madras Observatory participated in observations of the important total solar eclipses that were visible from India during the nineteenth century. These were the eclipses that established the foundations of astrophysics and especially of solar physics, and in these observations the Madras Observatory's contributions were most significant. The first one of August 18, 1868 created the subject of solar physics, for at this eclipse the spectroscope was used for the first time to discover the gaseous nature of the prominences. The hydrogen emission lines seen in the prominence were so strong that the French astronomer Jansen reasoned they could be seen without the eclipse. The next day at the eclipse site the speculation was proved to be correct, making it possible for daily surveys of prominences thereafter, without the need of a total eclipse.

There were several eclipse teams scattered over the path of totality for this vital eclipse. The Madras Observatory had two teams, one at Wanarpati and the other at Masulipatam. Clouds at Wanarpati interfered with the success of the expedition. At Masulipatam, Pogson detected the hydrogen lines in emission, as had all the teams that had a programme of observation with the spectroscope. They also saw a bright yellow line near the position of the D lines of sodium. The line originated from a hitherto unknown element later termed helium, after the source of its earliest detection.

On June 6, 1872 an annular eclipse was visible at Madras. Pogson examining the region close to the moon's limb found the bright chrornospheric spectrum flash out for a short duration on the formation and again at the breaking up of the annulus. This is the first observation on record of viewing the flash spectrum at an annular eclipse.

An Indian Observatories Committee in England advised the Secretary of State on matters pertaining to the administration of the Madras Observatory. In many respects, with no adequate staff to help him, Pogson had taken on more programmes of work than he could bring to a successful termination. There were questions raised in London in 1867 whether the Madras Observatory need be continued at all, since the British had started some other observatories in their possessions in the Southern Hemisphere. It was even recommended that the Madras Observatory should concentrate more on publication of the observations already made; than make new ones. The work of Pogson was commended on, and questions on the closure of the Madras Observatory relegated to the time when Pogson would retire.

Meanwhile in May 1882, Pogson had proposed the need for a twenty-inch telescope, which could be located at a hill station in South India, engaged in photography and spectrography of the sun and the stars. The proposal received active support both in India and Britain and necessary authority given for the search of a suitable location in the southern highlands of India. Michie Smith undertook the survey of Palni and Nilgiri hills in 1883 and 1885, his observations covering both the requirements of transparency and steadiness of image during both day and night. But in 1884, the Astronomer Royal recommended that Pogson having accumulated large arrears in observations, saddling him with additional work connected with the new large equatorial would not be desirable — "On Pogson's retirement, the question of establishing a branch observatory or removing the Madras Observatory to a more favourable station might be considered. I am disposed to prefer the latter alternative . . . . . .”

The idea of making solar observations under tropical skies soon gained ground and the search for a suitable site extended over the entire Indian sub-continent. In the north, Leh, Mussoorie and Dehra Dun were examined for their suitability. In the southern part, the study was confined to Kodaikanal, Kotagiri and Madras. In his recommendation to the Government of India, the Meteorological Reporter, on the basis of his two year survey pointed out that the skies were seldom free of dust as to permit observations that called for high transparency. And so the new Observatory had to be located in the southern hills, with Kodaikanal becoming the obvious choice, on the basis of performance. At the Indian Observatories Committee meeting of July 20, 1893 with Lord Kelvin in the Chair, the decision was taken to establish a Solar Physics Observatory at Kodaikanal with Michie Smith as its Superintendent, the decision on the permanent site of the Astronomical Observatory being deferred to a later date. The observatory was to be under the control of the Government of India instead of under the Government of Madras, as it had been for a century earlier.

The last five years of the nineteenth century witnessed a rapid transformation of work from the Madras Observatory to Kodaikanal. The first observations were commenced at Kodaikanal in 1901, and these conformed to patterns in the “new astronomy” that were planned for the observatory. While the two observatories functioned together under the control of a Director at Kodaikanal, the astronomical observations at Madras were confined only to the measurement of time. The new observatory had a wide array of spectroscopic equipment specially acquired for solar studies. There were instruments to visually examine the prominences around the solar limb and the spectra of sunspots. Photographic studies included daily white light photography of the solar disc and monochromatic chromospheric pictures with the spectroheliograms in the light of ionized calcium and of hydrogen. This uninterrupted series photographs, continue unto the present day, and form one of the most unique collections of a record of solar activity available anywhere in the world. Only two other institutions, the observatory at Meudon in Paris and the Mount Wilson Observatory have a collection that spans an equivalent time interval.

Perhaps the most important result of these early years was the discovery by Evershed at Kodaikanal in 1909, of radial motion in sunspots. In the next few years numerous studies of this phenomenon now known as the **Evershed effect,** were made both at Kodaikanal and at a temporary field station in Kashmir. These early studies have been so comprehensive that little has been added to our information on it in the subsequent half century. In 1922, Evershed also discovered under conditions of good seeing, innumerable small displacements of lines equivalent to velocities of the order of a few tenths of a kilometre per second. Nearly fifty years later, with better spectrographic and image resolution, extension of this early discovery have added much information on wave phenomena in the solar photosphere and chromosphere.

For the thirty eight years between 1922 and 1960, the directors were Royds, Narayan and Das. The activity in solar physics was maintained at the pace it has been and work progressed in the traditions of the early years. Highlight of this era are the discovery of the oxygen lines in emission in the chromosphere without the aid of an eclipse, the centre-limb variations of the hydrogen lines and their use to study the solar atmosphere and the detailed study of the properties of the dark markings seen in H-alpha.

For studies of the physical properties of stars the observatory had limited instrumental resources. Nevertheless, some interesting results on comets and stellar spectra were obtained that substantiate the concept that at any such institution the men who use the instruments are more important than the instruments. Soon after his arrival in 1907, Evershed discovered the ultraviolet tail bands in Comet Daniel that are now ascribed to CO^+ Evershed made numerous studies of the planet Venus and of Nova Aquilae 1918. And his high dispersion spectra of Sirius have had the highest dispersion values employed in stellar spectroscopy until recently. . . . .

The IAU Colloquium on the 'Cyclical Evolution of Solar Magnetic Fields' was held in Kodaikanal to mark the Centenary of the founding of the observatory there. The above account of the origin of this observatory, and its activities during the first few decades, is from an unpublished note by the late M. K. V Bappu, a former Director of the Kodaikanal Observatory and the founding Editor of the Journal of Astrophysics and Astronomy.

The adjacent page carries a photo of Michie Smith, the first Director of the Kodaikanal Observatory, and the front cover shows one of the main buildings dating back to the early years. The discovery by John Evershed of radial motions in sunspots was undoubtedly the most seminal contribution from this distinguished observatory. The back cover carries a photograph of Evershed. We have also reproduced the first two pages of his discovery paper from the Bulletin of the Kodaikanal Observatory.

The Editor
J. A. A.

Foreword

The Kodaikanal Observatory was established in 1899. The accompanying note gives the historical background which led to the setting up of this Solar Observatory. To mark the CENTENARY of this Observatory, and in recognition of its many distinguished contributions to solar physics, a Colloquium on **Cyclical Evolution of Solar Magnetic Fields: Advances in Theory and Observations** was held at the Kodaikanal Observatory. We are very grateful to the International Astronomical Union for agreeing to sponsor this as the IAU COLLOQUIUM 179.

We are thankful to the **Indian Academy of Sciences** for agreeing to publish the Proceedings of this historic colloquium as one of the issues of the *Journal of Astrophysics and Astronomy*. The various papers appearing in these proceedings vouch for the continuing interest of solar physicists the world over in the fascinating interplay of magnetic fields and plasma dynamics leading to the sunspot cycle. These papers also demonstrate that the ramifications of the solar cycle extend from deep within the Sun out to the far reaches of the solar system.

The organization of an international meeting, and bringing out the proceedings involves a considerable amount of work. On behalf of the Scientific Organizing Committee we wish to record our gratitude to a number of people and organizations. The original initiative to hold such a meeting came from the solar physics group of the Indian Institute of Astrophysics in Bangalore. Later several astronomers, in particular Bob Howard, added substance to the idea. Members of the organizing committees of Commissions 10 and 12 of the IAU gave the final shape to the programme.

Mr. Brajesh Kumar of the Udaipur Solar Observatory has helped us in a major way with these proceedings, and we would like to express our sincere thanks to him. Thanks are also due to a number of referees who helped us in processing the written contributions. Finally, we would like to express our gratitude to Ms Hema Wesley at the Academy for taking the overall responsibility of editing this volume.

P. Venkatakrishnan
Oddbjorn Engvold
Arnab Rai Choudhuri
Guest Editors

J. Astrophys. Astr. (2000) **21,** 119–125

Active Region Magnetic Fields

Robert F. Howard, *National Solar Observatory, Tucson, Arizona 85726, U.S.A.*
e-mail: howard@noao.edu

Abstract. The tilt angles of sunspot groups are defined, using the Mount Wilson data set. It is shown that groups with tilt angles greater than or less than the average value (≈ 5 deg) show different latitude dependences. This effect is also seen in synoptic magnetic field data defining plages. The fraction of the total sunspot group area that is found in the leading spots is discussed as a parameter that can be useful in studying the dynamics of sunspot groups. This parameter is larger for low tilt angles, and small for extreme tilt angles in either direction. The daily variations of sunspot group tilt angles are discussed. The result that sunspot tilt angles tend to rotate toward the average value is reviewed. It is suggested that at some depth, perhaps 50 Mm, there is a flow relative to the surface that results from a rotation rate faster than the surface rate by about 60 m/sec and a meridional drift that is slower than the surface rate by about 5 m/sec. This results in a slanted relative flow at that depth that is in the direction of the average tilt angle and may be responsible for the tendency for sunspot groups (and plages) to rotate their magnetic axes in the direction of the average tilt angle.

Key words. Active regions—sunspot groups—group tilt angles.

1. Introduction

The study of the Sun has since the early 17th century and the work of Galileo, Scheiner and others been a field that has relied in part on long-term observational studies. The great majority of these programs have proved to be of great importance to the field of solar physics. In the history of our field we find many important contributions to solar physics, and indeed to the broader field of astrophysics, that have relied heavily on findings from these synoptic programs. Examples begin with the discovery by Galileo of the rotation of the Sun. Other later examples include the solar cycle itself, the latitude drift of sunspots during the cycle, differential rotation, the reversal of sunspot magnetic fields (and later the polar magnetic field) as each cycle progresses, cycle related variations in such things as filament distribution, coronal features, flares, plages, etc., latitude-dependent rotation variations (torsional oscillations), and more. None of these facts about the Sun would have been discovered without regular, persistent observations, in some cases over many decades.

One of the leading observatories in the world, with some of the longest runs of fundamental solar observations, is the Kodaikanal Observatory, now a station of the Indian Institute of Astrophysics. The value of the observational archives of the

Kodaikanal Observatory and other long-term archives has only in the last decade or two been fully appreciated and utilized. With the introduction of digitizing techniques, it is now possible to collect relatively easily the results of many years of observations and analyze these data to search for repeatable patterns that give us insight into the large-scale, long-term phenomena that are related to the mechanism of the activity cycle.

Here I will examine some interesting new phenomena of this sort, and discuss their relevance to the activity cycle. This work is just an example of the sort of thing that can be done with long, high-quality data sets. But analyses of this sort have only begun. There is very much more that remains to be done.

2. Tilt angles of sunspot groups

The tilt angle of a sunspot group (or an active region) is an important quantity. It is now generally thought to result from the action of the Coriolis force on the rising magnetic flux tube that erupts at the surface to form the active region (Schmidt 1968; Wang & Sheeley 1989; D' Silva & Howard 1993). This quantity was recognized as an important parameter in solar activity many years ago, and was the subject of an early paper that showed for the first time that the tilt angle varied systematically with solar latitude (Hale *et al.* 1919). It is this work that has led recently to calling this effect Joy/s law.

Here I will examine the tilt angles of sunspot groups derived from the Mount Wilson Observatory archive. The digitization and analysis of these data are described in an earlier paper (Howard, Gilman & Gilman 1984). The data extend from 1917 through 1985. The tilt angles are derived by the following means. The area-weighted centroid of the sunspot group is determined in solar latitude and central meridian distance. Then the sunspots to the west of the center are defined to be leading sunspots, and the others are defined to be following sunspots. Similar centroids are then determined separately for these leading and following sunspots. The angle between the line joining these centroids and the local parallel of latitude is defined to be the "tilt angle."

In Fig. 1 I have plotted Joy's law, the relationship between tilt angle and latitude, for two subsets of the data. The first is for tilt angles greater than +5 deg (the average tilt angle), and the second (dashed lines) is for tilt angles less than +5 deg. The solid lines represent least-squares solutions for straight lines. The slope of the upper curve is 0.084 ± 0.015. The slope of the lower curve is -0.100 ± 0.020. There are 12592 sunspot groups represented in the upper curve, and 11898 in the lower curve. These curves are plotted for groups with absolute latitudes less than 35 deg in order to avoid the influence of a small number of extreme cases. This result indicates that perhaps the relationship between Joy's law and the effect of the Coriolis force on rising flux tubes is not as simple as we had first thought and requires further consideration.

One possible explanation for this effect is that the width of the distribution of tilt angles increases with latitude. But plots of this function (not shown here) show no such systematic effect. Also it might be argued that the method used here to define the tilt angle in some way introduces a bias in the angles as a function of latitude in such a way as to produce the effect seen in Fig. 1. In order to eliminate such a possibility, a figure has been plotted which shows the same plot as Fig. 1, but for

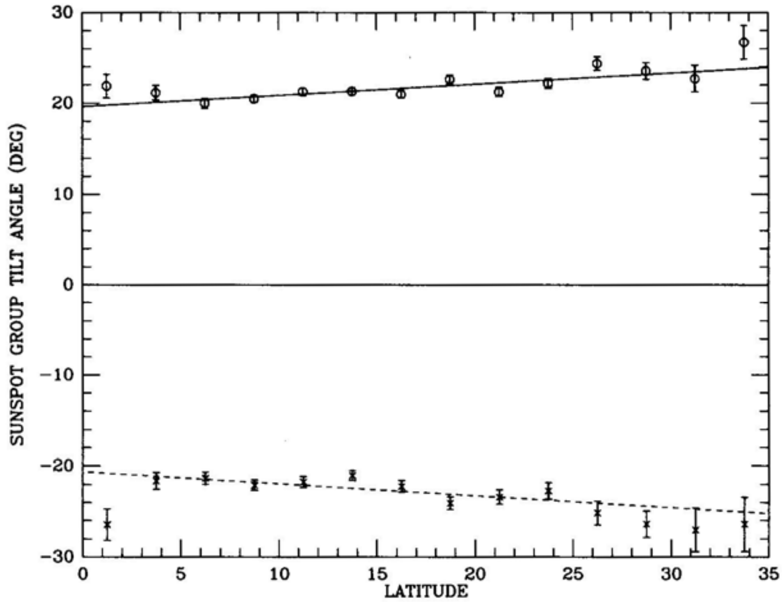

Figure 1. Tilt angle vs latitude, top plot for sunspot groups with tilt angles greater than the average value, and bottom for sunspot groups with tilt angles less than the average.

Mount Wilson plage (magnetograph) data (Howard 1989). Here the data set is of plages with normal (not reverse) magnetic orientation. This is a data set that is completely independent of the sunspot data. In this figure (not shown here) a very similar effect is seen, thus confirming this result and illustrating that the effect is not an artifact of the method of calculating the tilt angles, and that it holds for plages as well as sunspot groups.

If the broad distribution of tilt angles seen in Fig. 1 is due, as has been assumed, to the effect of random, large-scale convective motions on the rising flux loops of the active regions, then it is difficult to imagine how groups on one side of the average tilt angle in Fig. 1 could show a different latitude dependence of the tilt angle than groups on the other side. If the Coriolis force is the sole factor that determines the average tilt angle of the regions at the surface, then it should act on all of the rising flux tubes in the same manner. However, as will be discussed below, tilt angles of regions change once they reach the surface, and this mechanism of change may be the key to this extension of Joy's law.

3. The fraction of the sunspot group area in leading and following sunspots

Sunspot groups do not all have leading and following sunspots of equal area. Some groups have more area in their leading sunspots, and some in their followers. We do not know why this is so.

It is of interest to ask how the fraction of the total group area in leading sunspots is distributed among sunspot groups of various tilt angles. Is there a relationship between these two quantities that may provide information regarding the physics of

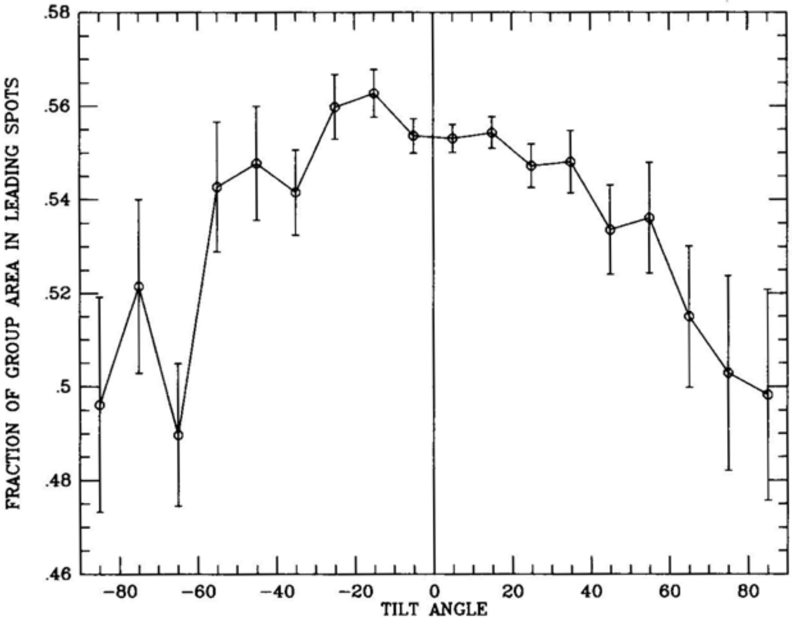

Figure 2. Averages of the fraction of the sunspot group area in the leading spots to the area in the following spots over 10-deg intervals of tilt angle for the full Mount Wilson data set.

the process that brings magnetic flux loops to the surface to form active regions? In an attempt to answer that question, Fig. 2 has been plotted.

It is clear from Fig. 2 that the smallest tilt angles correspond to the largest values of F, the fraction of the sunspot group area that is in the leading sunspots. On average, sunspot groups with extreme tilt angles tend to have the smallest values of F. It has been shown by Fan, Fisher & DeLuca (1993) that as the magnetic flux loop rises to the surface the magnetic fields of the leading portion of the loop tend to remain more vertical than the following portion, which they claim may be responsible for the fact that the largest sunspots are generally found in the leading part of the group ($F > 0.5$). Extreme tilt angles in one direction or another may provide an additional field line inclination that might further break up the original magnetic flux tubes and thus lead to a decrease in the size of leading or following sunspots in the group.

4. Tilt angle variations

The tilt angles of sunspot groups generally show variations with time. Most variations in the tilt angle are small, but the distribution extends to ±90 deg, although some of these extreme changes may be the result of processes such as the merging or separation of closely spaced multiple groups. Again, because of the lack of magnetic field information, we cannot determine tilt angle changes beyond ±90 deg.

Looking at the daily tilt angle change averaged over latitude drift bins (Fig. 3), we see a systematic behavior. Here the values of tilt angle change greater than ±40 deg have been omitted to avoid possible errors (i.e. tilt angle changes that are not really

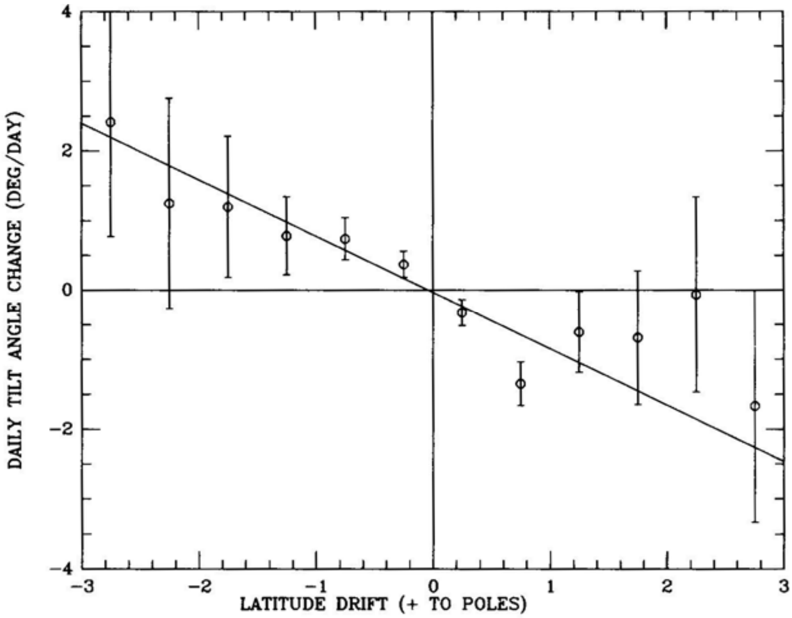

Figure 3. Average daily tilt angle change over intervals of 0.5 deg/day in latitude drift. Positive latitude drift represents poleward motion.

tilt angle changes, such as merging of nearby groups or eruption of new flux). In this plot the straight line is the linear, least-squares solution. The slope of this line, from this solution is –0.810 ± 0.096. The negative slope indicates that when sunspot groups are rotating to more positive tilt angles, the group shows an equatorward drift. This suggests that the rotation of the tilt angle of the group is about the following sunspots, or about some point closer to following than leading sunspots. This is in agreement with a recently derived result using the same data (and the Kodaikanal data) but from a quite different technique (Howard, Sivaraman & Gupta 2000).

The tilt angles of sunspot groups tend on average to rotate toward the average tilt angle (≈+5 deg). This is illustrated in Fig. 4. Here the data are limited to groups with absolute tilt angles less than 50 deg and absolute tilt angle changes less than 40 deg as discussed in the earlier study (Howard 1996). We see a surprising result here because if the tilt angle is determined by the effect of the Coriolis force during the rise of the magnetic flux tube to the surface, what turns the axis after the group appears, and why is it turned on average toward the average tilt angle? What is special about that angle after the group has arrived at the surface? The generally accepted view of the appearance of an active region at the surface is that the loop of magnetic flux that will form the region rises from a source toriodal flux bundle that is located just below the bottom of the convective zone (Parker 1955; Rosner 1980; DeLuca & Gilman 1986). The convective zone is a region where there are, of course, large- and small-scale motions which are a part of the convective process. It is difficult to imagine that a flux tube at the average tilt angle (or at any angle) could be stable at any level within the convection zone.

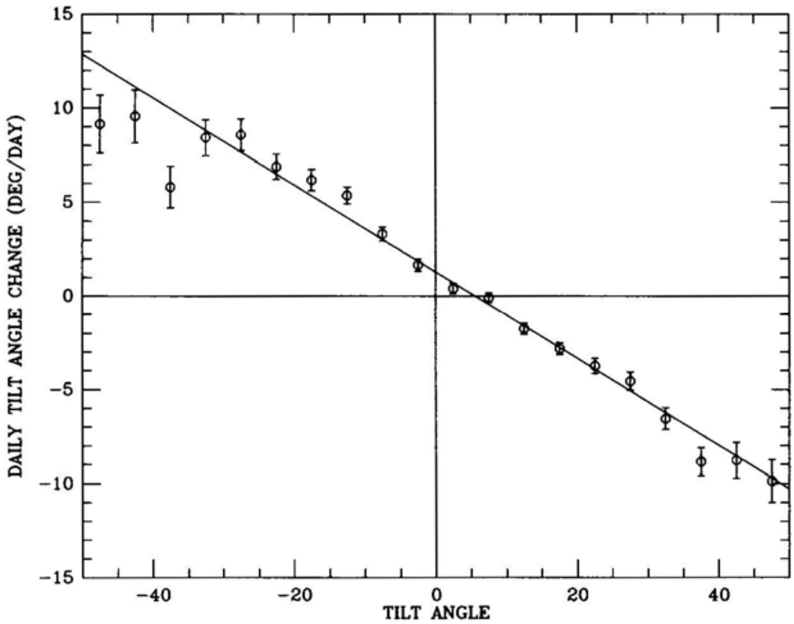

Figure 4. Average daily tilt angle change over 5-deg intervals of tilt angle for the full Mount Wilson data set.

5. A possible explanation

Another possible explanation presents itself, however. We know little about the dynamics of the solar interior. But helioseismology, using GONG and MDI data is beginning to shed some light on the depth dependence of solar rotation. Recent results (Beck 1999) have shown that the rotation rate at a small depth below the surface (say 0.93 R_0, or 50 Mm) is about 3% faster than the surface rate over a broad range of intermediate latitudes. This corresponds to a difference from the surface values of about 60 m/sec.

We know nothing about meridional flows at these depths, but we may hope that eventually global oscillations will give us some clues (Giles *et al.* 1997; Basu *et al.* 1999). In the meantime we can hypothesize that since at the surface we know that the plasma drifts poleward with a velocity of about 10–20m/sec, at some depth below the surface there must be a return flow, equatorward, at some rate - or at least that the magnitude of the poleward flow should decrease. We do not know the range of depths of the surface flow, but it is not unreasonable to assume that at 0.93 R_0 (or 50 Mm), where the rotation is faster than the surface rate, as mentioned above, we may expect a poleward flow that is lower in amplitude than the surface flow by perhaps 25–50.%, or about 5 m/sec. This is equivalent to a relative motion in the meridional direction equatorward at 5 m/sec. If we then combine the rotation rate, faster than the surface by 60 m/sec with a net 5 m/sec equatorward flow, we find a resultant streaming of material in a direction that makes an angle with the local parallel of latitude of about 5 deg, or about the same order of magnitude and in the same direction as the average tilt angle. This picture involves, of course, several assumptions. We don't really know anything about subsurface meridional motions yet, but we can expect that results from GONG or MDI data will open this area up to observational study before long.

Thus one suggestion to explain the tendency for sunspot (and plage (Howard 1996)) tilt angles to rotate toward the average is that there is a large-scale, persistent velocity field at the average tilt angle that acts to rotate the flux loop in that direction. Note that the rotation is principally about the following portion of the region, as discussed above.

Note that a slight variation in the latitude dependence of either the rotation rate difference from the surface to the subsurface layers or of the latitude drift rate difference could contribute to the latitude dependence of the tilt angle (Joy's law). We may note that if the subsurface meridional flow decreases with latitude, which one might expect because of the spherical geometry of the surface layers, then the difference between the magnitudes of the surface flow and the deeper flow will increase, thus increasing the difference between the two flow velocities, which will increase the flow angle, which is what we see in Joy's law.

If this is the explanation for the rotation of the magnetic axes of sunspot groups after their appearance at the solar surface, then perhaps this will also help explain the result described above concerning the different slope of Joy's law for groups with tilt angles less than and greater than the average value. It is possible that the effect on the tilt angle of the inclined subsurface flow is different for regions with tilt angles greater than and less than the average value.

Acknowledgement

This research is supported in part by Grants INT-9003847 and INT-9604920 from the US-India Cooperative Science Program of the Division of International Programs, US National Science Foundation. I wish to acknowledge the several generations of observers at Mount Wilson who made these observations covering many decades. Without their dedication and careful work this study would not have been possible.

References

Basu, S., Antia, H. M., Tripathy, S. C. 1999, *Astrophys. .J.,* **512,** 458–470.
Beck, J. G. 2000, *Solar Phys.,* **191,** 47–70.
DeLuca, E. E., Gilman, P. A. 1986, *Geophys. Astrophy. Fluid Dynamics.,* **37,** 85–127.
D' Silva, S., Howard, R. F. 1993, *Solar Phys.,* **159,** 63–88.
Fan, Y., Fisher, G. H., DeLuca, E. E. 1993, *Astrophys. J.;* **405,** 390–401.
Giles, P. M., Duvall, Jr., T. L., Scherrer, P. H., Bogart, R. S. 1997, *Nature,* **390,** 53–54.
Hale, G. E., Ellennan, F., Nicholson, S. B., Joy, A. H. 1919, *Astrophys. J.,* **49,** 153–178.
Howard, R. F. 1989, *Solar Phys.,* **123,** 271–284.
Howard, R. F. 1996, *Solar Phys.,* **167,** 95–113.
Howard, R. F., Gilman, P. A., Gilman, P. I. 1984, *Astrophys. J.,* **283,** 373–384.
Howard, R. F., Sivaraman, K. R., Gupta, S. S. 2000, *Solar Physics* (submitted).
Parker, E. N. 1955, *Astrophys. J.,* **121,** 491–507.
Rosner, R. 1980, in '*Cool Stars, Stellar Systems and the Sun,*' Smithsonian Astrophys. Obs. Report No. 389, (ed.) A. K. Dupree, pp 79–96.
Schmidt, H. U. 1968, in '*Structure and Development of Solar Active Regions,*' IAU Symposium No. 35, (ed.) K. O. Kiepenheuer, (Reidel: Dordrecht, The Netherlands), pp 95–107.
Wang, Y.-M., Sheeley, N. R., Jr. 1989, *Solar Phys.,* **124,** 81–100.

J. Astrophys. Astr. (2000) **21**, 127–134

New Initiatives for Synoptic Observations

C. U. Keller, *National Solar Observatory, 950 N. Cherry Ave., Tucson, AZ 85719, USA. e-mail:keller@noao.edu.*

Abstract. Several new synoptic facilities for long-term studies of the Sun will become operational within the next few years. This paper summarizes information on some of these projects, in particular GONG+, ISOON, GOES/SXI, and SOLIS. SOLIS, the Synoptic Optical Long-Term Investigations of the Sun, is currently being built by the National Solar Observatory and will become operational in 2001. It consists of a 50-cm vector spectromagnetograph, a 14-cm full-disk patrol, and an 8-mm sun-as-a-star spectrometer.

Key words. GONG—ISOON—SXI—SOLIS.

1. Introduction

Many new synoptic facilities and instruments will become available during the next few years. Here I summarize information on the initiatives that I am most familiar with.

2. GONG+

The Global Oscillation Network Group (GONG) is currently upgrading its instruments from the current 256 by 256 pixel format to 1024 by 1024 CCD cameras running at 60 Hz. In addition, the new system will provide magnetograms at this resolution once every minute. Slow network connections to some of the GONG sites will limit the real-time availability to about one averaged magnetogram every 5 minutes. GONG+ will become operational in mid-2000.

3. Improved Solar Observing Optical Network (ISOON)

The US Air Force (USAF) has a network of telescopes around the world called SOON (Solar Observing Optical Network). The improved version of this network, called ISOON, will consist of four optical telescopes at existing SOON sites: Holloman, New Mexico, USA; Learmonth, Australia; San Vito, Italy; and Ramey, Puerto Rico, USA. ISOON will transmit data in near-real time to the USAF and the Space Environment Center of NOAA for use in space weather forecasting. ISOON is an upgrade of the existing SOON facilities with a tunable, dual Fabry-Perot filter system and a 2048 by 2048 CCD camera. The prototype is currently being built at the National Solar Observatory/Sacramento Peak and should become operational in 2001. Table 1 lists the various data products of ISOON. In addition to these primary

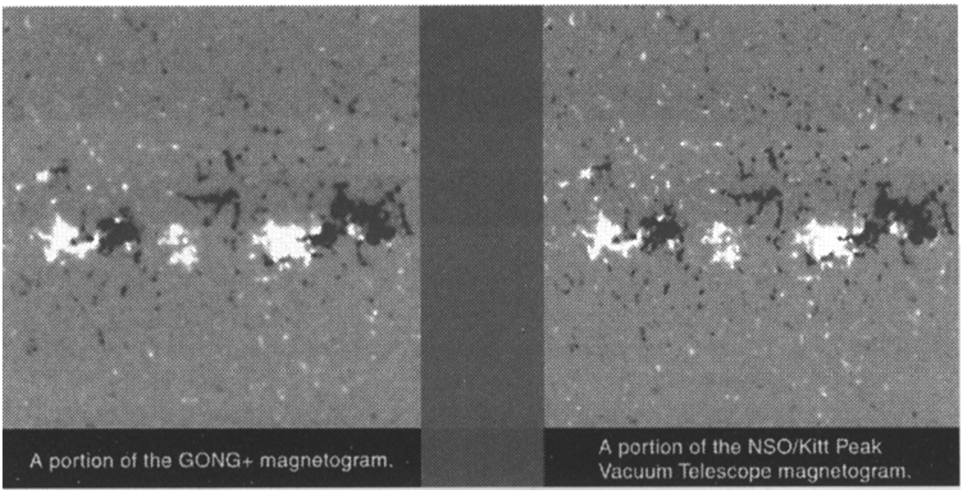

Figure 1. Comparison of magnetograms from the GONG+ prototype and the daily Kitt Peak magnetogram.

Table 1. ISOON data products.

Data Product	Frequency
Full disk Hα line center	1 per minute
Full disk continuum at 612.0 nm	1 per hour
Full disk photospheric magnetogram at 612.2 nm	1 every 3 hours
Off limb Hα line center	occasionally
Full disk Hα off band	occasionally

data products, data derivatives such as intensity histograms, flare area, brightness, location, start, maximum, and end will be provided.

The USAF is not interested in long-term data storage, since it is not required for space weather forecasting. Other agencies will need to take care of this. Also, public access to the data has not been defined at this time.

4. GOES/Solar X-ray Imager (SXI)

The next generation of US weather satellites (GOES) will have a small X-ray imager mounted on the solar array yoke. SXI will provide continuous monitoring of the Sun in X-rays. The data will be used by NOAA and the USAF to determine when to issue forecasts and alerts of space weather conditions that may interfere with ground and space systems.

SXI will provide full-disk 512 by 512 pixel images in 10 wavelength bands from 6 to 60 Å at one-minute intervals. The expected useful life is 3 years with a goal of 5 years. The first SXI instrument was built by NASA's Marshall Space Flight Center, subsequent models were built by Lockheed-Martin. The first satellite equipped with SXI should become operational in October 2000 and the subsequent ones in 2002 and 2003.

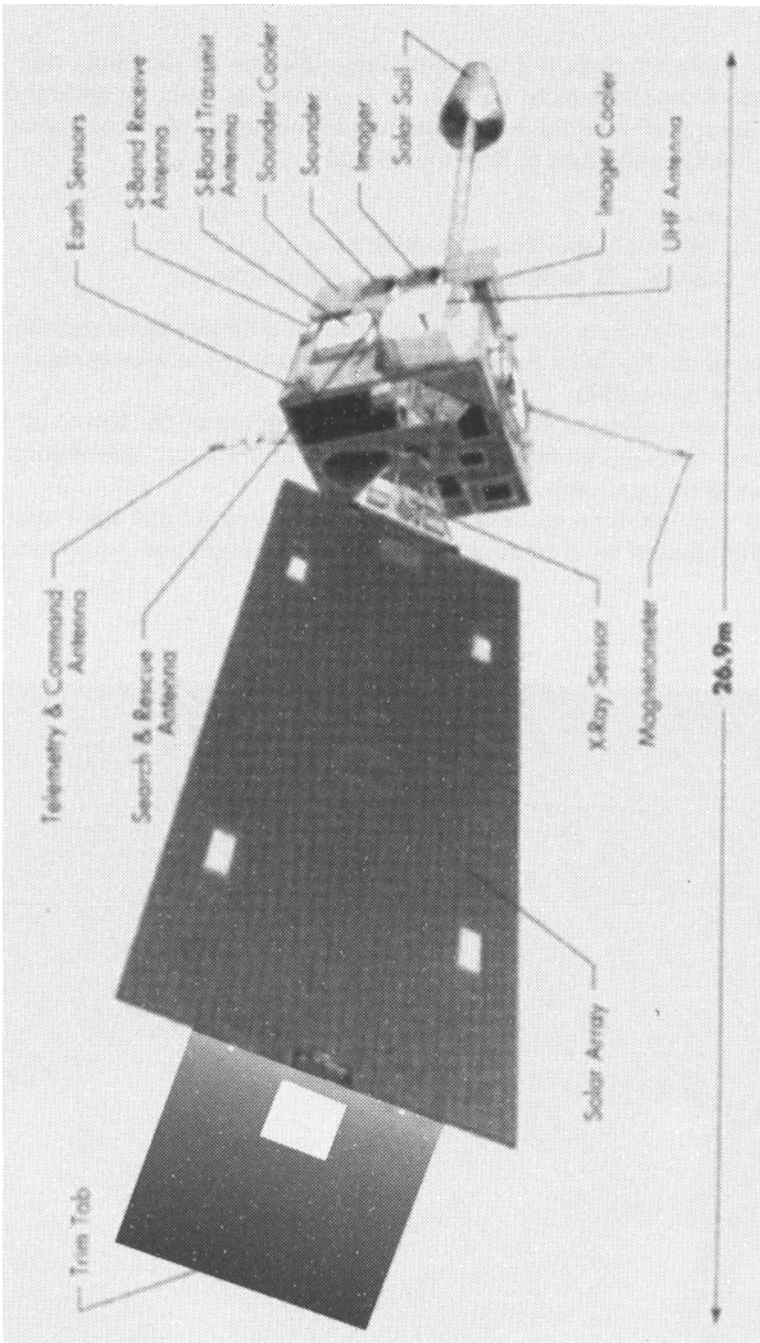

Figure 2. The GOES spacecraft.

5. SOLIS

5.1 *Overview*

SOLIS, the Synoptic Optical Long-term Investigations of the Sun, will provide unique, modern observations of the Sun on a continuous basis for several decades. These long-term studies of the most important astronomical object to humanity will provide the fundamental data to help understand

- the solar dynamo.
- flares, mass ejections, and their terrestrial effects.
- irradiance changes and their relationship to global change.

SOLIS consists of three instruments attached to a single equatorial mount (see Fig. 4). The mount has been finished and will be installed at a preliminary site for testing in early April 2000.

In its final configuration, SOLIS will be located on top of the Kitt Peak Vacuum Telescope and become operational in 2001 (see Fig. 3). More information can be found at www .nso .noao .edu/solis.

The next three sections describe the various instruments and their status as of March 2000, followed by a description of the data products and the operations.

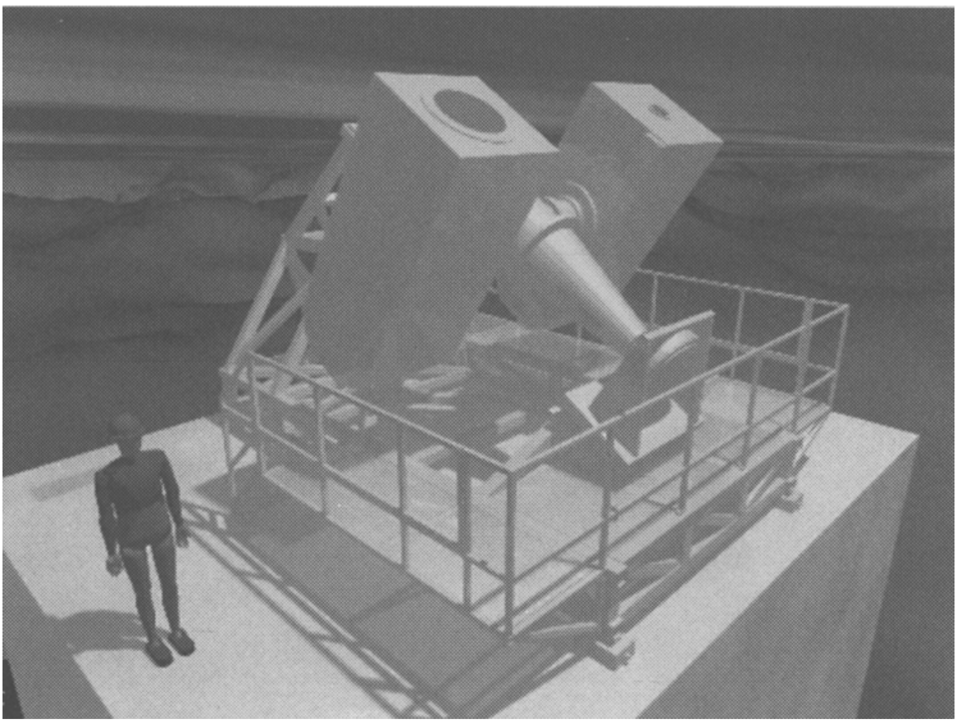

Figure 3. SOLIS on top of the Kitt Peak Vacuum Telescope.

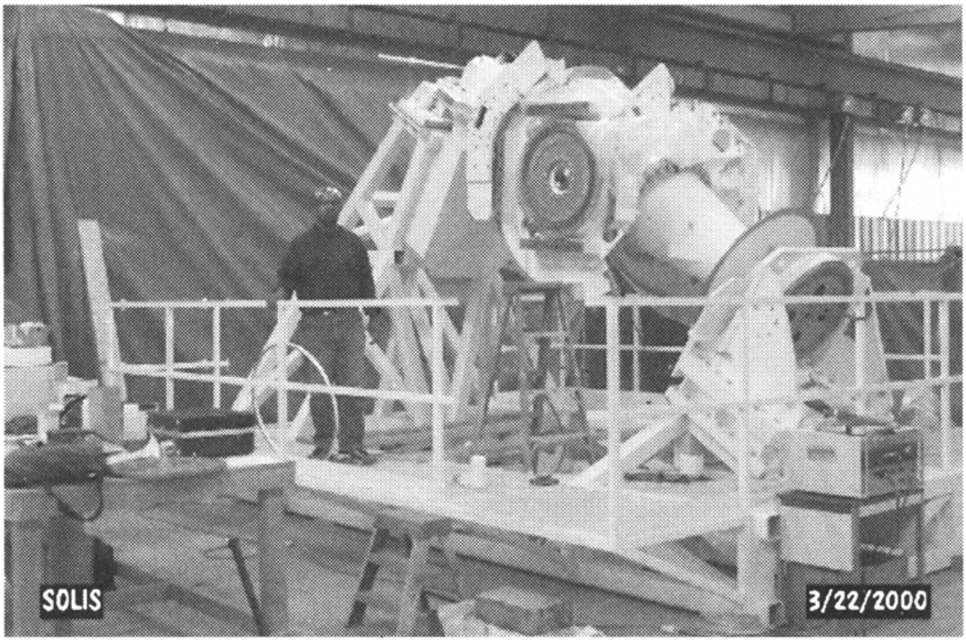

Figure 4. The SOLIS mount.

5.2 *Vector-Spectromagnetograph (VSM)*

The VSM is a 50-cm quasi-RC telescope with an active secondary mirror that compensates for image motion and telescope shake up to 40 Hz. The telescope is filled with helium to reduce internal seeing by about a factor of 10 and has a 6-mm thick fused silica entrance window. The guider consists of four linear arrays embedded in the focal-plane heat dump. The spectrograph has a Littrow design that is insensitive to temperature changes. The entrance slit is scanned in declination to provide 2048 by 2048 pixel scans of the full solar disk. The polarization modulation is performed by ferroelectric liquid crystals running at 300 Hz. Two 1024 by 256 pixel backside-illuminated CCD cameras record 300 frames per second, which are then analyzed to obtain the Stokes parameters. The VSM is capable of recording vector magnetograms in FeI 630.2 nm, deep longitudinal magnetograms in FeI 630.2 nm, longitudinal magnetograms in Ca II 854.2 nm, and intensity in HeI 1083.0 nm. The slit can be scanned in 1 arcsec increments with 0.1 to 5.00 seconds per slit position. This provides regular full-disk scans in 15 minutes while fast full-disk scans can be performed in 3 minutes.

As of March 2000, the optics and most of the mechanical parts have either been received or are in production.

5.3 *Full-Disk Patrol (FDP)*

The FDP is a 14-cm refractor with a fast tiptilt mirror for image motion compensation. It features a 0.25 Å universal birefringent filter working from CaII K to

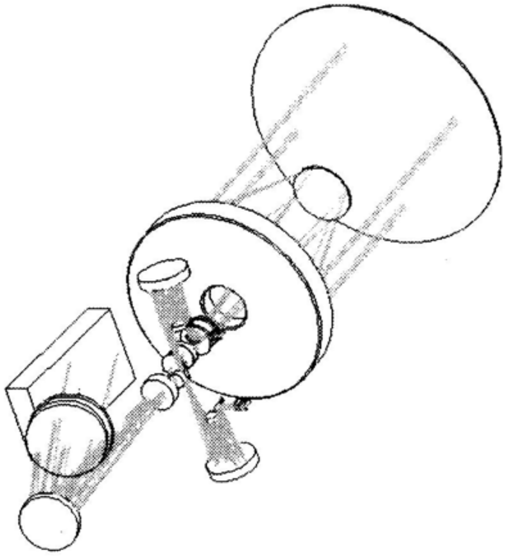

Figure 5. Optical schematic of the SOLIS Vector-Spectromagnetograph.

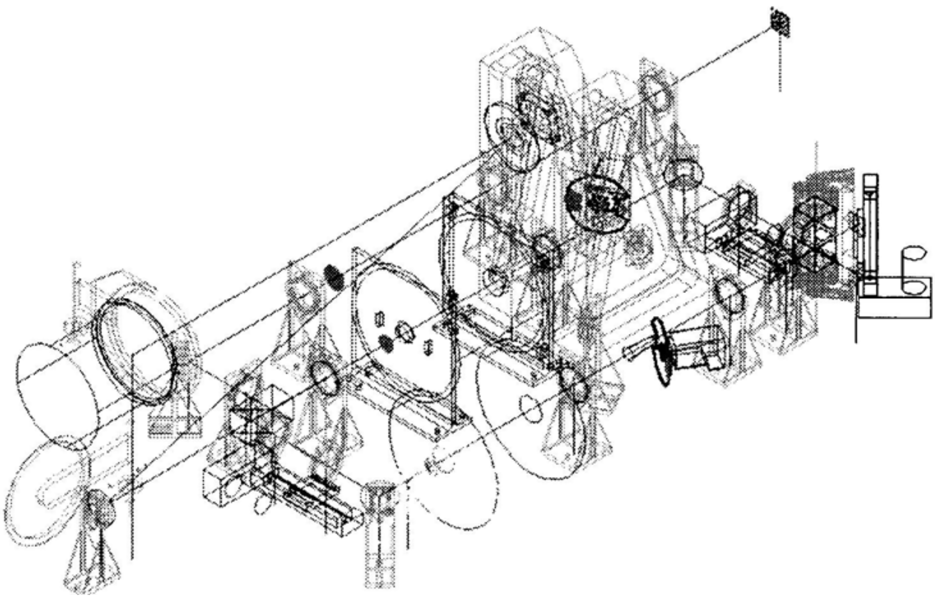

Figure 6. A wire-frame schematic of the FDP optics.

Hα. In addition, there is a separate HeI 1083.0 nm filter. The filter pass-band is monitored with the fiber-fed spectrograph (see below). Two 2048 by 2048 pixel CCD cameras will provide accurate intensity and Doppler measurements at about one full-disk image per second.

As of March 2000, many of the optical parts have been received and a preliminary mechanical design has been finished.

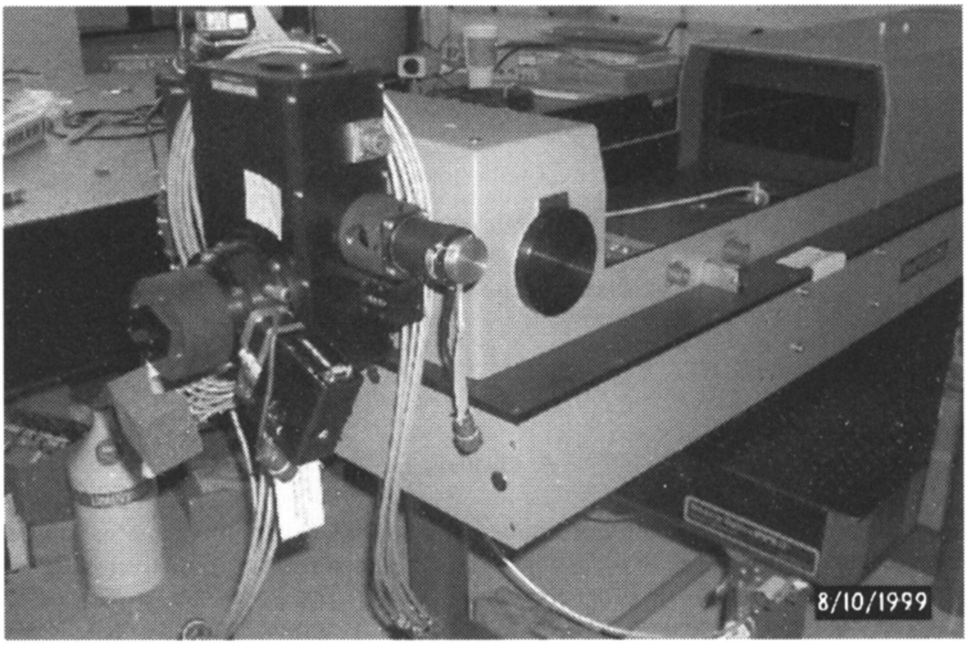

Figure 7. The SOLIS Integrated Sunlight Spectrometer during testing.

5.4 *Integrated Sunlight Spectrometer (ISS)*

The ISS consists of two 8-mm telescopes feeding fibers. One of the two beams goes through an iodine absorption cell for very precise Doppler measurements. The fibers are fed into a commercial 2-m double-pass spectrograph from McPherson that provides a choice of spectral resolution: 30,000 and 300,000. A 1024 by 1024 pixel CCD camera is mounted onto a movable stage for accurate flat-fielding. The ISS has a quartz lamp for flat-fielding and a U-Ar lamp for wavelength calibrations. The iodine cell will allow a spectrograph stability of 1 m/s. In addition to the two small telescopes, there will be an extinction monitor, which produces images of the Sun in 5 wavelengths to measure differential extinction across the solar disk.

As of March 2000, the ISS has already produced very accurate spectra.

5.5 *Operations*

SOLIS is a remote-controlled, autonomous system operating similar to a satellite. It records synoptic core as well as user-driven observations. It allows event-triggered observing (e.g. flares or rocket flights) and features automatic scheduling of observations with proposal submission and data access over the internet. There is a completely open data policy where reduced data will be available within minutes after they have been recorded and reduced.

The data handling relies on a 1 TB, 150 MB/s Storage Area Network (SAN) and a 45 Mb/s DS-3 line from Kitt Peak to Tucson, where data will be integrated into the existing Digital Library.

Table 2. SOLIS core data products.

Data Product.	Frequency
Photospheric vector magnetogram	3 per day
Chromospheric longitudinal magnetogram	3 per day
Helium 1083.0 nm (coronal proxy)	3 per day
Deep photospheric magnetogram	one per day
Hα core and wing intensity, velocity	1 per minute
He I 1083.0 nm core intensity and velocity	one per minute
Continuum (white light)	one per 10 minutes
Ca II K core and wing (chromospheric) intensities	
Oscillation-free photospheric velocity	one per day
Various sun-as-a-star profiles	2 per day

6. Outlook

Several new synoptic facilities are coming on-line in the next few years. Most of the reduced data will be readily accessible over the internet. Other initiatives such as STEREO, HESSI, and Solar-B in space and RISE/PSPT, helioseismology networks, and many university-based programs will provide a wealth of data.

The major drawback of SOLIS is the limitation to a single longitude. The mount can accommodate a range of latitudes.

J. Astrophys. Astr. (2000) **21**, 135–140

New High Resolution Observations of the Solar Diameter from Space and Ground with the Microsatellite Program PICARD

Luc Damé, *Service d'Aéronomie du CNRS, 91371 Verrières-le-Buisson, France*
e-mail: luc.dame@aerov.jussieu.fr

Abstract. The PICARD microsatellite mission will provide 2 to 6 years simultaneous measurements of the solar diameter, differential rotation and solar constant to investigate the nature of their relations and variabilities. The 100 kg satellite has a 40 kg payload consisting of 3 instruments which will provide an absolute measure (better than 10 milliarcsec) of the diameter and the solar shape, a measure of total solar irradiance, and UV and visible flux in selected wavelength bands. Now in Phase B, PICARD is expected to be launched before mid-2003. The engineering model of the diameter telescope will be used on ground simultaneously with the satellite to investigate the atmospheric bias and state on the possible accuracy of the ground measurements carried up to now. We review the scientific goals linked to the diameter measurement, present the payload, and give a brief overview of the program aspects.

Key words. Solar diameter—solar shape—long-period oscillations—g-modes—solar influence on climate.

1. Introduction

Since solar energy is one of the major driving inputs for terrestrial climate and since some correlations between surface temperature changes and solar activity exists, it appears important to know on what time scale the solar irradiance and other fundamental solar parameters, like the diameter, vary in order to better understand and assess the origin and mechanisms of the terrestrial climate changes.

Global effects, such as diameter changes, large convective cells, the differential rotation of the Sun's interior and the solar dynamo at the base of the convective zone, can probably produce variations in the total irradiance or, at least, correlate with these variations associated, during maximum, with the changing emission of bright faculae and the magnetic network. The aim of these correlations is twofold: on one side prediction and on the other explanation of the past history of climate, like the Maunder minimum period.

To establish long-term links and trends between solar variability and climate changes, it is necessary to achieve not only high precision but also absolute measurements, which the diameter measurements of PICARD aim at. Further, this high precision allows "instantaneous" monitoring of the diameter changes, i.e., with a proper orbit for the microsatellite, oscillations and, in particular, the gravity modes.

2. Scientific objectives

2.1 *Why the diameter?*

From 1666 to 1719, Jean Picard and his student Philippe de la Hire measured the solar diameter, observed the sunspots and determined the Sun rotation velocity. Fortunately, these measurements covered the Maunder minimum and some time after. The data were re-examined by Ribes *et al.* (1987) who, after removing the seasonal variation of the solar diameter, obtained the annual means at 1 AU. These values, averaged for the Maunder minimum period, show a significant difference of the order of 0.5 to 1 arcsec and after the Sun recovered a significant activity, corresponding to a larger Sun diameter during the Maunder minimum. As expected, few sunspots were observed. However, Picard's data also showed a slow down of the Sun's rotation velocity at the equator and more sunspots in the southern hemisphere than in the north.

2.2 *Diameter and earth's climate*

The solar constant measurements performed in space by the radiometers since 1978 were modeled using the sunspots number and faculae. This allowed the reconstruction of the solar constant variation back to 1610 (Lean 1997). This showed that the solar constant experienced a significant decrease during the Maunder minimum. The temperature in the northern hemisphere has been also reconstructed for the same period. The cooling of this period is known as the Little Ice Age. The similarity of the temperature and solar constant variations strongly suggests the Maunder minimum to be the cause of the Little Ice Age. To assess this suggestion, climate models were run by Sadourny (1994) that showed the Maunder minimum as the possible cause of the Little Ice Age. Volcanic eruptions (major ones) also play a certain role, but their effects do not extend over more than a few years.

In a similar fashion, the modern data of solar diameter measurements and sunspots number, set together by Laclare *et al.* (1996), reveal an increase of the Sun's radius for a decrease of the solar constant. We propose to operate from space by measuring simultaneously both quantities from the same platform and in non-magnetic lines or continua in order to establish experimentally without ambiguity the solar constant and diameter relationship. The importance of the measurements for climatology is straightforward, taking into account the Little Ice Age and the Maunder minimum events.

2.3 *Prediction and precision*

The total solar irradiance measurements made by radiometers from space over the last 20 years, is excellent in relative terms (10^5) but poor in absolute. The amplitude of the variation over the cycle (0.1%) is small and is about the same as the uncertainty on the absolute value from one instrument to the other. Prediction of climate change from such data is not straightforward and the adjustment of datasets of different origins is an art (cf. Fröhlich & Lean 1998). On the contrary, if the relation irradiance-diameter is established by PICARD, the diameter measure which is precise, reproducible and absolute to 10 mas (or even better when the HIPPARCOS data will be recalibrated by FAME or GAIA) and which, according to Laclare *et al.* (1996), has an amplitude over the solar cycle of 0.4–0.6 arcsec or so, provides a proper- and quantified-sampling of the activity change over the cycle.

2.4 *Lyman alpha monitoring*

PICARD will provide high resolution (1") Lyman alpha images which will complement the EOS/SOLSTICE measurements. These images will make it possible to account better for the observed Lyman alpha changes and also for a better reconstruction of a long-term Lyman alpha data set. Lyman alpha is important for the ozone changes and the formation of the ionospheric D-region in the Earth's atmosphere and this should result in progress in atmospheric science and aeronomy.

2.5 *Long-period oscillations*

Another major objective of PICARD is to attempt the detection of the gravity modes (g-modes) of the Sun. These modes are of prime importance to understand the structure and dynamics of the solar core which cannot be studied by using solar pressure modes (p-modes) alone. So far the g-modes have not been discovered by any set of instruments onboard the SOHO spacecraft (Appourchaux *et al.* 2000). The 1-σ upper limit of g-mode amplitude at around 200 μHz is typically 1 mm/s or 0.1 ppm (Fröhlich *et al.* 1998). Given a velocity amplitude of 1 mm/s at 200 μHz, the displaycement of the solar surface would be about 1.6 m pp which is equivalent to a variation of solar radius of about 2 μ arcsec. This level could be marginally detected by PICARD although this is not the method we are using for detecting the g-modes with the instrument. Nevertheless, it is worth noticing that MDI/SOHO was able - without an optimized, stable and distortion free telescope as SODISM/PICARD – to observe a 10 μ arcsec high frequency p-mode (5 min.) solar limb oscillation signal (Kuhn *et al* 1997).

With PICARD we want to detect intensity fluctuations at the solar limb that will perturb the equivalent solar radius signal. Appourchaux and Toutain (1997) reported p-modes detection using the limb data of the LOI instrument. In some case the amplification with respect to full-disk integrated data is about 4, i.e. it means that a p-mode with an amplitude of 1 ppm in full disk is observed with an amplitude of 4 ppm at the limb (of. Damé *et al.,* 1999). This amplification factor was roughly predicted by theory (Appourchaux & Toutain 1997). If we hope that the same amplification factor holds for the g-modes, we may detect them faster with the limb data of PICARD than with the SOHO data. A pessimistic derivation gave 20 years for the detection of the first few g-modes with SOHO: with PICARD we can seriously envisage detecting them in 16 months with the amplification factor above.

3. PICARD payload

To carry the proposed measurements PICARD has 3 instruments: SODISM, the "SOlar Diameter Imager and Surface Mapper", for the measure of the diameter and

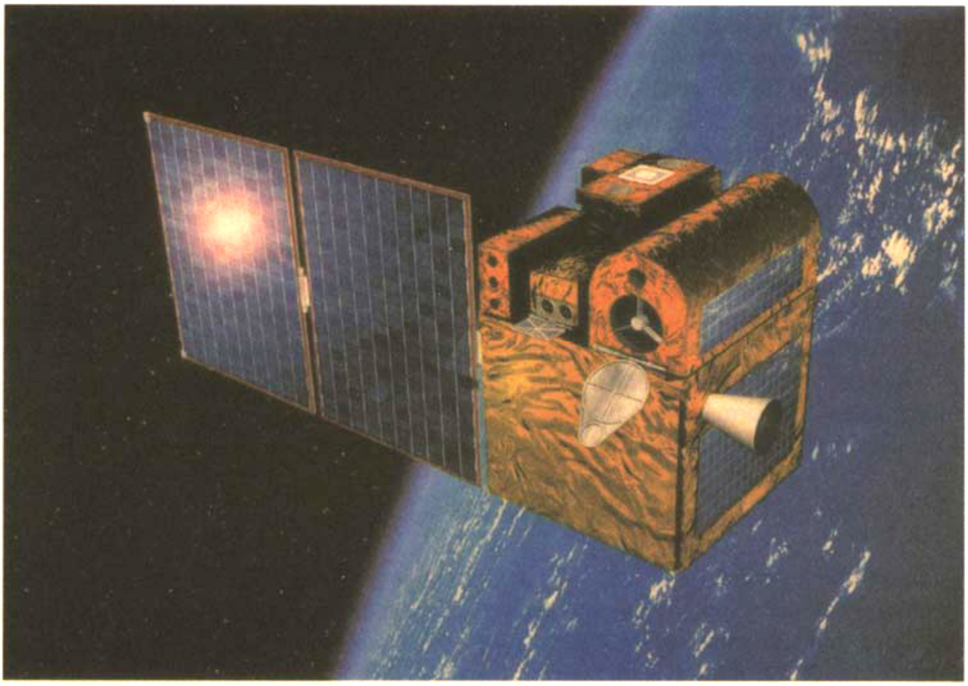

Figure 1. Artist view of PICARD microsatellite: 60 × 60 × 80 cm^3. Shown are the 3 instruments: SODISM, telescope and guiding (right) SOVAP, differential radiometer (center) and PREMOS (flux monitors) (left) near the solar panels. Behind, one can see the electronics box supporting two S-band antennae and a solar pointer (acquisition manoeuvers).

differential rotation (this is, therefore, a whole Sun imager), SOVAP (SOlar VAriability PICARD), for the measure of .the total absolute solar irradiance (correlation with SODISM measurements) and PREMOS (PRecision MOnitoring of Solar variability), a package of 3x4 UV photometers at 230, 311, 402 and 548 nm. Fig. 1 presents an artist view of PICARD's microsatellite. SODISM is realized by the Service d'Aéronomie du CNRS, France, in collaboration with the Space Science Department of ESTEC, SOVAP by the Royal Meteorological Institute of Belgium (RMIB), and PREMOS by the World Radiation Center of Switzerland.

SODISM is a telescope of useful diameter 110 mm which forms a complete image of the Sun on a large, back illuminated, CCD of 2048 × 2048 useful pixels. The pixel, 13.5 μm, corresponds to 1.05 arcsec (at 1 AU) and the effective spatial resolution is also about an arcsec (at the limb). SODISM observes in 4 wavelengths bands (8 nm bandwidth each) the whole Sun (230 nm, 548 nm, 160 nm and Lyman alpha) and 2 calibration channels (cf. Table 1) accessible through the use of 2 cascading filter-wheels, each with 5 positions.

PICARD provides an absolute diameter reference better than 10 mas (milliarcsec) in the "Star field" channel. It provides access to stellar fields in which (with a limit magnitude of 9) star-triplets of the HIPPARCOS reference catalog are imaged, allowing to scale our diameter measure and, if required, to identify and to follow any structural change in the focus or CCD dimensions which could affect the diameter measure.

Table 1. Observing and calibration modes of SODISM/ PICARD.

UV nominal mode	230 nm
Visible	548 nm
Active regions	160 nm
Prominences and ionosphere	Lyman alpha
CCD Flat Field	"Diffusion"
Scaling factor	"Star field"

SODISM has a sound optical concept allowing to achieve a distortion free and dimensionally stable image of the solar limb, using SiC mirrors on invar plates directly linked to a carbon-carbon tube.

The engineering model of SODISM will be used in CERGA, France, in conjunct-tion with the newly working DORAYSOL and the longstanding (25 years of observations) Astrolabe of Francis Laclare. As such, and for the first time, the same instrument will be used in space and on ground to measure the solar diameter, deduce atmospheric bias and estimate the ground instrument's possible accuracy. It is expected that the ground instrument will operate for more than a solar cycle. A new generation seeing monitor, measuring the coherence length and temporal coherence, will be used in conjunction with PICARDSOL and DORAYSOL to better assess atmospheric effects on the ground diameter measure (in order to validate the past historical measurements).

The measure of the total irradiance is made by the SOVAP instrument which is a differential absolute solar radiometer already flown 8 times in space from 1993 to 1998 (and recently on VIRGO/SOHO).

PREMOS consists of 3 sets of 4 "filter radiometers", based on the same principle as a radiometer (equilibrium of the flux inside a cavity) but with the preselection of a known and reduced spectral bandwidth. These photometers observe in the UV and the visible, at the same wavelengths, 230 and 548 nm as SODISM and with the same bandwidth (8nm). Two other wavelengths are also considered: 311 and 402 nm.

4. Mission scenario

Several scenarios are still under consideration for the PIGARD flight which is due before mid-2003 (the launch date is important since the diameter/constant relationship will definitively be better determined during the near linear part of the cycle, rising or falling – our case – than at minimum or maximum when the "constant" is mostly flat). The favored orbits are those providing only brief or non-eclipsing Sun-synchronous viewing in order to achieve both the thermal stability for the absolute long term diameter measurement and the near continuous sampling for long period g-modes oscillations. Nominal launch is either a Sun Synchronous Orbit (SSO) as a secondary passenger of the Indian PSLV rocket or with Radarsat 2 (Canadian satellite) which has a high (800 km) full Sun SSO orbit (also possible with a Dnietr Russian rocket dedicated launch from Plesetsk).

Note that the PICARD Mission Center will normally be operated by the RMIB and that, most probably, antennae (S band) in Toulouse and Kiruna will be used for

Table 2. Major characteristics of PICARD model payload. The 39.9 kg mass includes 2 electronics boxes of 9 and 4 kg over and under the platform. Telemetry depends on the selected orbit (eclipsing or not).

Characteristics	μ-sat PICARD	SODISM	SOVAP	PREMOS
Mass (kg)	39.9	17	5.8	4.1
Size (cm^3)	60 × 60 × 30	60 × 28 × 28	35 × 15 × 25	30 × 10 × 20
Power (W)	28.5	19.9	4.2	4.4
Thermal control (W)	19.8	16.3	2	1.5
Average Telemetry (Mbits/day)	1210–1810	1200–1800	5	5

telemetry needs (about 1.2 Gbits per day). In the case of a non-eclipsing orbit telemetry might be higher (1.8 Gbits per day) requiring a third antenna.

Acknowledgements

We are thankful to the CNES and in particular to B. Tatry, J.-Y. Prado and F. Dulac for their support to the mission, and would like to espress special thanks to direct collaborators to PICARD and this paper: A. Joukoff, S. Dewitte, W. Schmutz, T. Appourchaux, D. Cugnet, M. Hersé, G. Thuillier, J.-P. Rozelot and C. Delmas and, as well, to the 27 Co-Investigators of PICARD who are doing excellent work towards a successful PICARD's mission.

References

Appourchaux, T. *et al.* 2000, Observational Upper Limits for Low-Degree Solar g-Modes, *Ap. J.,* in press.

Appourchaux, T., Toutain, T. 1997, in *Sounding Solar and Stellar Interiors,* Symposium *IAU,* **181,** (eds.) Janine Provost and Francois-Xavier Schmider, 5.

Dame, L., Hersé, M., Thuillier, G. *et al.* 1999, PICARD: Simultaneous Measurements of the Solar Diameter, Differential Rotation, Solar Constant and their Variations, *Adv. in Space Research,***24(2),** 205–214.

Fröhlich, C. the Phoebus Group 1998, in *Structure and Dynamics of the Sun and Solar-like Stars* (SOHO 6 /GONG 98), *ESA SP–***418,** 67.

Kuhn, J. R., Bogart, R., Bush, R. *et al.* 1997, Precision Solar Astrometry from SOHO/MDI, in *Sounding Solar and Stellar Interiors,* Symposium *IAU,* **181,** (eds.) Janine Provost and Francois-Xavier Schmider, 103–110.

Laclare, F., Delmas, C., Coin, J. P., Irbah, A. 1996, Measurements and Variations of the Solar Diameter, *Solar Physics,* **166,** 211–229.

Lean, J. 1997, The Sun's Variable Radiation and its Relevance for Earth, *Annu. Rev. Astron. Astrophys.,* **35,** 33–67.

Ribes, E., Ribes, J. C, Barthalot, R. 1987, Evidence for a Larger–Sun with a Slower Rotation during the Seventeenth Century, *Nature,* **326,** 52–55.

Sadourny, R. 1994, Sensitivity of Climate to Long-term Variations of the Solar Output, in *The solar engine and its influence on terrestrial atmosphere and climate,* (ed.) E. Nesme-Ribes, (Springer Verlag), *NATO ASI Series I,* **25**, 479–491.

J. Astrophys. Astr. (2000) **21,** 141-147

Introduction to the Solar Space Telescope

G. Ai*, S. Jin, S. Wang, B. Ye, & S. Yang, *Beijing Astronomical Observatory/ National Astronomical Observatories, Chinese Academy of Sciences, Beijing 100012, China.*
**email: aigx@sun10.bao.ac.cn*

Abstract. The design of the space solar telescope (SST) (phase B) has been completed. The manufacturing is under development. At the end of 2000, it will be assembled. The basic aspect will be introduced in this paper.

Key words. Space telescopes.

1. Introduction

The world wide development of solar space-based observations went through two steps in the spatial resolution: low resolution (sun as a star) in the 60s–70s, and medium resolution (1"—10") in the 80S–90S. The next step will be high spatial resolution (~ 0.1") in the beginning of 21st century. The solar magnetic fields provide the major incentive to work on solar physics, the small spatial scale of magnetically constrained structures and processes in the solar atmosphere provide the major incentive for high resolution solar telescopes (Rutten & Pamel 1993), the 3-dimensional (multi-wave bands and multi-layers) high resolution and continuous evolutions provide the major incentive for space-base large and synthetic solar telescopes.

In the research of the solar magnetic field, there are two very important aspects: one is the accurate measurement of the vector magnetic field (Wang 1994, 1999); the other is the character of the solar magnetic element (Wang *et al.* 1995). In the space solar telescope, these two aspects will be the most important contents that can probably help achieve a breakthrough in our understanding.

The space solar telescope has been proposed since 1992 (Ai 1993; Ai *et al.* 1993; Ai 1996; Ai 1998). The phase A (assessment study) was completed in 1995–1998 and the design (phase B) was basically completed in the past two years. Now the telescope is under development.

2. Scientific objectives

The main scientific objectives are to achieve a breakthrough in solar physics through coordinated, high resolution observations of transient and steady state solar hydro-dynamic and magnetohydrodynamic processes, over 2-D polarized spectrum, UV, hard X-ray, soft X-ray, H_α image, and continuous time evolution. The practical contents of the scientific objectives are as follows: (1) Explore the 3-dimensional structure of the vector magnetic fields and the velocity fields with about 0.1"–0.15" spatial resolution by means of 2-D spectrometry. (2) Explore the fine structures of solar atmospheres, especially the heating of the chromosphere and the corona. (3) Study the energy build up, storage, triggering and release of solar flares. (4) Study the fine evolution of the solar active region, especially that of sunspots and prominences. (5) Study the various solar transient phenomena associated with solar terrestrial space environment. (6) Provide various parameters serving the purpose of forecasts of solar activity and associated calamities.

3. Basic parameters of the satellite

- Total weight — $\approx$ 2.0 ton
- Power — 1200 W, 16 m^2 solar cell panel
- Orbit altitude — 709 km, sun synchronous polar circular 6 am/6 pm nodal crossing
- Attitude — 3 axis stabilized, pointing to solar disc
  Pointing accuracy — $\pm 5''$ (solar disc)
  $\pm 40''$ (ecliptic pole)
  Control stability — $\pm 3''/s$ (solar disc)
  no constraint (ecliptic pole)
- Data recorder — 6 GB/day, (after data compression 5–10)
- Data storage — 4 GB
- Telemetry — down link rate: 30 Mb/s, X-waveband, 8200 MHz up link rate: 4 KB/s, S-waveband, 1700 MHz
- Rocket — LM-4B
- Size — $5 \times 2 \times 2\,m^3$
- Mission life — 3 years
- Launch Date — 2004

4. Payloads

4.1 *The main optical telescope (MOT)*

- 1 m diameter.
- Diffraction limit: ~ 0.1", FOV: 2.8' × 1.5'.
- 2-D real time polarization spectrograph for 2-D simulating Stokes parameter profile tunable wavelength range: 3900-7000 Å.
  Spectral resolution: $\Delta\lambda$ ~ 0.075 Å (λ5300Å).
  8-channels: distributed in a spectral line or several spectral lines.
  Spectral distance between two close channels can be selected.
  Spectral distance: 1$\Delta\lambda$; 3$\Delta\lambda$; 5$\Delta\lambda$.
  Corresponding wavelength bandwidth: 0.80 Å; 2.40Å; 4.00 Å.
  CCD: 8, 2048 pixels × 2048 pixels, 0.075"/pix.
- Accuracy of polarization analyzer: 2×10^{-4}.
- Wide band filter-graph: (3800-5500 Å; $\Delta\lambda$ ~30Å).
- CCD: 1024 pixels x 1024 pixels, 0.05"/pix, exposure time: 10^{-4}s.
- Accuracy of correlation tracker: ~ ±0.01"; 80 Hz.

Table 1. Parameters of the EUV images.

Telescope number	Wave length	Ion	$Log_{10}T$ (K)	Pixel size	Field of view	Focal length
1	12.9 nm	Fe XXI	7.0	0.25″	8.5′ × 8.5′	400
2	18.0 nm	Fe XI	6.1	0.25″	8.5′ × 8.5′	400
3	28.4 nm	Fe XV	6.3	2.5″	85′ × 85′	100
4	30.4 nm	He II	4.7	0.25″	8.5′ × 8.5′	400

4.2 *EUV imager for the solar telescope* (*EUT*)

The instruments consist of a bundle of four normal incidence astronomical telescopes with multi-layer coating: these coatings are reflecting selectively in narrow wavelength band passes, each a few per cent wide, covering EUV-lines of various Fe ions and the prominent He II 304 Å line (see Table 1). Several bandpass filters centered on different lines, which are radiated at different known plasma temperatures, are necessary to cover the whole range of temperatures of the corona from its ‘cool’ base, the hottest spots in active regions to even hotter flares.

Table 2. Instruments parameters.

Name	MOT	WIS	HAT	EUV	SIRA
Weight	800 kg	30 kg	50 kg	131 kg	8 kg
Size	450 × Φ120+ 250 × 80 × 30	30 × 40 × 15	200 × Φ20	300 × Φ50	100
Power	600 W	20 W	40 W	30 W	49 W
Data rate	5 Mb/s 23 GB/day	1 Kb/s 25 MB/day	1 Mb/s 2 GB/day	6 Mb/s 6 GB/day	1.3 GB/day

4.3 *Wide band spectrometer* (*WIS*)

The overall detector characteristics are as follows:

- Soft-X-ray spectrometer (SXS)

Detector	gas proportional counter Xe + CO_2
Energy range	2–30 keV
Number of energy channels	64
Geometric area	5 cm^2
Time resolution	1 s
Energy resolution	20% at 5.9 keV (^{55}Fe)
Power consumption	5 W
Weight	4 kg
Amount of data	10 MB/day
FOV	8° × 8°

• Hard X-ray spectrometer (HXS)

Detector	Nal, ϕ7.6 cm×2.0 cm
Energy range	15–450 keV
Number of energy channels	32
Time resolution	1 s
Energy resolution	15% at 60 keV (^{241}Am)
Power consumption	5 W
Weight	6 kg
Amount of data	5 MB/day

• Gamma-ray spectrometer (GRS)

Detector	Nal, ϕ7.6 cm ×7.6 cm
Energy range	0.3–14 MeV
Number of energy channels	256
Time resolution	4 s
Energy resolution	7% at 662 keV (^{137}Cs)
Power consumption	5 W
Weight	7 kg
Amount of data	10 MB/day

4.4 H_α and white light telescope (*HAT*)

- Diameter: 12 cm
- Full disk by wedge prisms (FOV~ 1°)
- 0.5 Å (λ 6563 Å)
- White light: ~5500 Å
- 2 CCD: 2048 pixels × 2048 pixels, l" /pix

4.5 *Solar and interplanetary radio-spectrometry* (*SIRA*)

The SIRA-instrument shall determine the flux density and the degree of circular polarization of the solar radio emission in two orthogonal components. The chirp transform spectrometer will be designed with the following characteristics:

Frequency range	1 MHz to 60 MHz
Integration time	100 ms
Frequency resolution	$\Delta/f/f < 0.1$ but $\Delta f_{max} = 1$ MHz
Frequency range 1 MHz to 10 MHz	$\Delta f = 100$ KHz
Frequency range 10 MHz to 60 MHz	$\Delta f = 1$ MHz
Number of channels	2 × 160

Some parameters of the above mentioned instruments can be seen in Table 2.

5. Optical design of SST main telescope

The optical design of SST main telescope has been principally completed. As shown in Fig. 1, the present system consists of a F/3.5 paraboloid primary 1 m in diameter, a collimator of 5 lens and a F/39 imaging objective of 2 lenses.

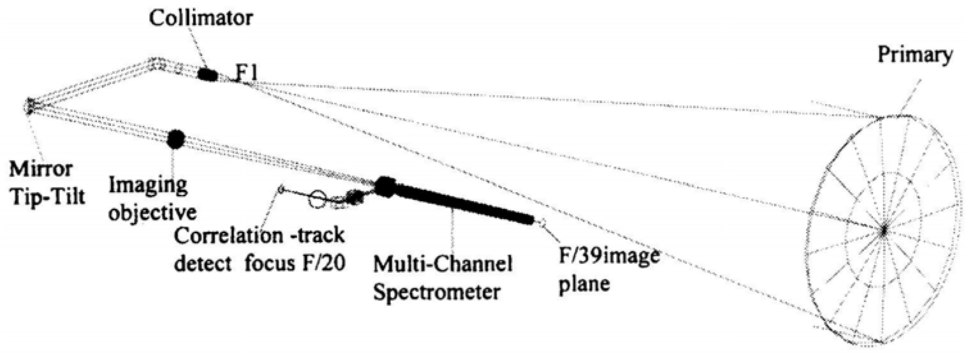

Figure 1. Optical system of SST main telescope.

- Parameters and specifications:

Telescope clear aperture	ϕ985 mm with stop at the primary
Center obstruction	17% in diameter
System focal length	38500 mm at 633 nm
Field of view	$2.8' \times 1.5'$
Detector CCD size	2048×1024 with $0.014\,\text{mm} \times 0.014\,\text{mm/pix}$
Operating wavelength	Any wavelength within 393–656 nm spectral ranges with a band width of 2 nm

- Optical performance: The calculated PSF results for the main telescope are shown in Table 3 and Fig. 2. The results demonstrate that the designed system image quality is very close to the diffraction limit (S.R. > 0.85), on any working wavelength and over a field of view of 1.6' in diameter. With such optical image quality, it will be possible to realize its required spatial resolution of 0.15" at wavelength 600 nm.

- Alignment tolerances studies: The alignment tolerances given in Table 4 correspond to the displacement and tilt that introduce in the system a spatial resolution degradation of 0.08".

Table 3. Strehl ratio values obtained by calculation at F/39 focal plane for SST main telescope.

Wavelength	393.3 nm	422.6 nm	517.8 nm	524.9 nm	532.4 nm	587.6 nm	656.3 nm
S.R.(0.0)	0.948	0.998	0.989	0.988	0.988	0.986	0.989
S.R.(0.707)	0.913	0.985	0.952	0.950	0.948	0.952	0.965
S.R.(1.0)	0.850	0.950	0.931	0.935	0.938	0.952	0.966

Assembly, integration and optical test configuration has been defined and will be carried out in Beijing Astronomical Observatory. It consists of a vibration isolation stand onto which the main telescope and all necessary test equipment may be installed. Auto-collimation method is chosen for testing telescope output wavefront errors introduced by either misalignment between the primary and lens collimator, or

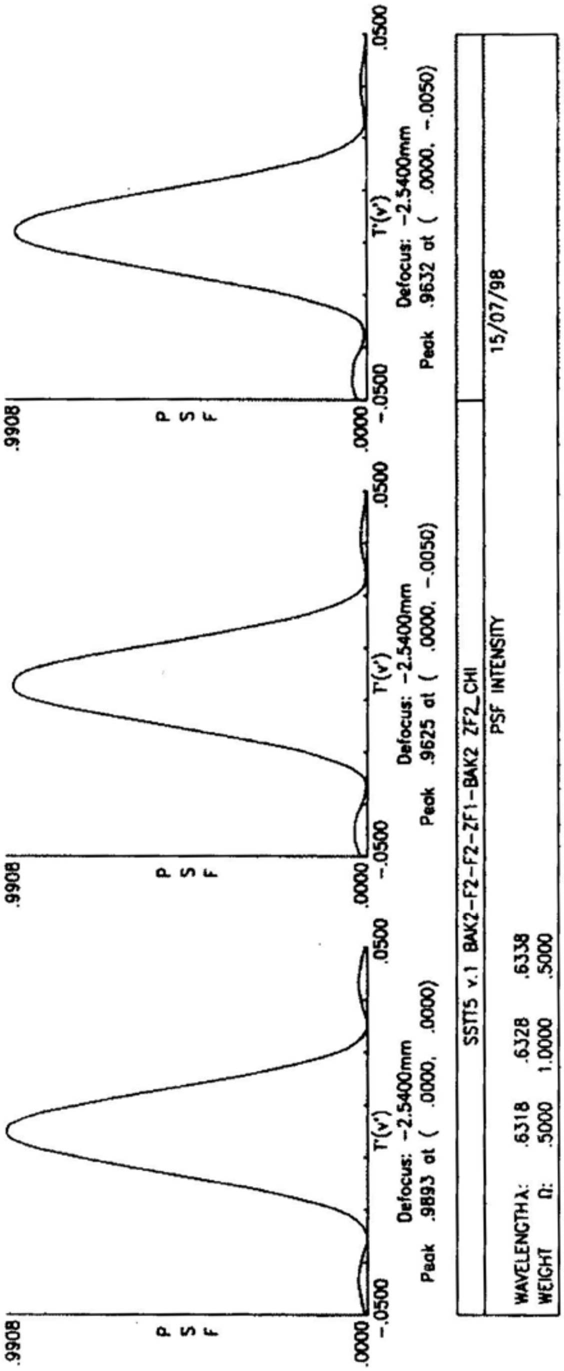

Figure 2. Calculated PSF at 633nm and with a field of view 3.24′ in diameter for SST main telescope.

Table 4. Alignment tolerance for SST main telescope.

	Tilt	Decentre	Defocus
Primary	$4''$	0.04 mm	
Collimator	$1'$	0.04 mm	0.04 mm
Imaging objective	$2'$	0.2 mm	0.1 mm

the primary surface distortion. In order to characterize wavefront of the telescope operating in full lm aperture, a plane mirror with the same diameter as the primary of surface quality $\lambda/60$(rms) will be used as reflector in the auto-collimation test optics. The gravity load effect and solar thermo effect simulation for primary after their integration on ground, has been also studied.

1m paraboloid primary and 1 m flat reflect has been manufactured. Zerodur is chosen as mirror glass and both mirrors need to be polished to a surface accuracy of $\lambda/60$(rms).

Acknowledgements

The Space Solar Telescope project is supported by the Chinese Academy of Sciences, the National Science Foundation of China, the Ministry of Science and Technology and the Office of 863-2.

References

Ai, G. X. 1993, in: *The Magnetic and Velocity Fields of Solar Active Regions,* (eds.) H. Zirin, G. X. Ai & H. M. Wang, IAU Colloquium No. **141,** page 149.

Ai, G. X. 1996, *Adv. Space Res.,* **17**, 343.

Ai, G. X. 1998, *Adv. Space Res,* **21**, 305.

Ai, G. X., Zhang, H. Q., Zhang, B. R. 1993, in *The Second Solar Magnetic and Velocity Fields,* (ed.) H. Q. Zhang, page 1.

Rutten, R., Pamel, L. 1993, in *The Magnetic and Velocity Fields of Solar Active Regions,* (eds.) H. Zirin, G. X. Ai & H. M. Wang, IAU Colloquium No. **141,** page 184.

Wang, J. X. 1994, *Sol. Phys.,* **155,** 285.

Wang, J. X. 1999, *Fund. Cos. Phys.,* **20**, 251.

Wang, J. X., Wang, H. M., Tang, F., Lee, J. W, Zirin, H. 1995, *Sol. Phys.,* **160,** 227.

J. Astrophys. Astr. (2000) **21,** 149–153

Results from Kodaikanal Synoptic Observations

K. R. Sivaraman, *Indian Institute of Astrophysics, Bangalore 560 034*
email:siva @ iiap. ernet. in

Abstract. The synoptic observations of Kodaikanal form one of the longest unbroken solar data from the beginning of the 20th century to the present day, and consists of the white light and monochromatic images of the sun. In this review, I shall discuss the results of the investigations in two areas using these data: (i) Tilt angles of the magnetic axes of bipolar spot groups, and (ii) structure and dynamics of large scale unipolar magnetic regions on the solar surface.

The observed properties and patterns of behaviour of the tilt angles can be used as effective diagnostics to infer the physical conditions in the subsurface layers of the sun, and thus get an insight into the physical effects that act on the rising magnetic flux tubes during their journey through the convection zone to the surface.

The second topic of discussion here, namely, the studies of the dynamics of unipolar regions over several solar cycles, show that the global solar activity has a high latitude component which manifests in the form of polar faculae, in addition to the well known sunspot activity at the middle and low latitudes. This raises the question about the origin of this high latitude component.

Key words. Synoptic observations—tilt angles of sunspot groups—global solar cycle.

1. Reduction of data and results

The synoptic observations of Kodaikanal starting from the beginning of the 20th century and continuing to the present day consist of:

- White light images from 1904,
- Ca II K_{232} spectroheliograms from 1907,
- H_{α} spectroheliograms from 1914.

1.1 *White light images*

The positions and areas of all sunspots were measured from the daily white light images for the period of 82 years (1906–1987). These measurements have been used for determining

- the solar rotation, differential rotation and their variations with the solar cycle (see S.S. Gupta *et al* in these proceedings),

- the tilt angles of the magnetic axes of bipolar spot groups and this will be discussed below.

Tilt angle of sunspot groups is a parameter that can be measured on the solar surface and that can serve as a good diagnostic to infer the relative effects of the forces (namely magnetic buoyancy, magnetic tension and Coriolis force) that act on the strands of magnetic flux tubes during their journey from (probably) the layers just beneath the convection zone all the way to the surface. The Coriolis force acting on the rapidly rising and expanding flux loop twists the loop such that it finally emerges at the surface with a tilt of the axis joining the centroids of the leading and following sunspots of a spot group with reference to the local parallel of latitude. Our study shows that the distribution of the tilt angles of the spot groups, their variations with latitudes of the spot groups, their areas, daily expansion rates, polarity separation, age and the derivatives of these parameters provide clues to infer the physical conditions and the forces that act on the these flux tubes while in the interior, and to the conditions that lead to the operation of the solar dynamo (Sivaraman *et al.* 1999; and Howard *et al.* 2000).

Main results from this study are:

1. It is the delicate balance among the forces – magnetic buoyancy, magnetic tension and the Coriolis force – that decides what the final value of the tilt angle of a sunspot group is.
2. The distribution of tilt angles shows a peak around +5° and not at zero (Fig. 1). It is seen that maximum number of spot groups possess this value of the tilt angle which is the equilibrium value. The tilt angle increases linearly with increase in latitude. Near the equator, the average tilt angle is about +2° and at 35° latitude the tilt angle increases to about +8°. This variation of tilt angle with latitude is known as the “Joy’s law”.
3. Spot groups with tilt angles greater than the average value (which is the most commonly occurring value of 5°) tend to rotate their axes towards the average value and this motion is more for the growing spot groups than for those decaying.
4. Sunspot group tilt angle changes are correlated with polarity separation changes (expansion or contraction), and is in the right direction, and of the correct magnitude one would expect if Coriolis force is the agency responsible for causing the tilt.
5. The average tilt angle for spot groups varies with solar cycle, being higher during solar minimum periods than during maximum periods. This variation in tilt angles can be caused by variation in the field strengths of the sub surface toroidal flux tubes, between the two phases of the cycle. A decrease in magnetic tension because of the weaker field strengths in the rising flux tubes would offer less resistance to the effect of the Coriolis force, which in turn tends to increase the tilt angle of the spot groups that appear during the minimum years.

2. Structure and dynamics of large scale unipolar magnetic regions on the solar surface

From the daily H_α spectroheliograms we have constructed the H_α synoptic charts for every rotation of the sun for the period 1910–1985 (Makarov & Sivaraman 1983).

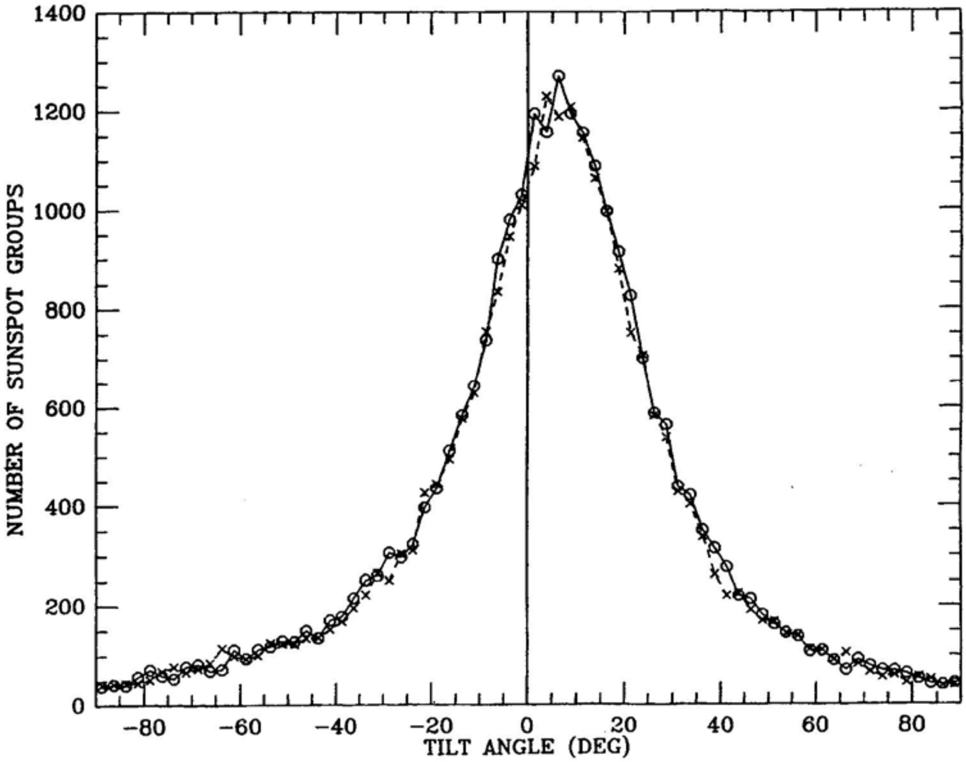

Figure 1. Distribution of tilt angles of multi-spot sunspot groups. The solid line is from Kodaikanal data for the years 1906–1987 and the dashed line from the Mount Wilson data for the years 1917–1985. Notice the peak around +5° and the close agreement between the results from the two stations.

Using these, we constructed the Latitude–Time diagrams for this period which show the poleward migration of the filament bands (and hence the migration of the unipolar magnetic regions) and the epochs of the polar field reversals (Makarov & Sivaraman 1989). The polar reversal marks the end of the current sunspot cycle. We have also plotted the distribution of the polar faculae for four cycles (for the years 1940–1985) picking up the faculae from the K-line spectroheliograms of Kodaikanal and Kislovodsk. These are shown in Fig. 2. During the years of solar minimum that follow the polar reversal, polar faculae appear first in the latitude zones 40–80°. The equatorward boundaries of the zones of appearance of the faculae progressively shift towards the respective poles as the cycle progresses. The polar faculae have strong magnetic fields in the range of 1600 Gauss associated with them (Homann *et al.* 1997).

Our study has brought out the fact that the polar faculae is the second component of the global solar activity, the first component being the well known sunspot activity and the butterfly diagram. These two components occur at different latitude belts each lasting for about 11 years but with a phase difference of 5–6 years, the polar faculae leading the sunspot activity (see Fig. 2). This gives rise to the concept of the extended solar cycle which starts from the appearance of the first polar faculae (following the polar reversal) and ends with the last sunspots of the cycle. The

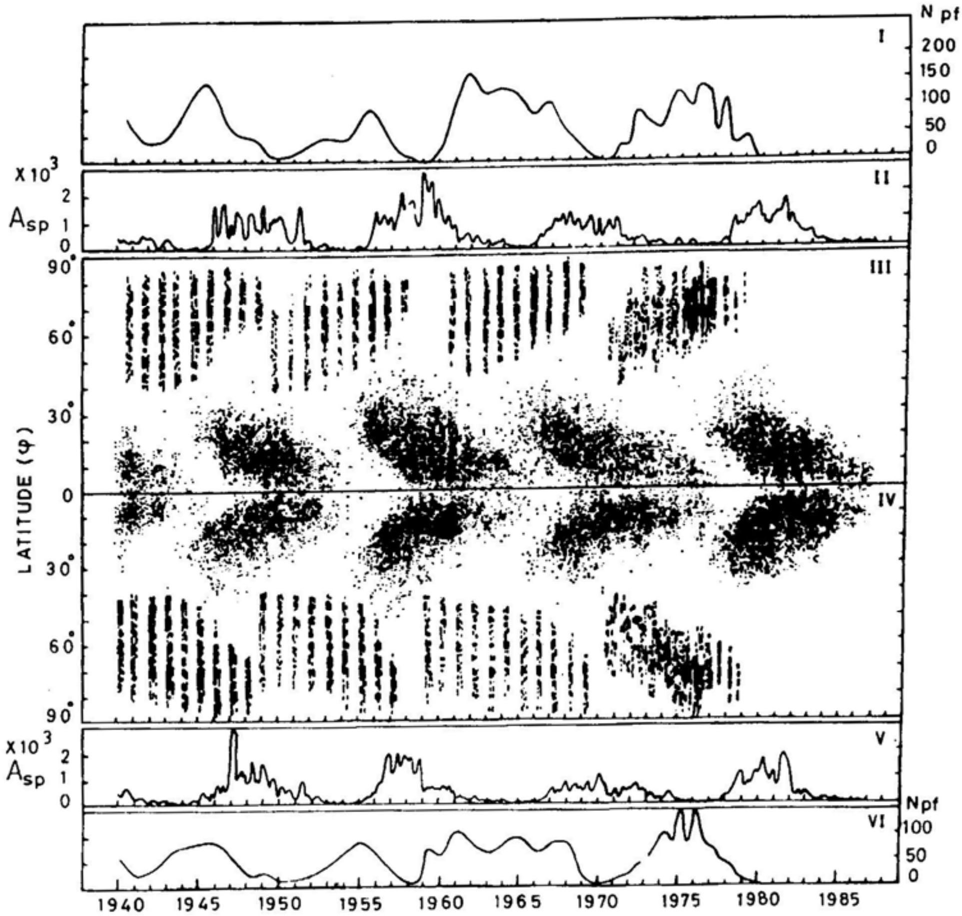

Figure 2. Latitude distribution of polar faculae and sunspots (butterfly diagram) in the N-hemisphere (box III) and in the S-hemisphere (box IV) for the years 1940–1985. Notice that the faculae appear first in the 40–80° latitude zones in the N and S hemispheres and the equatorward boundaries of these zones shift towards the respective poles as the cycle progresses. The plots of sunspot areas A(Sp) are shown in Boxes II and V and the number counts of polar faculae in Boxes I and VI for the N and S hemispheres for these years.

properties of the polar faculae such as their morphology, magnetic flux content, the duration and location they occur in relation to the sunspot activity raise the important poser whether these fields are due to a polar dynamo, and if so, how it is related to the main dynamo that generates the sunspot active region magnetic fields.

Acknowledgements

We wish to express our deep gratitude to the several generations of observers who made these observations covering many decades and which made these studies possible.

References

Homann, T., Kneer, F., Makarov, V. I. 1998, *Solar Phys.,* **175,** 81.
Howard, R., Sivaraman, K. R., Gupta, S. S. 2000, *Solar Phys.,* (in press).
Makarov, V. I., Sivaraman, K. R. 1983, *Solar Phys.,* **85,** 227.
Makarov, V. I., Sivaraman, K. R. 1989, *Solar Phys.,* **123,** 367.
Sivaraman, K. R., Gupta, S. S., Howard, R. 1999, *Solar Phys.,* **189,** 69.

J. Astrophys. Astr. (2000) **21,** 155–160

Sunspot Groups as Tracers of Sub-Surface Processes

M. H. Gokhale, *Indian Institute of Astrophysics, Bangalore 560 034, India.*
email: gokhale@ iiap.ernet.in

Abstract. Data on sunspot groups have been quite useful for obtaining clues to several processes on global and local scales within the sun which lead to emergence of toroidal magnetic flux above the sun's surface. I present here a report on such studies carried out at Indian Institute of Astrophysics during the last decade or so.

Key words. Sunspot group—solar cycle—solar rotation.

1. Introduction

Locations and epochs of sunspot groups can be specified much less accurately than those of individual sunspots. However, sunspot groups provide measures of toroidal magnetic flux emerging at the locations and epochs of their occurrence. Because of this the data on sunspot groups have been more useful than the data on individual sunspots, in studies of several subsurface processes leading to emergence of toroidal magnetic flux above the sun's surface. Extensive studies of sunspot cycle, its north-south symmetry (and small but significant asymmetry), its distribution on sun's surface and in time, sun's rotation, meridional motions of sunspots, etc., have been carried out by several authors using data on sunspot groups ever since such data have been available. Compilation of Greenwich ledgers of data on sunspot groups during 1874–1976 by Balthasar and Wöhl on magnetic tapes led to a large number of such studies during 1980's, especially of sun's differential rotation (Balthasar & Wöhl 1980; Balthasar *et al.* 1986; Zappalá & Zuccarello 1991 and references therein). Owing to shortage of time I restrict this review to present a report on the work done by our group at Indian Institute of Astrophysics which fits the title of this colloquium and the title of my talk. I shall point out the clues given by these studies for modeling the cyclical evolution of solar magnetic fields, but I shall not report on the follow-up work which is incomplete.

2. Solar magnetic cycle as global MHD oscillations

Using lifespan of a sunspot group as a measure of toroidal magnetic flux emerging during its life, and attaching to it the sign of polarity of bipolar magnetic regions in the respective wing of the butterfly diagram, Gokhale *et al.* (1992) determined the rate, Φ, of emergence of toroidal magnetic flux as a function of heliographic co-latitude θ and time t. Legendre-Fourier (LF) analysis of $\Phi(\theta, t)$ using Greenwich data during 1874–1976 showed (Gokhale & Javaraiah 1992) that it can be expressed

As superposition of at least *four* 'global' oscillations described by:

$$\dot{\Phi}(\theta, t) = \dot{\Phi}_{0s} + \dot{\Phi}_{0c} + \dot{\Phi}_{1s} + \dot{\Phi}_{1c} + \cdots, \tag{1}$$

where

$$\dot{\Phi}_{0s} = [\Sigma_{l=1,3,\ldots 13} A_s(0, l) P_l(\theta)] \sin(2\pi\nu_0 t), \tag{2a}$$

$$\dot{\Phi}_{0c} = [\Sigma_{l=3,5,\ldots 17} A_c(0, l) P_l(\theta)] \cos(2\pi\nu_0 t), \tag{2b}$$

$$\dot{\Phi}_{1s} = [\Sigma_{l=15,17,\ldots 29} A_s(1, l) P_l(\theta)] \sin(2\pi\nu_1 t), \tag{2c}$$

$$\dot{\Phi}_{1c} = [\Sigma_{l=19,21,23,25} A_c(1, l) P_l(\theta)] \cos(2\pi\nu_1 t), \tag{2d}$$

where $P_l(\theta)$ represent Legendre polynomials of order l in $\cos(\theta)$, '$A_s(0, l)$', etc., are coefficients of the respective LF terms determined by the analysis, and

$$\nu_0 = 1/21.6\,\mathrm{yr}^{-1}, \quad \nu_1 = 1/7\,\mathrm{yr}^{-1}.$$

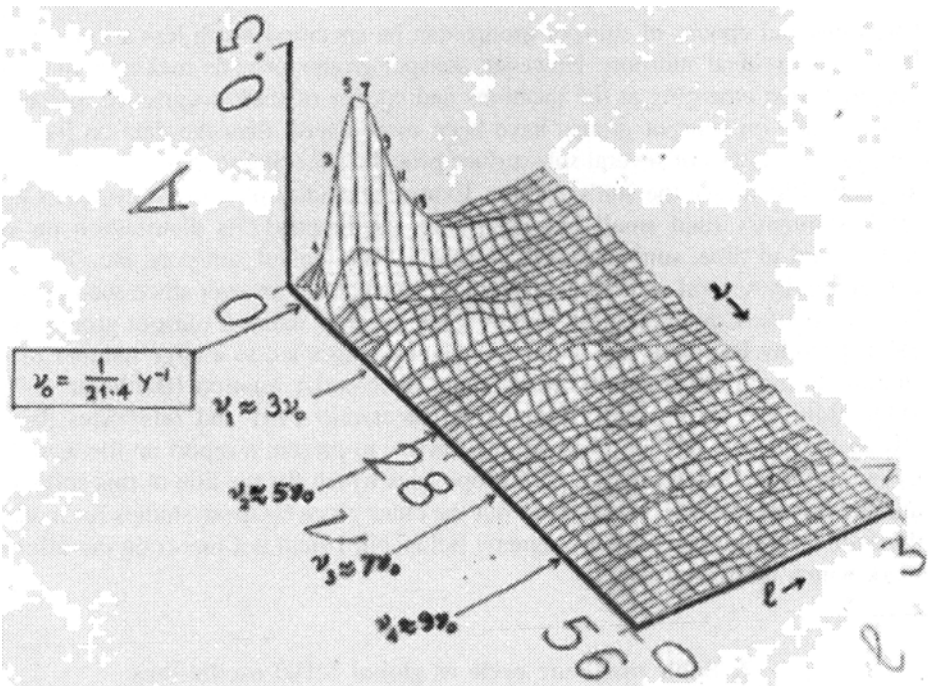

Figure 1. Legendre-Fourier spectrum of $\dot{\Phi}(\theta,t)$ during 1874–1976.

Each sum on the right side of equation (1) corresponds to a distinct and significant hump in the LF power spectrum (Fig. 1). The LF power in terms of l = even is much less though not insignificant. Further studies revealed the following facts:

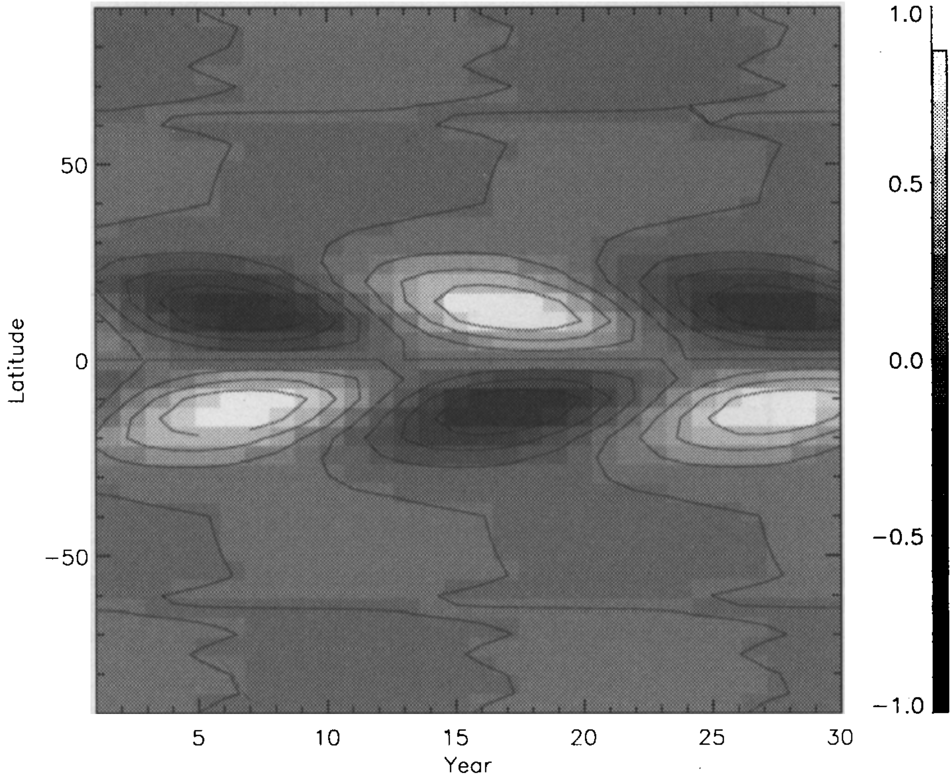

Figure 2. $\dot{\Phi}(\theta, t)$ given by sum of first four terms in equation (1). Numbers on the horizontal axis represent years. Different shades represent values of in an arbitrary unit. Continuous lines represent contour levels. Zero level contours migrate to poles.

- The relative amplitudes and phases of LF terms in each sum and those of terms in one sum to another, are nearly independent of the length and location of the sampled time interval, provided it is longer than 11 years.
- The relative amplitudes and phases of LF terms in $\dot{\Phi}_{0s}$ (the most dominant terms) are similar to those given by the *magnetogram* data during 1960–1985 (Stenfio 1988).
- Superposition of first four terms in equation (1) not only *reproduces* the 'butterfly diagrams', but also *predicts:* (i) migrations of 'weak' field and 'neutral lines' from "middle" latitudes to poles, and (ii) reversal of "polar" fields at appropriate phase in the cycle, *though the analysed data come only from the "low" latitudes.* (Fig. 2). (See Gokhale & Javaraiah 1992).
- The magnitude of a sunspot cycle number '*n*' has about 90% correlation to the change in the phase of oscillation Φ_{0c} from cycle number '*n* — 2' to cycle number '*n* — 1'. This fact can be used to *predict* the magnitude of a *new* sunspot cycle from the analysis of data during *previous two* cycles. (Gokhale & Javaraiah 1995; see Fig. 3).

The above facts strongly indicate that the expressions $\dot{\Phi}_{0s}$, $\dot{\Phi}_{0c}$ $\dot{\Phi}_{1s}$ and $\dot{\Phi}_{1c}$ represent *physically real* global oscillations of the sun. Concentration of LF power in ridges parallel to *l*-axis in Fig. 1 suggests that these oscillations may be 'forced' oscillations.

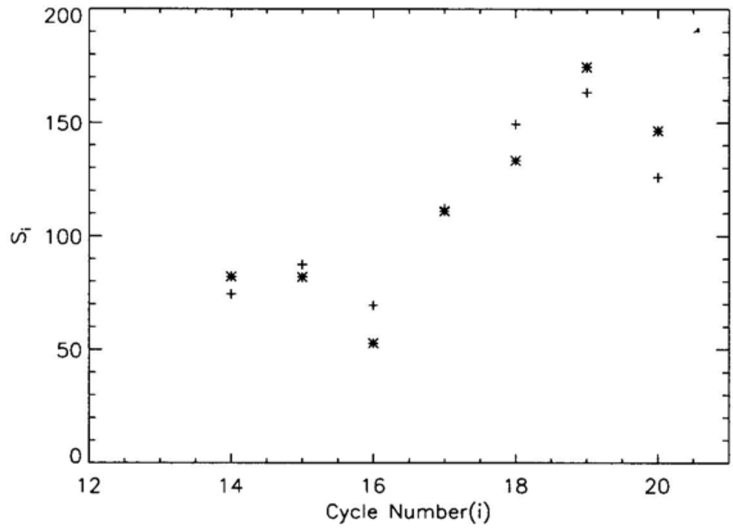

Figure 3. Observed magnitudes S_i of sunspot cycle numbers i compared to those predicted from their 90% correlation to the phase shift of Φ_{Oc} from cycle no. 'i – 2' to cycle number 'i — 1'. The observed and the predicted values are represented by '+' and * respectively.

3. 'Torsional nature of the MHD oscillations'

Year-to-year variations of the differential rotation coefficients 'A' and Fourier analysis of the temporal variations of the differential rotation coefficient 'B' computed from longitudinal motions of sunspot groups yield frequencies equal to, within uncertainties, the frequencies ν_0 and ν_1, in the rate of emergence of toroidal magnetic flux (of. section 2) with high statistical significance (Javaraiah & Gokhale 1995).

This suggests that the four oscillations found in $\dot{\Phi}$ may be "torsional MHD oscillations" of even parity in rotation (odd parity in toroidal field).

4. North-south asymmetry

Several common periodicities exist between the temporal variations of north-south asymmetries in the amount of sunspot activity and in the coefficients of differential rotation. However variations of asymmetries in activity and rotation are *poorly* correlated to one another (Javaraiah & Gokhale 1997a).

5. Initial anchoring and rate of emergence of magnetic structures associated with sunspot groups

From similarity of age and life-span dependencies of spot group rotation rate to the depth dependence of plasma rotation rate it is estimated that

- magnetic structures of spot groups rise at the rate of 21 Mm/day,
- magnetic structures of sunspot groups living less than or equal to 2 days are initially anchored near the Sun's surface.

- those of spot groups with life spans from 2 to 9 days are initially anchored at increasingly larger depths, at the rate of about 21 Mm for each extra day of life span (Javaraiah & Gokhale 1997b).

6. Depth-dependence of 'torsional' periodicity

The dominant periodicity in 'B' determined from 'young' longlived groups is '21 yr'. That determined from 'old' long-lived groups *and* from 'short-lived' groups is '11 yr'. This result, taken along with the estimated depths of 'initial anchoring' suggests that the '21 yr' periodicity in 'B' is dominant near the base of the convective envelope, and the '11 yr' periodicity is dominant near the surface (Javaraiah 1998).

7. Short term periodicities in differential rotation

Javaraiah & Komm (1999) have found several short term periodicities in the mean photospheric rotation rate $\bar{A}$ determined from Mt. Wilson velocity data during 1869–1994 and similar periodicities from sunspot group data during 1982-1994. However, the sunspot group data during 1874–1976 shows only harmonics of the solar magnetic cycle.

Periodicities of 'A' and 'B' determined from the spot group data differ considerably from those determined from dopplergram data, since sunspot group rotation is affected by plasma rotation sampled over several depths, latitude zones and solar cycle phases. Separated sunspot group samples are often too small to yield significant results.

The coefficient 'A' seems to undergo significant variation of magnitude ~ 0·01 μ rad s^{-1} during *odd* numbered cycles. Variations in 'B', determined from spot groups living 2–12 days and using superposed epoch analysis, are ~ 0.05 μ rad s^{-1}, and are during the odd numbered cycles opposite to the variations during the even numbered cycles, which confirms the existence of a 22 yr periodicity in 'B' (Javaraiah 2000, in these proceedings).

8. Meridional flows and their coupling to rotational flows

The meridional flows determined from the data during the last 2–3 days of spot groups living 10–12 days are found to have magnitudes (10–20 m/s) and directions (poleward), similar to those of the surface meridional plasma flows determined from the dopplergrams and magnetograms. This indicates global coupling of meridional and rotational flows (Javaraiah 1999).

Acknowledgements

I am thankful to J. Javaraiah for useful discussions and B. A. Varghese and J. S. Nathan for help in making Figures 2 and 3. I am also thankful to the referee, Professor J. O. Stenflo, for useful comments.

References

Balthasar, H., Vázquez, M., Wöhl, H. 1986, *Astr. Astrophys.,* **155,** 87–98.

Balthasar, H., Wöhl, H. 1980, *Astr. Astrophys.,* **92,** 111–116.

Gokhale M. H., Javaraiah, J. 1992, *Solar Phys,,* **138,** 399–410.

Gokhale, M. H., Javaraiah, J. 1995, *Solar Phys.,* **156,** 157–177.

Gokhale M. H., Javaraiah J., Kutty K. N., Varghese B. A. 1992, *Solar Phys.,* **138,** 35–47.

Javaraiah, J. 1998, in *Dynamics of the Interior of the Sun and Sun-like Stars,* (ed.) S. G. Korzennik & A. Wilson, ESA SP–418, (Noordwijk) 809–812.

Javaraiah, J. 1999, *Solar Phys.,* **189,** 289–304.

Javaraiah, J. 2000, in these proceedings.

Javaraiah, J., Gokhale, M. H. 1995, *Solar Phys.,* **158,** 173–195.

Javaraiah, J., Gokhale, M. H. 1997a, *Solar Phys.,* **170,** 389–410.

Javaraiah, J., Gokhale, M. H. 1997b, *Astr. Astrophys.,* **327,** 795–799.

Javaraiah, J., Komm, R. W. 1999, *Solar Phys.,* **184,** 41–59.

Stenflo, J. O. 1988, *Astrophys. Space Sci.,* **144,** 321.

Zappalá R. A., Zuccarello, F. 1991, *Astr. Astrophys.,* **242,** 480–487.

J. Astrophys. Astr. (2000) **21,** 161–162

The Large-Scale Magnetic Field and Sunspot Cycles

V. I. Makarov* & A. G. Tlatov, *Kislovodsk Solar Station of the Pulkovo Observatory, Kislovodsk 357700, P.O. Box 145, Russia.*
**email: makarov© gao.spb.ru*

Key words. Sun: magnetic field—sunspots—solar cycle.

Extended abstract

We report on the correlation between the large scale magnetic field and sunspot cycles during the last 80 years that was found by Makarov *et al.* (1999) and Makarov & Tlatov (2000) in H-α spherical harmonics of the large scale magnetic field for 1915–1999. The sum of intensities of the low modes 1 = 1 and 3, A(t), was used for comparison with the Wolf number, W(t). It was shown that the large scale magnetic field cycles, A(t), precede the sunspot cycles, W(t), by 5.5 years.

Let us consider the behaviour in time of the harmonics with low numbers 1 = 1 and 1 = 3. The radial component B(r) of the magnetic field may be expanded in terms of the spherical harmonics

$$B(r) = \sum_l \sum_m P_l^m (g_l^m \cdot \cos(m\phi) + h_l^m \cdot \sin(m\phi)),$$

where θ and ϕ are the latitude and longitude, P_l^m are Legendre polynomials and g_l^m and h_l^m 1are coefficients of expansion on the spherical functions.

$$g_l^m = \frac{(2l+1)}{2\pi} \cdot \frac{(l-m)!}{(l+m)!} \int_0^{2\pi} d\phi \cos(m\phi) \int_0^{\pi} B_r(\theta,\phi) P_l^m(\cos(\theta)) \sin(\theta)\, d\theta.$$

$$h_l^m = \frac{(2l+1)}{2\pi} \cdot \frac{(l-m)!}{(l+m)!} \int_0^{2\pi} d\phi \sin(m\phi) \int_0^{\pi} B_r(\theta,\phi) P_l^m(\cos(\theta)) \sin(\theta)\, d\theta.$$

The magnetic moments of a dipole (l = 1) and an octopole (1 = 3) are determined by the following equations:

$$\mu_1 = \left(\sum_{m,l=1} (g_l^m g_l^m + h_l^m h_l^m) \right)^{1/2}, \quad \mu_3 = \left(\sum_{m,l=3} (g_l^m g_l^m + h_l^m h_l^m) \right)^{1/2}.$$

Let us enter the parameter describing their intensity,

$$A(t) = (\mu_1^2 + \mu_3^2/3)^2.$$

The distribution of A(t) and W(t) is represented in Fig. 1 for 1915–1999. Both indices A(t) and W(t) have a cyclic character with a period of about 11-years. The phase shift between A(t) and W(t) is about 5.5 years. A comparison of the index A(t)

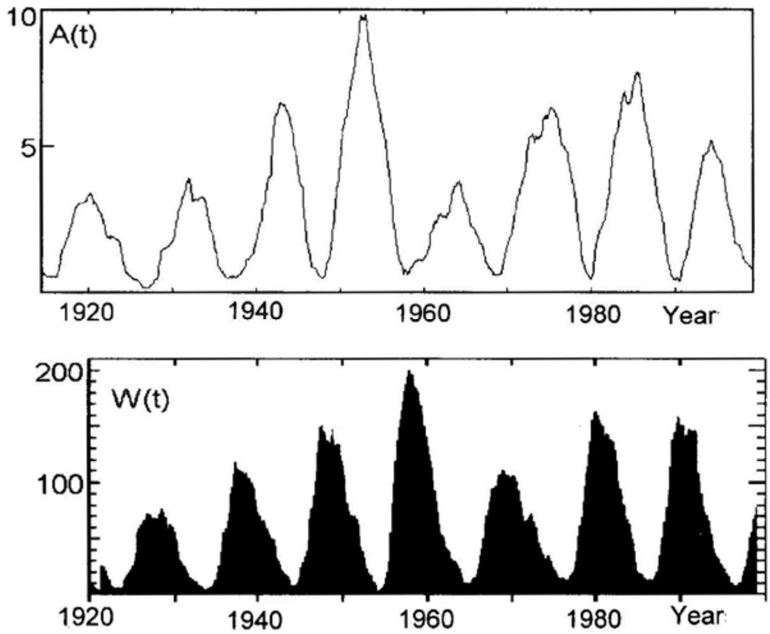

Figure 1. A(t) – the large-scale magnetic field cycles according to H-α magnetic charts for 1915–1999, W(t) – the sunspot solar cycles for 1920–1999.

with W(t) shows the possibility to forecast solar activity. The current cycle 23 is expected to be less than cycle 22 and will make $W_{max} \approx 130 \pm 10$.

Acknowledgement

Financial support for this work comes from the Russian Fund Basic Research, Grant 99-02-16200 and 00-02-16355, INTAS 98-1088 and NRA 98-OSS-08.

References

Makarov, V. I., Tlatov, A. G. 1999, in Proceedings of the 9th Meeting on Solar Physics (Italy), 125.

Makarov, V. L, Tlatov, A. G. 2000, *Astron. Rep.,* (in press).

J. Astrophys. Astr. (2000) **21,** 163–165

Cyclic Evolution of Sunspots: Gleaning New Results from Old Data

S. K. Solanki[1]*, M. Fligge[2], P. Pulkkinen[3] & P. Hoyng[4]

[1]*Max-Planck-Institut fiir Aeronomie, D-37191 Katlenburg-Lindau, Germany.*
[2]*Institute of Astronomy, ETH Zentrum, 8092 Zurich, Switzerland.*
[3]*Institute of Astronomy, University of Helsinki, Finland.*
[4]*SRON, Utrecht, The Netherlands.*
**email: solanki@linmpi.mpg.de*

Abstract. The records of sunspot number, sunspot areas and sunspot locations gathered over the centuries by various observatories are reanalysed with the aim of finding as yet undiscovered connections between the different parameters of the sunspot cycle and the butterfly diagram. Preliminary results of such interrelationships are presented.

Key words. Sunspots—solar dynamo.

1. Introduction

Much of our knowledge of solar activity in historic times is due to the Zürich relative sunspot number introduced by Rudolf Wolf. He started regular (daily) observations of sunspot number around 1850 and reconstructed the sunspot number to earlier times based on less regular observations. This is the oldest and longest record available of solar magnetic activity. Another long and equally important data set is that of sunspot positions and areas published by Greenwich Observatory since 1874 and now continued by other observatories. In this paper we use these data to find out if there is any relationship between some of the basic parameters describing the distribution of sunspots over the solar cycle. Kodaikanal Observatory recordings are an important component of the Greenwich compilations, so that it is particularly appropriate to publish this paper in the special issue marking the 100th anniversary of Kodaikanal Observatory.

2. Parameters

When sunspot latitudes as tabulated by Greenwich Observatory are plotted versus time one obtains the classical butterfly diagram. The butterfly diagram is a well-studied phenomenon (e.g. Antalova & Gnevyshev 1983, or for the corona Storini & Sykora 1997). For our analysis we first separate the sunspots belonging to each solar cycle using this diagram. With the exception of a very small fraction of the sunspots they can be uniquely assigned to a given cycle in a straightforward manner. Next we add together the areas of all sunspots within a given (narrow) latitude band over a whole sunspot cycle. In this manner we obtain the latitudinal distribution of the sunspot areas averaged over a whole sunspot cycle. This distribution is double-humped, with a maximum each in the southern and northern hemisphere and a minimum at the equator. Next we determine the following parameters (moments) of this distribution, separately for the two hemispheres:

1. total area of the distribution (in the northern and southern hemispheres separately), i.e. the sunspot number integrated over the cycle, *n*;
2. the mean latitude of the north and south lobes of the distribution, *l*;
3. the width of each of the lobes, *w*.

When determining these parameters we neglect the change in the centre-of-gravity of the whole distribution with a 90-year period found by Pulkkinen *et al.* (1999).

3. Relationships

In the next step we check whether there is any relationship between these three parameters for the different solar cycles. This can be done for each hemisphere individually or for the whole sun (by averaging the absolute values of the parameters from both hemispheres). It turns out that the hemispheres and the whole sun exhibit almost the same behaviour, although the scatter is larger for the individual hemispheres. Therefore, for the rest of this paper we consider only the relationships for the whole sun.

In Fig. 1 we plot the mean latitude of the sunspot distribution versus the strength of the cycle. Each triangle represents a solar cycle. Obviously the two quantities are related; the correlation coefficient reads 0.87. The relationship between the width of the distribution and the strength of the cycle is of similar quality (correlation coefficient 0.88).

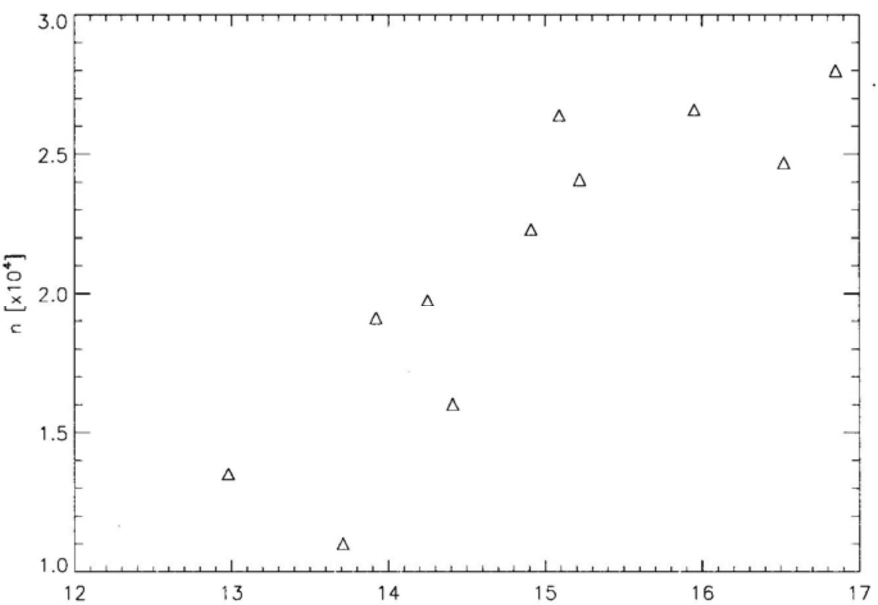

Figure 1. Integrated sunspot number, *n* vs. mean latitude, *l*. Each symbol represents a solar cycle.

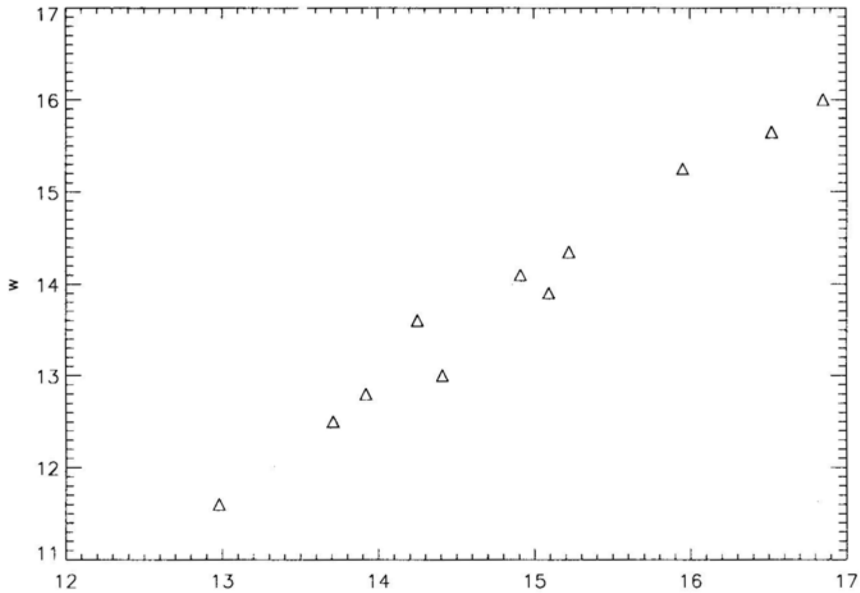

Figure 2. Width of sunspot distribution, w, vs. mean latitude, l.

An even tighter relationship is obtained when we plot the width of the sunspot distribution versus the mean latitude (Fig. 2). The correlation coefficient in this case is almost 0.99.

Both linear and quadratic least-squares fits were made to the data points. Only in the case of the mean-latitude l versus cycle strength n relationship (1) is the fit significantly improved by introducing a quadratic term. In that case the χ^2 value is reduced from 3.5 to 2.9.

The coefficients of the linear fits, which are in general adequate, are:

$$w = -1.388 + 0.562l,$$
$$l = 10.976 + 1.868n,$$
$$w = 4.723 + 1.064n$$

where w = width, l =mean latitude and n = total sunspot number.

The tightness of the above relationships suggests that they reflect a general property of the solar dynamo. These relations thus represent a new observational constraint that a successful dynamo model needs to reproduce.

References

Antalova, A., Gnevyshev, M. N. 1983, Latitudinal distribution of sunspot areas during the period 1874–1976, *Contributions of the Astronomical Observatory Skalnate Pleso,* **11,** 63–93.

Pulkkinen, P. J., Brooke, J., Pelt, J., Tuominen, I. 1999, Long-term variation of sunspot latitudes, *Astr. Astrophys.,* **341,** L43–L46.

Storini, S., Sykora, J. 1997, Coronal activity during the 22-year solar magnetic cycle, *Solar Phys.,* **176,** 417–430.

J. Astrophys. Astr. (2000) **21,** 167–170

22-Year Periodicity in the Solar Differential Rotation

J. Javaraiah, *Indian Institute of Astrophysics, Bangalore 560 034,. India.*
email:jj @ iiap.ernet.in

Abstract. Using the data on sunspot groups compiled during 1879–1975, we determined variations in the differential rotation coefficients *A* and *B* during the solar cycle. The variation in the equatorial rotation rate *A* is found to be significant only in the odd numbered cycles, with an amplitude ~ 0.01 μ rads^{-1}. There exists a good anticorrelation between the variations of the differential rotation rate *B* derived from the odd and even numbered cycles, suggesting existence of a '22-year' periodicity in *B*. The amplitude of the variation of *B* is ~ 0.05 μ rad s^{-1}.

Key words. Sunspot group—solar cycle—solar rotation.

1. Introduction

Study of solar cycle variations of the Sun's differential rotation is important for understanding the solar cycle mechanism and has been studied by several authors using the Greenwich data on sunspot groups (for references see Javaraiah & Gohkale 1995). Recently, we determined periodicities in the solar differential rotation through the power spectrum analysis of the differential rotation parameters derived from the data on sunspot groups compiled from Greenwich Photoheliographic Results (GPR) during 1879–1976 and from Mt. Wilson velocity data during 1969–1994 (Javaraiah & Gokhale 1995, 1997a; Javaraiah 1998; Javaraiah & Komm 1999). A periodicity at 18.3 ± 3 year was found to be dominant in *B* determined from the spot group data. This periodicity might be related to the solar magnetic cycle (Gokhale & Javaraiah 1995; Gokhale 2000). Hence, it is interesting to study, in detail, the temporal behavior of the differential rotation in the adjacent solar cycles. We have now analyzed the upgraded GPR sunspot group data during 1879–1975 and study variations of the differential rotation coefficients *A* and *B* during the odd numbered solar cycles (ONSCs) and during the even numbered solar cycles (ENSCs). This study is carried out by using the method of superposed epoch analysis (see Balthasar *et al.* 1986). This method provides adequate samples of spot groups in different phases of the solar cycle.

2. Data and analysis

We have used the data on sunspot groups compiled from GPR during 1879–1975. This data is compiled by the National Geophysical Data Center, USA and include the observation time (the date and the fraction of the day), heliographic latitude and longitude, central meridian longitude (CML), etc., for each day observation. We have computed the sidereal rotation velocities (ω) for each pair of consecutive days in the life of each spot group using its longitudinal and temporal differences between these days. We fitted this data to the standard formula of differential rotation, $\omega(\lambda) = A + B \sin^2 \lambda$, where $\omega(\lambda)$ is the solar rotation rate at latitude λ, the parameters A and B are measures of the equatorial rotation rate and latitude gradient of rotation rate, respectively. We have excluded the data corresponding to the $|CML| > 75°$ on any day of the spot group life span and also did not use the data from non-consecutive days of spot groups life span. Further, we excluded the data corresponding to the

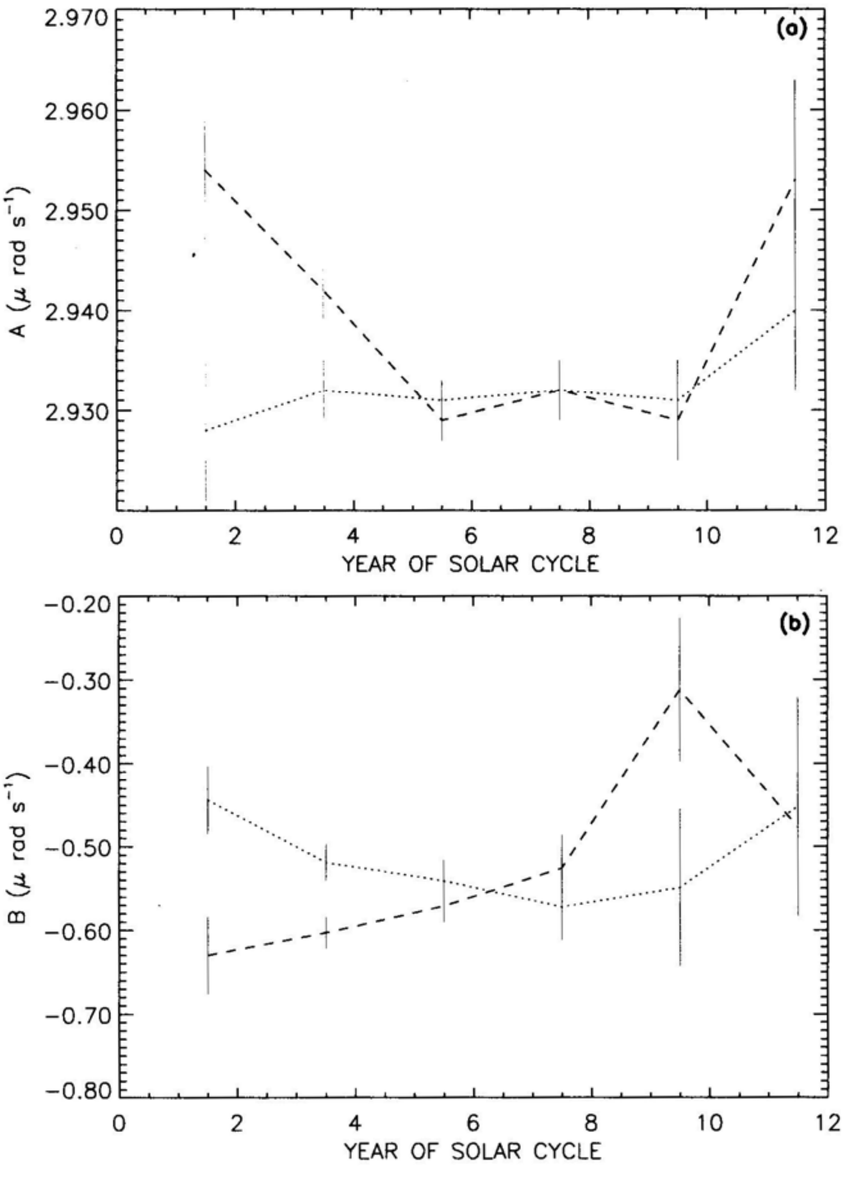

Figure 1. The mean variations of A and B during ONSCs (dashed curves) and ENSCs (dotted curves). Averages taken over 2-year intervals. Activity maximum is around 4–5 years.

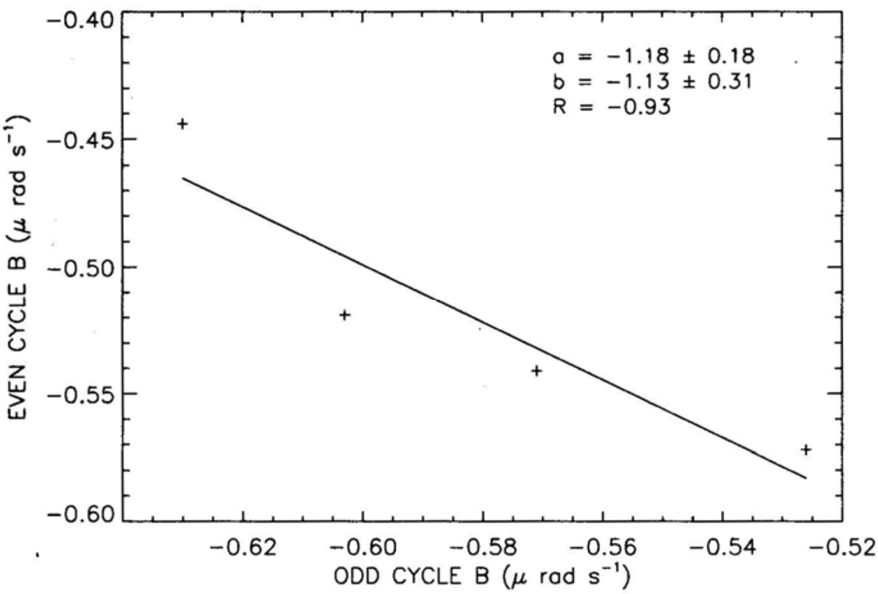

Figure 2. Correlation between *B* of ONSCs and that of ENSCs during the first eight years of the cycles. The solid line represents the values of *B* of ENSCs obtained from the linear regression analysis. The values of intercept *a,* slope *b* and correlation coefficient *R* are also given.

'abnormal' motions, e.g., displacements exceeding 3° day^{-1} in the longitude or 2° day^{-1} in latitude. This precaution substantially reduces the uncertainties in *A* and *B* (cf., Javaraiah & Gokhale 1995). We have determined the variations of *A* and *B* by superposing the data during 1879–1975, according to the years relative to the nearest sunspot minimum (1879, 1890, 1902, 1913, 1923, 1934, 1944, 1954, 1965, 1976).

3. Results and discussion

Fig. 1 shows the mean variations of A and *B* during the ONSCs (Waldmeier cycle numbers 13, 15, 17, 19) (dashed curves) and the ENSCs (12, 14, 16, 18, 20) (dotted curves). From this figure, it can be seen that the variation in *A* is significant only in the ONSCs, with amplitude ~ 0.01 μ rads^{-1}. The variation in *B* is quite significant in both ONSCs and ENSCs with amplitude ~ 0.05 μ rads^{-1}. There exists a good anti-correlation between the dashed and dotted curves (in Fig. 1 (b)) suggesting existence of a '22-year' periodicity in *B*. However, the amplitude of the anticorrelation depends on the phase of the solar cycle. The value of the correlation coefficient (R) is only –0.33 from all the 6 points. Exclusion of the last point (average value of 11th and 12th years) yielded R = –0.53. The exclusion of last two points yielded R = –0.93 and this is shown in Fig. 2. The linear fit shown in this figure (solid line) suggests existence of a good inverse linear relationship between the *B* of ONSCs and that of ENSCs, in the first eight years of the cycles.

The so-called 'torsional oscillations' discovered by Howard & LaBonte (1980) and LaBonte & Howard (1982) using Mt. Wilson Doppler measurements during

1967–1982, consist of alternating bands of rotation, faster (or slower) than average, and moving in each hemisphere from the pole to the equator in ~ 22 years. In a given latitude, the velocity of torsional oscillation changes its direction from east to west and vice versa during 11 years with amplitude of about 3 ms^{-1} . Ternullo (1990) has found evidence of equator-ward moving bands of torsional oscillation using the sunspot drawings made during cycle 21 at Catania Astrophysical Observatory. It is interesting to note that Ternullo used for each spot group only the data collected from the 4th day of observation until the last observation available (i.e., the data of old spot group). Using the anchoring depths of magnetic structures of spot groups of different life spans and age (Javaraiah & Gokhale 1997b), we suggested that the '22-year' and '11-year' periodicities in B might be dominant in the rotation perturbations near the base of the convection zone and near the surface, respectively (Javaraiah 1998).

References

Balthasar, H., Vázquez, M., Wöhl, H. 1986, *Astr. Astrophys.,* **155,** 87–98.

Gokhale, M. H. 2000, in these proceedings.

Gokhale, M. H., Javaraiah, J. 1995, *Solar Phys.,* **156,** 157–177.

Howard, R., LaBonte, B. J.1980, *Astrophys. J.,* **239,** L33–L36.

Javaraiah, J. 1998, in *Dynamics of the Interior of the Sun and Sun-like Stars,* (eds.) S. G. Korzennik & A. Wilson, (Noordwijk: ESA SP-418), pp. 809–812.

Javaraiah, J., Gokhale, M. H. 1995, *Solar Phys.,* **158,** 173–195.

Javaraiah, J., Gokhale, M. H. 1997a, *Solar Phys.,* **170,** 389–410.

Javaraiah, J., Gokhale, M. H. 1997b, *Astr. Astrophys.,* **327,** 795–799.

Javaraiah, J., Komm, R. W. 1999, *Solar Phys.,* **184,** 41–59.

LaBonte, B. J., Howard, R. 1982, *Solar Phys.,* **75,** 161–178.

Ternullo, M. 1990, *Solar Phys.,* **127,** 29–50.

J. Astrophys. Astr. (2000) **21,** 171–172

Is a Sunspot in Static or Dynamic Equilibrium?

P. Venkatakrishnan, *Udaipur Solar Observatory, Physical Research Laboratory, Post Box No. 198, Badi Road, Udaipur 313 001, India.*
email:pvk @ plume.uso.ernet.in

Key words. Sun—sunspot—structure.

Extended abstract

Sunspots have been studied ever since their discovery by Galileo, but the investtigation of sunspot structure remains a current issue. The theoretician's ideal, isolated sunspot is rarely observed. However, most of the discussions about the stability and dynamics of sunspots are based on this ideal model. In what follows, we shall examine the evolution of a similar idealised model of a sunspot and comment on the implications of this study on the use of sunspots as tracers of subphotospheric dynamics.

To simplify matters, let us assume a sunspot where the vertical or z-component of the field varies with ρ direction as;

$$B_z = B_0 \exp(-\rho^2/L^2).$$

This component alone will produce a cylindrical spot model quite unlike what is generally observed. However, this cylindrical model can serve as an approximation for a sunspot when we consider a small height range of the spot. As can be seen later, this assumption is not central to the issue being discussed. Generally, any such model is considered to be in static equilibrium because the electrical resistivity of the plasma is very high, leading to diffusion times that are much larger than the life-time of the sunspot. In a recent paper Schrijver, C. J. *et al.* (1998) showed that reconnection events at the network boundary enhance the effective mean free path for magnetic field diffusion to 30000 km. They also note that the typical time between events is about 6 hours or roughly 20000 s. Thus the magnetic diffusivity η realised by this process is 10^{15} cm^2 s^{-1}. This diffusion cannot be ignored as can be seen in what follows.

The diffusion equation of the magnetic field can be written as:

$$\frac{\mathrm{d}}{\mathrm{d}t} B_z = \eta \frac{\mathrm{d}^2}{\mathrm{d}x^2} B_z.$$

For an initial field at $t = 0$, as given earlier, the time evolution turns out to be:

$$B_{z(t)} = B_0 \exp(-\rho^2/(L^2 + \eta\, t)).$$

For a sunspot of initial size of 30000 km, the time taken for doubling of its size by diffusion is roughly 6 hours. For smaller spots, it is smaller, scaling as the Square of the size. Actually, these estimates are conservative estimates, since the initial ρ-profile chosen was a gaussian. The effect would be more severe for a sharper

profile. Clearly then, diffusion cannot be ignored and a static sunspot is not physically realisable.

The way out of the apparent dilemma posed above is to have a spot in dynamic equilibrium. In this case, the diffusion is halted by a plasma flow that converges towards the spot. The surface flows like the Evershed flow, runs counter to such a requirement. It would seem therefore, that converging flows are beneath the surface. Recent work based on time distance seismology has indeed pointed towards such an inference. The sunspot thus seems to exist due to the effect of flows acting at and near the solar surface. Furthermore, the position of a sunspot is then decided by the location of such a flow pattern. The pattern can, in principle, move independent of the general plasma flow, which is basically solar rotation. Thus, the use of spots as tracers of subsurface rotation becomes debatable.

References

Schrijver, C. J. *et al.* 1998, *Nature,* **394,** 152.

J. Astrophys. Astr. (2000) **21,** 173–176

Periodic Variation of the North-South Asymmetry of Solar Activity Phenomena

V. K. Verma, *U. P. State Observatory, Manora Peak, Naini Tal, India 263 129.*
e-mail: verma@upso.ernet.in

Abstract. We report here a study of various solar activity phenomena occurring in both north and south hemispheres of the Sun during solar cycles 8–23. In the study we have used sunspot data for the period 1832–1976, flare index data for the period 1936–1993, Hα flare data 1993–1998 and solar active prominences data for the period 1957–1998. Earlier Verma reported long-term cyclic period in N-S asymmetry and also that the N-S asymmetry of solar activity phenomena during solar cycles 21, 22, 23 and 24 will be south dominated and the N-S asymmetry will shift to north hemisphere in solar cycle 25. The present study shows that the N-S asymmetry during solar cycles 22 and 23 are southern dominated as suggested by Verma.

Key words. Sunspots—solar activity—solar cycles.

1. Introduction

The north-south (N-S) asymmetries of several manifestations of solar activity have been studied earlier by various authors. The literature also indicates that several solar activity phenomena show some form of the N-S asymmetry (Bell & Glazer 1959; Bell 1962; Roy 1977; Verma 1987). Bell (1962) finds long term N-S asymmetry in the sunspot area data. Roy (1977) studied the N-S distribution for flares, sunspots and white light (WL) flares for a period of more than two solar cycles and found that the asymmetry in the northern hemisphere increases with the importance of solar events. Hansen & Hansen (1975) are of the view that the overall filament configuration and their evolution with time compactly represent the general topology of the photospheric magnetic field and its evolution during the course of solar activity cycles. Reid (1968) reported N-S asymmetry in favour of northern hemisphere for the period 1958–1965. Howard(1974) studied solar magnetic flux data for 1967 to 1973 and found that the northern hemispheric flux exceeds by 7% over the southern hemispheric flux. White & Trotter (1977) investigated asymmetry of sunspot area and found that on an average the solar magnetic field cycle occurs uniformly in the northern and southern hemisphere. Swinson *et al.* (1986) also examined relative sunspot numbers and sunspot area. Their analysis shows that the N-S asymmetry of sunspot numbers favours northern hemisphere in the period 1947–1984 (Solar cycles 18–20). Verma (1987) studied six types of solar phenomena for solar cycles 19, 20 and 21. These include major flares, type II radio bursts, white light (WL) flares, Solar gamma-ray (SGR) bursts, hard X-ray (HXR) bursts and coronal mass ejection (CME) events. Verma (1987) found that the asymmetries in major flares, type II radio bursts and WL flares favour the northern hemisphere during solar cycles 19 and 20, asymmetries in type II radio bursts, WL bursts, SGR bursts, HXR bursts and CME events favour the southern hemisphere during solar cycle 21. Vizoso & Ballester (1987) studied the N-S asymmetry in sudden disappearances of solar prominences during solar cycles 18–21 and found that asymmetry curve can be fitted by a sinusoidal function with a period of 11 years. Verma (1992,1993) studied the N-S asymmetry of various solar activity phenomena and reported cyclic behaviour of N-S asymmetry. According to the study of Verma (1992, 1993) the N-S asymmetry has a trend of long term period of 12 solar cycles (110 years). Further, Verma (1992) predicted that the N-S asymmetry in solar cycles 22, 23 and 24 may be southern dominated and N-S asymmetry will shift to northern hemisphere in solar cycle 25. Recently Atac & Ozguc (1996) studied the N-S asymmetry in flare index and found a periodic behaviour.

The present study has been carried out to know the trend of N-S asymmetry in solar activity phenomena after the research works of Verma (1992, 1993). We also discuss the results obtained in the present study in the light of earlier works.

2. Observational data and analysis

In the present study the data for the solar activity phenomena includes sunspot area (SA), solar flares (SF), sudden disappearing filaments (SDF) and solar active prominences (SAP) are taken from various sources. The types of solar activity phenolmena and sources of their references are given in Table 1.

The N-S asymmetry of solar activity phenomena during solar cycles 8–23 has been calculated using the following formula:

$$A_{ns} = \frac{N_n - N_s}{N_n + N_s}.$$

Here, A_{ns} is the N-S asymmetry index, N_n is the number of solar activity phenomena in northern hemisphere and N_S is the number of solar activity phenomena in southern hemisphere. Thus, if $A_{ns} > 0$, the activity in the northern hemisphere dominates, and if $A_{ns} < 0$, the reverse is true. To study the N-S asymmetry of solar activity events with long term period we have calculated the N-S asymmetry for solar cycles period

Table 1. Shows types of solar activity phenomena, period and their references.

Solar Activity Phenomena	Period	References
Sunspot area	1832–1871	Wolbach (1962)
	1874–1954	Janes (1955)
	1955–1976	Annals Royal Greenwich Observatory, England
Solar flares	1936–1993	Atac & Ozguc (1996)
	1994–1998	Solar Geophysical Data (1995–1999)
Solar prominences	1957–1998	Verma (2000)
Sudden disappearing filaments	1945–1985	Vizoso & Ballester (1987)

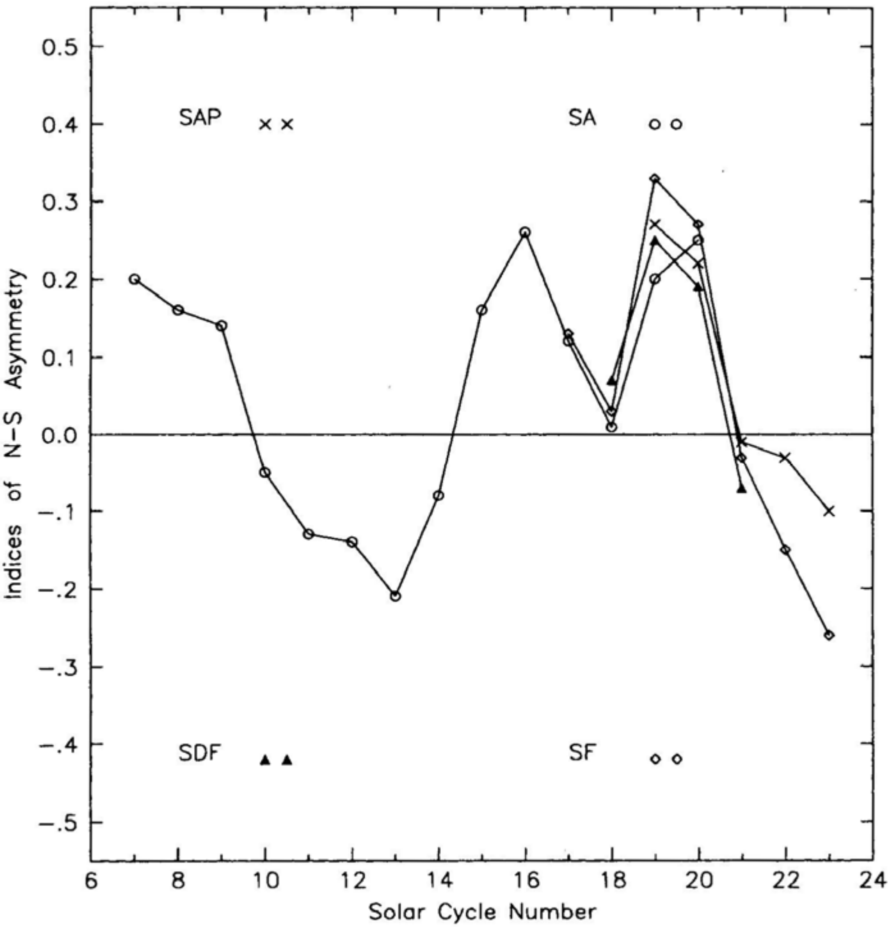

Figure 1. Plot of N-S asymmetry of Various Solar Active Phenomena versus Solar Cycle Number.

between 8–23. The plot of the N-S asymmetry indices versus solar cycle number is shown in Fig. 1.

3. Results and discussions

The present study examines the N-S asymmetry for solar active phenomena which includes sunspot area, solar flares, solar active prominences etc. between solar cycles 8–23. According to the earlier works of Verma (1992, 1993) the N-S asymmetry of solar active phenomena has a periodicity about 12 solar cycles (110 years) and Verma (1992) had also predicted that the solar cycles 22, 23 & 24 may be southern dominated and N-S asymmetry will shift to the northern hemisphere in the solar cycle 25. From Fig. 1 it is clear that the N-S asymmetry of solar active phenomena during solar cycles 22 & 23 favours southern hemisphere as predicted by Verma (1992). Thus the present investigations support and confirm the results of Verma (1992).

References

Atac, T., Ozguc, A. 1996, *Solar Phys.,* **166,** 201.
Bell, B. 1962, *Smithsonian Contr. Astrophys.,* **5,** 187.
Bell, B., Glazer, H. 1959, *Smithsonian Contr. Astrophys.,* **3,** 25.
Hansen, R., Hansen, S. 1975, *Solar Phys.,* **44,** 225.
Howard, R. 1974, *Solar Phys.,* **38,** 59.
Janes, H.S. 1955, *Sunspot and Geomagnetic Storm Data, 195* Her Majesty's Stationary Office, (London, UK).
Reid, J. H. 1968, *Solar Phys.,* **5,** 207.
Roy, J. R. 1977, *Solar Phys.,* **52,** 53.
Solar Geophysical Data 1995–1999, *NOAA,* (Boulder, USA).
Swinson, D. B., Koyama, H., Saito, T. 1986, *Solar Phys.,* **106,** 35.
Verma, V. K. 1987, *Solar Phys.,* **114,** 185.
Verma, V. K. 1992, *ASP Conf. Series,* **27,** 429.
Verma, V. K. 1993, *Astrophys. J.,* **403,** 797.
Verma, V. K. 2000, *Solar Phys.,* **194,** 87.
Vizoso, G., Ballester, J. L. 1987, *Solar Phys.,* **112,** 317.
White, O. R., Trotter, D. E. 1977, *Astrophys. J. Suppl.,* **33,** 391.
Wolbach, J. G. 1962, *Smithsonian Contr. Astrophys.,* **5,** 195.

J. Astrophys. Astr. (2000) **21,** 177–183

Solar Filaments as Tracers of Subsurface Processes

D. M Rust, *Applied Physics Laboratory, Johns Hopkins University, 11100 Johns Hopkins Road, Laurel, MD 20723, USA.*
e-mail: david.rust@jhuapl.edu

Abstract. Solar filaments are discussed in terms of two contrasting paradigms. The standard paradigm is that filaments are formed by condensation of coronal plasma into magnetic fields that are twisted or dimpled as a consequence of motions of the fields' sources in the photosphere. According to a new paradigm, filaments form in rising, twisted flux ropes and are a necessary intermediate stage in the transfer to interplanetary space of dynamo-generated magnetic flux. It is argued that the accumulation of magnetic helicity in filaments and their coronal surroundings leads to filament eruptions and coronal mass ejections. These ejections relieve the Sun of the flux generated by the dynamo and make way for the flux of the next cycle.

Key words. Solar filaments—solar dynamo—magnetic fields.

1. Introduction

Filaments are clouds of relatively cool and dense gas in the solar atmosphere. The Standard paradigm of filament formation invokes condensation of plasma from the corona into dimpled magnetic fields, which are usually supposed to be twisted by shearing and reconnection of existing loops in the corona driven by surface motions. There is, however, a new paradigm about filaments, and twisted fields in general, according to which, probably all the magnetic flux that emerges into the photosphere is twisted. Twisted flux forms sunspots, active regions (ARs) and filaments. The twist accumulates in filaments and coronal arcades. Eventually the accumulated, highly-twisted fields become unstable and erupt. From a study of filament magnetic fields and filament eruptions, then, one might hope to discover important properties of the subsurface processes of the solar dynamo.

2. General properties of filament magnetic fields

The magnetic fields in filaments are nearly horizontal and generally exhibit a helical structure inside an arcade of coronal loops (Athay *et al.* 1983, Rust & Kumar 1994). Fig. 1 is a sketch of an idealized twisted-field filament and its magnetic arcade. The orientation of the axial fields in polar crown filaments, those generally above 50° latitude, shows a distinct dependence on the solar cycle (Leroy *et al.* 1983, Martin *et al.* 1992). In the years leading up to the maximum of even-numbered cycles, for example, the magnetic vectors in polar crown filaments point westward in the

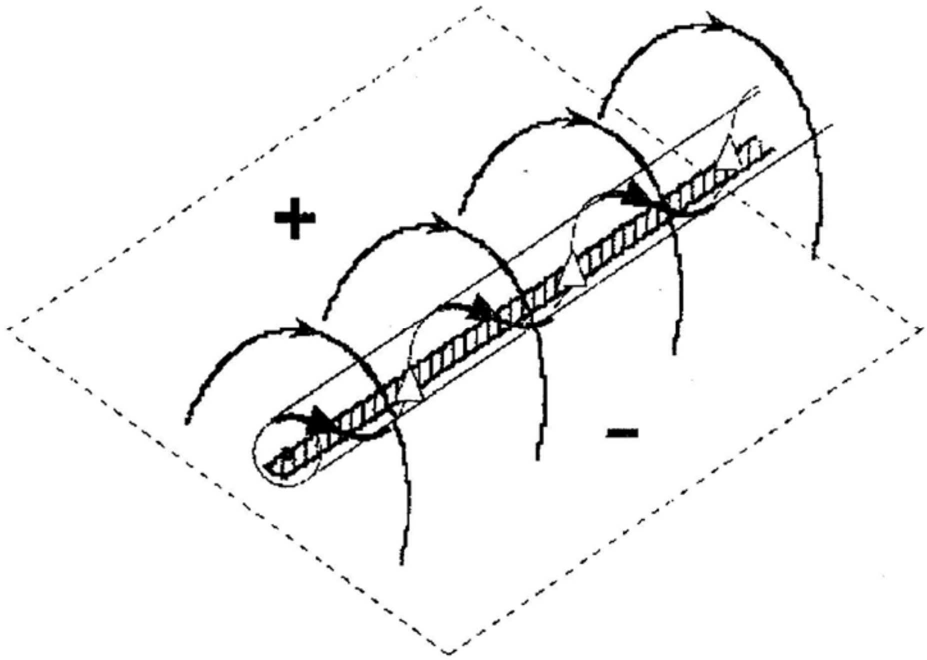

Figure 1. Perspective view of a filament (hatched strip) trapped in a twisted magnetic flux rope. An arcade of coronal loops encloses the filament. Filaments invariably lie on the borders separating positive and negative photospheric fields as shown here.

northern hemisphere and eastward in the southern hemisphere. Thus, these filaments collectively might be thought of as forming two magnetic toroids around the Sun, north and south with a flux of about 10^{20} Mx in each hemisphere. The filaments in ARs also generally follow the same pattern: they extend from a 'leader' spot eastward to a 'follower' spot or to non-spot fields of the same polarity as follower spots, so they could be viewed as segments of toroids as well.

Beginning 4–5 yrs after the onset of each cycle, an increasing number of filaments appears at mid-latitudes, i.e., 30°–45°. These are the so-called 1st tier or between-AR filaments. Their axial fields point eastward in the northern hemisphere and westward in the southern hemisphere in even-numbered cycles, i.e., they are opposite the fields in the polar-crown and AR filaments (Tang 1987).

First-tier filaments may be related to a peculiar feature of the solar dynamo. Stix (1976) published numerical solutions from a typical dynamo model that suggest that each cycle begins with toroidal fields at latitudes of 35° to 40°. We can identify the fields in the ARs of the cycle with these toroids. But the dynamo also produces weaker, reversed toroids about five years after the onset of the cycle. These toroids strengthen gradually for several years, all the while staying at latitudes above 35°. Thus, their behavior is similar to that of 1st-tier filaments, which also maintain a nearly constant mean latitude, ca. 50°, through most of the cycle. Toward solar minimum, these reversed toroidal fields strengthen and become the source of the ARs of the next cycle. Thus, the patterns of the toroidal fields in normal AR filaments and lst-tier filaments are consistent with some features of the model of the solar dynamo. First-tier filaments may be the earliest sign of the next solar cycle.

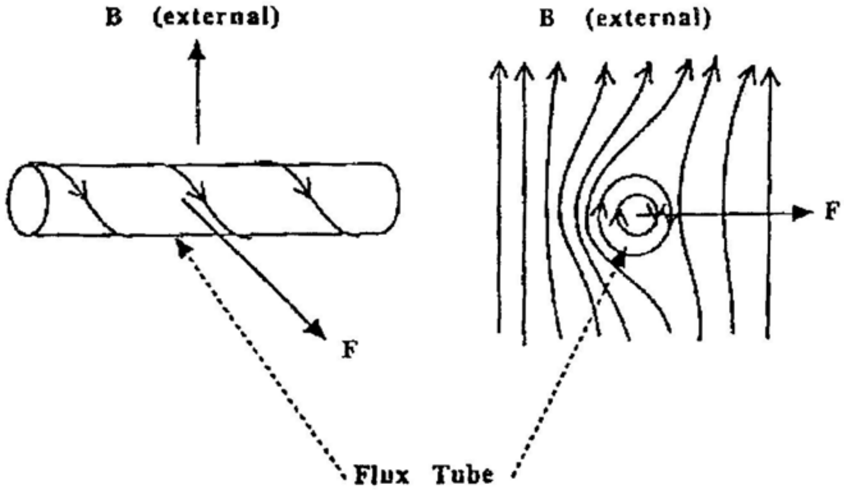

Figure 2. A horizontal flux rope in vertical external fields experiences a force *F* that is repulsive on one side and attractive on the other.

Twisted horizontal fields thrown up by the dynamo should collect at polarity boundaries. As shown in Fig. 2, there is a lateral force on a horizontal flux rope surrounded by vertical fields. If the flux rope has a net current flowing along its axis, the Lorentz force acting on it, in the presence of an external field will force the flux rope to move until it reaches a polarity boundary, where the horizontal force vanishes. Thus, weak-field horizontal flux ropes will be in stable equilibrium and they will collect at polarity boundaries.

3. Global pattern of filament helicity

Filaments resemble twisted ropes, giving inspiration to the flux rope model (Low & Hundhausen 1995, Amari *et al.* 1999, Rust & Kumar 1994). The recent model of Aulanier & Demoulin (1998) and Aulanier *et al.* (1998) now seem to account quite convincingly for the barbs on filaments in terms of a helical flux rope model distorted by underlying fields. The chirality of the twist, left-handed in the north and right-handed in the south, is consistent with an origin in the dynamo.

Evidence that filaments erupt as the result of an instability in a twisted flux rope was obtained with the X-ray telescope aboard the Yohkoh satellite. A sigmoid (S-shaped) brightening usually appears in X-rays at the onset of filament eruption. The ratio R of sigmoid length to width in a large sample of eruptives peaks at R = 5 (Rust & Kumar 1996). This is exactly the ratio of the most likely helical kink instability in a twisted magnetic field. Furthermore, most sigmoid brightenings in the southern hemisphere are S-shaped, as predicted for a helical instability in a field with right-handed twist. Sigmoid brightenings in the north are usually mirror image (reversed) S-shaped, as expected for instabilities in left-handed flux ropes.

Despite some sophisticated calculations (Van Ballegooijen *et al.* 1998), models based on surface motions have not yet explained the global pattern of filament axial fields in the polar crown and in the first tier of filaments. The basic problem is that differential rotation, which is the only systematic surface motion outside ARs, will shear coronal arcades so that, in even-numbered cycles, the magnetic field vectors in polar crown filaments point eastward in the northern hemisphere and westward in the southern hemisphere, contrary to observations.

Mackay *et al.* (1998) combine surface motions and emergence of twisted flux ropes to show how first tier filaments might form with the required negative helicity in the north and positive helicity in the south. But the key ingredient in their model is the correct helicity of the emergent flux.

If surface motions cannot reproduce the observed toroidal and helical field patterns, then -we can turn to subsurface motions. Suppose that filament fields originate in AR flux ropes and accumulate in the chromosphere and corona. Then the problem becomes one of showing how the AR fields are twisted. Longcope *et al.* (1999) consider how much twist could be imparted by the Coriolis force acting during a flux rope's flight from the base of the convection zone to the photosphere. They conclude that the effect would produce an average twist in ARs at least an order of magnitude lower than that observed by Pevtsov *et al.* (1995). Similarly, they find that subsurface differential rotation falls short by an order of magnitude. They develop a model of subsurface twist imparted by turbulent motions in the convection zone that they call the ∑-effect and that, according to them, could produce the observed average twist in AR fields. They do not consider surface motions, but their ∑-effect model is the first attempt at a quantitative correspondence between the observed amount of helicity on the Sun and plausible subsurface motions.

The amount of helicity K injected into the solar atmosphere by AR fields in each solar cycle can be estimated from the number N of active regions, each with an average flux ϕ and twist per unit length q. Taking N = 3000 ARs per cycle, $\phi = 10^{21}$ Mx per AR, q = 0.02 rad Min^{-1} as measured by Pevtsov *et al.* (1995), then we find $K = 1.3 \times 10^{45}\ \mathrm{Mx}^2$ per solar cycle. This is nearly the same value escaping the Sun as estimated by Bieber & Rust (1995) from interplanetary magnetic field (IMF) measurements and from estimates of the helicity in filaments and coronal arcades. Thus it is plausible that the helicity emerging in ARs accumulates in filaments and coronal arcades. As shown in Parker's (1979) book, the twist in an emerged flux rope will migrate into the emerged portion of the rope.

Now that there is so much data on the distribution and quantity of magnetic helicity in the solar atmosphere (Brown *et al.* 1999), it is important to calculate the magnetic helicity from dynamo models. Gilman & Charbonneau (1999) pointed out that most dynamo theories can only calculate the mean fields and helicity that might occur at the base of the convection zone. They say nothing about what might happen to the fields as they rise to the visible surface, but it is useful to review dynamo results here because important features of the predicted cyclic behavior and helicity patterns should be preserved when the fields emerge at the photosphere.

Gilman & Charbonneau (1999) computed mean field strengths for the toroidal and poloidal components and the mean positive and negative current helicity produced by a variety of dynamo models. Current helicity has the same sign as magnetic helicity (Seehafer 1990), so current helicity calculations are useful to see if a realistic dynamo model can reproduce the observed magnetic helicity pattern. Gilman & Charbonneau (1999) computed the helicity from a 'flux transport' model developed by Dikpati & Charbonneau (1999). It is similar to Babcock's (1961) original model of the sunspot cycle. The results are in good general agreement with observations since the toroidal component is much stronger than the radial component. And while negative (positive) helicity dominates in the north (south), each hemisphere has mixed helicities in the sunspot zones, also in agreement with observations. There is an interesting pattern of added helicity near the poles, and this may be due to the fact that the model does not account for flux escape from the Sun.

Parker (1984) and Vainshtein & Rosner (1991) argued on theoretical grounds that one of the features fundamental to all solar cycle models, namely, the escape of dynamo-generated flux from the Sun, cannot take place at anything close to the apparent rate of emergence in ARs. Parker (1984) estimated that $\leq 3\%$ of the flux can escape. However, Parker's argument was based on much lower rates of reconnection among emerged flux ropes than seems reasonable after the evidence of the TRACE mission.

Vainshtein & Rosner (1991) accepted the possibility of coronal reconnections releasing toroidal flux, but they mistakenly assumed it could take place only above ARs. They then concluded that the coronal fields above ARs would have to average 2300 G, an unlikely value. If, however, the vehicles of flux accumulation in the corona are filaments and coronal arcades and not ARs, then Vainshtein & Rosner's (1991) reasoning would lead to an estimated average field of 23 G in the corona, in approximate agreement with observations.

Observational evidence of flux escape is accumulating. Smith & Bieber (1991) observed an apparent overwinding of the IMF and suggested it could be explained if toroidal fields escape into the solar wind. Also from IMF measurements, Bieber & Rust (1995) estimated that $\sim 10^{24}$ Mx of toroidal flux escapes the Sun per cycle and they went on to argue that CMEs and eruptive filaments could remove 100% of this toroidal flux. Smith & Phillips (1995) found that most of the IMF overwinding occurred during the periods with CMEs; that is, the fields in the CMEs account for the toroidal field in the solar wind, aside from that produced by rotation of the Sun.

In the same way that filaments with right- (left-) handed twisted fields dominate in the south (north), a like chirality segregation is also seen in the IMF (Bieber *et al.* 1987, Smith & Bieber 1993). This is an important further indication that the escaping toroids threading filaments and CMEs can be identified with the excess azimuthal component of the IMF. According to theory, the helicity of the fields should be preserved as they erupt, even if there is substantial reconnection (Taylor 1986).

Since the helicity in each hemisphere is the same for successive cycles the fields generated in a cycle cannot be canceled by oppositely directed fields from the next cycle. Helicity will accumulate in the solar atmosphere in filaments and coronal arcades until it drives them to instability and expulsion.

4. Concluding remarks

Since at least the time of the Skylab flare workshops, solar researchers have implicitly assumed that the fields in filaments could be derived from some combination of photospheric footpoint motions and reconnections in the corona. It now seems unlikely that such motions, i.e., differential rotation, meridional flow or convection, can impress the observed patterns of helicity on coronal fields. Still, an appeal to subsurface processes should be resisted, but surface motion models have been able to reproduce neither the pattern of filament field orientations nor the correct sign of helicity.

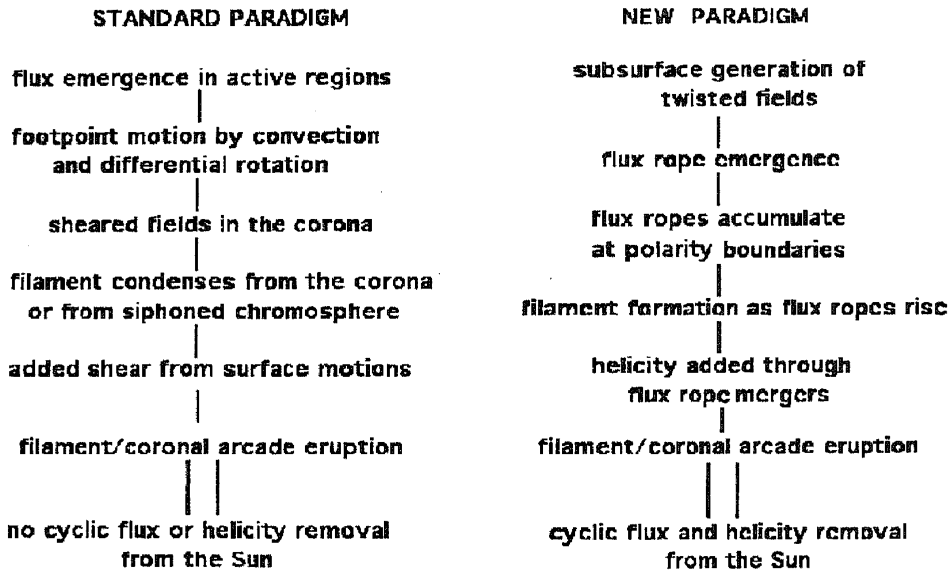

Figure 3. The new paradigm vs. the standard paradigm for filament evolution.

The new paradigm (Fig. 3) starts with some subsurface mechanism-which one(s) is not at all clear-imparting helicity to the magnetic fields before they emerge. The paradigm relies heavily on the concept of twisted flux ropes as agents of helicity transfer from the interior to the visible photosphere and subsequently to the corona.

Many of the steps between subsurface generation of twisted fields and their removal from the Sun are speculative and need to be tested by observation. Nevertheless, the new paradigm of filament formation and eruption is likely to be important in the research on the solar cycle. Magnetic flux and helicity leave the Sun in eruptive filaments and coronal mass ejections. The total flux and helicity measured in the IMF during each 11-year solar cycle is equal to the estimated total flux and helicity of the eruptives and CMEs. It is also equal to the flux and helicity in the 3000 active regions seen in a typical cycle. This is strong evidence that eruptive filaments and CMEs carry off very nearly all of the magnetic fields generated in each solar cycle.

Acknowledgements

I am grateful to Sara Martin for many interesting discussions and to J. O. Stenflo, who presented this paper when I couldn't be at the conference in person. This work was sponsored by NASA grant NAG5-7921.

References

Amari, T., Luciani, J. F., Mikic, Z., Linker, J. 1999, *Astrophys. J.,* **518,** L57–L60.

Athay, R. G., Querfeld, C. W., Smartt, R. N., Deglinnocenti, E. L. 1983, *Solar Phys.,* **89,** 3–30.

Aulanier, G., Demoulin, P. 1998, *Astr. Astrophys.,* **329,** 1125–1137.

Aulanier, G., Demoulin, P., Van Driel-Gesztelyi, L., Mein, P., Deforest, C. 1998, *Astr. Astrophys.,* **335,** 309–322.

Babcock, H. W. 1961, *Astrophys. J.,* **133,** 572.

Bieber, J. W., Evenson, P. A., Matthaeus, W. H. 1987, *Astrophys. J.,* **315,** 700–705.

Bieber, J. W., Rust, D. M. 1995, *Astrophys. J.,* **453,** 911.

Brown, M. R., Canfield, R. C., Pevtsov, A. A. (ed.) 1999, *Magnetic Helicity in Space and Lab. Plasmas,* Geophys. Monograph **111,** Amer. Geophys. U.

Dikpati, M., Charbonneau, P. 1999, *Astrophys. J.,* **518,** 508–520.

Gilman, P. A., Charbonneau, P. 1999, in *Magnetic Helicity in Space and Laboratory Plasmas,* Geophys. Monograph **111,** (eds.) M. R. Brown, R. C. Canfield, A. A. Pevtsov, Amer. Geophys. U., 75–82.

Leroy, J. L., Bommier, V., Sahal-Brechot, S. 1983, *Solar Phys.,* **83,** 135–142.

Longcope, D., Linton, M., Pevtsov, A., Fisher, G., Klapper, I. 1999, in *Magnetic Helicity in Space and Laboratory Plasmas,* (eds.) M. R. Brown, R. C. Canfield, A. A. Pevtsov, Geophys. Monograph **111,** Amer. Geophys. U., 39–101.

Low, B. C., Hundhausen, J. R. 1995, *Astrophys. J.,* **443,** 818–836.

Mackay, D. H., Priest, E. R., Gaizauskas, V., Van Ballegooijen, A. A. 1998, Solar Phys., **180,** 299–312.

Martin, S. F., Marquette, W. H., Bilimoria, R. 1992, in *The Solar Cycle,* (eds.) K. L. Harvey, K. L. Harvey, pp 53–66, Astron. Soc. Pacific.

Parker, E. N. 1979, *Comical Magnetic Fields,* (Oxford: Clarendon Press).

Parker, E. N. 1984, *Astrophys. J.,* **281,** 839.

Pevtsov, A. A., Canfield, R. C., Metcalf, T. R. 1995, *Astrophys. J.,* **440,** L109–L112.

Rust, D. M., Kumar, A. 1994, *Solar Phys.,* **155,** 69–97.

Rust, D. M., Kumar, A. 1996, *Astrophys. J.,* **464,** L199–L202.

Seehafer, N. 1990, *Solar .Phys.,* **125,** 219.

Smith, C. W., Bieber, J.W. 1991, *Astrophys. J.,* **370,** 435–441.

Smith, C. W., Bieber, J.W. 1993, *J. Geophys. Res.,* **98,** 9401–9415.

Smith, C. W., Phillips, J. L. 1995, *Delaware Univ., Intl. Solar Wind,* **8,** 93.

Stix, M., 1976, in *Basic Mechanisms of Solar Activity, IAU Colloq.* **71,** (eds.) V. Bumba, J. Kleczek, (Reidel) 367.

Tang, F. 1987, Solar *Phys.,* **107,** 233–237.

Taylor, J. B. 1986, *Rev. Mod. Phys.,* **58,** 741.

Vainshtein, S. I., Rosner, R. 1991, *Astrophys. J.,* **376,** 199.

Van Ballegooijen, A. A., Cartledge, N. P., Priest, E. R. 1998, *Astrophys. J.,* **501,** 866.

J. Astrophys. Astr. (2000) **21,** 185–192

Coronal Structures as Tracers of Sub-Surface Processes

Alexei A. Pevtsov & Richard C. Canfield, *Montana State University, Bozeman, MT 59717, U.S.A.*
**e-mail: pevtsov@physics.montana. edu*

Abstract. The solar corona – one of the most spectacular celestial shows and yet one of the most challenging puzzles – exhibits a spectrum of structures related to both the quiet Sun and active regions. In spite of dramatic differences in appearance and physical processes, all these structures share a common origin: they are all related to the solar magnetic field. The origin of the field is beneath the turbulent convection zone, where the magnetic field is not a master but a slave, and one can wonder how much the coronal magnetic field "remembers" its dynamo origin. Surprisingly, it does. We will describe several observational phenol-mena that indicate a close relationship between coronal and sub-photo-spheric processes.

Key words. Sun—solar corona—magnetic field—helicity.

1. Introduction

The corona – a tenuous portion of the solar upper atmosphere – was observed as early as 1063 BC (Golub & Pasachoff 1997). The real surprise came in 1939, when Grotrian discovered that the coronal gas is a few million degrees hotter than the underlying photosphere and chromosphere. Since then, many models of the coronal heating have been proposed (e.g. Mandrini, Démoulin & Klimchuk 2000); but the question "how does the corona get so hot?" is still open. Considering the possible processes that can affect the appearance of coronal structures, one can divide them into two categories: ones that take place above the photosphere and require no connection with the sub-photospheric layers and those that, even if they occur in the corona, may have close ties with sub-photospheric processes. Below we examine several coronal phenomena and explore their sub-photospheric origin.

2. The hemispheric helicity rule in the solar corona

2.1 *Sigmzoidal loops of solar active regions*

Soft X-ray images of the solar corona (Fig. 1), routinely observed by Yohkoh, give numerous examples of bright coronal structures reminiscent of the letters S and inverse-S. Such sheared structures, discovered in earlier Yohkoh observations (e.g. Acton *et al.* 1992), were collectively named *sigmoidal* loops by Rust & Kumar

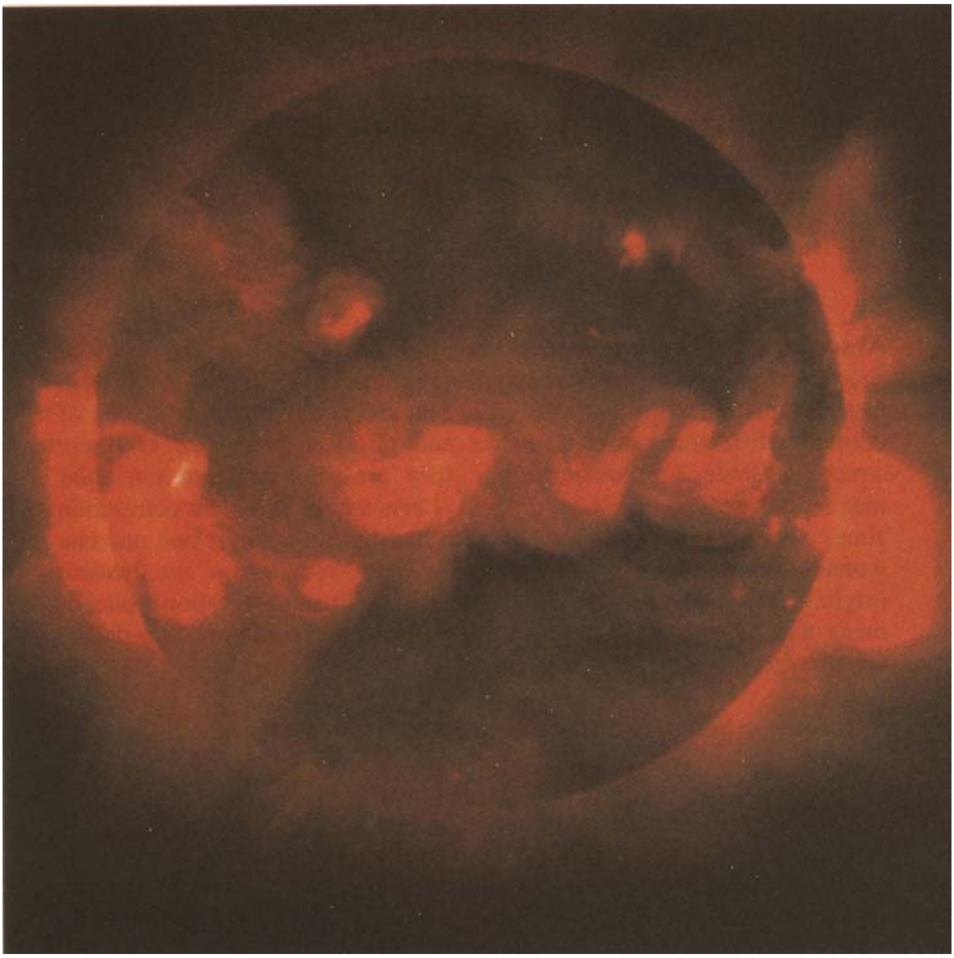

Figure 1. Yohkoh soft X-ray telescope image showing sigmoidal coronal loops.

(1996). There is a close similarity in appearance between the shape of sigmoidal loops and linear force-free field lines projected on the image plane. Pevtsov, Canfield & McClymont (1997) compared the value of α ($\nabla \times B = \alpha B$) computed independently for ~ 100 active regions using photospheric magnetograms and coronal images and found good agreement between the photospheric and coronal α values. They interpret their results as an indication of field-aligned electric currents flowing from below the photosphere through to the corona. The currents may be the result of near-surface sunspot proper motions (e.g. van Driel Gesztelyi *et al.* 1997) or may be of subphotospheric origin (Leka *et al.* 1996).

The distribution of sigmoidal loops shows a clear hemispheric dependency: S-shaped loops are typical in the southern hemisphere, and inverse-S loops prevail in the northern hemisphere. This dependency is the coronal signature of the hemispheric helicity (chirality) rule (for a review, see Pevtsov & Canfield 1999). According to the rule, magnetic fields in the northern (southern) hemisphere tend to have negative (positive) helicity. Table 1 shows the distribution of sigmoidal loops for solar cycles

Table 1. Distribution of coronal sigmoids by hemisphere.

	Cycle 22 (1991–95)		Cycle 23 (1997–98)	
	Forward S	Inverse S	Forward S	Inverse S
Northern Hemisphere	41%	59%	29%	71%
Southern Hemisphere	68%	32%	87%	13%

22 and 23. Both cycles exhibit the same hemispheric preference in chirality (sign of helicity), in agreement with the photospheric vector magnetographic data (e.g., Bao & Zhang 1998). Both strong magnetic fields of active regions (e.g. Pevtsov, Canfield & Metcalf 1995) and weak magnetic fields on large scales (Pevtsov & Latushko 2000) follow the same hemispheric asymmetry. The rule has also been observed in chromospheric filaments, sunspot penumbra filaments, superpenumbrae, and even the interplanetary magnetic field (Richardson 1941; Martin, Bilimoria & Tracadas 1994; Bieber, Evenson & Matthaeus 1987).

There are two important properties of the hemispheric helicity rule that are critical for its understanding.

- The rule is global and independent of the solar cycle. The same sign-asymmetry. was observed during cycles 20, 21, 22 and 23 (e.g. Seehafer 1990; Pevtsov, Canfield & Metcalf 1995; Bao & Zhang 1998; Hagyard & Pevtsov 1999). Solar features of different origin and size exhibit the same hemispheric preference in their helicity. Thus, it seems highly unlikely, that the small scale (local) processes such as, say, sunspot proper motions can explain this general tendency.
- The rule is not very strong, only 60–70% of all active regions follow it. Mechanisms that depend strongly on the solar hemisphere (e.g., Coriolis force, differential rotation) should result in much stronger hemispheric dependency. Hence, although such mechanisms may play a role, they are not the only ones of importance.

Several different mechanisms can in principle explain the hemispheric helicity rule (Table 2), but most of them fail to explain specific details. For example, differential rotation produces the correct sense of shear in coronal loops. However, it will also introduce twist of opposite sign into the magnetic flux tubes, in disagreement with observations (e.g. Pevtsov & Canfield 1999). The Coriolis force acting on the apex of a magnetic flux tube rising through the convection zone will deflect it. This action will produce the correct hemispheric asymmetry in twist and writhe, but the resulting

Table 2. Mechanisms of the hemispheric helicity rule.

Mechanism	Hemispheric helicity rule?
Near surface proper motions	No
Differential rotation	No (wrong sign of twist)
Coriolis force	Yes
Sigma-effect	Yes
CZ mean-field dynamo	No (wrong sign)
Overshoot region dynamo	Yes

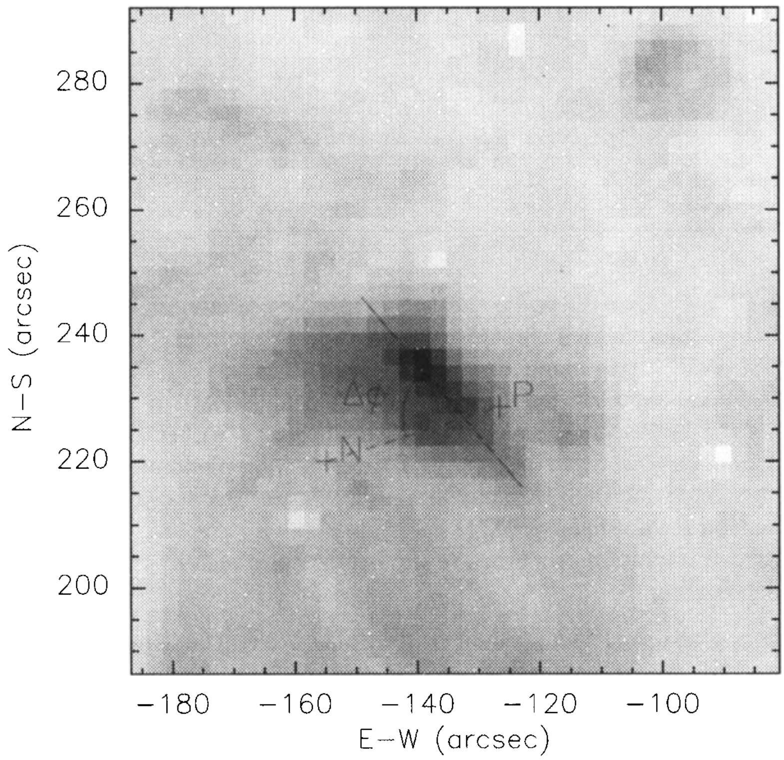

Figure 2. Example of X-ray bright point (halftone) and corresponding magnetic bipole (letters N and P connected by dashed line). Symbols N and P indicate negative and positive polarities and ΔΦ is misalignment between magnetic bipole (dashed) and XBP orientation (solid line).

hemispheric preference should be much stronger than observed. Two mechanisms can correctly explain the hemispheric helicity rule: an interaction between magnetic flux tubes and turbulent convection (∑-effect, Longcope, Fisher & Pevtsov 1998) and an overshoot region dynamo (Gilman & Charbonneau 1999). However, the expected contribution of the overshoot region dynamo is significantly less than that of the ∑-effect (Longcope *et al.* 1999).

2.2 *X-Ray bright points*

Another coronal feature – X-ray bright points (XBP) – may also follow the hemispheric helicity rule, although their hemispheric dependency is not as clear as for the sigmoidal loops of active regions. Fig. 2 shows an example of XBP which is tilted relative to the underlying bipole. In fact, many XBPs show such misalignment of their axes (Kankelborg *et al.* 1996). Longcope (1998) developed a topological model to describe the XBP phenomena as the result of magnetic reconnection. between two independent flux systems. In his model, reconnection and energy deposit occur along a separator field line, and the separator appears as the XBP loop in the corona. The misalignment between the X-ray bright point and the magnetic

Table 3. X-ray bright point misalignment fraction by hemisphere.

Hemisphere	All data (285 XBPs)		Strongly elongated only (154 XBPs)	
	Positive	Negative	Positive	Negative
Northern	42%	58%	36%	64%
Southern	54%	46%	50%	50%

bipole depends on the mutual orientation of the large-scale ambient magnetic field and the reconnecting bipole. On the other hand, one can also consider XBP to be a single bipolar active region loop. If the loop carries electric currents it may appear to be sheared, similar to the sigmoidal loops of active regions (e.g. Fig. 1). If the electric currents (magnetic field twist) in the XBPs follow the same hemispheric helicity rule as the active regions, the orientation of the XBPs should also exhibit the hemispheric dependency. In Longcope (1998) model XBPs are formed via random encounters of two independent flux systems, and hence, should exhibit no hemispheric preference in their orientation relative to the bipole axis. Recently, Kankelborg et al. (1999) surveyed the SOHO-EIT and MDI data set and identified 764 X-ray bright points. They analyzed 285 XBPs and found that magnetic bipoles have no preference either in their polarity orientation (no Hale polarity rule, Hale & Nicholson 1938) nor in their tilt relative to the equator (no Joy's law, Zirin 1988). However, the orientation of XBPs relative to the axis of the associated bipole shows a weak hemispheric preference, which is in agreement with the hemispheric helicity rule (Table 3).

Thus, it seems that at least some XBPs do follow the hemispheric rule and hence can be explained in the framework of a flux tube model. However, a more restricted subset, including only XBPs with strongly elongated shape, shows no hemispheric preference in the southern hemisphere (Table 3). Clearly, the presence (or absence) of the hemispheric helicity rule in orientation of the X-ray bright points needs further investigation, perhaps separately for XBPs that are associated with reconnection of existing magnetic fluxes, as distinguished from those associated with emerging/submerging bipoles.

3. Large scale patterns in the corona

The topology-of the magnetic field is one of the most important factors determining the appearance of coronal structures. There is good correlation between unsigned magnetic flux and X-ray brightness of coronal loops (e.g. Fisher et al. 1998). Thus, it is not surprising that the brightest coronal areas are related to the active regions. However, some coronal features persist much longer than individual active regions. Fig. 3 shows a stackplot of Yohkoh synoptic maps for 8 solar rotations. One can clearly see several areas of enhanced coronal activity which persist for many solar rotations. Sandborgh et al. (1998) used full disk soft X-ray telescope images from Yohkoh to identify boundaries of coronal flux systems. A flux system was defined as a bright closed area (not a coronal hole, for instance) with coronal loops connecting sub-areas inside the system and no loops crossing its outer boundary. The shape of the loops (sigmoidal structure) was used to determine the chirality of each flux system.

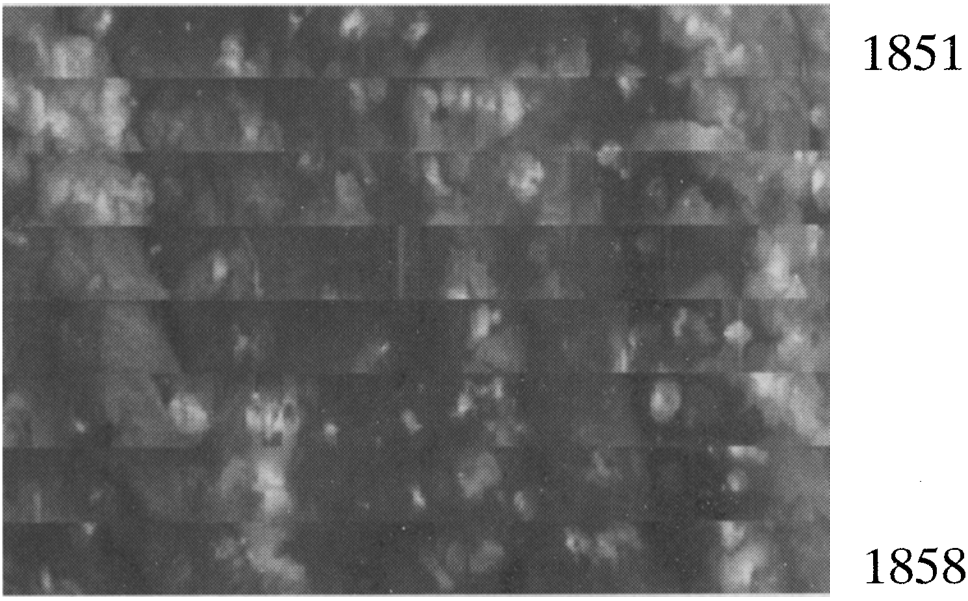

Figure 3. Stackplot of Yohkoh synoptic maps for 8 solar rotations (1851-1858). Each strip covers 360° in Carrington longitude and 0-20° in latitude in the northern hemisphere. Longitude runs from left (0°) to right (360°).

Table 4. Coronal flux systems observed in 1991–1992.

	Extension in		Lifetime		
No.	Latitude	Longitude	First CRN	(rotations)	Chirality
1	−40° to −20°	300° to 360°	1851	3	positive
2	−20° to 0°	90° to 120°	1851	3	complex
3	−40° to −5°	60° to 90°	1852	3	negative
4	−40° to −10°	140° to 180°	1852	3	negative
5	−40° to 0°	320° to 20°	1854	4	negative
6	−30° to 0°	90° to 130°	1855	3	zero
7	−10° to 40°	320° to 20°	1856	3	negative
8	0° to 30°	240° to 280°	1857	5	negative
9	−15° to 15°	20° to 40°	1858	4	positive
10	0° to 20°	300° to 340°	1858	3	positive

Table 4 lists size, a lifetime and chirality of several flux systems found by Sandborgh et al. (1998) during 11 consecutive solar rotations.

The coronal flux systems listed in Table 4 are significantly larger than a typical active region (up to 50° in latitude and 60° in longitude, flux system No. 7). They persist for up to 5 solar rotations (e.g. No. 8) maintaining the same chirality.

Large scale structures of similar size have been observed in magnetic fields (e.g. Ambroz 1992) and photospheric flows (Hathaway et al. 1998). Close similarity in size and lifetime suggests a common origin for all these different structures. However, without co-temporal comparison of the features, their relationship remains questionable.

Transequatorial loop systems (TLS) connecting independent active regions across the solar equator are another example of large-scale organization in the corona. Pevtsov (2000) studied the distribution of TLS observed during 1991–1998 and found that such loops are formed only in selected areas on the Sun. Such areas persist for several consecutive solar rotations and exhibit no significant difference in rotation rates between its northern and southern hemisphere ends. The majority of TLS exhibit sheared loops, implying the presence of electric currents. As a rule, magnetic fields in areas connected across the equator have the same chirality, which suggests continuity of electric currents flowing between connected active regions.

The coronal flux systems and TLS can be seen as coronal counterparts of complexes (nests) of activity, previously observed in the distribution of solar active regions (e.g. Brouwer & Zwaan 1990). The size and persistence of the activity nests can not be easily explained by photospheric processes alone and may, for instance, indicate an asymmetry in the solar dynamo and/or large-scale persistent pattern inside the convection zone (e.g. giant cells).

Acknowledgements

This work was supported by NASA through SR&T grant NAG5–6110. A.A.P. would like to acknowledge partial travel support by the International Astronomical Union to attend the IAU Colloquium 179 in Kodaikanal, India.

References

Acton, L. W., et al. 1992, Science, **258,** 618.

Ambroz, P., 1992, in *The Solar Cycle,* (ed.) K. Harvey (San Francisco: ASP), **27,** 35.

Bao, S., Zhang, H. 1998, *Astrophys. J.,* **496,** L43.

Bieber, J. W., Evenson, P., Matthaeus, W. 1987, *Astrophys. J.,* **315,** 700.

Brouwer, M. P., Zwaan, C. 1990, *Solar Phys.,* **129,** 221.

Fisher, G. H.; Longcope, D. W., Metcalf, T. R., Pevtsov, A. A. 1998, *Astrophys. J.,* **508,** 885.

Gilman, P. A., Charbonneau, P. 1999, in *Magnetic Helicity in Space and Laboratory Plasmas,* (eds.) M. Brown, R. Canfield & A. Pevtsov, vol. **111** of Geophysical Monographs Series (Washington, D.C.: American Geophysical Union).

Golub, L., Pasachoff, J. M. 1997, *The Solar Corona* (Cambridge: Cambridge Univ. Press).

Hagyard, M., Pevtsov, A. 1999, *Solar Phys.,* **189,** 25.

Hale, G. E., Nicholson, S. B. 1938, *Magnetic observations of sunspots, 1917–1924...* (Washington, D.C.: Carnegie institution of Washington)

Hathaway, D. H., Bogart, R. S., Beck, J. G. 1998, *Eos Trans. AGU,* **79**(17), S281.

Kankelborg, C. C., Walker, II, A. B. C., Hoover; R. B., Barbee, T. W. J. 1996, *Astrophys. J.,* **466,** 529.

Kankelborg, C. C., Nelson, J., Longcope, D. W., Pevtsov, A. A. 1999, *BAAS,* **194,** 1601.

Leka, K. D., Canfield, R. C., McClymont, A. N., van Driel-Gesztelyi, L. 1996, *Astrophys. J.,* **462,** 547

Longcope, D. W. 1998, *Astrophys. J.,* **507,** 433.

Longcope, D. W., Fisher, G. H., Pevtsov, A. A. 1998, *Astrophys. J.,* **507,** 417.

Longcope, D. W., Linton, M. G., Pevtsov, A. A., Fisher, G. H., Klapper, I. 1999, in *Magnetic Helicity in Space and Laboratory Plasmas,* (eds.) M. Brown, R. Canfield & A. Pevtsov, vol. **111** of Geophysical Monographs Series (Washington, D.C.: American Geophysical Union), 93.

Mandrini, C. H., Demoulin, P., Klimchuk, J. A. 2000, *Astrophys. J.,* **530,** 999.

Martin, S. F., Bilimoria, R., Tracadas, P. W. 1994, in *Solar Surface Magnetism,* (ed.) C. J. Rutten & C. J. Schrjiver (Dordrecht: Kluwer Academic Publishers).

Pevtsov, A. A. 2000, *Astrophys. J.,* **531,** 553.

Pevtsov, A. A., Canfield, R. C., McClymont, A. N. 1997, *Astrophys. J.,* **481,** 973.

Pevtsov, A. A., Canfield, R. C., Metcalf, T. R. 1995, *Astrophys. J.,* **440,** L109.

Pevtsov, A. A., Canfield, R. C. 1999, *Magnetic Helicity in Space and Laboratory Plasmas,* (ed.) M. Brown, R. Canfield & A. Pevtsov, vol. **111** of Geophysical Monographs Series (Washington, D.C.: American Geophysical Union) 103.

Pevtsov, A. A., Latushko, S. M. 2000, *Astrophys. J.,* **528,** 999.

Richardson, R. S. 1941, *Astrophys. J.,* **93,** 24.

Rust, D. M., Kumar, A. 1996, *Astrophys. J.,* **464,** L199.

Sandborgh, S. C., Canfield, R. C., Pevtsov, A. A. 1998, *Eos Trans. AGU,* **79**(17), S285.

Seehafer, N. 1990, *Solar Phys.,* **125,** 219.

van Driel-Gesztelyi, L., Csepura, G., Schmieder, B., Malherbe, J. M., Metcalf, T. 1997, *Solar Phys.,* **172,** 151.

Zirin, H., 1988, *Astrophysics of the Sun* (Cambridge: Cambridge University Press).

J. Astrophys. Astr. (2000) **21**, 193–196

Polar Magnetic Field Reversals of the Sun in Maunder Minimum

V. I. Makarov* & A. G. Tlatov, *Kislovodsk Solar Station of the Pulkovo Observatory, Kislovodsk 357700, P.O. Box 145, Russia.*
**e-mail: makarov@ gao.spb.ru*

Abstract. A possible scenario of polar magnetic field reversal of the Sun during the Maunder Minimum (1645–1715) is discussed using data of magnetic field reversals of the Sun for 1880–1991 and the ^{14}C content variations in the bi-annual rings of the pine-trees in 1600–1730 yrs.

Key words. Sun: cycle—magnetic field—maunder minimum.

1. Introduction

Topology and polar magnetic field reversals for 1880–1991 were described in the papers (Makarov & Sivaraman 1989; Makarov 1994). In this paper we continue to discuss a possible scenario of polar magnetic field reversal of the Sun in the Maunder Minimum (1645–1715). Preliminary result has been published in the paper (Makarov & Callebaut 1999).

2. Observational data

The data on polar migration of solar magnetic fields were obtained on the basis of H-alpha magnetic synoptic charts for 1880–1991 using Kodaikanal, Kislovodsk and Italian observations, and Atlas of H-alpha charts (Mclntosh 1979; Makarov & Fatianov 1980; Makarov & Sivaraman 1989; Makarov 1994). The Wolf numbers were taken from Jones (1955), Hoyt & Schatten (1998) and Makarov & Makarova (1996). We used ^{14}C content variations in the biannual rings of the pinetrees in 1600–1730 yrs (Kocharov *et al.* 1995).

3. Results

A comparison of H-alpha magnetic charts with the Stanford magnetographic observations shows that the pattern of the largescale magnetic fields can be derived with greater accuracy than can be inferred from magnetograms (Duval *et al* 1977; Makarov & Tlatov 1999). Thus, H-alpha charts represent data for investigation of global properties of large-scale magnetic fields during many solar cycles when magnetographic observations are not available.

The poleward migration rate of the magnetic fields, V (ms^{-1}), depends on the solar activity. To quantify this we take as an independent variable quantity the sum of the

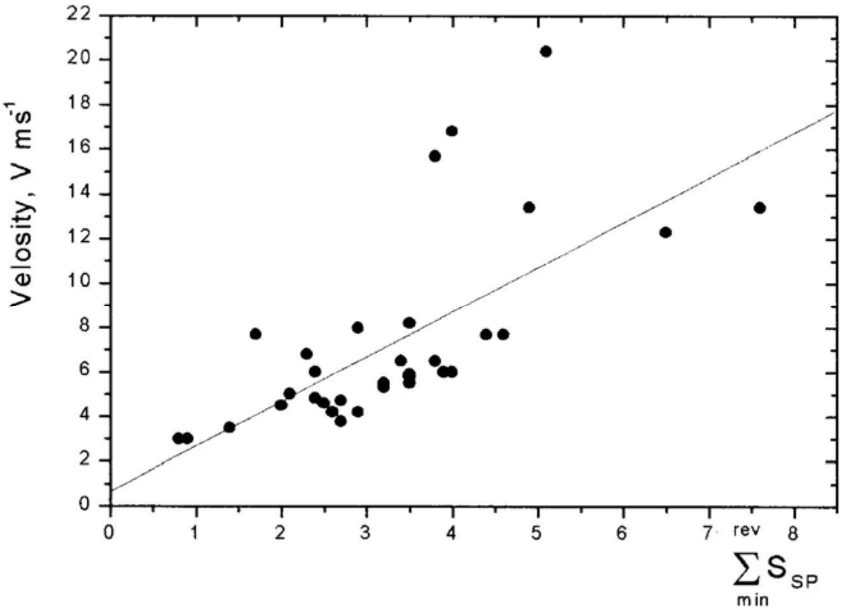

Figure 1. Poleward migration rate, V (ms^{-1}), of the magnetic field vs the sum of the yearly mean Wolf numbers $\sum_{\rm min}^{\rm rev}$ W(t) from a minimum of the solar activity to polar magnetic field reversal for 1880–4991 yrs.

yearly mean Wolf number $\sum_{\rm min}^{\rm rev}$ W(t) starting at a minimum activity, min, up to polar magnetic field reversal, rev, or the Wolf number maximum, $W_{\rm max}$ We found that the poleward migration rate of the magnetic fields according to Fig. 1 is:

$$V(\mathrm{ms}^{-1}) = 0.7 + 0.015\Sigma_{\rm min}^{\rm rev} W(t); \quad \text{or} \quad V(\mathrm{ms}^{-1}) \approx 0.7 + 0.06 W_{\rm max}.$$

One can see that the value V (ms^{-1}) at very low solar activity is about 0.7 ms^{-1}. In those cycles the latitude zones of magnetic field migrate to the poles during more than 20 yrs and this process determines length of a solar cycle. But according to Beer *et al.* (1998) the magnetic cycles persisted throughout the Maunder Minimum. As the intensity of the solar cycle determines the poleward migration rate it also determines which latitude of the zonal boundary will reach. The higher W(t), the higher the latitúde which is reached. According to Makarov & Callebaut (1999) the minimum intensity of solar cycle for polar magnetic reversal requires the $\sum_{\rm min}^{\rm rev} W(t) \approx 200$, or $W_{\rm max} \approx 40 \pm 10$. According to Hoyt & Schatten (1998), Nagovitsyn (1997) $W_{\rm max}$ has been significantly less than 40 during 1640–1715.

4. Discussion

According to Ribes *et al.* (1993) in the Maunder Minimum the active regions were observed only near the equator. This fact of long occurrence of the sunspots near the equator is unique. In the normal solar cycles active regions practically do not emerge in a zone of ±5° around the equator. The occurrence of active regions during a long time near the equator of the Sun may be taken to testify as a case of a "long

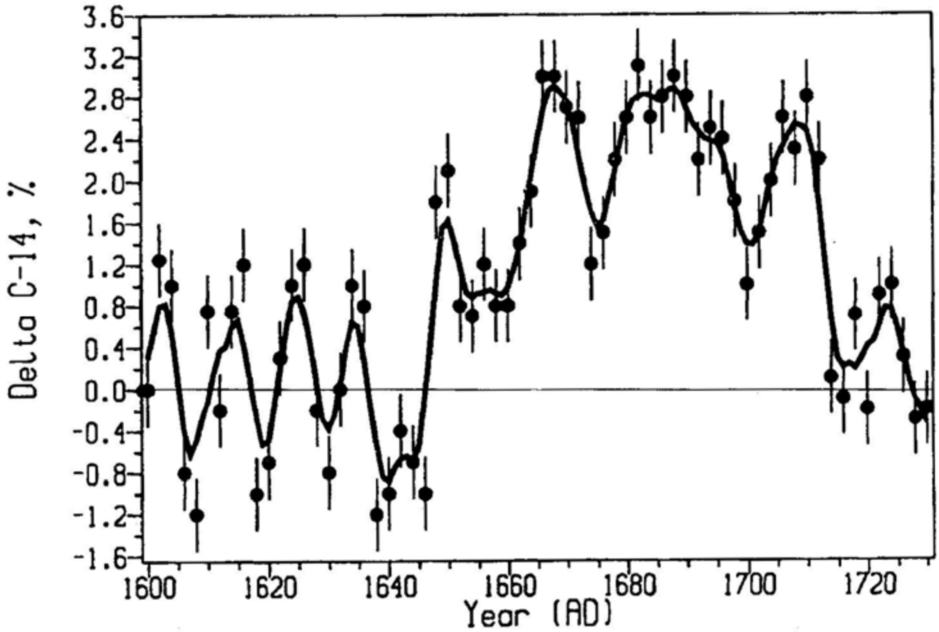

Figure 2. ^{14}C content variations in the bi-annual rings of the pine-trees from South Urals for AD 1600–1730. (By courtesy of Kocharov *et al.* 1995).

solar cycle". This version of a "long solar cycle" is confirmed by the study of the ^{14}C content variations in the bi-annual rings of the pine-trees from South Urals over AD 1600–1730, Kocharov *et al.* (1995) (Fig. 2). In fact, ^{14}C content shows the cycle length to be about 20 yrs in 1640–1715 in accordance with poleward migration rate.

According to Waldmeier (1957), solar activity on a branch of growth of a century cycle dominates in the northern hemisphere, and on a branch of decay in the southern hemisphere. Actually, in 1672–1704 practically no sunspots were observed in the northern hemisphere (Ribes & Nesme-Ribes 1993). At such low activity of the Sun in the northern hemisphere polar magnetic field reversal was possible only in the southern hemisphere. In this epoch the structure of the magnetic field of the Sun was of a "monopole" type, i.e: both poles of the Sun had the same polarity. Such state of solar magnetic field was repeatedly observed in 1955–1982 yrs (Makarov 1984). In 1705 the Wolf number increased and became sufficient for polar magnetic field reversal and hence the structure of a magnetic field was restored.

5. Conclusion

In Maunder Minimum, poleward migration rate of magnetic fields was about 0.7 ms^{-1} and solar cycle length was about 20 yrs. The minimum strength of solar cycle, $W_{\max} \approx 40 + 10$, is required for polar magnetic field reversal. We used these results to show that probably polar magnetic field reversal in Maunder Minimum occurred in the one hemisphere.

Acknowledgements

We thank the LOC of the IAU Colloquium 179 for their financial support and the referee for helpful criticism. This work was partially supported by the RFBR, grants No. 99-02-16200 and 00-02-16355, INTAS, grant No. 98-1088.

References

Beer, J., Tobias, S., Weiss, N. 1998, *Solar Phys.,* **181,** 237.
Duval, T. L., Wilcox, J. M., Svalgaard, L., Scherrer, P., McIntosh, P. S. 1977, *Solar Phys.,* **55,** 63.
Hoyt, D. V., Schatten, K. H. 1998, *Solar Phys.,* **157,** 340.
Jones, H. S. 1955, *Sunspot and Geomagnetic-Storm Data,* (London).
Kocharov, G. E., Ostryakov, V. M., Peristykh, A. N., Vasil'ev, V. A. 1995, *Solar Phys.,* **159,** 381.
Makarov, V. I., Fatianov, M. P. 1980, *Soln. Dann.,* **10,** 96.
Makarov, V. I. 1984, *Solar Phys.,* **93,** 393.
Makarov, V. I., Sivaraman, K. R. 1989, *Solar Phys.,* **119,** 35.
Makarov, V. I. 1994, *Solar Phys.,* **150,** 359.
Makarov, V. I., Makarova, V. V. 1996, *Solar Phys.,* **163,** 267.
Makarov, V. I., Callebaut, D. K. 1999, in *Proc. 9th European Meeting on Solar Physics, "Magnetic Fields and Solar Processes"*, (ed.) A. Wilson, p. 117.
Makarov, V. I., Tlatov, A. G. 1999, in *Proc. 9th European Meeting on Solar Physics, "Magnetic Fields and Solar Processes",* (ed.) A. Wilson, p. 125.
McIntosh, P. S. 1979, "*Annotated Atlas of H-alpha charts*", NOAA.
Nagovitsyn, Yu, A. 1997, *Astronomy Reports,* **23,** 742.
Ribes, J. C., Nesme-Ribes E. 1993, *Astron. Ap.,* **276,** 549.
Waldmeier, M. 1957, Zs. *Astrophys.,* **43,** 29.

J. Astrophys. Astr. (2000) **21**, 197–200

Periodic Variations in the Coronal Green Line Intensity and their Connection with the White-light Coronal Structures

Milan Minarovjech*, Milan Rybanský & Vojtech Rušin, *Astronomical Institute of the Slovak Academy of Sciences, 05960 Tatranská Lomnica, Slovak Republic.*
**e-mail: milanmin@ta3.sk*

Abstract. We present an analysis of short time-scale intensity variations in the coronal green line as obtained with high time resolution observations. The observed data can be divided into two groups. The first one shows periodic intensity variations with a period of 5 min. the second one does not show any significant intensity variations. We studied the relation between regions of coronal intensity oscillations and the shape of white-light coronal structures. We found that the coronal green-line oscillations occur mainly in regions where open white-light coronal structures are located.

Key words. Sun—solar corona—5 min variations—solar activity.

1. Introduction

The heating mechanism of the solar corona is one of the important but unsolved problems in solar physics. It is supposed that this heating is done through certain types of waves (e.g., Ulmschneider 1991). The 5 min. oscillations are one of such candidates. The oscillations have already been observed many times, not only in the emission-line corona but in the white-light corona as well (Tsubaki 1988; Rušin & Minarovjech 1994; Singh 1997). However, regions in the solar corona where these oscillations were observed is not known yet. In this paper we will show a possible connection between 5 min. intensity oscillations of the green-line corona and corresponding structures in the white-light corona (WLC).

2. Observations

Since 1990, observations of the green (530.3 nm) and red (637.4 nm) coronal lines have been made with a photoelectric photometer at the Lomnicky Stit coronal station (Minarovjech & Rybansky 1992). This photoelectrical method is based on spectral flux measurements in the wavelengths where coronal emission lines are located. To subtract scattered light in the spectrum, a nearby continuum is measured simultaneously. Measurements are expressed in absolute coronal units. We note that 'final' coronal intensity is independent neither of the shape nor of the Doppler shift of the emission lines. Measurements of the coronal line intensities are made, mostly, at the height of 55 arcsec above the solar limb. The photometer can provide coronal line intensity measurements with time resolution of 0.04 s. However, an averaging over 2.56 s is usually applied, and at the fixed position angle the measurements are continued for 20–30 min. (the coronagraph is automatically guided). Examples of such measurements are shown in Rušin & Minarovjech (1994). To compare the green-line oscillations and the corresponding WLC structures, data from Manua Loa High Altitude Observatory MARK-III K-coronameter (Mk3) were used.

3. Data processing

We have processed 541 records of the green-line oscillations and corresponding white-light images corona images as measured on the Mk3 K-coronameter. For each record of green-line data, we computed standard deviation and fast Fourier transform (FFT). The results can be separated into three groups. The first one represents quiet records without significant changes in the coronal line intensity. The second one represents records with maximum FFT power in the range of 250–450 s (5 min.). The last one contains all records that did not belong to the former two groups. These data were not taken into an account in the following studies. To obtain corresponding WLC structures, the qualitative Mk3 image data were processed using digital unsharp masking. Resulting shapes of the WLC structures situated in the position angles corresponding to those of green-line oscillations can also be separated into three groups: open, closed, and uncertain, respectively. We note that such a separation is difficult in cycle maxima, where very complicated systems of structures occur both in the WLC and green-line corona. The separation of WLC structures around solar cycle minima is possible with higher precision. Examples of separation are depicted in Fig. 1. The white line represents the patrol measurements of the green-line intensity. The position angles where 5 min. oscillations of the green-line intensity occur are marked with white circles, while regions quiet in oscillatory variations are marked with white squares.

4. Results and short discussion

Of particular interest here is the relation between regions of coronal green-line oscillations and the shape of corresponding WLC structures. The observations of the green-line oscillations were made mostly at the peaks of the green-line intensity. The local intensity maxima in the green-line corona and WLC structures obtained from processed Mk3 measurements are correlated, as was discussed by Minarovjech (2000). The data analysis shows that quiet records of coronal line intensity are found where the closed WLC structures are located. On the other hand, the records of coronal line oscillations are found where the open WLC structures are located. As a next step, an attempt to observe short period oscillations in the green-line intensity has been done. The presented results make possible an explanation in different behaviour of data results as discussed by Tsubaki (1988) in the green corona line intensity. In order to find more exactly the connection between the white-light corona and the green-line oscillations, simultaneous observations of white-light and emission-line coronae are required.

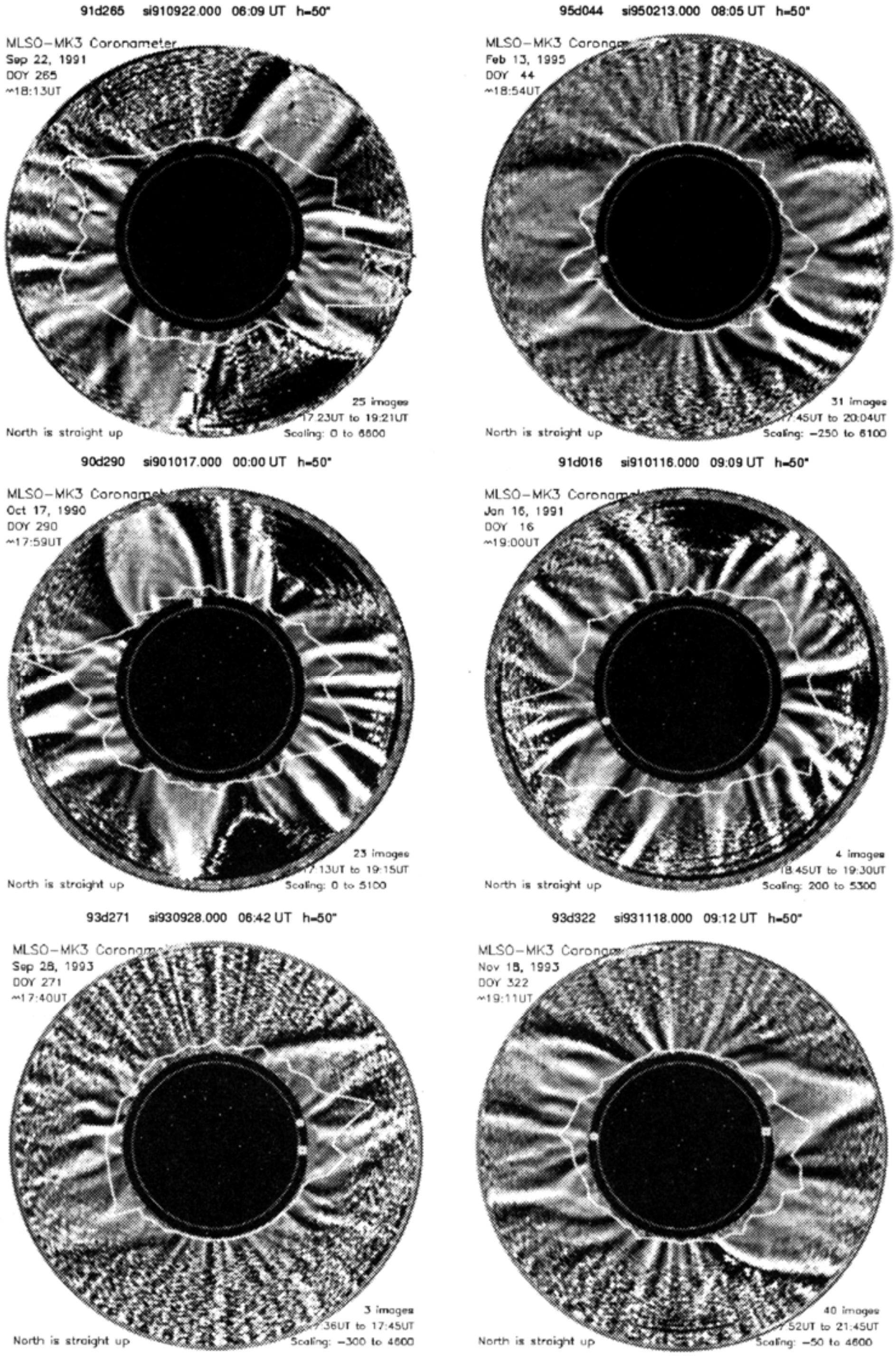

Figure 1. Position angles where the 5 min. oscillations in the green line intensity is observed and is not observed are shown with white circles and squares, respectively. White line polar diagram depict the green line patrol intensity measurement.

Acknowledgments

This work was partly supported by the Grant Agency (5017/98) of the Slovak Academy of Sciences. One of us (M. M.) thanks IAU for travel support. M. M. and V. R. express their deepest thanks to the LOC, headed by Prof. S. Hasan, for providing them pleasant hospitality during their stay in India, realized in the framework of cooperation between SAS and INSA. We wish to thank the unknown referee for his critical comments that improved this paper.

References

Minarovjech, M. 2000, in *The Last Total Solar Eclipse of the Millenium in Turkey,* ASP Conference Series **205,** (ed.) Livingston, W. & Ozguc, A. (Bratislava: Veda) p. 32, in press.

Minarovjech, M., Rybansky, M. 1992, *Solar Phys.,* **139,** 1.

Rušin, V., Minarovjech, M. 1994, in *Solar Coronal Structures, Proceedings of IAU 144 Coll.,* Rušin, V., Heinzel, P. & Vial, J.-C. (Bratislava: Veda).

Singh, J., Cowsik, R., Raveendran, A. V., Bagare, S. P., Saxena, A. K., Sundararaman, K., Vinod Krishan, Nagaraja Naidu, Samson, J. P. A., Gabriel, F. 1997, *Solar Phys.,* **170,** 235.

Tsubaki, T. 1988, in *Proceedings of 9th Sacramento Peak Summer Meeting,* (ed.) Altrock, R. C. (New Mexico: Sacramento Peak Observatory).

Ulmschneider, R., Priest, E. R., Rosner, R.1991, *Mechanism of Chromospheric and Coronal Heating,* (Berlin: Springer Verlag).

J. Astrophys. Astr. (2000) **21**, 201–204

Long-term Cyclic Variations of Prominences, Green and Red Coronae over Solar Cycles

Vojtech Rušin*, Milan Minarovjech & Milan Rybanský *Astronomical institute, Slovak Academy of Sciences, 059 60 Tatranska Lomnicá, Slovak Republic*
** e-mail: vrusin@ta3. sk*

Abstract. Long-term cyclic variations in the distribution of prominences and intensities of green (530.3 nm) and red (637.4 nm) coronal emission lines over solar cycles 18-23 are presented. Polar prominence branches will reach the poles at different epochs in cycle 23: the north branch at the beginning in 2002 and the south branch a year later (2003), respectively. The local maxima of intensities in the green line show both poleward- and equatorward-migrating branches. The poleward branches will reach the poles around cycle maxima like prominences, while the equatorward branches show a duration of 18 years and will end in cycle minima (2007). The red corona shows mostly equatorward branches. The possibility that these branches begin to develop at high latitudes in the preceding cycles cannot be excluded.

Key words. Prominences — emission corona — cycle activity.

1. Introduction

So far a wide variety of phenomena have been used to study solar activity, e.g. sunspots, irradiance in the whole range of the electromagnetic spectrum, coronal mass ejections, and so on (see for example Pap *et al.* 1994). These studies have led to a better understanding of magnetic activity of the Sun as a star, and its influence upon Earth. Individual features of this activity in the outer layers of the solar atmosphere are caused by both small- and large-scale magnetic fields stored at the base of the convection zone. Active regions emerge as a result of occasional disturbances given to this toroidal field by the convection (dynamo mechanism). Prominences and the corona are observed around the entire solar disk. Thus, these phenomena allow us to study magnetic activity not only around the equator and/or mid-heliographic latitudes, but at high latitudes and around the poles as well, and will help improve our knowledge on the origin of solar activity. In this paper we present some results on ‘cyclic’ variations as obtained from prominences and green and red coronal emission lines.

2. Observations

Observations of prominences have been regularly made at the Lomnicky Štít coronal station since 1967. Data on the green-line corona over the period 1939-1996 were taken from the compiled homogeneous coronal data set (e.g. Altrock *et al.* 1997 and references therein). Data for 1997-1999 were taken from Kislovodsk and Lomnický Štít. Coronal red-line intensities were taken from data published in Quarterly Bulletin on Solar Activity and Solar Geophysical Data.

3. Results

1. Prominences clearly show poleward-migrating branches which are separated in cycle minima from the main zone in mid-latitudes, and then shift to the poles, where they decay in cycle maximum. Our results confirm the former results presented by many researches, e.g., Secchi, Waldmeier, d'Azambuja, Makarov and others, e.g. Rušin, Rybanský & Minarovjech (1998). However, the time of arrival of these branches to the poles differs between northern (N) and southern (S) hemispheres. The N-branch comes to the pole about one year earlier than the S-branch, at present. There are two polar branches observed in some cycles, e.g. in cycle 20 in the N-hemisphere and in cycle 22 in the S-hemisphere. Similar cases have occurred in some former cycles as can be seen from filament observations (e.g., Coffey & Hanchett 1998). Comparison of the prominence distribution in the present cycle 23 with former prominence cycle distributions indicates that the north branch will reach the north pole at the beginning of 2002, the south one a year later (2003), respectively. More details about the time-latitude distribution of prominences can be found in Minarovjech, Rybanský and Rušin (1998).

2. The local maxima in latitude distribution of the green line intensity show also poleward and equatorward branches (Fig. 1). Sequences of their development are as follows: The main equatorial branch begins to develop approximately 2-3 years after the previous minimum, in latitudes of 50-60 degrees, separating from the principal zone of the previous cycle. Then, these increased intensities move to the heliographic latitudes of 70 degrees, and turn off (around cycle maxima) to move to the equator,

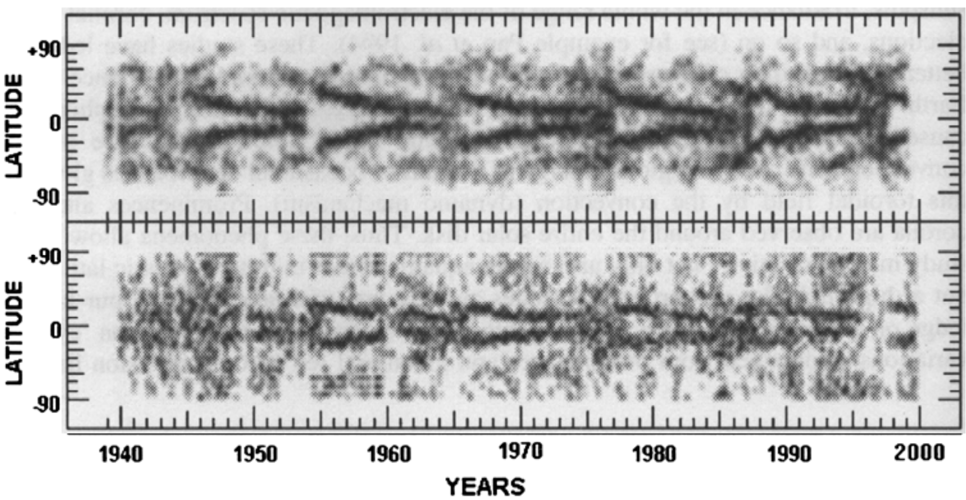

Figure 1. Time-latitude diagrams of local maxima of the green- (top) and red- (bottom) line intensities, respectively, indicating how solar cycles overlap for several years.

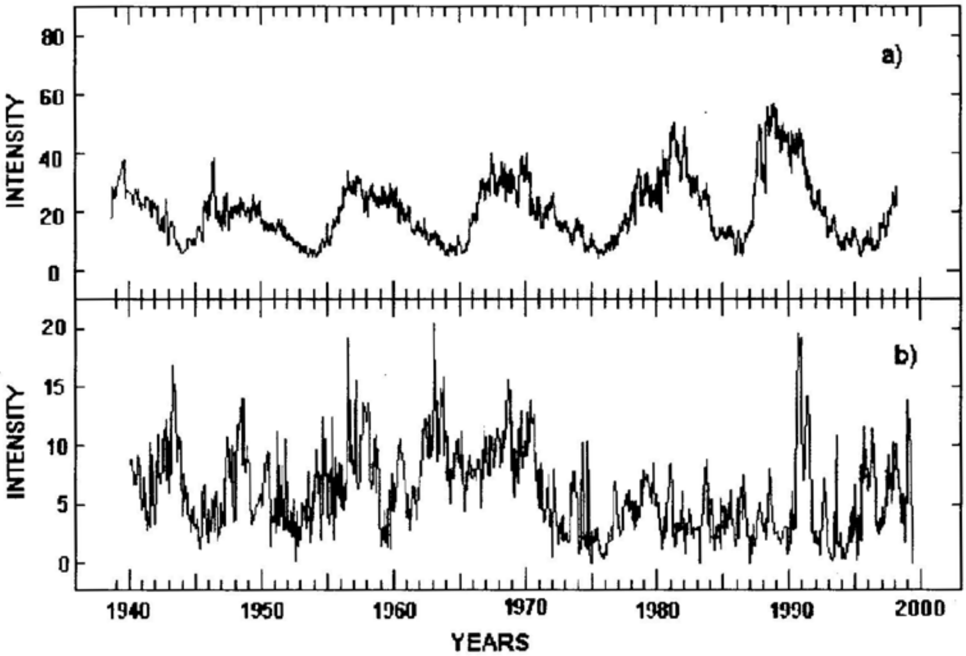

Figure 2. Changes in solar activity over monthly scales, as evident in the green (top) and red (bottom) coronae for the entire Sun.

where they end (decay) in the following minimum in latitudes around 5-10 degrees. The whole process takes 17-18 years. The poleward-migrating branches reach the poles around cycle maximum, and decay when the polar magnetic field reversal occurs. These branches are separated in cycle minimum just 2-3 years prior to the beginning of the next principal equatorward-migrating branch. The poleward-migrating branches of the green-line corona are better seen when only one poleward migration branch occurs in prominences.

3. Distribution of the red line (637.4 nm) intensities shows only the principal equatorward-migrating branches (Fig. 1). They begin clearly to develop around cycle minima at heliographic latitudes of 20-25 degrees (their maxima are 5 degrees closer to the equator than those of the green-line corona), and end in the next minimum. Nevertheless, one may recognize, in some cycles, outlines of high-latitude branches that migrate to the mid-latitude principal branches.

4. The long-term behavior of the green-line corona (Fig. 2) indicates that the peak amplitudes increased over the period of 1939-1998 by a factor of 2. We did not see double or multiple maxima in cycle 20 as discussed by Sýkora (1992). The changes in intensity over scales of months are complicated due to the quasí-biennial periodicity during the '11-year' cycles (e.g. Rusin & Zverko 1990). The peaks of the green-líne emission mostly coincide with the sunspot numbers, even though a shift of two years was observed in cycles 20 and 21. We did not confirm the existence of two red-line peaks, in sunspot maximum and minimum, as discussed by Waldmeier (1971) in cycle 21. The peak of the red-line intensity is only one, nearly coincident with that of the green-line corona. Nevertheless, increased intensities were observed around cycle minima (Rušin, Rybanský & Minarovjech 1998), and the changes of the red-line

intensities are much more complicated than for the green-line corona. Even though ’chaotic’ changes in the red-line corona are seen in data of monthly averages, the existence of low-latitude branches confirm a long-term development that is similar to the green-line corona.

4. Conclusion

We have presented here distributions of prominences, and green and red coronal intensities over the period of 1939 (1967)-1999. All observed phenomena confirmed cycle variations, even though with a very complicated manner, and sometimes are confused. This stresses the necessity of coordination in both ground-based and space solar observations.

Acknowledgements

This work was partially supported by the Grant Agency (5017/98) of the Slovak Academy of Sciences. Attendance in the meeting was realized thanks to the Indian-Slovak co-operation (SAS and INSA). One of us (M.M.) would like to thank IAU for the travel support.

References

Altrock, R. C. 1997, *Solar Physics,* **170**, 411.

Coffey, H. C., Hanchett, C. D. 1998, In *Synoptic Solar Physics,* ASP Conference Series, Vol. 140, (eds.) K. S. Balasubramaniam, J. W. Harvey and D. M. Rabin, 447.

Minarovjech, M., Rybanský, M., Rušin, V. 1998, In *New Perspectives on Solar Prominences,* ASP Conference Series, (San Francisco), (eds.) D. Webb, D. Rust and B. Schmieder, 484.

Pap, J. M., Frohlich, C, Hudson, H. S., Solanki, S. K. 1994, *The Sun as α Variable Star* (Cambridge University Press).

Rušin, V., Zverko, M. 1990 *Solar Phys.* **128,** 261.

Rušin, V., Rybanský, M., Minarovjech, M. 1998, In *Synoptic Solar Physics,* ASP Conference Series 140, (eds.) K. S. Balasubramaniam, J. W. Harvey and D. M. Rabin, 353.

Sýkora, J. 1992, *Contr. Astron. Obs. Skalnaté Pleso* 22, 55.

Waldmeier, M. 1957, *Die Sonnenkorona,* Vol II., Birkhauser, Basel.

J. Astrophys. Astr. (2000) **21**, 205–208

Large-scale Motion of Solar Filaments

Pavel Ambrož, *Astronomical Institute of the Acad. Sci. of the Czech Republic, CZ-25165 Ondrejov, The Czech Republic.*
e-mail: pambroz@asu.cas.cz

Alfred Schroll, *Kanzelhöehe Solar Observatory of the University of Graz, A-9521 Treffen, Austria.*
e-mail: pambroz@asu.cas.cz

Abstract. Precise measurements of heliographic position of solar filaments were used for determination of the proper motion of solar filaments on the time-scale of days. The filaments have a tendency to make a shaking or waving of the external structure and to make a general movement of whole filament body, coinciding with the transport of the magnetic flux in the photosphere. The velocity scatter of individual measured points is about one order higher than the accuracy of measurements.

Key words. Sun—filaments—horizontal motions.

1. Introduction

The aim of our study was focused on the feasibility of obtaining detailed information about the horizontal displacement of filaments in solar atmosphere. According to the papers of Glackin (1974), Adams & Tang (1977), Brajša *et al.* (1991) and Japaridze & Gigolashvili (1992), there exists a large scatter of the zonal averages of zonal displacements. Another conclusion is that the rotation rate, derived for the solar filaments (Van Tend & Zwaan 1976), differs from rotation rate of solar photosphere. Both conclusions can be understood in terms of the radial dependence of solar rotation rate.

Filaments are vertically structured phenomena, projected on the solar disc. Although the outer structure of filaments appear to vary in time, long-lived reference points are absent. The 'seeing' dependent contrast of the H_α pictures is the source of uncertainties during the measurements on the contour and the feet of filaments. On the other hand, all filaments are located above the neutral line of largescale background magnetic fields. This shows that the position of the filament is above all determined by the distribution of magnetic field in the solar photosphere.

2. Results of measurements and conclusions

Heliographic position of the filaments is measured on the full disc H_α pictures taken at the Kanzelhöhe solar observatory (KHSO) during the regular patrol program. Our measuring procedure is based on the method of multiple measurements of contour points around the filament during the whole observing day. The initial data set contain about 170 thousand position measurements. The possible errors due to the projection (Roša *et al.* 1998) of the vertical structure on the sphere are much lower than the adopted error limit 100 ms^{-1}. Conversion to the heliographic co-ordinates was made according to the standard procedure, developed at KHSO. Each final velocity value is the best fit from zonal velocities, derived from more than 20 (maximum is 144) measurements per day. The most accurate values are determined with an error 20ms^{-1}.

The filament velocities are relative to Carrington reference system time dependent from day to day. Sometimes, the obtained velocities have a different magnitude on opposite sides of the filament and they change also in orientation in some cases. The different parts of the filament move with different velocity. Filaments make the shaking (oscillations) perpendicular to the filament axis or wave-like movement in direction of the filament axis on the time scale of one day. The average velocity of all points characterizes a general displacement of the whole filament body.

The latitude dependence of the zonal velocities of the filaments is presented in Fig. 1. The scatter plot of the zonal velocity values is combined with the set of fitted curves of the rotation laws, derived by different authors. The scatter of the curves is lower than 200 ms^{-1} and the scatter of the individual velocity values is nearly 800 ms^{-1}, although the internal accuracy of the measured points on the filament edge is only 100 ms^{-1}. From such differences, one can conclude that the possible axially symmetric flow is combined with the much more spatially variable velocity field, dependent on the latitude and longitude position on the solar surface. The great scatter of the individual velocity values is probably caused by small-scale displacements, related to the random walk of small-scale magnetic elements in solar photosphere.

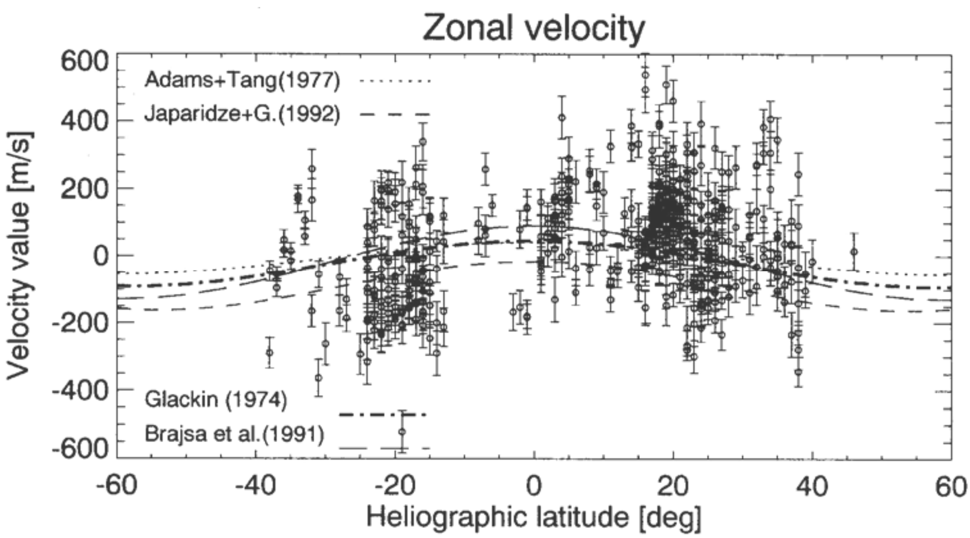

Figure 1. Latitude distribution of measured zonal and meridional velocities. Each measured value is drawn with the corresponding error bar. Only the measurements with errors lower than 100 ms^{-1} are used. The plot of the axially symmetric rotation rate curves, derived according to the different authors, demonstrate the presence of the non-axially symmetric component of the velocity field, oriented zonal or meridional.

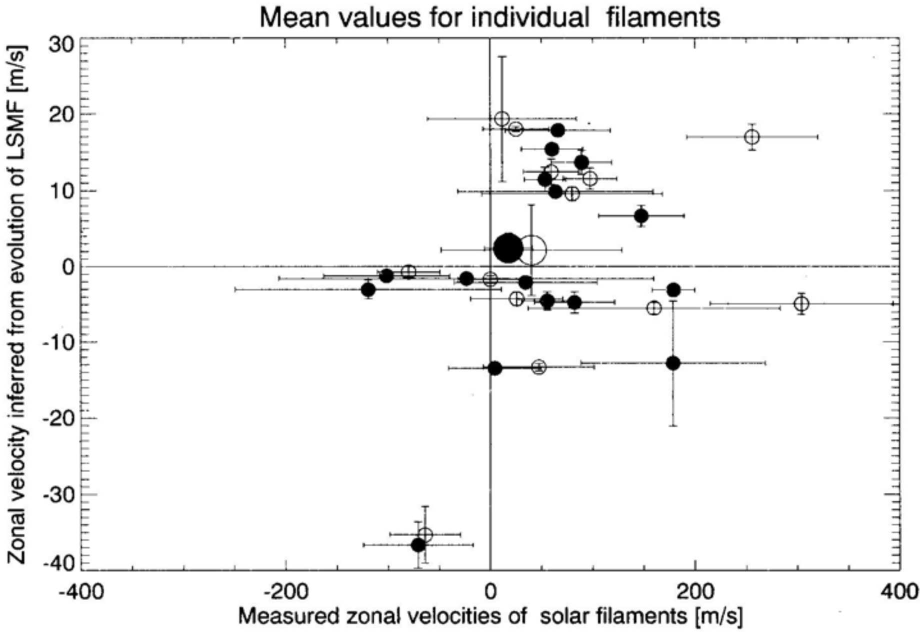

Figure 2. The scatter plot of the corresponding mean values of zonal velocities, as derived from filament displacements and from evolution of the large-scale magnetic field. The full and empty circles are related with the left and right contour of the filament, respectively. The pair of large circles show the position of the total averages of all measurements.

The plotted velocities relate with fine parts of the filaments, and do not characterise the filaments as whole.

Corresponding values of the zonal velocity field in the photosphere can be also derived from the temporal evolution of large-scale magnetic field. The magnetic data from Wilcox Solar Observatory of Stanford University were transformed into series of spherical harmonic functions with maximal principal index $l = 12$. Only the large scale long-lived structures were used. The velocity structure, responsible for the time evolution of large scale magnetic flux was inferred (Ambrož 1993, 2000) with help of the "Local correlation tracking" method (November, 1986) applied on the pair of consecutive magnetic synoptic charts.

Two arrays of corresponding velocities are plotted in Fig. 2. A substantial number of the plotted points is located mainly in the first and also in the third quadrant. It supports our assumption about the large-scale magnetic field displacement due to the large-scale velocity flow: Proper motions of filaments relate proportionally with a displacement of the magnetic inversion line. Except three points with extremely great errors, the error bars of other points penetrate into the third quadrant. Only one point cannot be explained by relationship with the large-scale velocity transport.

The use of filaments as "tracers" for detection of large-scale velocities is possible if the accuracy is better than 100 ms^{-1}. On the chart of horizontal velocities, inferred from the displacement of the magnetic flux, the filaments do not coincide with regions of the velocity extremes and are located in regions with high velocity gradient (zonal or meridional).

Acknowledgements

The present research was partially granted by the Austrian Academy of Sciences under agreement with the Academy of Sciences of the Czech Republic. Wilcox Solar Observatory data used in this study was with courtesy of J.T. Hoeksema. The Wilcox Solar Observatory is supported by NASA, NSF, and ONR. Present work was made under support of grant of GA/AVCR No. A3003806 and the Key Project AVCR No. Kl-003-601.

References

Adams, W. M., Tang, F. 1977, *Solar Phys.,* 55, 499

Ambrož, P. 1993, in *The Magnetic and Velocity Fields of Solar Active Regions,* ASP Conf. Ser. Vol. **46**, (eds.) H. Zirin, G. Ai; H. Wang, p. 495.

Ambrož P. 2000, *Solar Phys.,* in press.

Brajsa, R., Vršnak, B., Ruždjak, V., Schroll, A., Pohjolainen, S., Urpo, S., Terasranta, H. 1991, *Solar Phys.,* 133, 195.

Glackin, D. L. 1974, *Solar Phys.,* 36, 51.

Japaridze, D. R., Gigolashvili, M. Sh. 1992, *Solar Phys.,* 141, 267.

November, L. 1986, *Appl. Optics,* 25, 391.

Van Tend, W., Zwaan, C. 1976, in *Basic Mechanism of Solar Activity,* IAU Symposium No. 71, (eds.) V. Bumba, J. Kleczek, p. 45.

Roša, D., Vršnak, B., Božic, H., Brajša, R., Ruždjak, V. , Schroll, A., Wöhl, H. 1998, *Solar Phys.,* 179, 237.

J. Astrophys. Astr. (2000) 21, 209–212

The Magnetic Sun from Different Views: A Comparison of the Mean and Background Magnetic Field Observations made in Different Observatories and in Different Spectral Lines

M. L. Demidov, *Institute of Solar-Terrestrial Physics, Irkutsk, P.O. Box 4026, 664033, Russia.*
email: demid@iszf.irk.ru

Abstract. A comparison is made of observational data on the mean magnetic field of the Sun from several observatories (a selection of published information and new measurements). Results of correlation and regression analyses of observations of background magnetic fields at the STOP telescope of the Sayan solar observatory in different spectral lines are also presented. Results obtained furnish an opportunity to obtain more unbiased information about largescale magnetic fields of the Sun and, in particular, about manifestations of strong (kilogauss) magnetic fields in them.

Key words. Sun: magnetic fields—magnetographs.

1. Introduction

The statement that reliable information on largescale magnetic fields (LSMF) of the Sun (i.e. the background field (BMF), and the mean magnetic field (SMMF)) is of the utmost importance in the study of many problems in solar and solar-terrestrial physics, is beyond question at present. One of the unassailable reliability criteria of experimental data has always been the reproducibility of these results with different instruments. Therefore, the need for such a comparison of solar data appears also quite explicable. For this purpose, this paper analyzes SMMF observations from different observatories using earlier published data (but collected together), as well as invoking the new observations obtained at the STOP telescope of the Sayan solar observatory (SSO).

A substantial drawback to the present situation of investigations of the solar LSMF is the fact that they are based on observations virtually in only one line-FeI λ 525.0 nm. It has been demonstrated in a large number of publications that it is fruitful to compare high resolution magnetic fields measurements made in different spectral lines. As far as the LSMF are concerned, such investigations were initiated by Demidov (1998). Results of BMF observations in the new lines are presented in following sections.

2. Comparison of the solar mean magnetic field observations

SMMF observations that were initiated over 30 years ago are of significant scientific value for a variety of reasons and in particular for investigations of long-term

Table 1. Comparison of SMMF observations from different observatories: CAO – Crimean astrophysical observatory, MWO – Mt.Wilsonobservatory, WSO – Wilcox solar observatory, SSO – Sayan solar observatory. R – correlation coefficient, N – number of points.

Reference	Observatories being compared and coefficients of difference	R	N	Time interval
Scherrer 1973	CAO/MWO = 0.76			1968–1972
Scherrer *et al.* 1977	CAO/MWO = 0.8	0.4	464	1971–1974
Kotov &	CAO/MWO = 1.22			1968–1976
Severny 1983	MWO/WSO = 1.76			1975–1976
	CAO/WSO = 2.04			1975–1976
Grigoryev & Demidov 1987	SSO/WSO = 1.51	0.88	228	1980–1982
Kotov *et al.* 1998a	CAO/WSO = 1.25	0.95	26	1991
Kotov *et al.* 1998b	CAO/WSO = 1.2	0.86	732	1991–1993
	SSO/WSO = 0.89	0.85	93	1994
Kotov *et al.* 1998c	WSO/CAO = 0.43			1973–1976
	WSO/MWO = 0.59			1975–1982

variations in global magnetism and solar rotation. Since SMMF observations are carried out at several observatories, it is natural to question the degree of quantitative correspondence of different observational series. Some relevant information from different publications is presented in Table 1. It turns out that the degree of correlation of the series and the amount of their systematic difference depend on the particular combination of the series being compared and also change with the time. There can be several reasons for the existence of such systematic differences: calibration, instrumental weighting functions, methods of zero level monitoring, etc. Also, one of the serious reasons is most probably the difference of parameters of photometers in magnetographs at different observatories and, as a consequence, a different character of signal attenuation in strong fields. Such an explanation is supported by, for example, the following fact. According to Table 1, the coefficient of difference of the SMMF observations at SSO and WSO during 1982–1984 was: Hsso/Hwso = 1.51. A comparison of the data from these observatories for 1993–1997 gives the following relationship (number of points N = 487, R = 0.71):

$$H_{\mathrm{WSO}} = -5.4(\pm 1.4) + 0.91(\pm 0.03) \times H_{\mathrm{SSO}}, \tag{1}$$

showing that the degree of correspondence of the observational series has improved considerably. The most probable reason for a change in the character of correspondence of the data from the two observatories implies that in 1991 in the course of a STOP upgrade the photometer parameters were modified significantly: the mean distance of the slits from the line center became 4.2 pm instead of 8.2 pm (it will be recalled that at WSO and at Mt. Wilson this value is 4.4 pm, and at Crimea it is 6.2 pm). As a consequence, the SSO measurements has become more sensitive to the saturation effects in the strong magnetic fields. But more convincing evidence for the manifestation of strong fields in the LSMF observations follows from an analysis of the SMMF and BMF observations in different spectral lines.

Table 2. Results of correlation and regression analyses of the BMF observations in different combination of spectral lines. The parameters of the linear regression equation $H_{\text{lineY}} = A(\pm\Delta A) + B(\pm\Delta B) \times H_{\text{line}}\text{X}$ were calculated using the method of reduced major axis.

Line Y	Line X	N	A	ΔA	B	ΔB	R
525.0	513.7	365	37	27	0.38	0.01	0.87
524.7	513.7	249	44	37	0.46	0.02	0.77
525.0	525.1	635	−6	23	0.58	0.01	0.86
524.7	525.1	522	−5	14	0.65	0.01	0.95
525.0	524.7	4506	1	2	0.83	0.005	0.89

3. BMF observations in different lines, and their analysis

Observations of the background magnetic fields at STOP are carried out with an angular resolution of (usually) 120 seconds of are, with the time difference between magnetogram recordings in different lines of about 1.5^h. A special investigation of the influence of such a time difference on the results has shown that it can be considered negligible. The lines used in the observations are: λ 513.7 nm Nil (Lande factor g = 1), λ 524.7 nm Fel (g = 2), λ 525.02 nm Fel (g = 3), and λ 525.06 nm Fel (g = 1.5). The mean position of the photometer slits relative to the line centre was 4.2pm in all cases.

Results of correlation and regression analyses of the BMF observations in different combinations of spectral lines are summarized in Table 2. It is evident from the data in this table that the BMF observations in different lines are correlated very well with each other, but they differ greatly in amplitude of the measured strengths. If it is assumed (Ulrich 1992) that the effects that distort the magnetograph signal have no (or only a minor) influence on the observations in lines with a small Lande factor, for example, in our case in the line λ 513.7 nm Nil with g = 1 , then one has to recognize that measurements in the most frequently used line λ 525.02 nm Fel give strengths underestimated by a factor of 3, not by a factor of 1.8 as believed previously. It will be recalled here that according to (Ulrich 1992) and (Wang & Sheeley 1988) this factor even might be 4. It is worthwhile to note, however, that the lines λ513.7 nm Nil and λ525.02nm Fel, as well as the lines λ523.3 nm Fel and λ525.02nm Fel, used by Ulrich (1992), are not magnetic ratio lines (as a wellknown pair of lines λ 524.7 nm Fel and λ 525.02 nm Fel).

Acknowledgement

I'm very grateful to the local IAU Colloquium 179 Organizing Committee and to the RFBR for partial financial support, which allowed me to attend this interesting conference.

References

Demidov, M. L. 1998, in *Synoptic Solar Physics, ASP Conference Series,* **140**, (eds.) K. S. Balasubramaniam *et al,* 171.

Grigoryev, V. M., Demidov, M. L. 1987, *Solar Phys.,* **114,** 147.

Kotov, V. A., Severny, A. B. 1983, *The Mean Magnetic Field of the Sun as a Star: Catalogue 1968–1976,* materials of the World data Center B, (Moscow).

Kotov, V. A., Demidov, M. L., Haneychuk, V. I., Tsap, Y. T. 1998a, *lzv. Krymsk. Astrofiz. Obs.,* **94,** 110.

Kotov, V. A., Demidov, M. L., Haneychuk, V. I., Grigoryev, V. M., Tsap, Y. T. 1998b, *lzv. Krymsk. Astrofiz. Obs.,* **94,** 118.

Kotov, V. A., Scherrer, P. H., Howard, R. F., Haneychuk, V. I. 1998c, *Astrophys. J. Suppl. Ser.,* **116,** 103.

Scherrer, P. H. 1973, *Ph.D. Dissertation,* Stanford University, SUIPR Rep., 554.

Scherrer, P. H., Wilcox, J. M., Kotov, V. A. Severny, A. B., Howard, R. 1977, *Solar Physics,* **52,**3.

Ulrich, R. K., 1992, in *Seventh Cambridge Workshop on Cool Stars, Stellar Systems, and the Sun,* ASP Conference Series, **26,** (eds.) Giampapa & J. A. Bookbinder, 38.

Wang, J. M., Sheeley, N. R. 1988, *J. Geophys. Res.,* **93(A10)**, 11.227.

J. Astrophys. Astr. (2000) **21,** 213–220

Vector Magnetic Fields, Subsurface Stresses and Evolution of Magnetic Helicity

Richard Canfield* & Alexei Pevtsov, *Department of Physics, Montana State University, Bozeman, Montana 59717–3840.*
**email: canfield@physics.montana. Edu*

Abstract. Observations of the strength and spatial distribution of vector magnetic fields in active regions have revealed several fundamental properties of the twist of their magnetic fields. First, the handedness of this twist obeys a hemispheric rule: left-handed in the northern hemisphere, right-handed in the southern. Second, the rule is weak; active regions often disobey it. It is statistically valid only in a large ensemble. Third, the rule itself, and the amplitude of the scatter about the rule, are quantitatively consistent with twisting of fields by turbulence as flux tubes buoy up through the convection zone. Fourth, there is considerable spatial variation of twist within active regions. However, relaxation to a linear force-free state, which has been documented amply in laboratory plasmas, is not observed.

Key words. Magnetic fields—currents—magnetic helicity.

1. Introduction

The magnetic fields of the Sun and stars are believed to be produced by dynamos, whose physical nature is one of the most interesting topics of modern solar and stellar research. The last two decades have seen dramatic advances in our knowledge of how such dynamos work. It is now widely believed that the solar dynamo is located at the radial shear zone revealed by helioseismology near the base of the convection zone. Magnetic flux generated there is buoyant and rises through the convection zone as Ω-loops, whose ends are anchored in the convectively stable core. Great progress has been made in understanding flux emergence processes (e.g., Spruit 1981, Chou & Fisher 1989; D'Silva & Choudhuri 1993; Fan, Fisher & McClymont 1994; Caligari, MorenoInsertis & Schüssler 1995). Observational data have been matched accurately by nonlinear models of thin magnetic flux tubes rising buoyantly to the solar surface (D'Silva & Choudhuri 1993, Fan, Fisher & McClymont 1994). These models, and their comparison to observed active region data, provide the most compelling evidence that flux does indeed originate beneath the convection zone. Many observed attributes of solar activity may ultimately be understood in terms of either dynamo processes or flux transport processes, or both.

2. Measures of helicity

Before proceeding further, it is appropriate to formally define various quantities relevant to magnetic helicity, including those that can be measured. Consider a magnetic field $B(x) = \nabla \times A(x)$ in a domain D on whose surface $n \cdot B = 0$. The magnetic helicity H of this flux system is then $H = \int_D A \cdot B \, dV$. Consider a thin tube T with local $B(r,\theta,z)$ defined by its axial component $B_a = (0,0,B_z(r))$ and meridional component $B_m = (0, B_\theta(r),0)$. Moffatt & Ricca (1992) showed that the total magnetic helicity H is given by $H= \int_T A_a \cdot B_a \, dV + 2 \int_T A_m \cdot B_m \, dV$. The axial term gives the *writhe* contribution $W = \int_T A_a \cdot B_a \, dV$, and the meridional term gives the *twist* contribution $T = 2\int_T A_m \cdot B_m \, dV$, where $B_a = \nabla\times A_a$ and $B_m = \nabla\times A_m$. Twist and writhe are illustrated in Fig. 1.

We *cannot* observe a full flux system D of an active region, since it extends below the visible surface, so we cannot observationally determine H W, or T. We *can* measure local values of quantities that contribute to the integrand $A \cdot B$. Using vector magnetograms, we determine the photospheric vertical current density j_z over a horizontal area S: $j_z= (\mu_0 S)^{-1} \int B \cdot d\ell = \mu_o^{-1} (\nabla\times B)_z$. For a force-free field $(\nabla \times B)_z = (\alpha B)_z = \mu_0 j_z$. For a linear (constant–α) force-free field $A \cdot B = \alpha^{-1} B^2$. We use the force-free field parameter α to describe our data, since it can be derived

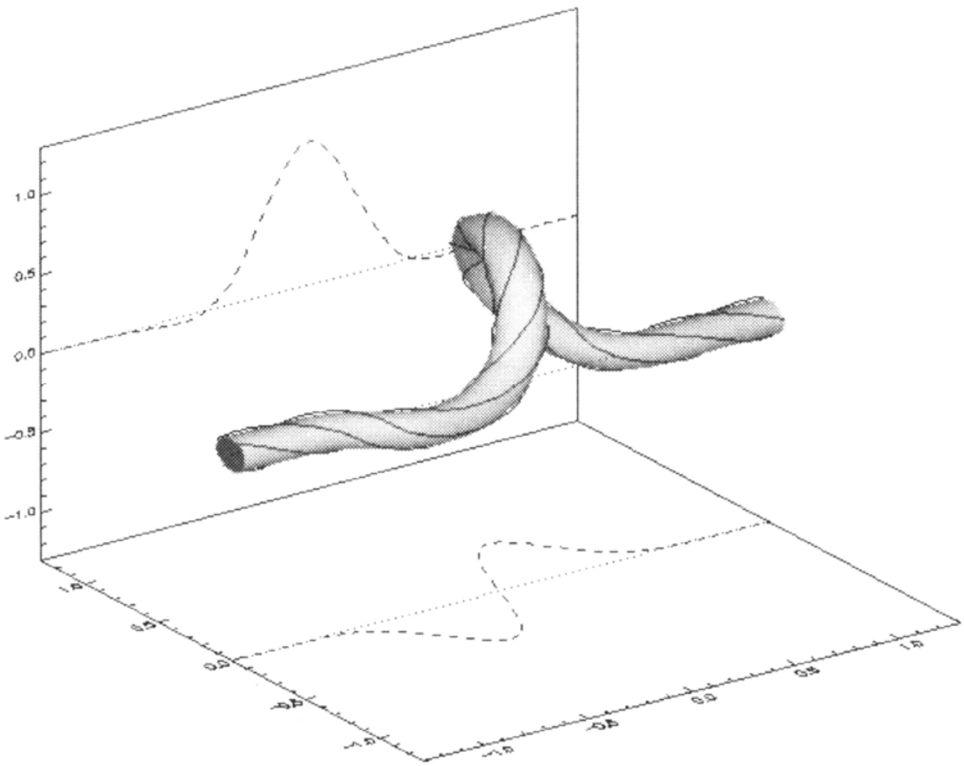

Figure 1. A section of a flux tube with local contributions to twist (right-handed) and writhe (left-handed), defined in section 2.

from observations whether B is force free or not, and it is a local measure of the integrand of *H* if B is force-free, as in the Sun's corona.

The magnetic vector potential A(x) cannot be derived from photospheric vector magnetograms, but both the current helicity ($h_c \equiv B \cdot \nabla \times B$) and the parameter α can be. The quantities *H*, h_c, and α are related: for a force-free model, for example, *H*, and h_c are proportional to the magnetic energy density and α . The sign of α is a measure of the handedness (chirality) of the field; $\alpha>0$ for right-handed fields. The nonlocal quantity *H* is conserved in ideal MHD, and nearly so in circumstances relevant to the Sun, when a suitably defined relative helicity is used (Berger 1999). On the other hand, the local quantity h_c is not conserved. It is important to recognize that although h_c is not conserved, it is observed, and can be related to the physics of the convection zone and the dynamo through modeling.

3. Vector magnetic fields and subsurface stresses

Pevtsov, Canfield & Metcalf (PCM, 1995), introduced α_{best} as a quantitative measure of the magnetic field line twist at the photospheric level. This least-squares best-fit value quantifies the amount of twist in the active region as a whole. Independent evidence (Leka *et al.* 1996) suggests that the photospheric twist is a characteristic of the field *prior* to its emergence.

A data set has been compiled of α_{best} measured for 203 different active regions over the period 1991–1995 (Longcope, Fisher & Pevtsov (1998), see Fig. 2). Many of the active regions were observed repeatedly, each observation providing an independent measurement of α_{best}. This offers an estimate of the error in the measured value. Fig. 2 shows point-to-point scatter much greater than the error bars. There is, however, a tendency for α_{best} to vary with latitude; this tendency is statistically significant. The unique strength of these data is their quantitative basis.

Until recently, models of the rise of flux tubes through the convection zone assumed the magnetic field within the tube to be *untwisted,* contrary to this observational evidence. Longcope & Klapper (1997) formulated a model for the dynamics of a twisted thin flux tube. These equations provide the basic theoretical tool necessary to understand the introduction of twist during flux tube rise.

The first application of the Longcope-Klapper equations to a rising magnetic flux tube have yielded a very promising comparison to the PCM dataset (Longcope *et al.* 1998). During its rise the axis of the flux tube is distorted into a sinuous shape by turbulent convective flows. The turbulence is influenced by the Coriolis force, which endows it with kinetic helicity. As a result, the sinuous distortions to the rising flux tube have a slightly helical nature, contributing writhe. The Longcope-Klapper equations describe how these helical (writhing) distortions twist the magnetic field within the tube; they term this coupling between writhe and twist the Σ-*effect.*

The sense of twist within the flux tube is *opposite* to the sense of the helical distortions to the axis. The internal twist therefore has the same handedness as the turbulence. This is opposite to the sign of the well-known α-effect of Parker (1955) and Steenbeck & Krause (1966). Monte Carlo simulations of the Σ-effect compare remarkably well to the data (Fig. 2). There is a statistical trend with the correct sign and latitudinal dependence (solid line). On top of this trend there is substantial statistical scatter (dashed lines) in good quantitative agreement with observations.

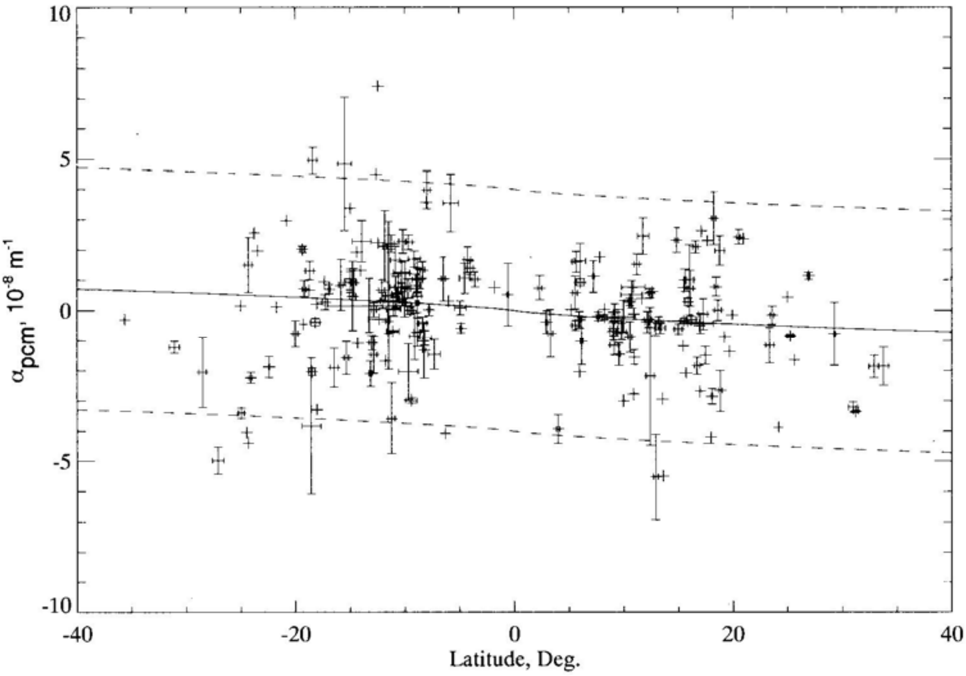

Figure 2. A measure of overall twist (α_{best}) of 203 active regions. Error bars reflect the variation in α_{best} from independent measurements of the Same active region. The mean twist predicted by a Σ-effect model is shown (solid), as well as its standard deviation (dashed), for a flux tube of $\Phi = 10^{22}$ Mx (see section 3).

The success of this simple model is striking, and its implications must be considered. Gilman & Charbonneau (1999) have shown that the creation of twist at the core-convection zone interface produces a variety of "butterfly diagrams" such as those in Fig. 3. The noteworthy aspect of these calculations is that they allow observations of the current helicity to be used to discriminate between dynamo models. However, we must ask—does the convection zone impose such a strong imprint on the current helicity of photospheric magnetic fields that it drowns out any signature of the dynamo? Longcope *et al.* (1999) argue that the amplitude of the twist generated in the dynamo region will be much less than that produced by convection zone turbulence through the Σ-effect. It remains to be seen whether any twist signature of dynamo processes at the base of the convection zone can be detected at the photosphere.

4. Evolution of magnetic helicity inside active regions

Considerable spatial variation of the current helicity is found in both solar and laboratory plasmas, and it is interesting to contrast what is known on the Sun to what has been learned from laboratory research. Studies of relaxation phenomena in laboratory plasmas show that such plasmas relax toward a minimum energy state, while keeping their relative magnetic helicity roughly constant, as originally proposed by Taylor (1974, 1986). During this evolution magnetic reconnection takes place and

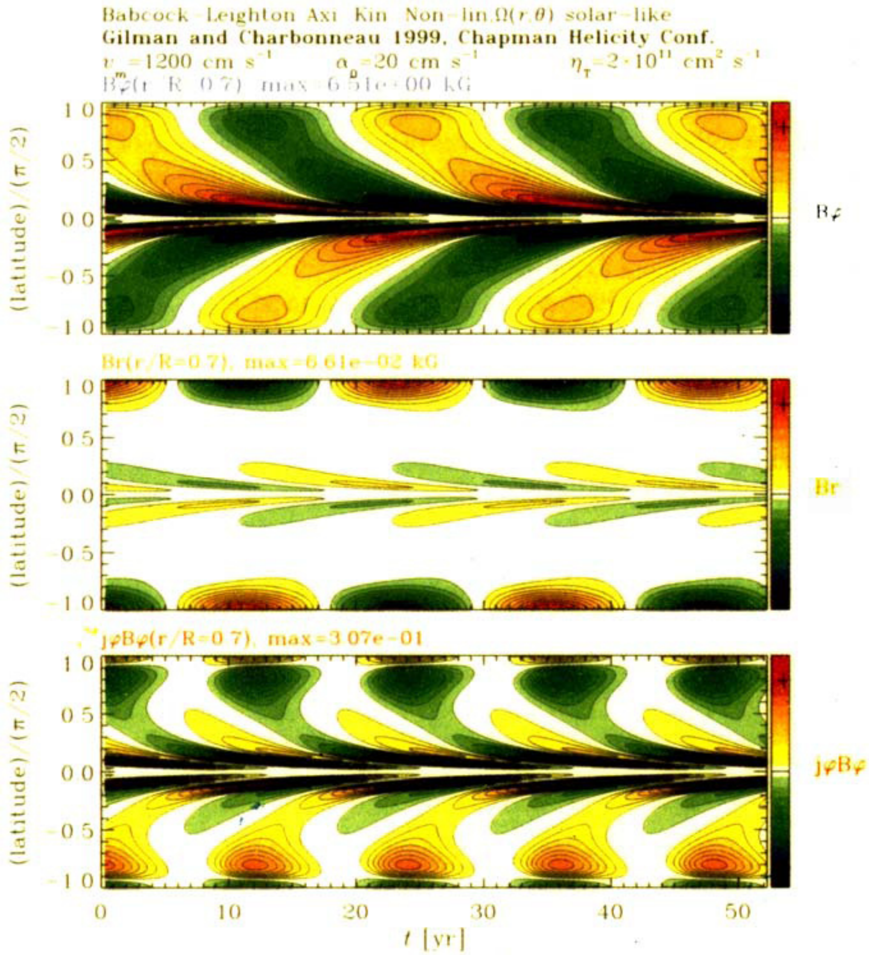

Figure 3. Butterfly diagram for the toroidal field, the radial field, and the current helicity at the interface between the core and the convection zone. Results of a model of Gilman & Charbonneau (1999), by permission.

energy is released, but magnetic helicity is much better conserved than energy (Yamada 1999).

It is well known that electric currents are nonuniform within active regions and sunspots, where they can be measured with vector magnetographs (e.g., Gary *et al.*1987). Pevtsov, Canfield & Metcalf (1994) used $\alpha_z = (\nabla \times B)_z/B_z$, as a measure of the vertical current helicity h_{cz}. They found that patches of both signs of h_{cz} are typically present inside active regions. Although these pattern evolve, individual patches can be identified for up to 4 days. Such patterns of h_{cz} were confirmed by Abramenko & Yurchishin (1996) and Wang (1999).

Though it is not understood in detail, it is plausible that local current helicity patterns will form as flux bundles rise through the convection zone. Numerical simulations imply that structures of a given size, but opposite kinetic helicity, will form as a single magnetic flux tube bifurcates due to drag forces (Longcope, Fisher & Arendt 1996).

Bogdan (1984) found that flux tubes of the same sense of twist will merge if their relative velocities are slow enough to allow their magnetic fields to reconnect. Zweibel & Rhoads (1995) estimated an upper limit to the critical velocity and concluded that colliding twisted flux tubes may coalesce at the base of the convection zone, but not in the photosphere. In their estimate, however, they used the convective velocity for this estimate, an obvious overestimate. One might speculate that in many cases, particularly in strong field regions such as sunspots, different conclusions might result from a more exact treatment.

Pevtsov & Canfield (1999) described the evolution of the α_z-pattern late in the decay of a sunspot. Fig. 4 shows values of the cross-correlation coefficient for successive α_z-patterns inside this sunspot. The characteristic decay time of the pattern was found to be $\tau \sim 47$ hours. However, despite the presence of short term evolution, the data show no convincing indication of relaxation of the pattern towards larger spatial scales or smaller values of α_z, as we would expect from energy release and Taylor relaxation. Using Haleakala Stokes Polarimeter vector magnetograms of 18 different active regions observed for more than 8 days, we computed contours of a_z corresponding to a single fixed level $\pm 10^{-9}\mathrm{m}^{-1}$ and calculated averaged areas of patches (S_{avg}) and averaged values of α (α_{avg}) inside each patch. Fig. 5 shows the variation of α_{avg} and S_{avg} for the magnetograms observed within ±45° of the central meridian. Despite significant scatter, the data show no systematic trend either in averaged size nor in averaged α_z.

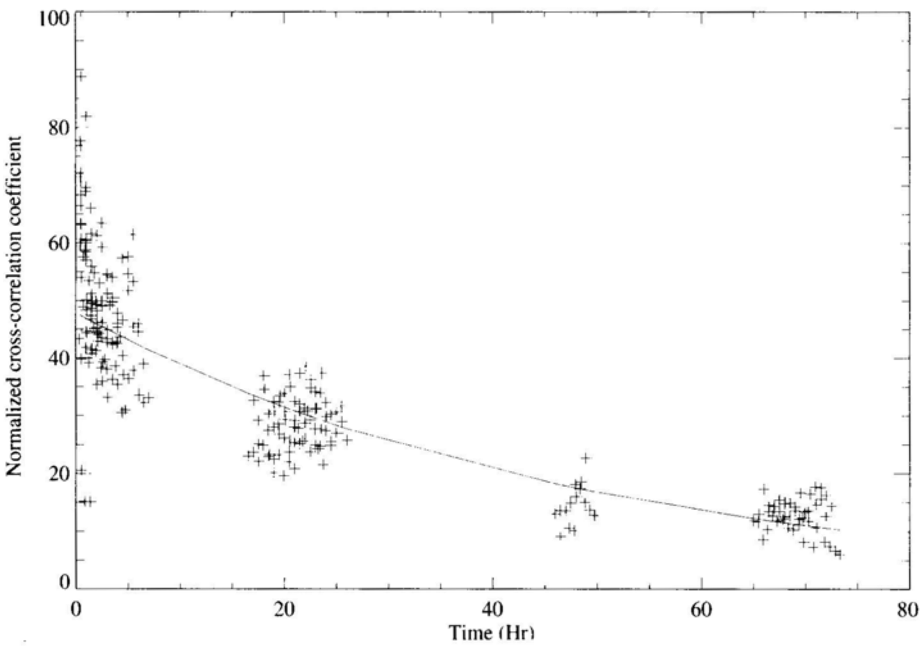

Figure 4. Cross-correlation function computed using α-maps of decaying active region NOAA 7926.

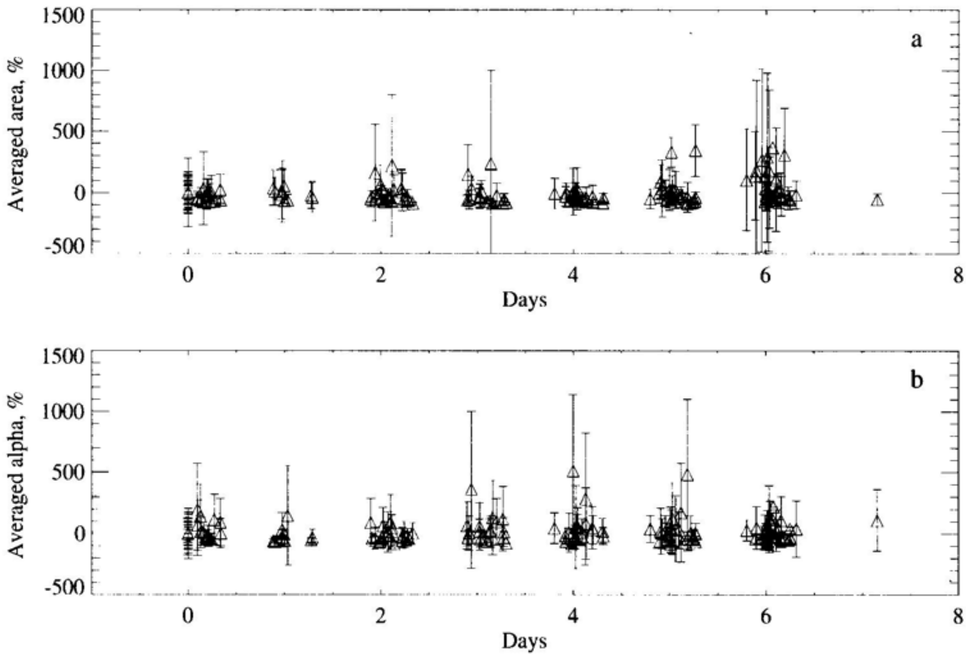

Figure 5. Evolution of averaged size of contours corresponding to $\pm 10^{-9}\mathrm{m}^{-1}$ (**a**) and averaged value of α inside areas (**b**) for 18 active regions.

The presence of short term evolution (Fig. 4) and the lack of long-term evolution (Fig. 5) suggests to us that the local helicity pattern inside active regions evolves mostly via rearrangement of existing individual α_z patches. We see no indication of a Taylor relaxation process in our data.

References

Abramenko, V. I., Yurchishin, V..B. 1996, *Solar Phys.,* **168**, 47.

Berger, M. A. 1999, in *Magnetic Helicity in Space and Laboratory Plasmas,* (ed.) M. R. Brown, R. C. Canfield & A. A. Pevtsov, **111** of Geophys. Monogr. Ser. (Washington, D.C. AGU), 1–10.

Bogdan, T. J. 1984, *Phys. Fluids,* **27**, 994.

Caligari, P., Moreno-Insertis, F., Schüssler, M. 1995, *Astrophys. J.,* **441**, 886.

Chou, D.-Y, Fisher, G. H. 1989, *Astr. Astrophys.,* **341**, 533.

D'Silva, S., Choudhuri, A. R. 1993, *Astr. Astrophys.,* **272**, 621.

Fan, Y, Fisher, G. H., McClymont, A. N. 1994, *Astrophys. J.,* **436**, 907.

Gary, G. A., Moore, R. L., Hagyard, M. J., Haisch, B. M. 1987, *Astrophys. J.,* **314**, 782.

Gilman, P. A., Charbonneau, P. 1999, in *Magnetic Helicity in Space and Laboratory Plasmas,* (ed.) M. R. Brown, R. C. Canfield & A. A. Pevtsov, **111** of Geophys. Monogr. Ser. (Washington, D.C. AGU), 75–82.

Leka, K. D., Canfield, R. C., McClymont, A. N., Van Driel Gesztelyi, L. 1996, *Astrophys. J.,* **462**, 547.

Longcope, D. W., Fisher, G. H., Arendt, S. 1996, *Astrophys. J.,* **464**, 999.

Longcope, D. W., Fisher, G. H., Pevtsov, A. A. 1998, *Astrophys. J.,* **507**, 417.

Longcope, D. W., Klapper, I. 1997, *Astrophys. J.,* **488**, 443.

Longcope, D. W., Linton, M., Pevtsov, A. A., Fisher, G. H., Klapper, I. 1999, in *Magnetic Helicity in Space and Laboratory Plasmas,* (ed.) M. R. Brown, R. C. Canfield & A. A. Pevtsov, **111** of Geophys. Monogr. Ser. (Washington, D.C. AGU), 93–101.

Moffatt, K. H., Ricca, R. L. 1992, *Proc. R. Soc. Lond. A,* **439**, 411.

Parker, E. N. 1955, *Astrophys. J.,* **122**, 293.

Pevtsov, A. A., Canfield, R. C. 1999, in *Magnetic Helicity in Space and Laboratory Plasmas,* (ed.) M. R. Brown, R. C. Canfield & A. A. Pevtsov, **111** of Geophys. Monogr. Ser. (Washington, D.C. AGU), 103–110.

Pevtsov, A. A., Canfield, R. C, Metcalf, T. R. 1994, *Astrophys. J.,* **425**, L117.

Pevtsov, A. A., Canfield, R. C, Metcalf, T. R. 1995, *Astrophys. J.,* **440**, L109.

Spruit, H. C. 1981, *Astr. Astrophys.,* **98**, 155.

Steenbeck, M., Krause, F. 1966, *Z. Naturforsch,* **21a**, 1285.

Taylor, J. B. 1974, *Phys. Rev. Lett,* **33**(19), 1139.

Taylor, J. B. 1986, *Rev. Mod. Phys.,* **58**(3), 741.

Wang, J. 1999, *Fundamentals of Cosmic Physics,* **20**, 251.

Yamada, M. 1999, in *Magnetic Helicity in Space and Laboratory Plasmas,* (ed.) M. R. Brown, R. C. Canfield & A. A. Pevtsov, **111** of Geophys. Monogr. Ser. (Washington, D.C. AGU), 129–140.

Zweibel, E. G., Rhoads, J. E. 1995, *Astrophys. J.,* **440**, 407

J. Astrophys. Astr. (2000) **21**, 221–227

Cyclical Variability of Prominences, CMEs and Flares

J. L. Ballester, *Departament de Física, Universitat de les Illes Balears. E-07071 Palma de Mallorca, Espana.*
e-mail: dfsjlb0 @ps, uib. es

Abstract. Solar flares, prominences and CMEs are well known manifestations of solar activity. For many years, qualitative studies were made about the cyclical behaviour of such phenomena. Nowadays, more quantitative studies have been undertaken with the aim to understand the solar cycle dependence of such phenomena as well as peculiar behaviour, such as asymmetries and periodicities, occurring within the solar cycle. Here, we plan to review the more recent research concerning all these topics.

Key words. Sun: Activity—prominences—flares—CMEs.

1. Introduction

The long-term evolution of solar activity, on time scales of the solar cycle and beyond, has been studied from different perspectives using a variety of phenomena that have timescales shorter than 11 years. Two of the most studied topics have been the time-latitude distribution of filaments, CMEs and flares and the asymmetry of solar activity. However, sixteen years ago an unexpected short-term periodicity in high-energy flares was discovered by the solar maximum mission satellite and nowadays we have some hypothesis about when and why it occurs. In the following, I would like to review the more recent research done on those topics.

2. Time-latitude distribution of filaments, CMEs and flares

2.1 *Filaments*

Regularities in the time-latitude distribution of the prominences were already described by D'Azambuja's (1948). Later, Waldmeier (1973) pointed out that prominences are distributed in three narrow zones, which show different types of time-latitude behaviour. These zones are: (a) Zone of sunspot type prominences which move along with sunspots originating between 30° and 50°; (b) Zone of long-lived prominences which develop from active centers, migrating towards the equator at a latitude 15° higher than the spot zone; (c) Polar zone at latitudes higher than 45°. Since Secchi (1872) discovered the zone of polar prominences and its poleward motion, this phenomenon has been observed in every cycle and is independent of the intensity of the cycle. The characteristic pattern of the polar zone is a "rush to the poles" and the development of a secondary polar crown on the next neutral line equatorward of the first. This behaviour was well documented by Evershed & Evershed (1917).

Mclntosh (1992) discriminated between high-latitude filaments with "correct" polarity – which means that the polarity of the magnetic field lying poleward of east-west oriented filaments is the one appropriate for that cycle (true polar crown) – from those with "opposite polarity" (emergent polar crown). The kinematic model of the solar cycle tries to explain the polar crown "rush" to the poles as the consequence of diffusion of magnetic fields which accumulated from the dispersion of active regions earlier in the solar cycle. Then, the movement of the polar crown should reflect the numbers and intensities of the active regions while the onset of poleward motion should await some accumulation of flux from numerous active regions. Instead, the motion of the polar crown begins very soon after the sunspot minimum, long before there are active regions. Furthermore, the rate of motion varies little during the rise of the cycle, even though there is a large increase in the number of active regions. Mclntosh (1992) argued that this steady progress must reflect some fundamental subsurface process rather than the surface diffusion of decaying active-region field.

During solar cycle 20, two polar zones appeared in the northern hemisphere (Waldmeier 1973). The first was regular and reached the pole shortly after the sunspot maximum. The second one, irregular and weaker, appeared at lower latitudes only when the regular zone was already disappearing. This anomalous zone also moved towards the pole and disappeared at the beginning of 1971, migrating faster than the regular one. Curiously, the phase shift (1.4 years) between regular polar zones in both hemispheres seems to be related with the phase shift (1 year) between the main zones of activity in both hemispheres. On the other hand, an anomaly which appeared in the migration, towards the equator, of the main zone of sunspots belonging to the northern hemisphere seems to be the cause of the apparition of the second polar zone. This points out the existence of a coupling between the activity in low and high latitudes. Also, in this cycle, a three-fold reversal of the magnetic field occurred in the northern hemisphere as the secondary polar crown followed the first into the polar region (Makarov *et al.* 1983). Benevolenskaya & Makarov (1992) have claimed that triple reversals have happened during all even cycles since cycle 12 and that the mechanism could be the superposition of a high frequency variation on the basic 22-year magnetic cycle. However, there are doubts about the reliability of the records used for this hypothesis. Dermendjiev *et al.* (1994) pointed out that during the ascending phase of the solar cycle 22 a triple structure developed in the southern hemisphere.

2.2 *Coronal mass ejections*

Webb (1991) and Webb & Howard (1994) studied CMEs from 1973 to 1989 concluding that: (1) the frequency of occurrence of CMEs tends to follow the solar activity cycle in both amplitude and phase; (2) considering only long-term averages, all solar activity indices are equally correlated with CME rate.

Cliver *et al.* (1994) obtained Carrington rotation averaged daily rates of CMEs for the period 1979–1989 and performed a correlation plot with the tilt angle of the heliospheric current sheet. A quasi-discontinuity appears in October 1988, when the average daily rate doubled and remained high until the end of solar maximum mission observations in late 1989. Another quasi-discontinuity appeared in 1982 with a decrease in the CME rate. Also, they inferred a similar discontinuity (increase) in the CME rate during 1978.

These discontinuities occur at about the time of the onset of the poleward motion of the true polar crown or at the time of return to the equilibrium position. If the increase in the CME rate in late 1988 is related to the dynamics of the high latitude filaments, then we would expect a change in the latitude distribution of CMEs around the time of the quasi-discontinuity.

Hundhausen (1993) found that the distribution of apparent central latitudes of CMEs for different years shows significant changes in the spread about the equator. For instance, 41° in 1980, 38° in 1989, but only 13° in 1986. The changes in the distribution of CMEs latitudes do not correspond to those for solar features related to small-scale magnetic structures such as sunspots, active regions, or Hα flares. Instead, Hundhausen's (1993) findings support the hypothesis that the latitude distribution of CMEs mimics that of solar filaments. This analysis suggests that there is a close, physical relationship of coronal mass ejections with the disruption of large-scale magnetic structures. Cliver & Webb (1998) made a statistical comparison of high-latitude CMEs with disappearing solar filaments (DSFs) finding that: (1) Beginning with the "rush to the poles", DSFs occur at an increasing rate from the "emerging" polar crown. At maximum, these filaments are the dominant source of high-latitude DSFs. Following polarity reversal, the new true polar crown becomes the source of all high-latitude DSFs; (2) At the last two solar maxima, there were ≈ 4 times as many high-latitude (≥ 60°) CMEs as high latitude (≥ 45°) DSFs. They offer the following plausible reasons for this discrepancy: (a) under-reporting of small DSFs, (b) propagation effects or (c) some combination of both effects.

2.3 *Flares*

A detailed study of Hα flares (1938–1992) and X-ray flares (1982–1992) reveals that flare energy release systematically follows the solar cycle and extends well beyond the main activity zone into higher latitudes (Balasubramanian & Regan 1994). The butterfly diagram for Hα flares is similar to butterfly diagram for sunspots and follows the solar cycle with an extension of the zone of flare activity outside the sunspot activity zone during solar cycles 19, 20 and 21. Also, this diagram already suggests flare asymmetry between hemispheres. The butterfly diagram for X-ray flares shows its concentration in the main activity zone. Concerning the latitude distribution of X-ray flares energies, the majority of X-ray flares extending outside the main activity zone (± 30°) are low intensity C-class flares while only few high intensity X-ray flares occur at latitudes higher than ±40°. On the other hand, the number of flares drastically drops off above a flux of 10^{-3} watts m^{-2} and most of the flare energy appears to be released in the mid-latitudes around ±17°. Then, models that attempt to describe the large scale solar activity should include an explanation of this observed location of maximum energy release.

3. The near 158-day periodicity in high-energy solar flares

The near 158-day periodicity was detected during solar cycle 21 in γ-ray flares (Rieger *et al.* 1984); X-ray flares (Kiplinger *et al.* 1985; Dennis 1985; Kile & Cliver

1991); flares producing interplanetary electrons (Droöge *et al.* 1990); microwave flares (Bogart & Bai 1985) and proton flares (Bai & Cliver 1990). However, during solar cycle 22 there has been no evidence for the presence of this periodicity in any solar flare related indicator. Why do high-energy flares display this periodicity only sporadically?

Energetic solar flares are based on reconnection between emergent magnetic flux and old flux (Forbes 1991; Priest 1990). Then, one could suspect that a periodic behaviour in the occurrence rate of energetic flares could be related to a periodic emergence of magnetic flux, giving place to a periodic variation of the total sunspot area on the Sun's surface (Carbonell & Ballester 1990). To test this hypothesis, we need to prove that the occurrence of the periodicity in high-energy flares coincide with a similar occurrence of periodicity in sunspot areas.

To this end, we applied wavelet analysis to a time series made of daily sunspot areas between 1874 and 1993 in order to study the temporal variation with time scales around 160 days. The analysis reveals the existence of a periodic variation in the emergence of magnetic flux at epochs that coincide with the periodicity found in high-energy solar flares, which suggests a close relationship among them (Oliver, Ballester & Baudin 1998). Recently, a complete re-analysis of solar activity historical archives has been made (Hoyt & Schatten 1998) and the result is a homogeneous database of group sunspot numbers spanning along a 386-year period (1610-1995). This database is compiled from the daily number of observed sunspot groups. We have started our analysis in 1750 and have applied the wavelet technique to a time series made of daily group sunspot numbers between 1750 and 1995, in order to study the temporal variation with time scales around 160 days (Ballester, Oliver & Baudin 1999). After analyzing the whole time series, we find that an episode of the 158-day periodicity occurred around the maximum of solar cycle 2, this being the first time that such a periodicity is detected prior to the twentieth century. After this epoch, a signal appears around the maxima of solar cycles 16 to 21. The detection of the periodicity in this solar activity index provides a strong confirmation for the existence of a periodic emergence of magnetic flux around the maxima of some solar activity cycles. During the twentieth century, the periodicity has appeared simultaneously in sunspot areas and group sunspot numbers, but the periodicity does not manifest with the same strength in both data sets as pointed out by means of Lomb-Scargle periodograms. In order to explain this behaviour, we suggest that the periodic emergence of magnetic flux, which triggers the flares, can occur either by forming new sunspot groups in previously spotless photospheric regions or by creating new sunspots within already formed sunspot groups.

According to the first type of behaviour, new sunspot groups would periodically appear, increasing simultaneously the number of sunspot groups and the total sunspot area, such as could have occurred during solar cycles 16 and 17.

According to the second type of behaviour, the periodic emergence of new magnetic flux gives place to a periodic variation of sunspot areas but not to a variation in the number of sunspot groups. A good example of this case would be solar cycles 20 and 21. Finally, when none of the previous types of periodic emergence takes place, the periodicity in flare occurrence does not appear, as in solar cycle 22. Having this in mind, one can suggest that when the periodicity appears in sunspot as are only, i.e. when the magnetic flux emerges mostly within already formed active regions, a similar periodicity should appear in high-energy solar flares, such as occurred during solar cycle 21. On the other hand, when the periodic emergence of magnetic flux is produced in the form of new and scattered sunspot groups, no periodicity should appear in energetic solar flares.

4. The north – south asymmetry of solar activity

The asymmetry of solar activity between hemispheres has been known for a long time and it has been detected in: (a) Solar flares (Roy 1977; Knoska 1985; Garcia 1990; Joshi 1995; Özgüç & Ataç 1996); (b) Prominences (Waldmeier 1971; Hansen & Hansen 1975; Vizoso & Ballester 1987; Joshi 1995); (c) Magnetic flux (Howard 1974; Tang *et al.* 1984; Rabin *et al.* 1991).

Verma (1992, 1993) has performed the most complete study of N–S asymmetry using different solar activity indicators for solar cycles 8–22. He has suggested that the N–S asymmetry may have a period, or long term trend, around 110 years, however, one has to be careful since we only have data for about 160 years. The presence of this trend has been also studied by Oliver & Ballester (1994) and Özgüç & Ataç (1996).

The most important result is that the shape of the trend indicates that during solar cycle 22 the dominance of solar activity has moved to the southern hemisphere, changing thus the behaviour exhibited during the most recent solar cycles. Also, Verma (1992, 1993) has predicted that the dominance of the southern hemisphere will continue during cycles 23 and 24.

Roy (1977) and Yau (1988) argued that the N–S asymmetry in spots is anti-correlated with solar cycle while Swinson *et al.* (1986) suggested that there is a 22-year periodicity in the N–S asymmetry of spots. However, Garcia (1990) suggested that N–S asymmetry of flares is out of phase with the solar activity cycle and with the N–S asymmetry in spots. All the above are qualitative conclusions based on the shapes of the curves of solar activity and asymmetry versus time while Rank Correlation tests, using sunspot data, suggest anticorrelation although this conclusion has to be taken with care.

The solutions of the linear (Kinematic) dynamo problem have pure dipole or quadrupole symmetry; i.e. toroidal field are antisymmetric or symmetric about the equator. These symmetries can only be broken in the non-linear regime, which lead to the appearance of spatially asymmetric mixed-mode (mixed-parity) solutions (Jennings & Weiss 1991). Brandenburg *et al.* (1989) have studied oscillatory non-linear dynamos finding that one of the features of the solutions is that the symmetry type can vary on a very long time scale compared to the magnetic cycle frequency. Pulkkinen *et al* (1999) have determined the long-term variation (1853–1996) of the latitude of the magnetic equator of the Sun. This latitude is computed as the sum of mean latitude of solar activity in each hemisphere.

The period of this variation is about 8.4 sunspot cycles or 90 years, and the amplitude 1.3 degrees. This variation in latitude can be explained as a mixed-parity mode in which a quadrupolar component is oscillating with this period; however, Stenflo & Vogel (1986) found a small quadrupolar component in the radial field at the solar surface, which oscillates on time scales much shorter than the solar cycle! Thus there is great scope for improvement in the understanding of non-linear dynamos as related to observed N–S asymmetries in occurrence of flares & sunspots.

References

Ataç, T., Özgüç, A. 1996, *Sol. Phys.,* **166**, 201.

Bai, T., Cliver, E. W. 1990, *Astrophys. J.,* **363**, 299.

Balasubramanian, K. S., Regan, J. 1994, in *Solar Active Region Evolution,* ASP Conf. Ser. 68, (eds.) K. S. Balasubramanian and G. W. Simon, 17–23.

Ballester, J. L., Oliver, R., Baudin, F. 1999, *Astrophys. J.,* **522**, L153.

Brandenburg, A., Krause, F., Tuominen, I. 1989, in *Turbulence and Nonlinear Dynamics in MHD flows,* (eds.) M. Meneguzzi, A. Pouquet and P. L. Sulem (Elsevier), 35–40.

Benevolenskaya, E. E., Makarov, V I. 1992, in *The Solar Cycle,* ASP Conf. Ser. 27, (ed.) K. L. Harvey, 532–535.

Bogart, R. S., Bai, T. 1985, *Astrophys. J.,* **299**, L51.

Carbonell, M., Ballester, J. L. 1990, *Astron. Astrophys.,* **238**, 377

Cliver, E. W., St Cyr, O. C, Howard, R. A., Mcintosh, P. S. 1994, in *Solar Coronal Structures,* (eds) V. Rusin, P. Heinzel, J. C. Vial, (VEDA Publishing Co.), 83–89.

Cliver, E. W., Webb, D. F. 1998, in *New Perspectives on Solar Prominences,* ASP Conf. Ser. 150, (eds.) D. Webb, D. Rust, and B. Schmieder, 479–83.

D'Azambuja, L., D'Azambuja, M. 1948, *Ann. Obs. Meudon,* **6,** 52.

Dennis, B. R. 1985, *Sol. Phys.,* **100**, 465.

Dermendjiev, V. N., Stavrev, K. Y., Rusin, V., Rybansky, M. 1994, *Astron. Astrophys.,* **281**, 241.

Dröge, W., Gibbs, K., Grunsfeld, J. M., Meyer, P., Newport, B. J., Evenson, P., Moses, D. 1990, *Astrophys. J. Suppl. Sen,* **73**, 279.

Evershed, J., M. A. 1917, *Mem. Kodaikanal Obs. I,* part II.

Forbes, T. G. 1991, *Geophys. Astrophys. Fluid Dynamics,* **62**, 15.

Garcia, H. 1990, *Sol. Phys.,* **127,**185.

Hansen, R., Hansen, S. 1975, *Sol. Phys.,* **44**, 225.

Howard, R. 1974, *Sol. Phys.,* **38**, 59.

Hoyt, D. V., Schatten, K. H. 1998, *Sol. Phys.,* **181**, 491.

Hundhausen, A. J. 1993, *J. Geophys. Res.,* **98**, A8, 13177.

Jennings, R. L., Weiss, N. O. 1991, *Mon. Not. R. Astr. Soc,* **252**, 249.

Joshi, A. 1995, *Sol. Phys.,* **157**, 315.

Kile, J. N., Cliver, E. W. 1991, *Astrophys. J.*, **370**, 442.

Kiplinger, A. L., Dennis, B. R., Orwig, L. E. 1985, *Bull. A. A. S.,* **6**, 891.

Knoska, S. 1985, *Contrib. Astron. Obs. Skalnat Pleso,* **13**, 217.

Makarov, V. I., Fatianov, M. P., Sivaraman K. R. 1983, *Sol. Phys.,* **85**, 215.

Mclnstosh, P., 1992, in *The Solar Cycle,* ASP Conf. Ser. 27, (ed.) K. L. Harvey, 14–34.

Oliver, R, Ballester, J. L. 1994, *Sol .Phys.,* **152**, 481.

Oliver, R., Ballester, J. L., Baudin, F. 1998, *Nature,* **394**, 552.

Priest, E. R. 1990, in *Basic Plasma Processes on the Sun,* (eds.) E. R. Priest and V. Krishnan, (Kluwer Academic Publishers), 271–291.

Pulkkinen, P. J., Brooke, J., Pelt, J., Tuominen, I. 1999, *Astron. Astrophys.,* **341**, L43.

Rabin, D. M., DeVore, C. R., Sheeley, N. R., Harvey, K. L., Hoeksema, J. T. 1991, in *Solar Interior and Atmosphere,* (eds.) A. C. Cox, W. C. Livingston and M. S. Matthews, (The University of Arizona Press), 781–843.

Rieger, E., Share, G. H., Forrest, D. J., Kanbach, G., Reppin, C, Chupp, E. L. 1984, *Nature,* **312**, 623.

Roy, J. R. 1977, *Sol. Phys.,* **52**, 53.

Secchi, P. A. 1872, *Die Sonne,* Braunschweig, p. 520.

Stenflo, J. O., Vogel, M. 1986, *Nature,* **319**, 285.

Swinson, D. B., Koyama, H., Saito, T. 1986, *Sol. Phys.,* **106**, 35.

Tang, F., Howard, R., Adkins, J. M., 1984, *Sol. Phys.,* **91**, 75.

Verma, V. K. 1992, in *The Solar Cycle,* ASP Conf. Ser. 27, (ed.) K. L. Harvey, 429–435.

Verma, V. K. 1993, *Astrophys. J.,* **403**, 797.

Vizoso, G., Ballester, J. L. 1987, *Sol. Phys.,* **112**, 317.

Waldmeier, M. 1971, *Sol. Phys.,* **29**, 232.

Waldmeier, M. 1973, *Sol. Phys.,* **28**, 389.

Webb, D. F. 1991, *Adv. Space Res.,* **11(1),** 37.
Webb, D. F., Howard, R. A. 1994, *J. Geophys. Res.,* **99,** A3, 4201.
Yau, K. K. C, 1988, in *Secular Solar and Geomagnetic Variations in the last 10000 years,* (eds.) F. R. Stephenson and A. W. Wolfendale (Kluwer Academic Publishers), 161–185.

J. Astrophys. Astr. (2000) **21**, 229–232

Analysis of the 9th November 1990 flare

Anita Joshi & Wahab Uddin, *U. P. State Observatory, Manora Peak, Naini Tal 263129, India*
e-mail: anita@upso.ernet.in wahab@upso.ernet.in

Abstract. In this paper we present complete two-dimensional measurements of the observed brightness of the 9th November 1990 *Hα* flare, using a PDS microdensitometer scanner and image processing software MIDAS. The resulting isophotal contour maps, were used to describe morphological-cum-temporal behaviour of the flare and also the kernels of the flare. Correlation of the *Hα* flare with SXR and MW radiations were also studied.

Key words. *Hα* flare—isophotal contour maps—flare kernels.

1. Introduction

In this paper, we present two-dimensional isophotal contour maps made from the analysis of 9th November 1990 flare, with the aid of isodensitometry and image processing of photographic *Hα* observations. We have given salient information about the morphological changes in the flare using the isophotal contour maps. With the help of isophotal contour maps along with three-dimensional (3D) pictures, the location of kernels of the flare have also been investigated. We have also studied the nature of the flare in soft X-ray (SXR) and microwave (MW) radiations, with the help of the limited data available with us.

2. Isophotal contour maps

We have carried out photographic monitoring of 9th November 1990 flare, using 15 cm, f/15 Coudé refractor in conjunction with Daystar *Hα* and Ca II K filters, at Uttar Pradesh State Observatory (UPSO), Naini Tal. The density on the film of the images were digitized, at Indian Institute of Astrophysics (IIA), Bangalore, with the help of a positional densitometer system (PDS) and analysis has been carried out at UPSO (Joshi 1996).

Selected H_α filtergrams of the flare (1N/N06E36, AR 6359B) are shown in Fig. 1. To visualize flare kernels in this figure we have also shown isophotal contour map and 3D (*x, y, I*) intensity plot at the maximum phase of the flare. The figure shows a question-mark shape filament, before the onset of the flare. The flare erupted from the lower part (towards south) of the filament and from the upper part (towards north) of the filament a dark surge erupted. At the maximum, the flare produced about six minute duration remote chromospheric brightening. Selected *Hα* isophotal contour

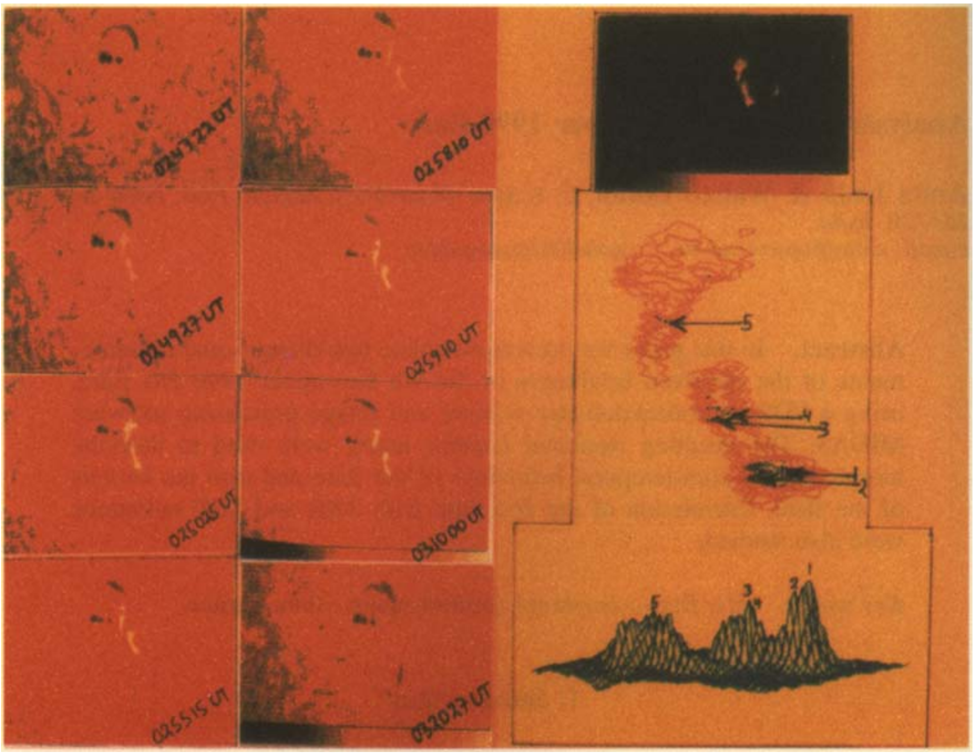

Figure 1. Selected *Hα* filtergrams (left) and isophotal contour map with 3D intensity plot (right) at the maximum phase of the flare.

maps of the flare are given in Fig. 2. The isophotes were set at a chosen intensity ratio between flare intensity (I_f) and background intensity (I_b). In the figure, the first isophote was set at $I_f / I_b = 1.61$ and the increment between two contour levels was 0.29. The flare occurred at 024836 UT in the form of two ribbons. The two flare ribbons were denoted as A and B. During the rise phase of the flare the thickness of the ribbons increased with time till the maximum at 024927 UT. As the ribbons thickness increased, the separation between ribbons decreased and ribbons appeared closest to each other at the flare maximum. After the maximum there was a decline in the flare activity. During the decline the ribbons A and B were noticed to separate speedily, followed by the fragmentation of ribbon A. At 025810 UT again a slight increase in flare activity was noticed which later showed gradual decay of flare activity. To confirm this chronology of event, in Fig. 2 we have also presented intensity and area plots of the flare as a function of time, wherein, intensity is expressed in arbitrary scale and area is in millionths of solar disk. It is clear from the data points (only in decay-phase) that the flare in Ca Π K (crosses) shows similar trend as in *Hα,* whereas in Ca II K the flare covers a larger area than H_α . There are five bright points among these bright points the two most intense points (number 1 and 2) may be flare kernels (cf. Fig. 1). These two points have intensities 2.45 and 2.38 times of the surrounding flare intensity. Thus, the selection criterion for the flare kernels is the bright points, having intensities 2.4 times of surrounding flare intensity.

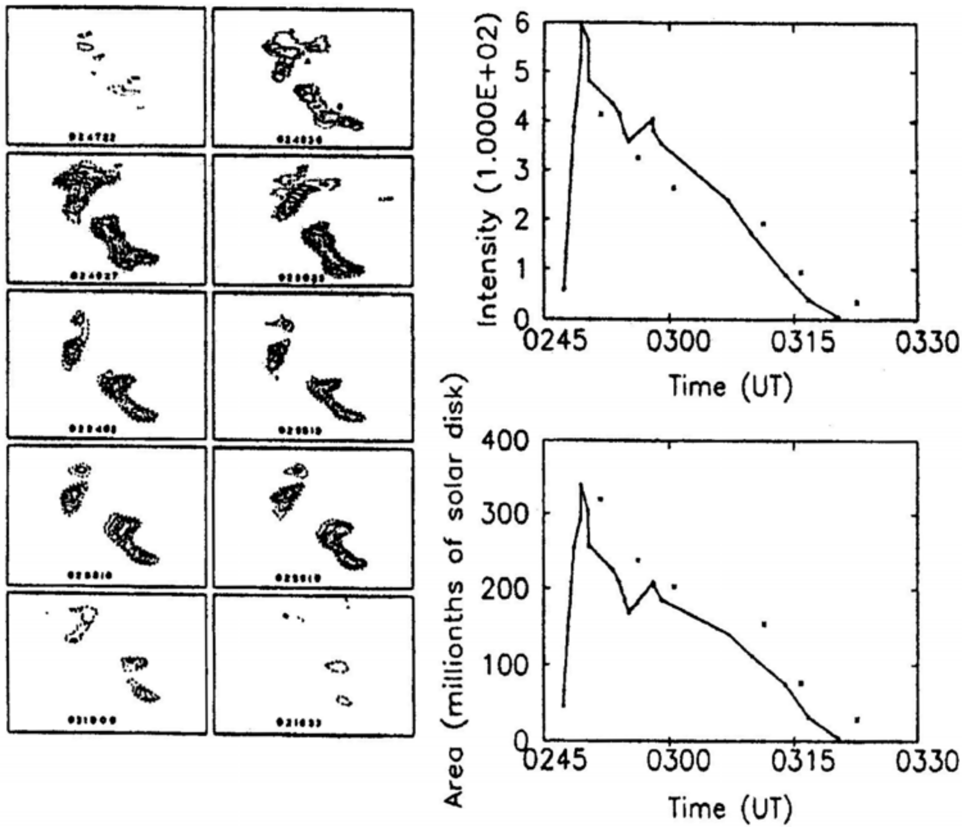

Figure 2. Flare isophotal contour maps and intensity and area time profiles.

3. SXR and MW radiations

The flare associated with radiations in SXR and MW (SGD 1991) GOES SXR time profiles shows a sharp rise to maximum, followed by a gradual decayas in *H*α. The profiles of 1–8 Å and 0.5–4 Å bands show peak-fluxes as 6.1 × 10^{-6}Wm^{-2} and 4.9 × 10^{-7} W m^{-2} respectively. The peak value of the flux in 1-8 Å band suggest X-ray importance class C6.1. By using SXR time profiles, we can determine effective temperature (T_{eff}) and emission measure (EM) of SXR emitting source. For determining these quantities, we have followed Thomas *et al.* (1985). The calculated values came out to 0.8 × 10^7 K and 1.3 × 10^{49} cm^{-3}.

The flare associated MW burst recorded in frequencies 410, 610, 1000, 2000, 2840, 3750 and 9400 MHz respectively (SGD 1991, Joshi 1996). From the radio data, we have estimated the values of the magnetic field perpendicular to the electron density ($B_\perp$) in gauss, electron energy (E) in MeV and the angular size (ϕ) in arcsec of the MW burst source. For this we followed the method given by Degaonkar *et al.* (1981). The estimated values are 204 gauss, 1.4 MeV and 12.4 arcsec.

4. Results and discussions

The triggering of the flare appeared to be due to filament existing in the vicinity of the active region (Fig. 1). The flare produced remote chromospheric brightening. Isophotal contour maps (Fig. 2) given by us chalk out a detailed scenario of flare. The nature of the evolution of the flare can also be studied very well by time profiles. It is a dynamic two ribbon flare. The flare shows the expanding motion of two flare ribbons with the velocity of separation of 3.75 km s^{-1} during the maximum phase of the flare. The $H\alpha$ classification of the flare corresponds to class 1N (SGD 1991). The area (338 millionths of solar disk) measured by us at the maximum of the flare also corroborate to this class. The isophotal contour maps along with 3D pictures help in visualizing the location of flare kernels, whereas the clear cut detection of flare kernels is only possible in the wings of H_α (Tang 1985).

The flare is also associated with radiations in SXR (C6.l-class) and MW (spiky burst). The estimated values of T_{eff} (0.8×10^7 K) and EM (1.3×10^{49} cm^{-3}) suggest that SXR emission originated in a hot plasma through thermal bremsstrahlung (Kawabata 1960). From the radio data, the calculated values of $B_\perp$, E and ϕ of radio source are 204 gauss, 1.4 MeV and 12.4 arcsec.

Acknowledgements

Thanks to an anonymous referee for improving the scientific content of the paper.

References

Degaonkar, S. S., *et al.* 1981, *Bull. Astron. Soc. India,* **9,** 291.
Joshi, A. 1996, Ph. D. *Thesis, Kumaun Univ. Nainital, India.*
Kawabata, K. 1960, *Rep. Ionos. and Space Res. Japan,* **14,** 405.
SGD, 1991, 557/1 & 561/II.
Tang, F. 1985, *Solar Phys.,* **102,** 131.
Thomas, R. J., Star, R., Crannell, C. J. 1985, *Solar Phys.,* **95,** 323.

J. Astrophys. Astr. (2000) **21**, 233–236

A Rapidly Evolving Active Region NOAA 8032 observed on April 15th, 1997

Shibu K. Mathew* & Ashok Ambastha, *Udaipur Solar Observatory, P. O. Box: 198, Udaipur 313 004, India.*
**e-mail: shibu@ iiap.ernet.in*

Abstract. The active region NOAA 8032 of April 15, 1997 was observed to evolve rapidly. The GOES X-ray data showed a number of sub-flares and two C-class flares during the 8-9 hours of its evolution. The magnetic evolution of this region is studied to ascertain its role in flare production. Large changes were observed in magnetic field configuration due to the emergence of new magnetic flux regions (EFR). Most of the new emergence occured very close to the existing magnetic regions, which resulted in strong magnetic field gradients in this region. EFR driven reconnection of the field lines and subsequent flux cancellation might be the reason for the continuous occurrence of sub-flares and other related activities.

Key words.

1. Introduction

There are number of observations suggesting new flux emergence as the cause for the flare trigger. Association of frequent occurrence of flares with EFR was reported by Rust (1972) in a number of cases. Examples of EFR triggered flares have been also reported by Wang *et al.* (1991), where they observed X-class flares near the sites of EFR. Wang & Shi (1993) suggested that emergence of new flux and its cancellation with the existing flux is wholly inseparable, elementary process in the active region for the occurrence of flares. In this paper we have carried out a similar study of flux emergence, cancellation and their relation to the occurrence of flares for the active region NOAA 8032.

2. **Observations**

The region NOAA 8032 of April 15th, 1997 was observed to evolve rapidly in its magnetic and chromospheric structures. The Solar Geophysical Data (SGD) reported a number of B-class and two C-class flares during its 10 hours of evolution. The SOHO/EIT Fe IX/X 171 Å images showed loop formation and repeated brightening due to new emerging flux regions. At Udaipur Solar Observatory we have taken near simultaneous photospheric white light and magnetic field observations of this active region using the USO video magnetograph (Mathew *et al.* 1998). The active region

NOAA 8032 showed up in Ca I 6122 Å image as a group of small pores with opposite polarities, the leading spot had a negative polarity.

3. Discussion and results

Figure l(a) to (d) shows the contour plots of magnetograms, obtained on April 15, 1997 at 05:23, 08:26, 09:05 and 10:01 UT. The contour plots show clear evidence of EFRs and corresponding magnetic field changes in this active region. Major changes in the field occurred during the initial stages of evolution, i. e., within 3 to 4 hours after the begining of our observations at 05:20 UT. As evident in the contour plots most of the new fluxes emerged near to the existing flux regions, i.e., within 10-15 arc-seconds. According to SGD (May 1997, Number 633, Part I, GOES X-ray data) the flare activity at this region started around 07:30 UT. Even though the magnetogram data were not available at the time of flare, the images obtained around 08:26 UT shows a clear evidence of EFRs at the flaring site. It can be inferred that emergence of new flux regions had started before the first X-ray flare and perhaps triggered the flare. Similar observations of surges and Hα compact flares due to the rapid emergence have been reported by Kurokawa (1998).

We have analysed the changes in the positive and negative fluxes. Flux changes were calculated in two specific areas of EFRs marked by small boxes on Fig. 1 (b) and listed in Table 1. In the magnetograms taken around 05:23 UT, more positive flux was present as compared to that at 08:36 UT, which implies a reduction of flux imbalance. Later an increase and then again a decrease was observed in the net positive flux. This oscillation of the magnetic flux can perhaps be attributed to the continuous emergence and cancellation of fluxes during the flare activity.

This study revealed that EFRs evolved considerably when flare occurred. At this region flux change at a rate approximately 10^{13} Mx/s was found which conforms with earlier observations by Ribes (1969) and Rust (1972). At the location *b* of EFR the magnetic flux of negative polarity gradually increased while the positive polarity decreased. This observation was in agreement with Ribes results that the flare occurred when the magnetic flux in one feature is increasing and decreasing in another adjoining area. Magnetic field gradient is another important parameter to decide the flare location. We have carried out the magnetic field gradient calculation for the above active region for two specific locations and found an increase in magnetic field gradient during 05:23 to 10:01 UT. This strong horizontal gradient might have favored the continuous occurrence of sub-flares, surges and related activities in NOAA 8032.

Potential field calculation is carried out for this active region using Schmidt technique and observed flux distribution from USO VMGs. A comparison has been carried out between the calculated potential field and SOHO/EIT images. The calculated transverse field shows the photospheric or low lying connections while the EIT UV images shows higher loops as observed in the coronal heights. The loop structure initially showed simple bipolar nature of the active region. A number of new loops are noticed on further development of the active region, which corresponds to the emergence of new magnetic flux. Comparing the USO longitudinal magnetic maps and SOHO/EIT images, we find that the bright areas in SOHO/EIT images correspond to the location of EFRs or high magnetic field gradient. Due to the low resolution of EIT it is difficult to distinguish a particular loop which connects to

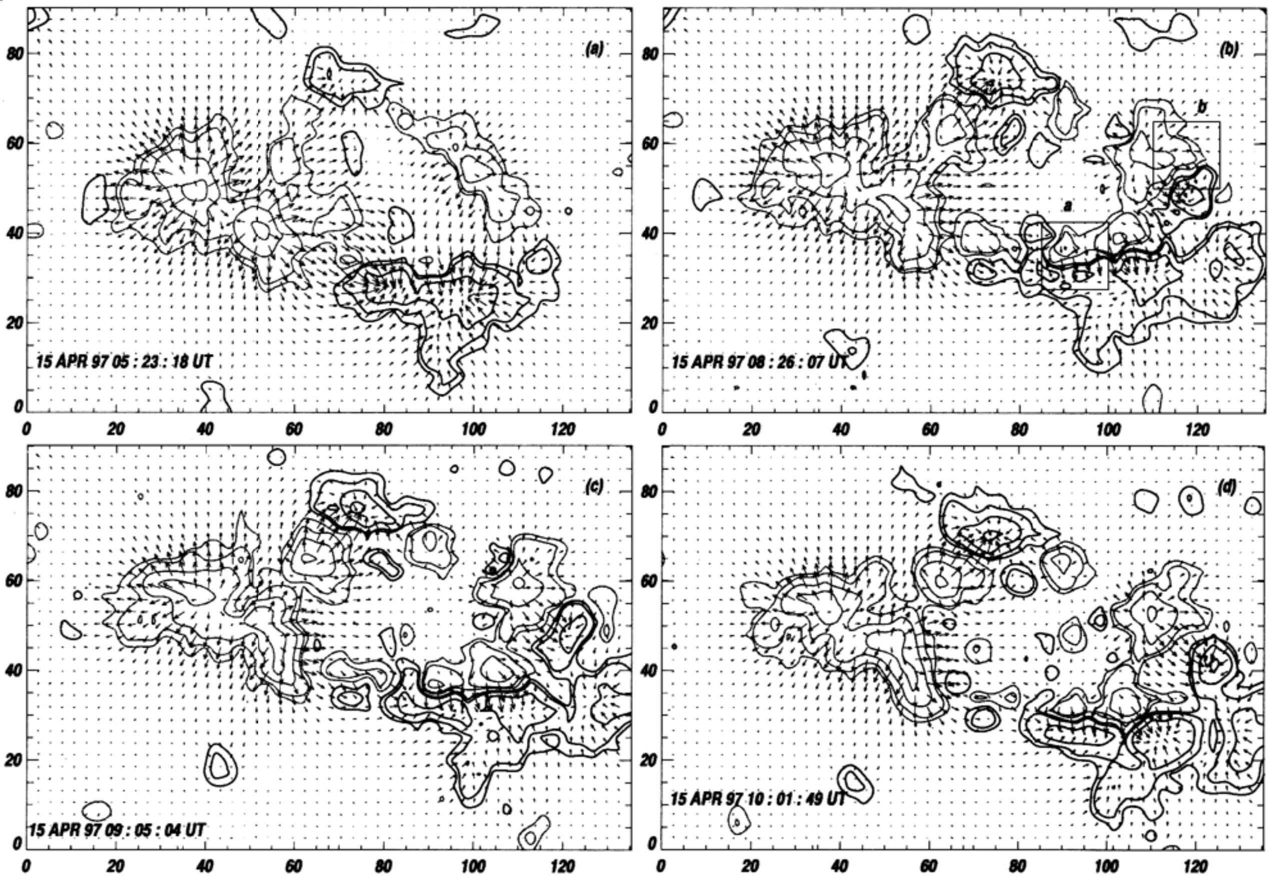

Figure 1. The evolution of active region NOAA 8032 for a time period of 05:23 UT to 10:01 UT. The contours (longitudinal field) are plotted at ±50, ±100, ±250, ±500, and ±750 G. Arrows indicate the calculated potential transverse field. The subscripts along x and y axes correspond to 10 arc-sec.

Table 1.
Location (a)

Flux in Maxwell	05:23 UT	08:26 UT	09:05 UT	10:01 UT
Positive flux	9.9×10^{16}	4.0×10^{17}	6.4×10^{17}	3.4×10^{17}
Negative flux	1.3×10^{18}	1.0×10^{18}	1.3×10^{18}	1.2×10^{18}

Location (b)

Flux in Maxwell	05:23 UT	08:26 UT	09:05 UT	10:01 UT
Positive flux	1.5×10^{18}	1.0×10^{18}	9.0×10^{17}	5.1×10^{17}
Negative flux	3.9×10^{16}	8.6×10^{17}	1.0×10^{18}	1.2×10^{18}

the opposite polarity near the locations of EFRs. This makes it difficult to obtain a measure of non-potentiality of the magnetic field structure using the loops. However it can be inferred that the system of loops connecting a simple bipolar structure evolved to a more complicated system as a result of new flux emergence in this region.

4. Conclusion

The GOES X-ray flare data showed a number of sub-flares and two C-class flares during the 89 hours of the evolution of NOAA 8032. Although no major flares were recorded in this region, continuous recurrence of sub-flares, surges, filament formation and re-orientation of structures were noticed. From the comparison of the magnetograms obtained around 05:23 UT and 08:20 UT, large changes were observed in magnetic field configuration. Due to the emergence of new magnetic flux, increase in magnetic field gradient and flux changes were observed throughout the evolution of this active region. The EFRs driven reconnection of field lines and the subsequent flux cancellation might be the reason for continuous occurrence of sub-flares and other related activities. The potential field calculation showed rearrangement of the field lines during the evolution of the active region. Similar loop formation and reorientation were also noticed in the transition region loops.

References

Kurokawa, H. 1998, *Space Sci. Rev.,* **51**, 49.
Mathew, S. K., Bhatnagar, A., Prasad, C. D., Ambastha, A. 1998, *A&AS,* **133**, 285.
Ribes, E. 1969, *Astrophys. J.,* **2**, 316.
Rust, D. M. 1972, *Solar Phys.,* **25**, 141.
Wang, J., Shi, Z. 1993, *Solar Phys.,* **143**, 119.
Wang, H., Tang, F., Zirin, H., Ai, G. 1991, *Astrophys. J.,* **380**, 282.

J. Astrophys. Astr. (2000) **21**, 237–240

Low Frequency Radio Emission from the 'Quiet' Sun

R. Ramesh, *Indian Institute of Astrophysics, Bangalore 560034, India, email: ramesh@iiap. ernet. In*

Abstract. We present observations of the 'quiet' Sun close to the recent solar minimum (Cycle 22), with the Gauribidanur radioheliograph. Our main conclusion is that coronal streamers also influence the observed radio brightness temperature.

Key words. Sun—corona—radio observations—streamers—scattering.

1. Introduction

It is well known that the appearance of the corona changes with frequency due to opacity and refraction effects. As we move towards low frequencies, the optical depth (τ) increases due to a rise in the absorption coefficient, which is inversely proportional to the square of the frequency. Therefore, the observed brightness temperature (T_b) should approach the electron temperature (T_e) of the medium (~ 10^6 K), since $T_b \approx T_e$ for large values of τ But the observed T_b at frequencies ≤100 MHz has always been low so far (Sheridan 1970; Aubier *et al.* 1971; Erickson *et al.* 1977; Sastry *et al.* 1981, 1983; Thejappa & Kundu 1992). Also, the observed peak brightness temperature varies by a factor of more than three, even during periods when the Sun is 'quiet' and free of any sunspots (Thejappa & Kundu 1992; Sastry 1994). In this paper, we discuss the effect of the streamers on the behaviour of the observed radio brightness temperature of the 'quiet' Sun at low frequencies.

2. Observations

The radio data reported were obtained with the Gauribidanur radioheliograph (GRH, Ramesh *et al.* 1998) during April–August 1997, close to the minimum of the last solar cycle (Cycle 22). The observing frequency was 75 MHz and the integration time used was 4.64 sec. The Sun was 'quiet' and no transient burst activity was noticed in our data. Table 1 shows the minimum and maximum values of the different parameters measured by us during the above period.

3. Discussions and conclusions

As scattering by smallscale (~ 100 km) density inhomogeneities is one of the major reasons attributed for low values of the observed T_b and the variations in it, one should

Table 1.

Parameter	Minimum	Maximum
Integrated flux density	7576 Jy	19283 Jy
Brightness temperature	0.25×10^6 K	0.83×10^6 K
E-W diameter	32′	51′
N-S diameter	33′	36′

expect an inverse correlation between the observed flux densities and the half-power widths (Aubier *et al.* 1971; Ramesh 1999). Fig. 1 shows the variation of the E-W diameter with the integrated flux density during our observational period, at 75 MHz. One can notice that the above two parameters are anti-correlated, indicating that scattering plays a major role in the solar corona. However, the correlation coefficient is small, ~ –0.52. The other possibility is the refraction effect due to the large scale structures in the solar atmosphere, since it is known that they contribute in a variable proportion to the observed flux of the ‘quiet’ Sun (Borkowski 1982). Fig. 2 shows the radioheliogram taken with the GRH for one of the observing days during the period mentioned earlier. The corresponding white light coronagraph picture

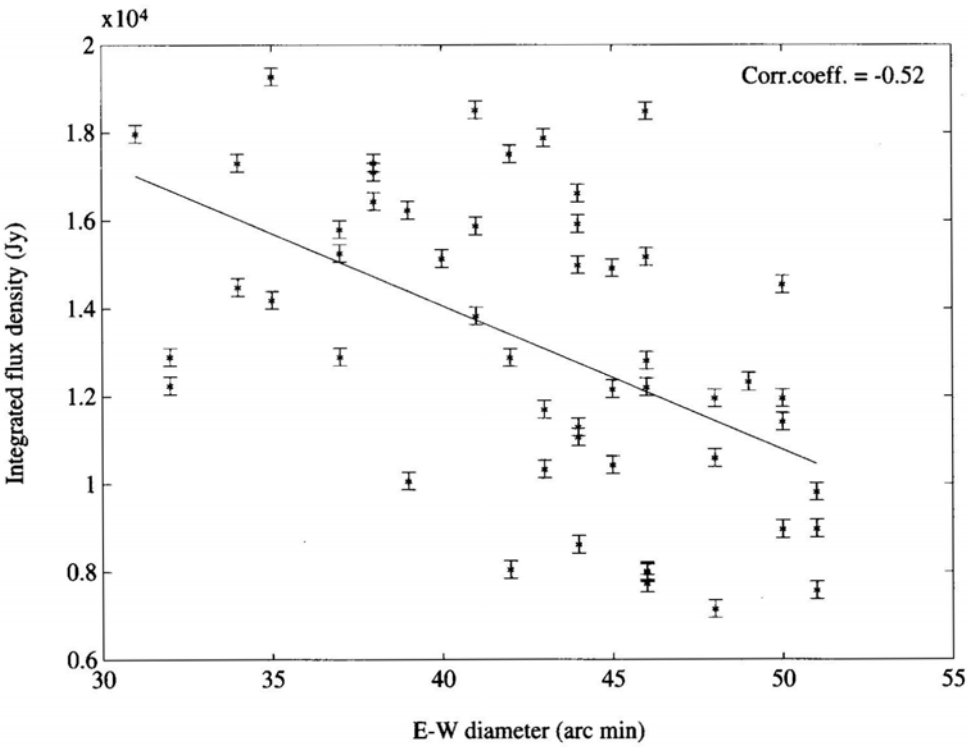

Figure 1. Variation of E-W diameter of the Sun with integrated flux density during 1997 April–August, at 75 MHz.

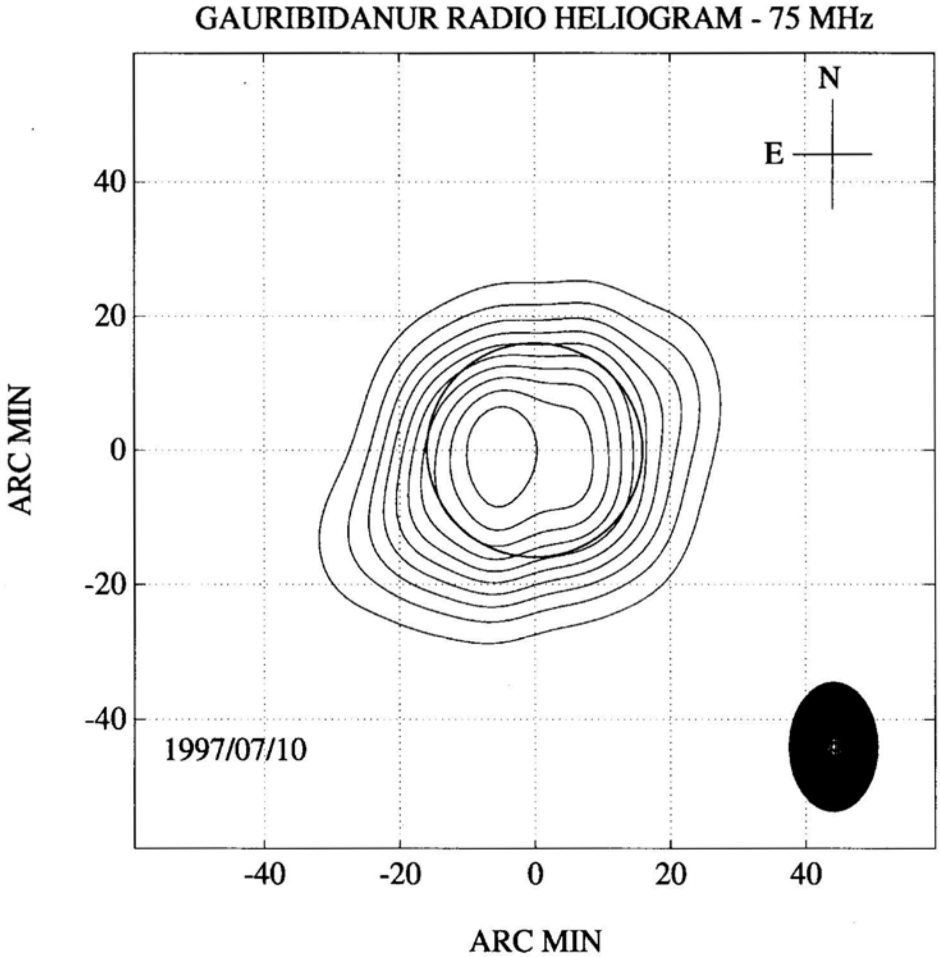

Figure 2. Radioheliogram obtained with GRH on 1997 July 10 at 06:30 UT. The open circle at the center is the solar limb and the filled circle at the bottom right corner is the beam of the instrument.

obtained on the same day is shown in Fig. 3. One can see that there is a good agreement between the elongated features off the limb in both the figures. In this connection we would like to point out that according to Thejappa & Kundu (1994), the shape of the radio corona depends on the position angle of the coronal streamers. The associated discrete source appears either as an enhancement or a depression depending on its shape and position on the disk (Riddle 1974; Thejappa & Kundu 1994). Therefore, it is possible that the variations in the integrated flux density, E-W diameter, and hence the T_b in the present case is a consequence of both scattering and the presence of coronal streamers.

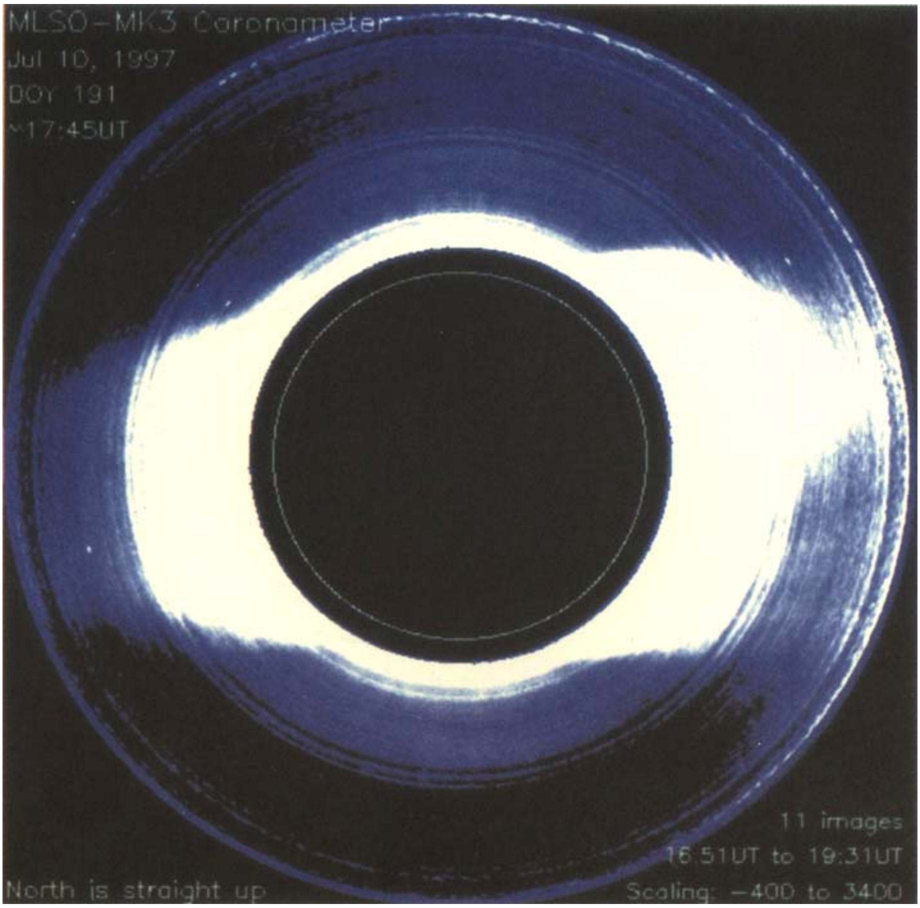

Figure 3. White light picture of the corona obtained with the Mauna Loa MKIII K-Coronameter. The occulting disk is at a height of $1.122R_{\odot}$ from the center.

References

Aubier, M., Leblanc, Y., Boischot, A. 1971, *Astr. Astrophys.,* **12**, 435.
Borkowski, K. M. 1982, *Sol. Phys.,* **81,** 207.
Erickson, W. C, Gergely, T. E., Kundu, M. R., Mahoney, M. J. 1977, *Sol. Phys.,* **54,** 57.
Ramesh, R., Subramanian, K. R., Sundararajan, M. S., Sastry, Ch. V. 1998, *Sol. Phys.,* **181,** 439.
Ramesh, R. 1999, *Ph.D. thesis,* Bangalore University.
Riddle, A. C. 1974, *Sol. Phys.,* **36**, 375.
Sastry, Ch. V, Dwarakanath, K. S., Shevgaonkar, R. K., Krishnan, V. 1981, *Sol. Phys.,* **73**, 363.
Sastry, Ch. V., Shevgaonkar, R. K., Ramanuja, M. N. 1983, *Sol. Phys.,* **87**, 391.
Sastry, Ch. V. 1994, *Sol. Phys.,* **150,** 285.
Sheridan, K. V. 1970, *Proc. Astr. Soc. Australia,* **1**, 304.
Thejappa, G., Kundu, M. R. 1992, *Sol. Phys.,* **140,** 19.
Thejappa, G., Kundu, M. R. 1994, *Sol. Phys.,* **149,** 31.

J. Astrophys. Astr. (2000) **21**, 241–244

Stokes Polarimetry at the Kodaikanal Tower Tunnel Telescope

K. Sankarasubramanian[1]*, G. Srinivasulu[1], A. V. Ananth[1] &
P. Venkatakrishnan[2]
[1]*Indian Institute of Astrophysics, Bangalore 560034, India*
[2]*Udaipur Solar Observatory, Udaipur 313004, India*
**e-mail: sankar@iiap.ernet. In*

Abstract. A Stokes Polarimeter has been developed using a masked CCD arrangement for the measurement of the vector magnetic field of sunspots. Charge shifting within the CCD is used to record near simultaneous orthogonal polarisation. The testing of the Stokes Polarimeter and the behavior of the integrated system combined with the Kodaikanal tower tunnel telescope will be discussed.

Key words. Solar polarimetry—charge shifting—vector magnetic field.

1. Introduction

Stokes spectro-polarimetric approach has been adopted at the Kodaikanal Tower Telescope (KTT) (Bappu 1967) in order to study sunspots and other active regions. The accurate estimation of vector magnetic field requires high accuracy in the polarisation measurements apart from the high spectral resolution. This can be achieved by using a two beam polarimeter (like the Advanced Stokes Polarimeter (ASP), Elmore *et al.* 1994) or by using high frequency chopping mechanism (like the ZIMPOL, Povel 1995) which eliminates seeing induced spurious polarisation signals. In an earlier attempt at the KTT (Ananth *et al.* 1994), a chopping scheme was utilised with a peltier cooled CCD detector achieving a rate of 0.5 Hz. However, this CCD had an inherent limitation on bias and flat fielding accuracies.

A new Stokes Polarimeter was designed for the KTT using a masked CCD sensor. An EEV P8603 CCD chip of size 578 × 385 pixels, is used as the sensor. The sensor array is divided into three regions using an aluminium mask of 1 mm thickness and 4 mm width which is held on to the surface of the CCD. This mask allows the central region (197 pixels) to be exposed to light and the upper and lower regions shielded from the light beam. The chopping mechanism used here is very similar to the one used by Stockman *et al.* (1982). The working principle of the Stokes polarimeter with the masked CCD and the image acquisition system has been discussed already (Srinivasulu *et al.* 1999).

2. Testing of the polarimeter

A laboratory test was carried out to look for the mis-alignments of the polarization optics used in the polarimeter. A linearly polarised collimated beam at 6302 Å is sent

Table 1. Measurement of the misalignments of the optical axis of the polaroid, QWP and the retardance error of QWP.

Component	Parameters for an ideal polarimeter	Parameters measured
QWP-Axis	45° from the slit direction	$43.0 \pm 0.3°$ from the slit direction
QWP-Retardance	90°	$95.5 \pm 0.5°$
Analyser-Axis	45° from the slit direction	$45.0 \pm 0.3°$ from the slit direction
Compensating polaroid	45° from the slit direction	$44.0 \pm 0.5°$ from the slit direction

through the polarimeter. The polarimeter consists of a rotating Glan-Thompson polariser (GTP) and an insertable quarter waveplate (QWP). Stokes Q, U and V are measured for different azimuth of the transmission axis of the input linearly polarized light. The mis-alignment in the fast axis of the QWP and the retardance error is found from the modulation in the measured V/I. The misalignment in the azimuth of the GTP's transmission axis is identified from the measured Q/I and U/I modulation. The composite Mueller matrix of the optical set up is modeled with three free parameters, viz. (a) the angular deviation of the fast axis of the QWP from the design angle (45°), (b) the angle of deviation of the azimuth of the GTP's transmission axis from 45°, and (c) the retardance error of the QWP. A non-linear least square fit is used to identify the best fit parameters with the observed data points. The parameters for an ideal polarimeter and the derived values from the best fit are compared in Table 1.

The Stokes polarimeter is then tested by integrating it with the KTT and the Littrow mount spectrograph. The response of the grating to light which is linearly polarised at different angles to the grating ruling was measured to compensate for the varying angle of the polarisation of the analysed light in the Q, U and V measurement respectively. A simple model for the grating response has been developed in order to estimate the response coefficients. Since the grating acts as a partial polariser, the output intensity can be written as,

$$I(\theta) = G_{11} + G_{12}\cos(2\theta) \tag{1}$$

where G_{11} and G_{12} are the response coefficients for the grating. The response coefficients derived after the model fit are, $G_{11} = 1.0$ and $G_{12} = 0.80$.

3. Measurement of instrumental polarisation

The instrumental polarisation of the 3-mirror coelostat system was measured with the above mentioned Polarimeter. The continuum polarisation was measured on 16th April 1999 at the disk center. We chose a continuum region near 6302 Å. Fig. 1 shows the measured data points for different observing times. The geometry of the KTT was used to calculate the theoretical instrumental polarisation using spherical trigonometry. The solid line shown in Fig. 1 is the best theoretical fit for the observed data points. The free parameters used are the refractive indices of the three mirror coating (aluminium) with an oxide layer. The oxide layer refractive index is fixed at a constant value of 1.77 and its thickness is varied. It was found that the fit is even better without the oxide layer. These observations are carried out within a few months of the mirror

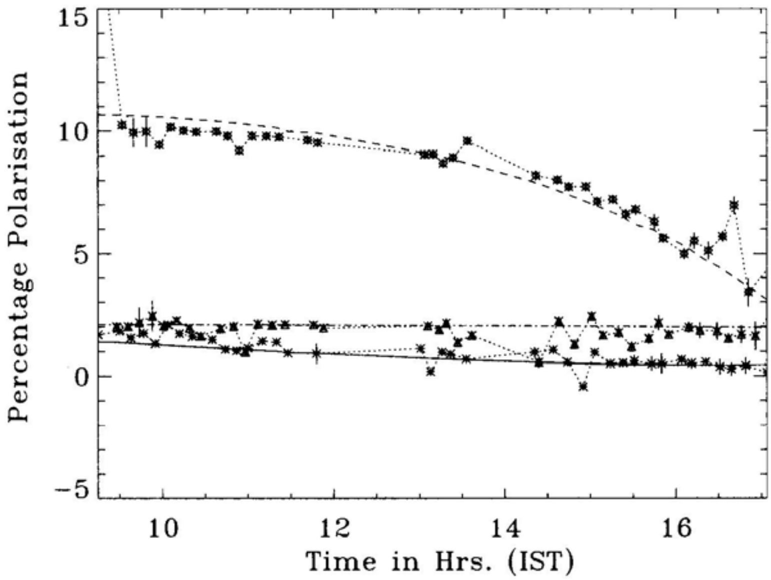

Figure 1. The measured polarisation at the disk center in the continuum for different observing time given in Indian Standard Time (IST). The star symbol is for Q/I, the diamond is for U/I and the triangle is for V/I. The solid, dashed and dot-dashed line is the best fitted model.

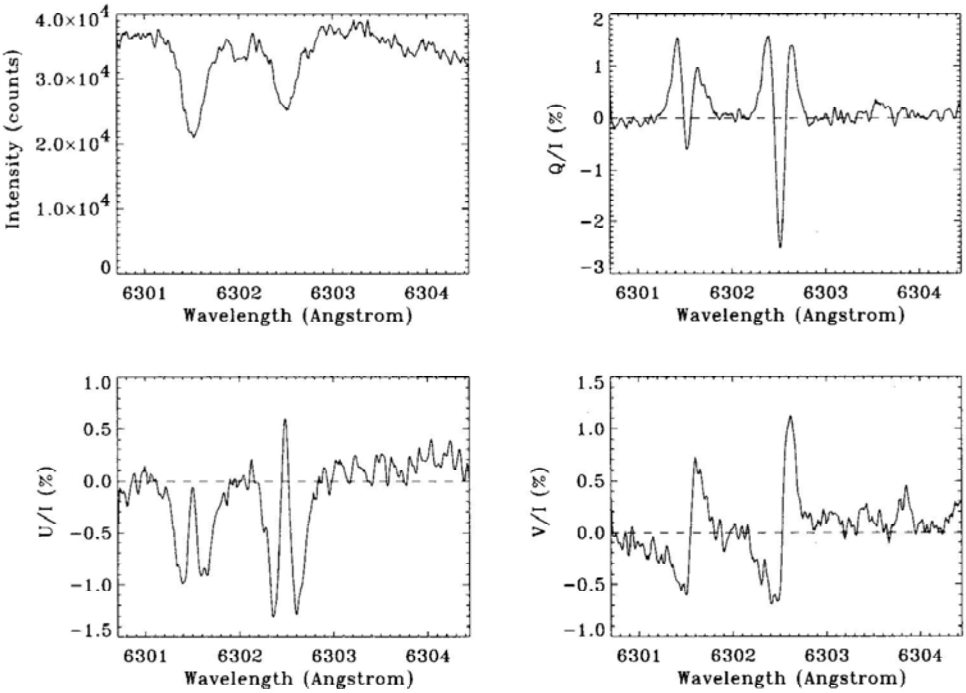

Figure 2. The Stokes profiles at a point in the umbra-penumbra boundary of the sunspot, after elimination of the telescope polarisation.

coating and hence we believe that there is not much oxide layer formed on it. The refractive index derived agreed well with the value for bulk aluminium.

Sunspot KKL21263 was observed for its vector magnetic field on 16th April 1999. The slit width used was 100μ. Fig. 2 shows the observed Stokes profiles at a point on the sunspot, after removing the polarisation introduced by the telescope. The exposure time was 1 sec and the rms noise in the continuum was about 0.3%.

Acknowledgements

We thank Mr. J. P. A. Samson, Mr. Jayavel and the mechanical staff at Kodaikanal and Bangalore for their help in mechanical design and fabrication. Mr. Devendran and Mr. Hariharan are acknowledged for their help during the observing runs.

References

Ananth, A. V., Venkatakrishnan, P., Narayanan, R. S., Bhattacharyya, J. C. 1994, *Solar Phys.,* **151**, 231.

Bappu, M. K. V. 1967, *Solar Phys.,* **1,** 151.

Elimore, D. F., Lites, B. W., Tomczyk, S., Skumanich, A., Dunn, R. B., Schuenke, J. A., Streander, K. V., Leach, T. W., Chambellan, C. W., Hull, H. K., Lacey, L. B. 1992, *SPIE,* **1746,** 22.

Povel, H. P. 1995, *Opt. Eng.,* **34,** 1870.

Srinivasulu, G., Sankarasubramanian, K., Ananth, A. V., Venkatakrishnan, P. 1999 (presented as a poster in the second international workshop on solar polarisation).

Stockman, H. S. 1982, *SPIE,* **331,** 76.

J. Astrophys. Astr. (2000) **21**, 245–247

Twist of Magnetic Fields in Solar Active Regions

Hongqi Zhang*, Lirong Tian, Shudong Bao & Mei Zhang, *Beijing Astronomical Observatory, National Astronomical Observatories, Chinese Academy of Sciences, Beijing 100012, China.*
email: zhq@sun10.bao.ac.cn

Key words. Solar active regions—solar magnetic fields.

1. Extended abstract

In the solar atmosphere, the magnetic and current helicity have played an important role in the study of twisted magnetic field. Current helicity parameter $h_{\|} = \mathbf{B}_{\|} \cdot (\nabla \times \mathbf{B})_{\|}$ and force free factor $\alpha = h_{\|} / B_{\|}^2$ can be used to analyze the distribution of twisted field (current helicity) in the photosphere (Seehafer 1990; Pevtsov *et al.* 1995; Bao & Zhang 1998). Bao & Zhang (1998) and Zhang & Bao (1999) computed the photospheric current helicity parameter $h_{\|}$ for 422 active regions, including most of the large ones observed in the period of 1988–1997 at Huairou Solar Observing Station of Beijing Astronomical Observatory.

The calculated results (Pevtsov *et al.* 1995; Abramenko *et al.* 1996; Bao & Zhang 1998) show that most current helicities in sunspot groups in the northern hemisphere show negative sign in the northern hemisphere, while positive in the southern hemisphere, which is consistent with Seehafer's result (Seehafer 1990). The distribution of current helicity parameter $h_{\|}$ in active regions also shows the butterfly pattern through the solar cycle. And, less than 30% of the active regions do not follow the general trend (Zhang & Bao 1998).

The longitudinal distribution of current helicity parameter $h_{\|}$ of active regions in both the hemispheres in the last decade was presented by Zhang & Bao (1999). We can find that the current helicities of solar active regions tend to be uniformly distributed in the different solar longitudes, but the reverse ones show a tendency to occur in some special longitudes. In these longitudes, the reversed magnetic helicities of active regions maintain some kind of coherence over a long period of time, e.g. about 20–40 solar rotation cycles (about 1.53 years).

Relationship in sign between twist parameters $h_{\|}$ and tilt angles of magnetic polarity axis have been investigated for 286 active regions in which bipolar magnetic fields are dominant from data set in the 22nd solar cycle. Fig. 1 shows the relationship in sign between tilt angles of magnetic polarity axis, that of a line joining N-S polarity with the equator (denoting writhe of an Ω-flux tube) and mean twist parameters $h_{\|} = (\mathbf{J}_{\|} \cdot \mathbf{B}_{\|})$ (denoting twist of magnetic lines in the flux tube) for the 262 bipolar active regions of which tilt angles are between –90° and 90° (Tian *et al.* 1999a, 1999b).

A positive/negative tilt is set for an active region of which the leading spot is S/N polarity and the polarity is closer to the equator in the northern/southern hemisphere. It is found that almost 60% of bipolar active regions have "normal chirality", with

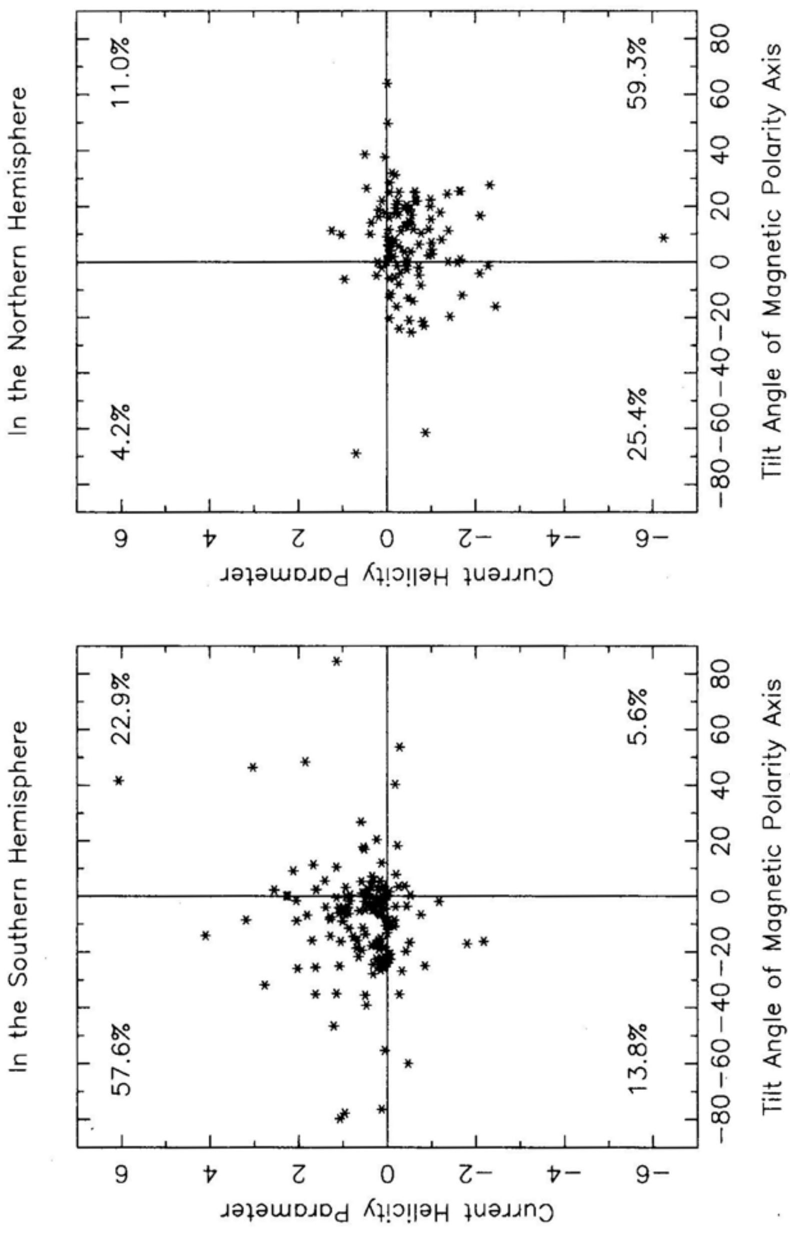

Figure 1. The relationship in sign between tilt angles of magnetic polarity axis and current helicity parameter $h_{\|}$ in the 22nd solar cycle.

magnetic fields twisted as left/right-handedness (denoted by a —/ + $h_{\|}$) in a flux tube writhed in right/left-handedness (denoted by a +/– tilt) in the northern/ southern hemisphere. But, about one-fourth of bipolar active regions have "abnormal chirality", with magnetic fields twisted as left/righth-andedness in a flux tube writhed in opposite-handedness in both hemispheres.

References

Abramenko, V. I., Wang, T. J., Yurchishin, V. B. 1996, *Solar Phys.,* **168**, 75.

Bao, S. D., Zhang, H. Q. 1998, *Astrophys. J.,* **496**, L43.

Canfield, R. C, Pevtsov, A. A. 1998, in *ASP Conf. Ser.,***140**, *Synoptic Solar Physics,* (ed.)K S. Balasubramanian, J. W. Harvey & D. M. Rabin, 131.

Pevtsov, A. A., Canfield, R. C, Metcalf, T. R. 1995, *Astrophys. J.*, **440**, L109.

Seehafer, N. 1990, *Solar Phys.,* **125**, 219.

Tian, L. R., Zhang, H. Q., Tong, Yi, Jing, H. R. 1999a, *Solar Phys.,* **189**, 305.

Tian, L. R., Zhang, H. Q., Bao, S. D. 1999b, *Astr. Astrophys.* (submitted).

Zhang, H. Q., Bao, S. D. 1998, *Astr. Astrophys.,* **339**, 880.

Zhang, H., Bao, S. 1999, *Astrophys. J.,* **519**, 876.

J. Astrophys. Astr. (2000) **21**, 249–250

The Photospheric Flow near the Flare Locations of Active Regions

Debi Prasad Choudhary, *Udaipur Solar Observatory, Physical Research Laboratory, Post Box No. 198, Badi Road, Udaipur 313001, India.*
e-mail: debi@ plume.uso.ernet.in

Key words. Active regions—magnetic field—velocity field—flare locations—shear.

Extended abstract

The observation of the photospheric velocity field along with the magnetic field is very important for understanding the origin and evolution of these locations of active regions. Earlier measurements have shown a general down flow with velocities of 0.2 to 0.3 km s^{-1} in the active regions along with few locations of upflows. The localised upflows are observed in the light bridges and emerging flux regions with different speeds (Beckers & Schroter 1969). The flow patterns of flare locations in the active regions are observed by using the tower vector magnetograph (TVM) of Marshall Space Flight Centre. The line-center-magnetogram (LCM) technique has been employed to determine the active region velocities (Giovanelli & Ramsay 1971). The LCM is based on finding the wavelength in the line profile where two opposite circularly polarised Zeeman-split components change sign. If the material in the magnetic field of different locations have relative line of sight velocities, their cross-over wavelength will be seen to be Doppler shifted. In order to use the LCM with TVM, a series of Stoke-V images are made as a function of wavelength and their cross-over wavelength at each pixel is determined. We have observed 12 active regions between June 25th and August 25th, 1998. Three of these active regions (NOAA 8253, 8264 and 8307) show flare activity associated with the flux emergence and/or changes in magnetic shear during their disk passage. The images of a selected field of view in left and right circularly polarised Zeeman components in the wavelength range of 5250.12 to 5250.30 Å are obtained at 10 mÅ steps. The time taken for obtaining one set of observations is about 10-15 minutes. In this mode of operation, the start and end wavelengths are specified and the filter is tuned at desired wavelength steps. In one observing sequence, two sets of left and right circularly polarized images are produced as a function of wavelength. These sets of images are processed and merged following a certain procedure to produce a data cube. The most important requirement for the Doppler shift measurements is the repeatability of the wavelength steps. In the recent improvement, the filter tuning was achieved with accuracy better than 0.3 mÅ by using an optical encoder. However, it has been shown that insufficient spectral resolution would lead to spurious zero-crossing shift of asymmetric Stokes-V. This effect of spectral smearing in the case of observations with TVM and the present data analysis procedure has been estimated by simulation. The individual images are flat fielded and registered in order to remove the pixel sensitivity variation

over the field of view and image motion during the observations. The two Zeeman components are subtracted to obtain a set of difference images as a function of wavelength. These processed images are merged to make Stokes-V data cubes, with two spatial and one-wavelength dimensions. The integrated Stokes-V profiles are obtained by averaging the profiles of the pixels with magnetic field values higher than a certain cut-off value depending on the noise level in each data set. These Stokes-V profiles are fitted with a synthetic profile by using the multidimensional minimization method (Debi Prasad 2000). The results obtained are listed below.

- The relative "zero-crossing" velocity between the leading and following polarity of large active regions showing the chromospheric and coronal activity are found to be ~ 70–770 km s^{-1}. The small and inactive regions show negligible Doppler velocity.
- The velocities between different sub-areas joined with the coronal loop structures vary widely. It is clearly evident in the case of NOAA 8293 that out of two following polarity spots, the velocity associated with one of them was higher. The velocities of parasitic polarities with respect to the dominant magnetic feature of same polarity are higher and blue shifted. In case of active regions NOAA 8253 and 8307, these locations were associated with high magnetic shear. Although, their counterpart on NOAA 8264 did not show magnetic shear, it displayed recurrent chromospheric activity.

References

Beckers, J. M., Schröter, E. H. 1969, *Solar Phys.*, **10**, 384.

Debi Prasad Choudhary 2000, *Solar Phys.,* to appear.

Giovanelli, R, G., Ramsay, J. V. 1971, in *Solar Magnetic Fields, IAU Sym. 43* (ed.) Howard, R. F. (Dordrecht: Kluwer Academic Publishers) p. 293.

J. Astrophys. Astr. (2000) **21**, 251–254

Solar Energetic Particle Events at the Rise Phase of the 23rd Solar Activity Cycle Registered aboard the Spacecraft "INTERBALL-2"

Vladislav Timofeev* & Sergey Starodubtsev, *Institute of Cosmophysical Research and Aeronomy, 31 Lenin Ave., 677891 Yakutsk, Russia.*
**e-mail: v. e. timofeev@ sci.yakutia. ru*

Abstract. The experiment with 10K-80 aboard the INTER-BALL-2 (which detects protons with energies >7, 27–41, 41–58, 58–88, 88–180 and 180–300 MeV) registered six events of the solar energetic particle (SEP) increase. These events are during the initial rise phase of the 23rd solar activity cycle. Solar flares with the SEP generation are accompanied by coronal mass ejection (CME). Here we analyze the dynamics of the differential energy spectrum at different phases of the SEP increase.

Key words. Solar energetic particles—coronal mass ejection—interplay-netary shock—differential energy spectrum.

1. Introduction

In recent years the paradigm to understand the events of SEP increases has been changed (Reames 1995). The SEP events are classified as the gradual and impulsive. In the first case, the energetic particles are accelerated at the point of intersection of the magnetic field lines on the surface of the shock wave formed by CME. It is important to note, that gradual events are observed in a wide range of heliolongitudes. On the other hand, the impulsive events are observed in a narrow cone of longitudes, <30°. In the present paper we analyze these two types of events.

2. Instrumentations

In this work we used the proton spectrometer data from the INTERBALL-2 satellite launched into the near-Earth orbit on August 29th, 1996. The apparatus 10K-80 registers protons in one integral channel $E_p > 7$ MeV and in five differential channels from 27 to 300 MeV.

3. Data

We describe below the six SEP events:

- **The event on November 4th, 1997** was observed associated with the active region NOAA 8100 where there was the flare X2/2B (S14W33). The maximum of brightness was observed at 0558 UT. The SOHO spacecraft registered the CME

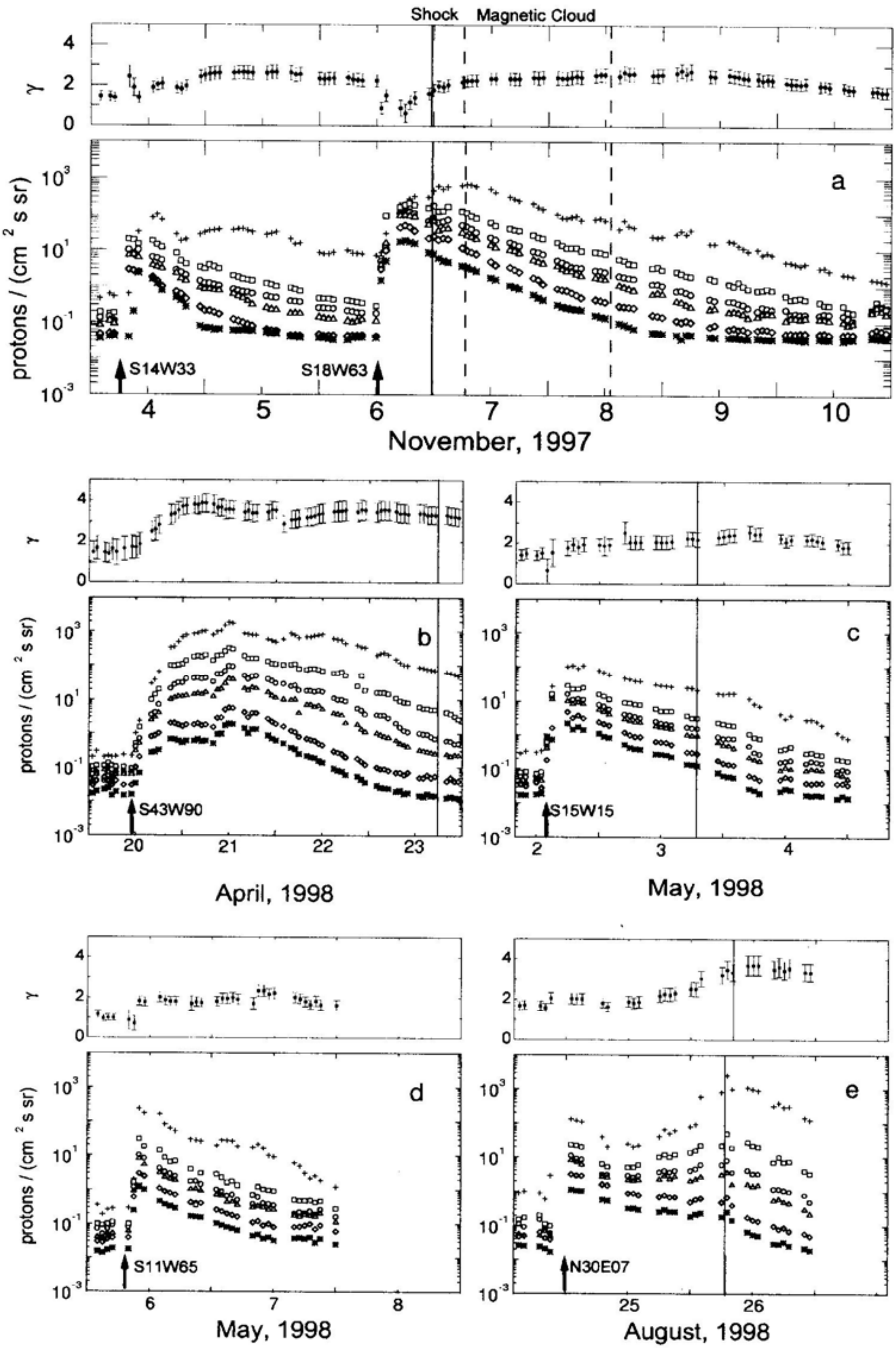

Figure 1. Temporal profiles of SEP increase from the considered solar events registered with the 10K-80 and corresponding evolution of differential energy spectra. The solid vertical lines are Shockwaves. The dashed vertical lines are magnetic cloud boundaries.

between 0552 and 0608 UT. At 0640 UT, ~ 40 min. after the flare, the 10K-80 detected the beginning of SEP intensity increase in all channels. Fig. l(a) presents times when the solar flare was observed.

- **The event on November 6th, 1997** is the largest one observed in the last nine years in the soft X-rays by many spacecrafts and which was detected with neutron monitors as GLE. The flare X9/2B was in the same active region NOAA 8100. Its coordinates were (S18W63) with a maximum intensity in H_α at 1155 UT on November 6. At that time the movement of the CME from the west limb of the Sun has been observed. About 30 min. later, a sharp increase was observed for the protons with energies from 27 to 300 MeV (Fig. l(a)).
- **The event on April 20th, 1998** is associated with the active region NOAA 8194 where the flare Ml/EPL (S43W90) with a maximum in H_α at 1021 UT followed by the CME with a velocity $V\sim$ 1000 km/s took place. One of the features of this event is that in about 40 hours the temporal profiles (Fig. l(b)) of SEP intensities have been essentially modulated, thereby both the character and the time are the same for all energetic channels. It led to the appearance of the second maximum. It appears to be connected with the interplanetary disturbance from the CME.
- **The event on May 2nd, 1998** (Fig. l(c)) is associated with the active region NOAA 8210, where the flare X1/3B (S15W15) with a maximum in H_α at 1342 UT took place, which was followed by a CME with a velocity $V \approx$ 2500 km/s. This event was detected with the neutron monitor network. The propagation time is ~ 40 min. This event is characterized by a short increase to the event maximum and a gradual decrease of the intensity for all energies.
- **The event on May 6th, 1998** (Fig. l(d)) is also associated with an active region NOAA 8210, where the flare X2 /1N (S11W65) with a maximum H_α at 0809 UT accompanied by the type IV radioburst has been taken place. This event was also detected with neutron monitors. Approximately 35 min. after the flare the sharp increase of SEP intensity in the energy region from 7 to 300 MeV started. This event is characterized by the rapid increase of the charged particle intensity to the maximum during a period of about one hour for the above energies.
- **The event on August 24th, 1998** is associated with an active region NOAA 8307 here the flare X1/3B (N30E07) with a maximum H_α at 2212 UT has taken place. This event was observed up to relativistic energies also. The temporal intensity profiles (Fig. l(e)) during the whole event have been repeatedly modulated. The modulation degree is inversely proportional to the magnetic rigidity of the charged particles. (See in detail Timofeev and Starodubtsev (1999, 2000) and references therein).

4. Discussion

Thus, it should be noted that only one event, namely that of April 20th, 1998 refers to the purely gradual events. The increase of SEP on May 6th, 1998 can be classified as an impulsive event. In our opinion, the rest events are mixed types.

The observed SEP events were accompanied by CMEs. On the boundary of these CMEs shock waves were formed, part of which reached the Earth's orbit as interplanetary shocks. In our experiment, during the initial SEP growth phase, a hard power spectrum of running particles from the shock wave was observed. (A theory of cosmic ray acceleration at the front of running shock wave was developed by Berezhko *et al.* (1988)). This spectrum monotonically increased up to the maximum value of the SEP (see Fig. 1). During the decay phase of SEP intensity, the flow isotropization was observed, and the spectrum became invariant within the experimental errors.

Acknowledgements

The authors would like to thank NOAA Space Environment Services Center and NASA GSFC for providing the solar flare and solar wind data.

References

Berezhko, E. G., *et al.* 1988, in *Generation of Cosmic Rays by Shock Waves,* (ed.) Kuzmin, A. L, (Novosibirsk: Nauka) p. 182. (in Russian)

Reames, D. V. 1995, *Adv. Space Res.,* **15**, 741.

Timofeev, V. E., Starodubtsev, S. A. 1999, *Proc. 26th* ICRC, Salt Lake City, Utah, **6,** 200.

Timofeev, V. E., Starodubtsev, S. A. 2000, *Proc. of International Symposium from Solar Corona through Interplanetary Space, into Earth's Magnetosphere and Ionosphere: Interball, ISTP satellites, and ground-based observations,* Kyiv, Ukraine, 7, 349.

J. Astrophys. Astr. (2000) **21**, 255–258

An Operator Perturbation Method of Polarized Line Transfer V. *Diagnosis of Solar Weak Magnetic Fields*

K. N. Nagendra[1,2]*, H. Frisch[2], M. FaurobertScholl[2] & F. Paletou[2]
[1]*Indian Institute of Astrophysics, Bangalore 560034, India.*
[2]*Observatoire de Iα Côte d'Azur, (CNRS/UMR 6529), BP. 4229, F06304, Nice Cedex 4, France.*
**email:knn@ iiap.ernet.in*

Abstract. We present an application of the PALI (Polarized Approximate Lambda Iteration) method to the resonance scattering in spectral lines formed in the presence of weak magnetic fields. The method is based on an operator perturbation approach, and can efficiently give solutions for oriented vector magnetic fields in the solar atmosphere.

Key words. Polarization—magnetic fields, radiative transfer—stars: atmospheres—methods: numerical.

1. Introduction

We refer to polarized spectral lines formed outside the active regions having 'weak' oriented fields ($0 \leq B \leq 300$ G) which cause de-polarization in Stokes-Q, and rotation of the plane of polarization in Stokes-U parameter of the 'resonantly scattered' line radiation. This phenomenon called 'Hanle Effect', is invoked to explain the linear polarization changes observed in lower chromospheric resonance lines such as Ca I 4227 Å, Sr 4607 Å and Sr II 4078 Å (see Bianda *et al.* 1999 for observational Hanle diagnostics). The theoretical interpretation of such data demands the solution of NLTE polarized line transfer equation, for several combinations of independent parameters.

2. Results and discussions

The details of the Hanle scattering problem are described in Nagendra *et al.* (1998, 1999). The coherent superposition of radiatively broadened Zeeman sub-states in weak fields ($\Delta\nu_L \leq \Gamma_R$), is responsible for the Hanle effect. The Stokes-V parameter is negligible in weak fields.

2.1 *The two-parameter polarization diagrams*

Determination of field parameters from observed data can be attempted with the help of 'two-parameter polarization diagrams' showing a network of *iso-strength* and

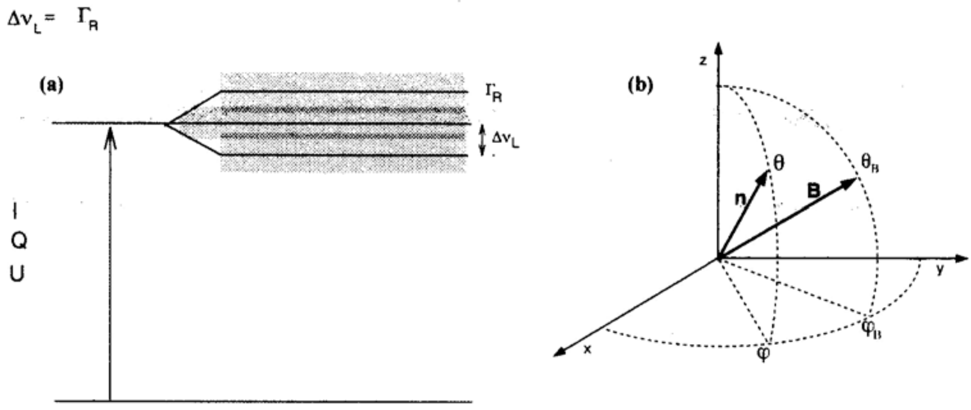

Figure 1. (**a**): Hanle effect in weak magnetic fields (B = 10 – 300 G), when ($\Delta v_L \approx \Gamma_R$). Pure Zeeman effect ($B$ = 1000 – 3000 G) corresponds to ($\Delta v_L \gg \Gamma_R$); (**b**): Geometry specifying the direction of the magnetic field **B** and of the line-of-sight **n**. Angles θ and θ_B are the co-latitudes of **n** and **B**, respectively. The azimuthal angles φ and φ_B are measured from the x-axis in an anti-clockwise direction in the xy-plane – that also represents the 1-D plane parallel slab atmosphere. The z-axis is the vertical direction. The light gray bands represent the radiative width Γ_R.

iso-azimuth curves. For a given line of sight, determined by the values of θ and φ (Fig. lb), we choose a value of θ_B and vary the two other parameters of the vector magnetic field, γ_B and φ_B. The field strength parameter is $\gamma_B = 2\pi\Delta v_L g_J/\Gamma_R$, where g_J is the Lande g-factor of the upper level with a radiative width Γ_R, and Δv_L is the Larmour frequency (Fig. la). If an observational data point (*U/I, Q/I*) falls within an interval defined by[$\Delta\gamma_B$,Δ φ_B], we get upper and lower limits on the possible values of γ_B and φ_B. This approach is useful when an independent estimate of θ_B is available. We now point out the generalization of the relevant equations in Nagendra *et al.* (1998, 1999), where the meaning of mathematical symbols in equations (1) and (2), can be found. For PRD mechanism, $\bar{\mathbf{J}}(\tau, x)$ is given by (when φ_B is constant with depth):

$$\bar{\mathbf{J}}(\tau, x) = \hat{R}(\varphi_B)\bar{\mathbf{J}}^0(\tau, x), \tag{1}$$

where $\bar{\mathbf{J}}^0(\tau, x)$ is the *reduced mean intensity* computed for the special case of field azimuth $\varphi_B = 0$. Notice that one can get the $\bar{\mathbf{J}}$ (τ, x) for an arbitrary value of φ_B , using the above equation. The corresponding line source vector is:

$$\mathbf{S}_l(\tau, x) = (1 - \varepsilon(\tau))\hat{H}_B(\theta_B, \varphi_B, B)\bar{\mathbf{J}}(\tau, x) + \mathbf{S}^{th}(\tau), \tag{2}$$

which gives the *reduced specific intensities* by application of a formal solution of the transfer equation. The iso-azimuth curves are computed by solving the Hanle transfer problem fully, for several values of γ_B . Iso-strength curves however are computed rapidly by taking advantage of the Hanle symmetry mentioned above. The polarization diagrams are easy to construct since one can express I, Q and U in terms of the six components of the 'azimuth independent reduced specific intensity vector' written as $\mathbf{I} = (I_I, I_Q, I_{+1}, I_{-1}, I_{+2}, I_{-2})^T$ (see equations (81)(83) in Nagendra *et al.* 1998).

Details of constructing the well known "two-parameter polarization diagrams" are presented in Nagendra *et al.* (1998). Exactly identical model parameters are employed

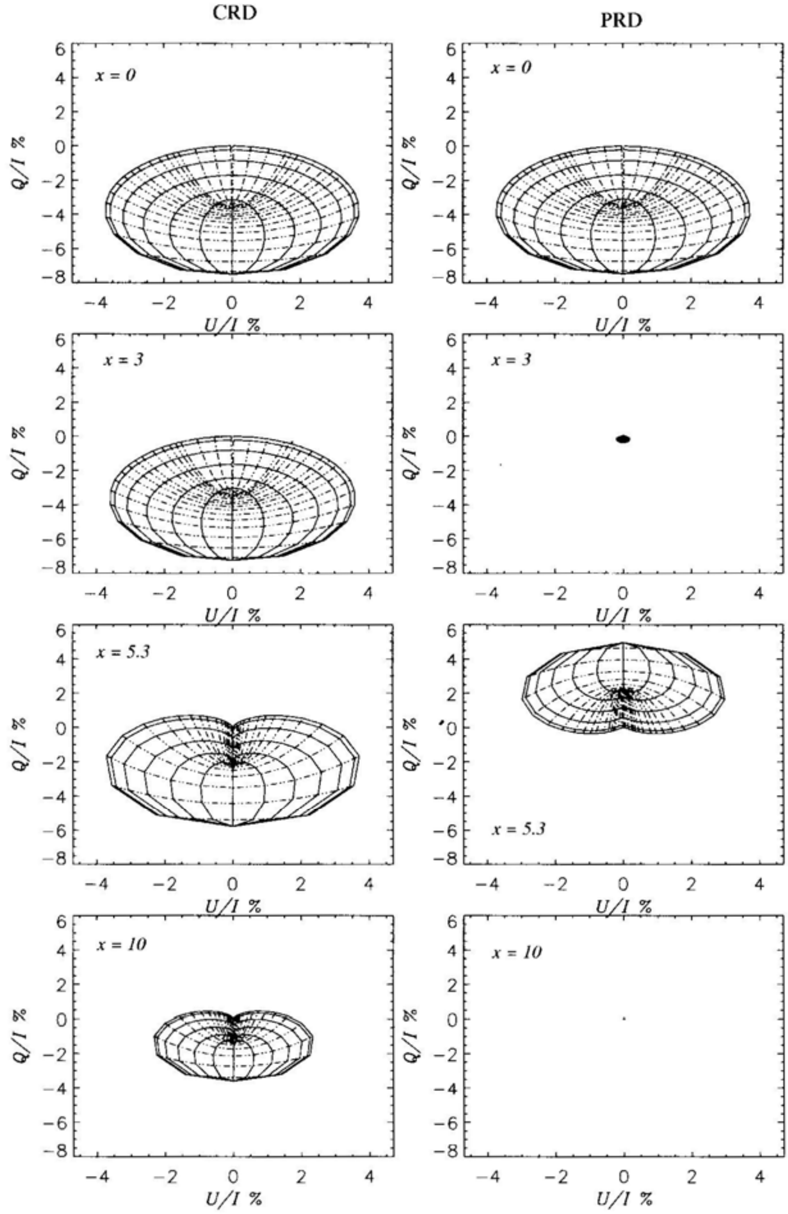

Figure 2. The twoparameter polarization diagrams for Hanle effect in an optically thin line. A comparison of CRD and PRD mechanisms is presented. The magnetic field is assumed to be horizontal (θ_B= 90°). The field strength parameter γ_B and field azimuth φ_B are independent parameters. γ_B varies from 0–100 (dashed horizontal lines moving down to up); and φ_B varies from 0-180° (solid vertical lines moving from left to right). The *iso-azimuth curves* (solid lines) are drawn by fixing φ_B and varying γ_B . The *iso-strength curves* (dashed lines) are drawn by fixing γ_B and varying φ_B. The line of sight (LOS) is fixed at (θ, φ) = (90°, 0°). The results for four frequencies x= 0,3,5.3 and 10 are presented. The iso-strength curves show the *Hanle de-polarization* and *saturation effects* clearly. The iso-azimuth curves show the effect of *rotation of the plane of polarization* when γ_B varies. Iso-azimuth curves meet at the point γ_B = 0 where (U/I = 0), and for φB = (90°, 270°), they are parallel to the (U/I) = 0 axis. The Hanle de-polarizing ability is maximum for θ_B = 90°.

in computing Fig. 15 of that paper, and the Fig. 2 in this paper. In Fig. 2, the two basic mechanisms of line scattering are considered: the *Partial Frequency Redistribution* (PRD) which is physically more realistic for resonance lines, compared to the *Complete Frequency Redistribution* (CRD). The CRD diagrams uniformly decrease in size (degree of linear polarization (Q/I, U/I)), and reach a constant level for frequencies $x > 10$. The PRD diagrams show a strong sign reversal at $x = 3$, where polarization is ≈ 0 (panel 2); become fully positive (panel 3); and reach zero polarization for large frequencies (panel 4). They follow the well known physical characteristics of CRD and PRD (see Fig. (lb) of Faurobert 1987).

3. Conclusions

The PALI is about 100 times faster than the conventional methods of solving the Hanle scattering problem. It is suitable for realistic modeling of the Hanle effect observations in spectral lines formed on the Sun. The Hanle effect is useful in exploring the spatially unresolved vector magnetic fields in a parameter space where the ordinary Zeeman effect is not practically useful.

References

Bianda, M., Stenflo, J. O., Solanki, S. K. 1999, in *Solar Polarization, 2nd SPW,* (ed.) K. N. Nagendra & J. O. Stenflo, (Dordrecht: Kluwer), ASS **243**, 31.

Faurobert-Scholl M. 1987, *Astron. Astrophys.* **178**, 269.

Nagendra, K. N., Frisch, H., Faurobert-Scholl, M. 1998, *Astron. Astrophys.* **332**, 610.

Nagendra, K. N., Paletou, F., Frisch, H., Faurobert-Scholl. 1999, in *Solar Polarization, 2nd SPW,* (ed.) K. N. Nagendra & J. O. Stenflo, (Dordrecht: Kluwer), ASSL **243**, 127.

J. Astrophys. Astr. (2000) **21**, 259–262

On the Possibility of Radio Emission from Quasi-parallel and Quasi-perpendicular Propagation of Shocks

A. Shanmugaraju[1,2] & S. Umapathy[1]
[1]*School of Physics, Madurai Kamaraj University, Madurai 625021, India*
[2]*Radio Astronomy Centre, TIFR, Ooty 623001, India*

Abstract. A set of 21 solar type II radio bursts observed using Hiraiso radio spectrograph have been analysed to study the direction of propagation of coronal shocks. A simple analysis is carried out to find the approximate angle between the shock normal and magnetic field by solving the Rankine-Hugoniot MHD relation with assumption of Alfven speed and plasma beta. From this analysis, it is suggested that both quasi-parallel shocks (favourable) and quasi-perpendicular shocks can generate type II bursts depending upon the circumstances of the corona.

Key words. Radio emission — shocks — type II bursts.

1. Introduction

The direction of propagation of shock with respect to the magnetic field is important for understanding of plasma hypothesis. It is very difficult to determine the angle by using the remote observations of solar type II radio bursts due to lack of direct knowledge about the magnetic field and the uncertainty about the location and trajectory of the source regions. Earlier attempts to resolve this issue using both theoretical as well as observational evidences contradict each other (e.g., McLean & Labrum 1985; Mann *et al.* 1995; Thejappa *et al.* 1997; Aurass *et al.* 1998)

2. Analysis of type II bursts

2.1 *Relative instantaneous bandwidth*

The relative instantaneous bandwidth of the backbone of type II bursts can be estimated from the relation, $\Delta f/f = (f_u - fi)/fi$, where f_u and fi are the upper and lower frequencies at a particular time of a type II burst (Mann *et al.* 1995). The mean relative instantaneous bandwidth for the 21 type II bursts is in the range of 0.17 — 0.7 (the fifth column in Table 1). The error in estimating this value would be 10—15% due to the diffuse edges of the backbone of type II bursts.

Table 1. List of properties of type II bursts from Hiraiso

Date	Burst time(UT)	Freq. range	$\langle f_h/f_f \rangle$	$\langle \Delta f/f \rangle$	$\langle N2/N1 \rangle$	D_f MHz s^{-1}	V^*_{shock} km s^{-1}
950203	0155 – 0214	130 – 55	..	0.28	1.90	0.25	875
950221	0328 – 0342	90 – 50	2.15	0.27	1.61	0.07	405
950313	0656 – 0711	60 – 40	1.97	0.31	1.72	0.05	517
950702	0002 – 0010	170 – 80	?	0.24	1.54	0.21	475
950702	0007 – 0017	95 – 50	2.0	0.23	1.51	0.08	437
950702	0017 – 0023	80 – 40	2.0	0.36	1.85	0.13	978
950916	2110 – 2114	50 – 30	2.0	0.34	1.80	0.05	773
951012	0306 – 0312	300 – 120	?	0.17	1.37	0.43	440
951012	0604 – 0620	350 – 50	2.0	0.48	2.19	0.50	550
951013	0504 – 0520	400 – 45	2.05	0.57	2.47	0.52	636
960422	0446 – 0449	300 – 30	1.95	0.41	2.00	0.41	603
960822	0759 – 0807	110 – 70	2.10	0.34	1.80	0.13	497
970512	0454 – 0508	80 – 30	..	0.39	1.93	0.06	525
970521	2011 – 2023	140 – 30	2.0	0.50	2.25	0.17	808
970727	2025 – 2031	130 – 35	2.05	0.34	1.80	0.25	945
970924	0248 – 0258	80 – 30	?	0.34	1.80	0.08	700
971103	0437 – 0448	260 – 55	2.0	0.60	2.56	0.40	672
971104	0559 – 0606	230 – 30	?	0.70	2.89	0.45	957
971114	0131 – 0139	100 – 40	2.10	0.43	2.07	0.13	752
980126	2228 – 2243	95 – 30	2.0	0.29	1.67	0.08	570
980127	2215 – 2218	180 – 80	2.0	0.33	1.77	0.43	930

*This estimate is based on the observed drift rate noted above and a density enhancement factor 4.

2.2 *Density jump*

From *in situ* measurements of interplanetary shock waves it was suggested that the radiating source of solar type II radio bursts is in the vicinity of the transition region of upstream and downstream region of shocks (Mann *et al.* 1995). Also the instantaneous bandwidth of solar type II radio burst is assumed to be due to the density jump. Then the relative instantaneous bandwidth of a type II burst can be related to the density jump across the shock as, $\Delta f / f = \sqrt{N_2/N_1 - 1}$, where N_1 and N_2 are the electron densities in the upstream and downstream respectively. Using this relation and the derived values of relative instantaneous bandwidth, we obtained the density jump to be in the range 1.37–2.89.

2.3 *Angle between shock normal and magnetic field*

The Alfven–Mach number represents the strength of the shock: $M_A = V_{shock}/V_A$ To start with, assuming V_A = 350 km s^{-1} (possible explanation for assuming this value of V_A is given below), the Alfven–Mach number was estimated for each type II burst to be in the range between 1.2 and 2.8.

The Rankine–Hugoniot relation relates all the quantities of shocks in both upstream (ahead of the shock) and downstream (behind the shock) regions. For an oblique shock, the Rankine–Hugoniot MHD relation is given (Priest 1982) as,

$$(M_A{}^2 - X)^2\{\gamma\beta X + M_A{}^2\cos^2(\theta)[(\gamma-1)X - (\gamma+1)]\} + M_A{}^2 X\sin^2(\theta)\{[\gamma + (2-\gamma)X]M_A{}^2 - X[(\gamma+1) - X(\gamma-1)]\} = 0 \quad (1)$$

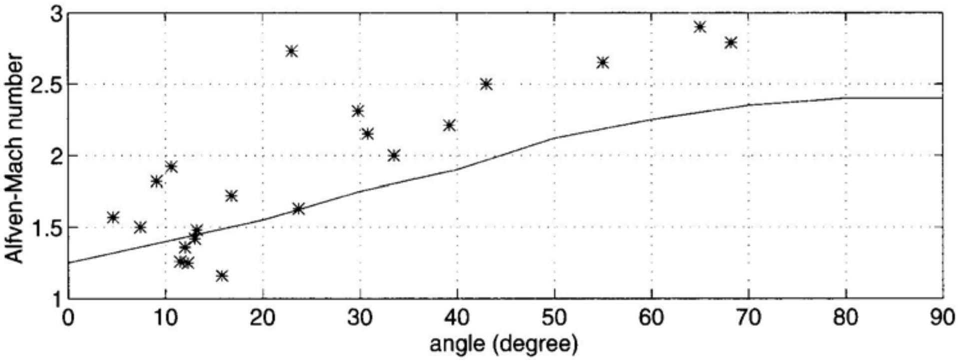

Figure 1. Plot showing the angle between shock normal and magnetic field for all type II bursts. (Please see the text for more details).

where $X= N_2 / N_1$, $\gamma = 5/3$ and β is the plasma beta. Utilizing the derived values of Alfven-Mach number and density jump and assuming a plasma beta of 0.4, the angle between shock normal and magnetic field has been determined for each type II burst using the above relation. The results are shown in Fig. 1. In this figure, the solid line is the dependence of critical Alfven-Mach number on the angle for a plasma beta = 0.4. (which was obtained theoretically by Mann *et al.* 1995). Our observations are shown by the symbol '*' which gives the derived values of Alfven-Mach number and the angle between the shock normal and magnetic field. It is apparent that many of the type II bursts (~ 18) show the angle below 45°. This means that these type II bursts may be generated by quasi-parallel shocks. Only three cases show the angle above 45° which means that they may be generated by quasi-perpendicular shocks. The spread in the Alfven-Mach number is due to the range of values of shock speed as given in Table 1.

3. Discussion

Earlier observational results have shown that the Alfven speed has a range of values depending upon the magnetic field and electron density. For example, assuming the basic plasma parameters, magnetic field B = 1G, coronal temperature $T = 2 \times 10^6$ K and electron density $N_e = 5 \times 10^{13}\ m^{-3}$ for a four-fold Newkirk's model at 60 MHz level, the Alfven speed (V_A.) and plasma beta (β) are estimated as 308 km s^{-1} and 0.4 respectively. These values are estimated using the relations V_A=2.18 × 10^{16} $B/(m_eN_e)^{1/2}$ m s^{-1} and $\beta = 3.47 \times 10^{-28}\ N_eTB^{-2}$ (McLean & Labrum 1985). A mean value of Alfven speed in the distance range 1.2 - 4$R_\odot$ where type II bursts are generated, lies between ~350 – 450 km s^{-1} (Bougeret 1985). Hence the assumption of V_A=350km s^{-1} and $\beta = 0.4$ seems to be a reasonable one in (1). The effect of variation of the parameters Alfven speed and plasma beta in the direction of propagation of shocks will be published elsewhere.

Our analyses are in agreement with Mann *et al.* (1995), Thejappa *et al.* (1997) and Aurass et al. (1998) that both quasi-parallel and quasi-perpendicular shocks are involved in the generation of type II radio emission. However, the shock normal angles estimated by using the assumption of Mann *et al* (1995) do not represent the actual values. Because, they suggested that the type II emission is originated at the transition regions and the bandwidth of the emission is a measure of density jump across the shock. But, recent spacecraft observations show that Langmuir waves occur only in the upstream regions, indicating that type II emission occurs only in the upstream regions (Lengyel-Frey *et al.* 1997; Thejappa *et al.* 1997; Bale *et al.* 1999). In any case, if the emission is assumed to occur at the fundamental, the bandwidth is determined by the spectral width of the Langmuir waves due to thermal motion of electrons, doppler broadening due to thermal motions of ions and due to the density fluctuations in the ambient plasma, not the density jump across the shock. The complexity of the processes involved is high and it may not be easy to understand all the features from solar spectrograph data alone.

Acknowledgements

We thank Dr. N. Gopalswamy, Catholic Univ. of America, and Dr. V. Balasubramanian, RAC-TIFR for useful suggestions; Dr. S. Nagai, Dr. E. Sagawa of Hiraiso, CRL, Japan and Dr. T. Kondo of KSRC, Japan for providing the data; the referee for his valuable comments.

References

Aurass, H., Hofmann, A., Urbarz, H.W. 1998, *Astr.Astrophys.*334,289.

Bale, S.D. *et al.* 1999, *Geophys. Res. Letters,* **26**(**11**), 1573.

Bougeret, J.L. 1985, in Collisionless shocks in the Heliosphere: Reviews of Current Research, AGU GN34, (eds.) B.T. Tsurutani and R.G. Stone, p. 13.

LengyelFrey, G. *et al.* 1997, *J. Geophys. Res.,* **102**, 2611.

Mann, G., Clasen, T., Aurass, H. 1995, *Astr. Astrophys.* **295**, 775.

McLean, D.J. and Labrum, N.R. (eds.) 1985, *Solar Radiophysics* (Cambridge University Press, Cambridge), 333.

Priest, E. 1982, *Solar Magneto Hydrodynamics* (Reidel, Dordrecht), p. 199.

Thejappa, G. *et al* 1997, in *Proc. 31st ESLAB Symp.,* p. 189.

J. Astrophys. Astr. (2000) **21**, 263–264

Emergence of Twisted Magnetic Flux Related Sigmoidal Brightening

K. Sundara Raman[1], K. B. Ramesh[2], R. Selvendran[1], P. S. M. Aleem[1] & K. M. Hiremath[2]
[1] *Indian Institute of Astrophysics, Kodaikanal 624103, India*
[2] *Indian Institute of Astrophysics, .Bangalore 560034, India*

Key words. Sun: Sigmoid—filament—sunspots.

Extended abstract

We have examined the morphological properties of a sigmoid associated with an SXR (soft X-ray) flare. The sigmoid is cospatial with the EUV (extreme ultra violet) images and in the optical part lies along an S-shaped H_α filament. The photoheliogram shows flux emergence within an existing δ type sunspot which has caused the rotation of the umbrae giving rise to the sigmoidal brightening.

It is now widely accepted that flares derive their energy from the magnetic fields of the active regions and coronal levels are considered to be the flare sites. But still a satisfactory understanding of the flare processes has not been achieved because of the difficulties encountered to predict and estimate the probability of flare eruptions. The convection flows and vortices below the photosphere transport and concentrate magnetic field, which subsequently appear as active regions in the photosphere (Rust & Kumar 1994 and the references therein). Successive emergence of magnetic flux, twist the field, creating flare productive magnetic shear and has been studied by many authors (Sundara Raman *et al.* 1998 and the references therein). Hence, it is considered that the flare is powered by the energy stored in the twisted magnetic flux tubes (Kurokawa 1996 and the references therein). Rust & Kumar (1996) named the S-shaped bright coronal loops that appear in soft X-rays as 'Sigmoids' and concluded that this S-shaped distortion is due to the twist developed in the magnetic field lines. These transient sigmoidal features tell a great deal about unstable coronal magnetic fields, as these regions are more likely to be eruptive (Canfield *et al.* 1999). As the magnetic fields of the active regions are deep rooted in the Sun, the twist developed in the subphotospheric flux tube penetrates the photosphere and extends in to the corona. Thus, it is essentially favourable for the subphotospheric twist to unwind the twist and transmit it through the photosphere to the corona. Therefore, it becomes essential to make complete observational descriptions of a flare from the magnetic field changes that are taking place in different atmospheric levels of the Sun, to pin down the energy storage and conversion process that trigger the flare phenomena.

In this work, we have attempted to correlate the soft X-ray and EUV brightening appeared in the active region NOAA 8688 of YOHKOH and SOHO pictures on 17th August 1999, with the corresponding features in Hα and white light photoheliograms observed at Kodaikanal. A bipolar δ type sunspot group appeared in the eastern limb on its second rotation on 14th August 1999. On 17th and 18th August, the spot had grown to its large size with a common penumbra. As a result of the successive emerging flux, the change in the orientation of the umbrae is well observed in the photoheliogram from 16th to 18th August 1999. The rotation of the umbrae within the δ type spot is calculated with respect to the rotation axis of the Sun (see Sundara Raman *et al.* 1998). The umbral structures are visible from 16th August 1999 and an umbral rotation of 16° is observed between 16th and 17th August, whereas, on the next day the rotation is only 4°. An overlying filament observed in the Hα spectroheliogram had grown in size from 16th to 17th August and appears as twisted S-shaped filament on 18th August. A coronal loop brightening is observed in a sigmoidal structure at 12.57.55 hrs UT on 17th August 1999. The observations show the occurrence of the brightening closely associated with the rotation of the umbrae, along with a corresponding development in the filament size and shape.

It can be concluded that the photospheric twist is transmitted to the filament as it is connected to the photosphere by its foot points. As a result, the geometry and structure of the filament becomes highly sheared and the overlying coronal magnetic field is observed as a sudden brightening in the sheared loop that appears in arcades spanning the S-shaped filament.

Reference

Canfield, R. C, Hudson, H. S., McKenzie, D. E. 1999, *Geophy. Res. Lett.,* **26**, 627.

Kurokawa, H. 1996 in *Magnetodynamic Phenomena in the Solar Atmosphere,* (ed.) Y. Uchida *et al,* (Dordrecht: Kluwer) p. 185.

Rust, D. M., Kumar, A. 1994, *Solar Phys.,* **155**, 69.

Rust, D. M., Kumar, A. 1996, *Astrophys. J.,* **464**, L199.

Sundara Raman, K., Selvendran, R., Thiagarajan, R. 1998, *Solar Phys.,* **180**, 331.

J. Astrophys. Astr. (2000) **21**, 265–268

Tessellation of SoHO Magnetograms

R. Srikant* & Jagdev Singh, *Indian Institute of Astrophysics, Bangalore 560034, India*
**e-mail: srik@iiap.ernet.in*

Abstract. A gradient based algorithm which divides arbitrary images into non-overlapping surface filling tiles of opposite polarity is used to study the flux and size distributions of large scale magnetic flux concentrations in solar and heliospheric observatory (SoHO) magnetograms. The mean absolute flux and size of the concentrations at the considered scale is found to be about 1.7×10^{18}Mx and 5.2Mm for both polarities. The form of the flux distribution is characterized by a skewness of $\alpha_3 = 4.9$ and a kurtosis of $\alpha_4 = 42.8$. The fall in the distribution in the range 6.5×10^{17} Mx to 5×10^{18} Mx is described by an exponential fit, in agreement with a model for the sustenance of quiet region flux.

Key words. Sun: granulation—magnetogram.

1. Introduction

The structure of magnetic flux on the solar surface is the result of the interaction of magnetic fields with the convective flows. Magnetic flux is not uniformly distributed, but, even at the scale of a few arcsecs, parcelled into flux concentrations with flux of the order of 10^{18} Mx. As a result of buffetting by granules, shear in the flow in which the concentrations are embedded, these concentrations constantly evolve by colliding, merging, cancelling and fragmenting (Martin 1990). The histogram of flux in concentrations is an effect of these processes, and can hence shed light on them. Here we describe a method to study flux concentrations statistically.

2. Data analysis

The data consists of full disk magnetograms from the Solar and Heliospheric Observatory (SoHO)/Michelson Doppler Imager (MDI) extending over 10.5 hr. A magnetogram is subjected to a procedure, whereby it is mapped into a pattern of surface filling non-overlapping tiles. In the version of the method followed by Hagenaar *et al.* (1997) and Srikanth *et al.* (2000), the local minima in the magnetogram are identified. Then, those pixels converging towards a given minimum according to the steepest descent criterion are collected into a single tile labelled by that minimum. This results in the entire image being tessellated. Fig. 1 is a result of the tessellation of a quiescent window of size 160" × 160".

Adapting the tessellation procedure to magnetograms requires a non-trivial extension in order to take into account the bipolarity of magnetic fields. The new method

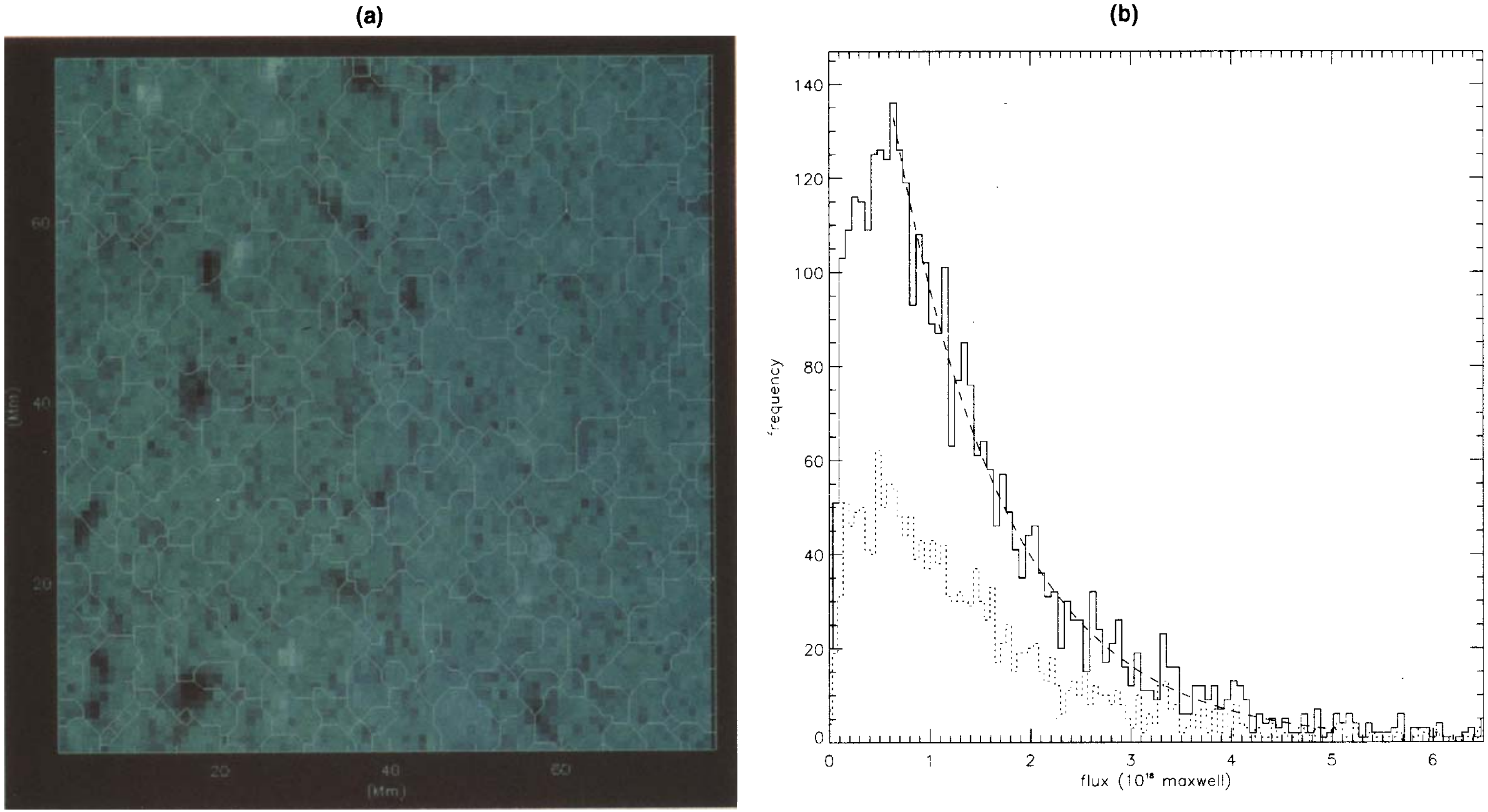

Figure 1. (**a**) Tessellation of a magnetogram window, with tiles enclosing positive and negative flux regions; when two same-signed extrema occur close to each other, the tile boundary apparently cuts through concentrations; (**b**) Histogram of the flux concentrations; the large histogram represents the combined flux values for both polarities, with an exponential fit indicated in the range 0.64×10^{18} to 5×10^{18} Mx. The smaller dotted histogram represents positive polarity flux concentrations.

consists in doubly tessellating the image: first, to determine the local minima and their associated tessellation according to steepest descent; and second, to determine the local maxima, and analogously their associated tessellation via ‘steepest ascent’, wherein the locus of a point is along the direction of the highest positive gradient. The part of the image covered by negative valued pixels in the first tessellation describes the discontinuous system of negative flux concentrations. Its exact area and flux complement is given by the part of the image covered by the positive valued pixels in the second tessellation. It might appear, at first, that the tessellation could be used to tile supergranules, given that supergranular outflows concentrate relatively large (mixed polarity) fields at their boundaries. However, this is thwarted by the discrete character of the flux. The tiles that constitute the tessellation are interpreted as flux concentrations. Their boundaries are neutral lines where the field changes sign.

Two advantages of the present method: (1) In the related work of Schrijver *et al.* (1997), the total flux of the concentrations is determined assuming the net flux as being three times the core flux. No such (possibly model dependent) assumption is made here. The total flux is obtained by integrating the absolute field over the tile; (2) We have a direct handle of the size of the concentrations, which can be used for geometric modelling of the latter.

For the present study, a total of seven such windows spanning about 10.5 hours of data were used. A total of 3559 tiles were obtained by the double tessellating procedure, with 1775 and 1784 tiles carrying negative and positive flux, respectively. Both temporal averaging and spatial smoothing of magnetograms increase the mean size of the observed tiles, by suppressing small-scale and short-term fluctuations (Srikanth *et al.* 2000).

3. Results

Fig. l(b) is the histogram of the tiles obtained from the double tessellation of SoHO magnetograms. The bold outline represents the combined graph for both polarities. The other represents the positive polarity taken separately. The distribution peaks around 6.4×10^{17} Mx, in agreement with the value obtained by Schrijver *et al.* (1997) for core fluxes, and not incompatible with that of Wang *et al.* (1995). The flux distribution function of the tiles is characterized by its skewness (α_3) (asymmetry) and kurtosis (α_4) (peakedness) given by:

$$\alpha_m = \frac{1}{n\sigma^m}\left(\sum_i (x_i - \bar{x})^m\right) \tag{1}$$

where σ is standard deviation. The mean flux, mean size, skewness and kurtosis for the positive, negative and combined flux concentrations are given in Table 1.

The mean absolute flux value of 1.7×10^{18}Mx, confirms earlier estimates. The larger mean compared to the mode of the distribution is reflected in the positive skewness of the flux distribution. As expected, the characteristics of the distribution are similar for both polarities. The mean size of the concentration emerges at about 5 Mm, suggesting that the tiles may be identified with large network elements. This somewhat large value, and its closeness to mesogranular size (Ploner *et al.* 2000), are points that merit further investigation. This size implies a mean flux for the quiet region of about 2.2 gauss (LaBonte & Howard 1980).

Table 1. Mean tile flux, size, and skewness and kurtosis of flux distributions of positive, negative and combined flux concentrations from SoHO magnetograms.

Type	Mean abs. flux	Mean size	Skewness	Kurtosis
Positive	1.7×10^{18} Mx	5.3 Mm	4.8	42.2
Negative	1.6×10^{18} Mx	5.1 Mm	5.0	43.3
Combined	1.7×10^{18} Mx	5.2 Mm	4.9	42.8

4. Discussion and conclusions

We find that an exponential fit well describes the fall in the distribution function in Fig. l(b) in the range between 6.4×10^{17} and 5×10^{18} The exponential character extends below the 10^{18} Mx point noted by Schrijver *et al.* (1997). According to their empirical model for the dynamics and sustenance of flux in quiet regions, this supports the scenario that flux concentrations are subject to fragmentation and that re-emergent flux is not entirely derived from previously cancelled flux. New flux from ephemeral regions accounts for the remaining flux required to sustain the quiet network. For values of flux smaller than 10^{17}, the noise in the data (about 2.5×10^{16} Mx per pixel) renders small magnetic concentrations unobservable. The turn-down from the exponential fit is, therefore, perhaps an artifact of the data, rather than intrinsic to the magnetic flux.

The present method can help us look for possible clustering properties among like-polarity concentrations. In future work, we will relate the large value of the kurtosis of the flux distribution to the flux-size relation, and hence, derive a geometrc model of the concentrations.

Acknowledgements

We thank Dr. P. H. Scherrer and the SoHO consortium for providing us with the MDI/ SOI magnetogram data.

References

Hagenaar, H. J., Schrijver, C. J., Title, A. M. 1997, *Astrophys. J.,* **481**, 988.

LaBonte, B. J., Howard, R. 1980, *Sol. Phys.,* **80**, 15.

Martin, S. F 1990, in *Solar Photosphere: Structure, Convection, and Magnetic Fields, IAU Symp. 138,* (ed) Stenflo, J. O. (Dordrecht: Kluwer) 129.

Ploner, S. R. O., Solanki, S. K., Gadun, A. S. 2000, *Astron. Astrophys.,* **356**, 1050.

Schrijver, C. J., Title, A. M., Ballegooijen, A., Hagenaar, H. J., Shine, R. 1997, *Astrophys. J.,* **481**,424.

Srikanth, R., Singh, J., Raju, K. P. 2000, *Astrophys. J.,* **534**, 1008.

Wang, J., Wang, H., Tang, F, Lee, J. W., Zirin, H. 1995, *Sol. Phys.,* **160**, 277.

J. Astrophys. Astr. (2000) **21**, 269

Parametric Study of Molecular Line Polarization in the Solar Atmosphere

K. E. Rangarajan* & D. Mohan Rao, *Indian Institute of Astrophysics, Bangalore 560034, India.*
**email: rangaraj@iiap.ernet.in*

Key words. Molecular polarization—scattering—radiative transfer.

1. Extended abstract

The polarimetric observations of the quiet sun show linear polarization in molecular lines of C_2, MgH, etc. The molecular lines are very faint in the intensity spectrum. Q branch transitions of MgH are considered in this study. Using radiative transfer calculations, we find that the intensity and polarization profiles of MgH lines can be matched for a range of inelastic collisional rates (Γ_1) and depolarizing elastic collision rates ($D^{(2)}$) of the transitions in solar atmosphere. It is shown that the physical constraints imposed on these parameters can be used to estimate them. This procedure also allows us to get the oscillator strength (f). It is found for the strong line 5156.652 Å, $f = 0.12$, $\Gamma_1 = 5.59 \times 10^7$ sec^{-1} and $D^{(2)} = 1.29 \times 10^8$ sec^{-1}. Most of the other lines observed are weak by a factor of 3 in intensity compared to the 5156.652 Å line but show a polarization value of the order of 0.08%. One such typical line is 5156.997 Å. This line can be fitted for the parameters $f = 0.04$, $\Gamma_1 = 1.22 \times 10^7$sec^{-1} and $D^{(2)} = 2.95 \times 10^7$ sec^{-1}.

J. Astrophys. Astr. (2000) **21**, 271–274

Relationship of Non–potentiality and Flaring: Intercomparison for an M–class Flare

Ashok Ambastha* & Shibu K. Mathew, *Udaipur Solar Observatory, Physical Research Laboratory, Udaipur-313 001, India*
**email* : *ashok@uso.ernet.in*

Abstract. We have made an attempt to obtain relationship of magnetic shear and vertical currents in NOAA AR7321. Intercomparison of changes observed at several flaring and non-flaring sites associated with an M4/2B flare observed on October 26, 1992 is reported.

Key words. Magnetic shear—electrical current—flare.

1. Introduction

The source of flare energy is believed to be in the form of excess energy stored in non-potential magnetic structures. One may expect to detect measurable flare related changes in magnetic field. Non-potentiality in active regions is generally described by angular or magnetic shear, electric currents, magnetic helicity or force-free parameter (Hagyard 1990; Canfield *et al.* 1993). Basic input for calculating these parameters is accurate, high spatial and temporal resolution, and multi-layer measurement of solar vector magnetic field. So far, this has been difficult to achieve to the desired accuracy. There remain difficulties in interpreting the results due to both solar and non-solar reasons. To redress the problem, quantitative descriptions based on averaging of non-potentiality parameters over an area-of interest have been suggested. A bewildering variety of flare-related changes have been reported, which include increase, decrease, or no change during flares (Ambastha, Hagyard, & West 1993; Wang H. 1992, 1997; Wang J. *et al* 1996; Hagyard, Stark & Venkatakrishnan 1999). There seems to be no direct relation of the strength of shear with the class of flare. Considering the importance of the problem, careful search for flare related changes is needed for large number of active regions in order to establish the results. No significant contribution to the magnetic energy is expected to come from areas of an active region where the longitudinal component $B_z = 0$, or $B_t \sim 0$ (Forbes 1993). Therefore, an areal averaging over the region between the umbra and the polarity inversion line should hopefully provide measurable changes. Also, H_α flare-ribbons form near the foot points of the magnetic fleldlines along which magnetic energy release takes place. A search for any flare-related change in non-potential index may be promising near flare-ribbons.

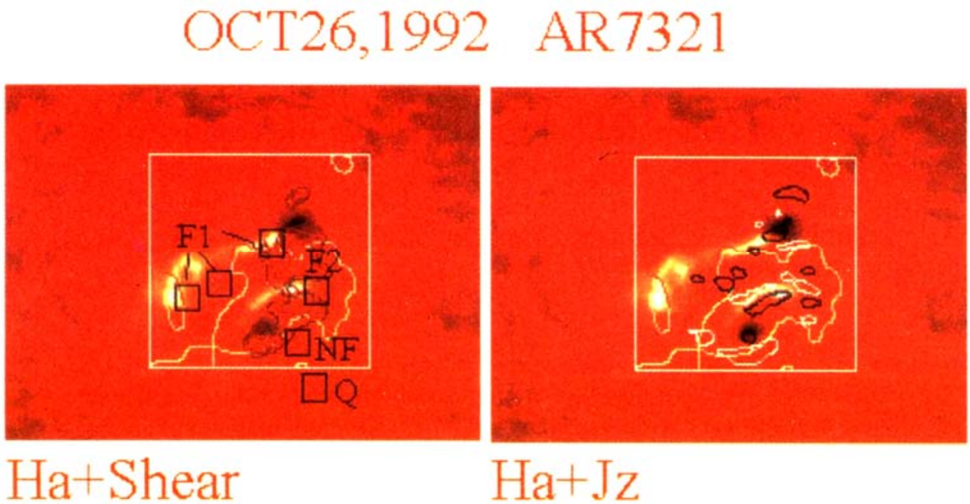

Figure 1. Overlays of shear and vertical currents J_z on H_α filtergrams of NOAA AR7321 on October 26, 1992/14:56 UT

2. Quantitative measure of magnetic non-potentiality and the observational data

We have made magnetic shear $\omega = B_t \times |\theta_{obs} - \theta_{pot}|$, and vertical current density $J_z = \frac{1}{4\pi}(\nabla \times \vec{B})_z$ maps for their comparison. Here θ_{obs} and θ_{pot} are azimuth angles of the observed and potential transverse fields. Overlays of these maps and co-temporal H_α filtergrams show the spatial correlation of flaring locations with shear and currents at 14:56 UT, i.e., before the flare onset (Fig. 1). However, it is usually rather difficult to identify changes in angular shear $|\theta_{obs} - \theta_{pot}|$ occurring at pixel level during the evolution of the flare because – (i) flare related changes in B_t (both in its magnitude and azimuth) are expected to be rather small, (ii) errors in B_t measurements are large, (iii) both solar and non-solar effects introduce ambiguities, and (iv) angular shear depends on the method of the calculated potential field.. Telescope tracking errors and atmospheric changes add further contamination to the data. Due to these difficulties, it is advantageous to use area-averaged shear parameter, which improves the signal-to-noise ratio, and provides a quantitative index. However, the precise location of changes is lost in the process of the spatial averaging. Also, the source of change becomes difficult to identify, i.e., whether the observed change in non-potentiality corresponds to a change in the magnitude of B_t, its azimuth θ_{obs}, or both. Area-averaging may be carried out over the spatial scale of the entire active region, giving the magnitude of non-potentiality for the active region, but any flare related changes occurring at much smaller spatial scales get suppressed. Therefore, it is desirable to select a suitably small area near the flare site. Further, it is important to have simultaneous high quality vector magnetograms and H_α filtergrams over the period of the flare.

We have analysed the vector magnetograms obtained for the active region NOAA7321 on October 26, 1992, obtained from the NASA Marshall Space Flight Center (MSFC). The active region underwent a rapid change in magnetic configuration and produced several flares from its birth on October 24, 1992, till the disappearance behind the western limb on November 2, 1992. A M4/2B flare was

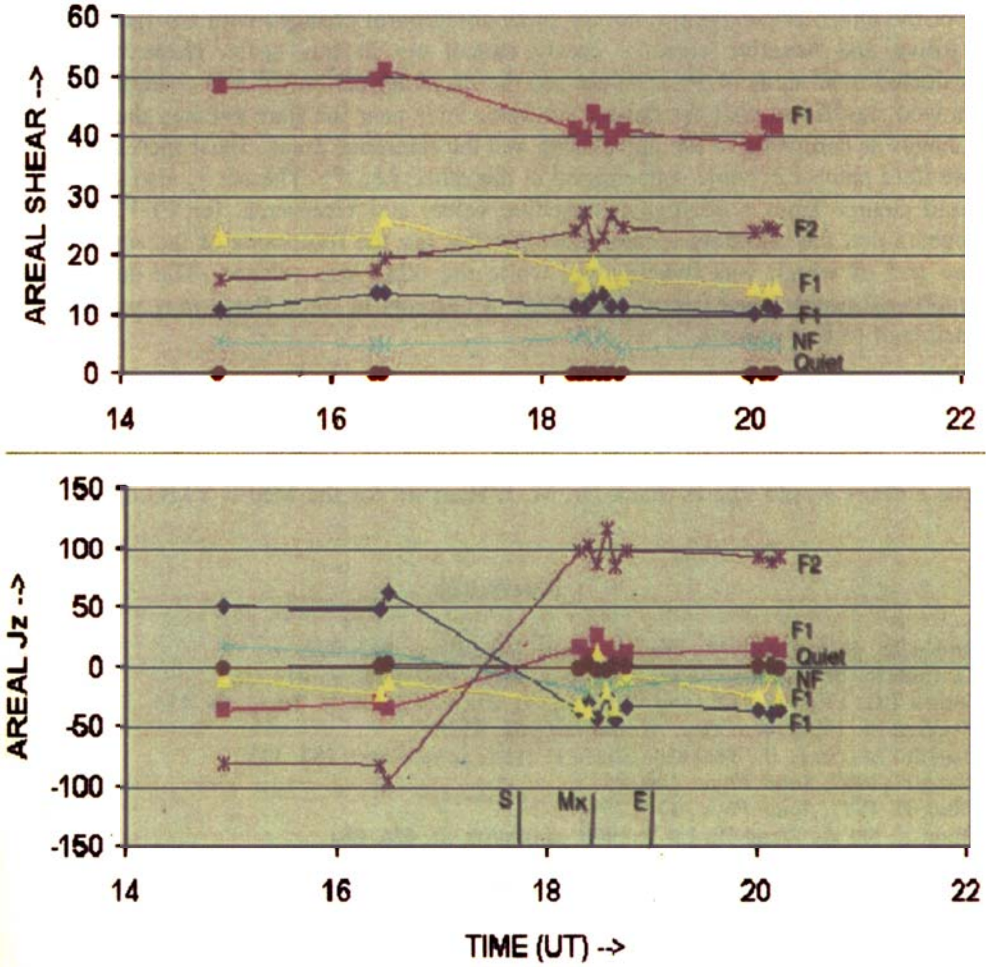

Figure 2. Time evolution of area-averaged shear and current indices.

observed on October 26, 1992/17:4518:34 UT in this active region at the location S21W18. Using the magnetograms available before, during, and after this flare, we have obtained the time profiles of the area-averaged shear and vertical current indices for certain sites near a reference quiet area, flaring (Fl and F2) and non-flaring (NF) locations (Fig. 2). Flare start, maximum phase and end time are marked on the time axis.

3. Results and conclusions

The shear and J_z maps of NOAA7321 show that the sites of large shear and currents generally correspond with locations of H_α flare patches, however, J_z appear to have a closer relationship. Some flare-ribbons are seen in areas having low or no shear, but they appear to be linked to remote sites of strong shear through loop structures, as inferred from the H_α filtergrams. Area-averaged shear and vertical current, obtained over the entire active region, do not show cotemporal changes with the flare, as the positive and negative currents nearly cancel out at this scale. However, when evaluated over areas of 30×30 arc-sec the carefully calibrated and coaligned maps showed significant changes during the flare. Sites near the flare patches show larger changes as compared to the non-flaring and the reference areas. Shear increased near one flare patch F2, while it decreased in the other, i.e., Fl. The net J_z also showed a rapid change from a positive to negative value, and vice-versa, for F1-F2 pair. It appears that the remotely located flare-patches are the footpoints of the same loop; one end of which was twisting up, while the other was relaxed. The conflicting reports of increase and decrease in shear or currents in some flares may perhaps be attributed to this process.

Acknowledgements

The authors would like to thank Dr. M. J. Hagyard for the MSFC VMG data.

References

Ambastha, A., Hagyard M., West E. 1993, *Solar Phys.,* **342,** 917.
Canfield R., de La Beaujardiere J.-F., et al. 1993, *Astrophys. J.,* **411**, 362.
Forbes T.G. 1993, in *ASP Conf, Ser. ,* (ed.) H. Zirin, G. Ai & H. Wang, **46**, 415.
Hagyard M. 1990, *Mem. Soc. Astron. Ital.,* **61**, 337.
Hagyard M, Stark B., Venkatakrishnan P. 1999, *Solar Phys.,* **184,** 133.
Wang H. 1992, *Solar Phys.,* **140,** 85.
Wang H. 1997, *Solar Phys.,* **174**, 265.
Wang J., Shi Z., Wang H., Lu Y. 1996, *Astrophys. J.,* **456**, 861.

J. Astrophys. Astr. (2000) **21**, 275–282

Properties of Flux Tubes and the Relation with Solar Irradiance Variability

M. Fligge[1] & S. K. Solanki[2]
[1] *Institute of Astronomy, ETH Zentrum, 8092 Zurich, Switzerland.*
[2] *Max-Planck-Institut für Aeronomie, D-37191 Katlenburg-Lindau, Germany,*
e-mail: fligge @ astro, phys. ethz. Ch

Abstract. At the solar surface the magnetic field is bundled into discrete elements of concentrated flux, often referred to as magnetic flux tubes, which cover only a small fraction of the solar surface. Flux tubes span a whole spectrum of sizes, ranging from sunspots to features well below the best currently obtainable spatial resolution.

Whereas sunspots have been well studied, our knowledge of the true brightness of small-scale magnetic features is hampered by the insufficient spatial resolution of the observations. A better understanding of the thermal and magnetic properties of these small-scale features, however, is crucial for an understanding of (climate-relevant) long-term solar irradiance variations.

Key words. Irradiance—flux tube—sunspot—plage.

1. Solar irradiance variations

Space-borne measurements of solar irradiance reveal a remarkably inconstant Sun with variations on time-scales of minutes up to the length of the solar cycle. Most prominent is a 0.1% increase of total irradiance in phase with the solar activity cycle. While sunspots and active region faculae dominate solar irradiance variations on time-scales of days to months (Fig. 1), the active network is also an important contributor to the long-term variations on the solar cycle time-scale.

Sunspots have been studied relatively well. Their large-scale magnetic field structure is rather simple and the temperature is close to that expected from radiative equilibrium (Severino *et al.* 1994; Del Toro Iniesta *et al.* 1994). Based on these simplifications, the influence of sunspots on solar irradiance can be modelled relatively accurately (Foukal 1981; Hudson *et al* 1982; Fligge *et al.* 1998, 2000). In contrast, our knowledge of the true brightness of small-scale magnetic features composing the faculae and active network is still very incomplete. Observations of these features are challenging and hard to perform due to their complex morphology (Fig. 2) and the low contrast relative to the quiet Sun. Their brightness signature depends on many factors such as limb distance, averaged field strength, wavelength or spatial resolution of the observations (see Solanki 1993, for an overview). The contribution of small-scale magnetic features to solar irradiance changes is one of the largest unknowns in present irradiance reconstructions — especially on time-scales of the solar cycle.

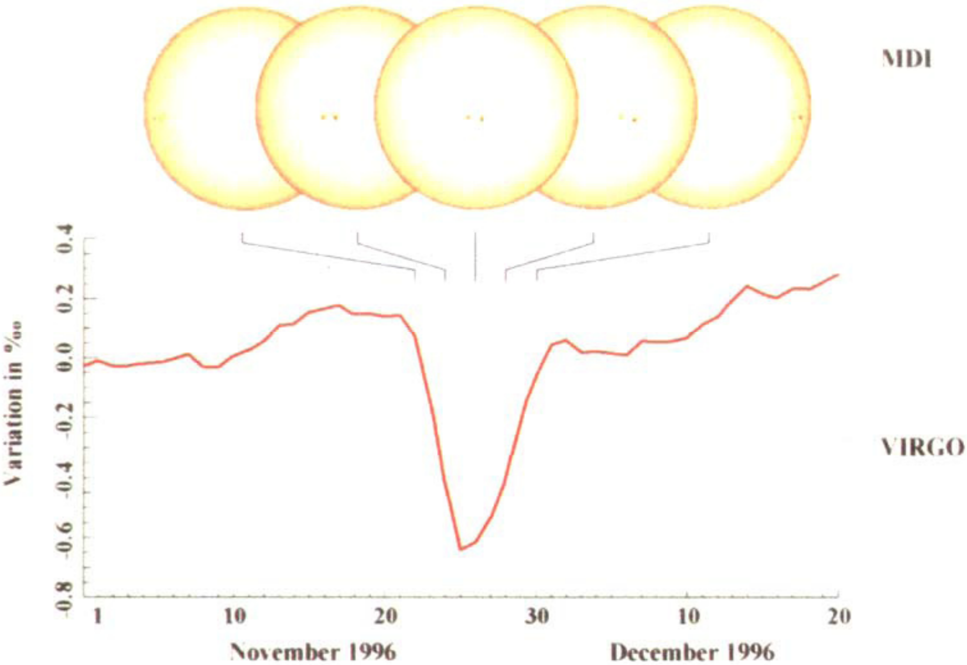

Figure 1. Top: A series of MDI continuum intensity images illustrating the passage of a spot dominated active region across the solar disc at the end of 1996. **Bottom:** Simultaneously recorded values of total irradiance variations measured by VIRGO. The dark spots show up as a distinct dip in the solar irradiance record.

2. Basic properties of flux tubes

At the solar surface the magnetic field is bundled into discrete elements with field strength of the order of 1 kG. The physical properties of these magnetic elements are generally interpreted using the framework of magnetic flux tubes (Spruit 1981; Solanki 1993).

At photospheric heights, the kinetic energy of the gas inside the flux tube is comparable to the energy of the flux tube's magnetic field. The magnetic field, therefore, inhibits the convective energy transport within the flux tube and attenuates the heat flux from below; the flux tube is cooled. In addition, the internal gas pressure is reduced to preserve the pressure equilibrium between the inside of the flux tube and its surrounding, leading to a lowering of the $\tau = 1$ level within the flux tube (Wilson depression, Fig. 3). As a result deeper layers become visible. The walls of the flux tube below the external $\tau = 1$ level are hot due to the rapid rise in temperature with depth.

For small (optically thin) flux tubes the radiative inflow through the hot walls is able to significantly heat up the middle and upper parts of the flux tube's photosphere making these layers hotter than in the quiet Sun (Grossmann-Doerth *et al.* 1989). This leads to an increased contrast within spectral lines compared to the continuum (Frazier 1971) — something which is also seen in MHD models of the solar photo-sphere (Fig. 4, Gadun *et al* 2000). As the diameter and, thus, the optical thickness of

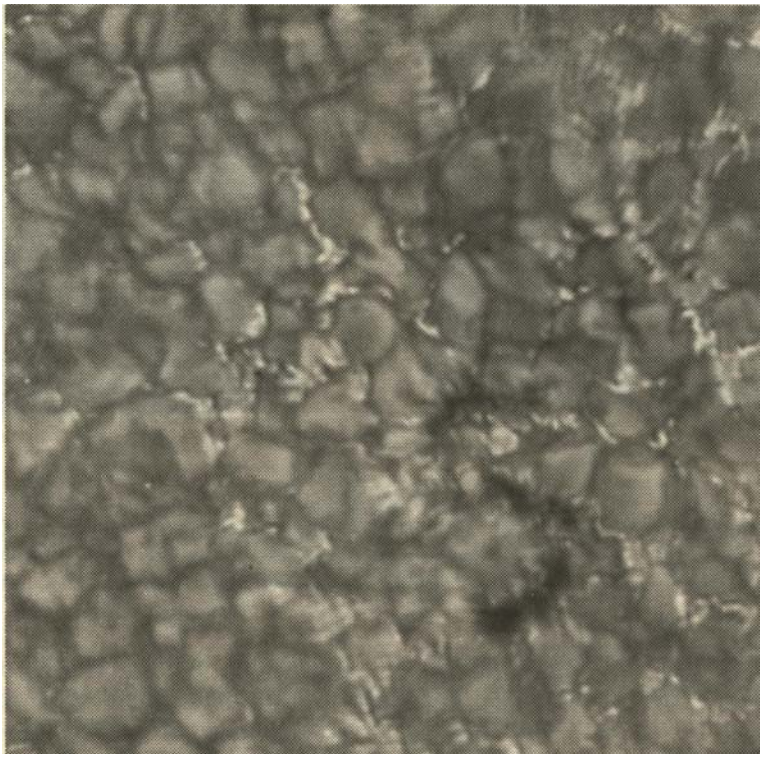

Figure 2. High resolution g-band (430.5 nm) image of an active network region. The bright points along the intergranular lanes mark the presence of small-scale magnetic features. (Courtesy of NSO/KP).

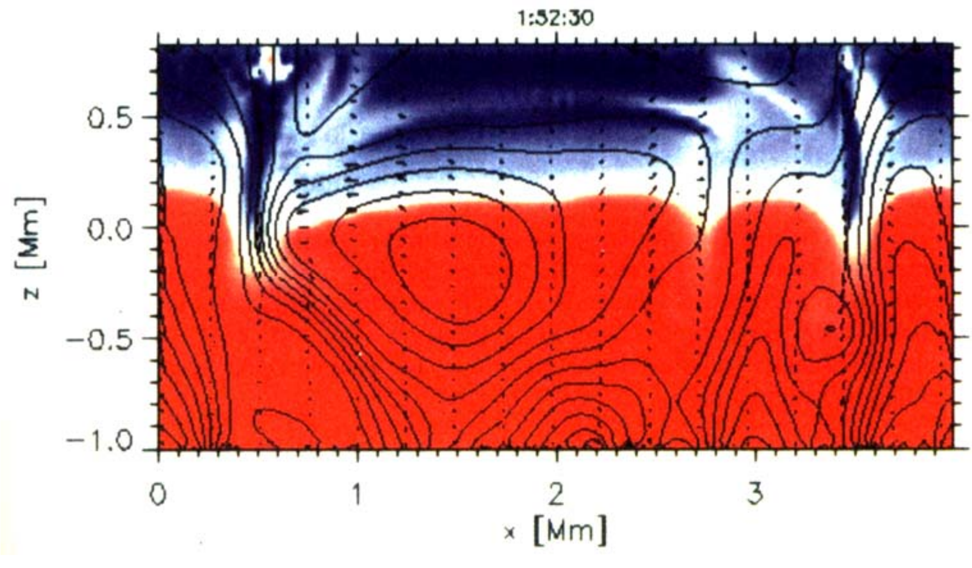

Figure 3. Vertical cut through the solar surface from a 2D-MHD simulation of the solar granulation. It illustrates the concentration of the magnetic field lines and the formation of flux tubes. Two such concentrations are seen: near x= 0.5 Mm and 3.5 Mm. (Figure provided by S.R.O. Ploner based on the simulations of Gadun *et al.* 2000).

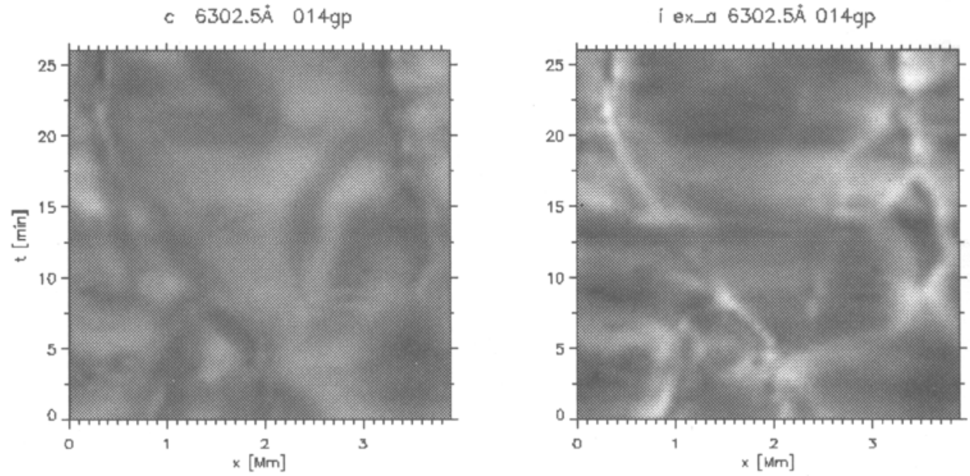

Figure 4. Temporal evolution of the emergent radiation of a vertical cut through the solar atmosphere using a 2D MHD model of the solar granulation (Gadun *et al.* 2000). The x-axis covers roughly 4 Mm. As expected, these simulations show an increased contrast in the core of a spectral line (right panel) compared to the continuum (left panel) for regions of concentrated flux.

the flux tube increases, the effectiveness of the heating by the inflowing radiation from the hot walls decreases. The brightness of a flux tube therefore, is to a large extent determined by its diameter. However, the brightness of flux tubes also shows a very pronounced center-to-limb variation (CLV) since the visibility of the hot walls increases towards the limb (Spruit 1976).

In summary, large flux tubes (pores and sunspots) are dark while small flux tubes (composing the faculae and active network features) usually are bright. This is plotted schematically in Fig. 5 (from Solanki 1999). Flux tubes of intermediate size are bright at the limb and dark at disc centre in the continuum, although they may be bright in some spectral lines.

3. Irradiance models

Following section 2, the brightness of a flux tube is basically determined by two parameters: size and limb distance. The size of the flux tubes within an active region increases with average field strength, i.e. with increasing filling factor (Solanki and Brigljevisć 1992; Grossmann-Doerth *et al.* 1994).

Solar irradiance variations can, therefore, be reconstructed based upon the following two ingredients:

(1) A detailed description of the distribution of the solar surface magnetic field and its evolution in time.

(2) The brightness of individual magnetic features as a function of limb distance μ and filling factor α.

The first can, to a large extent, be obtained by examining full-disc magnetograms. The latter, however, requires detailed magneto-hydrodynamic and radiative transfer modelling of flux tubes and their surroundings (e.g. Steiner *et al.* 1996; Gadun *et al.*

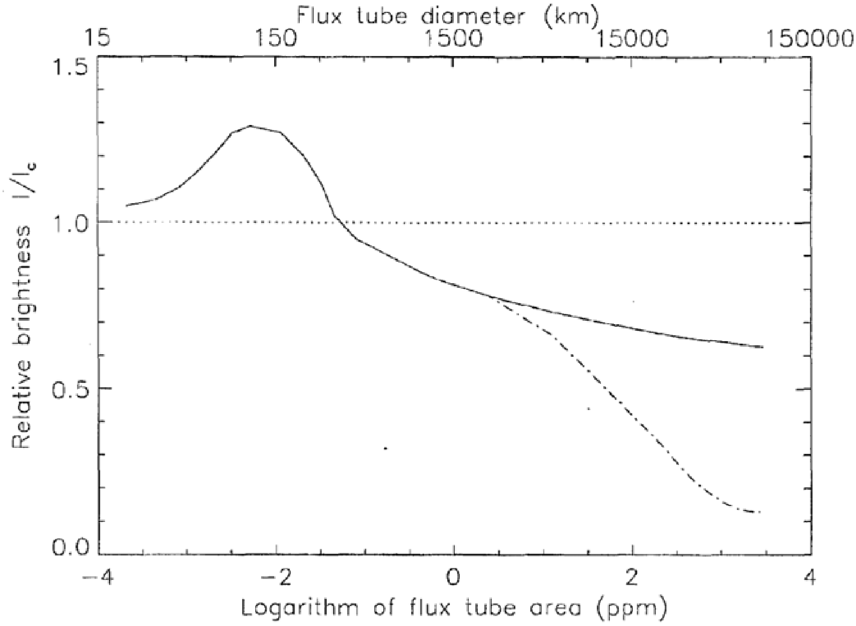

Figure 5. White-light contrast of flux tubes relative to the quiet Sun as a function of flux tube diameter, i.e. logarithmic flux tube area (in ppm). The solid line represents the relative brightness averaged over the whole spot while the dashed-dotted line is for the umbra only.

2000), or the empirical determination of their properties based upon, e.g., sophisticated inversion techniques (Ruiz Cobo & Del Toro Iniesta 1992, 1994; Frutiger *et al.* 1999).

To bypass the difficulties arising from such multidimensional or multi-component approaches, we present a method to reconstruct solar irradiance variations based on the representation of sunspots and faculae (and the quiet Sun) by simple 1-component models whose brightness can be derived using ATLAS, a spectral synthesis code developed by Kuracz (1992).

In this model the intensity $I_{i,\,j}(\lambda;\,t)$ of an element (i,j) on the solar surface at time t and wavelength λ is given by

$$\begin{aligned} I_{i,j}(\lambda;t) = & (1 - \alpha^s_{i,j}(\Phi;t) - \alpha^f_{i,j}(\Phi;t)) \cdot I^q(\mu(i,j),\lambda) \\ & + \alpha^s_{i,j}(\Phi;t) \cdot I^s(\mu(i,j),\lambda) \\ & + \alpha^f_{i,j}(\Phi;t) \cdot I^f(\mu(i,j),\lambda), \end{aligned} \tag{1}$$

where $I^q\ (\mu(i,j),\lambda)$, $I^s(\mu(I,j),\lambda)$ and $I^f\ (\mu(i,j),\lambda)$ are the calculated intensity spectra of the quiet Sun, the sunspot and the facular model, respectively. The fractional coverage of the solar surface element (i,j) by the three components is described by the filling factors $\alpha^s_{i\,j}$ $(\Phi;t)$ (sunspots) and $\alpha^f_{i\,j}$ $(\Phi;t)$ (faculae). The filling factors are deduced from full-disc magnetograms by converting the measured magnetic flux within the element (i,j) into a corresponding filling factor.

The model has been used by Fligge *et al.* (2000) to reconstruct short-term solar total and spectral irradiance variations measured by VIRGO. The high correlation (roughly

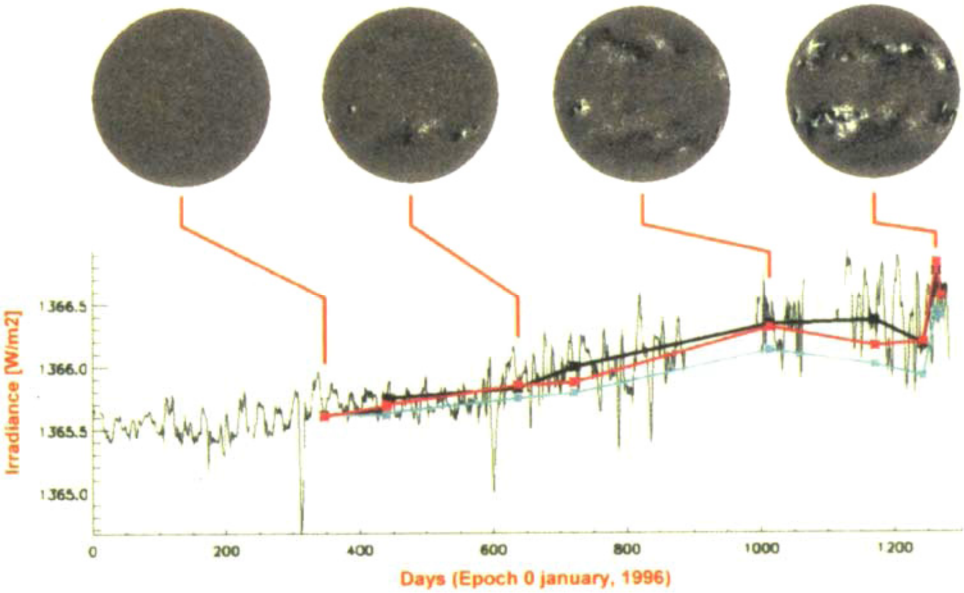

Figure 6. Upper part: Full-disc magnetograms of MDI indicating the increase of solar activity from the minimum of cycle 22/23 towards the maximum of cycle 23, **Lower part:** Total solar irradiance as measured by VIRGO (thin line). The black squares represent VIRGO measurements on 10 selected days. The reconstruction of irradiance on these days using 20-minutes averaged magnetograms is given by the dark gray squares, the reconstruction using standard 1-minute magnetograms by light gray ones.

0.95) between the measured and reconstructed time-series confirms the dominant influence of sunspots and active region faculae to irradiance changes on time-scales of a few weeks.

It is still under debate as to what extent long-term changes of solar irradiance, i.e. the increase of the solar brightness between activity minimum and maximum can be explained by models based on solar surface magnetic fields only. Addressing these time-scales, the slowly varying contribution of the active network must be carefully taken into account.

In a preliminary analysis, we applied the method described above to reconstruct solar irradiance changes during the onset of cycle 23. To this end, we picked out 10 days between 1996 and 1999 when complete sequences of at least 20 successive MDI full-disc magnetograms taken at a cadence of 1 per minute were available. Finally, we reconstructed relative solar irradiance values for each day using either a single 1-minute (recA) or an average over 20 1-minute (recB) magnetograms, thereby, increase-ing the signal-to-noise ratio by a factor of ≈ 4.5.

This is illustrated in Fig. 6. The four magnetograms on the top denote the increase of solar magnetic activity during the time period considered. The VIRGO time-series of daily total solar irradiance measurements is shown by the thin line, while the measured irradiance values for the 10 selected days are marked with squares and connected with a thick, black line.

The predicted increase of total solar irradiance due to recA (light gray) is too small. Due to the higher noise level within the 1-minute magnetograms (20 G) most network points elude detection. The network contribution, therefore, is heavily underestimated.

However, recB, represented by the gray line, closely follows the VIRGO measurements. This indicates that even on these timescales, it is the solar surface magnetic field that produces most of the observed solar irradiance changes.

4. Conclusions and outlook

In recent years there has been increasing evidence that the solar surface magnetic field is by far the most important driver of solar irradiance variations on times-scales of days up to the solar activity cycle length (and probably even longer). Models based purely on the evolution of solar surface magnetic features have been highly successful in reproducing not only total and spectral irradiance variations but also a number of other solar phenomena related to solar activity like, e.g., the variation of the ratio of facular to sunspot areas (Fligge *et al.* 1998) or variations of the amount of line-blanketing over the solar cycle (Unruh *et al.* 1999).

Although solar irradiance modelling has made substantial progress many details have still to be worked out. One major simplification implicit in current models is that they completely neglect the physical nature of faculae, namely that they are composed of small-scale flux tubes. A way to improve the irradiance models and to deepen our understanding about the brightness variations produced by solar surface magnetic features is to derive the atmospheric parameters from spectro-polarimetric measurements using inversion techniques (Ruiz Cobo & Del Toro Iniesta 1992; Frutiger *et al.* 1999). By simultaneous inversion of multiple spectral lines different layers of the solar atmosphere can be probed and thermal stratification can be derived. New techniques, such as the use of *response functions* (Ruiz Cobo & Del Toro Iniesta 1994) are able to dramatically speed up the inversion of depth-dependent quantities making such investigations feasible. To validate future models, however, new experiments providing irradiance records of high temporal *and* spectral resolution are needed. Such measurements are expected to become available within the next few years.

References

Del Toro Iniesta, J. C, Tarbell, T. D., Ruiz Cobo, B. 1994, *Astrophys. J.,* **436**, 400.

Fligge, M., Solanki, S. K., Unruh, Y. C. 2000, *Astmn. Astrophys.,* **353,** 380.

Fligge, M.,Solanki, S.K., Unruh,Y. C, Fröhlich, C, Wehrli, C. 1998, *Astron. Astrophys.,* **335,** 709.

Foukal, P., 1981, in *The Physics of Sunspots,* Proceedings of the Conference, Sunspot, NM, Sacramento Peak Observatory, pages 391–423.

Frazier, E. 1971, *Sol. Phys.,* **21,** 42.

Frutiger, C, Solanki, S. K., Fligge, M., Bruls, J. H. J. M. 1999, in *Solar Polarization. Proc. 2nd SPW,* (eds.) K. N. Nagendra & J. O. Stenflo, pages 281–290, (Kluwer Dordrecht).

Gadun, A. S., Solanki, S. K., Sheminova, V., Ploner, S. 2000, *Astrophys. J.,* (submitted).

Grossmann-Doerth, U.,Knoelker, M., Schuessler, M.,Solanki, S.K.1994, *Astron. Astrophys.,* **285,**648.

Grossmann-Doerth, U.,Schuessler,M.,Solanki, S. K.1989, *Astron. Astrophys.,* **221,** 338.

Hudson, H. S., Silva S., Woodard, M, Willson, R. C. 1982, *Sol Phys.,* **76,** 211.

Kurucz, R. L. 1992, *Revista Mexicana de Astronomia y Astrofisica,* **23,** 187.

Ruiz .Cobo, B., Del Toro Iniesta, J. C. 1992, *Astrophys. J.,* **398,** 375.

Ruiz .Cobo, B., Del Toro Iniesta, J. C. 1994, *Astron.***283,** 129

Severino, G., Gomez, M. T., Caccin, B. 1994, in *Solar Surface Magnetism,* (eds.) R. J. Rutten & C. J. Schrijver, pages 169–177, (Kluwer Dordrecht).
Solanki, S. K. 1993, Space *Science Reviews,* **63,** 1.
Solanki S. K. 1999, in *ASP Conf. Ser. 158: Solar and Stellar Activity: Similarities and Differences,* page 109.
Solanki, S. K., Brigljević, V. 1992, *Astron. Astrophys.,* **262,** L29.
Spruit, H. C. 1976, *Sol. Phys.,* **50,** 269.
Spruit, H. C. 1981, n *NASA. Goddard Space Flight Center. The Sun as a Star,* pages 385–413.
Steiner, O., Grossmann-Doerth, U., Schussler, M., Knoelker, M. 1996, *Sol Phys.,* **164,** 223.
Unruh, Y. C, Solanki, S. K., Fligge, M. 1999, *Astron. Astrophys.,* **345,** 635.

J. Astrophys. Astr. (2000) **21**, 283–287

Dynamical Processes in Flux Tabes and their Role in Chromospheric Heating

S. S. Hasan, *Indian Institute of Astrophysics, Bangalore 560034, India,*
e-mail: hasan@iiap.ernet.in

Abstract. We model the dynamical interaction between magnetic flux tubes and granules in the solar photosphere which leads to the excitation of transverse (kink) and longitudinal (sausage) tube waves. The investigation is motivated by the interpretation of network oscillations in terms of flux tube waves. The calculations show that for magnetic field strengths typical of the network, the energy flux in transverse waves is higher than in longitudinal waves by an order of magnitude. But for weaker fields, such as those that might be found in internetwork regions, the energy fluxes in the two modes are comparable. Using observations of footpoint motions, the energy flux in transverse waves is calculated and the implications for chromospheric heating are pointed out.

Key words. MHD — Sun: magnetic fields, oscillations.

1. Introduction

It is now generally accepted that the solar photosphere is threaded with vertical magnetic fields clumped into elements or flux tubes with field strengths in the kilogauss range and diameters of the order of 100 km (e.g., Frazier & Stenflo 1972). These flux tubes occur preferentially in the magnetic network, which essentially outlines the boundaries of supergranules (convection cells typically 30 Mm) that are clearly visible as bright points in G-band and Ca II images. High resolution observations suggest that these network bright points, located in intergranular lanes, are in a highly dynamical state, due to the buffeting effect of random convective motions (e.g., Muller 1983; Muller *et al.* 1994; Berger & Title 1996; van Ballegooijen *et al.* 1998). It is likely that the interaction of the motions with the magnetic elements can excite MHD oscillations in the flux tubes, which can contribute to chromospheric and coronal heating.

The dynamical behaviour of bright points has been examined in great detail extensively (e.g., Muller *et al.* 1994, Berger *et al.* 1998; van Ballegooijen *et al.* 1998). Many observations have confirmed that the chromosphere in the magnetic network of the quiet Sun oscillates with periods of around 7 min. (e.g., Damé 1983; Lites, Rutten & Kalkofen 1993; Curdt & Henzel 1998).

Many numerical simulations of dynamical effects associated with the interaction of magnetic fields and convection have been carried out (e.g., Nordlund & Stein 1989; Nordlund *et al.* 1992; Steiner *et al.* 1998). The simulations of Steiner *et al.* clearly show the bending of a flux sheath through the buffeting action of granules. This interaction can excite MHD oscillations in the magnetic element which can propagate upwards and heat the chromosphere and corona (Spruit 1981; Ulmschneider, Zähringer & Musielak 1991.) The excitation of transverse (kink) waves by the foot-point motions of magnetic elements has been modelled by Choudhuri, Auffret & Priest (1993). They suggest that rapid motions (with a time constant less than 300 s) with velocities larger than 2 km s^{-1} can excite transverse oscillations which carry adequate energy for coronal heating. Calculations show that transverse waves get converted to longitudinal waves in the chromosphere (Ulmschneider *et al.* 1991; Zhugzhda, Bromm & Ulmschneider 1995); the latter can easily dissipate through shock formations and contribute to the heating of the atmosphere. Chromospheric oscillations with a period of 7 min. have been interpreted as transverse waves in a magnetic flux tube oscillating at their cutoff period (Kalkofen 1997).

The main aim of the present contribution is to quantitatively study the interaction of a magnetic flux tube that is buffeted by a granule from the ambient medium and examine the excitation of wave flux tubes modes (transverse and longitudinal) for the *same* external impulse, with a view to determine the partitioning of vertical energy flux in the two modes. Using observations of footpoint motions, the energy flux of transverse waves is calculated and the implications for chromospheric heating are pointed out.

2. Model

Consider a vertical magnetic flux tube extending through the photosphere, which we assume to be "thin" and isothermal. It is convenient to use the "reduced" displacement, $Q(z,t)$, which is related to the physical Lagrangian displacement, $\xi(z, t)$, by $Q(z, t) = \xi_{\perp}(z, t)e^{-Z/4H}$, where H denotes the scale height of the atmosphere.

It can be shown that Q_{α} ($\alpha = \kappa$ for transverse waves and $\alpha = \lambda$ for longitudinal waves) satisfies the Klein-Gordon equation (Hasan & Kalkofen 1999, henceforth Paper I). Once Q_{α} is determined, the vertical energy flux in the two modes can easily be calculated (Paper I).

3. Results

We use the following default parameters: temperature T = 6650 K, scale height H = 155.4 km, sound speed c_s = 8.4km s^{-1}, β = 0.3 ($B \approx 1600$ G at z = 0), where $\beta = 8\pi B^2/\rho$, B and p are respectively the magnetic field and pressure at the tube axis. The wave speed and cutoff period are 7.3 km s^{-1} and 534 s for kink waves and 7.5 km s^{-1} and 227 s for longitudinal waves. Note that the latter period is almost the same as the acoustic cutoff period. We assume that the flux tube is buffeted by a single granule with a speed of 1 km s^{-1} in a single impact with an interaction time of 50 s.

Fig. 1 shows the time variation of F_{wave}/f_0 (where f_0 denotes the filling factor of magnetic flux tubes at z = 0), the wave energy flux in the vertical direction, in transverse (solid lines) and longitudinal (dotted lines) modes at two different heights, using the default parameters. Note that the energy flux in longitudinal waves is measured by the scale on the right. The impulse delivered to the tube at z = 0 creates an oscillation that transports energy to the higher layers. The first maximum

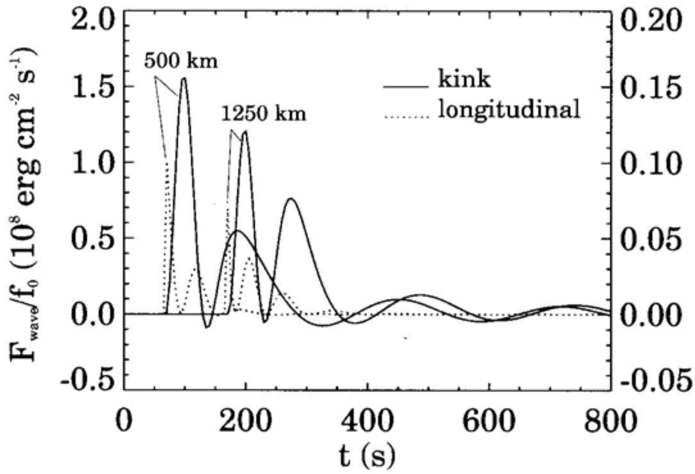

Figure 1. Time variation of F_{wave}/f_0 (where f_0 denotes the filling factor of magnetic flux tubes at z = 0), the vertical energy flux in transverse waves (solid lines) and longitudinal (dotted lines) at two heights for $\beta = 0.3$.

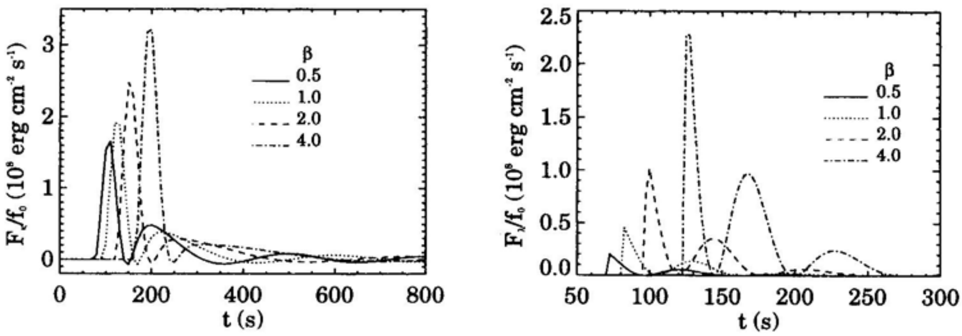

Figure 2. Time variation of the vertical energy flux in transverse waves (left panel) and longitudinal waves (right panel) at z = 500 km for different β.

corresponds to the initial impulse associated with the buffeting action of the external granule. It should be noted that the vertical energy flux in transverse waves is about 15 times larger than the energy flux in longitudinal waves.

Fig. 2 depicts the time variation of the vertical energy flux in transverse (left panel) and longitudinal waves (right panel) at z = 500 km for various values of β. We find that, whereas the maximum value of the flux associated with the primary pulse increases gradually with β (i.e. with decreasing magnetic field strength) for transverse waves, the variation is much sharper for longitudinal waves. As β increases, the energy flux in the two modes becomes comparable (typically for $\beta \geq 2$).

4. Discussion

The generic behaviour is the same for transverse and longitudinal wave excitation: the buffeting action of a granule on a flux tube impulsively excites a pulse that travels away from the source region (with the kink or longitudinal tube speed). After the passage of the pulse, the atmosphere oscillates at the cutoff period of the mode, with an amplitude that slowly decays in time. We find that the initial pulse carries most of the energy; subsequently the atmosphere oscillates as a whole in phase, without energy transport. The wave period observed in the magnetic network is interpreted as the cutoff period of transverse waves, which leads naturally to an oscillation at this period (typically in the 7 min. range).

For strong magnetic fields, most of the energy goes into transverse waves, and only a much smaller fraction into longitudinal waves. Observationally this model is consistent with the interpretation of network bright points in terms of transverse waves, where the power spectrum observed in H_3 by Lites *et al.* (1993) shows a high peak at 2.5 mHz (the cutoff frequency of transverse waves) and a much smaller peak at 3 mHz, perhaps a contribution made by longitudinal flux tube waves. These calculations therefore support the hypothesis that mainly transverse flux tube waves are dominantly excited and the observed velocity signal measures the cutoff period of the transverse waves in the photosphere.

For weaker magnetic fields the energy fluxes in the two modes are comparable. From the absence of a strong peak at low frequencies in the power spectrum of the cell interior (CI) we conclude that both transverse and longitudinal waves must make a negligible contribution to K_{2V} bright point oscillations. The absence of the magnetic modes then implies that the waves in the CI are probably acoustic waves, and the observed 3 minute period is therefore the acoustic cutoff period — and not the cutoff period of longitudinal flux tube waves. This implies that the magnetic field structure in the CI is likely to be different from that of flux tubes in the magnetic network.

4.1 *Chromospheric heating*

Since the energy flux in transverse waves is significantly higher for magnetic elements in the network, we examine their role in chromospheric heating. We calculate the vertical energy flux in transverse waves excited due to the footpoint motion of magnetic elements using observations of G band bright points (obtained at the Swedish Solar Observatory at La Palma during 1995). The motion of the bright points was followed using a tracking technique with "corks" as tracers of bright points (van Ballegooijen *et al.* 1998). Let us assume that the motion of the G band bright points can be taken as a proxy for the footpoint motion of flux tubes at the base (z = 0) of the photosphere. Then by specifying the horizontal displacement of the tube at z = 0, the displacement at any height and hence the vertical energy flux can be determined (for details see Hasan, Kalkofen & van Ballegooijen 2000).

Fig. 3 shows the vertical energy flux in transverse waves versus time at a height z = 750 km for a typical magnetic element in the network. We find that the injection of energy into the chromosphere takes place in brief and intermittent bursts, lasting typically 30 s, separated by longer periods (longer than the time scale for radiative losses in the chromosphere) with lower energy flux. The peak energy flux into the chromosphere is as high as 10^9 erg cm^{-2}s^{-1} in a single flux tube, although the time-averaged flux is ~ 10^8 erg cm^{-2} s^{-1}.

In summary, we find that transverse waves are more efficiently excited than longitudinal waves in the magnetic network. For magnetic field strengths of the order of

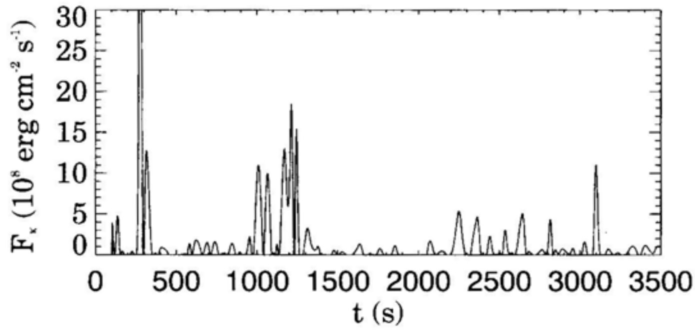

Figure 3. Time variation of the vertical energy flux in transverse waves in a single flux tube at z = 750 km due to footpoint motions taken from observations.

1500 G, the energy flux in transverse waves is an order of magnitude larger than in longitudinal waves. However, for weaker magnetic fields, the fluxes in the two modes become comparable.

The energy flux in upward propagating transverse waves has been calculated for a representative magnetic element in the network. We find that these waves supply energy to the chromosphere in short-duration sporadic bursts (lasting typically 30-60 s), separated by longer periods with low energy flux. From an observational point of view, such a scenario for heating the magnetic network would suggest a high variability in Ca II emission. A possible remedy to this difficulty would be to consider the effect of high frequency motions (Hasan, Kalkofen & van Ballegooijen 2000).

References

Berger, T. E., Löfdahl, M. G., Shine, R. A., Title, A. M. 1998, *Astrophys. J.,* **495,** 973.

Berger, T. E., Title, A. M. 1996, *Astrophys. J.,* **463,** 365.

Choudhuri, A. R., Auffret, H., Priest, E. R. 1993, *Solar Phys.,* **143,** 49.

Curdt, W., Henzel, P. 1998, *Astrophys. J.,* **503,** L95.

Dame, L., 1983, Thèse, Université de Paris VII.

Frazier, E. N., Stenflo, J. O. 1972, *Solar Phys.,* **85,** 113.

Hasan, S. S., Kalkofen, W. 1999, *Astrophys. J.,* **519,** 899 (Paper I).

Hasan, S. S., Kalkofen, W., van Ballegooijen, A. A. 2000, *Astrophys. J.,* (in press).

Kalkofen, W. 1997, *Astrophys. J.,* **486,** L145.

Lites, B. W., Rutten, R. J., Kalkofen, W. 1993, *Astrophys. J.,* **414,** 345.

Muller, R. 1983, *Solar Phys.,* **85,** 113.

Muller, R., Roudier, Th., Vigneau, J., Auffret, H. 1994, *Astr. Astrophys.,* **283,** 232.

Nordlund, ., Stein, R. F. 1989, In *Solar and Stellar Granulation,* NATO ASI Series, Vol. 263 (ed.) Rutten, R. J. and Severino, G. (Kluwer: Acad. Publ.), p. 453.

Nordlund, Å., Brandenburg, A., Jennings, R. L., Rieutord, M., Ruokainen, J., Stein, R. F., Tuominen, I. 1992, *Astrophys. J.,* **392**, 647.

Spruit, H. C. 1981, *Astr. Astrophys.,* **98**, 155.

Steiner, O., Grossmann-Doerth, U., Knölker, M., Schüssler, M. 1998, *Astrophys. J.,* **495,** 468.

Ulmschneider, P., Zähringer, K., Musielak, Z. E. 1991, *Astr. Astrophys.,* **241,** 625.

van Ballegooijen, A., Nisenson, P, Noyes, R. W., Löfdahl, M. G., Stein, R. F., Nordlund, Å., Krishnakumar, V. 1998, *Astrophys. J.*, **509,** 435.

Zhugzhda, Y. D., Bromm, V, Ulmschneider, P. 1995, *Astr. Astrophys.,* **300,** 302.

J. Astrophys. Astr. (2000) **21**, 289-292

Infrared Photometry of Solar Active Regions

M. Sobotka[1,2], M. Vázquez[1], M. Sánchez Cuberes[1], J. A. Bonet[1] &
A. Hanslmeier[3]
[1]*Institute de Astrof'isica de Canarias, E-38200 La Laguna, Tenerife, Spain.*
[2]*Astronomical Institute, Academy of Sciences of the Czech Republic, CZ-25165 Ondrejov, The Czech Republic.*
[3]*Institut für Geophysik, Astrophysik und Meteorologie, Universitätsplatz 5, A-8010 Graz, Austria.*

Abstract. Simultaneous time series of broad-band images of two active regions close to the disk center were acquired at the maximum (0.80 μm) and minimum (1.55 μm) continuum opacities. Dark faculae are detected in images obtained as weighted intensity differences between both wavelength bands. The elements of quiet regions can be clearly distinguished from those of faculae and pores in scatter plots of brightness temperatures. There is a smooth transition between faculae and pores in the scatter plots. These facts are interpreted in terms of the balance between the inhibition of convective energy transport and the lateral radiative heating.

Key words. Solar photosphere—faculae—pores.

1. Introduction

Observations of active photospheric structures in the infrared are of particular interest, because the opacity minimum is at 1.6 μm, so that the deepest layers of the photosphere can be probed at this wavelength. Foukal and his colleagues have published a series of papers based on such observations (see Foukal *et al.* 1990) and reported that many faculae are dark at the disk center. Moran, Foukal & Rabin (1992) found that the dark infrared contrast increases with the magnetic flux beyond a threshold value of about 2×10^{18} Mx. Similar observations with spatial resolution of 1" were obtained by Wang *et al.* (1998). In this work we use the infrared photometry of faculae and pores to obtain information about their brightness temperatures in the layers corresponding to the minimum and maximum continuum opacities.

2. Observations and data analysis

Series of broadband CCD images of active regions were obtained at the Swedish Vacuum Solar Telescope (Observatorio del Roque de los Muchachos, La Palma) simultaneously in two channels: λ = 0.8000 ± 0.0025 μm (continuum opacity maximum) and λ = 1.5542 ± 0.0046 μm (continuum opacity minimum). We observed two active regions close to the center of solar disk:

(1) 23rd June 1997, 08:0909:24 UT, NOAA 8055, a growing group of very small pores.
(2) 25th June 1997, 08:3110:07 UT, NOAA 8056, a rapidly developing group of large pores.

After the bias and gain corrections, all frames were normalized to the mean intensity of the undisturbed photosphere $\overline{I_{\rm phot}}$ ·The images show details near the diffraction limit of the telescope (0.″45 for 0.80 μm and 0.″89 for 1.55 μm). The frames were aligned, de-stretched, and corrected for the theoretical point-spread function of the telescope. Acoustic waves were removed by subsonic filtering. Frames in both channels were re-sampled to a common scale 0."166 pixel^{-1}. To enable a direct comparison of intensities in both wavelength bands the 0.80 μm images were degraded to the resolution of the 1.55 μm ones.

Using the models of a plage (Solanki & Steenbock 1988), quiet photosphere (Gingerich *et al.* 1971), and a small Sunspot (Collados *et al.* 1994) as proxies of real structures, we found that the differences between the effective formation heights of the 0.80 μm and 1.55 μm continua increases with decreasing mean temperature of the model: 28 km for the plage, 41 km for the quiet photosphere, and 64 km for the small spot.

3. Results

To compare the intensities in both wavelength bands we computed weighted difference images $I_{\rm dif} = F\,[I(1.55) - 1] - [I(0.80) - 1]$, where "1" stands for normalized $\overline{I_{\rm phot}}$ and the factor $F=[\Delta I^{\rm OR}_{\rm rms}\ (0.80)]/[\Delta I^{\rm OR}_{\rm rms}\ (1.55)]$, calculated from the rms granular contrasts in the quiet region (QR) for each pair of frames, enhances the contrast at 1.55 μm. This enhancement is necessary because $\Delta I_{\rm rms}$ in the 1.55 μm band is lower than that in 0.80 μm by factor of about 2.3 and a simple subtraction of images does not give a clear result. The difference images (Fig. 1) show dark structures which look

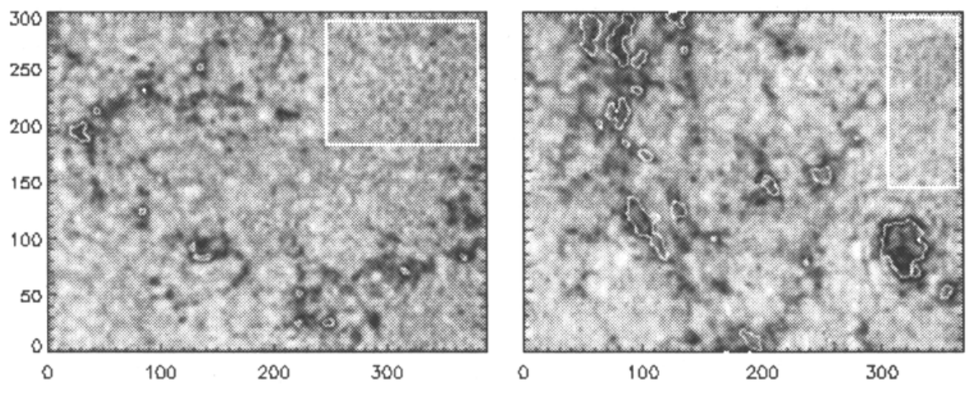

Figure 1. Difference images of NOAA 8055 (left) and NOAA 8056 (right) showing dark faculae and pores. The contours indicate borders of pores for λ0.80μm. White rectangles enclose quiet regions. The coordinate unit is 1 pixel, i.e., 0.166.

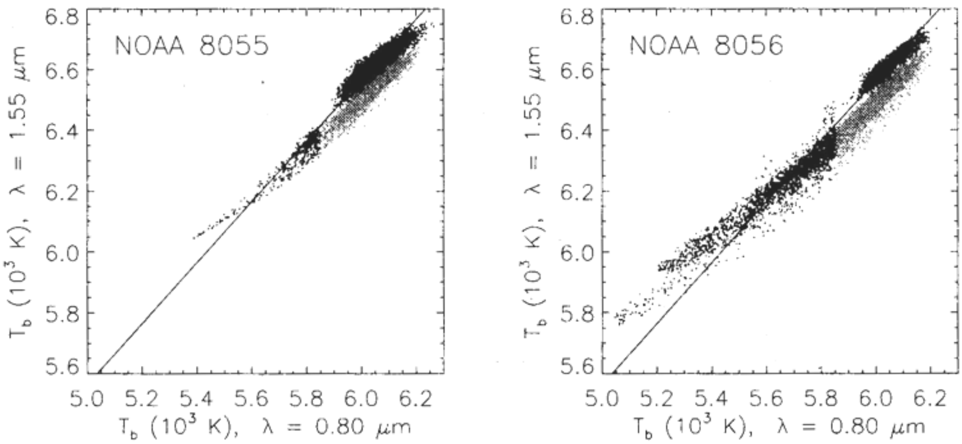

Figure 2. Scatter plots of brightness temperatures. Elements of quiet regions and of pores are black, facular elements are gray.

very similar to plages or faculae. The comparison of histograms of intensity distributions in QRs and in dark structures has shown that these darkenings appear due to reduced intensities in the 1.55 μm band as compared to 0.80 μm, so that they correspond to dark faculae.

The normalized intensities were converted to the absolute ones using the calibration factors of Neckel & Labs (1984) and Makarova, Roshchina, & Sarychev (1994), and the brightness temperatures $T_{\rm b}$ were computed for each position in the best frames of the series. Pixel-to-pixel scatter plots of $T_{\rm b}(1.55)$ versus $T_{\rm b}(0.80)$ are shown, in Fig. 2. The pixels belonging to QRs are clearly distinguished from those of faculae and the pixels of pores smoothly extend the cloud of facular pixels toward lower temperatures. The temperature difference $\Delta T_{\rm b} = T_{\rm b}(1.55) - T_{\rm b}(0.80)$ is an important parameter which depends on the temperature stratification in the atomsphere. The straight line in the scatter plots represents the constant temperature difference $\Delta T_b(QR)$ = 560 K, corresponding to an average QR. It can be seen that in magnetized regions ΔT_b gradually increases with decreasing temperature. All facular pixels show ΔT_b lower than the quiet ones. Some parts of the pores have $\Delta T_b < \Delta T_b(\mathrm{QR})$, similar to faculae. These parts are observed in ΔT_b maps as "rings" outlining the borders of pores. Inner parts of pores are characterized by $\Delta T_b > \Delta T_b(\mathrm{QR})$.

4. Discussion

Magnetic field is distributed in the photosphere in the form of discrete elements of different sizes and filling factor. When the magnetic flux reaches a certain value, a facula is formed and the inhibition of convective energy transport reduces the temperature in the lowest photospheric layers, observed at 1.55 μm. In the upper layers, this temperature deficit is balanced by lateral radiative heating, so that faculae are nearly as hot as their surroundings. This explains the discontinuity between QRs and faculae in the temperature scatter plots. In case of pores, the size of magnetic features is so large that the lateral radiative heating cannot compensate the temperature deficit due to the inhibition of convective energy transport, and photospheric layers become cooler than the surroundings at all heights. The observed increase of ΔT_b with decreasing T_b could be partially explained by increasing difference between the effective formation heights of the 0.80 and 1.55 μm continua, indicated by model calculations (see Sect. 2), although different temperature gradients should also be taken into account.

Acknowledgements

M.S. thanks the Spanish Ministry of Education for a sabbatical stay. This work was partially funded by the Spanish DGES project 95-0028 and by the Grant Agency of the Academy of Sciences of the Czech Republic (grant A 3003903).

References

Collados, M., Martínez Pillet, V., Ruiz Cobo, B., del Toro Iniesta, J.C., Vázquez, M. 1994, *Astron. Astrophys.,* **291,** 622.
Foukal, P., Little, R., Graves, J., Rabin, D., Lynch, D. 1990, *Astrophys. J.,* **353,** 712.
Gingerich, O., Noyes, R. W., Kalkofen, W., Cuny, Y. 1971, *Solar Phys.,* **18,** 347.
Makarova, E. A., Roshchina, E. M., Sarychev, A. P. 1994, *Solar Phys.,* **152,** 47.
Moran, T., Foukal, P., Rabin, D. 1992, *Solar Phys.,* **142,** 1.
Neckel, H., Labs, D. 1984, *Solar Phys.,* **90,** 205.
Solanki, S. K., Steenbock, W. 1988, *Astron. Astrophys.,* **189,** 243.
Wang, H., Spirock, T., Goode, P.R., Lee, C., Zirin, H., Kosonocky, W. 1998, *Astrophys. J.,* **495,** 957.

J. Astrophys. Astr. (2000) **21,** 293–297

CaII K Imaging to Understand UV Irradiance Variability

R. Kariyappa, *Indian Institute of Astrophysics, Bangalore 560034, India.*
email: rkari@ iiap.ernet. in

Abstract. To identify and understand the underlying physical mechanisms of total solar and UV irradiance variability and to estimate the contribution of various chromospheric features to UV irradiance, detailed analysis of spatially resolved data is required. The various chromospheric features have been segregated and different parameters have been derived from CaII K Spectroheliograms of NSO/Sac Peak and Kodaikanal Observatory and compared with UV irradiance flux measured in MgII h and k lines by NOAA 9 satellite. The important results of this detailed analysis of CaII K Images of 1992 together with UV irradiance data will be discussed in this paper.

Key words. Chromosphere: CaII K Emission—UV Irradiance.

1. Introduction

The CaII H and K resonance lines have been recognized as useful indicators for identifying regions of chromospheric activity on the solar surface. A two-dimensional image of the Sun (spectroheliogram) obtained in these lines shows that the three agencies responsible for CaII emission are: the plages, the network, and the intranetwork elements. The changes in the network and intranetwork elements related to solar activity are less understood, especially because of the lack of systematic and quantitative measurements of these chromospheric features.

In our earlier paper (Kariyappa & Pap 1996, hereafter Paper I), we have discussed the observational details, a new method of analysis, and the preliminary results of the CaII K spectroheliograms of the National Solar Observatory at Sacramento Peak (NSO/Sac Peak). The main purpose of the present paper is to separate and to derive the relative intensity and area of various chromospheric features from 424 images for the years 1980 and 1992. The results of the relative intensity and the area of the chromospheric features compared to UV irradiance will also be discussed.

2. Results and discussion

To analyze the CaII K spectroheliograms and to separate various chromospheric magnetic features, we have calculated histograms over the complete full-disc image (Paper I). We have applied the corrections for the background emulsion noise, the limb darkening, and for the disk center intensity to all the images before extracting the intensity and area of the chromospheric features. In general, the pixel intensity values for intranetwork elements will fall in the ‘toe’ portion, for network elements in the ‘peak’ portion and for plages in the ‘tail’ portion of the histogram plot (Paper I, figure 2). Using the relative intensity levels in the histogram plots, the K-images containing individual features have been displayed to examine the morphological structures to make sure the fixed intensity range for the features is correct. The main criteria used here to distinguish between various features are: very bright, large and compact structures correspond to plages, the cellular structures with bright boundaries correspond to network elements and the remaining features are associated to background and intranetwork regions. We first assumed the intensity levels that might bound the plage pixels in a histogram, and then examined images in which the pixels with greater or lesser intensities than those bounds were masked. The bounding intensities were then adjusted until the masked images accurately mapped the plage regions. Similar processes were used for the network and intranetwork features. The relative intensity and the number of pixels for different features have been derived. The uncertainties in the determination of the intensity as well as the area are $\pm$ 5 in intensity units and $\pm$600 pixels respectively.

In Fig. 1, we show the time series of the variation in averaged relative intensity of plage, network, and intranetwork elements and MgII c/w ratio of NOAA9/SBUV2 for the year 1992. The intensity of plages and the network decrease from maximum activity conditions to solar minimum (e.g. Foukal & Lean 1988), in a fashion similar to that of the full-disk Ca K intensity values, FWHM, and MgII c/w ratios (Paper I). It is interesting to note that the intranetwork elements also show a behavior during 1992 similar to that of the plages and the network, and all the parameters of these chromospheric features are well correlated with the MgII c/w ratio.

The time series of the variation in the area (total number of pixels) of plages, network, and intranetwork elements and MgII c/w ratio for 1992 is plotted in Fig. 2. It can be seen, the plage area shows a variation over similar 1992 to that of the plage intensity, indicating that during high solar activity conditions the plages cover a larger area. However, our results indicate an anticorrelation between the relative intensity and area of network elements for the time interval of 1980 and 1992. We find that the general behavior in relative intensity and area of the various chromospheric features of 1980 is similar to that of the variation seen in 1992.

The anticorrelation found between the intensity and area of the network indicates that during solar minimum the network is fainter but it covers a larger area, and therefore it may give a significant contribution to irradiance changes. We note that from an independent analysis of Kodaikanal CaII K-spectroheliograms for a longer period between 1957 and 1983, it has been shown that the area of the network elements at the center of the solar disc in a quiet region of the Sun’s surface is anticorrelated with the solar cycle (Kariyappa & Sivaraman 1994). Muller & Roudier (1994) have shown that the number variation in photospheric network bright points (NBPs) is in antiphase with the sunspot number. In addition, recently Berrilli *et al.* (1999) have found from an analysis of PSPT CaII K images that the network cell size is anticorrelated with the solar activity.

The scatter plot diagrams (not shown here) between the relative intensity and area of the various features and the MgII c/w ratio show that the variation of the relative intensity and the area of the listed features contributes significantly to the changes in UV irradiance. This result demonstrates that both the intensity and area of the various spatial structures have to be taken into account in the irradiance models. Although the

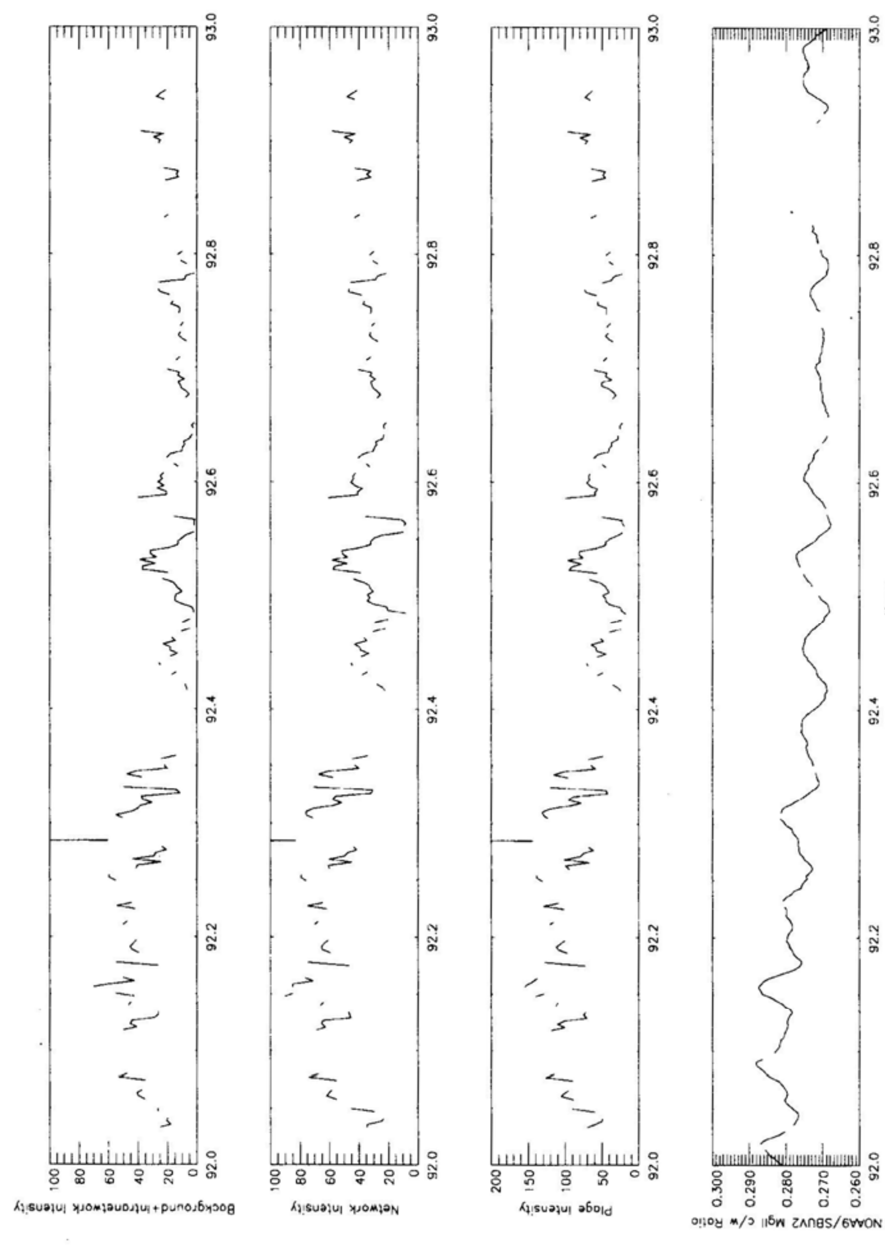

Figure 1. Time series (*from bottom to top*) of NOAA9/SBUV2 MgII c/w ratio, averaged relative intensity of plages, network and intranetwork elements for the time interval of 1992.

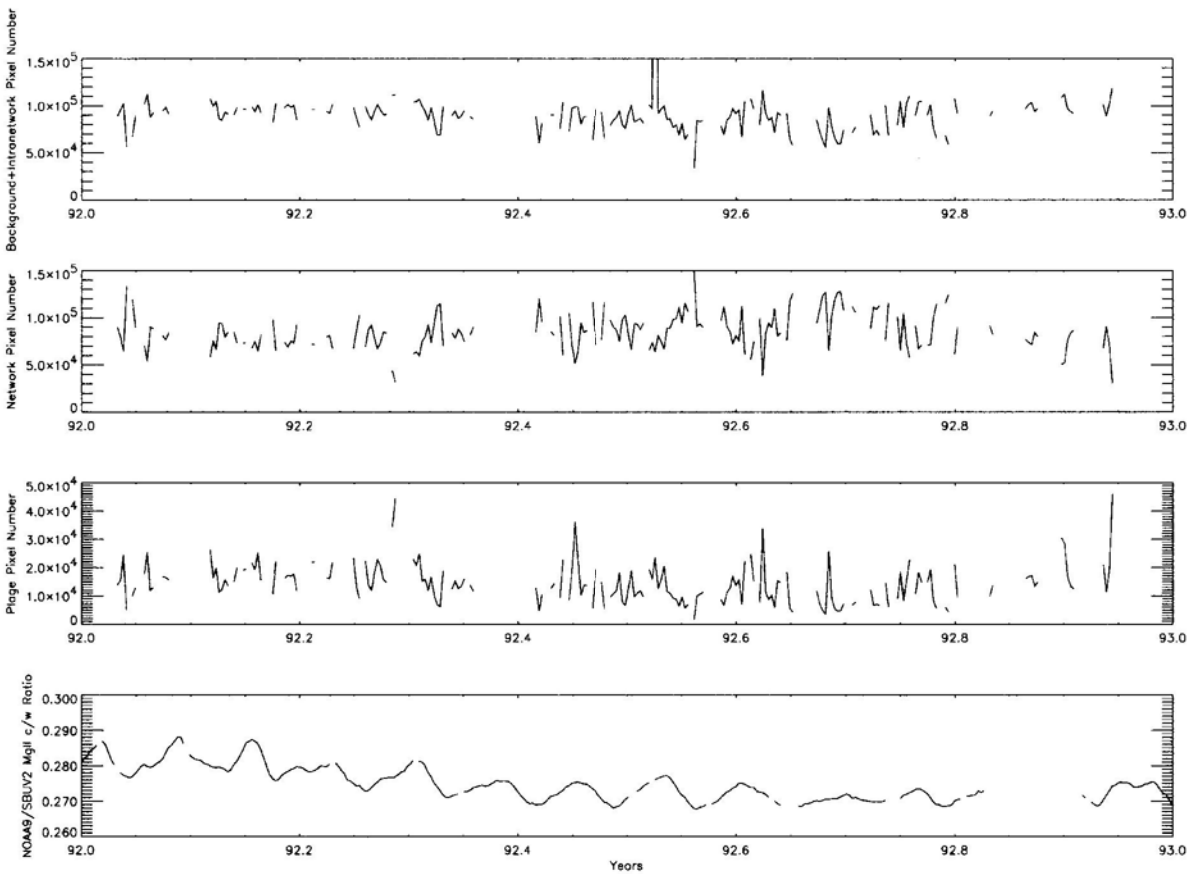

Figure 2. Time series (*from bottom to top*) of NOAA9/SBUV2 MgII c/w ratio, area of plages, network, and intranetwork elements for the time interval of 1992. Note that there is a peak-to-peak anticorrelation in the area of network with that of the variation of plages and intranetwork elements.

network and intranetwork elements are much fainter than the plages, they cover a large fraction of the solar disk. Therefore, they may contribute significantly to the changes in UV (and total) irradiance. These results may explain the discrepancy between the UV models (Foukal & Lean 1988; Pap 1992) and measurements at the time of solar minimum.

References

Berrilli, R, Ermolli, L, Florio, A., Pietropaolo, E. 1999, *Astr. Astrophys.,* **344,** 965–972.
Foukal, P., Lean, J. 1988, *Astrophys. J.,* **328,** 347–357.
Kariyappa, R., Sivaraman, K. R. 1994. *Solar Phys.,* **152,** 139–144.
Kariyappa, R., Pap, J. M. 1996, *Solar Phys.,* **167,** 115–123 (Paper I).
Muller, R., Roudier, Th. 1994, *Solar Phys.,* **152,** 131–137.
Pap, J. 1992, *Astr. Astrophys.,* **264,** 249–259.

J. Astrophys. Astr. (2000) **21,** 299–302

Models of Flux Tubes from Constrained Relaxation

A. Mangalam* & V. Krishans† *Indian Institute of Astrophysics, Koramangala, Bangalore 560 034, India.*
**e-mail: mangalam @ iiap. ernet. in*
†email: vinod@iiap.ernet.in

Abstract. We study the relaxation of a compressible plasma to an equilibrium with flow. The constraints of conservation of mass, energy, angular momentum, cross-helicity and relative magnetic helicity are imposed. Equilibria corresponding to the energy extrema while conserving these invariants for parallel flows yield three classes of solutions and one of them with an increasing radial density profile, relevant to solar flux tubes is presented.

Key words. Hydromagnetics—Sun: atmosphere, magnetic fields.

1. Invariants of the system

There is a remarkable concentration of the magnetic field of the Sun into isolated flux tubes at the visible surface, and also in the form of coronal loops, where the field strengths are of the order of 1500 G. It is our aim to seek equilibrium structures appropriate to these flux tubes, using principles of plasma relaxation. The subject of turbulent relaxation of a plasma has been examined by several workers with the aim of predicting a set of equilibria after the plasma has passed through a disruptive phase (e.g. Woltjer 1960; Taylor 1974; Rieman 1980). The results have been applied to fusion devices as well as to astrophysical plasmas (krishan 1996; Finn & Antonsen 1983). For a review of the utility of the helicity concept see Brown *et al.* (1999).

Taylor (1974) hypothesized the existence of a global helicity invariant while the system would resistively relax to a state of minimum energy which would be topologically inaccessible in perfect MHD. Berger & Field (1984) allowed for open field lines in the volume and constructed a relative helicity invariant which has the equivalent form (Kusano *et al.* 1985)

$$H_R = H(\mathbf{B}_c,\mathbf{B}_c) + 2H(\mathbf{P},\mathbf{B}_c), \tag{1}$$

where $\mathbf{B}_c$ is the closed field in the volume under consideration and $\mathbf{P}$ represents the open field lines in the volume, whose self-helicity is taken to be zero. By taking a variation of this expression, we find, using $\delta H(\mathbf{B}) = 2\int d^3x\delta\mathbf{B} \,.\, \mathbf{A}$, that

$$\begin{aligned}\delta H_R &= 2\int_v \mathrm{d}^3x\delta\mathbf{B}_c \cdot \mathbf{A}_c + 2\int_v \mathrm{d}^3x\delta\mathbf{B}_c \cdot \mathbf{A}_P \\ &= 2\int_v \mathrm{d}^3x\delta\mathbf{B}_c \cdot \mathbf{A} = 2\int_v \mathrm{d}^3x\delta\mathbf{B} \cdot \mathbf{A} = \delta H(\mathbf{B}),\end{aligned} \tag{2}$$

where we have employed the fact that $\delta \mathbf{A}_p = 0$ and $\delta \mathbf{P} = 0$ as $\mathbf{P}$ is determined completely by the fixed boundary conditions (there is an alternate route in the Appendix A of Berger (1984)). We emphasize the result that the variation of the relative helicity is equal to the variation of the helicity itself.

Here, we investigate a three dimensional model of relaxed states, drawing on the framework of Finn & Antonsen (1983), who assume ideal MDH, but with large thermal conductivity. This has two consequences; the cross-helicity, $K = \int d^3x v \cdot \mathbf{B}$, an invariant in ideal MHD remains conserved in the limit of large thermal conductivity and it turns out under same assumptions, that the entropy functional, $S = \int d^3x \rho \ln (p/\rho^\gamma)$ is also an invariant. Note however that adiabaticity is not assumed to allow for entropy change during the relaxation process.

We consider the usual system of MHD equations with the energy equation suitably modified to include large parallel thermal conductivity. It can be shown, in spite of parallel heat flux, due to the boundary condition $B \cdot \hat{n} = 0$, that the total energy, $E = \int d^3x(\frac{1}{2}\rho v^2 + \frac{1}{8\pi}\mathbf{B}^2 + \frac{p}{\gamma-1})$, is conserved. In all H_R, K, S, and the total mass, $M = \int d^3x \rho$, and E are the global invariants of the system. The entropy functional increases for finite thermal conductivity and is invariant, if it is infinite. The standard variational method of extremizing $E_* = E - \frac{1}{2}\mu H_R - \alpha K - nS - \delta M$ yields the following equations

$$p = nT = n(\gamma - 1)\eta m, \tag{3}$$

$$v = \frac{\alpha \mathbf{B}}{\rho}, \tag{4}$$

$$\nabla \times \left[\left(\frac{1}{4\pi} - \frac{\alpha^2}{\rho}\right)\mathbf{B}\right] = \mu \mathbf{B}, \tag{5}$$

$$\frac{m\alpha^2 \mathbf{B}^2}{2\rho^2} + T \ln (n/n_0) = 0, \tag{6}$$

where $\ln n_0 = m\delta/T + (\ln (T/m\gamma) - \gamma)/(\gamma - 1)$

2. Analysis of the parallel flow

We study the parallel flows by introducing the parameters, $v = n/n_0$, $v_1 = 4\pi\alpha^2/(mn_0)$, $\mathbf{b} = \mathbf{B}/B_{max}$, $e_0 = v_1 B^2_{max}/(8p n_0 T)$ and $\mu_0 = \mu R$, where R is the length scale in the problem and B_{max} is the maximum field strength. The system then reduces to

$$\nabla \times [(1 - v_1/v)\mathrm{b}] = \mu_0 \mathrm{b}, \tag{7}$$

$$v^2 \ln v = -\varepsilon_0 \mathrm{b}^2. \tag{8}$$

There are two branches evident from the above equations: for $\varepsilon_0 > 1/(2e)$, there are no solutions and for $\varepsilon_0 < 1/(2e)$, two solutions exist. The solution with $v < 1/\sqrt{e}$ has v monotonically decreasing with b^2 and viceversa for $v > 1/\sqrt{e}$. The Taylor state, $\nabla \times \mathbf{B} = \mu \mathbf{B}$ is found in the limit $v_1 \rightarrow 0$. For a fixed μ_0, the equilibria exist only in the restricted part of the $\varepsilon_0 - v1$ plane, where solutions with $v < 1/\sqrt{e}$ called class I solutions and solutions with $v > 1/\sqrt{e}$ can be distinguished as class II and class III by the sign of $dB^2/d\rho$. So, there are three classes of solutions possible; class I with radially decreasing density and magnetic energy, class II with radially increasing magnetic energy but a decreasing density profile and finally, class III with increasing density and decreasing magnetic energy profile.

In cylindrical symmetry, the equations reduce to

$$b'_\phi = \frac{\mu_0}{\sigma} b_z - \frac{b_\phi}{r} - \frac{\sigma'}{\sigma} b_\phi, \tag{9}$$

$$b'_z = -\frac{\sigma'}{\sigma} b_z - \frac{\mu_0}{\sigma} b_\phi, \tag{10}$$

where $\sigma = 1 - v_1/v$. The solutions were obtained by solving the coupled non-linear equations (9-10) with the constraint, (8), and the boundary conditions, $b_\phi(0) = 0$ and $b^2 = 1$ at the appropriate boundary ($r/R = 0$ or 1) decided by the solution class. A point to note is that by forcing $b_\phi(1) = 0$, one can ensure that no net current, I_z, is carried by the flux tube and B_{max} can then be consistently determined. However, this solution can also be obtained by enforcing $b^2 = 1$ at 1 or 0 (depending on the solution class, whether it is increasing or decreasing) and truncating the solution at the point where $b_\phi = 0$, with the value of μ scaled appropriately. Zero net current flux tubes are qualitatively similar to the flux tube with carrying finite current.

3. Application to solar flux tubes

Class III solutions (see Fig. 1) with hollow profiles, holds for $v < 1/\sqrt{e}$, or if the condition v In (ev^2) > $v1$ holds. Therefore, $n < 0{\cdot}6\ n_0$ or the Mach number of the flow, $M > 0{\cdot}5$. Typical solar flux tubes ($\rho \simeq 3 \times 10^{-7}$ g/cc, $\beta \simeq 1$, $p \simeq 1{\cdot}4 \times 10^5$ dyn/cm^{-2}) with an underlying ultra subsonic flow, satisfy the condition for class III solution. For stable flux tubes of $B \simeq 1500$ G and v ~ 3 km/sec, the parameters are of the order, $v_1 \approx 0$ 16, $\varepsilon_0 \approx 0{\cdot}1$, indicating that the flow is of class III. The restricted types of equilibria, taking into account open field boundary conditions, which may be present in a plasma immediately after disruptive or turbulent process, have been discussed here. The parameter range for the solar flux tubes (in the photosphere) indicate that the radial density need not be peaked but can have a hollow (increasing density) profile which pertains to class III solutions. The validity of this analysis depends upon the thermal conductivity being dominant in the turbulent process.

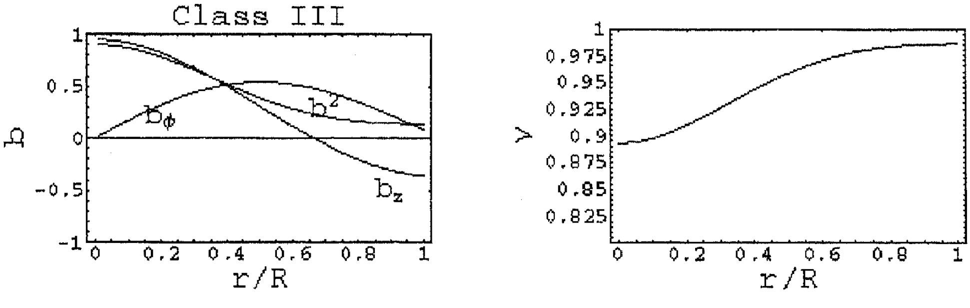

Figure 1. Class III solution with decreasing **B** and increasing density for the choice of parameters, $v_1 = 0{\cdot}16$, $\mu = 3$ and $\varepsilon_0 = 0{\cdot}1$.

The second variation of E^* indicates that the flows are stable if $\tau > 0$. Further, we plan to include other invariants like angular momentum and explore axisymmetric systems and other geometries. The predictions can be tested by numerical simulations and future observations.

Acknowledgement

We thank Prof. Richard Canfield for useful discussions during the meeting.

References

Berger, M. A. 1984, *Geophys. Astrophys. Fluid Dyn.,* **30**, 79.
Berger, M. A., Field, G. B. 1984, J. *Fluid Meek*, **147**, 133.
Brown, M. R., Canfield, R. C, Pevstov, A. A. 1999, in *Magnetic Helicity in Space and Laboratory Plasmas,* (Washington: American Geophysical Union).
Finn, J. M., Antonsen, T. M. 1983, *Phys. Fluids*, **26**, 3540.
Krishan, V. 1996, *J. Plasma Physics,* **56**, 427.
Kusano, K., Suzuki, Y., Nishikawa, K. 1995, *Astrophys. J.*, **441**, 942.
Reiman, A. 1980, *Phys. Fluids*, **24**, 956.
Taylor, B. 1974, *Phys. Rev. Lett*, **35**, 1139.
Woltjer, L. I960, *Rev. Mod. Phys.*, **32**, 914.

J. Astrophys. Astr. (2000) 21, 303–306

The Hemispheric Sign Rule of Current Helicity during the Rising Phase of Cycle 23

S. D. Bao*, G. X. Ai & H. Q. Zhang, *Beijing Astronomical Observatory/National Astronomical Observatories, Chinese Academy of Sciences, Beijing 100 012, China*
**email: bshd@sun10.bao.ac.cn*

Abstract. We compute the signs of two different current helicity parameters (i.e., α_{best} and H_c) for 87 active regions during the rise of cycle 23 The results indicate that 59% of the active regions in the northern hemisphere have negative α_{best} and 65% in the southern hemisphere have positive. This is consistent with that of the cycle 22. However, the helicity parameter H_c shows a weaker opposite hemispheric preference in the new solar cycle. Possible reasons are discussed.

Key words. Sun: activity—magnetic fields—photosphere.

1. Introduction

In the last decade observations have revealed that a hemispheric preference of mag netic chirality (handedness) exists throughout the solar atmosphere, such as sunspot whirls (Richardson 1941), signs of current helicity in active regions (see Table 1), quiescent filaments (Martin *et al.* 1994), sigmoid coronal loops (Rust & Kumar 1996) and interplanetary magnetic clouds (Rust 1994). Table 1 shows that the hemispheric asymmetry in sign of current helicity seems to be stronger in the Huairou Solar Observing Station (HSOS) data (Abramenko *et al.* 1996, Bao & Zhang 1998) than in the Mees Solar Observatory (MSO) data (Pevtsov *et al.* 1995, Longcope *et al.* 1998) Bao *et al.* (2000) studied the origin of this phenomenon and concluded that it is mostly due to a choice of two different helicity parameters (α_{best} and H_c) used in these studies, rather than a disagreement between the two data sets. The interpretation of all these patterns and their possible connection to the dynamo are open to question. In addition, current helicity of magnetic fields also plays an important role in solar flare evolution (Bao *et al.* 1999). The purpose of this paper is to examine whether the hemispheric helicity changes its sign from one solar cycle to another.

2. Data analysis and results

We chose 87 active regions observed with the vector magnetograph at HSOS during the rising phase of cycle 23 to compute the sign of their current helicity. All data used in our study were acquired with favorable weather and seeing conditions during the time in which active regions were located near the central meridian. Considering that the noise level of transverse field measurements is generally higher than that of

Table 1. Signs of photospheric current helicity computed by different groups.

Group	Hemisphere	α_{best} Negative	α_{best} Positive	H_c Negative	H_c Positive	Total
Pevtsov *et al.* (1995)	Northern	25(76%)				33
	Southern		25(69%)			36
Longcope *et al.* (1998)	Northern	58(62%)				93
	Southern		73(66%)			110
Abramenko *et al.* (1996)	Northern			15(79%)		19
	Southern				18(86%)	21
Bao & Zhang (1998)	Northern			168(84%)		199
	Southern				177(79%)	223

Table 2. Distribution of hemispheric helicity signs for the two cycles.

Cycle	Hemisphere	α_{best} Negative	α_{best} Positive	H_c Negative	H_c Positive	Total
22	Northern	152(76%)		168(84%)		199
	Southern		159(71%)		177(79%)	223
23	Northern	26(59%)		14(32%)		44
	Southern		28(65%)		21(49%)	43

line-of-sight field measurements by an order of magnitude, we did not transform our data into disk-center heliographic coordinates to avoid dirtying the vertical components by the projection correction. The 180° azimuth ambiguity was resolved following Wang *et al.* (1994). A detailed description of the HSOS instrument and observational technique may be found elsewhere (e.g., Bao *et al.* 2000).

Table 2 shows the signs of both α_{best} and H_c for 87 active regions during the rise of cycle 23. The value of the parameter α_{best} is determined by the best match between the x and y components of the computed constant-α force-free and observed horizontal magnetic field in the sense of a minimum least-squares difference (Pevtsov *et al.* 1995), and the other parameter H_c is given by computing $B_z\ (\nabla\times \mathrm{B})_z$ (Bao & Zhang 1998).From this table we can notice that 59% of active regions in the northern hemisphere have negative α_{best} , and 65% in the southern hemisphere have positive α_{best} This result is consistent with those results of cycle 22. However, H_c shows a weak opposite hemispheric preference, in disagreement with the cycle 22. The variation of current helicity with solar latitude for all 87 active regions is displayed in Fig. l(a)–l(b). Each plus symbol marks the value of α_{best} or H_c and the latitude (of magnetogram center) for one active region. For comparison, Fig. l(c)–l(d) shows the variation of α_{best} and H_c with solar latitude for the data of cycle 22. These plots demonstrate that current helicity has a maximum at about 15°–25° latitude and decreases toward both the equator and the poles (Pevtsov *et al.* 1995). On the other hand, we can clearly see that there is consistency between two dashed lines in Fig. l(c)–l(d). Fig. l(a)–l(b) show no consistency between attitudinal trends in α and H_c. This means that H_c no longer follows the hemispheric sign rule in the current cycle.

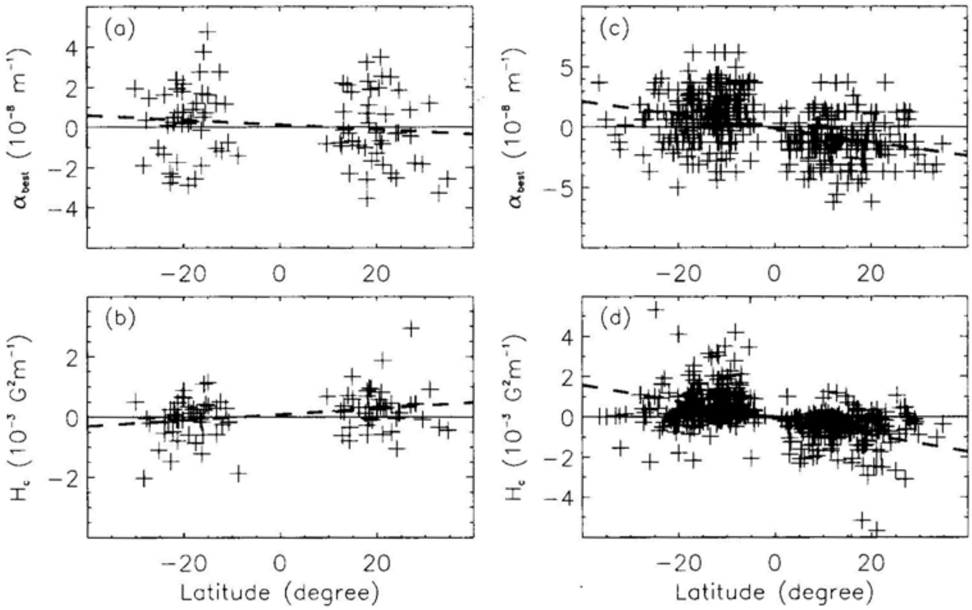

Figure 1. (a)–(b) variation of α_{best} and H_c with solar latitude for 87 active regions observed during the rise of cycle 23. (c)–(d) variation of these two parameters with solar latitude for 422 active regions studied by Bao & Zhang (1998), respectively. The dashed line shows a linear fit to the data.

3. Discussion

The hemispheric sign rule of photospheric current helicity in active regions was established for the cycle 22 (see Table 1). We expect to see the same hemispheric asymmetry for both α_{best} and H_c in a new solar cycle. However, our observations indicate that the helicity parameter H_c does not obey such a hemispheric rule during the rising phase of cycle 23, unlike α_{best}. How to explain it? Our views are that:

- Although such a primary result is interesting, it would be premature to make a serious conclusion based on these data. More samples are required to answer this question.
- Since the Faraday rotation will produce a counterclockwise rotation of the azimuth for a line-of-sight field of positive polarity, and during cycle 23 the polarity of leading sunspots is positive in the northern hemisphere, some active regions with negative current helicity in the northern hemisphere may reverse their original twist and show positive helicity as a result of Faraday rotation. In addition H_c may be more susceptible to Faraday rotation than α_{best} because it is mainly related to the areas where the line-of-sight field is strong. Considering the Hale-Nicholson polarity rule, the Faraday rotation action should be opposite to cycle 22 (see Table 2).
- The cause of the hemispheric tendency is still uncertain. Perhaps these two parameters reflect different physical nature of subphotospheric origin.
- A single sign of α_{best} or H_c averaged over a whole active region is not appropriate. It ignores the small-scale patterns of oppositely directed twist which are known to exist inside active regions.

Acknowledgements

This work was supported by the National Science Foundation of China under grant 19791090 and 19973008.

References

Abramenko, V. I., Wang, T. J., Yurchishin, V. B. 1996, *Solar Phys*., **168**, 75.
Bao, S. D., Pevtsov, A. A., Wang, T. J., Zhang, H. Q. 2000, *Solar Phys*., **175**, 75.
Bao, S. D., Zhang, H. Q. 1998, *Astrophys. J*., **496**, L43.
Bao, S. D., Zhang, H. Q., Ai, G. X., Zhang, M. 1999, *Astr. Astrophys. Suppl. Ser*, **139**, 311.
Longcope, D. W., Fisher, G. H., Pevtsov, A. A. 1998, *Astrophys. J*., **507**, 417.
Martin, S. F., Bilimoria, R., Tracadas, P. W. 1994, in *Solar Surface Magnetisms*, (eds.) R. J. Rutten & C. J. Schrijver, (Dordrecht: Kluwer), 303.
Pevtsov, A. A., Canfield, R. C, Metcalf, T. R. 1995, *Astrophys. J*., **440**, L109.
Richardson, R. S. 1941, *Astrophys. J.,* **93**, 24.
Rust, D. M. 1994, *Geophys. Res. Lett*., **21**, 241.
Rust, D. M., Kumar, A. 1996, *Astrophys. J.,* **464**, L199.
Wang, T. J., Xu, A. A., Zhang, H. Q. 1994, *Solar Phys*., **155**, 99.

J. Astrophys. Astr. (2000) **21,** 307–313

Magnetoconvection and the Solar Dynamo

Å. Nordlund[1], S. B. F. Dorch[2] & R. F. Stein[3]
[1]*Astronomical Observatory & Theoretical Astrophysics Center, Juliane Maries Vej 30, 2100 Copenhagen Ø, Denmark, e-mail: aake@astro.ku.dk*
[2]*The Royal Swedish Academy of Sciences, Stockholm Observatory, SE-13336 Saltsjöbaden Sweden, e-mail: dorch@astro.su.se*
[3]*Dept. of Physics and Astronomy, Michigan State University, East Lansing, MI 48824, USA e-mail: rstein@pa.msu.edu*

Abstract. We review current understanding of the interaction of magnetic fields with convective motions in stellar convection zones. Among the most exciting recent results is the discovery that magnetic fields need not primarily be confined to the stable layer below the convection zone; numerical simulations have shown that surprisingly, strong magnetic fields can be maintained in the interior of the convection zone.

Key words. Magnetic fields—convection—dynamo—Sun.

1. Introduction

The main ingredients of the solar dynamo are thought to be 1) differential rotation, that is able to wind up an initially poloidal magnetic field into a strong, toroidal magnetic flux system, 2) magnetic flux storage, which is able to keep the magnetic field in the convection zone, while the toroidal field strength is building up, 3) magnetic buoyancy, that tends to bring sufficiently strong magnetic fields up to the surface, 4) systematic and or random horizontal velocities, that control the spreading of emerged magnetic fields across the solar surface, and 5) meridional circulation, that may play a role in the migration of magnetic fields towards the equator and towards the poles.

When considering these effects, it must be remembered that the unobserved, subsurface magnetic field is likely to be as intermittent as the observed, surface magnetic field is, and that the fundamental reason for the interrnittency is interaction between the magnetic field and the turbulent convection in the solar convection zone. The solar convection zone covers about 7-8 orders of magnitude in density. The innermost half of the (logarithmic) density range occupies about 95% of the convection zone depth with a nearly polytropic (index 3/2) stratification, while the remaining 5% (about 10 Mm) accounts for the remaining 3–4 orders of magnitude in density, with significant ionization effects considerably influencing the equation of state of the gas.

The range of temperatures is more moderate but, nevertheless, corresponds to a range of pressure scale heights that covers two and a half orders of magnitude, and turn over times that vary from minutes in the surface layers to weeks or months near the bottom of the convection zone.

As explained in more detail below (section 2), the strong density stratification is of crucial importance for the interaction between the magnetic field and the turbulent convection, giving rise to a powerful "stratification pumping" effect that is able to hold the magnetic field down, and thus counterbalance the effects of magnetic buoyancy. These properties of solar magnetoconvection are likely to be of crucial importance for the workings of the overall solar dynamo mechanism (section 3).

2. Magnetoconvection: stratification pumping

During the last decade a series of magneto-convective numerical simulations have been performed (e.g. Hurlburt & Toomre 1988; Brandenburg *et al.* 1990; Jennings *et al.* 1992; Nordlund *et al.* 1992; Hurlburt *et al.* 1994; Nordlund *et al.* 1994; Brandenburg *et al.* 1996).

Simulations of stratified convection have shown that trace particles initially placed in a horizontal layer of a highly stratified model on the average are transported downwards, as a result of the asymmetric vertical transport in stratified convection (Stein & Nordlund 1989). In the context of magnetic fields, such a tendency has also been seen in convective dynamo simulations (Nordlund *et al.* 1992; Brandenburg *et al.* 1996). Most recently Tobias *et al.* (1998) have studied the same phenomenon, and Mcleod (1998) discussed similar ideas as presented here.

Numerical experiments are indeed very helpful in revealing and quantifying the types of effects mentioned in the Introduction, but precisely because of the strong stratification, it is very difficult to make numerical experiments that cover the whole solar convection zone, and that cover the whole range of relevant time scales. Instead, one may choose to model only part of the convection zone, and also, to narrow the range between dynamic and thermal time scales, to scale convective fluxes and thermodynamic fluctuations to much larger values than the ones in the solar convection zone.

From general scaling arguments, one expects that convective velocities scale as $v_{\rm conv} \sim F^{1/3}{}_{\rm conv}$, and that temperature fluctuations scale as $\delta T_{\rm conv} \sim F^{2/3}{}_{\rm conv}$ This is corroborated by recent numerical experiments (Brandenburg *et al.* 2000), that show that the expected scalings indeed are obeyed quite accurately. It is thus possible to explore the dynamics of the lower solar convection zone using models where the total flux is increased by, for example, a factor of 10^5, corresponding to an increase of velocities (and hence a reduction of time scales) by a factor of $10^{5/3} \sim 50$. By using a scaled Kramer's opacity (decreased with a factor of 10^5), one maintains the ratio between radiative and convective fluxes, as well as the overall temperature structure.

In experiments with magnetic fields, scaling of the magnetic field with $B \sim F_{\rm conv}^{1/3}$ maintains the ratio between ordinary velocities and the Alfven velocity, as well as the ratios between magnetic, inertial, and buoyancy forces. Numerical experiments may thus be used to obtain not only qualitative but even semi-quantitative information about the distribution of magnetic fields inside the solar convection zone.

A sequence of such experiments show that stratified convection is able to retain a distribution of surprisingly strong magnetic fields *inside* the convection zone (Dorch 1998; Dorch & Nordlund 2000); cf. Fig. 1.

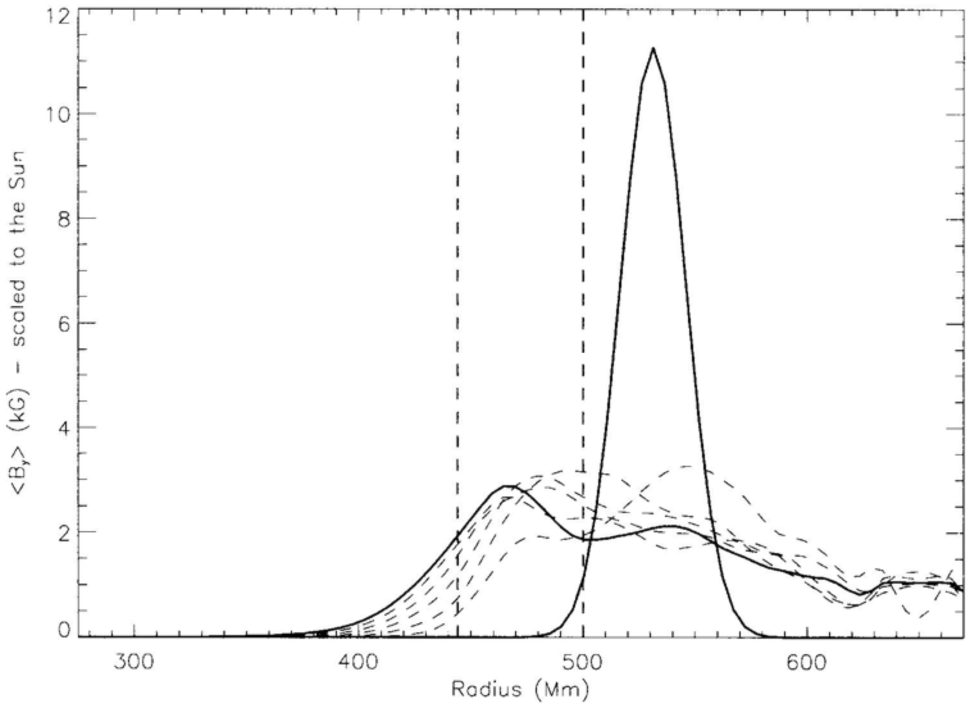

Figure 1. The horizontally averaged magnetic field as a function of radius for 7 different times: t=0 (initial field – thick solid curve), 3.3, 6.5, 9.8, 13.0, 16.3 (thin dashed curves), and 19·5 (solid curve) turn-over times. The approximate bottom and top of the undershoot layer are indicated by two vertical dashed lines. Further illustrations may be found at http://www.as-tro.ku.dk /%71 aake/ talks /Kodaik99.

In these experiments, a horizontal "sheet" (with Gaussian profile) is placed inside the convection zone, in a snapshot with well developed, convectively driven turbulence, and its subsequent evolution is followed. The strength of the magnetic field is varied between experiments. Experiments were performed with both closed and open upper boundary conditions.

In brief, the results of the experiments show that:

- In the kinematic limit (weak magnetic field), a triangular distribution of magnetic field develops, with most of the flux residing near the bottom of, but still *inside* the convection zone.
- While the horizontally averaged magnetic flux peaks in the undershoot layer, below the convection zone proper, the peak magnetic field strengths, as well as the majority of the magnetic flux, resides inside the convection zone.
- With an open upper boundary, some amount of magnetic flux is lost per unit time at the upper boundary. But this effect diminishes when the boundary is moved closer to the real solar surface, and the effect would be much smaller if it was possible to model the entire convection zone.
- With a closed upper boundary, magnetic flux tends to accumulate at the upper boundary, which makes it difficult to study the long time evolution of strong magnetic fields.

- Nevertheless, the experiments show that the limit where buoyancy overcomes the effects of "stratification pumping" exceeds several tens of kG, and may well be consistent with 100 kG flux ropes forming *inside* the convection zone.

As may be illustrated with a simple Interactive Data Language program (shown at the symposium, available from the authors upon request), that traces field line evolution in a 2-D or 3-D polytrope with a schematic, horizontally sinusoidal velocity field, the basic effect is a purely kinematic, anisotropic transport effect, that does *not* require an asymmetry between up and down flows. Thus, the effect is different from the "topological pumping" discussed by Drobyshevski & Yuferev 1974 (see also Drobyshevski *et al.* 1980; Arter *et al.* 1982; Arter 1983; Galloway & Proctor 1983). Rather, it is a simple consequence of mass conservation. Because of the density stratification, most of the mass that is ascending at any one level must overturn into descending motion within about one density scale height, while most of the descending mass continues to descend. As a consequence, if magnetic field lines are traced by following the motion of weightless trace particles attached to the field lines, one observes that after a turn over time there has been a substantial downwards transport of magnetic flux.

With this picture in mind, it becomes possible to relate the flux loss at the upper boundary in the numerical experiments with an open upper boundary to the (much smaller) flux loss at the real solar surface. From the density contrast one may estimate that only about 0·01% of the ascending mass flux at the upper boundary of the numerical model would actually reach the real solar surface; because of mass conservation the rest of the ascending fluid has to turn over before reaching the solar surface. The magnetic field lines attached to the overturning fluid overturns as well, which explains why the magnetic flux loss at the real solar surface is much less than it is in the numerical model.

One may model the influence of rotation at least qualitatively even in these Cartesian models of the convection zone by including a Coriolis force whose direction and magnitude depends sinusoidally on one of the horizontal coordinates, which plays the role of the "latitude". Differential rotation modeled by enforcing a systematic, "latitude" dependent background velocity in the other ("longitudinal") direction. Models which include differential rotation spontaneously generate "toroidal" flux systems, by shearing magnetic flux that was initially poloidal. Again, the strongest fields reside *inside* the convection zone, and flux concentrations with several tens of kG field strength are easily held down by the stratification pumping effect. Models with higher density contrast (and hence smaller flux losses at the surface) are needed to determine the limiting field strength where buoyancy is able to over-power the stratification pumping.

When magnetic flux concentrations reach, and break through the (numerical) surface, bi-polar flux regions are formed. Because of the influence of the Coriolis force, the leading and following polarities are displaced in the same sense as is observed on the Sun; with leading polarity closer to the equator and following polarity closer to the poles. As pointed out by van Ballegooijen (1995), subsurface connections between the (poleward displaced) following polarity of one bi-polar region with the (equatorward displaced) leading polarity of a subsequent bi-polar region tend to have opposite tilt, and hence opposite signs of the poloidal component of the magnetic field. When differential rotation acts on such a U-loop, it tends to "unwind" the magnetic field, by turning the toroidal component into a poloidal one with the opposite polarity relative to the initial one.

A sufficient number of such events would lead to a reversal of the poloidal component, and such a mechanism could be responsible for the periodic field reversals. We have not yet observed such field reversals in the models, but this may be due to the numerical limitations; insufficient numerical resolution and/or density contrast. It will indeed be interesting to see if improved numerical simulations in the future will be able to produce spontaneous, periodic field reversals via this mechanism.

3. Discussion and conclusions

In order to better understand the essential ingredients of solar and stellar dynamos, we must gradually abandon the simplifying assumptions that have been necessary in the past, and move on to more realistic models. Here, we have discussed some of the interesting effects that appear when one allows for the interaction of magnetic fields with three-dimensional, strongly stratified convection.

Perhaps the most important outcome is that stratified convection unavoidably leads to a strong downward pumping of magnetic flux. This "stratification pumping" is a direct consequence of mass conservation, and does not require an asymmetry between ascending and descending motion pattern. (Up or down asymmetries are also a consequence of mass conservation, and may in practice contribute to the pumping effect but, as shown by the IDL example program, it is not a necessary ingredient.)

The main conclusion, which is a rather revolutionary one, is that "flux storage" in the stable layer below the solar convection zone is, after all, not a necessary ingredient in the solar dynamo. Instead, the indication from the numerical experiments is that the majority of the toroidal flux resides inside the convection zone, and that the maxima of magnetic field strength occur there as well. It should be noted that, because of the scaling of fluxes and velocities in the models, the undershoot layer is much more extended in the models that it is in the Sun.

In a scenario with the toroidal flux system residing inside the convection zone, flux emergence occurs when differential rotation has increased the field strength of a toroidal flux structure sufficiently, so that buoyancy is finally able to over-power the downward pumping associated with stratified convection.

An attractive feature of such a scenario is that the resulting, buoyant flux tubes may be appreciably shorter than if they were due to a Parker instability in flux tubes stored in the stable undershoot layer. The Parker instability works only for perturbations longer than about 12 local scale heights, and it is a common property of global, thin flux tube studies that it is the m = 1 and m = 2 modes that are most unstable (Spruit 1981; Moreno-Insertis 1986, 1992; Choudhuri 1989; Fan *et al.* 1993, 1994; Caligari *et al.* 1995, 1998).

The Parker instability driven modes are uncomfortably long, and produce emerging flux regions with too rapid separation between the two polarities (van Ballegooijen 1998). Also, flux tubes need to be twisted, or have internal structure, in order to not be broken up by a Rayleigh-Taylor like instability (Dorch 1995; Emonet & Moreno-Insertis 1996ab; Dorch & Nordlund 1998; Dorch *et al.* 1999). Flux tubes subjected to the turbulent motions in the convection zone may be expected to have such characteristics.

Several other features of the solar activity cycle come out naturally from a scenario where most of the magnetic flux resides near the bottom of, but inside, the convection zone. One example is the observed chirality of active region magnetic fields; statistically significant but randomly varying twists of the magnetic field lines, with opposite signs in the two hemispheres (see the review by Canfield (2000) in this volume). A twist with the correct sense of orientation results from the radial shear near the bottom of the convection zone (the "tachocline"), acting on the poloidal connections between the toroidal flux systems in the two hemispheres.

Even though the loss of magnetic flux at the upper boundary is exaggerated in current numerical models with open boundaries, such a loss is certainly a real effect that is important to consider, since the Sun is known to loose a considerable amount of toroidal magnetic flux during an activity cycle (van Ballegooijen 1998).

The picture that is starting to emerge from the numerical simulations is reviving and re-enforcing the classical Babcock-Leighton model of the solar dynamo: Differential rotation winds up an initially poloidal magnetic field. Magnetic buoyancy brings the flux up to the solar surface. The Coriolis force causes a systematic tilt of the emerging flux regions, and subsequent drift of the surface magnetic field causes a poloidal field reversal.

The new type of scenario, where the magnetic field responsible for the activity cycle resides inside the convection zone is also attractive from the point of view of late type stars such as M dwarfs, where no undershoot storage is available (e.g. Chabrier & Baraffe 1997; Allard *et al.* 1997).

In summary it seems as if the "buoyancy dilemma" may have been solved, or, to put it differently, that it may have never existed; stratified convection is able to keep a toroidal flux system *inside* the convection zone while differential rotation is working on increasing its field strength. The effect is an unavoidable consequence of mass conservation, possibly enhanced by the asymmetry between up- and downwards motions (itself a consequence of the density stratification).

References

Allard, F,Hauschildt,P. H.,Alexander,D. R., Starrfield, S.1997,*Ann. Rev. Astr. Astrophys.*, **35**, 137.

Arter,W. 1983, *J. Fluid Meck*, **132**, 25.

Arter, W., Proctor, M. R. E.Galloway, D. 1982, *Mon. Not. R.Astr. Soc*, **201**, 57P

Brandenburg, A., Nordlund, A., Pulkkinen, P., Stein, R. R, Tuominen, I. 1990, *Astr. Astrophys.*, **232**, 277-291.

Brandenburg, A., Jennings, R. L., Nordlund, Å., Rieutord, M., Stein, R. R, Tuominen, I. 1996, *J. Fluid Meck,* **306**, 325-357.

Brandenburg, A., Chan, K. L., Nordlund, Å., Stein, R. R 2000, *Astrophys. J.* (in preparation).

Caligari, P., MorenoInsertis, R,Schussler, M.1995, *Astrophys. J.*,**441**, 886-902.

Caligari, P., M.Schussler, R Moreno-Insertis 1998, *Astrophys. J.,* **502**, 481.

Canfield, R.2000, *J.Astrophys. Astr.* (this issue).

Chabrier, G., Baraffe, I. 1997, *Astr. Astrophys.*, **327**, 1039.

Choudhuri, A. R. 1989, *Solar Phys*., **123**, 217-239.

Dorch, S. B. F 1995, On the origin and properties of buoyant magnetic fields and flux tubes in the sun. Master's thesis, NBI Copenhagen University.

Dorch, S. B. F 1998, *The Solar Dynamo: A Conceptual Jigsawpuzzle.* PhD thesis, Copenhagen University.

Dorch, S. B. F, Nordlund, Å. 1998, *Astr. Astrophys*., **338**, 329-339.

Dorch, S. B. F,V. Archontis, Nordlund,Å.1999, *Astr. Astrophys*., **52**, L79–L82.

Dorch, S. B. F., Nordlund, Å. 2000, *Astr. Astrophys*., (in preparation)
Drobyshevski, E., Yuferev, V. 1974, *J. Fluid Meck*, **65**, 38.
Drobyshevski, E., Lokesnikova, E. N., Yuferev, V. 1980, *J. Fluid Meck*, **101**, 65
Emonet, T., Moreno-Insertis, F. 1996a, *Astrophys. J*., **458**, 783-801.
Emonet, T., Moreno-Insertis, F. 1996b, *Astrophys. J*., **472**, L53.
Fan, Y, Fisher, G. H., DeLuca, E. E. 1993, *Astrophys.* J., **405**, 390-401.
Fan, Y, Fisher, G. H., McClymont, A. N. 1994, *Astrophys.* J., 4**36**, 907-928.
Galloway, D., Proctor, M. R. E. 1983, *Geophys. & Astrophs. Fluid Dyn*., **24**, 109
Hurlburt, N. E., Toomre, J. 1988, *Astrophys. J*., **327**, 920-932.
Hurlburt, N. E., Toomre, J., Massaguer, J. M., Zahn, J.P. 1994, *Astrophys. J*., **421**, 245-260.
Jennings, R. L., Brandenburg, A., Nordlund, Å., Stein, R. F. 1992, *Mon. Not. R. Astr. Soc*, **259,** 465-473.
Mcleod, A. D. 1998, in *Numerical Astrophysics*, (ed.) Miyama, S. M. *et al*., 331.
Moreno-Insertis, F. 1986, *Astr. Astrophys*., **166,** 291-305.
Moreno-Insertis, M. 1992, The motion of magnetic flux tubes in the convection zone and the subsurface origin of active regions. in *Sunspots: Theory and Observation*, (Kluwer: Academic Publishers) 385–410.
Nordlund, Å., Brandenburg, A., Jennings, R. L., Rieutord, M., Roukolainen, J., Stein, R. F., Tuominen, I. 1992, *Astrophys. J.,* **392**, 647-652.
Nordlund, Å.,Galsgaard, K., Stein,R. F.1994,Magnetoconvection and magnetoturbulence. In *Solar Surface Magnetic Fields*, (ed.) R. J. Rutten and C. J. Schrijver, vol. 433, NATO ASI Series.
Stein, R. F., Nordlund, Å. 1989, *Astrophys. J*., **342**, L95-L98.
Spruit, H. C. 1981, *Astr. Astrophys*., **98**, 155-160.
Tobias, S. M.,Brummel, N. H., Clune, T. L.,Toomre, J. 1998, *Astrophys. J*., **502**, L177-L180.
van Ballegooijen, A. A. 1995, (Private communication),
van Ballegooijen, A. A. 1998, in *Synoptic Solar Physics*, vol. 140, (Kluwer: Academic Publishers) 17.

J. Astrophys. Astr. (2000) **21,** 315-318

Large-scale Flow and Transport of Magnetic Flux in the Solar Convection Zone

P. Ambrož, *Astronomical Institute of the Acad. Sci. of the Czech Republic, CZ-25165 Ondřejov, The Czech Republic*,
e-mail: pambroz@asu.cas.cz

Abstract. Horizontal large-scale velocity field describes horizontal displacement of the photospheric magnetic flux in zonal and meridian directions. The flow systems of solar plasma, constructed according to the velocity field, create the large-scale cellular-like patterns with up-flow in the center and the down-flow on the boundaries. Distribution of the large-scale horizontal eddies (with characteristic scale length from 350 to 490 Mm) was found in the broad equatorial zone, limited by 60° latitude circles on both hemispheres. The zonal averages of the zonal and meridian velocities, and the total horizontal velocity for each Carrington rotation during the activity cycles no. 21 and 22 varies during the 11-yr activity cycle. Plot of RMS values of total horizontal velocity is shifted about 1·6 years before the similarly shaped variation of the magnetic flux.

Key words. Sun—large-scale flow—cyclic variations.

The large-scale flows, characterizing the intermediate scale between the small-scale and solar rotation are expected from the theoretical considerations, but still the knowledge of such flows is very meagre. The main problem of large-scale velocity field measurements consists in the low velocity values of the order from 50 to 100 ms^{-1},blended by at least one order higher values of small-scale flows and also by the velocities of solar oscillations and rotation.

Movement of the large-scale magnetic flux is a well known characteristic of the magnetic field evolution in solar photosphere. In the past Wilcox & Howard (1970), Snodgrass (1983), Stenflo (1989) and Latuschko (1996) used the distribution of the background magnetic flux as "tracer" for measurements of horizontal velocity. The lifetime of large-scale magnetic phenomena is much longer than one Carrington Rotation Period (CRP, 27.275 days). We used CRP as the elementary time step of our data and the analysis was carried out during a time interval covering two 11-yr cycles of solar activity.

Surface distribution of magnetic flux is considered as a continuous scalar field. Displacements in zonal and meridional directions are measured by the local correlation technique (November 1986). The horizontal velocity field is inferred relative to the Carrington reference system in 2701 homogeneously distributed points in the photosphere from differences of pairs of the consecutive synoptic charts (Ambrož 2000). The large-scale velocity field is a continuously varying quantity in both orthogonal directions and in time. The velocity field structure differs during the whole period of activity cycle from the axially symmetric zonal velocity. It is significantly heterogeneous for different points in the photosphere. The solar equator defines a dominant plane for the north-south symmetry of the vector structures.

Semiempirical simulation of the horizontal flow in the photosphere is made by the "cork" procedure. The free testing particles, driven by inferred horizontal velocity are displaced in the solar photosphere during the time. The particle trajectories illustrate the streamlines of stationary flow. The flow structure, integrated between two consecutive Carrington rotations is the simplest picture of the large-scale flow in the solar photosphere. The nearly zonal flow was indicated in the circumpolar regions, polewards from 60° parallels on both hemispheres. Equatorwards from such limits large-scale eddies are observed (Ambrož 1987). The frequency of occurrence and the vorticity is temporally variable. Dominant vortices rotate on the northern hemisphere in the counterclockwise sense and their rotation on the southern hemisphere is opposite. The vorticity structure is much more developed during the period of maxima of the solar activity cycle. The flow structure changes slowly during a few CRPs and a temporal evolution of eddies was observed. The short-lived eddies (during one CRP) are frequent. The great, well developed eddies have a few phases of formation. The initial phase covers formation of eddy or integration of two or more small eddies respectively. The main phase is characterized by formation of one great eddy. During the decaying phase, one can observe the fragmentation of the main eddy into smaller vorticity phenomena. Finally, in the last step, the whole phenomenon disappears. Such a process is realized during 3 to 6 CRPs. On the synoptic chart during one CRP we usually see only one eddy, but also observed were five main eddies in different stages of their evolution.

The study of flow structure shows the discrete character of the flow systems. The free "cork" testing particles are initially homogeneously distributed in solar photosphere. After time interval of one or more CRPs, the testing particles are redistributed due to the inhomogeneous velocity structure. The cellular-like phenomena are formed with a characteristic dimension of about 40° in longitude. They contain positive and negative values, distributed into large-scale regions. The positive and negative regions form large-scale patterns, covering the whole photosphere. The structure of such divergence patterns contains the non-axially symmetric component. The accumulation of testing particles correlates well with the negative horizontal divergence regions.

According to the assumption about the 3D divergence-free flow of the incomepressible medium, the positive regions may indicate the large-scale up-flow, whereas the negative regions correspond with the down-flowing plasma. The character of the empirically simulated flow evokes an image of large-scale flow phenomena with a possible relationship with the large-scale convection in the deep layers of solar convection zone. The structure of convection cell is characterized by possible up-flow in the central part and by down-flow on the peripheries with more or less horizontal eddy flow between the vertical flow regions.

The horizontal divergence chart, calculated from the inferred velocity field, is projected on the sphere and shown in Fig. 1. The white regions in the left column contain the positive divergence values, the negative horizontal divergence relates with the dark regions. Both regions create the separate and cellular-like patterns on the solar surface with mean characteristic dimension about 420 ± 70 Mm. The shape and the position of the cellular patterns vary in time.

Figure 1. Composition of the horizontal divergence map derived from displacement of the magnetic flux distribution during one CRP (left), the streamlines during two CRP (center) and the end points of the "cork" trajectories after three CRP (right) when nearly "immediate" stationary velocity field was used for simulation of the transport during sufficiently long time. The velocities are inferred for the time interval from CR 1866 to CR 1867 in the year 1993. The ends of streamlines correlate well with black (negative) areas in the left picture. The white regions show the positive values of the horizontal divergence. The shadow areas relate with horizontal divergence free regions with nearly parallel streamlines.

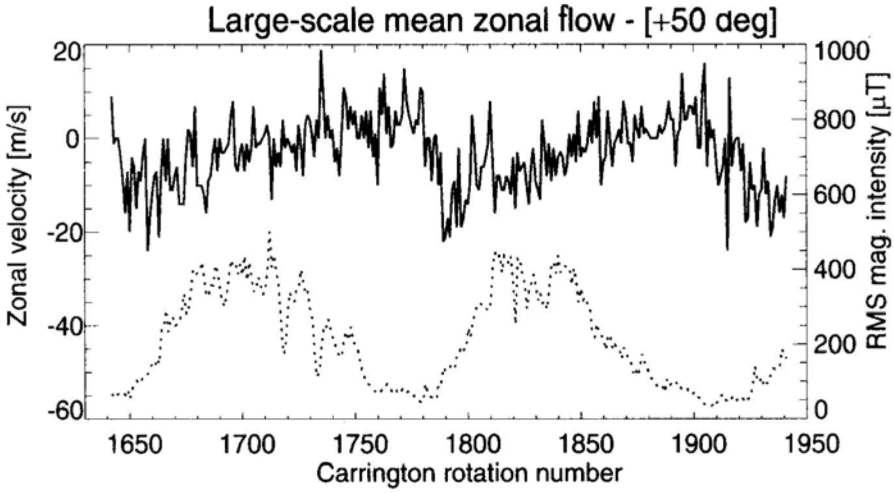

Figure 2. Plot of the time dependent mean zonal velocity (full line and scale on the left). The plot drawn by dotted line corresponds with the mean absolute value of the magnetic flux, corresponding with the scale on the right (for details see in text).

The mean horizontal velocities in Fig. 2 were calculated from each synoptic chart in the latitude belt from 50°N to 50°S for all longitudes. The investigated time interval covers the period of two cycles of solar activity, starting from CR1642 to CR1943. On the plot is zonal velocity compared with absolute value of magnetic flux. Both curves anti-correlate and the time lag of minimum-maximum is about 22 CRPs. The RMS horizontal velocity values were also correlated with magnetic flux. The RMS zonal velocity maximum is in the increasing part of the 11-yr solar activity cycle. The velocity curve is also shifted 21 CRPs (about 1.6 years) before the curve of the magnetic field. The cross correlation coefficients in extremes are -0.47 and 0.34, respectively.

Acknowledgement

Wilcox Solar Observatory data was used with the courtesy of J.T. Hoeksema. The Wilcox Solar Observatory is supported by NASA, NSF, and ONR. The present work was under the support of grant of GA/AVCR No. A3003806 and the Key Project AVČRNo. Kl003601.

References

Ambrož, P. 1987, *Bull Astron. Inst. Czechosl*, **38**, 110.
Ambroz, P.2000, *Solar Phys*., (in press).
Latuschko, S.1996, *Solar Phys*., **163**, 241.
November, L. J. 1986, *Appl. Opt*, **25**, 392.
Stenflo, J. O. 1989, *Astr. Astrophys*., **210**, 403.
Snodgrass, H. B. 1983, *Astrophys. J.,* **270**, 288.
Wilcox, J. M., Howard, R. 1970, *Solar Phys*., **13**, 251.

J. Astrophys. Astr. (2000) **21**, 319-322

The Space Stellar Photometry Mission COROT: Asteroseismology and Search for Extrasolar Planets

Annie Baglin[1]*, Gérard Vauclair,[2] & the COROT team

[1]*DESPA, UMR CNRS 8632 Observatoire de Paris, 92195 Meudon, France*
[2]*LAT, UMR CNRS 5572, Observatoire de Midi-Pyrénées, 31 400 Toulouse, France*
**email: annie. baglin@obspm.fr*

Abstract. The main scientific objectives, asteroseismology and search for extrasolar planets for the COROT photometric mission are presented, and its interest in terms of stellar variability. A description of the payload, details of the scientific program, the ground based preparatory observations and bibliography can be found at http://www.astrsp-mrs fr/corot/ pagecorot html.

Key words. Space—photometry—asteroseismology—extrasolar planets.

1. The asteroseismology programme

COROT will realise both an “exploratory programme”, to detect oscillations in a large variety of stars and to classify the asteroseismologic properties of stars in the Hertzprung-Russel diagram, and a more specific one called “central programme” for a detailed study of a few stars, specially chosen to test the hydrodynamics of the internal layers and the physical state of the stellar cores.

1.1 *The exploratory programme*

Its purpose is to determine the domain of stellar parameters for which oscillations are detectable, and the relation between the amplitudes of the solar-like oscillators and their global characteristics.

To achieve this, one has to observe a sample of objects with a variety of stellar parameters, i.e. mass, age, chemical composition, state of rotation...but with moderate signal to noise ratio. A frequency resolution of 0.5 μ Hz is sufficient for this purpose, corresponding to observing runs of 10 to 20 days. Stars down to the 9th magnitude are appropriate targets; 5 to 10 targets will be observable at the same time. Let us note that COROT is up to now the only seismology project which has this multiplex capability.

Several tens of stars will have to be followed, corresponding to a total observing time of at least 2 to 4 months.

1.2 *The central programme*

It is more ambitious and more time consuming than the exploratory one; it corresponds to the second step in the development of space asteroseismology. It aims at observing very precisely a small set of objects, selected for their diagnostic power. The choice of these targets will be partly based on the results of the exploratory phase.

Using the solar case as a template, we fix the accuracy of the frequency measurement at 0.1 μ Hz to have access to mode profiles and rotational splitting and to measure precisely the distribution of the mode frequencies. For a 6th magnitude star, the detection threshold will be less than 1 ppm. For A and F stars close to the main sequence, it will then be possible to measure the size of the convective cores, the size of the outer convective zones and their helium content or the rotation profile of δ Scuti stars.

A least 5 runs are planned, during which one bright star (the main target) and several fainter ones in the surrounding field of view will be followed.

2. The exoplanet programme

The detection of a telluric planet is a major challenge and is expected to be the next big step in astronomy, and recent discoveries of a few tens of giant planets have upset our vision of the formation of planetary systems. A sensible approach for the search and study of extrasolar planets around stars is first searching for giant exoplanets, then searching for telluric ones, and finally spectroscopically analysing them, with an emphasis on telluric ones.

The first step has been made with the discovery of 51 Peg b in 1995, but presently we do not have an unbiased statistics of these planets. The second objective is ONLY accessible to the COROT mission (or to similar ones, such as KEPLER or EDDINGTON, which are not approved yet). The third one will be the main goal of future very ambitious missions which will probably fly in a few decades.

This detection of telluric planets around solar type stars is very difficult because of their small masses. Before the achievement of ambitious space projects (interferometers, coronographs), only gravitational amplification and transits are available on a short or mid term. The transit method is the only one which allows the precise determination of the orbital period and the size of the planet. Yet this method needs a high precision photometry (10^{-3} to 10^{-4}) and continuous observations during a long period (several months). Particularly well adapted to the telluric planets, it can also detect giant extra-solar planets (detectable by spectroscopy from the ground) and determine their albedo.

As COROT is devoted to stellar photometry, aiming at both a high precision and a long observation time, the search for exoplanets by the transit method can easily be integrated in the payload and in the mission profile.

Presently, we do not know the statistical distribution of telluric exoplanets as function of their size. In fact, we do not even know if they exist! Though COROT is not a mission devoted specifically to telluric exoplanets detection, it will demonstrate the “existence theorem”. This piece of information is crucial for the future projects which will aim to perform the spectroscopy of such objects.

One major difficulty in the detection of a planetary transit is to get rid of false alarms due to photometric variations of stellar origin, as stellar activity. To do so a dispersive element (prism) has been included in the exoplanet field giving a little spectrum (3–4 resolution). It has been shown that this coloured information decreases significantly the false-alarm probability. In order to estimate the number of possible transits due to telluric planets, we have to estimate the number of solar type stars escorted a priori with at least one planet. Since 50 % of the young stars have a dust disc, it is reasonable to assume a priori that half of the stars have got telluric planets and that 20% of them have got planets whose radius is superior to the earth. The number of events depends on the radius and the distance of the planet to its parent star, so it is difficult to give numbers. With a photometry optimised up to $m_v = 15.5$ (which corresponds to the COROT field with a hundred thousand stars observed during the mission) the expected number of detections is:

- 25 planets having a radius of 1.6 earth radius at 0.3 a.u.
- 40 planets having a radius of 2 earth radius at 0.3 a.u.
- A few planets of around 2 earth radius in the "habitable" zone thanks to the chromatic information.
- Several hundreds of hot Jupiters and Uranus like planets, with detailed light curves.

3. The additional programmes and the stellar photometry data base

COROT will provide extremely long and uninterrupted sequences of photometric data of more than hundred thousand stars, of magnitude between 12 and 16, acquired by the exoplanet field. The time sampling is 15 minutes, the accuracy on an individual measurement is a few 10^{-4}, and the duration varies from 10 to 150 days. For the brightest ones two colours will be available, with the same accuracy. The only available data of this type come from the microlensing surveys, with looser time sampling (1 day) and very rough photometry (1%). They have shown that these sets of wide complete samples are extremely useful to probe scenarios of evolution and stellar physics. They nicely complement seismology of much smaller samples of targets.

For instance, COROT will obtain light curves of binary stars, with a level of precision which will allow to study tidal modulations and tidal lags which can provide a direct measurement of the viscosity of the stellar material.

Colour photometry can supply, through the use of surface tomography, relevant information concerning the evolution of cold spots and differential rotation axes of single and binary stars and can give a direct measurement of limb and gravity darkening laws.

For stellar activity, the high photometric precision and long time series provided by COROT will allow us to extend· the analysis of the dependence of magnetic activity upon rotation to moderately active stars and moderate rotators, thus providing powerful observational tests to dynamo theories.

Analogous to planets, comets will produce transits detectable by COROT; Kuiper Belt objects of very small size could also be observed.

To perform such studies called "Additional Programmes", scientists will bid against an Announcement of Opportunity to access data and/or observing time.

4. Mission requirements

To achieve the scientific objectives, the mission lifetime has to reach at least 3 years, and the programme asks for long and continuous exposures on the same targets, as to reach the frequency resolution of 0.1 μ Hz up to 150 days are necessary. The Small Mission of CNES Programme imposes a low altitude orbit; polar inertial orbits are the only ones to allow 150 days continuously on the same field. To avoid eclipses and straylight from the Earth, the observable zone is restricted to two circles, centered on the equator, in opposite direction, with a radius of approximately 12 to 14 degrees.

The selection of targets inside these fields is the responsibility of the Scientific Council. The working group on “Ground Based Programme” is responsible for gathering all the data necessary to make this choice.

J. Astrophys. Astr. (2000) **21**, 323–329

Helioseismology and the Solar Interior Dynamics

S. Vauclair, *Laboratoire d'Astrophysique de Toulouse, 14, Avenue Edouard-Belin, 31400-Toulouse, France*
e-mail: sylvie.vauclair@obs-mip.fr

Abstract. The inversion of helioseismic modes leads to the sound velocity inside the Sun with a precision of about 0.1 per cent. Comparisons of solar models with the "seismic sun" represent powerful tools to test the physics: depth of the convection zone, equation of state, opacities, element diffusion processes and mixing inside the radiative zone. We now have evidence that microscopic diffusion (element segregation) does occur below the convection zone, leading to a mild helium depletion in the solar outer layers. Meanwhile this process must be slowed down by some macroscopic effect, presumably rotation-induced mixing. The same mixing is also responsible for the observed lithium depletion. On the other hand, the observations of beryllium and helium 3 impose specific constraints on the depth of this mildly mixed zone. Helioseismology also gives information on the internal solar rotation: while differential rotation exists in the convection zone, solid rotation prevails in the radiative zone, and the transition layer (the so-called "tachocline") is very small. These effects are discussed, together with the astrophysical constraints on the solar neutrino fluxes.

Key words. Helioseismology—diffusion—light elements—abundances.

1. Introduction

The Sun is the most well known of all the stars. Its mass, radius, luminosity and age have been widely discussed in the present conference. The study of its internal structure entered a new age with helioseismology. Several ground based networks, as well as several instruments aboard the space mission SOHO, continuously observe the solar oscillations. Millions of solar p-modes have been detected. The inversion of the measured frequencies yields accurate and detailed information about the sound velocity in the Sun's interior, which in turn leads to constraints on the equation of state, opacities, chemical composition. Studies of the mode splitting also give precise information on the internal differential rotation (Chitre 2000).

The photospheric abundances of the Sun have been precisely determined (Grevesse 1991; Grevesse & Sauval 1999). For the light elements, the abundance determinations show that lithium has been depleted by a factor of about 140 compared to the protosolar value while beryllium is not depleted by more than a factor 2 (Balachandran & Bell 1998).

Observations of the $^3He/^4He$ ratio in the solar wind and in the lunar rocks (Geiss 1993; Gloecker & Geiss 1998) show that this ratio may not have increased by more than ≅ 10% since 3 Gyr in the Sun. While the occurence of some mild mixing below the solar convection zone is needed to explain the lithium depletion and, as we will see below, is consistent with helioseismology, the $^3He/^4He$ observations put a strict constraint on its efficiency.

In the present paper we discuss the constraints on the internal structure of the Sun, including element settling and mixing processes, obtained from helioseismology and abundance measurements. Implications on the solar neutrino fluxes are also presented.

2. Element settling in the Sun and solar type stars

Element settling inside the Sun has now become detectable from the comparison of the observed oscillation modes with the results of the theoretical models. This settling is due, not only to gravitation, but also to thermal diffusion and radiative acceleration (although this last effect is small compared to the two others). It leads to abundance variations of helium and heavy elements of order ≅ 10% below the convective zone. Although not observable from spectroscopy, such variations lead to non negligible modifications of the solar internal structure and evolution. Helioseismology is a powerful tool to detect such effects, and its positive results represent a great success for the theory of stellar evolution.

2.1 *Theory of element settling in the Sun and the stars*

The importance of element settling inside the stars during their evolution is now widely recognized as a “standard process”. As soon as condensed from interstellar clouds, the self-gravitating spheres built density, pressure and temperature gradients which forced the various chemical species present in the stellar gas to move with respect to one another. This process is believed to be the reason for the large abundance variations observed in main-sequence type stars, horizontal branch stars and white dwarfs (Vauclair & Vauclair 1982).

Inside the convective regions, the rapid macroscopic motion mixes the gas components and forces their abundance homogenisation. The chemical composition observed in the external regions of the cooler stars is thus affected by the settling which occurs below the outer convective zones. Since the settling time scales vary within the first approximation like the inverse of the density, the expected variations are smaller for cooler stars, which have deeper convective zones. While the abundances of some elements can be seen to vary by several orders of magnitude in the hottest Ap stars, the maximum variations in the Sun are not larger than a few per cent (≅ 10%.).

The computation of element settling is based on the Boltzmann equation for dilute collision-dominated plasmas. In case of thermodynamical equilibrium, solution of the equation is the maxwellian distribution function. In stars like the Sun, the distribution is not maxwellian, due to the influence of the local gravity (or pressure gradient), thermal gradient, radiative acceleration and concentration gradient. However the deviations from the maxwellian distribution are very small and can be treated in the framework of a perturbation theory.

Two different methods have been used to solve the Boltzmann equation in such an approximation. The first method relies on the Chapman-Enskog procedure (described in Chapman & Cowling 1970), using convergent series of the distribution function. This procedure is applied to binary mixtures, leading to expressions with successive approximations for the binary diffusion coefficients. For the diffusion of charged particles in a plasma, a ternary mixture approximation is introduced, including the electrons. This method was widely used in the first computations of diffusion processes in stars (see Vauclair & Vauclair 1982). Even recently, similar methods have been used by many authors, for example Bahcall & Loeb (1990), Bahcall & Pinsonneault (1992), Richard *et al.* (1996). The second method is that of Burgers (1969), in which separate flow and heat equations for each component of a multi-component mixture are solved simultaneously. Descriptions of this method may be found for example in Cox, Guzik & Kidman (1989), Richer & Michaud (1993), Thoul, Bahcall & Loeb (1994).

In any case the diffusion equation has to be solved simultaneously for all the considered elements. The order of magnitude of the time scales generally implies the computation of many iterations of the diffusion process for a single evolutionary time step. For each computation of a new model along the evolutionary track, the tables of abundances inside the star have to be transferred for every element, as a function of the internal mass. For the model consistency, these abundance profiles must be taken into account in the interpolation of the opacity tables.

For the Sun, the whole process has to be iterated several times from the beginning, with small changes in the original helium mass fraction and mixing length parameter, to obtain the right Sun and the right age (luminosity and radius with a precision of at least 10^{-4}).

2.2 *Treatment of collisions*

The element settling is in fact the result of a competition between two kinds of processes. First the individual atoms want to move due to the various gradients. Second their motion is slowed down due to collisions with the other ions as they share the acquired momentum in a random way. The diffusion time scales are direct functions of the collision probabilities for the considered species. A good treatment of collisions is thus necessary to obtain the abundance variations with a high degree of precision.

For collisions between charged ions, problems similar to those encountered for the equations of state have to be solved. The basic question concerns the divergence of the Coulomb interaction cross sections. In the first computations of diffusion, the "Chapman & Cowling approximation" was used, assuming a cut-off of the cross section equal to the Debye shielding length. Average values of the shielding factor were used for analytical fits of the resulting diffusion coefficients.

Paquette *et al.* (1986) proposed a more precise treatment of this problem. They pointed out that the Debye shielding length has no physical meaning as soon as it is smaller than the interionic distance. They proposed a screened coulomb potential with a characteristic length equal to the largest of the Debye length and interionic distance, and they gave tables of collision integrals which can be used in the computation of diffusion processes in the stellar gases. The Paquette *et al.* approximation should be generally used in the computation of stellar structure. It may however in most cases be replaced by an analytical expression given by Michaud & Proffitt (1992).

2.3 *Radiative acceleration*

Turcotte *et al.* (1998) have consistently computed the radiative acceleration on the elements included in the OPAL opacities. They have found, contrary to current belief, that the effect of radiation can, in some cases, be as large as $\cong$ 40% that of gravity below the solar convective zone. This is important only for metals however, and not for helium. When radiative acceleration is neglected, the abundance of most metals changes by about $\cong$ 7.5% if complete ionisation is assumed below the convective zone, and by $\cong$ 8.5% if detailed ionisation rates are computed. When radiative acceleration is introduced, with detailed ionisation, the results lie in-between. The resulting effect on the solar models is small and can be neglected (although it becomes important for hotter stars).

2.4 *Influence of macroscopic motions*

Macroscopic motions do not prevent element settling. Their influence consists in reducing the abundance gradients, thereby increasing the settling time scales and decreasing the final abundance variations. They are definitely needed in stars to account for the observed abundances, which would show much larger anomalies if settling was occurring alone (see Vauclair 2000).

Computations including rotation-induced macroscopic motions have been described by many authors, including Zahn (1992), Richard *et al.* (1996), Maeder & Zahn (1998), Bran *et al.* (1999), Vauclair (1999). Two kinds of effects may be important in the solar interior: the classical meridional circulation which, according to Zahn's theory, leads to a large horizontal turbulence and a small vertical mixing of chemical species, and instabilities induced by the large shear which occurs below the convective zone, the so-called "tachocline". (Spiegel & Zahn 1992). In the presence of a vertical μ-gradient, the meridional circulation velocity is the sum of two terms which leads to motion in the opposite directions, the "Ω-currents", and the "μ-currents". In case of helium gravitational settling, a μ-gradient builts up which soon counteracts the standard meridional circulation below the convective zone. In the deeper layers, the nuclearly induced μ-gradient plays a similar role. Such an effect is important to explain the constancy of beryllium and the isotopic helium ratio in the Sun, while lithium is destroyed by two orders of magnitude (see below).

3. The solar case

3.1 *Evidence of element settling inside the sun from helioseismology*

Solar models computed in the old "standard" way, in which the element settling is totally neglected, do not agree with the inversion of the seismic modes. This result has been obtained by many authors, in different ways. There is a characteristic discrepancy of a few per cent, between the sound velocity computed in the models and that of the seismic Sun just below the convective zone. Introducing the element settling reconciliates the two results. It is also possible to reduce the discrepancy between sound velocity in the old solar standard models and in the seismic Sun by adding effects other than element settling. For example changes in the opacities could possibly lead to similar results (Tripathy & Christensen-Dalsgaard 1998). However, as already pointed out, element settling must not be considered as a new parameter in the computations. It represents second order effects in the physics of auto-gravitational spheres, precisely and without any free parameter. Introducing element settling in the standard models means improving the physics. The fact that the models with settling lie closer to the seismic Sun than the models without settling is quite encouraging.

3.2 *Discussion: necessity of mild mixing, ^{7}Li and ^{3}He*

Although the introduction of pure element settling in the solar models considerably improves consistency with the seismic Sun, some discrepancies do remain, particularly below the convective zone where a "spike" appears in the sound velocity (Richard *et al.* 1996; Brun *et al.* 1998). The helium profiles directly obtained from helioseismology (Basu 1997; Antia & Chitre 1997) indeed show a helium gradient below the convective zone which is smoother than the gradient obtained with pure settling. Furthermore, standard solar models including element settling do not reproduce the observed lithium depletion.

In Richard *et al.* 1996, a mild mixing below the convective zone, attributed to rotation-induced shears (Zahn 1992), was introduced to account for the lithium depletion. It was shown that such a mixing may also reduce the spike in the sound velocity, leading to more consistent solar models than the ones computed with pure element settling. In these models however the abundance of ^{3}He increased in the convective zone, due to a small dredge up from the tail of the ^{3}He peak.

Studies of the influence of a mild mixing on the sound velocity profile have been carried out by several authors recently (see Brun *et al.* 1999). They confirmed that it may reduce the spike below the convective zone. It is difficult however to prevent ^{3}He from increasing in the observed layers.

Vauclair & Richard (1998) have tried several parametrizations of mixing below the solar convective zone, which could reproduce both the ^{7}Li and the ^{3}He constraints. The only way to obtain such a result is to postulate a mild mixing, efficient down to the lithium nuclear burning region but not too far below, to preserve the original ^{3}He abundance. This may be explained by a cut-off in the rotationally-induced mixing due to the presence of a μ-gradient. Also a mixing effect decreasing with time, as obtained with the rotation-induced shear hypothesis, helps destroying lithium without increaseing too much ^{3}He, as the ^{3}He peak itself builts up during the solar life. Vauclair & Richard (1998) showed that, in this case, lithium can be destroyed as observed while ^{3}He is not increased by more than a few percent. Then beryllium is not destroyed by more than $\cong$ 20%.

3.3 *Consequences for the solar neutrino problem*

The comparison between the computed solar models and the "seismic Sun" is also able to rule out the core mixing processes which have been invoked to account for the solar neutrino deficiency (e.g. Morel & Schatzman 1996, Cumming & Haxton 1996). Such a mixing, which could be induced by internal waves, nuclear instabilities or any other process, would be able to decrease the solar neutrino flux. The basic reason is that it brings ^{3}He down towards the solar center and increases the rate of the ^{3}He (^{3}He, 2p) ^{4}He nuclear reaction yield, while the ^{3}He (^{4}He, γ) ^{7}Be reaction is reduced.

Richard & Vauclair (1997), and later Bran *et al.* (1998) have introduced in the best solar models, a parametrized mixing region located at the edge of the nuclear burning core. In Richard & Vauclair (1997), this extra-mixing has been introduced in the form of a gaussian centered at a radius $r/R_\odot = .2$, with a maximum turbulent diffusion coefficient of 1000 cm^2.s^{-1}, and a width $\delta/R_\odot = .04$, similar to the parametrization introduced by Morel & Schatzman (1996). They showed that such a core mixing can indeed reduce the neutrino fluxes. However this solar model is inconsistent with helioseismology. Introducing mixing in the central regions of the Sun changes the energy production: the constraint of obtaining the "right Sun" at the right age then leads to modifications of the sound velocity even in the regions where it is very precise, which is unacceptable.

4. Conclusion

In summary, the constraints implied by both the helioseismic inversions arid abundance determinations in the Sun converge towards the existence of a small mild mixing region below the convection zone, which would extend down to a depth of the order of one scale height. The implied mixing region must be very mild, with diffusion coefficients of 10^3 – 10^4 cm^2.s^{-1} only. This is quite different from a traditional adiabatically stratified overshooting zone, which is excluded from helioseismology (Christensen-Dalsgaard *et al.* 1993 & 1995; Basu 1997). It could be related to the differential rotation which occurs below the convection zone (tachocline).

Such a mild mixing zone can lead to a lithium depletion by a factor of 140 as observed, without increasing the $_3$He/$_4$He ratio by more than ≅ 10%. Beryllium is not depleted, which is consistent with the Balachandran & Bell (1998) result.

In any case this localized mixing region must be completely disconnected from the solar core. The μ-gradient may play the role of a cut-off in this respect. No mixing can indeed be allowed in the nuclear energy production region as it would lead to a sound velocity incompatible with helioseismology. In particular the mixing processes invoked by Cumming & Haxton (1996) to decrease the neutrino fluxes are excluded.

References

Antia, H. M., Chitre, S. M. 1998, *Astr. Astrophys.*, **339**, 239.
Bahcall, J. N., Loeb, A. 1990, *Astrophys. J.*, **360**, 267.
Bahcall, J. N., Pinsonneault, M. H. 1992, *Reviews of Modern Physics*, **64**, 885.
Balachandran, S., Bell, R. A. 1998, *Nature*, **392**, 791
Basu, S. 1997, *Mon. Not. R. Astr. Soc.*, **288**, 572.
Bran, A. S., Turck-Chieze, S., Morel P. 1998, *Astrophys. J.*, **506**, 913.
Bran, A. S., Turck-Chieze, S., Zahn, J. P. 1999, *Astrophys. J.*, **525**, 1023.
Burgers, J. M. 1969, *Flow Equations for Composite Gases*, (New York: Academic Press).
Chapman, S.,Cowling,T. G.1970, *The mathematical Theory of Non-Uniform Gases,* 3rd ed. (Cambridge University Press).

Chitre, S. M. 2000, (this Issue).
Christensen-Dalsgaard, J., Monteiro, M. J. P. F. G., Thompson, M. J. 1995, *Mon. Not. R. Astr. Soc*.,**276**, 283.
Christensen-Dalsgaard, J., Proffitt, C. R., Thompson, M. J. 1993, *Astrophys. J*., **408**, L75.
Cox, A. N., Guzik, J. A., Kidman, R. B. 1989, *Astrophys. J*., **342**, 1187.
Cumming, A., Haxton, W. C. 1996 *Phys. Rev. Lett*., **77**, 4286.
Geiss, J. 1993, in *Origin and Evolution of the Elements*, (ed.) Prantzos, Vangioni-Flam & Casse (Cambridge Univ. Press), **90**.
Gloecker, G., Geiss, J. 1998, *S S Rev*., **84**, 275.
Grevesse, N.1991, *Astr. Astrophys*.,**242**, 488.
Grevesse, N., Sauval, A. J. 1999, *Astr. Astrophys*., **347**, 348.
Maeder, A., Zahn, J. P. 1998, *Astr. Astrophys*., **334**, 1000.
Michaud, G., Proffitt, C. R. 1992, in *Inside the Stars*, (ed.) W. W. Weiss & A. Baglin, **371**, IAU, (San Francisco: PASPC), 246-259.
Morel, P., Schatzman, E. 1996, *Astr. Astrophys*., **310**, 982.
Paquette, C., Pelletier, C, Fontaine, G., Michaud, G. 1986, *Astrophys. J. Suppl*., **61**, 177.
Richard, O., Vauclair, S., Charbonnel, C., Dziembowski, W. A. 1996, *Astr. Astrophys*., **312**, 1000.
Richard, O., Vauclair, S. 1997, *Astr. Astrophys*., 322, 671.
Richer, J., Michaud, G. 1993, *Astrophys. J*., **416**, 312.
Spiegel, E., Zahn, J. P. 1992, *Astr. Astrophys*., **265**, 106.
Tripathy, S. C, Christensen-Dalsgaard, J. 1998, *Astr. Astrophys*., **337**, 579.
Thoul, A. A., Bahcall, J. N., Loeb, A. 1994, *Astrophys. J*., **421**, 828.
Turcotte, S., Richer, J., Michaud, G., Iglesias, C. A., Rogers, F. J. 1998, *Astrophys. J*., **504**, 539.
Vauclair, S. 1999, *Astr. Astrophys*., **351**, 973.
Vauclair, S. 2000, astro-ph 0002351.
Vauclair, S., Vauclair, G. 1982, *Ann. Rev. Astr. Astrophys.* **20**, 37.
Vauclair, S., Richard, O. 1998, in Proceedings of the SOHO6/GONG98 Workshop, Boston, Mass., 427.
Zahn, J. P. 1992, *Astr. Astrophys*., **265**, 115.

J. Astrophys. Astr. (2000) **21**, 331–337

Perspectives on the Interior of the Sun

S. M. Chitre, *Tata Institute of Fundamental Research, Homi Bhabha Road, Mumbai 400 005, India.*
e-mail: chitre@astro, tifr. res. in

Abstract. The interior of the Sun is not directly accessible to observations. Nonetheless, it is possible to infer the physical conditions inside the Sun with the help of structure equations governing its equilibrium and with the powerful observational tools provided by the neutrino fluxes and oscillation frequencies. The helioseismic data show that the internal constitution of the Sun can be adequately represented by a standard solar model. It turns out that a cooler solar core is not a viable solution for the measured deficit of neutrino fluxes, and the resolution of the solar neutrino puzzle should be sought in the realm of particle physics.

Key words. Sun: Oscillations, rotation, interior.

1. Introduction

The Sun has been aptly described as the Rosetta Stone of astronomy, and its internal layers provide an ideal cosmic laboratory for testing atomic and nuclear physics, high-temperature plasma physics, and neutrino physics and even general relativity. The interior of the Sun is shielded by the solar material beneath the visible surface, but, nevertheless, it is possible to study its internal constitution with the help of equations governing its structure together with the boundary conditions provided by observations. The outstanding question concerns the correctness of the theoretically constructed models of the Sun. It turns out the solar interior is transparent to neutrinos released in the energy-generating core, and also to seismic waves generated through the bulk of the solar body. These serve as complementary probes which furnish reasonably accurate information about the physical conditions prevailing inside the Sun.

The standard solar model (SSM) is the simplest possible configuration with a minimum number of assumptions and physical processes. The Sun is assumed to be a spherically symmetric object with negligible effects of rotation, magnetic fields, mass loss and tidal forces on its global structure. It is supposed to be in a quasi-stationary state maintaining hydrostatic and thermal equilibrium. The energy generation takes place in the central regions by thermonuclear reactions which convert hydrogen into helium mainly by the pp-chain. The energy is transported outwards principally by radiative processes, but the region extending over about a third of the solar radius below the surface is convectively unstable and in these layers the energy flux is carried largely by convection modelled in the framework of a local mixing length theory. There is supposed to be no mixing of nuclear reaction products outside the convection zone, except for the slow gravitational settling of helium and heavy elements by diffusion beneath this zone into the radiative interior. There is no transport of energy by any wave motion and the standard nuclear and neutrino physics is adopted for theoretical models satisfying the observed constraints, namely, mass, radius, luminosity and ratio of chemical abundances (Z/X). Here X and Z refer respectively, to the fractional abundance by mass of hydrogen and elements heavier than helium.

2. Solar neutrinos

The early investigations in solar physics were largely devoted to an extensive collection of spectroscopic data for studying the temperature, density and chemical composition in the surface layers of the Sun. Since the 1960s, there have been experiments set up to measure the flux of neutrinos generated by the nuclear reaction network operating in the solar core (Bahcall & Pinsonneault 1995). The neutrino fluxes are sensitive to the temperature and composition profiles in the central regions of the Sun, and it was hoped that the steep temperature dependence of some of the nuclear reaction rates would enable a determination of the Sun's central temperature to better than a few percent.

There have been valiant attempts since the 1960s to measure the flux of neutrinos released by the nuclear reaction network generating energy in the central regions of the Sun. The predicted capture rate for the Homestake experiment for the standard solar model (SSM) is 7.3±1.2 SNU (1 SNU = 10^{-36} captures per target atom per second) (cf. Bahcall *et al.* 1998). Davis, however, reports measurement of the solar neutrino counting rate to be 2.56 ± 0.22 SNU which clearly shows a puzzling deficit by nearly a factor of 3 over the SSM prediction. The Superkamiokande experiment is sensitive only to the high-energy ^8B neutrinos released by the pp-chain of nuclear reactions. The measured neutrino flux from the Superkamiokande experiment again shows a deficit by about 50% of the flux predicted by SSM.

These two experiments are sensitive only to the intermediate and high energy neutrinos. There are currently two radiochemical experiments using the gallium detector which have a low threshold of 0.233 MeV and are capable of measuring the low-energy pp-neutrinos. The GALLEX and SAGE experiments report measurement of the solar neutrino counting rate of 72.5 ± 6.0 SNU, while the SSM prediction of the neutrino capture rate for the gallium experiment is 129 ± 8 SNU. There is evidently a clear discrepancy between the measured and calculated neutrino fluxes. There have been a number of ingenious suggestions (cf. Chitre 1995) proposed to lower the central temperature of the Sun, in the process causing a depletion of the expected fluxes of medium and high energy neutrinos. But such a cooler solar core is inconsistent with the current experimental measurements, as this leads to even larger suppression of high energy ^8B neutrino flux to which the Superkamiokande experiment is sensitive. The Homestake experiment that detects the intermediate as well as high energy neutrinos shows even a larger reduction in the counting rate. We are thus faced with a paradoxical situation!

One of the primary goals of contemporary solar neutrino experiments is to probe the physics of thermonuclear reactions operating in the central regions of the Sun and, importantly, to constrain the properties of neutrinos. It has been demonstrated by Hata *et al.* (1994) and Castellani *et al.* (1997) that none of the existing solar neutrino experimental measurements are consistent with each other, provided we make the assumptions that neutrinos have standard properties, namely, no mass and hence no magnetic moment and no flavour-mixing during transit, and that the Sun is in thermal equilibrium with a constant luminosity, $L_\odot$. These deductions based on fairly general considerations are independent of any underlying solar model and in fact, they lead to an unphysical situation in that the ^7Be neutrino flux turns out to be negative. A cooler solar core, therefore, does not seem like a viable solution for the missing solar neutrino problem. A possible resolution of this paradox is the operation of propagation effects (cf. Bahcall & Bethe 1990) which would permit the electron neutrinos, by virtue of their tiny mass, to get transformed, during their transit through the solar body or through the space between the Sun and Earth, into neutrinos of a different flavour and as a result a fraction of them go undetected in the current solar neutrino experiments. This has been the conundrum plaguing the community over the past four decades which has prompted solar physicists to look for an independent, complementary tool to probe the thermal conditions inside the Sun.

3. Solar seismology

The surface of the Sun undergoes a series of mechanical vibrations which manifest themselves as Doppler shifts oscillating with a period centred around 5 minutes (Leighton *et al.* 1962). These have now been identified as acoustic modes of pulsation of the entire Sun (Ulrich 1970; Leibacher & Stein 1971; Deubner 1975) representing a superposition of millions of standing waves with amplitude of an individual mode of the order of a few cm/s. The frequencies of many of these modes have been determined to an accuracy of better than 1 part in 10^5. The accurately measured oscillation frequencies provide very stringent constraints on the admissible solar models. The determination of the mode frequencies to a high accuracy, of course, requires continuous observations extending over very long periods of time and this is achieved with the help of ground-based networks observing the Sun almost continuously. The most prominent amongst these networks is the Global Oscillation Network Group (GONG) which comprises six stations located in contiguous longitudes around the world (Harvey *et al.* 1996). Satellite-borne instruments have also been observing the solar oscillations and particularly, the Michelson Doppler Imager (MDI) on board the Solar and Heliospheric Observatory (SOHO) with its higher spatial resolution has been able to study solar oscillations with small associated length scales. The accurate helioseismic data of oscillation frequencies may be analyzed in two ways: i) Forward method, ii) Inverse method. In the Forward method, an equilibrium standard solar model is perturbed in a linearized theory to obtain the eigenfrequencies of solar oscillations, and these are compared with the accurately measured mode frequencies (Elsworth *et al.* 1990). The fit is naturally seldom perfect, but comparison indicated the thickness of the convection zone to be close to 200,000 km and the helium abundance, Y in the solar envelope was found to be 0.25. The direct method has had only a limited success, although it led to an improvement of the input microphysics like opacities and equation of state and emphasized the role of diffusion of helium and heavy elements into the radiative interior (Christensen-Dalsgaard *et al* 1993). A number of inversion techniques (Gough & Thompson 1991) have, therefore, been developed using the equation of mechanical equilibrium to infer the acoustic structure of the Sun.

One of the major accomplishments of the inversion methods was an effective use of the accurately measured solar oscillation frequencies for a reliable inference of the internal structure of the Sun (Gough *et al.* 1996; Kosovichev *et al.* 1997). The profile of the sound speed, $c = \sqrt{\Gamma_1 P/\rho}$ (where $\Gamma_1 = (\partial \ln P/\partial \ln \rho)_s$ is the adiabatic index) can now be determined through the bulk of the solar interior to an accuracy of better than 0.1% and the profiles of density and adiabatic index to somewhat lower accuracy (Gough *et al.* 1996). The agreement between the sound speed profile deduced from helioseismic inversions and SSM is remarkably close except for a pronounced discrepancy near the base of the convection zone and a noticeable difference in the energy-generating core. The hump below $0.7R_\odot$ may be attributed to a sharp change in the gradient of helium abundance profile on account of diffusion. A moderate amount of rotationally-induced mixing immediately beneath the convection zone can smooth out this feature. The dip in the relative sound speed difference around $0.2R_\odot$ may be due to ill-determined composition profiles in the SSM, possibly resulting from the use of inaccurate nuclear reaction rates.

From the recently available seismic data, the helium abundance in the solar envelope is deduced to be 0.249 ± 0.003 (Basu & Antia 1995) and the depth of the convection zone is estimated to be $(0.2865 \pm 0.0005)R_\odot$ (Basu 1998). It has also been possible to surmise the extent of overshoot of convective eddies beneath the base of the convection zone. The measured oscillatory signal is found to be consistent with no overshoot, with an upper limit of $0.05H_p$ (H_p being the local pressure scale height) (Monteiro *et al.* 1994; Basu *et al*. 1994).

The seismic structure of the Sun which we have discussed so far is based on the equations of mechanical equilibrium. The equations of thermal equilibrium have not been used because on oscillatory time scales of several minutes, the modes are not expected to exchange significant amount of energy. The frequencies of solar oscillations are, therefore, largely unaffected by the thermal processes in the interior. However, in order to determine the temperature and chemical composition profiles we need to supplement the seismically inferred structure obtained through primary inversions by the equations of thermal equilibrium, together with the auxiliary input physics such as the opacity, equation of state and nuclear energy generation rates (Gough & Kosovichev 1990; Antia & Chitre 1998; Takata & Shibahashi 1998). It turns out that the inverted sound speed, density, temperature and composition profiles, and consequently the neutrino fluxes, come pretty close to those given by the SSM. In general, the computed total luminosity resulting from these inverted profiles would not necessarily match the observed solar luminosity. The discrepancy between the computed and observed solar luminosity, $L_\odot$ can, in fact, be effectively used to provide a test of the input nuclear physics; in particular, it can be demonstrated that the cross-section for the proton-proton reaction needs to be increased slightly to $(4.15 \pm 0.25) \times 10^{-25}$MeV barns (cf. Antia & Chitre 1998). Note this cross-section has a crucial influence on the nuclear energy generation and neutrino fluxes, but it has never been measured in the laboratory. Indeed, it can be readily shown that the current best estimates for the proton-proton reaction cross-section and metallicity, Z are only marginally consistent with the helioseismic constraints and probably need to be increased slightly by a few per cent (Antia & Chitre 1999).

The seismic models enable us to estimate the central temperature of the Sun which is found to be $(15.6 \pm 0.4) \times 10^6$K, if we allow for upto 10% uncertainty in the opacities (Antia & Chitre 1995). It turns out that it is possible to determine only one parameter specifying the chemical composition and we assume the heavy element abundance, Z, to be known and attempt to surmise the helium abundance profile, Y The inferred helium abundance profile is in fairly good agreement with that in the SSM which includes diffusion, except in the regions just beneath the convection zone where the profile is essentially flat (Antia & Chitre 1998). This is suggestive of some sort of a mixing, possibly arising from a rotationally-induced instability. Interestingly, the temperature at the base of the solar convection zone is $\lesssim 2.2 \times 10^6$ K, which is not high enough to burn lithium. However, if there is some amount of mixing that extends a little beyond the base of the convection zone to a radial distance of $0.68R_\odot$, temperatures exceeding 2.5×10^6 K will be attained for the destruction of lithium by nuclear burning, and this may explain the low lithium abundance.

The remarkable feature that emerges from these computations is that even if we allow for arbitrary variations in the input opacities and relax the requirement of thermal equilibrium, but assume standard properties for neutrinos, it turns out to be difficult to construct a seismic model that is simultaneously consistent with any two of the three existing solar neutrino experiments within 2σ of the measured fluxes (Roxburgh 1996; Antia & Chitre 1997). This suggests that the persistent discrepancy between measured and predicted solar neutrino fluxes is likely to be due to non-standard neutrino physics. In this sense, helioseismology may be regarded to have highlighted the importance of the Sun as a cosmic laboratory for studying the novel properties of neutrinos.

We have been hitherto discussing the spherically symmetric structure of the Sun. It is also possible to determine helioseismically the rotation rate in the interior from the accurately measured rotational splittings. The first order effect of rotation yields splittings which depend on odd powers of the azimuthal order. These odd splitting coefficients can be used to infer the rotation rate as a function of depth and latitude. It is found that the surface differential rotation persists through the solar convection zone, while in the radiative interior the rotation rate appears to be relatively uniform (Thompson *et al.* 1996). The transition region near the base of the convection zone (the tachocline) is centred at a radial distance, $r = (0.7050 \pm 0.0027)R_\odot$ with a half-width of $(0.0098 \pm 0.0026)R_\odot$ (Basu 1997). There is distinct evidence of a shear layer just beneath the solar surface extending to $r \simeq 0.95R_\odot$ where the rotation rate increases with depth.

The helioseismically inferred rotation rate is, indeed, consistent with the measured solar oblateness of approximately 10^{-5} (Kuhn *et al.* 1998). The resulting quadrupole moment turns out to be $(2.18 \pm 0.06) \times 10^{-7}$ (Pijpers 1998), implying a precession of perihelion of the orbit of planet Mercury by about 0.03 arcsec/century, which is clearly consistent with the general theory of relativity.

The even order terms in the splittings of solar oscillation frequencies reflect the Sun's effective acoustic asphericity and can provide a valuable handle to probe the presence of a large-scale magnetic field or a latitude-dependent thermal fluctuation in the solar interior. Further, the local helioseismic techniques like ring diagrams or time-distance helioseismology provide a powerful tool for studying large-scale meridional flows inside the Sun (Kosovichev & Duvall 1999).

It has now been well demonstrated that the frequencies of solar oscillations vary with time and that these variations are correlated with the solar activity (Elsworth *et al.* 1990; Libbrecht & Woodard 1990; Dziembowski *et al.* 1998; Bhatnagar *et al.* 1999). It is expected that these frequency variations should result from structural changes in the layers close to the solar surface in order to show fluctuations over timescales of order 11 years. With accumulating GONG and MDI data over nearly five years during the rising phase of solar cycle 23, it has, indeed, been possible to study temporal variations of the solar rotation rate and other characteristic features associated with the solar envelope. In fact, helioseismic inversions have revealed small temporal variations of the rotation rate in the subsurface layers. These alternating bands of fast and slow rotational bands appear to migrate towards the equator as the solar cycle progresses, reminiscent of the torsional oscillations detected at the solar surface (Howard & LaBonte 1980; Snodgrass 1984), but extending to a depth of some 60 Mm (Howe *et al.* 2000; Antia & Basu 2000).

The frequencies of fundamental, or *f*-modes which are surface modes, are largely determined by the surface gravity and thus provide a valuable tool to probe the near-surface regions as well as an accurate measurement of the solar radius. (Schou *et al.* 1997; Antia 1998). The temporal variations in solar radius by a few kms have also been found to be correlated with solar activity indices (Antia *et al.* 2000). An important application of the accurately measured *f*-mode frequencies is their potential use as a diagnostic of solar oblateness and of magnetic fields just beneath the solar surface, in addition to studying the solar cycle variations of these quantities.

The ongoing efforts in helioseismology will hopefully, reveal the nature and strength of magnetic fields present inside the Sun and will also help in highlighting the processes that drive the cyclical magnetic activity and also locate the seat of the solar dynamo. The accumulating seismic data during the ascending and descending phases of cycle 23 will enable us to study the temporal variation of mode frequencies and amplitudes which should be indicative of the changes in the solar cycle and dynamics. In the process we may also learn how the magnetic field of the Sun changes with the solar cycle and what causes the solar irradiance to vary synchronously with the sunspot cycle. Finally, an unambiguous detection of buoyancy driven gravity modes would furnish a powerful tracer of the energy-generating regions of our Sun!

References

Antia, H. M. 1998, *Astr. Astrophys*., **330**, 336

Antia, H. M., Chitre, S. M. 1995, *Astrophys. J*., **442**, 434

Antia, H. M., Chitre, S. M. 1997, *Mon. Not. R. Astr. Soc*., **339**, 239,

Antia, H. M., Chitre, S. M. 1998, *Astr. Astrophys*., **339**, 239.

Antia, H. M., Chitre, S. M. 1999, *Astr. Astrophys*., **347**, 1000.

Antia, H. M., Basu, S. 2000, *Astrophys. J*., in press.

Antia, H. M., Basu, S., Pintar, J., Pohl, B. 2000, *Solar Phys*., in press.

Bahcall, J. N., Bethe, H. A. 1990, *Phys. Rev. Lett*., **65***,* 2233.

Bahcall, J. N., Pinsonneault, M. H. 1995, *Rev. Mod. Phys*., **67**, 781.

Bahcall, J. N., Basu, S., Pinsonneault, M. H. 1998, *Phys. Lett. B.*, **433**, 128.

Basu, S. 1997, *Mon. Not. R. Astr. Soc*., **288**, 572.

Basu, S. 1998, *Mon. Not. R. Astr. Soc.,* **298**, 719.

Basu, S., Antia, H. M. 1995, *Mon. Not. R. Astr. Soc*., **276**, 1402.

Basu, S., Antia, H. M., Narasimha, D. 1994, *Mon. Not. R.Astr. Soc*., **267**, 209.

Bhatnagar, A., Jain, K., Tripathy, S. C. 1999, *Astrophys. J*., **521**, 885.

Castellani, V., Degl'Innocenti, S., Fiorentini, G., Lissia, M., Ricci, B. 1997, *Phys. Rep*., **281**, 310.

Chitre, S. M. 1995, *Bull. Astr. Soc India*, 23, 379.

Christensen-Dalsgaard, J., Proffitt, C. R., Thompson, M. J. 1993, *Astrophys. J.,* 403, L75.

Deubner, F.-L. 1975, *Astr. Astrophys.*, **44**, 371.
Dziembowski, W. A., Goode, P. R., DiMauro, M. P., Kosovichev, A. G., Schou, J. 1998, *Astrophys. J.*, **509**, 456.
Elsworth, Y., Howe, R., Isaak, G. R., McLeod, C. P., New, R. 1990, *Nature*, **345**, 322.
Gough, D. O., Kosovichev, A. G. 1990, in *Proc. IAU Colloquium No. 121*, *Inside the Sun*, (eds.) Berthomieu, G., Cribier, M., (Kluwer: Dordrecht) p. 327.
Gough, D. O., Thompson, M. J. 1991, in *Solar Interior and Atmosphere,* (eds.) Cox, A. N., Livingston, W. C., Matthews, M., (University of Arizona Press: Tucson) p. 519.
Gough, D. O. *et al.* 1996, *Science*, **272**, 1296.
Harvey, J. W. *et al.* 1996, *Science,* **272**, 1284.
Hata, N., Bludman, S., Langacker, P. 1994, *Phys. Rev.*, **D49**, 3622.
Howard, R., LaBonte, B. J. 1980, *Astrophys. J.*, **239**, L33.
Howe, R., Christensen-Dalsgaard, J., Hill, F, Komm, R. W., Larsen, R. M., Schou, J., Thompson, M. J., Toomre, J. 2000, *Astrophys. J.*, **533**, L163.
Kosovichev, A. G., Duvall, T. L. 1999, *Curr. Sci.*, **77**, 1467.
Kosovichev, A. G. *et al.* 1997, *Solar Phys.*, **170**, 43.
Kuhn, J. R., Bush, R. I., Scheick, X., Scherrer, P. 1998, *Nature*, **392**, 155.
Leibacher, J., Stein, R. F. 1971, *Astrophys. Lett.*, **7**, 191.
Leighton, R. B., Noyes, R. W., Simon, G. W. 1962, *Astrophys. J.*, **135**, 474.
Libbrecht, K. G., Woodard, M. F. 1990, *Nature,* **345**, 779.
Monteiro, M. J. P. F. G., Christensen-Dalsgaard, J., Thompson, M. J. 1994, *Astr. Astrophys.*, 283, 247.
Pijpers, F. P. 1998, *Mon. Not. R. Astr. Soc.*, **297**, L76.
Roxburgh, I. W. 1996, *Bull. Astr. Soc. India*, **24**, 80.
Schou, J., Kosovichev, A. G., Goode, P. R., Dziembowski, W. A. 1997, *Astrophys. J.*, **489**, L197.
Snodgrass, H. B. 1984, *Solar Phys.*, **94**, 13.
Takata, M., Shibahashi, H. 1998, *Astrophys. J.*, **504**, 1035.
Thompson, M. J. *et al.* 1996, *Science*, **272**, 1300.
Ulrich, R. K. 1970, *Astrophys. J.,* **162**, 993.

J. Astrophys. Astr. (2000) **21**, 339–342

Seismic Tomography of the Near Solar Surface

L. Gizon[1], T. L. Duvall Jr[2] & R. M. Larsen[1,3]
[1]*HEPL, Stanford University, Stanford CA 94305, USA.*
[2]*NASA/Goddard Space Flight Center, Greenbelt MD 20771, USA.*
[3]*SCCM, Stanford University, Stanford CA 94305, USA.*
e-mail: lgizon @ solar. Stanford. edu

Abstract. Surface gravity waves have been used to probe flows in the two megameters beneath the photosphere using the techniques of time-distance helioseismology. The results suggest that supergranule velocities are smaller than at the surface. The outward flow outside a sunspot penumbra (the moat) is observed, as is an inward flow in the region beyond the moat.

Key words. Helioseismology—supergranulation—sunspots.

1. Time-distance helioseismology with surface gravity waves

Local helioseismology diagnostics open the prospect of mapping the three-dimensional structure and dynamics of the upper solar convection zone. Duvall & Gizon (2000) recently applied time-distance helioseismology to surface gravity waves, to probe horizontal flows in the first two megameters below the photosphere. Promising results were obtained using a simple calibration instead of a proper inversion.

Here we have analyzed an 8-hour long time series of dopplergrams observed on 1998 December 6 in the MDI high-resolution field of view (Scherrer *et al.* 1995). Rotation was removed. The datacube was Fourier transformed in time and space, and acoustic waves filtered out. The temporal cross correlations were computed and averaged using the quadrant geometry, as described by Duvall & Gizon (2000). For each pixel location, x, we obtained three cross-correlation functions, denoted C^{EW}, C^{SN} and C^{IO}, which depend on correlation time τ and distance Δ from x. They respectively contain local information about the westward component, northward component, and divergence of the flow. A fourth cross-correlation function, C^0, was constructed by averaging over all possible pairs of points; it is symmetric with respect to correlation time. Flows introduce a correlation-time asymmetry in C^{EW}, C^{SN} and C^{IO}, which we measure by cross correlation with the template C^0. We finally get time-asymmetry maps $\delta\tau^{\mathrm{EW}}$, $\delta\tau^{\mathrm{SN}}$, and $\delta\tau^{\mathrm{IO}}$ for each distance Δ. Further averaging over Δ in the range 4.5–11.9 Mm provides us with three maps, labeled $\overline{\delta\tau}^{\mathrm{EW}}$, $\overline{\delta\tau}^{\mathrm{SN}}$ and $\overline{\delta\tau}^{\mathrm{IO}}$, which are functions of x.

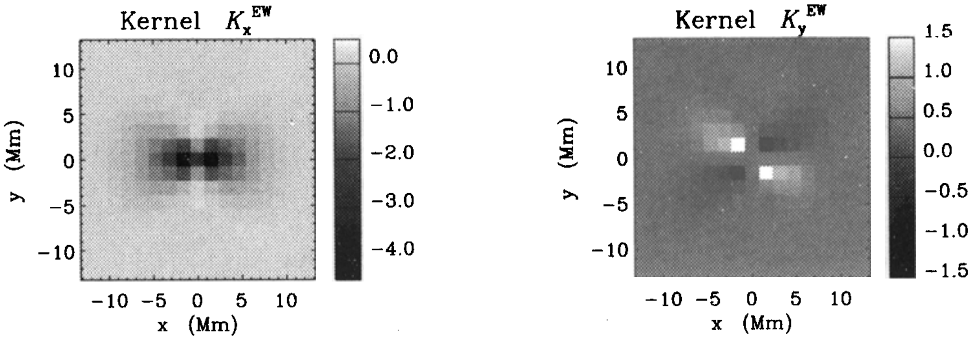

Figure 1. Kernels K_x^{EW} and K_y^{EW} which provide a relationship between the time-asymmetry map $\overline{\delta\tau}^{\mathrm{EW}}$ and the horizontal flow U. The kernels were averaged down to a resolution of 1.64 Mm. They are expressed in units of 10^{-3} s ^{2}m $^{-1}$ per pixel.

2. 2-D sensitivity kernels for horizontal flows

It is not appropriate to employ ray theory to solve the forward problem, because the flow can vary on a horizontal scale smaller than the wavelength, which is ~ 5 Mm for a 3-mHz surface gravity wave. Instead, we calculated the wavefield in the first Born approximation (see Woodward 1992). We restricted our attention to a simplified problem, in which the prescribed flow (U) is steady, horizontal, and depth independent. Furthermore the random sources of oscillations are assumed to be of pressure type, uniformly distributed on the surface, and spatially uncorrelated (Woodard 1997). Realistic frequency-dependent damping is included. Dispersion is built in. Under these conditions the scattered wavefield can be expressed as a 2-D surface integral. We can then relate time-asymmetry measurements (as defined above) to the two horizontal components of the flow following the procedure described in Tong *et al.* (1998). We write $\overline{\delta\tau}^{i} = K^{l}{}_{x} * U_x + K^{l}{}_{y} * U_y$ for $i \in$ {EW, SN, IO}, where '$*$'denotes 2-D convolution. The kernels K_x^{EW} and K_y^{EW} are shown in Fig. 1. Wave effects are smeared out by the spatial averaging over quadrants and distances.

3. Iterative deconvolution

To obtain the horizontal components U_x and U_y of the flow we solve the overdetermined system of equations mentioned above in the least squares sense. We apply the iterative LSQR algorithm and use the 2-D FFT to compute the convolutions involved. A regularized solution with small l_2-norm is obtained by stopping LSQR after a small number of iterations, k.

The inversion procedure was tested on artificial data corresponding to a hexagonal convective flow pattern. For moderate (10-100) signal-to-noise levels, the values of k found by the L-curve criterion or by Monte-Carlo generalized cross validation (Hansen 1998) are close to optimal and result in very accurate recovery of the artificial velocity signals. For the real observations, which are noisier, this is not possible, and instead we choose $k = 2$ based on inversions of artificial data with low signal-to noise.

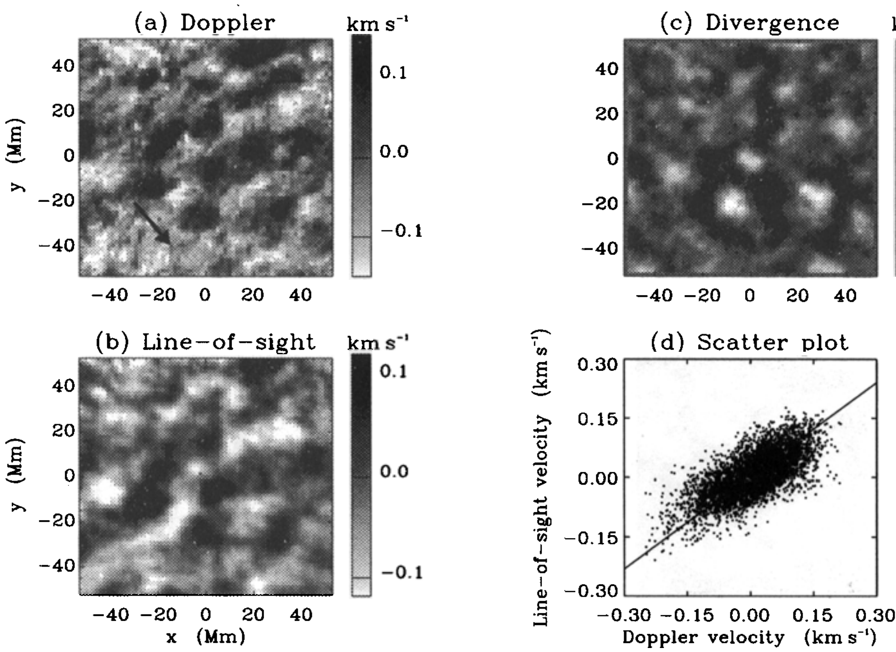

Figure 2. **(a)** 8-hour averaged dopplergram. The arrow points towards disk center. (**b**) Line-of-sight projection of the inferred horizontal velocity field obtained by deconvolution. (**c**) Horizontal divergence of the inferred flow. (**d**) Scatter plot of (b) versus (a); the straight line with slope 0.8 is a fit assuming equal errors in both coordinates. All maps have a spatial resolution of 1.64 Mm.

4. Results

Fig. 2 displays inversions obtained for a relatively quiet region. The supergranulation cells are easily identified in the divergence map. Also shown is the line-of-sight component of the inferred flow. The correlation with the average dopplergram is high (correlation coefficient 0.7). It appears that there is less high spatial frequency signal in our image. Perhaps this is a consequence of measuring a flow averaged over 2 Mm in depth. We also find the inferred flow to be weaker than the surface flow by a factor of 0.8. Supergranular motion may indeed depend on depth since density varies very rapidly in the near surface layers.

Results for a region including a sunspot are shown in Fig. 3. We detect a radial outflow from the sunspot center extending out to 30 Mm, with values up to 1 km s^{-1} . This is a manifestation of the moat flow. The moat is surrounded by a counter flow, suggestive of a downflow at the moat boundary. In the penumbra, the inferred outflow is significantly smaller than the Evershed flow observed in the Doppler image. The Evershed flow may thus be very shallow. It is not straightforward to reconcile the present findings with previous observations of downflows below sunspots (Duvall *et al.* 1996). We caution that spatially varying damping could introduce an additional time-asymmetry component (Woodard 1997) which is not accounted for in this study.

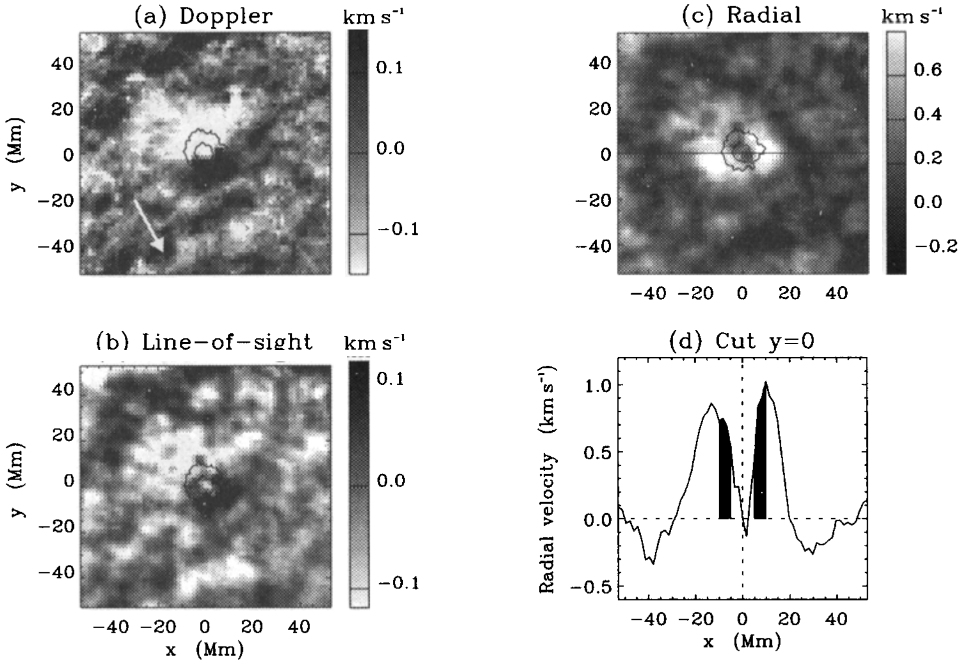

Figure 3. (a) 8-hour averaged dopplergram. The contour lines mark the boundaries of the umbra and penumbra. Doppler velocities vary between –0.8 and 0.3 kms^{-1} in the penumbra. (**b**) Line-of-sight projection of the inferred horizontal velocity field. The correlation coefficient between (a) and (b) is 0.6. (**c**) Radial component of inferred flow measured from sunspot center. (**d**) Cut at y = 0 through (c); the shaded regions indicate the location of the penumbra.

This work was supported by NASA grant NAG5-3077. SOHO is a mission of cooperation between ESA and NASA. We thank Phil Scherrer for discussions.

References

Duvall, T. L. Jr *et al.* 1996, *Nature*, **379**, 235.
Duvall, T. L. Jr, Gizon, L. 2000, *Solar Phys*., **192**, 177.
Hansen, P. C. 1998, *Rank-Deficient and Discrete III-Posed Problems: Numerical Aspects of Linear Inversion*, SIAM, (Philadelphia).
Scherrer, P. H. *et al*. 1995, *Solar Phys*., **162**, 129.
Tong, J. *et al*. 1998, *Geophys. Res*. Lett., **25**, 1983.
Woodard, M. F. 1997, *Astrophys. J.*, **485**, 890.
Woodward, M. J. 1992, *Geophys.*, **57**, 15.

J. Astrophys. Astr. (2000) **21**, 343–347

Helioseismic Search for Magnetic Field in the Solar Interior

H. M. Antia[1], S. M. Chitre[1] & M. J. Thompson[2]

[1]*Tata Institute of Fundamental Research, Homi Bhabha Road, Mumbai 400 005, India.*
[2]*Astronomy Unit, Queen Mary and Westfield College, Mile End Road, London E1 4NS, U.K.*

Abstract. The observed splittings of solar oscillation frequencies can be utilized to study possible large-scale magnetic fields present in the solar interior. Using the GONG data on frequency splittings an attempt is made to infer the strength of magnetic fields inside the Sun.

Key words. Sun: oscillations, magnetic field, interior.

The frequencies of solar oscillations are split due to departures from spherical symmetry caused by rotation, magnetic field or any other aspherical perturbations in solar interior. The odd splitting coefficients arise from rotation and can be inverted to infer the rotation rate in solar interior. The even splitting coefficients arise from second order effects of rotation, magnetic field or latitudinal temperature variations. In this work we attempt to infer the magnetic field strength in the solar interior using data from Global Oscillation Network Group (GONG).

Note that forces associated with rotation or magnetic field are much smaller than the gravitational forces in solar interior, and hence a perturbative treatment can be applied to treat these departures from spherical symmetry. We adopt the formulation due to Gough & Thompson (1990), with the difference that we include perturbation in the gravitational potential and also assume differential rotation in the interior, though the symmetry axis of magnetic field is taken to coincide with rotation axis. We use only the toroidal magnetic field taken to be of the form,

$$\mathbf{B} = \left[0, 0, a(r)\,\frac{dP_k}{d\theta}\,(\cos\theta)\right], \tag{1}$$

$$a(r) = \begin{cases} \sqrt{8\pi p_0 \beta_0}\left(1 - \left(\dfrac{r - r_0}{d}\right)^2\right) & \text{if} \quad |r - r_0| \le d \\ 0 & \end{cases}. \tag{2}$$

Here $P_k(x)$ is the Legendre polynomial of degree k, p_0 is the gas pressure, β_0 is a constant giving the ratio of magnetic to gas pressure, r_0 and d are constants defining the mean position and thickness of the layer where the field is supposed to be concentrated.

We use the rotation rate inferred from GONG data for the months 4–14 (Antia, Basu & Chitre 1998) to estimate second order contributions to the splitting coefficients a_2 and a_4. We incorporate all the second-order contributions arising from rotation, including those from the distortion of equilibrium state and perturbation to the eigenfunctions. These contributions can be subtracted from observed splitting coefficients obtained from the GONG data (Hill *et al.* 1996) to give residuals which may be due to magnetic field or any other aspherical perturbation in the solar interior. The resulting residuals can be compared with calculated splittings from magnetic fields concentrated in different regions of solar interior.

There have been some suggestions that a significant toroidal magnetic field may be concentrated in a layer around the base of the convection zone (Dziembowski & Goode 1992). We therefore first investigate splittings that are expected from such a field and the results are shown in Fig. l(a). These splittings include both the direct and distortion contributions as defined by Gough & Thompson (1990). It is clear from this figure that the splitting coefficients from such a field have a characteristic signature for modes with turning point near the base of the convection zone; it should be possible to detect such a signal in the observed splittings if a strong enough magnetic field is, indeed, present in these layers. Unfortunately, the errors in observed splitting coefficients are too large to detect small features expected from such magnetic field. In order to reduce the errors we take averages over 30 modes with nearby values of the lower turning point r_t and the results, after subtraction of expected contribution from rotation, are shown in Fig. l(b). There is no clear signature of any feature near the base of the convection zone and hence we can only set an upper limit on the strength of magnetic field in this layer. This will, of course, depend on the thickness of the magnetic layer. For a half-thickness of $0.02R_\odot$ the upper limit on magnetic field strength turns out to be 300 kG. This limiting value is close to what was obtained by Basu (1997) using a similar technique and is also consistent with the value independently inferred by D'Silva & Choudhuri (1993).

After addressing the issue of a possible magnetic field at the base of the convection zone, where theory suggests a field might be stored, we consider where else the data might indicate the presence of a magnetic field. There is no signature for the presence of significant magnetic field in the radiative interior, since the averaged residual splittings after correcting for rotation do not show any variation with r_t. However, within the convective envelope there is some significant residual splitting, which could be due to a moderately strong magnetic field. This residual appears, interestingly, to rise towards the surface. If it is due solely to magnetic field, the field may be distributed around a depth of ≈ 30000 km. It may be noted that this is approximately the depth to which the surface shear layer seen in solar rotation profile extends (Antia, Basu & Chitre 1998; Schou *et al.* 1998). Fig. 2 shows the splittings due to a few magnetic field configurations which are concentrated in the upper part of the convection zone. A comparison of these with the observed splittings indicates that there may be an azimuthal magnetic field with $\beta \approx 10^{-4}$ (i.e., $B \approx 20$ kG), with peak around r = $0.96R_\odot$. The non-zero value of these coefficients for $r_t < 0.7R_\odot$ could be easily explained by magnetic field in outer layers as can be seen from the computed splittings.

In this study we have assumed a smooth toroidal magnetic field, but in practice we do not expect such a field inside the convection zone. Turbulence may be expected to randomize the magnetic field and such a field may not be expected to produce any significant distortion in the equilibrium state. The direct effect of a magnetic field will still be felt though the contribution would be different. Thus our results may be treated as indicating an order of magnitude of field that may be expected if the observed splitting coefficients are indeed due to the presence of a magnetic field. If

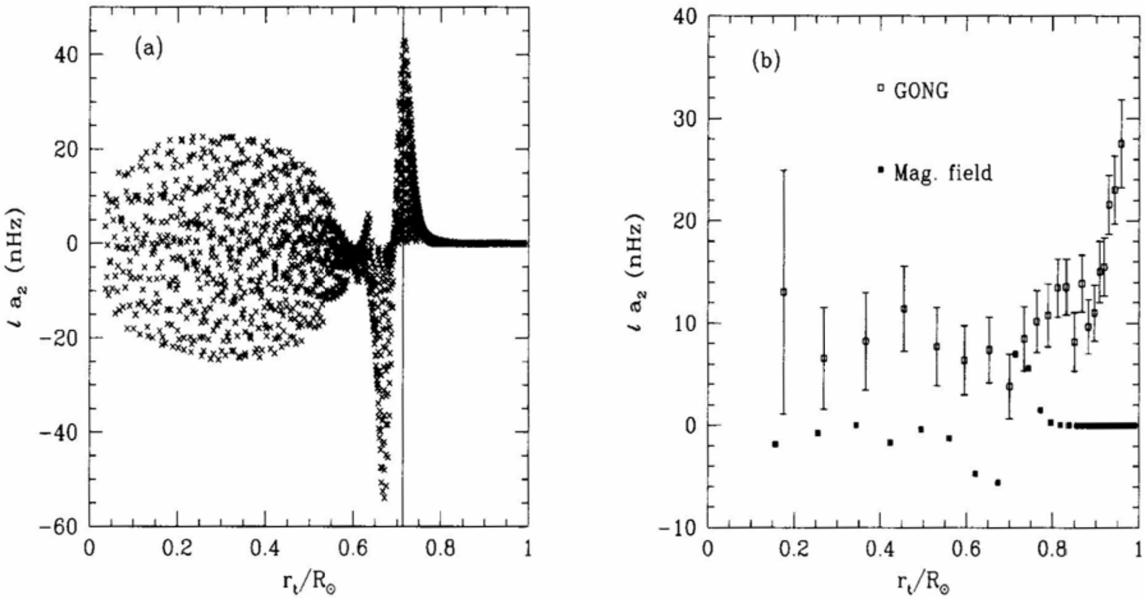

Figure 1. The splitting coefficient a_2 from a toroidal magnetic field concentrated near the base of the convection zone, plotted as a function of the lower turning point for the mode. Magnetic field is given by equations (1,2) with $k = 2$, $\beta_0 = 10^{-4}$, $r_0 = 0.713R_\odot$ (shown by the vertical line in the figure) and $d = 0.02R_\odot$. The left panel shows the splitting coefficients from each mode separately, while the right panel shows the results after averaging over 30 neighboring modes. The right panel also includes the observed splittings averaged over the same set of modes.

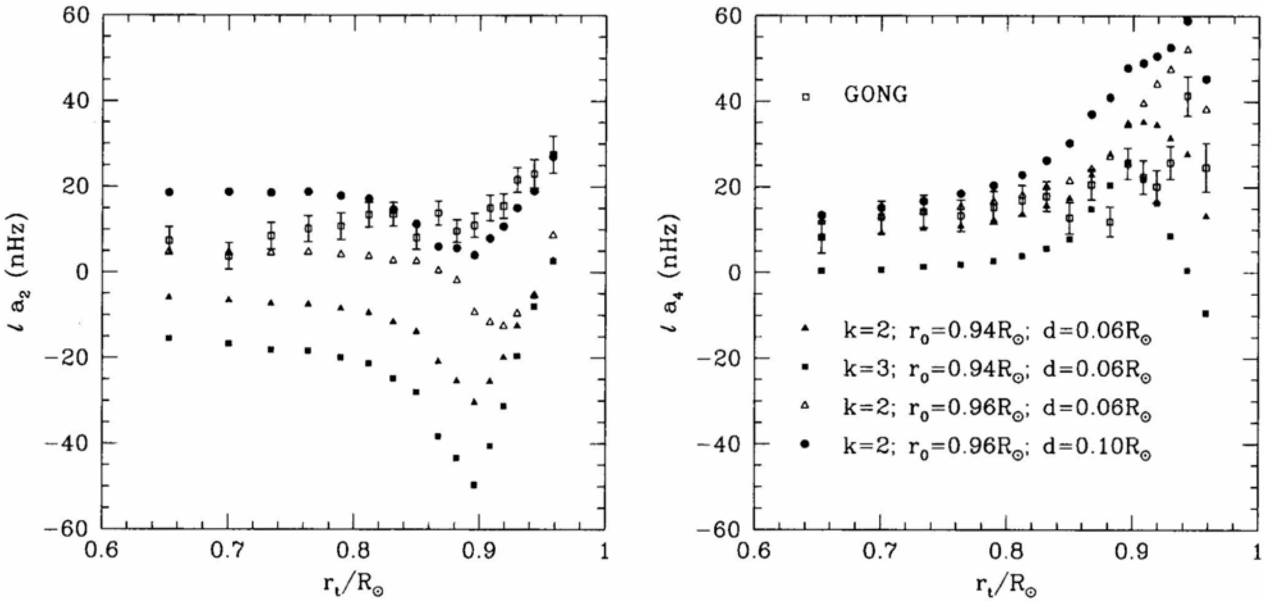

Figure 2. The splitting coefficients a_2 and a_4 from a toroidal magnetic field concentrated in the upper part of the convection zone, plotted as a function of the lower turning point. The estimated contribution from rotation has been subtracted from the observed splittings plotted in the figure. Magnetic field is given by equations (1,2) with $\beta_0 = 10^{-4}$, and the value of r_0, d and k as marked in the figure.

the field is concentrated in flux tubes which occupy only a small fraction of the volume, then the required magnetic field could be correspondingly larger. If we assume that the flux tubes occupy a fraction f of the total volume, the magnetic field strength should increase by $1/\sqrt{f}$. Alternately, a nonmagnetic latitudinally-dependent perturbation to the wave propagation speed might be responsible for the signal we have detected (cf. Gough & Zweibel 1995). Once again we may expect a perturbation of order 10^{-4} located in the region around $r = 0.96R_\odot$ for accommodating the observed splittings. Using the splitting coefficients alone it is not possible to distinguish between these two possibilities.

This work utilizes data obtained by the Global Oscillation Network Group (GONG) project, managed by the National Solar Observatory, a Division of the National Optical Astronomy Observatories, which is operated by AURA, Inc. under a cooperative agreement with the National Science Foundation. The data were acquired by instruments operated by the Big Bear Solar Observatory, High Altitude Observatory, Learmonth Solar Observatory, Udaipur Solar Observatory, Instituto de Astrofisico de Canarias, and Cerro Tololo Interamerican Observatory.

References

Antia, H. M., Basu, S., Chitre, S. M. 1998, *Mon. Not. R. Astr. Soc*, **298**, 543.
Basu, S. 1997, *Mon. Not. R. Astr. Soc*, **288**, 572.
D'Silva, S., Choudhuri, A. R. 1993, *Astr. Astrophys*., **272**, 621.
Dziembowski, W. A., Goode, P. R. 1992, *Astrophys. J.,* **394**, 670.
Gough, D. O., Thompson, M. J. 1990, *Mon. Not. Roy. Astmn. Soc*, **242**, 25.
Gough, D. O., Zweibel, E. G. 1995, in *Proc 4th SOHO workshop*, (eds.) J. T. Hoeksema, V. Domingo, B. Fleck, B. Battrick, ESA SP-376, ESTEC, (Noordwijk), p 73.
Hill, F., Stark, P. B., Stebbins, R. T. *et al* 1996, *Science*, **272**, 1292.
Schou, J., Antia, H. M., Basu, S. *et al* 1998, *Astrophys. J*., **505**, 390.

J. Astrophys. Astr. (2000) **21**, 349–352

Helioseismic Solar Cycle Changes and Splitting Coefficients

S. C. Tripathy, Kiran Jain & A. Bhatnagar, *Udaipur Solar Observatory, Physical Research Laboratory, PO Box No. 198, Udaipur 313 004, India.*

Abstract. Using the GONG data for a period over four years, we have studied the variation of frequencies and splitting coefficients with solar cycle. Frequencies and even-order coefficients are found to change significantly with rising phase of the solar cycle. We also find temporal variations in the rotation rate near the solar surface.

Key words. Solar cycle—rotation—activity.

1. Introduction

With the installation of the GONG instrument in 1995, the network has produced unprecedented amount of p-mode frequency data covering the descending phase of solar cycle 22 and the rising phase of cycle 23. These data sets have enabled us to make a detailed analysis of the cyclic variation of the p-mode frequency shifts and splitting coefficients. Using the subset of GONG data, Bhatnagar *et al.* (1999) studied the shift in mode frequencies for a period of two years starting from August, 1995 and confirm that the frequencies vary with the level of solar activity.

2. Data sets

The mode frequencies used in this study were estimated from the 3-month power spectra using the standard GONG analysis. The period under study extends from 1995 May 7th to 1999 August 1st. The data were divided into 41 overlapping time series with start dates spaced by 36 days (GONG months 2-42) and contains m-averaged p-mode multiplets in the frequency range of 1.5 mHz to 3.5 mHz and $\ell_{\max} = 150$. The mode frequencies are defined by

$$\nu_{n,\ell,m} = \nu_{n,\ell} + L \sum_{s=1}^{m} a_s^{n,\ell} P_s(m/L), \tag{1}$$

where $a_{s,n,l}$ are the splitting coefficients and $L^2 = \ell(\ell+1)$.The remaining symbols have their usual meanings.

3. Analysis and results

The temporal evolution of the frequency shifts over the period of four years is shown in Fig. 1. In the same figure, we also show the activity indices represented by means

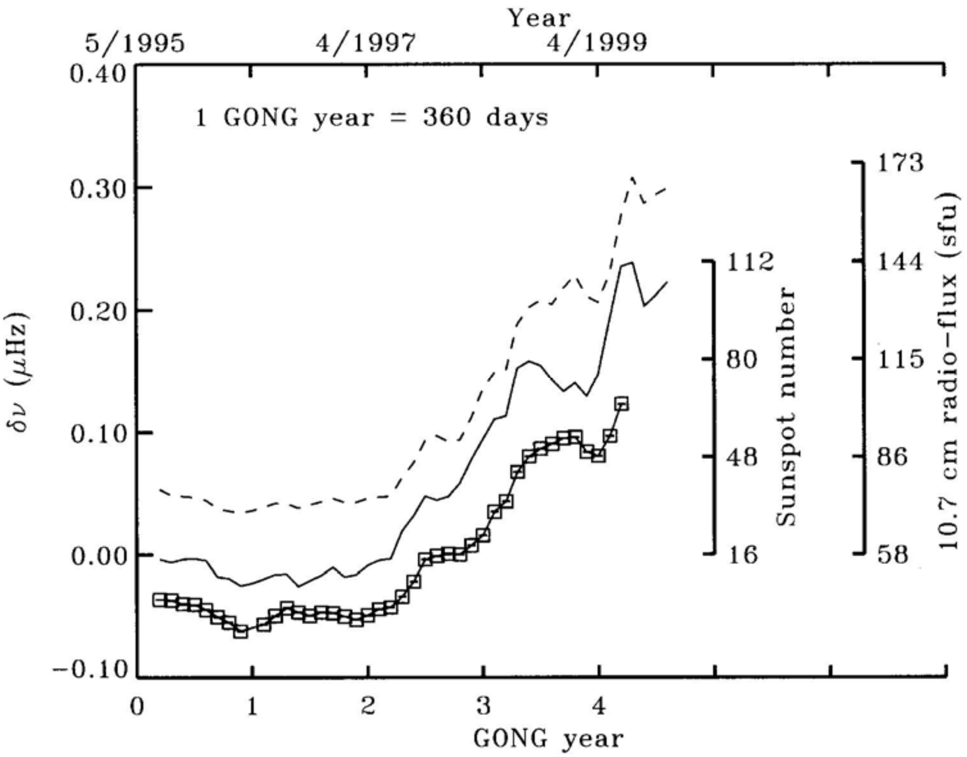

Figure 1. The temporal evolution of frequency shifts over a period of four years is shown by the solid line with squares. The solid and dashed lines represent the scaled mean sunspot number and 10.7 cm radio flux.

of sunspot number (R_I) and 10.7 cm radio flux (F_{10}). It is noted that the frequency shifts follow the trend of solar cycle. The regression analysis between the shifts and the activity indices shows a strong linear correlation with correlation coefficients of 0.99.

It is known that the solar differential rotation and other symmetric breaking factors like magnetic field can lift the degeneracy of the solar acoustic modes and split the eigen frequencies as defined in equation (1). The solar cycle variation of the even order splitting coefficients are shown in Fig. 2. We find that a_2 has a strong correlation with activity while a_4, a_6, and a_8 coefficients are anti-correlated. Howe *et al.* (1999) also investigated the temporal behaviour of these coefficients at 3 mHz and had obtained similar results.

The odd-order splitting coefficients measure the solar rotation. The variation of solar rotation rate with depth and latitude is studied by using analytical methods proposed by Morrow (1988). In an asymptotic limit, the appropriate combination of odd order coefficients reflects the depth variation of the angular velocity at a chosen co-latitude, ϕ (= 90° — θ, where θ is latitude).

$$\Omega^{nl}(\phi) \approx \sum_{i=0}^{s_{\max}} d_{2i+1}(\phi) a_{2i+1}^{nl}, \tag{2}$$

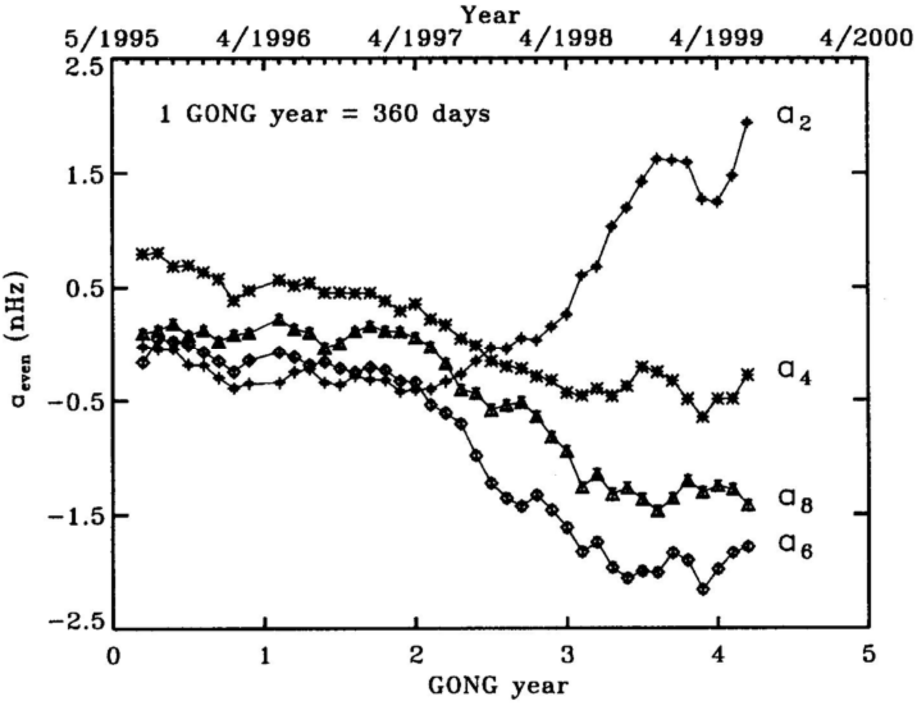

Figure 2. The temporal evolution of even order splitting coefficients.

where

$$d_1 = 1, \tag{3}$$

$$d_3 = [1 - 5\cos^2\phi], \tag{4}$$

$$d_5 = [1 - 14\cos^2\phi + 21\cos^4\phi], \tag{5}$$

$$d_7 = [1 - 27\cos^2\phi + 99\cos^4\phi - \frac{429}{5}\cos^6\phi], \tag{6}$$

$$d_9 = [1 - 44\cos^2\phi + 286\cos^4\phi - 572\cos^6\phi - \frac{2431}{7}\cos^8\phi]. \tag{7}$$

In the earlier studies (Mirror (1988; Jain *et al.* 2000), the summation in equation (2) was terminated by setting s_{max} = 2. With the availability of higher order coefficients in GONG data, the summation is extended to s_{max} = 4 (terms involving a_9^{nl}). The corresponding rotation rate at equator is given by

$$\Omega^{nl}(90^\circ) \approx a_1^{nl} + a_3^{nl} + a_5^{nl} + a_7^{nl} + a_9^{nl}. \tag{8}$$

In Fig. 3, we show the time variation of rotation rate for four different latitudes near the surface i.e. ν/L = 30. A small but significant change in rotation rate of the order of 3 nHz over a period of more than four years is clearly seen. These changes have been interpreted in terms of zonal flows earlier seen in BBSO data for cycle 22 (Woodard & Libbrecht 1993) and Doppler measurements (Howard & LaBonte 1980). Recently using inversion techniques, Basu & Antia (1999) have also found a systematic zonal flow migrating towards lower latitudes during the rising phase of cycle 23.

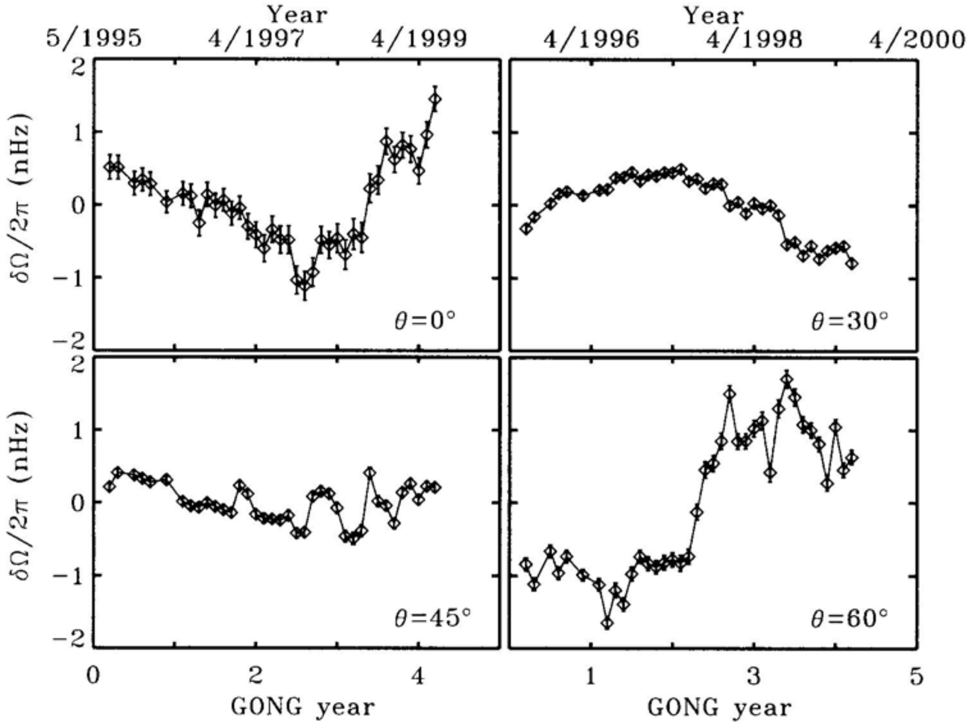

Figure 3. The temporal evolution of solar rotation rate as a function of GONG year (1 GONG year = 360 days) for different latitudes.

Acknowledgements

This work utilises data obtained by the GONG project, managed by the NSO, a Division of the NOAO, which is operated by AURA, Inc. under cooperative agreement with the NSF. The data were acquired by instruments operated by Big Bear Solar Observatory, High Altitude Observatory, Learmonth Solar Observatory, Udaipur Solar Observatory, Institute de Astrophsico de Canaris, and Cerro Tololo Interamerican Observatory. This work is partially supported under the CSIR Emeritus Scientist Scheme and Indo-US collaborative programme-NSF Grant INT-9710279.

References

Basu, S., Antia, H. M. 1999, *these proceedings*.

Bhatnagar, A., Jain, K., Tripathy, S. C. 1999, *Astrophys*. J., **521**, 885.

Jain, K., Tripathy, S. C, Bhatnagar, A. 2000, *Astrophys*. J., **542**, 521

Howard, R., LaBonte, B. J. 1980, *Astrophys*. J., **239**, L33.

Howe, R., Komm, R., Hill, R 1999, *Astrophys*. J., **524**, 1084.

Morrow C.A.1988, *Seismology of the Sun and Sun like Stars*, ESA-SP-286,(ed.) Rolfe, E.J (Noordwijk: ESA), p. 137.

Woodard, M. F., Libbrecht, K. G. 1993, *Astrophys. J.*, **402**, L77.

J. Astrophys. Astr. (2000) **21**, 353–356

Temporal Variation of Large Scale Flows in the Solar Interior

Sarbani Basu[1]* & H. M. Antia[2]

[1]*Institute for Advanced Study, Olden Lane, Princeton .. J. 08540, U.S.A.* and *Astronomy Department, Yale University, New Haven, CT 06520-8101, U.S.A.*
[2]*Tata Institute of Fundamental Research, Homi Bhahha Road, Mumbai 400 005, India.*
**e-mail: basu@astro.yale.edu*

Abstract. We attempt to detect short-term temporal variations in the rotation rate and other large scale velocity fields in the outer part of the solar convection zone using the ring diagram technique applied to Michelson Doppler Imager (MDI) data. The measured velocity field shows variations by about 10 m/s on the scale of few days.

Key words. Sun: Oscillations, Rotation, Interior.

The ring diagram technique has been used to study large scale flows in the outer parts of the solar convection zone (Hill 1988; Patron *et al.* 1997; Basu, Antia & Tripathy 1999). The accumulation of MDI data over the last four years has made it possible to study temporal variations in both the zonal and meridional components of the velocity field (Basu & Antia 1999). While long term variations (time-scales of years) in the rotation rate (zonal flow) are reasonably well established from both Doppler and helioseismic studies, short term variations have not been clearly identified. There is some indication from Doppler measurements at the solar surface that these velocity field change on a shorter time-scale of a few days (Snodgrass 1992; Hathaway *et al.* 1996). Similarly, some variation in the interior has also been found in ring diagram study (Patron *et al.* 1998). In this work, we try to study changes in meridional and zonal flows over a time scale of several days.

We use a set of 3d spectra obtained from full-disk Dopplergrams taken during May – June 1996. Each region covers approximately 15° × 15° in latitude and longitude and is tracked for 4096 minutes. We have selected the regions centered at Carrington longitudes of 90°, 60°, 30° for rotation 1909 and at 360°, 330°, 300° for rotation 1910. For each longitude we select regions centered at latitudes of 0°, ±10°, ±20°, ±30°, ±40°, ±50° and ±60°. These spectra cover half of a solar rotation period. For each of these regions, we find the horizontal components of velocity as a function of depth, as explained by Basu *et al.* (1999).

In order to isolate the time-dependent part of the large scale flows, we subtract the mean velocity over the six longitudes covered in this study from the estimated velocity at each latitude, longitude and depth. Fig. 1 shows the resulting velocities at different depths. There is no obvious pattern on spatial scales covered by our study, though it is clear that there is significant variation with longitude (or time). There is also a pronounced north-south asymmetry in the flow pattern.

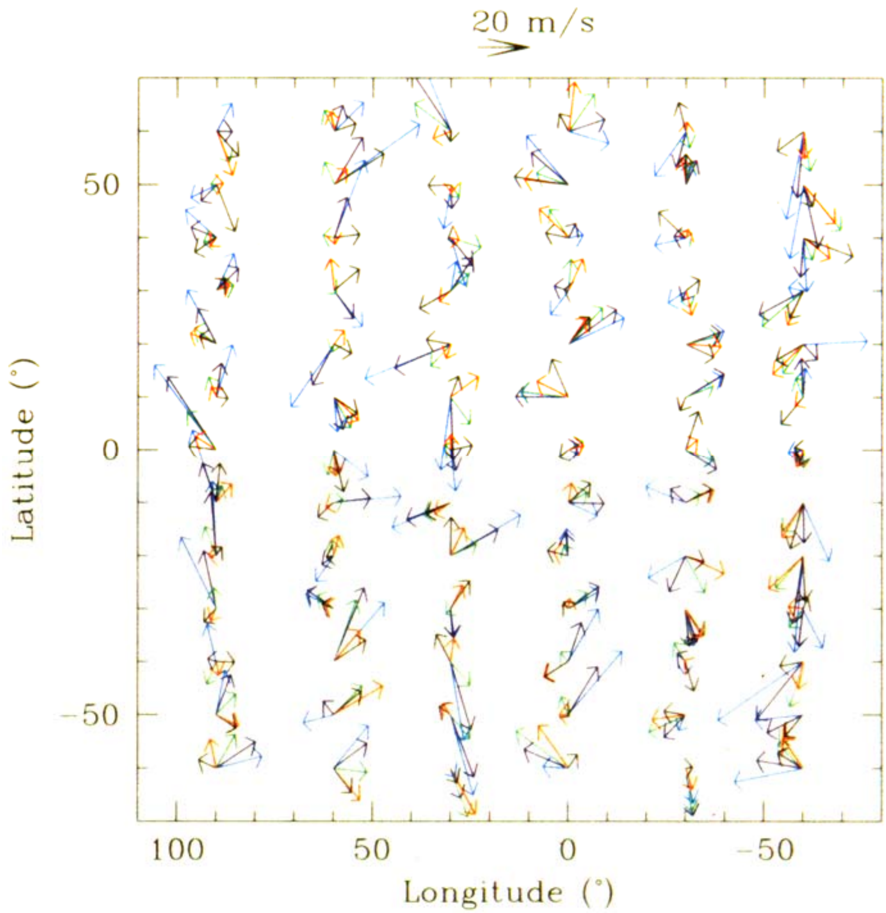

Figure 1. Horizontal flow velocities in horizontal planes at various depths obtained after subtracting the mean over six longitudes covered in this study. Each arrow represents the departure from the mean velocity at the corresponding latitude and longitude. The black, red, green, blue and cyan arrows correspond to depths of 0.995, 0.99, 0.985, 0.98, 0.975R$_\odot$ respectively. The arrow at the top marks the scale and the direction of rotation. The errors in these measurements are not shown but they are typically 2 –5 m/s depending on latitude and depth. Note that the flow direction changes with depth at most points.

Fig. 2 shows the zonal (u_x) and meridional (u_y) component of the residual velocity as a function of longitude and latitude at a few selected depths. Fig. 3 shows these components as a function of depth and longitude at various latitudes. Once again it is clear that there is some variation, but there is no clear pattern. A part of this variation could be due to convective cells of differing sizes present in the solar convection zone. The averaging over a small fraction of solar surface may not remove the convective signal completely. Similar changes have been seen in Doppler measurement at the solar surface (Hathaway *et al.* 1996). If these changes indeed represent real changes in solar rotation rate, then we will also need to examine the long term variations carefully. These variations have been detected in data sets which are averaged over the entire longitude range and over a few months

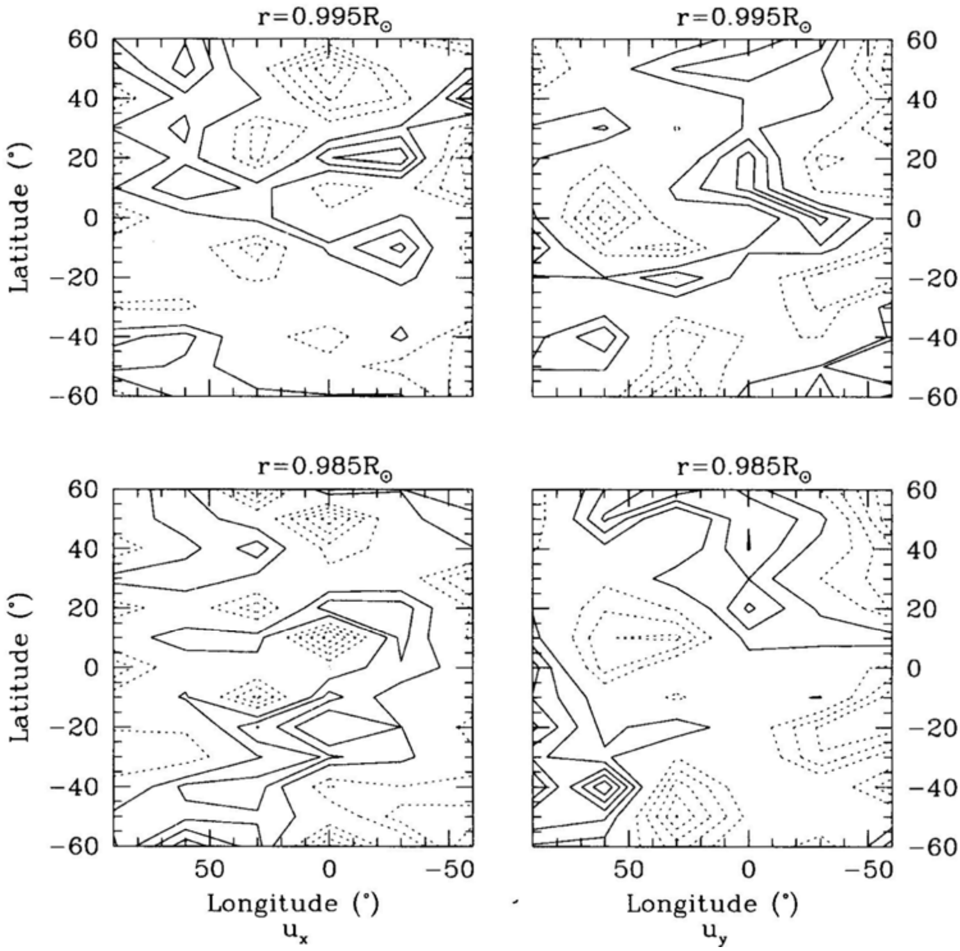

Figure 2. Zonal and meridional components of the time-dependent residual velocity at a few selected depths as marked above each panel, are plotted as contours of constant velocity in the longitude-latitude plane. The left panels show the zonal component, while the right panels show the meridional component. The continuous contours denote positive values while dotted contours display negative values. Contours are drawn at interval of 4 m/s.

in time (e.g., Howe *et al.* 2000). This averaging will tend to suppress the variations on a short time scale, but the entire contribution may not be removed. This residual contribution may produce some noise over the real signal of long-term temporal variations.

Acknowledgements

This work utilizes data from the Solar Oscillations Investigation/Michelson Doppler Imager (SOI/MDI) on the Solar and Heliospheric Observatory (SOHO). SOHO is a project of international cooperation between ESA and NASA.

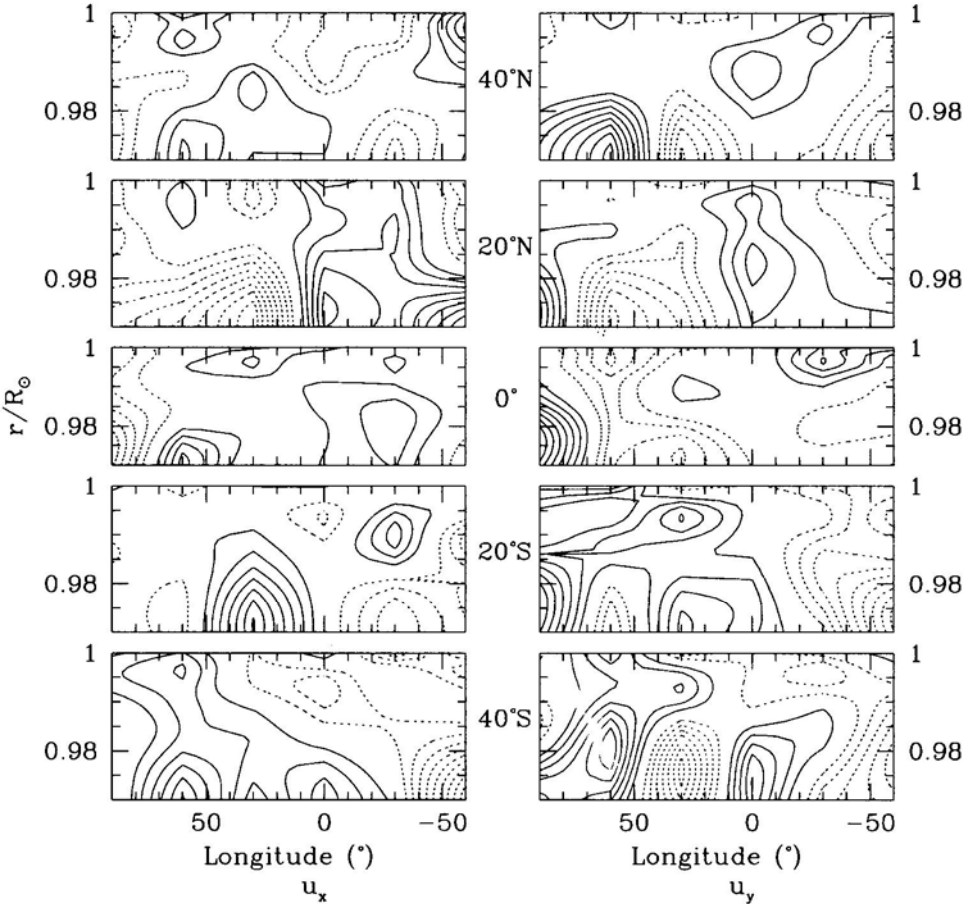

Figure 3. Zonal and meridional components of the time-dependent residual velocity at a few selected latitudes as marked in the center, are plotted as contours of constant velocity in the longitude-depth plane. The left panels show the zonal component, while the right panels show the meridional component. The continuous contours denote positive values while dotted contours display negative values. Contours are drawn at an interval of 4 m/s.

References

Basu, S., Antia, H. M. 1999, *Astrophys. J.*, **525**, 517.

Basu, S., Antia, H. M., Tripathy, S. C. 1999, *Astrophys. J.*, **512**, 458.

Hathaway, D. H., Gilman, P. A., Harvey, J. W. *et al.* 1996, *Science*, **272**, 1306.

Hill, F. 1988, *Astrophys. J.*, **333**, 996.

Howe, R., Christensen-Dalsgaard, J., Hill, F., Komm, R. W., Larsen, R. M., Schou, J., Thompson, M. J., Toomre, J. 2000, *Astrophys. J. Lett.,* **533**, L33.

Patron, J., Gonzalez Hernandez, L, Chou, D.-Y. *et al.* 1997, *Astrophys. J.*, **485**, 869.

Patron, J., Gonzalez Hernandez, I., Chou, D.-Y. *et al* 1998, *Astrophys. J.*, **506**, 450.

Snodgrass, H. B. 1992, in *The Solar Cycle,* proc. NSO 12th Summer Workshop, ASPS 27, p. 205.

J. Astrophys. Astr. (2000) **21**, 357–360

Observation of Hysteresis between Solar Activity Indicators and *p*-mode Frequency Shifts for Solar Cycle 22

S. C. Tripathy*, Brajesh Kumar, Kiran Jain & A. Bhatnagar, *Udaipur Solar Observatory, Physical Research Laboratory, P. B. No. 198, Dewali, Off Bari Road, Udaipur 313 004, India.*
**e-mail: sushant@uso.ernet.in*

Abstract. Using intermediate degree *p*-mode frequency data sets for solar cycle 22, we find that the frequency shifts and magnetic activity indicators show a "hysteresis" phenomenon. It is observed that the magnetic indices follow different paths for the ascending and descending phases of the solar cycle while for radiative indices, the separation between the paths are well within the error limits.

Key words. Sun: oscillations, activity.

1. Introduction

Ever since the discovery of global modes in the Sun, it has been expected that solar cycle changes in the Sun's interior would be reflected as a variation in the *p*-mode frequencies. Woodard *et al.* (1991), for the first time, showed that the mode frequencies varied on monthly time scales and were correlated with the average magnetic flux density on the Sun in short time intervals. Bachmann & Brown (1993) pointed out that the frequency shifts were correlated differently with magnetic and radiative indices and was later confirmed by Bhatnagar *et al.* (1999). A recent low ℓ analysis (Jiménez-Reyes *et al.* 1998) also indicated that the correlation between mode frequencies and magnetic activity indices is complex; it varies between rising and falling phases of the solar activity cycle. Here, we analyse the intermediate degree modes for the solar cycle 22 and find a "hysteresis" phenomenon between the centroid frequency changes and magnetic activity indicators.

2. Frequency data sets and analysis

The intermediate degree mode frequencies are obtained from different observing stations as these are not available from a single instrument or station for the solar cycle 22. Here we use frequency data sets obtained from HAO/NSO (FTACH) for the period May 1986 to November 1990 (17 sets), Big bear solar observatory (BBSO) data from March 1986 to September 1990 (4 sets), LOWL data from February 1994 to February 1996 (2 sets), GONG data from June 1995 to August 1999 (14 non-overlapping sets). The centroid frequency shifts are calculated by using the frequencies of BBSO station obtained in 1988 as these are also the reference frequencies for the FTACH data (Bachmann & Brown 1993). Thus, our analysis is restricted to the spherical harmonic degree range $20 \leq \ell \leq 60$ and frequency range 2600 μHz $\leq \nu \leq$ 3200 μHz. The activity indices considered are: KPMI, (Kitt Peak Magnetic Index) obtained from Kitt peak full disk magnetograms; MPSI, (Magnetic Plage Strength Index) from Mount Wilson magnetograms; R_I , the international sunspot number from the Solar Geophysical Data (SGD); F_{10} , integrated radio flux at l0.7 cm from SGD; FI, total flare index from SGD; He I, equivalent width of He 110830 Å line, averaged over the whole disk from Kitt Peak.

3. Results and conclusion

In Figs. 1 and 2, the variation in frequency shifts are plotted against the solar activity indices. It is observed for solar cycle 22 that the magnetic field index represented by KPMI follows different paths for the ascending and descending phases of solar cycle; the descending path always follows a higher track than the ascending one. However, in case of radiative indices represented by F_{10} here, the separation between the ascending and descending paths are small and within the error limits. This is further confirmed by carrying out the Spearman's rank correlation between the mean frequency shifts and activity indices. The correlation coefficients (r_s) for the ascending, descending and the full solar cycle 22 are summarised in Table 1. It is evident from the results that the radiative indices have a better rank correlation than the magnetic field indices. In Figs. 1 and 2, we have also shown the trend of variation in frequency shifts with activity indices for cycle 23 (up to August 1999).

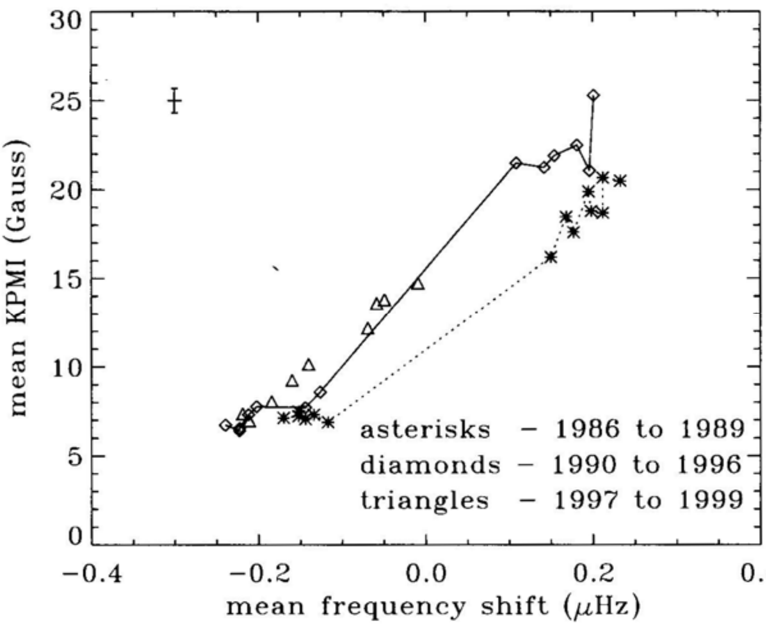

Figure 1. Variation of Kitt Peak Magnetic Index (KPMI) with frequency shift. It is observed for solar cycle 22 that the descending phase follows a higher track than the ascending one showing "hysteresis" phenomenon. The error-bars at the top left comer indicate 1σ values.

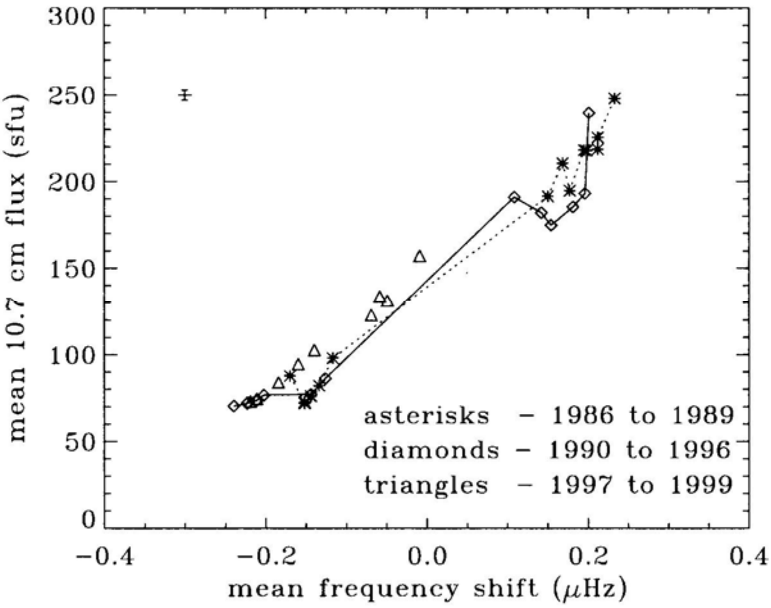

Figure 2. Variation of 10.7 cm radio flux (F_{10}) with frequency shift. It is observed for solar cycle 22 that the descending and ascending paths cross each other and the separation between the paths is well within the error limits. The error-bars indicate 1σ values.

Table 1. Spearman's rank correlation statistics for solar cycle 22.

Activity index	r_s (ascending phase)	r_s (descending phase)	r_s (full solar cycle)
KPMI	0.87	0.91	0.79
MPSI	0.83	0.96	0.88
R_I	0.92	0.93	0.94
F_{10}	0.94	0.96	0.95
FI	0.94	0.85	0.93
HeI	0.89	0.91	0.90

Table 2. Values of the parameter $\oint \Delta\nu$ for different activity indices for cycle 22

Activity index	$\oint \Delta\nu$ (nHz)
KPMI	110 ± 8.56
MPSI	60 ± 8.39
R_I	20 ± 8.36
F_{10}	-10 ± 8.93
FI	-10 ± 8.83
HeI	-20 ± 8.43

We have further evaluated the parameter $\oint \Delta\nu$ (Jiménez-Reyes *et al.* 1998) which represents the mean frequency difference between the descending and ascending phases of solar activity cycle as shown in Table 2. We find that the integral is nearly zero for radiative indices indicating that there is no "hysteresis" phenomenon for these indices. We believe that this phenomenon may explain the reason for the better correlation of radiative indices with the frequency shift than the magnetic indices.

To summarise, we find that the intermediate degree frequencies of solar cycle 22 show a "hysteresis" phenomenon with the magnetic indices whereas no such effect exists for the radiative indices.

Acknowledgement

The BBSO data were acquired by K. Libbrecht and M. Woodard, Caltech and the LOWL data from (http:/www hao.ucar.edu/public). This work utilises data obtained by Global Oscillation Network Group. Partial financial support from CSIR-ES scheme and Indo-US programme – NSF Grant INT-9710279 is acknowledged.

References

Bachmann, K. T., Brown, T. M. 1993, *Astrophys. J.*, **411**, L45
Bhatnagar, A., Jain, Kiran, Tripathy, S. C. 1999, *Astrophys. J.*, **521**, 885
Jiménez-Reyes, S. J., Regulo, C, Palleé, P. L., Roca Cortés, T. 1998, *Astr. Astrophys.*, **329**, 1119.
Woodard, M. F., Kuhn, J. R., Murray, N., Libbrecht, K. G. 1991, *Astrophys. J.*, **373**, L81.

J. Astrophys. Astr. (2000) **21**, 361–364

Non-Radial Oscillations in an Axisymmetric MHD Incompressible Fluid

A. Satya Narayanan, *Indian Institute of Astrophysics, Bangalore 560 034, India.*
e-mail: satya@iiap.ernet.in

Abstract. It is well known from Helioseismology that the Sun exhibits oscillations on a global scale, most of which are non-radial in nature. These oscillations help us to get a clear picture of the internal structure of the Sun as has been demonstrated by the theoretical and observational (such as GONG) studies. In this study we formulate the linearised equations of motion for non-radial oscillations by perturbing the MHD equilibrium solution for an axisymmetric incompressible fluid. The fluid motion and the magnetic field are expressed as scalars U, V, P and T, respectively. In deriving the exact solution for the equilibrium state, we neglect the contribution due to meridional circulation. The perturbed quantities U_*, V_*, P_*, T_* are written in terms of orthogonal polynomials. A special case of the above formulation and its stability is discussed.

Key words. Non-radial oscillations—MHD—axisymmetry.

1. Introduction

Studies of stellar pulsations, in particular the Sun, is interesting both from the theoretical and observational point of view. Stars such as the Cepheids are known to pulsate with large amplitudes. In the case of the Sun, several thousand individual modes have been identified. With careful observation, frequencies for as many as 10^6 modes can be determined accurately. Helioseismology deals with the study of the interior of the Sun from the observed frequencies of modes of oscillations. It is interesting to note that most of the modes are non-radial in nature. For more details about non-radial oscillations, refer to Unno *et al.* (1989), Christensen-Dalsgard (1997).

In order to study oscillations, it is important to determine the equilibrium state of stars which are under the combined action of gravitational, thermal and magnetic forces. In most of the studies related to Helioseismology, the equilibrium state is taken to be hydrostatic, where the pressure gradients are balanced by gravity in the absence of fluid motions. However, stars like the Sun have magnetic field both inside as well as on the outer atmospheres. It would be interesting to study the equilibrium state with magnetic field and motions included, before venturing into the study of oscillations. There have been several studies on the equilibrium of stars, in particular the Sun by Chandrasekhar (1956), Ferraro (1954), Pendergast (1956), Nakagawa & Trehan (1968), Gokhale & Hiremath (1993), Satya Narayanan (1996), Del Zanna & Chiuderi (1996), Neukirch & Tastatter (1999) who have investigated the combined effects of fluid motions and magnetic fields.

2. Equilibrium solution

In a cylindrical coordinate system (y, ϕ, z), the hydromagnetic equations for equilibrium in an incompressible medium with infinite electrical conductivity in which axial symmetry prevails can be written in the form of the following system of coupled partial differential equations for the scalars P, T, U, V which define the magnetic and velocity fields (Satya Narayanan 1996).

$$[y^2U, y^2P] = 0, \quad [y^2U, T] + [V, y^2P] = 0, \tag{1}$$

$$[y^2T, y^2P] + [y^2U, y^2V] = 0, \tag{2}$$

$$[\Delta_5 P, y^2P] - [\Delta_5 U, y^2U] + y\frac{\partial}{\partial y}\{T^2 - V^2\} = 0. \tag{3}$$

Here, $[X, Y] = \partial X/\partial y \partial Y/\partial - \partial X/\partial z \partial Y/\partial y$. In stars like the Sun, the meridional motion U is negligible. Neglecting U, equations (l)–(3) can be simplified to yield

$$\Delta_5 P + \frac{1}{y^2}G(y^2P) + y^2 g(y^2P) = \Phi(y^2P). \tag{4}$$

G, g and Φ are arbitrary functions of y^2P. Equation (4) represents the general integral of the equilibrium solution for the case $U = 0$. The above equation is highly nonlinear. However, for certain specific choices of G, g and Φ , the equation can be made linear.

The linear equation is

$$\Delta_5 P + \alpha^2 P = k - \beta y^2/2 \tag{5}$$

where α, β and k are constants.

The solution in spherical polars (by a simple transformation) is

$$P = \sum_{n=0}^{\infty} A_n \frac{J_{n+3/2}(\alpha r)}{(\alpha r)^{3/2}} C_n^{3/2}(\mu) + \frac{k}{\alpha^2} + \frac{4\beta}{\alpha^4} - \frac{\beta}{2\alpha^2} r^2(1 - \mu^2) \tag{6}$$

$\mu = r \cos \theta$. The boundary condition is similar to that discussed by Hiremath & Gokhale (1995).

3. Oscillations

In order to study the oscillations, we perturb the scalars U, V, P, T as follows

$$U = U_0 + \delta U, V = V_0 + \delta V, P = P_0 + \delta P, T = T_0 + \delta T. \tag{7}$$

The linearised equations for the oscillations can be written as

$$\frac{\partial \delta P}{\partial t} = [y^2 \delta U, y^2 P_0], \tag{8}$$

$$\frac{\partial \delta T}{\partial t} = [V_0, y^2 \delta P] + [\delta V, y^2 P_0] - [T_0, y^2 \delta U], \tag{9}$$

$$y^3 \frac{\partial \delta V}{\partial t} = [T_0, y^2 \delta P] + [y^2 \delta T, y^2 P_0] - [y^2 V_0, y^2 \delta U], \tag{10}$$

$$y \triangle_5 \frac{\partial \delta U}{\partial t} - [\triangle_5 P_0, y^2 \delta P] - [\triangle_5 \delta P, y^2 P_0] = 2y \frac{\partial}{\partial z}(T_0 \delta T - V_0 \delta V). \tag{11}$$

δU, δV, dP, δT denote perturbations while V_0 , P_0 , T_0 denote the basic state. U_0 has been neglected.

The basic equations which are derived in the cylindrical coordinate system can be recast in the spherical polars because of the spherical symmetry. The perturbed quantities are written in terms of spherical harmonics

$$f(r, \theta, \phi, z) = \sum_{l,m} f_r(r) Y_l^m(\theta, \phi) \exp(-i\omega t). \tag{12}$$

If we plug in the above equations in the linearised equations of motion, the resulting equations will be quite complicated as the number of terms in each of the expansion is rather large and one will end up in closure problem. However, for the sake of simplicity, we shall restrict our analysis to only the first few terms of the expansion (say l,m =7). The resulting equations are still complicated and will have to be solved numerically. This is in progress and will be reported subsequently.

An interesting stationary solution of the MHD equations is given by

$$V = \frac{B}{(4\pi\rho)^{1/2}} \quad \text{and} \quad \frac{p}{\rho} + \frac{B^2}{8\pi\rho} = \text{const.} \tag{13}$$

The linearised equations of motion can be simplified to yield a single equation for the poloidal field as

$$\frac{d^2 P}{dy^2} + \frac{1}{y}\frac{dP}{dy} + \left\{ k^2 \chi^2 - \frac{m^2}{y^2} \right\} P = 0 \tag{14}$$

Where $\chi^2 = 1/p^2(K + \sigma/2V_A)^2 - 1$. The solution of the above equation is given by $P = AJ_m(kXy)$ where $J_m(x)$ is the Bessel function of order m and A is an arbitrary constant. The boundary condition can be shown to be $P(y = R) = 0$. The frequency of oscillation of the system can be shown to be $\sigma/2V_A = \pm 1/p(1 + q^2)^{1/2} - \{k + m/p\}$, where $q^2 = j^2_{m,n}/(kR)^2$ and $j_{m,n}$ is the nth root of $J_m(x) = 0$. It is easy to see that the frequency of oscillation σ is always real and hence the system is stable to small perturbations.

4. Conclusions

An exact solution of the MHD equilibrium with the assumption of axial symmetry and large conductivity has been presented. The meridional circulation has been neglected. We have formulated the linearised equations of motion for oscillations about the equilibrium solution. We retain only a few terms in the expansion. The resulting equations will be solved later. Finally, a specific steady solution and its stability has been discussed.

References

Chandrasekhar, S. 1956, *Astrophys. J.*, **124**, 232.
Christensen-Dalsgard, J. 1997, *Lecture Notes on Stellar Oscillations.*
Del Zanna, L., Chiuderi, C. 1996, *Astr. Astrophys.*, **310**, 341.
Ferraro, V. C. A. 1954 *Astrophys. J.*, **119**, 407.
Gokhale, M. H., Hiremath, K. M., 1993, *Astrophys. J.*, **407**, 350.
Hiremath, K. M., Gokhale, M. H. 1995, *Astrophys. J.*, **448**, 437.
Nakagawa, Y., Trehan, S. K. 1968, *Astrophys. J.*, **151**, 1111.
Neukirch, T., Rastatter, L. 1999, *Astron. Astrophys*, (in press).
Pendergast, K. H. 1956, *Astrophys. J.*, **123**, 498.
Satya Narayanan, A. 1996, *Physica Scripta*, **53**, 638.
Unno, W., Osaki, Y., Ando, H., Shibahashi, H. 1989, *In Nonradial Oscillations of Stars*, (University of Tokyo Press).

J. Astrophys. Astr. (2000) **21,** 365–371

Mechanism of Cyclically Polarity Reversing Solar Magnetic Cycle as a Cosmic Dynamo

Hirokazu Yoshimura, *Department of Astronomy, University of Tokyo, Tokyo, Japan 113-0033.*
e-mail: yoshimura@astron. s.u-tokyo.ac.jp

Abstract. We briefly describe historical development of the concept of solar dynamo mechanism that generates electric current and magnetic field by plasma flows inside the solar convection zone. The dynamo is the driver of the cyclically polarity reversing solar magnetic cycle. The reversal process can easily and visually be understood in terms of magnetic field line stretching and twisting and folding in three-dimensional space by plasma flows of differential rotation and global convection under influence of Coriolis force. This process gives rise to formation of a series of huge magnetic flux tubes that propagate along iso-rotation surfaces inside the convection zone. Each of these flux tubes produces one solar cycle. We discuss general characteristics of any plasma flows that can generate magnetic field and reverse the polarity of the magnetic field in a rotating body in the Universe. We also mention a list of problems which are currently being disputed concerning the solar dynamo mechanism together with observational evidences that are to be constraints as well as verifications of any solar cycle dynamo theories of short and long term behaviors of the Sun, particularly time variations of its magnetic field, plasma flows, and luminosity.

Key words. Dynamo—solar cycle—polarity reversal—differential rotation—turbulence—global convection.

1. Solar dynamo and cyclically polarity reversal process in terms of magnetic field line stretching and twisting and folding inside the convection zone of the sun

The basic process of the solar cycle can easily and visually be understood without the help of a computer in terms of magnetic field line stretching and twisting and folding process by a flow of differential rotation and a non-axisymmetric flow such as global convection inside the solar convection zone in three-dimensional space (Yoshimura 1972, 1983, 1993).

It is well known that the magnetic field line stretching by the plasma flow of differential rotation, observed at the surface of the Sun as the equatorial acceleration, can explain the following part of the Hale's polarity rules of the solar cycle.

- The magnetic axis of a bipolar sunspot group of the Sun is almost always parallel to the equator.

- The polarity relation of preceding and following sunspots of the bipolar sunspot group is almost always the same for each northern or southern hemisphere during one solar cycle.
- This polarity relation of one hemisphere is opposite to that of the other hemisphere (Babcock 1961).

However, there was some confusion in this model about the mechanism of the polarity reversal part of the Hale's polarity rules and about the mechanism of how the latitudes of appearance of the sunspot groups migrate from mid-latitudes toward the equator as the solar cycle progresses.

This reversal process also can be understood in terms of magnetic field line deformation by plasma flows in the same way as the magnetic field line stretching by the flow of differential rotation. All we need for this process is an additional non-axisymmetric flow twisted by Coriolis force with spatial scale of the order of the diameter of the Sun. An example of such a flow is a convection which flows upward first and then horizontally and later downward to return horizontally to the upflow motion. This makes one cell of the flow system. The helicity vector of the twist is horizontal in the direction of the rotation, contrary to the case of many turbulent dynamo models whose helicity vector is generally vertical.

The first step in the understanding of the process is the deformation of the magnetic field lines by upward and downward motion of a non-axisymmetric flow. Suppose, first of all, that there are horizontal magnetic field lines stretched in the direction of rotation by the flow of differential rotation. The magnetic field lines are raised (pushed down) by upflow (downflow) motion of the non-axisymmetric flow.

The second step is the twisting of the magnetic field lines deformed by the process of the first step. The twisting is due to the fact that the horizontal motion of the non-axisymmetric flow is deflected to the right (left) in the northern (southern) hemisphere by Coriolis force. The horizontal flow in the same (opposite) direction as (to) the rotation is deflected toward the equator (poles) in both hemispheres. As a result of this process, a horizontal helical structure is formed in the streamlines of the flow. The direction of the twist of the helical structure, or the helicity vector of the structure, is horizontal and is in the same (opposite) direction as (to) the rotation in the upper (lower) part of the cell in the northern hemisphere. In the southern hemisphere, the direction of the twist is opposite to the case of the northern hemisphere. The magnetic field lines are twisted by the flow so that the field lines become almost parallel to the streamlines of the flow.

The third step is stretching of the deformed and twisted magnetic field lines by the flow of differential rotation. If the equator is rotating faster than the poles as in the case of the Sun, for example, the flow of differential rotation acts on the twisted magnetic field lines in the following way. The horizontal portions of the magnetic field lines, which are deflected by the twisted non-axisymmetric flow toward the equator, are carried in the direction of rotation at a rate faster than that of the portions deflected toward the poles in both hemispheres. In a reference frame rotating with the mean speed of the differential rotation, the portions deflected toward the equator look like being stretched in the same direction as the rotation while the portions deflected toward the poles look like being stretched in the opposite direction to the rotation. As a result of this process, the flow of equatorial acceleration of this step acts on the magnetic field lines in the following two different ways for the upper and lower parts of the flow cell. In the upper part, the magnetic field lines near the surface in the horizontal portions of the flow cell moving in the same (opposite) direction as (to) the rotation are deflected toward the equator (poles) and are stretched toward the same (opposite) direction as (to) the direction of the rotation. In the lower part, the magnetic field lines near the bottom behave in the same way as the field lines of the upper part near the surface.

The fourth step is the polarity reversal of the magnetic field and formation of a reversed magnetic field line system. When the processes in the three steps described above continue, the magnetic field lines near the surface (bottom) in the upper (lower) part of the flow cell, deflected both toward the equator and the poles, keep being stretched toward the same direction as the rotation and the field is strengthened. On the other hand, the magnetic field lines away from the surface (bottom) in the upper (lower) part of the cell, deflected both toward the equator and the poles, are folded to reverse their direction. One reversed magnetic field line system is formed and replaces the original magnetic field line system in the layer away from the surface (bottom) in the upper (lower) part of the cell. Since the whole process take place sequentially and continuously, a cyclically polarity reversing magnetic field line system is formed in the upper (lower) part of the cell which propagates toward the surface (bottom).

The equatorial acceleration, which we assumed in the above example, is not a special form of the differential rotation. The differential rotation can take any form which is determined by dynamics of the convection zone. In any case of the form of the differential rotation, a cyclically polarity reversing magnetic field line system is formed and the direction of propagation of the field line system is perpendicular to the gradient of the differential rotation. In other words, the waves propagate along iso-rotation surfaces. In the upper (lower) part of the cell, the propagation is toward the left-hand (right-hand) direction with respect to the gradient vector of the differrential rotation in the meridional plane in the northern hemisphere. In the southern hemisphere, the direction of propagation is opposite to the case of the northern hemisphere.

Since stretching of a magnetic field line gives rise to strengthening of its magnetic field and hence production of a magnetic field energy, this process is a dynamo mechanism. The wave is called a dynamo wave. When one magnetic field line system of the dynamo wave appears on the surface of the Sun, one solar cycle activity occurs. The butterfly diagram of the solar cycle reflects a cross section of the field line system of the dynamo wave at the surface of the Sun. The wave propagates along iso-rotation surfaces inside the Sun and obliquely encounters the surface of the Sun.

The requirements for the non-axisymmetric flow that can act as a dynamo together with the flow of differential rotation of the Sun by the processes described above are the followings.

- The whole pattern of the non-axisymmetric flow cell must propagate around the rotational axis of the Sun. Then in the reference frame that is rotating with the speed of the propagation, the flow of rotation looks like a zonal flow passing through the propagating cell. Only in this case, the magnetic field lines are not wound up and are not entangled around the cell. Global convection and Rossby. waves in a rotating system have such characteristics due to the influence of Coriolis force.
- Speed of the flow and the influence of Coriolis force on the flow which makes the flow pattern twist and propagate to drive the dynamo must be strong enough to

withstand the diffusive action of smaller scale flows. Diffusive smaller scale flows are defined as those flows that cannot feel the influence of Coriolis force strongly enough to act as a dynamo and disperse the magnetic field energy.

2. Historical review of formulation of solar cycle dynamo as a generation and polarity-reversing mechanism of the magnetic field of the sun

In order to understand the meaning of the solar cycle in a broader context of science and technology, we briefly review in the following a history of the concept of a cosmic dynamo.

When understanding of the nature of electricity and magnetism was in its infancy, Siemens invented a self-excited dynamo in laboratory (see Krause 1993). A dynamo is a machine that generates electric current and associated magnetic field. It was discovered by Faraday that electric current is generated in electrically conducting wires when the wires move across magnetic field lines created by a permanent magnet or by electric current flowing in an independent set of wires. A self-excited dynamo is a dynamo without a permanent magnet or a battery that generates electric current. Siemens demonstrated that such a machine is possible with two sets of wires that rotate with respect to each other. The first set of wires was set on a table of laboratory. The second set of wires rotated inside the first set of wires. However, generation of electric current and associated magnetic field of this machine was unstable in the sense that generation did not always occur.

The two sets of wires of the Siemens' self-excited dynamo were embedded in the magnetic field of the Earth. When the second set of wires rotated, it moved across the magnetic field lines of the Earth to generate a seed current that was feeded to the first set of wires. This seed current, flowing in the first set of wires, gave rise to a magnetic field. The rotating second set of wires moved across the field lines of this magnetic field to generate electric current in the second set of wires which was feeded to the first set of wires. This process continued to amplify the current and the associated magnetic field. Thus generation of the current and magnetic field was sensitive to the direction of the second set of wires with respect to the magnetic field lines of the Earth. Whether or not the seed current was strong enough to start the whole process depended on the direction of the second set of wires with respect to the magnetic field lines of the Earth.

The present day industrial dynamo originated by Siemens' invention uses a smaller secondary dynamo with a permanent magnet or a magnet produced by a small amount of electric current to feed the seed current of the Siemens' self-excited dynamo.

The basic question of a cosmic dynamo driven by plasma flows is closely related to the situation of the Siemens' dynamo. It also requires a seed current and field. The dynamo does not generate a magnetic field out of nothing. It amplifies an infinitesimal seed field to a field of finite amplitude. The infinitesimal seed field is present in any plasma where particles with electric charges are always present in micro space to move around and produce magnetic field. When this magnetic field in micro space is averaged over some macro space, it is difficult to completely cancel out the magnetic field. Some infinitesimal field is always present even in macro space. The question of a cosmic dynamo is whether or not there is any plasma flow that can amplify this infinitesimal field to a field of finite level without wires and rods that guide electric current and without permanent magnets and batteries. The question is essentially linear with respect to the magnetic field in the sense that the Lorentz force of the produced magnetic field acting on the flow does not come into this basic question. Only when we ask about the level and magnitude of the generated electric current and magnetic field or the amplitude of the solar cycle, we need to consider the nonlinear action of the Lorentz force on the dynamo driving flows and mechanical motions. When we investigate the long-term behavior of the solar cycle, this nonlinear aspect of the problem becomes essential.

We here return to the era when understanding of the nature of electricity and magnetism was still in its infancy. When Maxwell formulated the basic equation governing electricity and magnetism, he proposed that any rotating body with electric charges should be accompanied by a magnetic field. This rotation of electric charges is equivalent to a motion of electric charges and hence is equivalent to electric current. After Rowland proved this claim, Schuster pushed this proposition further that any rotating body which is electrically neutral should possess a magnetic field. Maxwell and Schuster conjectured that rotation and magnetic field should be related with each other in a fundamental way as a part of nature of space and time.

This proposition or conjecture prompted Hale in 1908 to test the idea for the case of sunspots. The H_α features around sunspots observed by Hale showed a pattern that was similar to that of a vortex motion of plasma. Hale thought that this must be equivalent to rotation and hence sunspots should have a magnetic field. By applying the Zeeman effect to the spectrum of light emitted from sunspots, he discovered magnetic field of sunspots. Although Hale's conjecture that the H_α features around sunspots represent vortex and rotational motions was wrong, this was the first suggestion that plasma motions without wires and rods could generate a magnetic field. This is the birth of concept of a cosmic dynamo. Since Larmor included this mechanism in his paper in 1919 as one of possible mechanisms of generation of magnetic field in cosmos, Larmor is often erroneously cited as the first person who suggested dynamo mechanism for generation of magnetic field in cosmos by plasma flows. He visited Mt. Wilson Observatory.

This concept of generation of magnetic field by vortex or rotational or axisymmetric plasma flows alone was proved to be unable to amplify and maintain magnetic field by Cowling in 1933–1934. This theorem, called Cowling's anti-dynamo theorem, was a great challenge to the concept of a cosmic dynamo driven by plasma flows.

A more fundamental meaning of the rotation-magnetic field relation was implied by Einstein's general relativity. In his paper of general relativity, he started his discussion of general relativity by Mach's Gedanken (thought) experiment where two bodies are rotating with respect to each other in an empty space. Since a person standing on each body can measure that one body is a perfect sphere and the other is an ellipsoid, for example, it can be concluded that the body with the ellipsoidal figure is rotating and hence centrifugal force is acting on the body. However, according to the principle of general relativity, both bodies should be equivalent. Why should one body have an ellipsoidal figure? Einstein's answer was that the nature of space and time of the two bodies are determined by distribution of mass at a far distance. This means that there could be no pure empty space. Even when we do not discuss the problem of contradiction of the concept of existence of ether by the name of structure of space and time as an absolute reference frame and the concept of general relativity which denies the existence of any absolute reference frame, we see in this answer of Einstein a limitation of the 20th century physics. Although Einstein's general relativity theory discussed only the aspect of equivalence of gravity and acceleration, the Mach's Gedanken (thought) experiment and Einstein's answer implied that existence of magnetic field of a rotating body is determined by mass distribution at far distance. As we have seen in the previous section, the solar dynamo works only under the influence of Coriolis force. This means that existence of a cyclically polarity reversing magnetic field depends on the mass distribution at a far distance according to the Einstein's thinking. Can existence of magnetic field in a local space be related to existence of mass distribution at a far distance?

To add a few words to this fundamental question, it was discovered by Barnett in 1914, at around the times of Einstein's general relativity which was published in 1916, that when a ferromagnetic material was rotated rapidly, it was magnetized around the rotational axis. Conversely, it was found by Einstein and de Haas in 1915 that when a ferromagnetic material was magnetized, it began to rotate around an axis. These two findings led many scientists to believe that there must be a fundamental relation between rotation and magnetic field.

On the other hand, facing the Cowling's challenge against the concept of a cosmic dynamo that the plasma motions could not generate magnetic field and could not drive electric current in cosmos, Elsassar, a friend of Einstein, proposed that non-axisymmetric flows could work as a dynamo even if axisymmetric flows alone could not work as a dynamo.

Several candidates of these flows have been studied. One class of flows is turbulence. The other class is laminar flows.

In order to avoid confusion, we should state here that there are two classes or concepts of turbulent dynamos. One class of dynamos generates magnetic field locally in a space on the order of the size of the turbulence itself. In this class, the presence of rotation as a whole is not important. It is similar to the case of plasma in micro space in general where charged particles move around to produce electric current and magnetic field. If there are no counteracting smaller scale turbulence that disperse the generated magnetic field, the field can be maintained in principle. In this class of turbulent dynamos, there need not necessarily be a net amount of magnetic field once averaged over some macro space. The other class of turbulent dynamos is under influence of rotation as a whole. In this class, the net amount of magnetic field is expected to exist even when the field is averaged over some macro space and the rotation-magnetic field relation is expected to exist.

In the initial phase of development of dynamo theories, however, the concept of magnetohydrodynamics was hot fully understood. Although existence of the two candidates of dynamo driving flows of global convection and Rossby waves was already theoretically known as the two possible types of oscillatory flow in a rotating spherical system by Margules and Hough in the late 19th century, its relevance to the dynamo problem was not noticed for a long time.

3. Solar cycle

For solar physics, the question is whether or not the global convection exists in the convection zone. If it exists, together with the action of the differential rotation flow, it cannot avoid driving the solar cycle under influence of Coriolis force of rotation to make its flow pattern twist and propagate.

One of the disputes which are related to the present solar cycle model is the structure of the differential rotation. The fact that the dynamo wave propagates along iso-rotation surfaces was first found by a numerical simulation experiment and was later proved analytically (Yoshimura 1975a, b). The theorem can now be seen and proved visually in terms of magnetic field line behavior without any difficulty and ambiguity. The dynamo wave is a powerful tool for investigation of the structure of the differential rotation. The dynamo model shows that the rotation rate must decrease poleward and increase inward in the layer where the observed sunspot groups originnate. We are not sure, however, about the depth where the sunspot groups originate. This structure was often claimed to be inconsistent with the results of the helioseismology. I rather see this difference as another source of information, as well as another observational contraint for further understanding the layer where the sunspot groups originate and for further understanding the vertical stratification of the solar convection zone.

Another source of information concerning the vertical stratification and the related nonlinear long-term behavior of the solar cycle is the solar total irradiance change which I discussed in separate literatures (Yoshimura 1994; 1996; 1997a,b; 1998; and references cited therein).

In conclusion, the cyclically polarity reversing magnetic field is a natural phenolmenon of a cosmic dynamo under influence of Coriolis force of rotation. The solar cycle is a representative example of such a cosmic dynamo.

References

Babcock, H. W. 1961, *Astrophys. J*, **133,** 572.

Krause, F. 1993, in *The Cosmic Dynamo,* IAU Symp. No. 157, (eds.) F. Krause *et al*., (Dordrecht: Kluwer Academic Publishers), 487.

Yoshimura, H. 1972, *Astrophys. J.*, **178,** 863.

Yoshimura, H. 1975a, *Astrophys. J. Suppl*., **29**, 467.

Yoshimura, H. 1975b, *Astrophys. J*., **201,** 740.

Yoshimura, H. 1983, *Astrophys. J. Suppli* **52,** 363.

Yoshimura, H. 1993, in *The Cosmic Dynamo*, IAU Symp. No. 157, (eds.) F. Krause *et al*., (Dordrecht: Kluwer Academic Publishers), 463.

Yoshimura, H. 1994, *Astron. Nachr*., **315,** 371.

Yoshimura, H. 1996, *Proc. Japan Acad*., **72B,** 197.

Yoshimura, H. 1997a, *Proc. Japan Acad*., **73B,** 115.

Yoshimura, H. 1997b, *Proc. Japan Acad*., **73B,** 120.

Yoshimura, H. 1998, *Solar Phys*., **177,** 329.

J. Astrophys. Astr. (2000) **21**, 373–377

The Current Status of Kinematic Solar Dynamo Models

Arnab Rai Choudhuri, *Department of Physics*, *Indian Institute of Science*, *Bangalore 560012*, *India*
e-mail: arnab@physics.iisc. ernet. in

Abstract. This review provides a historical overview of how research in kinematic solar dynamo modeling evolved during the last few decades and assesses the present state of research. The early pioneering papers assumed the dynamo to operate in the convection zone. It was suggested in the 1980s that the dynamo operates in a thin layer at the bottom of the convection zone. Some researchers in recent years are arguing that the poloidal field is produced near the surface—an idea that goes back to Babcock (1961) and Leighton (1969).

Key words. Sun—MHD—dynamo theory.

1. Introduction

The aim of solar dynamo theory is to explain how solar magnetic fields are generated and maintained by the nonlinear interactions between the solar plasma and magnetic fields. In the full dynamo problem, therefore, one has to study how the magnetic field $\mathbf{B}(x, t)$ and the velocity field $\mathbf{v}(x, t)$ act on each other. This is a problem which can be attacked only numerically in any non-trivial situation and is a formidable problem even by the standard of today's computers. This led to the development of kinematic dynamo theory, in which one assumes the velocity field to be 'given' and studies only the behaviour of the magnetic field. In the early years of kinematic dynamo research, very little was known about the conditions of the solar interior and researchers were free to assume any interior velocity field that would give a good match with observations. Our knowledge of the interior physics has increased dramatically in the last few years due to the development of helioseismology and various kinds of numerical simulations. These developments are putting tight constraints on the types of dynamo model which can be allowed, although we are still far from evolving a 'standard' model of the solar dynamo. Lack of space unfortunately compels us to omit any discussion of important nonlinear processes and fluctuations around the mean (irregularities of the solar cycle, field concentration in flux tubes, etc,).

Let us begin by summarizing the relevant observational data. The most important observation is the equatorward migration of the belt of sunspots, which leads to the well-known *butterfly diagram*. We believe that the sunspots are produced by the magnetic buoyancy of a strong toroidal magnetic field underneath the Sun's surface—an idea first propounded by Parker (1955a). Hence, the butterfly diagram implies an equatorward migration of the subsurface toroidal field. Although the sunspots are the regions of strongest magnetic field on the solar surface, there definitely exist magnetic fields outside sunspots. In low-resolution magnetograms, one finds patches of unipolar field with magnitude of the order 1 G propagating *poleward.* Even when averaged over latitude, one finds predominantly one polarity in a belt of latitudes and these latitude belts move poleward (see Wang *et al.* 1989 and references therein). The most plausible explanation for the weak field outside sunspots is that this is a manifestation of the poloidal magnetic field, which plays a crucial role in dynamo theory. The early dynamo theorists neglected the weak field outside sunspots and focused their attention on the butterfly diagrams of sunspots. It is now becoming clear that the weak field outside sunspots gives us valuable clues about the dynamo process and a dynamo model should attempt to explain its behaviour in addition to explaining the butterfly diagram.

2. Fundamentals of dynamo theory

The basic theory of the turbulent dynamo was developed in a classic paper by Parker (1955b) and then put on a firm mathematical basis by Steenbeck *et al.* (1966). The central idea is that the poloidal and the toroidal components of magnetic field sustain each other, drawing the energy from the reservoir of kinetic energy of motion. The differential rotation can stretch out the poloidal field lines to produce the toroidal field. On the other hand, the toroidal field is twisted by helical turbulence to give rise to the poloidal field again (a process now known as the α-effect). Basics of turbulent dynamo theory can be found explained in Choudhuri (1998).

If we assume axisymmetry and use spherical coordinates, the magnetic field can be written as

$$\mathbf{B} = B\,\mathbf{e}_\phi + \nabla \times (A\,\mathbf{e}_\phi), \tag{1}$$

where $B(r, \theta)$ and $A(r, \theta)$ correspond to the toroidal and the poloidal components respectively. Let us write the velocity field in the following way

$$\mathbf{v} = \mathbf{v}_p + r\sin\theta\,\Omega\,\mathbf{e}_\phi, \tag{2}$$

where $\Omega\ (r, \theta)$ is the angular velocity and $v_p(r, \theta)$ corresponds to any circulation in the meridional plane. If the magnetic and the velocity fields are written as in (1) and (2), then the turbulent dynamo theory leads to the following equations for the evolution of poloidal and toroidal components:

$$\frac{\partial A}{\partial t} + \frac{1}{s}(\mathbf{v}_p.\nabla)(sA) = \eta\left(\nabla^2 - \frac{1}{s^2}\right)A + \alpha B, \tag{3}$$

$$\frac{\partial B}{\partial t} + s(\mathbf{v}_p.\nabla)\left(\frac{B}{s}\right) = \eta\left(\nabla^2 - \frac{1}{s^2}\right)B + s(\mathbf{B}_p.\nabla)\Omega. \tag{4}$$

where $s = r\sin\theta$ and η is the diffusivity. The last terms in the above two equations are the dynamo source terms. The last term in (4) corresponds to the generation of toroidal field by the stretching of poloidal field $\mathbf{B}_p = \nabla\times (A\mathbf{e}_\phi)$ due to differential rotation, whereas the last term in (3) incorporates the α-effect, i.e. the twisting of toroidal field lines by helical turbulence to produce the poloidal component. In the kinematic dynamo approach, one essentially solves (3) and (4) after specifying som 'reasonable' distribution of α, Ω, η and v_p. Most calculations until recently did not include any meridional circulation, i.e. v_p was taken as 0. The other parameters could not be specified completely arbitrarily. It was found (Parker 1955b) that the kinematic dynamo equations admit a wave-like solution which propagates equatorward only if the dynamo criterion

$$\alpha \frac{\partial \Omega}{\partial r} < 0 \tag{5}$$

is satisfied in the northern hemisphere of the Sun. Since we believe that the equatorward migration of the sunspot belt results from a dynamo wave propagating towards the equator, early dynamo theorists used to choose their parameters in such a way that the inequality (5) was satisfied.

3. Historical development of solar dynamo models

If one looks at the historical development of solar dynamo models, then one can clearly discern three distinct phases. In the first phase during the approximate period ≈1965-1980, most dynamo models assumed that the two main ingredients of the dynamo process—the production of toroidal field by differential rotation and the production of poloidal field by α-effect—both took place in the convection zone of the Sun. During the second phase lasting over ≈ 1980–1995, it was assumed that both of the above-mentioned main ingredients of the dynamo process occurred in a thin layer at the base of the convection zone. Models developed in the third phase beginning around 1995 will be discussed in the next section.

Since the dynamo process is ultimately powered by the kinetic energy of motion, it was natural to assume in the beginning that the whole dynamo process takes place in the convection zone where kinetic energy is most abundant. The researchers of the first phase (Steenbeck & Krause 1969; Roberts 1972; Köhler 1973; Yoshimura 1975; Stix 1976) were able to produce reasonable-looking butterfly diagrams by solving (3)–(4) in the convection zone of the Sun, provided the inequality (5) was satisfied. Soon it started becoming clear that magnetic buoyancy would be particularly destabilizing in the body of the convection zone and remove any magnetic flux from there rather quickly, without allowing time for amplification by the dynamo (Parker 1975). Several authors (Spiegel & Weiss 1980; van Ballegooijen 1982; Parker 1987; van Ballegooijen & Choudhuri 1988) suggested ways of suppressing magnetic buoyancy at the bottom of the convection zone. This led to the idea that the whole dynamo process takes place in a thin layer at the base of the convection zone. When helioseismology found a layer of concentrated shear at the base of the convection zone, this idea found further support. Several authors in the second phase of dynamo research explored the idea of the dynamo operating in a thin layer (Gilman *et al.* 1989; Schmitt & Schussler 1989; Choudhuri 1990; Belvedere *et al.* 1991; Rüdiger & Brandenburg 1995).

If the dynamo operates at the base of the convection zone and the strong toroidal field is produced there, then this field has to rise through the convection zone to produce sunspots. Choudhuri & Gilman (1987) showed that the Coriolis force plays a very important role in this problem, trying to divert the rising flux to the poleward direction. Subsequent simulations of the flux rise made it clear that the toroidal field at the base of the convection zone has to be about 10^5 G (one order larger than the equipartition value) if we are to explain various surface features of sunspots (Choudhuri 1989; D'Silva & Choudhuri 1993; Fan *et al.* 1993). Since there is a shear layer at the base of the convection zone, most researchers still believe that the toroidal magnetic field is produced there. If this toroidal field is as strong as 10^5 G, then it would completely quench the α-effect and the traditional scenario of the dynamo process would definitely not work. It has been suggested that the buoyancy instability of this strong toroidal field itself may give rise to configurations similar to what was believed to be produced by the traditional α-effect (FerrizMas *et al.* 1994). Based on such ideas, some efforts have been made to develop new types of interface dynamo models (Parker 1993; Charbonneau & MacGregor 1997). Section 4 describes a different school of thought to tackle this problem of strong toroidal field, which we call the third phase of solar dynamo research.

4. Revival of interest in Babcock-Leighton models

When the active regions on the solar surface decay, they spread some magnetic flux around. The leading sunspot in a bipolar pair is usually found at a lower latitude, due to the action of the Coriolis during the rise (D'Silva & Choudhuri 1993). It was pointed out by Babcock (1961) and Leighton (1969) long time ago that the decay of such a tilted bipolar active region contributes to the poloidal field. This effect was not included in most of the detailed dynamo models during the first and second phases, when the primary emphasis was on explaining the equatorward migration of the sunspot belt. The poleward migration of the weak field was explained by assuming that this is the poloidal component which is carried by a meridional circulation flowing towards the pole near the solar surface (Wang *et al.* 1989; Dikpati & Choudhuri 1994; Choudhuri & Dikpati 1999).

Since traditional α-effect would be inoperative on a 10^5 G strong toroidal field at the base of the convection zone, some theorists are now exploring the Babcock-Leighton idea that the poloidal field is produced near the solar surface by the decay of active regions (Choudhuri *et al.* 1995; Durney 1995, 1997; Dikpati & Charbonneau 1999; Nandi & Choudhuri 2000). One way of incorporating this effect in dynamo calculations is to take the α-coefficient concentrated near the surface, while the shear layer is taken at the base of the convection zone. A meridional circulation which is poleward near the surface and equatorward in the interior has to play an important role in these dynamo models. This circulation brings down the poloidal field created at the surface to the base of the convection zone where it can be stretched by the differential rotation. One difficulty with such models is that the α coefficient arising out of the decay of active regions has to be positive, whereas $\partial\Omega/\partial r$ at lower latitudes is also positive. It may appear at the first sight that this would violate the dynamo criterion (5) and the dynamo waves would propagate in the poleward direction. It has been shown by Choudhuri *et al.* (1995) that an equatorward propagation may still be possible in this situation if meridional circulation plays a very significant role—the time scale of meridional circulation being less than the time scale of diffusion across the convection zone. This result shows that this new type of model is viable and such models are now being investigated in detail by several groups.

5. Conclusion

It appears that the kinematic dynamo models developed in the third phase may be free from the difficulties of the earlier models, while explaining the behaviour of both sunspots and weak magnetic fields in a unified way. We are, however, still far from developing a model which can explain all the different aspects of observation in detail.

It may be mentioned that in this review we have concentrated on those kinematic calculations which attempt to model the regularities of solar cycle. A very important problem of kinematic dynamo research is to model the irregularities of solar cycle. Although the present author has worked in this field and it is a subject close to his heart, the limitation of space made it impossible even to touch upon this subject. The reader may turn to a bigger review by the present author (Choudhuri 1999) for a discussion of some other aspects which are left out here.

References

Babcock, H.W. 1961, *Astrophys. J.*, **133,** 572.

Belvedere, G., Lanzafame, G., Proctor, M.R.E. 1991, *Nature*, **350,** 481.

Charbonneau, P., MacGregor, K.B. 1997, *Astrophys. J.*, **486,** 502.

Choudhuri, A.R. 1989, *Solar Phys.*, **123,** 217.

Choudhuri, A.R. 1990, *Astrophys, J.*, **355,** 733.

Choudhuri, A.R. 1998, *The Physics of Fluids and Plasmas: An Introduction for Astrophysicists* (Cambridge University Press).

Choudhuri, A.R. 1999, *Curr. Sci*,, **77,** 1475.

Choudhuri, A.R., Dikpati, M. 1999, *Solar Phys.*, **184,** 61.

Choudhuri, A.R., Gilman, P.A. 1987, *Astrophys. J*; **316,** 788.

Choudhuri, A.R., Schussler, M., Dikpati, M. 1995, *Astr. Astrophys.,* **303,** L29.

Dikpati, M., Charbonneau, P. 1999, *Astrophys. J.*, **518,** 508.

Dikpati, M., Choudhuri, A.R. 1994, *Astr. Astrophys.*, **291,** 975.

D'Silva, S., Choudhuri, A.R. 1993, *Astr. Astrophys*., **272,** 621.

Durney, B.R. 1995, *Solar Phys.*, **160,** 213.

Durney, B.R. 1997 , *Astrophys. J.*, **486,** 1065.

Fan, Y., Fisher, G.H., DeLuca, E.E. 1993, *Astrophys. J.*, **405,** 390.

Ferriz-Mas, A., Schmitt, D., Schussler, M. 1994, *Astr. Astrophys*., **289,** 949.

Gilman, PA., Morrow, C.A., DeLuca, E.E. 1989, *Astrophys. J.*, **338,** 528.

Köhler, H. 1973, *Astr. Astrophys*., **25,** 467.

Leighton, R.B. 1969, *Astrophys. J*,, **156,** 1.

Nandi, D., Choudhuri, A.R. 2000, *Astrophys. J.*, submitted.

Parker, E.N. 1955a, *Astrophys. 1*, **121,** 491.

Parker, E.N. 1955b, *Astrophys. J.*, **122,** 293.

Parker, E.N. 1975, *Astrophys. J.*, **198,** 205.

Parker, E.N. 1987, *Astrophys. J.*, **312,** 868.

Parker, E.N. 1993, *Astrophys. J.*, **408,** 707.

Roberts, P.H. 1972, *Phil Trans. Roy. Soc*, **272,** 663.

Rüdiger, G., Brandenburg, A. 1995, *Astr. Astrophys*., **296,** 557.

Schmitt, D., Schussler 1989, *Astr*, *Astrophys*., **223,** 343.

Spiegel, E.A., Weiss, N.O. 1980, *Nature*, **287,** 616.

Steenbeck, M., Krause, F. 1969, *Astr Nachr*., **291,** 49.

Steenbeck, M., Krause, F., Rädler, K.H. 1966, Z. *Naturfor.*, **21a,** 1285.

Stix, M. 1976, *Astr. Astrophys*., **47,** 243.

van Ballegooijen, A.A. 1982, *Astr. Astrophys*., **113,** 99.

van Ballegooijen, A.A., Choudhuri, A.R. 1988, *Astrophys. J.*, **333,** 965.

Wang, Y.-M., Nash, A.G., Sheeley, N.R. 1989, *Astrophys. J.*, **347,** 529.

Yoshimura, H. 1975, *Astrophys. J. Suppl*., **29,** 467.

J. Astrophys. Astr. (2000) **21**, 379–380

Solar Internal Rotation and Dynamo Waves: A Two-Dimensional Asymptotic Solution in the Convection Zone

Gaetano Belvedere[1]*, Kirill Kuzanyan[2] & Dmitry Sokoloff[3]
[1]*Department of Physics and Astronomy, University of Catania, Astronomy Unit, Via Santa Sofia 78, 95125 Catania, Italy.*
[2]*IZMIRAN, Troitsk, Moscow Region, 142092 Russia.*
[3]*Moscow State University, Department of Physics, 119899 Moscow, Russia.*
**e-mail: gbelvedere@alpha4. ct. astro. it*

Key words. Sun: magnetic fields, rotation, activity.

Extended abstract

Here we outline how asymptotic models may contribute to the investigation of mean field dynamos applied to the solar convective zone. We calculate here a spatial 2-D structure of the mean magnetic field, adopting real profiles of the solar internal rotation (the Ω-effect) and an extended prescription of the turbulent α-effect. In our model assumptions we do not prescribe any meridional flow that might seriously affect the resulting generated magnetic fields. We do not assume apriori any region or layer as a preferred site for the dynamo action (such as the overshoot zone), but the location of the α- and Ω-effects results in the propagation of dynamo waves deep in the convection zone. We consider an axially symmetric magnetic field dynamo model in a differentially rotating spherical shell. The main assumption, when using asymptotic WKB methods, is that the absolute value of the dynamo number (regeneration rate) $|D|$ is large, i.e., the spatial scale of the solution is small. Following the general idea of an asymptotic solution for dynamo waves (e.g., Kuzanyan & Sokoloff 1995), we search for a solution in the form of a power series with respect to the small parameter $|D|^{-1/3}$ (short wavelength scale). This solution is of the order of magnitude of $\exp(i|D|^{1/3}S)$, where S is a scalar function of position.

To use the helioseismological data on the solar internal rotation rate (e.g., Schou *et al.* 1998) we approximate the angular velocity **Ω** by an analytic fitting function. For the latitudinal dependence of the α-effect we adopted the estimate given by Krause that is proportional to $\sin\theta$ (θ latitude). For the radial dependence we assumed that the α-effect changes its sign near the bottom of the convection zone. There are two maxima of the generation sources which are situated at latitudes 16° and 61°. For the first one, the radial gradient of **Ω** is positive, while, for the second one, is negative. In our approach, we find two distinct independent non-overlapping dynamo waves: the first wave in low latitudes propagates equatorwards and the second one in high latitudes propagates polewards. The approximate solution of this two dimensional problem is represented in Fig. 1. One can see that, at low latitudes, the dynamo wave propagates mainly equatorwards with some inclination with respect to the bottom of the solar convection zone. The location of the maximum of the generated magnetic

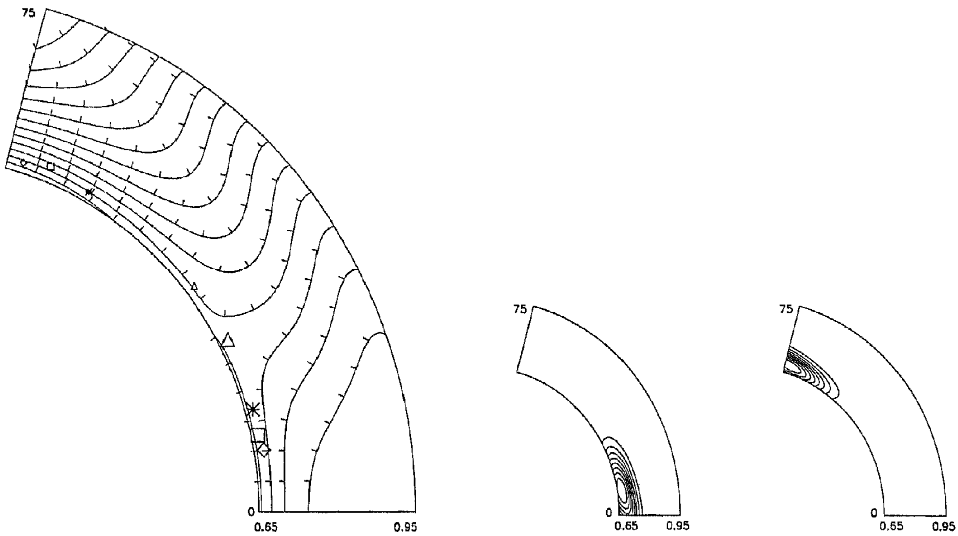

Figure 1. Contour plot of the angular velocity versus radius ($0.65 \leq r \leq 0.95$ units of the solar radius) and latitude ($0 \leq \theta \leq 75°$) after the data obtained by helioseismologists (Schou *et al.* 1998). The points of the dynamo wave maxima are shown as diamonds. Stars indicate the maxima of the sources asymptotic solution (left panel). Contour plots represent the envelope of the asymptotic solution in low (middle) and high (right panel) latitudes.

field is shifted towards the direction of the dynamo wave propagation, and is consistent with the results of (Kuzanyan & Sokoloff 1995) for the one dimensional model. It appears to be beneath the convection zone at the location $\theta = 12°$. For the poleward wave, we obtain similar properties, with the maximum located at $\theta = 68°$.

Summarizing, our analysis reveals two centers of dynamo wave generation: one at low latitudes and the other at high latitudes. The solution was found in the form of a travelling wave, which is shown to possess properties consistent with Yoshimura law (Yoshimura 1975) (dynamo waves propagate mainly along the lines of constant angular velocity).

References

Kuzanyan K. M., Sokoloff D. D. 1995, *Geophys. Astrophys. Fluid Dyn.,* **81**, 113.
Schou J., *etal.* 1998, *Astrophys. J.*, **505**, 390.
Yoshimura H. 1975, *Astrophys. J.*, **201**, 740.

J. Astrophys. Astr. (2000) **21**, 381–385

The Role of Magnetic Buoyancy in a Babcock-Leighton Type Solar Dynamo

Dibyendu Nandy* & Arnab Rai Choudhuri, *Department of Physics, Indian Institute of Science, Bangalore 560012.*
**e-mail: dandy@physics. iisc. ernet . in*

Abstract. We study the effects of incorporating magnetic buoyancy in a model of the solar dynamo—which draws inspiration from the Babcock-Leighton idea of surface processes generating the poloidal field. We present our main results here.

Key words. MHD—Sun: interior, magnetic fields.

1. Introduction

The review by Choudhuri (2000) in these proceedings points out the recent resurgence of interest in Babcock-Leighton (BL) type solar dynamos, in which the poloidal field is assumed to be generated near the solar surface due to the decay of active regions (Choudhuri *et al.* 1995; Durney 1997; Dikpati & Charbonneau 1999). Incorporating magnetic buoyancy (MB) in such a model is more tricky than it is in the case of a more traditional dynamo model, where MB could be treated merely as a flux loss mechanism. In a BL type dynamo, MB plays a more central role. It brings the toroidal flux from the bottom of the convection zone (where it is created at the tachocline) to the surface where the active regions thereby formed finally give rise to the poloidal flux. The meridional flow moving poleward and sinking near the poles then brings the poloidal flux back to the bottom of the solar convection zone (SCZ) for the production of toroidal flux. The model of Choudhuri *et al.* (1995) did not include MB, whereas Durney (1997) and Dikpati & Charbonneau (1999) treated MB through some simple prescriptions. Here we study the effects of MB by including it in the model of Choudhuri *et al.* (1995) and then looking for the changes in the results arising out of that. We present the details of our model in the next section.

2. Model

We solve the following equations within the northern quadrant of the SCZ (i.e. within $R_b = 0.7R_\odot \leq r \leq R_\odot$, $0 \leq \theta \leq \pi/2$):

$$\frac{\partial A}{\partial t} + \frac{1}{s}(\mathbf{v}_p.\nabla)(sA) = \eta\left(\nabla^2 - \frac{1}{s^2}\right)A + Q, \tag{1}$$

$$\frac{\partial B}{\partial t} + \frac{1}{r}\left[\frac{\partial}{\partial r}(rv_r B) + \frac{\partial}{\partial \theta}(v_\theta B)\right] = \eta\left(\nabla^2 - \frac{1}{s^2}\right)B + s(\mathbf{B}_p.\nabla)\Omega, \tag{2}$$

where $s = r \sin\theta$ and $B_p = \nabla \times (A e_\phi)$ is the poloidal field and B is the toroidal field. We have added one extra term Q on the right-hand side of equation (1), which governs the evolution of the poloidal field. This term does not follow from the induction equation. The usual $\alpha\Omega$ dynamo is given by the equations (1) and (2), with $Q = \alpha B$ We use the same distribution of α and Ω as in Choudhuri *et al.* (1995)—taking α concentrated near the surface and a layer of radial shear at the bottom of the convection zone.

We now adopt the following algorithm to incorporate buoyancy in our model:

* At intervals of time τ, we check whether the toroidal field B exceeds a certain critical field B_c, anywhere in the bottom of the SCZ.
* If B exceeds B_c at any point near the bottom of the SCZ, then a certain fraction f of it is made to erupt to regions close to the surface, where the α effect is concentrated.
* The erupted field is algebraically added to the field already present near the surface and the field at the bottom from where the eruption takes place is appropriately depleted, so that flux is conserved in the whole process.

The α effect works on this erupted field and generates the weak and diffuse poloidal field that we see on the surface—the essence of which is captured by the phenomenological source term Q in our equation (1).

There are three parameters which define this flux eruption process completely. One is τ (the time between successive eruptions) which we fix at $\tau = 8.8 \times 10^5$ s, approximately corresponding to an order of a thousand eruptions in a complete dynamo period. The second is B_c, the critical field, for which we use a value of $B_c = 1$ (in dimensionless units), for most of the calculations. The third is the fraction f of the toroidal field which is made to erupt. We study the dependence of the dynamo on some of these parameters and present our main results in the next section. The only nonlinearity in our problem comes through the α-quenching which is adjusted such that the peak value of the magnetic field turns out to be of order unity.

3. Results

In Fig. 1 we plot the variation of the dynamo time period T_d with the control parameter f, for three different values of the critical field B_c. It is seen that T_d decreases with increasing f and reaches an asymptotic value of 25.5 years. The fall in the value of T_d with f is quite drastic and it is obvious that making magnetic buoyancy more important (by increasing the control parameter f) has a significant effect on the working of the dynamo.

The primary role of buoyancy is to transport toroidal flux from the bottom of SCZ to the top. By making buoyancy stronger (with larger f), one makes the flux transport process more rapid and thereby reduces the dynamo period. Also, as the toroidal field belt travels equatorward with the progress of the dynamo cycle as is apparent from Fig. 2 (*left*), its strength decreases due to eruptions and becomes lower than B_c . In such a scenario, if B_c is also decreased, then we will find eruptions at lower and lower latitudes, which will effectively increase the zone of activity of the dynamo. This will result in an increase in the dynamo period

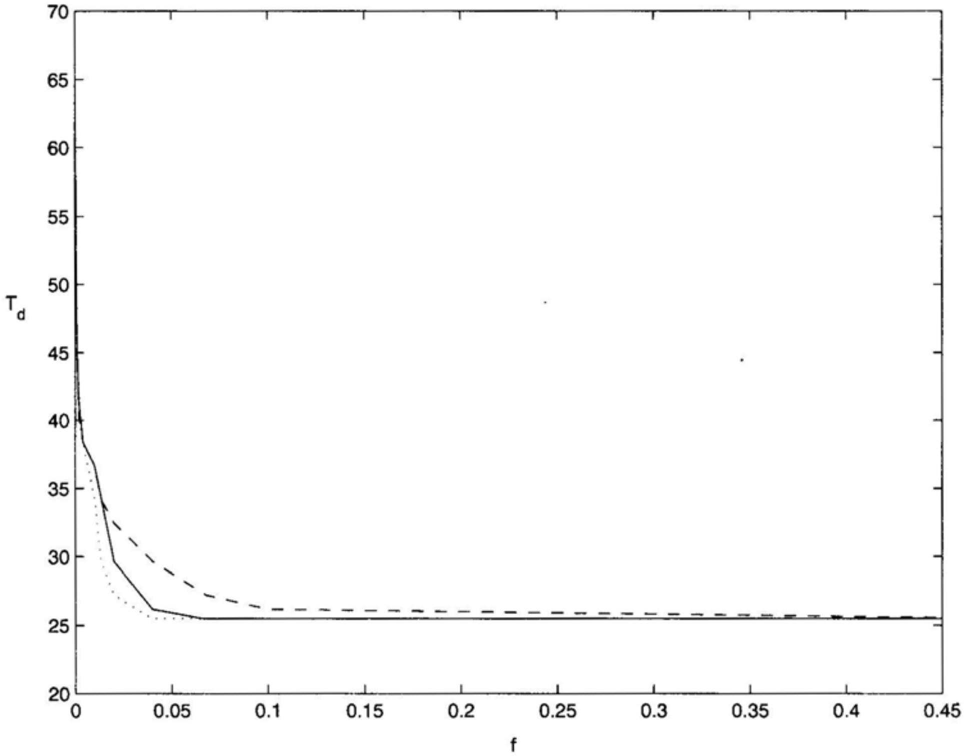

Figure 1. T_d in years vs f: the dotted line is for B_c = 2.0, the solid line for B_c = 1.0 and the dashed line for B_c = 0.5.

and obviously it will fall more slowly with f (for a lower B_c) as is evident from Fig. 1.

Fig. 2 (*left*) is a butterfly diagram for the toroidal field near the bottom of the SCZ. This figure is obtained with B_c = 1 and f = 0.1 and the contour levels that we have plotted are: 0.5, 1,2, 4, 8 and 16 respectively. We clearly see an equatorward propagation of the fields with time, in keeping with the equatorward propagation of sunspots. Note however that we do not see any strong toroidal field belt at low latitudes near the equator, which may be contradictory to observations of sunspots at low latitudes in the Sun. The reason for this becomes clear when we look at the plot of eruption latitude vs time, shown in Fig. 2 (*right*). We see that eruptions start occuring at very high latitudes—where we find the strongest toroidal fields, a feature present in Durney's (1997) results as well.

It is clear that all the recent calculations on Babcock-Leighton type solar dynamos are still of rather exploratory nature, since none of the authors have succeeded yet in producing butterfly diagrams resembling observations closely. With the basic physics of incorporating magnetic buoyancy having been explored, we are now in the process of developing more realistic models of the dynamo incorporating a solar-like profile of the angular velocity distribution and other improvements. It remains to be seen if the improved models will succeed in explaining the observational data more satisfactorily.

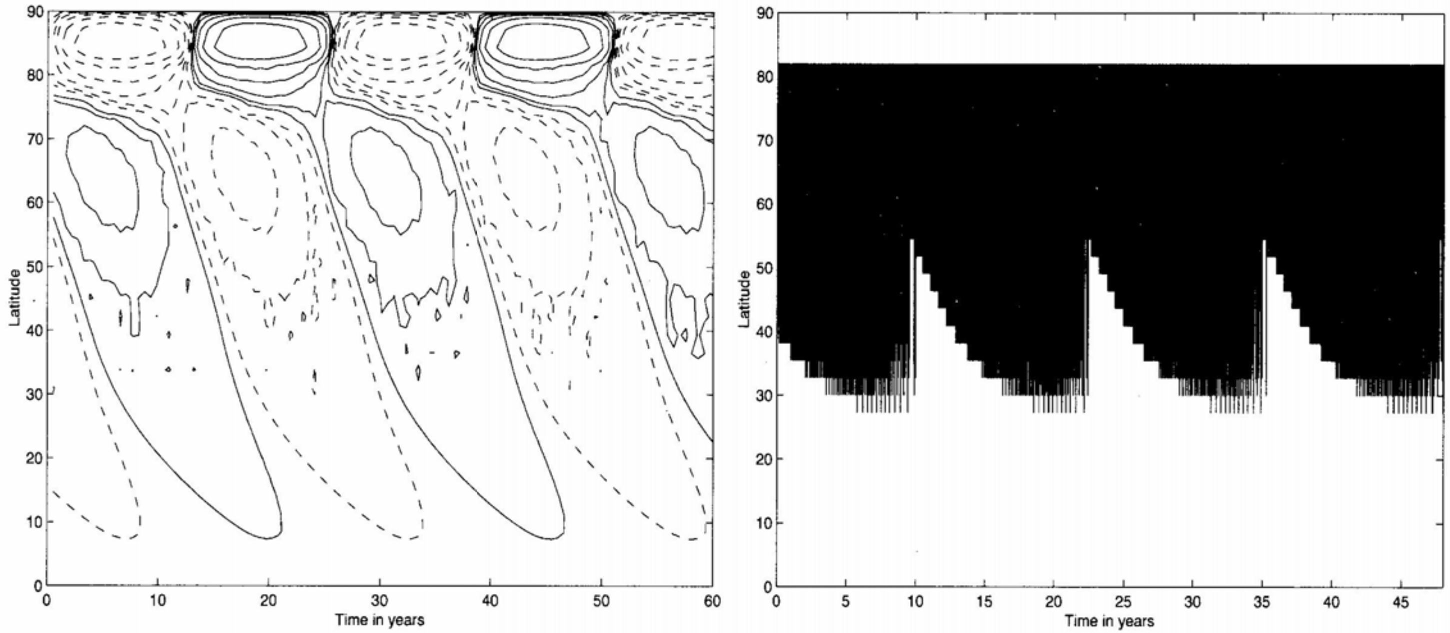

Figure 2. **Left**: Time-latitude plot of the contours of constant toroidal field B at the bottom of the convection zone. The solid lines denote positive B and the dashed lines negative B. Time is in years. **Right**: Eruption latitude vs time in years. The solid portion of the plot shows at which latitude eruptions are occurring.

References

Choudhuri, A. R. 2000, these proceedings.
Choudhuri, A. R., Schüssler M., Dikpati M. 1995, *Astr. Astrophys.*, **303**, L29.
Dikpati, M., Charbonneau, P. 1999, *Astrophys. J.*, **518**, 508.
Durney, B. R. 1997, *Astrophys. J* **.,** **486**, 1065.

J. Astrophys. Astr. (2000) **21**, 387–388

Alpha-Effect, Current and Kinetic Helicities for Magnetically Driven Turbulence, and Solar Dynamo

Gaetano Belvedere[1]*, V. V. Pipin[2,3] & G. Rüdiger[1,3]
[1]*Institute of Astronomy, University of Catania, Viale A. Doria 6, 95125 Catania, Italy.*
[2]*Institute for Solar-Terrestrial Physics, P.O. Box 4026, 664033 Irkutsk, Russia.*
[3]*Astrophysikalisches Institut Potsdam, An der Sternwarte 16, D-I4482 Potsdam, Germany.*
**e-mail: gbelvedere @alpha4. ct. astro, it*

Key words. Sun—dynamo, helicity, turbulent convection.

Extended abstract

Recent numerical simulations lead to the result that turbulence is much more magnetically driven than believed. In particular the role of *magnetic buoyancy* appears quite important for the generation of α-effect and angular momentum transport (Brandenburg & Schmitt 1998). We present results obtained for a turbulence field driven by a (given) Lorentz force in a non-stratified but rotating convection zone. The main result confirms the numerical findings of Brandenburg & Schmitt that in the northern hemisphere the α-effect and the kinetic helicity $\mathcal{H}_{\rm kin} = \langle \mathbf{u}' \cdot \mathrm{rot}\,\mathbf{u}' \rangle$ are positive (and negative in the northern hemisphere), this being just opposite to what occurs for the current helicity $\mathcal{H}_{\rm curr} = \langle \mathbf{j}' \cdot \mathbf{B}' \rangle$, which is negative in the northern hemisphere (and positive in the southern hemisphere). There has been an increasing number of papers presenting observations of current helicity at the solar surface, all showing that it is *negative* in the northern hemisphere and positive in the southern hemisphere (see Rüdiger *et al.* 2000, also for a review).

Mass conservation requires that $\partial \rho'/\partial t + \bar{\rho}\,\mathrm{div}\,\mathbf{u}' = 0$.Notice, that density has been assumed as homogeneous and density fluctuations vary in time. We do *not* adopt the inelastic approximation. For the turbulent energy equation we simply adopt a polytropic relation. In the sense of the 'τ-approximation', the spectrum of the given magnetic fluctuations field has been approximated by $\mathcal{B} \propto \delta(k - \ell_{\rm corr}^{-1})\,\delta(\omega)$ with $\tau_{\rm corr} \simeq \ell_{\rm corr}^2/\nu$. The turbulence may develop under the influence of a large-scale magnetic field $\bar{\mathbf{B}}$ and the gravity g. For the current helicity we find

$$\mathcal{H}_{\rm curr} = \frac{2}{5}\frac{\tau_{\rm corr}^3}{\ell_{\rm corr}^2}\frac{\bar{B}^2}{\mu_0}\frac{\langle {B^{(0)}}^2 \rangle}{\mu_0 \rho c_{\rm ac}^2}(\mathbf{g}\cdot\mathbf{\Omega}). \tag{1}$$

The current helicity is thus *negative* in. the northern hemisphere.

The next step is the α-effect. Only the most important component, $\alpha_{\phi\phi}$, will be discussed. We obtain

$$\alpha_{\phi\phi} = -\frac{1}{5}\frac{\tau_{\rm corr}^2}{c_{\rm ac}^2}\frac{\langle {B^{(0)}}^2 \rangle}{\mu_0 \rho}(\mathbf{g}\cdot\mathbf{\Omega}). \tag{2}$$

The α-effect proves thus to be *positive* in the northern hemisphere and negative in the southern hemisphere. Current helicity and α-effect have opposite signs, their ratio being

$$\frac{\alpha_{\phi\phi}\bar{B}^2}{\mathcal{H}_{\rm curr}} = -\frac{\mu_0}{2}\frac{\ell^2_{\rm corr}}{\tau_{\rm corr}}. \tag{3}$$

The observed negative sign of the current helicity is reproduced, as well as the positive sign of the α-effect (in the northern hemisphere).

Our model yields for the kinetic helicity

$$\mathcal{H}_{\rm kin} = -\frac{8}{15}\frac{\tau^3_{\rm corr}}{\ell^2_{\rm corr}}\frac{\bar{B}^2}{\mu_0\rho}\frac{\langle B^{(0)^2}\rangle}{\mu_0\rho c^2_{\rm ac}}(\mathbf{g}\cdot\mathbf{\Omega}), \tag{4}$$

which is *positive* in the northern hemisphere and *negative* in the southern hemisphere. If a rising eddy can expand in a density-reduced surrounding, then a *negative* value of the kinetic helicity is expected. The magnetic-buoyancy model, however, leads to another result. There is *no* minus sign between α-effect and kinetic helicity, but nevertheless the minus sign is present in the relation between α-effect and current helicity, and the α-effect is positive.

Thus, for the solar dynamo, there is no indication, at least in the bulk of the convection zone, for a negative α-effect, which, in current dynamo theory, is necessary to account for the butterfly diagram of solar activity in the light of helioseismology. Of course, this does not exclude the location of the dynamo action deeply in the convection zone, or in the boundary layer (Belvedere *et al.* 1991), where a negative α is expected. Otherwise, we should abandon traditional dynamo theory and investigate a possible dynamo action strongly modified by meridional circulation, that is usually neglected in conventional dynamo.

References

Belvedere, G., Proctor M. R. E., Lanzafame, G. 1991, *Nature*, **350**, 481.
Brandenburg,. A., Schmitt, D. 1998, *Astr. Astrophys.*, **338**, L55.
Rüdiger, G., Pipin, V. V, Belvedere, G. 2000, *Solar Phys.* (submitted).

J. Astrophys. Astr. (2000) **21**, 389–395

Cyclical Variation of the Quiet Corona and Coronal Holes

Takashi Sakurai, *National Astronomical Observatory, Japan,*
e-mail: sakurai@solar.mtk.nao.ac.jp

Abstract. Recent advances in the understanding of the quiet corona and coronal holes are reviewed. The review is based on long-term accumulation of data from eclipse observations, coronagraph observations, helium 10830 Å spectroheliograms, and X-ray observations.

Key words. Coronagraphs—solar activity cycle—solar corona—total eclipses—X-ray observations.

1. Introduction

The study of the solar cycle variation of the corona requires observational data spanning eleven years or more. The longest record comes from eclipse observations made from time to time over one hundred years, although they give only snap shot data of the corona. The invention of the coronagraph by Lyot in 1930 has made possible persistent observations of the solar corona. Observations of the solar corona from space started in the 1960s, and in 1973-74 the Skylab mission has made, for the first time, high quality and continuous observations of the solar corona in X-rays, EUV, and white light. Since then, the coronagraph (C/P) on board SMM (1980–1989), the soft X-ray telescope (SXT) on Yohkoh (1991-present), EIT and LASCO imagers on SOHO (1995–present), and XUV telescope on TRACE (1998–present) followed. At the same time period of Skylab, helium 10830 Å observations started at Kitt Peak, giving additional information of the corona.

2. Eclipse observations

The overall shape of the corona seen at the occasion of total eclipse changes during an activity cycle (Loucif & Koutchmy 1989). The size of polar coronal holes, indicated by the absence of streamers, is largest in activity minimum. The corona is most elliptical in activity minimum, and most circular in activity maximum. This is usually interpreted as follows: there are many streamers in activity maximum, and overlapping of these makes the corona nearly circular, while in activity minimum there are only a few streamers along the equatorial current sheet, making the corona elongated in the equatorial plane. However, recently Gulyaev (1992) and Koomen *et al.* (1998), among others, proposed that the current sheet, which is responsible for an elongated corona in activity minimum, warps or rotates out of the equatorial plane and tends to be seen more and more face-on toward activity maximum. The current sheet seen face-on gives a nearly circular shape of the corona. In the case of the eclipse of 1991 July, the corona looked like an elongated minimum corona, but the orientation of elongation was highly inclined with respect to the equator since we were looking at the inclined current sheet from its edge. This idea of rotating heliospheric current sheet was originally proposed by Saito *et al.* (1978).

3. Coronagraphic observations

A Lyot-type coronagraph usually observes at the wavelengths of strong coronal emission lines .The three most frequently used lines and their representative temperatures are:

Red line	6374 Å	Fe X	1 MK
Green line	5303 Å	Fe XIV	2 MK
Yellow line	5694 Å	Ca XV	3.5 MK

The yellow line is observable only at the occasion of high activity related to flares. The continuum corona (K-corona) due to the Thomson scattering of photospheric light by coronal free electrons can be observed with a K-coronameter, by using the polarization of the K-corona to discriminate it from the sky background.

Fig. 1 shows the latitude distribution of the green line intensity in the form of a butterfly diagram. Superposed dots are the locations of sun spots, namely the conventional sunspot butterfly diagram. The intensity of the green line generally follows the sunspot number (Rusin 1998). However, the latitude distribution of the green-line corona is wider than that of the sunspot belt. In particular, in the activity minimum the corona is bright above the magnetic neutral line surrounding the polar regions. This neutral line migrates from the mid latitude to the pole, with a phase shift of about half a cycle with respect to the migration of the sunspot belt. This picture of the so-called ‘extended solar cycle’ will be discussed later.

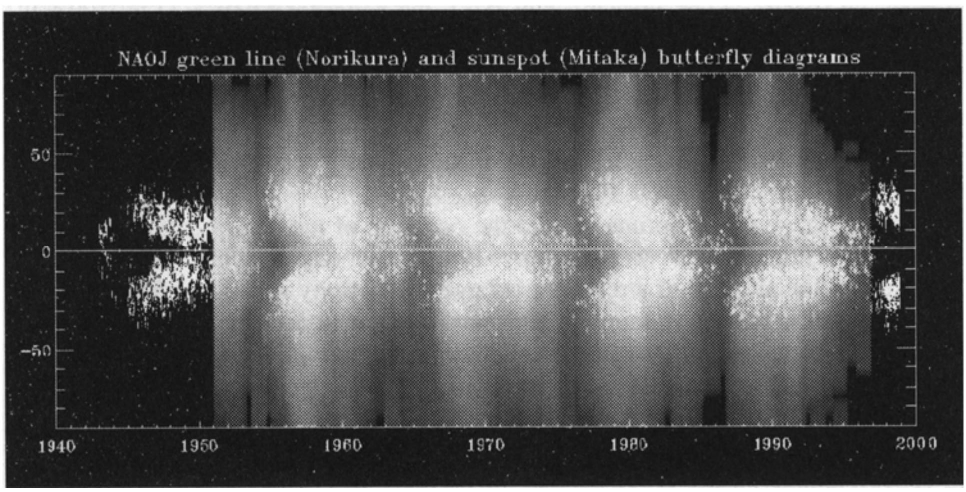

Figure 1. The latitude distribution of the coronal green line observed at Norikura in the period of 1951–1997. The superposed dots represent the sunspot distribution observed at Mitaka (1943-1998).

Contrary to the green line intensity, the red line intensity does not clearly follow the sunspot number (Rusin 1998). This is presumably because the 1 MK plasma represented by the red line is cooler than, and therefore is not, the main constituent of the coronal plasma.

The temperature derived from the intensity ratios of green and red lines shows a variation in a solar cycle. The temperature at the poles is highest (1·7 MK) at activity maximum, and lowest (1.3 MK) at activity minimum (Altrock 1998). The distribution of temperature shows an enhancement in high latitudes, above the neutral line encircling the polar regions (Guhathakurta *et al.* 1993), hotter by about 0·5 MK with respect to the temperature of the poles in activity minimum. The increase in temperature at the poles near activity maximum could be due to the approach of the magnetic neutral line toward the poles.

4. X-ray observations

The total X-ray flux from the sun varies with the activity cycle. Fig. 2 shows the soft X-ray flux observed by Yohkoh from 1991 to 1999. The total flux at activity maximum is about a factor of 100 larger than that at minimum.

Hara (1996) compared the contributions to the X-ray flux from quiet and active components of the corona. At a certain intensity level, the X-ray emitting structures can be divided into the quiet sun (including coronal holes) and active regions. The total flux comes predominantly from the active region component. The flux variation is due to the change in area occupied by the active regions. The brightness of the active region component, estimated by the ratio between the flux and the area, does not vary significantly within the cycle. The quiet sun component, though it occupies most of the solar surface, is a minor contributor to the total X-ray flux.

The butterfly diagram of the soft X-ray sun observed with Yohkoh (Hara 1996) shows, in addition to the familiar sunspot-related strong emissions, activities in high

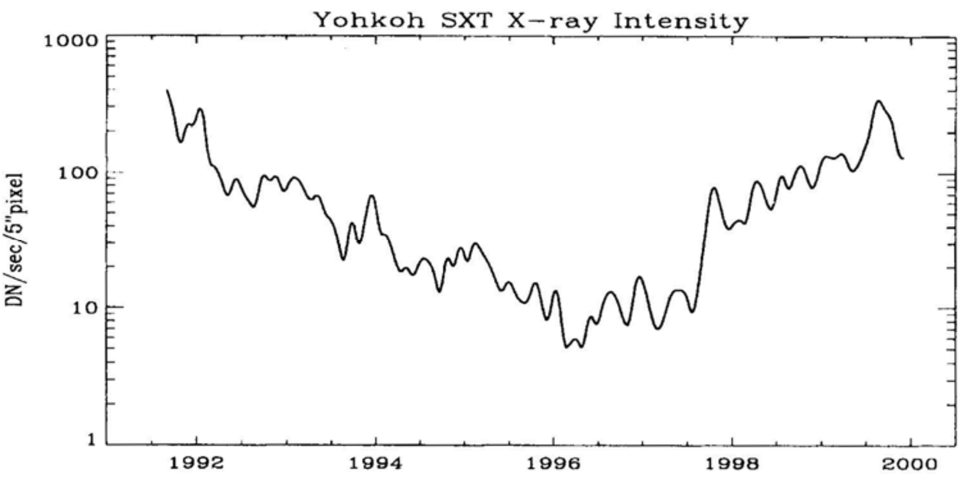

Figure 2. Variation of total soft X-ray flux of the sun observed with the soft X-ray telescope of Yohkoh in the period of 1991–1999.

latitudes. Hara (1996) identified that these high-latitude X-ray activities come from the polar ends of coronal large-scale X-ray loops. Probably they can also be explained as the enhanced emission above the magnetic neutral line encircling the poles.

The relation between the activity in the sunspot belt and that of high latitude regions has attracted attention and is termed as 'the extended solar cycle'. Here the meaning of 'extended' needs some clarification. At any point on the sun, the variation of, say, magnetic field strength shows a periodicity of eleven years. If the activity is created by a sub-surface flux tube that migrates toward the equator in the course of the activity cycle, there may exist two or more main flux tubes in the Sun. This is generally the case, since sunspots of the new cycle in mid latitudes and those of the old cycle near the equator coexist in activity minimum.

High latitude activities, which show migration toward the poles, may originate from the poloidal component of the magnetic field, as predicted by the dynamo theory. Since the poloidal field is the seed for the stronger, toroidal magnetic field that produces the sunspot belt later, the beginning of a particular cycle may be traced back to the poloidal component (polar fields) of the previous cycle. The predecessors known so far are; coronal emissions, prominences, torsional oscillations, high-latitude ephemeral regions, and so on.

5. Coronal holes

Coronal holes, dark regions in the corona formed where magnetic fields are open to the interplanetary space, have been studied by using X-ray and helium 10830 Å data. The helium 10830 Å absorption is due to the triplet helium whose ground level is 19·7 eV above the ground state, and is believed to be created by the photoionization by the XUV photons from the corona. Therefore the helium 10830 Å spectroheliograms generally mirror the X-ray images.

X-ray observations were intermittent up to the launch of Yohkoh, which is in operation for more than eight years now. A unique data set of helium 10830 Å spectroheliograms obtained at Kitt Peak since the 1970s provides a proxy to the X-ray corona, with continuity and time span superior to X-ray observations.

The rotation rate of coronal holes has been studied based on the helium 10830 Å spectroheliograms by Navarro-Peralta & Sanchez-Ibarra (1994), and by Insley *et al.* (1995). These authors divided the coronal holes into two classes: (a) equatorward extensions of polar coronal holes (in short, polar holes), and (b) isolated equatorial coronal holes (in short, equatorial holes). At activity maximum the equatorial holes dominate, while at activity minimum the polar holes dominate. This variation of fractional contributions from the two classes during an activity cycle makes it difficult to unambiguously derive the evolution of the differential rotation of coronal holes in an activity cycle. Therefore, Insley *et al.* (1995) only discussed the differential rotation averaged over the cycle, and questioned the results of Navarro-Peralta & Sanchez-Ibarra (1994) who presented the activity-phase dependence of differential rotation.

The equatorial holes migrate toward the equator as the sunspots do, and are interpreted to be phenomena related to active regions. The differential rotation of equatorial holes can be fitted by a quadratic function of $[\cos(\text{latitude})]^2$. The degree of differential rotation for these holes is not as large as for sunspots, but is not negligible as in rigid rotation either. For polar holes, fitting by a quadratic function of $[\cos(\text{latitude})]^2$ gives an almost rigid rotation, but the residuals are quite large and the fitting may not be justified. This character of the rotation of polar holes seems to conform with the theory of Wang *et al.* (1996), in that the holes or open field regions form by a balance of magnetic flux, and bear no definitive relationship with the motion of the surface where the flux originates.

6. X-ray bright points

X-ray bright points (XBPs) are small regions ($5–20 \times 10^4$ km) in X-ray images. XBPs can also be identified in helium 10830 Å heliograms as dark points. Part of XBPs originate from ephemeral regions (short-lived, small magnetic bipolar regions), but they also form where two patches of opposite magnetic polarities come across.

Earlier results by Skylab and rocket experiments (Davis 1988) showed that the number of XBPs varies in anti-phase with activity cycle. Since ephemeral regions vary in phase with sunspot numbers, a significant fraction of XBPs do not come from ephemeral regions. Now it is thought that XBPs predominantly form in quiet, mixed polarity regions where opposite polarity patches come across. Such mixed polarity areas are more numerous in activity minimum.

Since XBPs are small and relatively faint objects, their detectability will depend on the level of background X-ray emission, which also varies with the activity cycle. Therefore, Nakakubo & Hara (1999) re-examined the XBP number counts by taking care of different background levels. Their results are shown in Figs. 3 and 4. Fig. 3

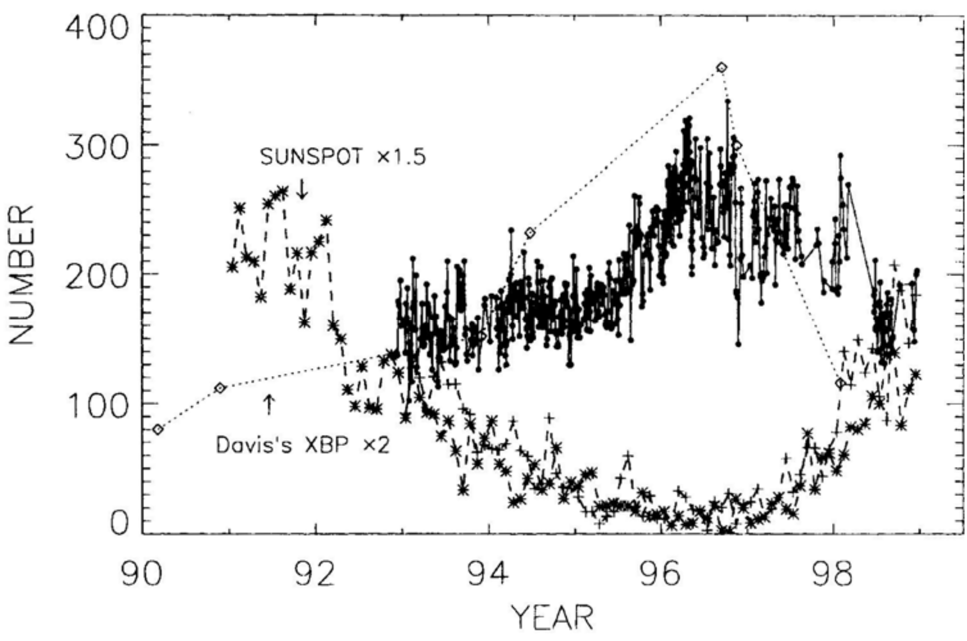

Figure 3. Variation of the number of XBPs observed by Yohkoh in the period of 1991-1998. The earlier results of Davis (1988) and the sunspot relative numbers are superposed at the same phases of the activity cycle. (After Nakakubo and Hara 1999).

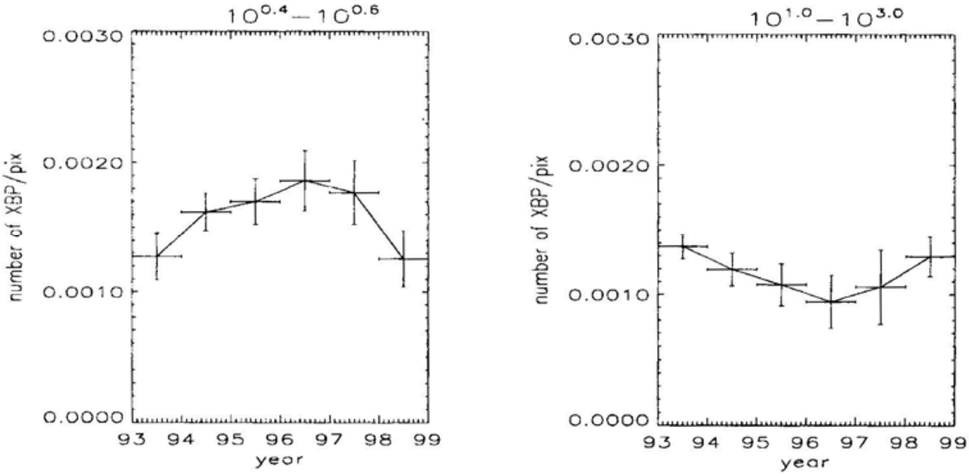

Figure 4. The number of XBPs in low (left) and high (right) background levels (Nakakubo & Hara 1999).

shows the total number of XBPs they detected as a function of time. Also plotted are the earlier results by Davis (1988) shifted in time so as to fit into the same activity cycle phase. Their study confirmed the variation of XBP counts to be in anti-phase with the activity cycle. However, it turned out that the situation is not so straight-forward. Fig. 4 shows the number of XBPs in regions of low and high background levels. The number of XBPs found in low-background regions are larger at activity minimum (namely, anti-phase with sunspot number), but XBPs found in high-background regions vary in phase with the sunspot number.

XBPs found in high-background regions are intrinsically bright XBPs, while XBPs found in low-background regions, in principle, can include both bright and faint XBPs. However, Fig. 4 indicates that, in regions of low background levels, there are very few XBPs that are bright. Bright XBPs which vary in phase with activity cycle may be a smaller end of active region spectrum, or ephemeral regions, and they tend to form in regions of high X-ray background (presumably in regions of strong magnetic fields). Faint XBPs make another class of objects, e.g. magnetic pairs in mixed polarity regions.

7. Final remarks

The orbital life of Yohkoh is estimated to be beyond this activity maximum, and Yohkoh will complete observations over a full solar cycle. GOES Solar X-ray Imager (SXI) of NOAA, planned to commence in 2000, will establish continuous monitoring of the solar corona and will provide valuable data base of the solar activity, more so compared with the GOES X-ray flux.

For ground-based observations, it is welcome that the initiative of SOLIS (Keller, in this issue) at U.S. National Solar Observatory has been funded. A similar plan is being developed in Japan (Sakurai 1998). Let me point out that the time scale of the solar activity is long compared to human cycle. Persistent observations are therefore necessary, and no quick solution is generally possible. We all have to transfer this endeavor generation after generation, in order to clarify the mechanism of solar activity cycle.

Acknowledgements

The author thanks Dr. H. Hara and Miss K. Nakakubo for discussion.

References

Altrock, R. 1998, in *Synoptic Solar Physics*, (ed.) K. S. Balasubramaniam *et al*., ASP Conf. Ser. **140**, (San Francisco: Astron. Soc. of the Pacific), 339.
Davis, J. 1988, *Solar Phys*., **88**, 337.
Guhathakurta, M., Fisher, R. R., Altrock, R. C. 1993, *Astrophys. J. Letters*, **414**, L145.
Gulyaev, R. A. 1992, *Solar Phys*., **142**, 213.
Hara, H. 1996, in *Magnetodynamic Phenomena in the Solar Atmosphere*, (ed.) Y. Uchida *et al*., (Dordrecht: Kluwer Academic Publishers), 321.
Insley, J. E., Moore, V., Harrison, R. A. 1995, *Solar Phys*., **160**, 1.
Koomen, M. J., Howard, R. A., Michels, D. J. 1998, *Solar Phys*., **180**, 247.
Loucif, M. L., Koutchmy, S. 1989, *Astron. Astrophys. Suppl*, **77**, 45.
Nakakubo, K., Hara, H. 1999, in *Explosive Phenomena in Solar and Space Plasmas*, (ed.) T. Kosugi *et al*., (Japan: The Institute of Space and Astronautical Science), 57.
Navarro-Peralta, P., Sanchez-Ibarra, A. 1994, *Solar Phys*., **153**, 169.
Rusin, V. 1998, in *Synoptic Solar Physics*, (ed.) K. S. Balasubramaniam *et al.,* ASP Conf. Ser. **140**, (San Francisco: Astron. Soc. of the Pacific), 353.
Saito, T, Sakurai, T, Yumoto, K. 1978, *Planet. Sp. Sci*., **26**, 413.
Sakurai, T. 1998, in *Synoptic Solar Physics*, (ed.) K. S. Balasubramaniam *et al.,* ASP Conf. Ser. **140**, (San Francisco: Astron. Soc. of the Pacific), 483.
Wang, Y. M., Hawley, S. H., Sheeley, N. R., Jr. 1996, *Science*, **271**, 464.

J. Astrophys. Astr. (2000) **21**, .397–401

The EUV Spectrum of Sunspot Plumes Observed by SUMER on SOHO

W. Curdt,[1] B. N. Dwivedi[2] & U. Feldman[3]
[1]*Max-Planck-Institut fiir Aeronomie, D-37191, Katlenburg-Lindau, Germany.*
[2]*Department of Applied Physics, Banaras Hindu University, Varanasi-221005, India.*
[3]*E.O. Hulburt Center for Space Research, NRL, Washington DC 20375, USA*
e-mail: curdt@linmpi.mpg.de

Abstract. We present results from sunspot observations obtained by SUMER on SOHO. In sunspot plumes the EUV spectrum differs from the quiet Sun; continua are observed with different slopes and intensities; emission lines from molecular hydrogen and many unidentified species indicate unique plasma conditions above sunspots. Sunspot plumes are sites of systematic downflow. We also discuss the properties of sunspot oscillations.

*Key words***.** Sun: EUV spectroscopy—sunspot—oscillation.

1. Introduction

According to Foukal (1974), sunspot plumes (SP) are regions with bright emission in transition region lines, I, with $I \geq 5\ \bar{I}$, which have an extent of a significant part of the white light sunspot. Interestingly, the percentage of sunspots which carry a plume varies with the solar cycle and seems to peak around solar minimum, an effect which is not yet understood. We will present a brief account of recent findings of spectroscopic features seen in SP and also on sunspot oscillations. In contrast to earlier, moderately resolved observations (e.g., Noyes *et al.* 1985), we have a selection of SP EUV spectra with unprecedented spectral resolution. We report on spectral features as continua and emission lines, including molecular emission, and present plasma diagnostic results using line pairs in our spectral range. The systematic downflow observed in SP and the coherent oscillation seen in the sunspot umbra may both be associated with the observation of more than 100 peculiar lines, which are not observed anywhere else on the Sun.

2. The instrument and data acquisition

The Solar Ultraviolet Measurements of Emitted Radiation (SUMER) is a high-resolution telescope and spectrometer on board SOHO (Solar and Heliospheric Observatory). SOHO orbits around the first Lagrange point, $L1$, in continuous view of the Sun. The spectrometer disperses stigmatic images of the slit covering the wave length range from 660 Å to 1610 Å in first order. Second order lines are superimposed on the first order spectrum. The angular scale of a pixel is ≈ 1 arcsec. Doppler flows down to 1–2 km s^{-1} can be detected with centroiding techniques. The instrument has been described in detail by Wilhelm *et al.* (1997).

Until now more than 30 sunspots have been observed. This includes studies with high temporal resolution in selected emission lines as well as spectral scans which cover the full spectral range of the instrument

2.1 *Observation of continua and emission lines*

From a spectral scan, obtained at a sunspot area on 1999 March 18th, we have separated the plume profile for comparison to an average quiet-Sun spectrum (Curdt *et al.* 1999). This shows that the thermal continuum around 1400 Å is depressed by a factor of ≈ 10, compatible with a temperature drop of 600 K at the bottom of the atmosphere. It is also seen that the Lyman continuum of the SP has a steeper slope and is enhanced by almost a factor of two near the Lyman limit (cf. Fig. 1). The plasma is optically thin for Lyman lines, thereby suggestive of low-density in the emitting source.

The emission peaks in lines with a formation temperature of $10^{5\cdot5}$ K and there is no emission from lines hotter than 10^6 K, an observational fact in support of results of Maltby *et al.* (2000). Within our spectral.range we found >100 peculiar lines, which are not present in quiet-Sun spectra and are also not observed in the corona. Some of them are seen in streamer spectra and half of them remain unidentified. They seem to belong to the 3- to 6-fold ionized species, and their emission requires plasma conditions not found anywhere else on the Sun.

Eight lines of the H_2 Werner bands fall into the SUMER spectral range. They are excited by resonance fluorescence through the strong O VI 1032 line (Schühle *et al.* 1999). H_2 emission is found everywhere in the sunspot umbra, but not outside.

2.2 *Spectroscopic diagnostics and sunspot oscillations*

Systematic studies of Maltby *et al.* (2000) have shown that SP always have downflows of up to 25kms^{-1}; sunspots with no SP can also have upflows; redshifted features often terminate in the plume area; the plume contours appear displaced in lines formed at different temperatures.

Within the SUMER spectral range we have many line pairs which can be used for density diagnostics. In Table 1 we list measurements from 8 selected line pairs observed in SP, using the atomic calculations of Laming *et al.* (1997). The results are consistent and yield densities between 8.3 and 9.5, again an indication for low-density plasma compared to typical active region values.

Many authors have reported of periodic phenomena seen in sunspots. Recently, Maltby *et al.* (2000) and Brynildsen *et al.* (1999) found a coherent 3-minute oscillation in O V observations, affecting the whole umbra (cf. figure 3 in Brynildsen *et al.* 2000). They have shown that the oscillations seen in both intensity and in Doppler velocity have a phase shift of almost 180°. They also found phase differences between oscillations seen in lines of different temperatures and conclude, that this observation is compatible with the concept of upward propagating acoustic waves.

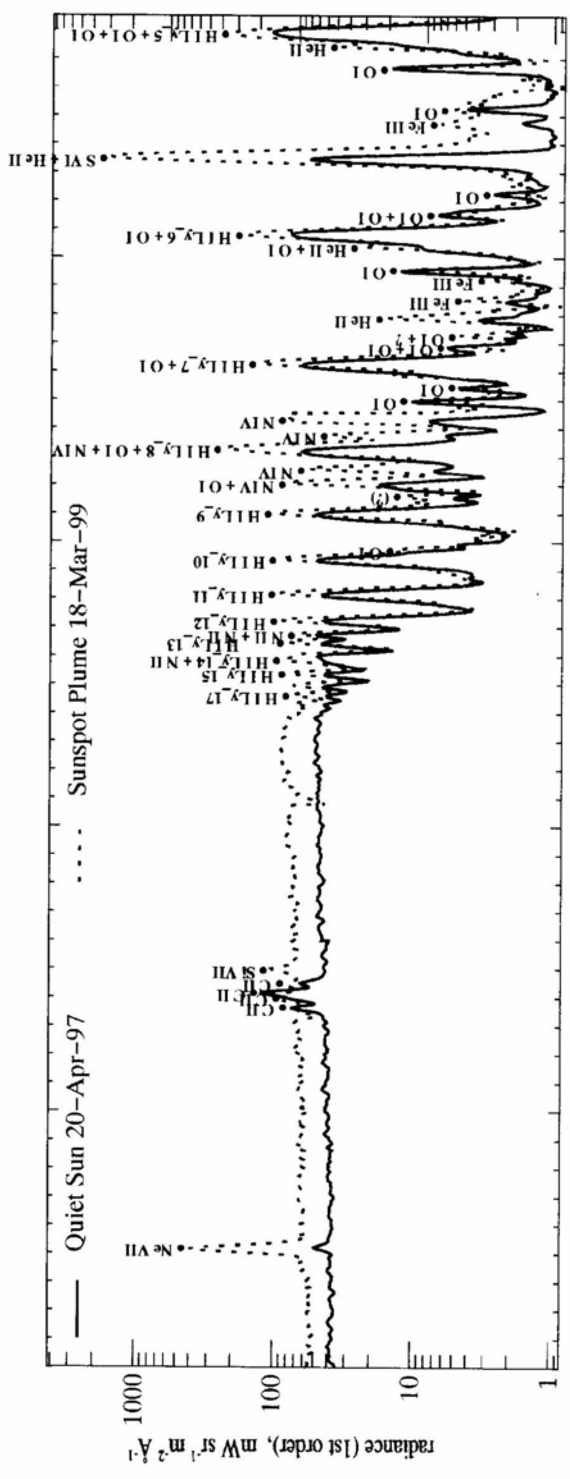

Figure 1. The average quiet-Sun spectrum around the Lyman limit (solid, lower curve) compared to the spectrum of a SP (dotted, upper curve).

Table 1. Density diagnostic measurement using selected line pairs.

Line pair	Species	Ratio	log N_e/cm^{-3}
895.15/887.27	Ne VII	>1000	>9
693.98/706.06	Mg IX	11	8.3
999.29/1005.84	Ne VI	1.6	9–10
872.12/880.33	Mg VIII	1.8	8–9
772.26/782.36	Mg VIII	1.8	9.3
1445.76/1440.49	Si VIII	10	>8
759.44/761.13	O V	8	9.6
922.52/923.60	N IV	1.9	9.5

3. Discussion

We suggest that the observations might all be related and fit into an interpretation model as shown in Fig. 2. We have demonstrated that the plasma seen in SP has low density. On the other hand, it is surprisingly cold, $10^{5.5}$ K to 10^6 K. Therefore we believe that the high emission measure is not compatible with thermal equilibrium. The non-collisional excitation process could be related to continuous inflow under high magnetic field conditions, finally hitting denser material – irrespective of whether this is proper bulk flow or not. Another source could be the damping of acoustic waves propagating upward from the oscillating surface.

4. Conclusion and Acknowledgements

Sunspots – subject to variations with the solar cycle – are possibly anchored deep in the solar interior. In conclusion, our effort has been to understand their transition into the solar atmosphere with spectroscopic techniques.

The SUMER project is financially supported by DLR, CNES, NASA and the ESA PRODEX Programme (Swiss contribution). SUMER is part of SOHO, the Solar and Heliospheric Observatory, of ESA and NASA.

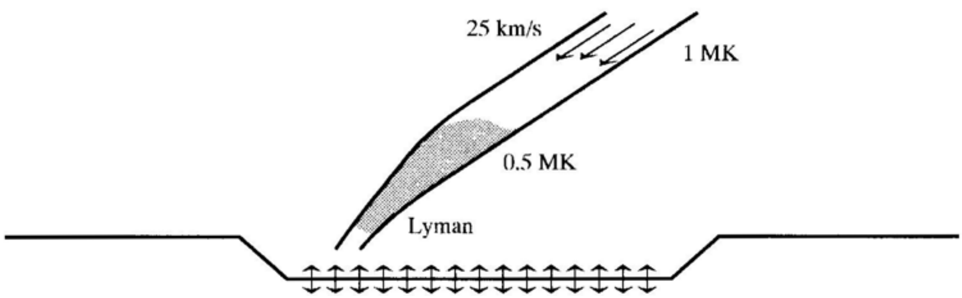

Figure 2. Cartoon showing an open loop sticking out of the oscillating sunspot umbra. Over the cold bottom of the atmosphere a spot of high emission plasma is located—the termination point of a colder loop supplying inflowing plasma, which is finally condensing and hitting denser material.

References

Brynildsen, N., Leifsen, T., Kjeldseth-Moe, O., Maltby, P., Wilhelm, K. 1999, *Astrophys. J.*, **511**, L121.

Brynildsen, N., Maltby, P., Leifsen, T., Kjeldseth-Moe, O., Wilhelm, K. 2000, *Solar Phys.*, **191**, 129.

Curdt, W., Brekke, P., Schühle, U., Wilhelm, K., Dwivedi, B. N. 1999, in Proceedings of the 8th SOHO workshop, (ed.) J. C. Vial & B. Kaldeich-Schürmann, (ESA SP-446), 251.

Foukal, P. V., Huber, M. C. E., Noyes, R. W. *et al.* 1974, *Astrophys. J.*, **193,** L143.

Laming, M, Feldman, U., Schühle, U., Lemaire, P., Curdt, W., Wilhelm, K. 1997, *Astrophys J.*, **485**,911.

Maltby, P., Brynildsen, N., Fredvik, T., Kjeldseth-Moe, O., Wilhelm, K. 2000, *Solar Phys.*, in press

Noyes, R. W., Raymond, J. C, Doyle, J. G., Kingston, A. E. 1985, *Astrophys. J.*, **297**, 805.

Schühle, U., Brown, C. M., Curdt, W., Feldman, U. 1999, in Proceedings of the 8th SOHO workshop, (ed.) J. C. Vial & B. Kaldeich-Schürmann, (ESA SP-446), 617.

Wilhelm, K., Lemaire, P., Curdt, W. *et al.* 1997, *Solar Phys.*, **170**, 75.

J. Astrophys. Astr. (2000) **21,** 403–406

Exploring Coronal Structures with SOHO

M. Karovska[1]*, B. Wood[1], J. Chen[2], J. Cook[2], & R. Howard[2]

[1] *Harvard-Smithsonian Center for Astrophysics, Cambridge, MA 02138 USA.*
[2] *Naval Research Laboratory, Washington DC, USA.*
**e-mail: karovska@cfa. harvard, edu*

Abstract. We applied advanced image enhancement techniques to explore in detail the characteristics of the small-scale structures and/or the low contrast structures in several Coronal Mass Ejections (CMEs) observed by SOHO. We highlight here the results from our studies of the morphology and dynamical evolution of CME structures in the solar corona using two instruments on board SOHO: LASCO and EIT.

Key words. Corona—CME.

1. Introduction

The Solar and Heliospheric Observatory (SOHO) provides unprecedented views of CMEs to heliocentric distances of up to 32 solar radii. CMEs are spectacular phenomena in the solar corona which have a wide variety of morphologies. Their exact three-dimensional magnetic topology is not generally clear because it is hard to infer the three-dimensional structure of a CME from two-dimensional images.

The roughly circular cavity observed in many CMEs might be interpreted to be the top of a broad flux rope viewed face-on, where the flux rope is still connected with the Sun. We present here the results of our study of several events of this kind observed using the Ultraviolet Imaging Telescope (EIT) and the Large Angle Spectrometric Coronagraph (LASCO) instruments on SOHO.

2. Observations and data analysis

The EIT instrument images the disk of the Sun in one of four different bandpasses and its field of view reaches to heliocentric heights of about 1.4 $R_\odot$ (Delaboudinière *et al.* 1995). The wavelengths and the dominant emission lines in these bandpasses are 171Å (Fe IX and Fe X), 195 Å (Fe XII), 284 Å (Fe XV), and 304 Å (He II). LASCO was designed to observe the solar corona from 1.1 $R_\odot$ 32 $R_\odot$ (Brueckner *et al.* 1995). This instrument contains three individual coronagraphs, CI, C2, and C3, which produce overlapping views of the corona.

We selected three CMEs with circular rim structures which were observed on 1997 April 30th and February 23rd, and on 1999 August 28th. In spite of the morphological similarities these CMEs were quite different. The February 23rd and August 28th CMEs were accompanied by dramatic prominence eruptions and significant GOES

Xray flares, while the April 30th was accompanied by no apparent prominence eruption and only a weak Xray flare.

The images of these CMEs contain many complex components with different spatial scales and a wide range of contrast levels. The morphology and distribution of the small spatial scale structures cannot readily be extracted directly from these images, either because of limited resolution and noise in the images, or because of the low contrast of the small-scale structures when compared to the large-scale features. Spatial and temporal characterization of these structures is extremely important for understanding the origin and the early evolution of these dynamical phenomena.

We applied image enhancement techniques to explore in detail the characteristics of the small-scale structures within the CMEs, especially to find the locations of the leading edges, trailing edges and the centroids of the circular rims. These techniques include an image enhancement algorithm (IEA) (Karovska *et al.* 1994), and an average-differencing technique used to improve the visibility of various dynamical coronal structures against the largescale slowchanging background.

3. Results

The set of CMEs that we studied can be followed from their points of origin near the limb to large distances from the Sun in the LASCO C3 field of view. We studied the kinematics of these structures by measuring the motions of their leading and trailing edges, and of the centroids, using the enhanced images. As an example, Fig. 1 shows the enhanced LASCO C2 images of the 1997 April 30th CME. The CMEs velocity and acceleration curves were computed from the second order polynomial fits to the height measurements.

Our results show that for the three CMEs, the acceleration takes place below heights of about 4 $R_{\odot}$. These CMEs appear to have begun very close to the limb of the Sun, so it is unlikely that there is a substantial motion along the line of sight that we are not detecting. Thus, the velocities we are measuring should be close to the true velocities.

Despite being similar in appearance in the C2 and C3 fields of view, these CMEs have dramatically different velocities. For example, the leading edge of the April 30th and August 28th CMEs reach relatively slow velocities of few hundreds km s^{-1} which is slightly faster than the ambient solar wind. However, the leading edge of the February 23rd CME levels out at a much higher speed of almost 1000 km s^{-1}.

We used the observed CME structures motions to test a MHD model of an expanding flux rope (Chen *et al.* 1996). We interpret the circular structures seen in the studied set of CMEs as outlining the apex of a flux rope viewed face-on. In the flux rope model, the CME is initiated by an increase of the poloidal component of the helical magnetic field within the flux rope. In fact, in the enhanced C2 observations of the April 30th CME, we do see helical lines which suggest the presence of a helical magnetic field.

We used only two free parameters to model the observed dynamics:

(1) the geometry of the initial flux rope, represented by the footpoint separation and (2) the profile of the poloidal flux injection (Chen *et al.* 1997; Wood *et al.* 1999).

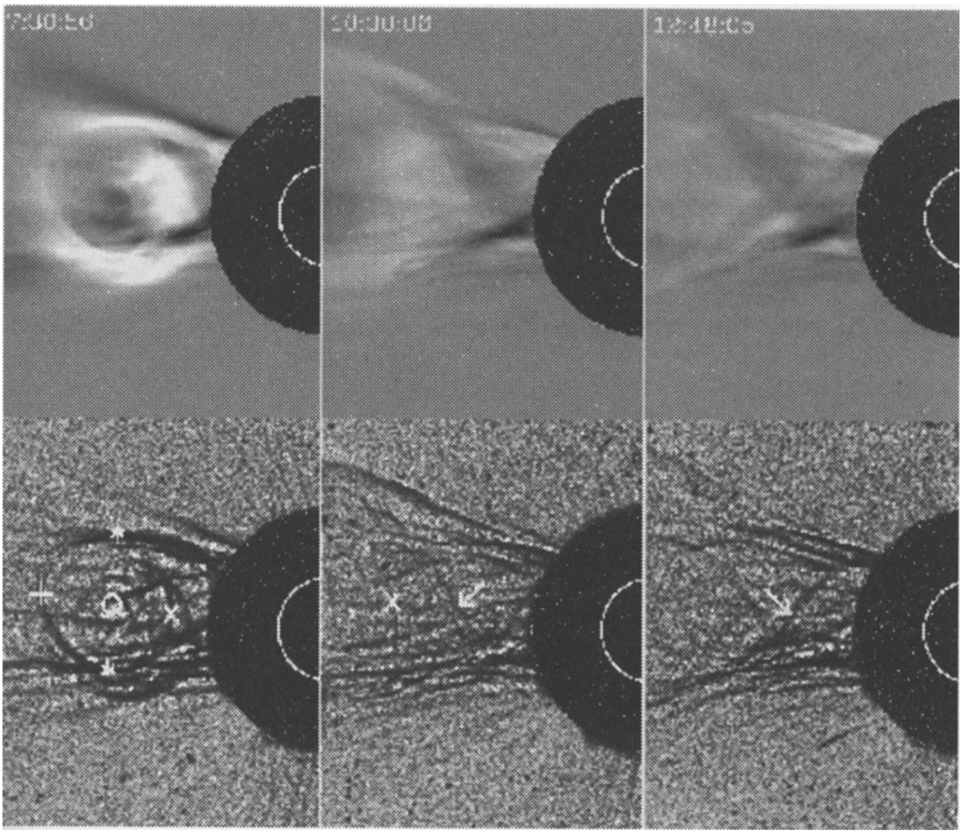

Figure 1. Average-differenced and edge-enhanced versions of three LASCO C2 images of the 1997 April 30 CME. These images were recorded at 7:00:56 UT, 10:30:06 UT, and at 12:40:05 UT, respectively. The locations of the leading edge (plus sign), trailing edge (X's), sides (asterisks), and centroid (circle) of the bright circular rim structure of the CME are indicated. Helical lines are seen below the rim which possibly trace the magnetic field. Two of these lines are identified with arrows.

For the April 30th CME, the initial position of the flux rope is observable in LASCO C1 Fe XIV λ5303 images as a bright semicircular region at the east limb, which starts to dim hours before the beginning of the CME. For the February 23rd CME, LASCO C1 images show a large loop in the northeast quadrant of the Sun which may mark the initial flux rope position.

We conclude that for 1997 February 23rd and April 30th CMEs, the trajectories are in good agreement with the flux rope model (Wood *et al.* 1999). We are currently testing the flux rope model using the measurements of the 1999 August 28th CME kinematics.

Acknowledgements

This project is supported by funding from the Naval Research Laboratory to the Harvard-Smithsonian Center for Astrophysics under contract N0014-97-1-G023.

M.K. is a member of the Chandra X-ray Observatory Center and is partially supported by NASA, Contract #NAS8-39073.

References

Brueckner, G. E., *et al,* 1995, *Sol. Phys.,* **162**, 357.
Chen, J., *et al.,* 1997, *Astrophys. J.*, **490**, L191.
Delaboudiniere, J. P., *et al,* 1995, *Sol. Phys.,* **162**, 291.
Karovska, M., Blundell, S. R, Habbal, S. R., 1994, *Astrophys. J.,* **428**, 854.
Wood, B. E., *et al,* 1999, *Astrophys. J.,* **512**, 484.

J. Astrophys. Astr. (2000) **21,** 407–411

Electron Density and Temperature Measurements, and Abundance Anomalies in the Solar Atmosphere

Anita Mohan[1], Bhola N. Dwivedi[1,2]* & Enrico Landi[2]
[1] *Department of Applied Physics, Institute of Technology, Banaras Hindu University, Varanasi 221005, India.*
[2] *Max-Planck-Institut für Aeronomie, 37191 Katlenburg-Lindau, Germany.*
**e-mail: dwivedi@banaras.ernet.in*

Abstract. Using spectra obtained from the SUMER (Solar Ultraviolet Measurements of Emitted Radiation) spectrograph on the spacecraft SOHO (Solar and Heliospheric Observatory), we investigate the height dependence of electron density, temperature and abundance anomalies in the solar atmosphere. In particular, we present the behaviour of the solar FIP effect (the abundance enhancement of elements with first ionization potential <10 eV in the corona with respect to photospheric values) with height above an active region observed at the solar limb, with emphasis on the so-called transition region lines.

Key words. Solar atmosphere—abundance anomalies—EUV diagnostics—emission lines.

Dwivedi, Curdt & Wilhelm (1997, 1999a) carried out an observing sequence based on a theoretical study by Dwivedi & Mohan (1995), with intercombination/forbidden Ne VI and Mg VI lines, which are formed at essentially the same temperature (4×10^5 K), according to Arnaud & Rothenflug (1985). The FIPs of Ne and Mg are 21.6 and 7.6 eV, respectively: they form a high-FIP/low-FIP pair. This observing sequence provided new observational facts in transition region emission lines in the corona (Dwivedi, Curdt & Wilhelm 1999a,b). In the present paper, we extend this investigation taking account of other high-FIP/low-FIP pairs such as K/Ar, Si/Ar and S/Ar present in the spectra. For want of space, we only present highlights of our findings and a full paper will be published elsewhere (Mohan, Landi & Dwivedi 2000).

The observations were made with the SUMER spectrograph on 1996 June 20 above an active region NOAA 7974 on the east limb, starting at 20:11 UT. Fig. 1 shows the position and extension of the SUMER raster superimposed on the He II 304 Å image of the eastern limb of the Sun taken at 19:41 UT with the EIT ultraviolet imager (Delaboudiniére *et al.* 1995). For the observations in the present contribution, Dwivedi, Curdt & Wilhelm (1997, 1999a) used the slit 4 arc-sec × 300 arc-sec with a raster step of 3.8 arc-sec to a total of 35 positions in the east-west direction. The raster started 40 arc-sec off-limb, above the position of the bright He II protrusion seen in the EIT image. With a step size corresponding to the slit width of 4 arc-sec, the spectrograph slit was stepped eastward for 133 arc-sec. At each

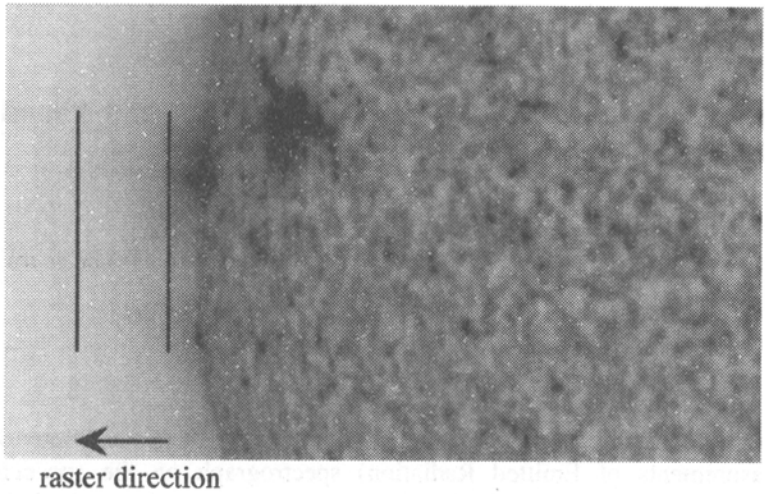

Figure 1. SUMER raster superimposed on a section of the He II 304 Å EIT image taken at 19:41 UT, showing the active region NOAA 7974 on the limb and its neighbour NOAA 7973 in photonegative representation. (Courtesy, EIT/SOHO consortium).

position, two 40Å wide spectra were obtained. The first spectrum was centered on the Ne VI 999 Å line, while the second spectrum was centered on the Mg VI 1192 Å line.

We have used density-sensitive 1196/1212 S X line ratio to determine N_e. In our dataset N_e is sufficiently low to let photoexcitation play an important role for S X density diagnostics. Using CHIANTI (atomic database described in Dere *et al.* 1997) and taking account of this process, the inferred log N_e values as a function of height are shown in Fig. 2. Uncertainties increase with height, and the last 5 density values are only an estimate of an upper limit, due also to the "flattening" of the theoretical ratio. Apart from the very last ratios, these values lie more or less on a straight line as a function of height which allows to measure density scale heights etc.

We measured electron temperature T from S X/Si XI line ratio shown in Fig. 3 as a function of height. We then calculated other lines' ratios using the N_e, T values we deduced as a function of height and compared them with observations. It is to be noted here that such a T measurement is biased to any problem in the relative S/Si abundance. Si is a low-FIP element while S is just at the border (its FIP is 10.4 eV), so this can be a bias to our results. We found from this ratio that the electron temperature was more or less constant with height. Its mean value is log T = 6.28 ± 0.03, maximum log T value = 6.31, and minimum log T value = 6.25.

In order to calculate theoretical line ratios, we need to use not only the correct N_e and T values, but also the ion fraction dataset. We made the comparison between the two most recent different ion fractions datasets found in the literature (Arnaud & Rothenflug 1985; Mazzotta *et al.* 1998). We calculated the Si XI/Ar XII and the S X/Ar XII ratios using these two ion fraction datasets. The difference between the two resulting values for each of these ratios are of a factor 2.2 (Si/Ar) and 2.5 (S/Ar). We, therefore, stress the fact that ion fraction datasets play a major role as uncertainty in quantitative FIP analysis. Our results show this in a clear way, which is also

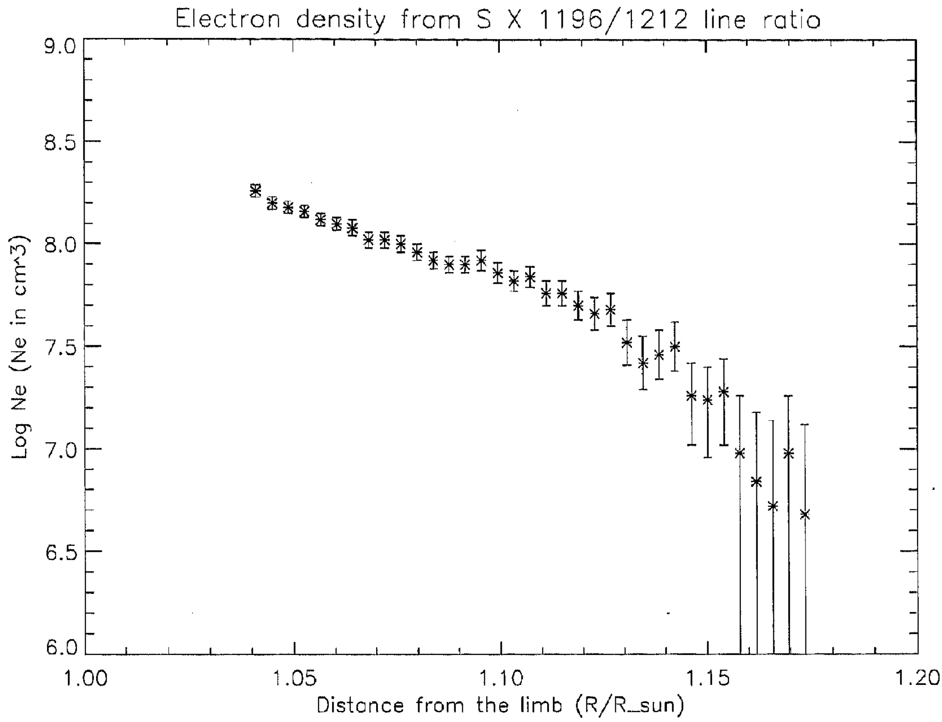

Figure 2. Height dependence of electron density from S X 1196/1212 line ratio.

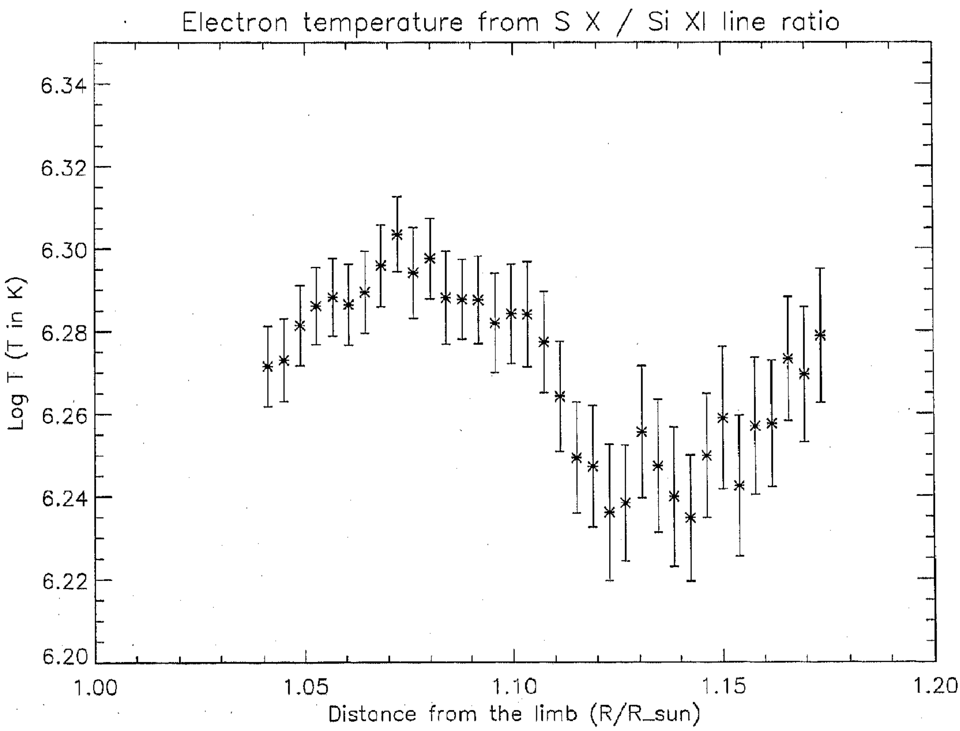

Figure 3. Height dependence of electron temperature from S X/Si XI line ratio.

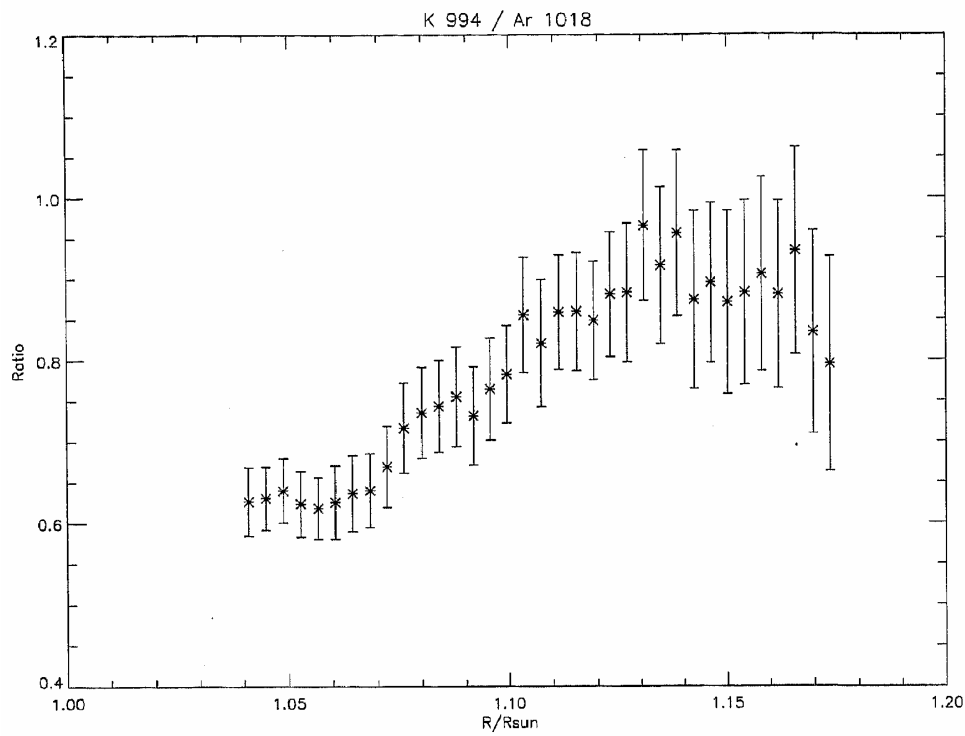

Figure 4. Height dependence of experimental K XIII/Ar XII (994/1018).

independent of possible temperature structure in the atmosphere as the plasma we have is isothermal.

We studied low-FIP/high-FIP pairs such as Si/Ar, S/Ar and K/Ar and their height dependence. The FIPs for K, Si, S and Ar are 4.3, 8.2, 10.4 and 15.8 eV respectively. We have investigated experimental K XIII/Ar XII, Si XI/Ar XII and S X/Ar XII. However, we report here only the height dependence of experimental K XIII/Ar XII as shown in Fig. 4. The observations reported in this paper have both active region at the limb and some plasma outside the structures of the active region. We, therefore, prepared the intensity maps from Ne VI, Mg VI and S X. We find that Ne VI and Mg VI maps are similar, thereby indicating that the plasma structures emitting both the ions are likely to be the same (although spatial resolution is not enough to be definitive on this conclusion). The S X, however, has no memory at all of the region, thereby indicating that the structures are cool. The results for the K/Ar, Si/Ar and S/Ar ratios outside the structures show different behaviour. This may be due to the fact that K, Si and S have an increasing FIP This could imply that the FIP effect bias depends on the magnitude of the FIP effect itself. However, further studies are required to confirm this.

In conclusion, this investigation provides new observational facts about electron density, temperature, and the FIP effect in the corona. A detailed analysis of this investigation can be found in Mohan, Landi & Dwivedi (2000).

References

Arnaud, M., Rothenflug, R. 1985, *Astr. Astrophys. Suppl.,* **60,** 425.

Delaboudiniere, J.-P. *et al.* 1995, *Solar Phys.,* **162,** 291.

Dere, K. P., Landi, E., Mason, H. E., Monsignori-Fossi, B. C, Young, P. R. 1997, *Astron Astrophys. Suppl* **125,** 149.

Dwivedi, B. N., Mohan, A. 1995, *Solar Phys.,* **157,** 135.

Dwivedi, B. N., Curdt, W., Wilhelm, K. 1997, *Paper presented at the JD19/IAU, Kyoto, August* **26**–27.

Dwivedi, B. N., Curdt, W., Wilhelm, K. 1999a, *Astrophys. J.,* **517,** 516.

Dwivedi, B. N., Curdt, W., Wilhelm, K. 1999b, *ESA SP-446,* **293.**

Mazzotta, P., Mazzitelli, G., Colafrancesco, S., Vittorio, N. 1998, *Astron. Astrophys. Suppl.,* **133,** 403.

Mohan, A., Landi, E., Dwivedi, B. N. 2000, *Astron. Astrophys.* (in press).

J. Astrophys. Astr. (2000) **21**, 413–417

Microwave Enhancement in Coronal Holes: Statistical Properties

N. Gopalswamy[1,2]*, K. Shibasaki[3], & M. Salem[4]
[1]*Bldg 26, Room G-l, Code 682.3, NASA/GSFC, Greenbelt MD, USA.*
[2]*Center for Solar Physics and Space Weather, The Catholic University of America, Washington DC 20064.*
[3]*Nobeyama Radio Observatory, Minamisaku, Nagano, 384-1305, Japan.*
[4]*Dept. of Physics, Case Western Reserve University, Cleveland, OH 44106, USA.*
**e-mail: gopals@fugee.gsfc. nasa.gov*

Abstract. We report on the statistical properties of the microwave enhancement (brightness temperature, area, fine structure, life time and magnetic field strength) in coronal holes observed over a period of several solar rotations.

Key words. Sun: radio radiation—coronal holes—EUV emission.

1. Introduction

Coronal holes appear as deficit in X-ray and EUV emissions as compared to the quiet Sun, except for a narrow microwave band (0.3 to 2 cm) in which they appear brighter than the quiet Sun (see, e.g. Kosugi *et al,* 1986 and references therein). The enhancement typically consists of diffuse and compact components with brightness temperatures of up to a few thousand K (Gopalswamy *et al,* 1999a,b). In the past, microwave enhancement has been studied using isolated holes. Since the advent of the Nobeyama radioheliograph (Nakajima *et al,* 1994), microwave enhancement is routinely observed in polar and low-latitude coronal holes enabling statistical studies. In this paper, we report on the results of a statistical investigation of a large number of coronal holes.

2. Data analysis and results

A large number of coronal holes were observed during January 1996 to April 1999 using (i) the Nobeyama radioheliograph at 17 GHz, (ii) the Solar and Heliospheric Observatory (SOHO) mission's Extreme-ultraviolet Imaging Telescope (EIT, Delaboudiniere *et al.* 1995) and (iii) the SOHO's Michelson Doppler Imager (MDI). By examining the EIT 195 Å images, we identified 71 coronal holes and verified them using Yohkoh/SXT and He 10830 Å data. Then we examined the microwave emission within the area occupied by the EUV coronal holes. We measured several parameters such as the coronal hole areas in EUV and microwaves, average and peak microwave brightness temperatures, average and peak magnetic field strengths, and life times of the coronal holes (in units of solar rotations). We considered only low-latitude coronal holes because they are free from limbbrightening in microwaves and they are potentially geo-effective.

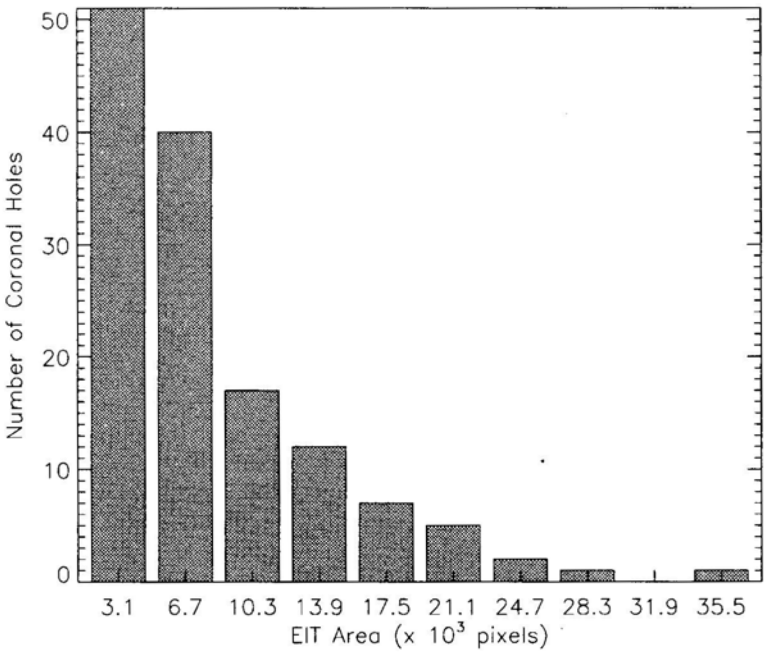

Figure 1. Distribution of areas of the 71 coronal holes as measured by SOHO/EIT. The areas are in units of EIT pixels (1 pixel = 5.2").

Fig. 1 shows that most of the holes have an area of ~3000 EIT pixels or 4.26 × 10^{20} cm^2 (1 pixel = 5.2″), very similar to the area of coronal holes reported by Harvey *et al* (1982). In Fig. 2, we see that a large number of coronal holes lived only for less than a single rotation period. This is in contrast to the long-lived holes studied during the *Skylab* era: most of the coronal holes lived for at least three rotations and some lived much longer (Bohlin 1977). Another surprising result is the large spread in area of the short-lived coronal holes, although the *Skylab* era trend of greater lifetime for larger holes seems to hold. The peak brightness temperature within the coronal holes was up to ~ 15,000 K. This is ~5000 K above the quiet Sun level. The peak values are due to compact sources within the coronal holes. Fig. 3 shows that the peak brightness temperature is weakly correlated with the peak magnetic field strength within the coronal holes. The microwave enhancement typically occupies only ~25% of the area seen in EUV (see Fig. 4). This is not a simple geometrical effect (microwave emission originates from the upper chromosphere whereas the X-rays and EUV originate from the corona) and seems to be determined by the area within the coronal hole where the magnetic flux is enhanced and unipolar. If there are regions of mixed polarity, the radio emission approaches quiet Sun level in these regions (see also Gopalswamy *et al.* 1999a, b).

3. Discussion and conclusions

The statistical results presented above confirm the close connection between the microwave enhancement and the magnetic field (structure and strength) within

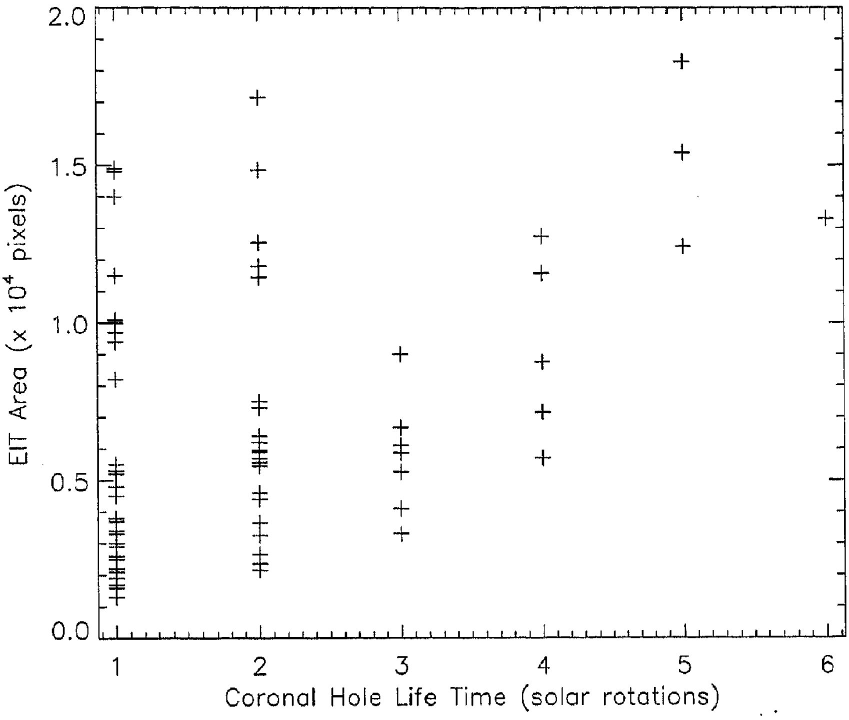

Figure 2. Lifetimes of 71 coronal holes (measured in units of solar rotations plotted against the measured area in EIT images (1 pixel = 5.2″).

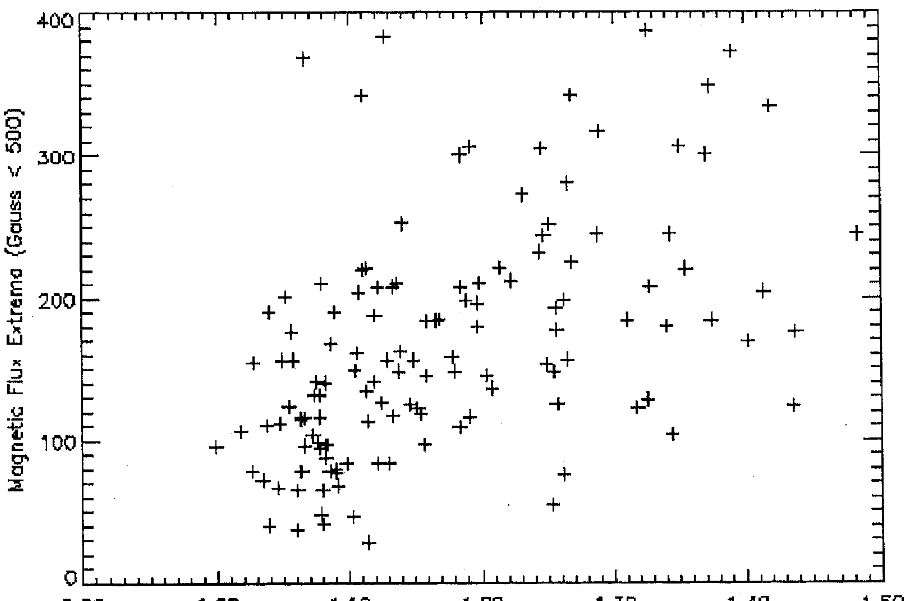

Figure 3. Scatter plot of the peak magnetic field strength and the peak brightness temperature within the 71 coronal holes.

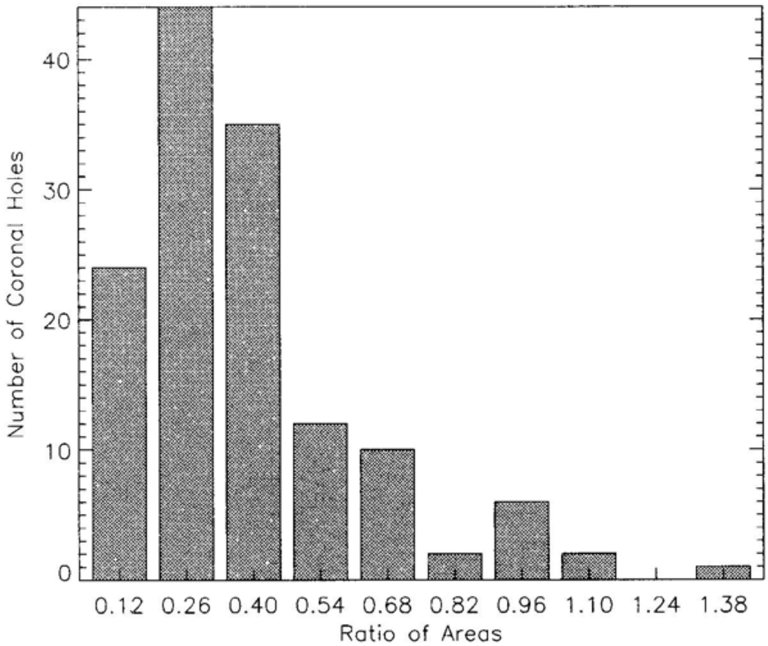

Figure 4. Fraction of the EUV coronal hole covered by microwave enhancement displayed as a histogram.

coronal holes. Combining the facts that microwave enhancement occupies only a fraction of the EUV coronal hole and the close relationship between the former with photospheric magnetic field structure, we can infer that the microwave emission is probably not "coronal". The quiet Sun in 17 GHz corresponds to the upper chromosphere, where the temperature is around 10,000 K. The microwave enhancement represents an enhancement over this quiet Sun level. Since the overlying corona is extremely thin, the easiest way to produce the enhancement is to increase the temperature of the optically thick layer by an amount equal to the observed enhancement. The highly variable, compact microwave sources seem to derive their energy from the enhanced network magnetic fields.

Acknowledgements

This research was partly supported by NASA's SOHO Guest Investigator program and NAG5-6139, NSF and AFOSR. SOHO is a project of international cooperation between ESA and NASA.

References

Bohlin, J. D. 1977, in *Coronal Holes and High Speed Wind Streams,* (ed.) Zirker,J. (Boulder: Colorado University Press) 27.

Delaboudiniere, J.-P., *et al.* 1995, *Solar Phys.,* **162,** 291.

Gopalswamy, N., Shibasaki, K., Thompson, B. J., Gurman, J. B., DeForest, C. E. 1999a, *J. Geophys. Res.,* **104,** 9767.

Gopalswamy, N., Shibasaki, K., Thompson, B. J., Gurman, J. B., DeForest, C. E. 1999b, in *Solar Wind Nine,* CP 471. (ed.) Habbal, S. *et al.* (New York: American Institute of Physics, Woodbury) 277.

Harvey, K., Sheeley, N. R., Harvey, J. W. 1982, *Solar Phys.,* **79,** 149.

Kosugi, T., Ishiguro, M. Shibasaki, K., 1986, *Phys,* **38,** 1.

Nakajima, H. *et al.* 1994, *Proc. IEEE,* **82,** 705.

J. Astrophys. Astr. (2000) **21,** 419–420

The Enhanced Coronal Green Line Intensity and the Magnetic Field Gradients

K. B. Ramesh*, B. S. Nagabhushana & B. A. Varghese, *Indian institute of Astrophysics, Bangalore 560 034.*
**e-mail: kbramesh@iiap. ernet. In*

Key words. Sun: Corona—emergence of magnetic flux.

Extended abstract

Ramesh, Nagabhushana and Varghese (1999) have shown that the green line intensity enhancement does not depend entirely on the strength of the underlying spot magnetic field though the coronal intensity enhanced feature is almost sure to occur at the locations of sunspots with strong magnetic fields and at the locations of plages having larger areas. Presented here are the results of an analysis of intensity of green line emission and the active region magnetic signatures as seen in Stanford magnetograms.

The data base used in this study consisted of homogeneous data set (HDS) of 5303 Å green coronal intensity measured at position angle intervals of 5° on any given day from several stations (see Rybansky, 1975) and brought down to the common scale of Lomnicky Štit. Daily maps of sunspots, and Ca plages are then superposed on the green line intensity maps of the corresponding day. Resultant composite maps are then compared with the Stanford magnetograms published in *Solar Geophysical Data.*

Careful scrutiny of the Stanford magnetograms in association with the composite maps of green line emission show the persistent presence of moderate to high field gradients along the neutral line at the locations of the intensity enhanced features. This result is in good agreement with the results obtained by Vaiana *et al.* (1973) in case of coronal X-ray emission.

In our next step we have measured the magnetic field gradients along the neutral line scanning from east limb to west limb for each individual event. Further analysis showed that the peak intensity does not depend on the level of field gradient though a threshold gradient of 3×10^{-5} G/km seems to be essential for the enhancement in green line emission.

Examination of the individual cases in a greater detail revealed the following. All the events showed consistently the development of moderate to high field gradients along the neutral line in the wake of either the fresh flux emergence in the vicinity of a persistent active region or the evolution of a new active region.

Case studies of individual intensity enhancement features and their associated active regions indicated that the enhancements are not the resultant of any flares. Continuous emergence of flux within or in the vicinity of a pre-existing active region leading to the formation of moderate to high field gradients along the neutral line seems to play a key role in heating the corona at the locations of 5303 Å intensity enhancement.

Wang *et al.* (1997) indicated that the magnetic energy residing near the base of the loop acts as the heating source for the green line corona by lifting chromospheric gas into the overlying loop and converting it into plasma with a temperature of around 2×10^6 K. Our work showed that a given degree of gradients does not always produce the same degree of brightness. Therefore, it appears that the degree of magnetic reconnection through which the stored magnetic energy is dissipated into the corona to raise the plasma temperature to the order of 2 MK plays an important role. Reconnection probably is determined by the nature of magnetic flux emergence through the photosphere.

Acknowledgements

Authors thank the observers of all coronal stations contributing to HDS. Data used here are obtained from WDC-A, STP, NOAA E/GC2, CO, USA.

References

Ramesh, K. B., Nagabhushana, B. S., Varghese, B. A. 1999, *Solar Phys.,* **188,** 99.
Rybansky, M. 1975, *Bull. Astron. Inst. Czech.,* **26,** 367.
Vaiana, G. S., Krieger, A. S., Timothy, A. F. 1973, *Solar Phys.,* **32,** 81.
Wang, Y. -M., *et al.* 1997, *Astrophys. J.,* **485,** 419.

J. Astrophys. Astr. (2000) **21,** 421–422

Multibaseline Observations of the Occultation of Crab Nebula by the Solar Corona at Decameter Wavelengths

K. R. Subramanian, *Indian Institute of Astrophysics, Bangalore 560 034, India, e-mail: subra@iiap.ernet.in*

Key words. Occultation—solar corona—density fluctuations.

Extended abstract

Information about the outer solar corona can be obtained by observing the occultation of radio sources by the solar corona. As the radio waves pass through the corona they get scattered due to the fact that the electron density and consequently the refractive index varies from point to point. The effect of scattering is manifested by an apparent increase in the angular size of the radio source which can be measured by suitable interferometers. We present here multibaseline observations on the occultation of Crab Nebula at 34.5 MHz with baselines extending upto 4.9 km during June 1986 and 1987.

Observations presented here were made with a compound grating interferometer with an East-West fan beam of 3 min of arc at 34.5 MHz. It consists of four grating units placed at intervals of 1.4 km on an East-West baseline starting from the western end of the East-West array of the Gauribidanur radio telescope (Sastry 1995). Each grating unit consists of 8 Yagi antennas combined in a branched feeder system. The ouput of each one of the grating units was correlated with the East-West array. Observations of the radio source Crab Nebula were made at the time of transit during June 1986 and 1987. The fringe amplitude V(S) for a baseline S was calibrated using the corresponding baseline fringe amplitude of radio source 3C123 or 3C134 and normalised to the preoccultation value V(O). Normalised fringe amplitudes V(S)/V(O) for baselines 0.7 km, 2.1 km, 3.5 km and 4.9 km were obtained for days when there was a fortuitous lull in the solar activity. The spatial coherence is described by a mutual coherence function given by τ (S) = V(S)/V(O). The structure function D(S) is related to mutual coherence function by τ (S) = exp(–D(S)/2) (Prokhorov *et al.* 1975). If the scattering medium is characterized by an electron density fluctuation spectrum of power-law, then the wave structure function also has a power-law form given by D(S) $\propto S^{\beta-2}$ for $2\leq \beta \leq 4$. A plot of log (D(S)) versus log(S) for the 4 baselines is used to obtain the value of β. The least square fitted spectral component β has a value in the range of 1.8 to 4.25 in the elongation range of 5 to 43 solar radii as shown in Fig. 1.

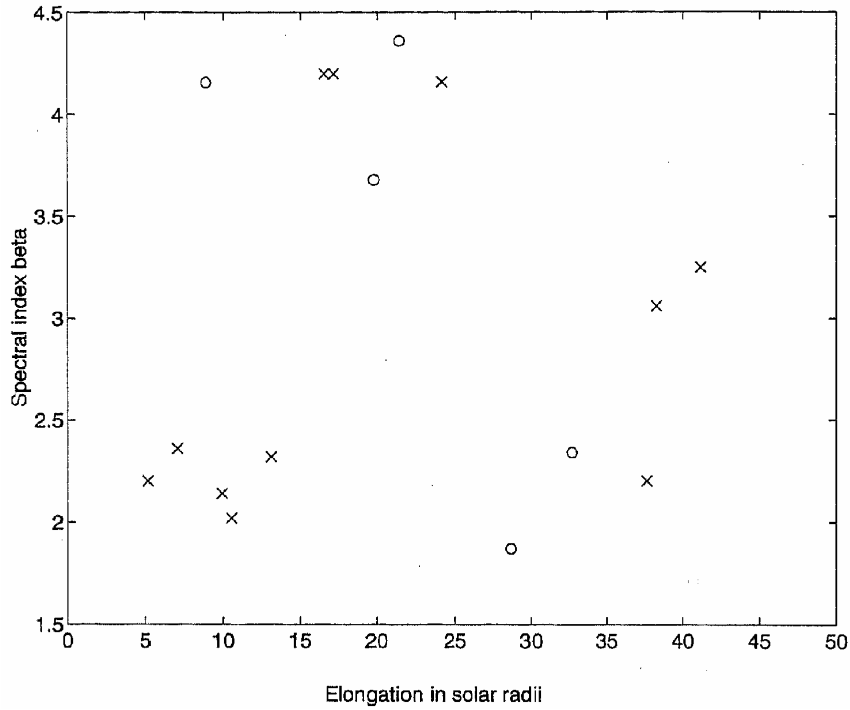

Figure 1. Variation of spectral index β with elongation during June 1986 and 1987 denoted respectively by crosses and open circles.

References

Blessing, R. G., Denission, P. A. 1972, *Proc. Astr. Soc. Australia,* **2**, 84.

Erickson, W. C. 1969, *Astrophys. J.*, **139**, 12901.

Prokhorov, A. M, Bunkin, F. V., Gochelashivily, K. S., Shishov, V. I. 1975, *Proc. IEEE.,* **63**, 790.

Sastry, Ch. V. 1995, *Space Sci. Rev,* **72**, 629.

J. Astrophys. Astr. (2000) **21**, 423–429

Solar Wind Variation with the Cycle

I. S. Veselovsky,* A. V. Dmitriev, A. V. Suvorova & M. V. Tarsina,
Institute of Nuclear Physics, Moscow State University, 119899 Moscow, Russia.
**e-mail: veselov@decl.npi.msu.su*

Abstract. The cyclic evolution of the heliospheric plasma parameters is related to the time-dependent boundary conditions in the solar corona. "Minimal" coronal configurations correspond to the regular appearance of the tenuous, but hot and fast plasma streams from the large polar coronal holes. The denser, but cooler and slower solar wind is adjacent to coronal streamers. Irregular dynamic manifestations are present in the corona and the solar wind everywhere and always. They follow the solar activity cycle rather well. Because of this, the direct and indirect solar wind measurements demonstrate clear variations in space and time according to the minimal, intermediate and maximal conditions of the cycles. The average solar wind density, velocity and temperature measured at the Earth's orbit show specific decadal variations and trends, which are of the order of the first tens per cent during the last three solar cycles. Statistical, spectral and correlation characteristics of the solar wind are reviewed with the emphasis on the cycles.

Key words. Solar wind—solar activity cycle.

1. Introduction

The knowledge of the solar cycle variations in the heliospheric plasma and magnetic fields was initially based on the indirect indications gained from the observations of the Sun, comets, cosmic rays, geomagnetic perturbations, interplanetary scintillations and some other ground-based methods. Numerous direct and remote-sensing spacecraft measurements *in situ* have continuously broadened this knowledge during the past 40 years, which can be seen from the original and review papers. We do not intend here to present the complete list of publications on this very popular topic and restrict ourselves by the selected set of references chosen more or less arbitrary for the introductory purposes only (Feldman *et al.* 1977; Crooker 1983; Veselovsky 1984; Schwenn 1990; Hapgood *et al.* 1991; King 1991; Gazis 1996; Richardson *et al.* 1996; El-Borie *et al.* 1997). See also related papers presented by S. Ananthakrishnan and P. Kiraly at the Kodaikanal meeting.

Interplanetary scintillation measurements demonstrated the existence of the helio-latitudinal solar wind velocity dependence on the solar cycle (Vlasov 1975, 1983, 1998; Coles *et al.* 1980; Bourgois & Coles 1989; Kojima *et al.* 1990; Lotova & Korelov 1991; Ricket & Coles 1991; Manoharan 1993; Coles *et al.* 1995). Ulysses measurements *in situ* confirmed and detailed these results regarding the solar minimum period. The solar cycle change in the solar wind dynamic pressure occurs at all solar latitudes, in both the fast and slow solar wind (Richardson *et al.* 1999).

The aim of this paper is to present a short review of recent studies of the solar wind variation with the cycles. More details and some working materials of the ongoing study can be found at the Web site (http://alpha npi.msu.su/alla).

2. Average parameters

Solar cycle variations of all heliospheric plasma and magnetic field parameters of an order of ten per cent are well documented (Veselovsky *et al.* 1998, 1999, 2000a, 2000b; Dmitriev *et al.* 2000). As an illustration, Fig. 1 shows the monthly averaged values of the main solar wind parameters. The curves are noisy, but some regular solar cycle changes can be recognized and they are confirmed by the detailed analysis. The solar cycle variations appear more clearly when longer time averages are invest-tigated. We performed this analysis with different kind of running averages, for example, over three, six and twelve months with the following results. The maximal densities are observed at the rising and declining solar cycle phases. The maximal velocities and temperatures appear at the declining phases, when the hotter and faster solar wind streams from large polar coronal holes reach the ecliptic plane. Helio-spheric and solar magnetic fields are well correlated and follow the activity cycle.

Solar cycles are clearly seen in the energy, momentum and mass fluxes of the solar wind. The Sun as a star emits by a factor of 1.5–2 more solar wind mass and energy during solar minima in comparison with solar maxima years. Moreover, the overall rising trend of the same order of magnitude during the past 30 years can be marked (see Fig. 2).

3. Statistical and spectral-time analysis

Not only average values, but also statistical properties of the solar wind parameters are solar cycle dependent. The physical reason for these lie in the solar activity regulation of the corona and wind sources.

The statistical distributions of the solar wind parameters are varying during solar cycle while remaining close to the log-normal laws with remarkable deviations. The information entropy is rather high, but different types of the solar wind flows are discernible. For example, fast solar wind "islands" are clearly seen in Fig. 3 for the velocity distributions during the declining phases (1974, 1985, 1994). More details can be found in the paper (Veselovsky *et al.* 2000b).

Multi-parametric cross-correlation analysis indicates that the best correlations between different solar wind parameters are observed under the averaging time of about one year. For the averaging times greater and less than this value one obtains a lower degree of correlation. The tentative explanation of this fact could be related to a relatively high level of fluctuations associated with the solar activity and the solar rotation, which is demonstrated in the next section.

Extremely high correlations were marked between the heliospheric magnetic field, the magnetic field of the Sun as a star and galactic cosmic ray variations (Belov *et al.* 1999). This allowed reconstructing heliospheric magnetic fields for the past times

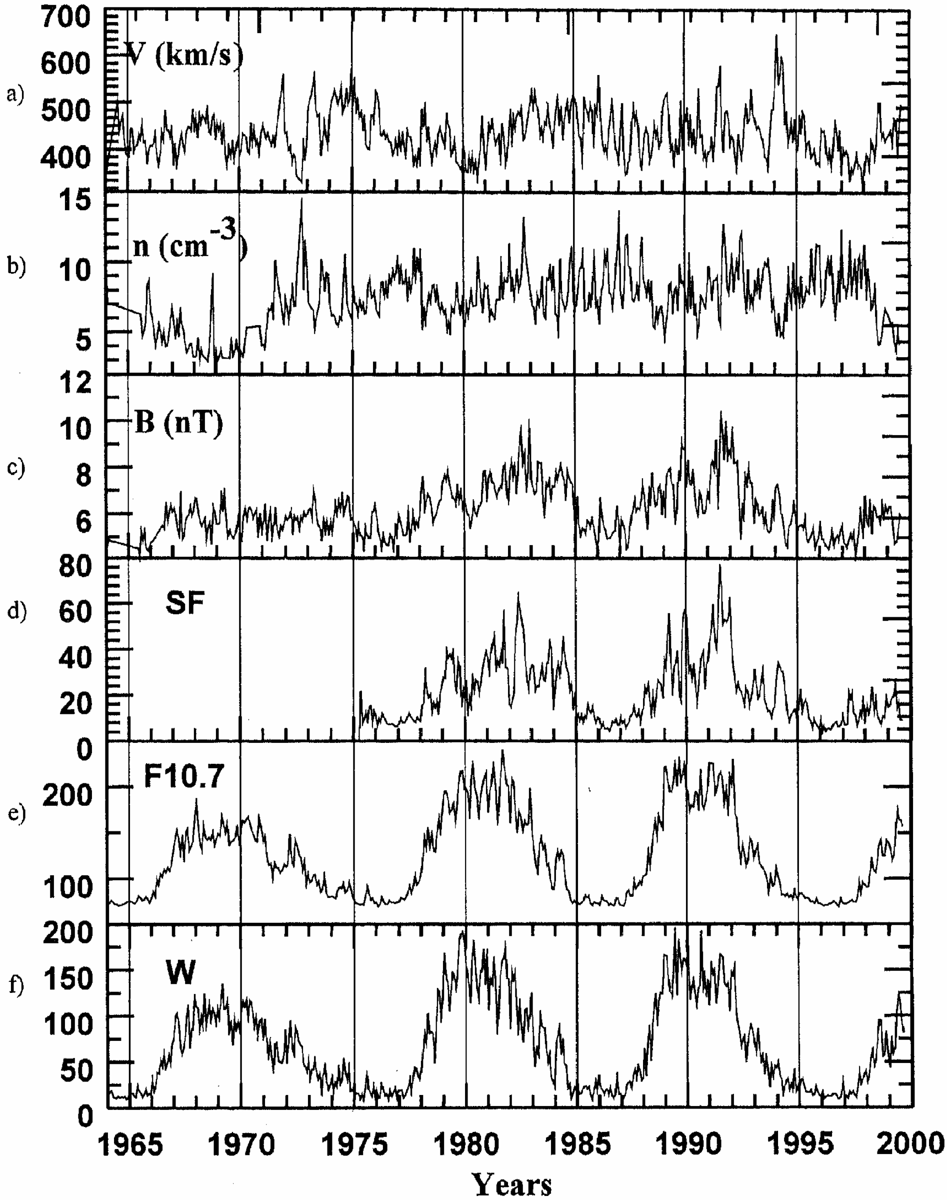

Figure 1. Monthly averaged values of the main solar wind parameters at the Earth's orbit and solar indexes: (**a**) solar wind velocity V (km/s); (**b**) solar wind number density n (cm^{-3}); (**c**) helisopheric magnetic field B (nT); (**d**) magnetic field of the Sun as a star SF; (**e**) solar radioemission index F10.7; (**f**) sunspot numbers W.

using neutron monitor data. Osherovich *et al.* (1999) described a strong correlation between the inverse square Alfven-Mach number M_A yearly medians and sunspot numbers.

Fast Fourier-transforms, spectral-time and wavelet analyses were applied for the investigation of the rythmic and non-rythmic long-term variations during the solar

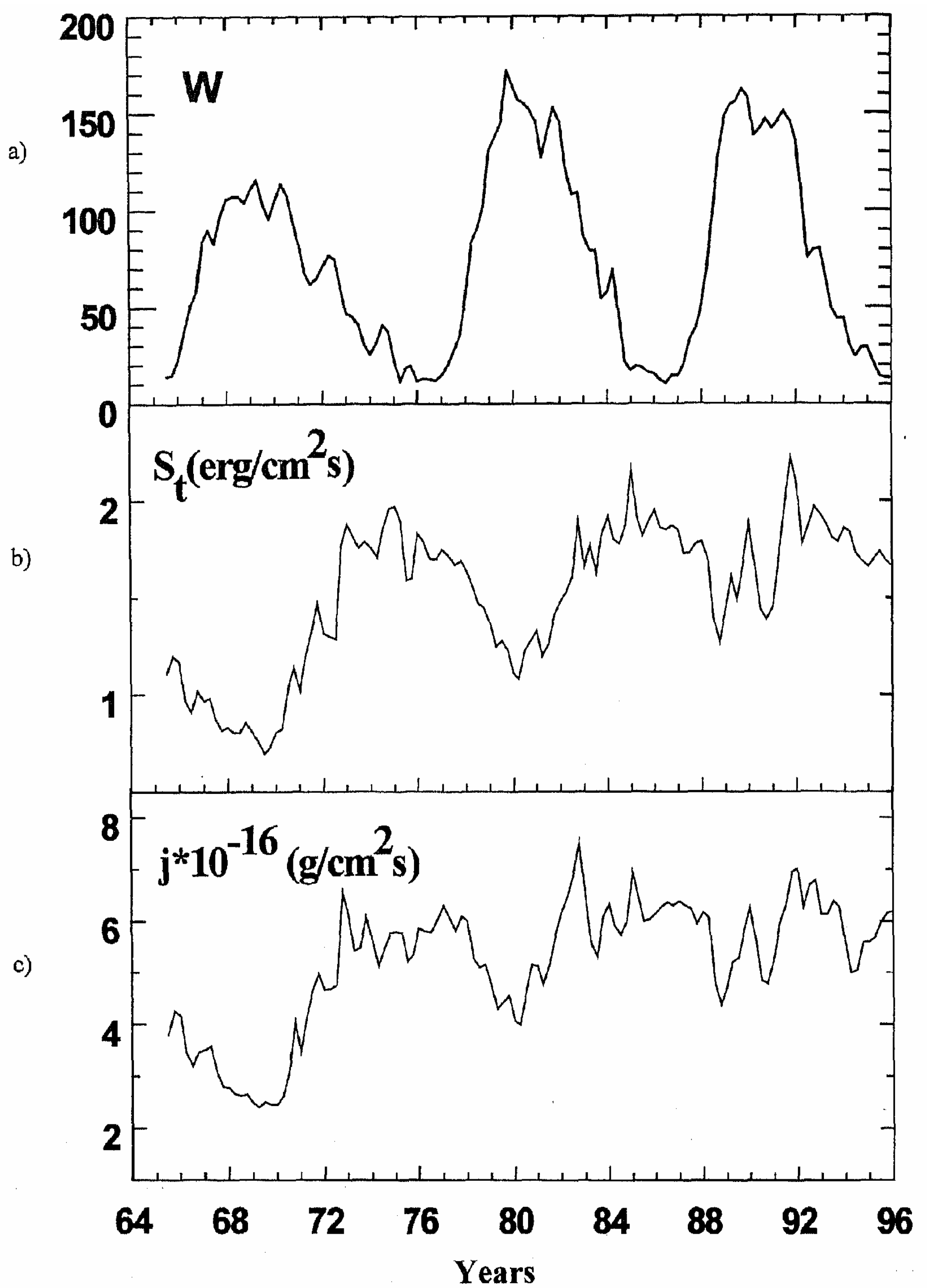

Figure 2. Solar wind, energy and mass flux densities during the 20–23 solar cycles. (**a**) sunspot numbers; (**b**) solar wind energy flux density S_t;(**c**) solar wind mass flux density j

cycles with time scales from days to tens of years. The results of this investigation (Veselovsky *et al.* 2000b) show a large manifold of the regular and irregular solar wind variations at the Earth's orbit which are explained by the following causes: 1) the solar variability; 2) the solar rotation with inhomogeneities in the corona; 3) the Earth's orbital motion.

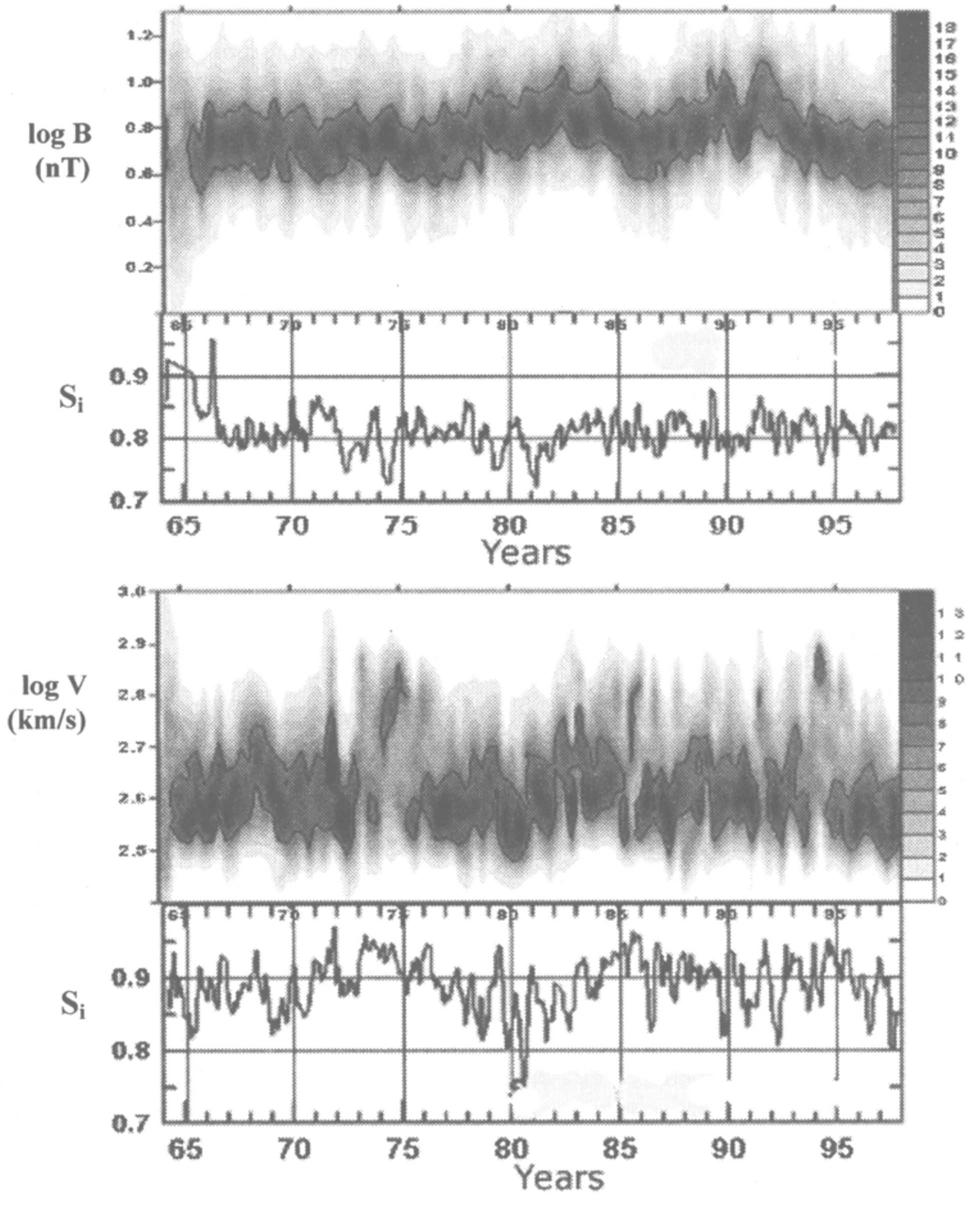

Figure 3. Statistical distributions and the information entropy of the hellisopheric magnetic field (upper panels) and the solar wind velocity (bottom panels). The color scale (right) was partially lost because of the white-black reproduction of the running histograms. Nevertheless, the level contours can be followed. In particular, the solid line is shown at the half-height of the histograms.

4. Discussion

It is well known that the large-scale 3-D organization of the solar corona and the heliosphere is regulated by the solar activity. Fast, tenuous and hot (slow, dense and cold) quasistationary solar wind flows usually correspond to the open (closed) magnetic configurations on the Sun represented by coronal holes (active regions). Coronal holes (active regions) are well developed around the solar minimum (maximum) years. The non-stationary transient flows, coronal mass ejections, or corpuscular streams according to the old terminology, correspond to more complicated and dynamical magnetic configurations on the Sun, both open and closed, as well as intermittent in space and time (Veselovsky 2000).

The demarcation between the non-stationary ($S \ll 1$) and quasistationary ($S \gg 1$) cases is given by the Strouhal number $S = Vt/l$, where V, t and l are characteristic velocity, time and space scales. The marginal value $S \approx 1$ corresponds to the time scales of the order of days for the Earth's orbit. Detailed knowledge is needed of the governing laws and different regimes in the heliosphere for a better understanding of the possible predictability limits when using neural network models (Veselovsky *et al.* 2000a).

5. Conclusions

- Heliospheric plasma parameters show solar cycle variations and longer-term trends. Both regular and irregular components are present. The regular changes are distinct in many instances, but they are relatively small and sometimes obscured by large fluctuations.
- The magnitude of the solar wind variations during the past solar cycles (20–23) is of the order of several tens of per cent.
- The cyclic variability of the Sun as a star on the factor about 1.5-2 is clearly seen in the integral mass and energy losses with the solar wind outflow.
- The observed variations do not contradict the concepts of the solar wind origins from the magnetically open, closed and intermittent structures in the solar corona.

Acknowledgements

The work was partially supported by the RFBR grants 98-02-17660, 98-01-00537, the Federal Program "Astronomy" and the Program "Universities of Russia". The IAU travel grant and the local support are gratefully acknowledged which facilitated the attendance and the presentation of the paper by the invited speaker (I.S.V.) at the Kodaikanal Colloquium.

References

Belov, A. V., Veselovsky, I. S., Gushchina, R. T., Dmitriev, A. V., Panassenko, O. V., Suvorova, A. V., Yanke, V. G. 1999, *Izvestiya Akademii Nauk. Ser Physica,* **63**, 1606 (in Russian).

Bourgois, G., Coles, W. A. 1989, in *Solar Wind Seven* (ed.) Marsch, E. and Schwenn, R., (Oxford: Pergamon) 155.

Coles, W. A., Grail, R. A., Klinglesmith, M. T., Bourgois, G. 1995, *J. Geophys. Res.,* **100**, 17069.

Coles, W. A., Ricket, B. J., Rumsey, V. H., Kaufman, J. J., Turley, D. G., Ananthakrishnan, S., Armstrong, J. W., Harmon's, J. K., Scott, S. L., Sime, D. G. 1980, *Nature,* **286**, 239.

Crooker, N. U. 1983, in *Solar Wind Five* (ed.) Neugebauer, M., (NASA, CP-2280) 303.
Dmitriev, A. V., Suvorova, A. V., Veselovsky, I. S. 2000, *Phys. and Chem. of the Earth.,* Part C, **25,** 113.
El-Borie, M. A., Duldig, M. L., Humble, J. E. 1997, *25th International Cosmic Ray Conference, Contributed Papers,* 1, SHl-3, 317.
Feldman, W. C, Asbridge, J. R., Bame, S. T., Gosling, J. T. 1977, in *The Solar Output and its Variations,* (ed.) White, O. R. (Boulder: Colorado University Press), Chapter V.
Gazis, P. R., *Rev. Geophys.,* 1996, **34**, 379.
Hapgood, M. A., Lockwood, M., Bowe, G. A., Willis, D. M. 1991, *Planet Space. Sci,* **39**, 411.
King, J. H. 1991, *J. Geomag. Geoelectr.,* **43**, 865.
Kojima, M., Kakinuma, T. 1990, *Space Sci Rev.,* **53**, 173.
Lotova, N. A., Korelov, O. A. 1991, in *Solar Wind Seven,* (ed.) Marsch, E., and Schwerin, R. (Oxford: Pergamon) 221.
Manoharan, P. K. 1993, *Solar Phys.,* **148**, 153.
Osherovich, V. A., Fainberg, J., Stone, R. G. 1999, *Geophys. Res. Lett,* **26**, 2597.
Richardson, J. D., Belcher, J. W., Lazarus, A. J. *et al.* 1996, in *Solar Wind Eight,* (ed.) Winterhalter *et al.,* (Woodbury: AIP Press) 483.
Richardson, J. D., Paularena, K. I., Wang, C. 1999, in *Solar Wind Nine,* (ed.) Habbal, S. R. *et al.* (AIP), CP471, 183.
Ricket, B. J., Coles, W. A. 1991, *J. Geophys. Res.,* **96**, 1717.
Schwenn, R. 1990, in *Physics of the Inner Heliosphere, Large-Scale Phenomena,* (ed.) Schwenn, R. and Marsch, E., (Berlin: Springer Verlag) 99.
Veselovsky, I. S. 1984, *Itogi Nauki i Techniki, "Issledovania Kosmicheskogo Prostranstva",* 22, Moscow VINITI.
Veselovsky, I. S. 2000, *Adv. Space Res.,* in press.
Veselovsky, I. S., Dmitriev, A. V, Orlov, Yu. V, Persiantsev, Yu. G., Suvorova, A. V. 2000a, *Solar System Research,* **33,** in press.
Veselovsky, I. S., Dmitriev, A. V, Panassenko, O. A., Suvorova, A. V. 1999, *Astronomy Reports,* **43,** 485.
Veselovsky, I. S., Dmitriev, A. V, Suvorova, A. V. 1998, *Solar System Research,* **32**, 310.
Veselovsky, I. S., Dmitriev, A. V, Suvorova, A. V, Ryazantseva, M. O. 2000b, *Solar System Research,* **34,** (in press).
Vlasov, V. I. 1975, *Geomagnetizm and Aeronomy,* **15**, 542 (in Russian, also translated in English).
Vlasov, V. I. 1983, *Geomagnetizm and Aeronomy,* **23**, 473 (in Russian, also translated in English).
Vlasov, V. I. 1998, *Interplanetary Plasma During 20–22 Solar Cycles According to Radio-astronomical Data,* (P. N. Lebedev Physical Institute, Russian Academy of Sciences, Preprint 52, Moscow).

J. Astrophys. Astr. (2000) **21**, 431–437

Heliospheric Magnetic Fields, Energetic Particles, and the Solar Cycle

Péter Király, *KFKI Research Institute for Particle and NuclearPhysics, H-1525 Budapest 114, POB 49, Hungary.*
e-mail: pkiraly@ sunserv.kfki.hu

Abstract. The heliosphere is the region filled with magnetized plasma of mainly solar origin. It extends from the solar corona to well beyond the planets, and is separated from the interstellar medium by the heliopause. The latter is embedded in a complex and still unexplored boundary region. The characteristics of heliospheric plasma, fields, and energetic particles depend on highly variable internal boundary conditions, and also on quasi-stationary external ones. Both galactic cosmic rays and energetic particles of solar and heliospheric origin are subject to intensity variations over individual solar cycles and also from cycle to cycle. Particle propagation is controlled by spatially and temporally varying interplanetary magnetic fields, frozen into the solar wind. An overview is presented of the main heliospheric components and processes, and also of the relevant missions and data sets. Particular attention is given to flux variations over the last few solar cycles, and to extrapolated effects on the terrestrial environment.

Key words. Heliosphere—heliopause—termination shock—solar cycle—energetic particles—interplanetary neutrals—anomalous component—cosmic rays—interplanetary magnetic fields.

1. Introduction

Heliospheric processes are mostly, but not exclusively controlled by solar activity that, in turn, reflects internal solar dynamics. Up to radial distances of 10 to 15 AU, solar wind (SW) streams directly control heliospheric structure. Fast streams from coronal holes interact with the slow wind; as a result, merged interaction regions (MIRs) appear which finally produce global merged interaction regions (GMIRs) in the distant heliosphere. Around solar minimum, during periods of stable coronal structure, forward and reverse shocks develop at the interfaces beyond 1 AU, and form corotating interaction regions (CIRs). Frozen-in magnetic fields are of solar origin, and alternating between inward and outward polarity sectors in the equatorial region, while both polar regions are unipolar. The two polarities are separated by the heliospheric current sheet (HCS), the heliospheric extension of the coronal neutral line.

Farther from the Sun, external influences become more competitive. Neutral atoms from interstellar space penetrate deep into the heliosphere before being ionized by charge exchange and solar UV radiation, and are then carried out by magnetic fields frozen into the solar wind; such pick-up (PU) ions get accelerated at the SW termination shock (TS), and can then access the inner solar system again as mainly singly charged anomalous cosmic rays (ACRs). With increasing energy, fully ionized galactic cosmic rays (CRs) can also access the inner heliosphere. In addition to the SW and the ionized component of the local interstellar medium (LISM), each of the PU, ACR and CR components influence the position and structure of the heliospheric boundary region. Reconnection between interstellar and heliospheric fields may also modify the boundary. Those distant processes, however, have only minute effects at 1 AU in comparison to SW ram pressure and local magnetic fields. The main role of high-energy particles in heliospheric studies is to provide information on heliospheric structure and on acceleration and propagation processes. As remote sensing of plasma processes is difficult, this is an important role. With increasing particle energy, information on larger and larger features of the heliosphere is gained.

The extent of external influences on heliospheric and possibly even on solar behaviour is a non-trivial problem. Interstellar conditions are expected to change rather slowly, thus at least the variable component of the influence should be small. There have been claims that planetary motion may assist in synchronizing the clock of the solar dynamo, even if the energy densities of the mass motions involved in the dynamo action vastly exceed planetary effects. On longer terms, the changing interstellar environment may certainly influence the extent of the heliosphere, and some back-reaction of those boundary conditions on SW sources and on flare and CME structure might result. Although SW is supersonic and excludes direct hydrodynamical inward propagating effects, it might be that energetic particles, supersonic thermal and suprathermal electrons, or magnetic fields provide some subtle ways of influencing the inner boundary of the heliosphere.

Magnetic fields and energetic particles, and their cyclic behaviour will be reviewed with particular emphasis on recent space-based measurements. Possible long-term effects of the variability of the Sun and of its galactic environment will also be discussed.

2. Heliospheric data sources

2.1 *Ground-based observations*

Prior to the advent of space age, variation of galactic CR intensity with solar activity provided the first clue for the presence of a changing magnetic shield between Earth at 1 AU and the distant galactic environment. For a vivid recollection on those early days, see J. A. Simpson's report (1985). It soon became known that CR intensity (as measured by secondary particles at sea level or higher in the atmosphere) is reduced not only during the general periods of sunspot maxima, but also short-term decreases (Forbush-decreases) appear after some bursts of solar activity, often also associated with geomagnetic disturbances. A rarer type of intensity changes called ground-level events (GLEs) is associated with solar energetic particles of sufficiently high energy (typically several GeV), so that secondaries can reach ground level. Since the early 40s about 60 such GLEs have been detected. Ground-based observations of magnetic field variations also provided important clues for the understanding of magnetospheric current systems and for their dependence on solar variability, and also for heliospheric fields.

The monitoring of CR flux levels by an extensive network of neutron and muon monitors still contributes to the understanding of both solar and global heliospheric processes. Recording of intensity variations of GeV to tens of GeV CR particles is more efficient by ground-based monitors than by space instruments, due to the much smaller size of the latter. Also, the terrestrial magnetosphere as a powerful magnetic analyzer helps to reconstruct the energy spectrum and the directional distribution for solar events. Neutron monitor data can be accessed through the cosmic ray pages of several groups active in that field (e.g. Chicago, Moscow, Yakutsk).

2.2 *Near-Earth missions*

IMP-8, launched in October 1973, has monitored local interplanetary (and to some extent also magnetospheric) conditions ever since. It has provided a 1 AU baseline e.g. to the Pioneer, Voyager, Helios, and Ulysses deep-space missions. The mean orbital radius of IMP-8 is about 35 Earth radii, with some variation during the mission, and it spends about 7 to 8 days of its 12.5 day orbit in the SW. After more than 26 years, most IMP-8 instruments still work well, performing at least part of their original tasks. Data from IMP-8 now cover 3 solar minima, and are in progress to cover the 3rd maximum. SW plasma parameters, magnetic fields, and energetic particles have been almost continuously covered during the past 26 years, and most data bases are accessible e.g. through the search machines CDAWeb, OMNIWeb and COHOWeb; COHOWeb also contains a wide range of other heliospheric spacecraft data in an easily (also graphically) accessible form. A recent review on IMP-8 performance, with the description of experiments and data sets as well as correlative studies with L1-based spacecraft, can be found in Paularena & King (1999).

SAMPEX, on low Earth orbit, should be mentioned for its ACR results. Mostly singly charged ACR ions, of interstellar neutral atom origin, have been detected since 1992 by extensively using the Earth's magnetosphere as a magnetic analyzer. Also, ACRs trapped inside magnetospheric radiation belts (after losing one or more additional electrons in the residual atmosphere) have been much studied.

Still close to 1 AU, on halo orbit around the L1 Lagrangian point upstream of Earth, was ISEE-3 between 1978 and 1982. It was the first spacecraft on that orbit, and studied SW, magnetic fields and low-energy particles undisturbed by terrestrial effects. The Wind spacecraft, launched in 1994, has also spent some time around that point. SOHO, launched late 1995 and ACE, launched in 1997 are now on similar orbits, their main objectives being observation of the Sun, and of SW and energetic particle composition, respectively.

2.3 *Deep-space missions*

The missions with utmost impact on both planetary and outer heliospheric research were the Pioneer and Voyager deep-space probes. Pioneer-10 was launched in 1972, Pioneer-11 in 1973, Voyager-1 and Voyager-2 both in 1977. While the Pioneer program was formally terminated in 1997, Pioneer-10 is still tracked. Since the last planetary encounter in 1989, all four probes have explored the distant heliosphere. Voyager-1, now farthest from the Sun, reached a heliocentric distance of 76 AU just at the time of the Kodaikanal IAU Colloquium. Both Voyagers are hoped to survive until 2015 or even 2020, and are now involved in the Voyager Interstellar Mission. Both are expected to pass the TS (Voyager-1 perhaps soon), and Voyager-1 should also cross the heliopause and provide *in situ* information from the LISM. Both Voyagers are heading upstream into the streaming LISM, while Pioneer-10 moves downstream.

The near-ecliptic region of the inner heliosphere between 0.29 and 1 AU was explored by the two Helios spacecraft (Helios-1: 1974–86, Helios-2: 1976–80). The range covered was important for a better *in situ* coverage of the radial development of SW structure and turbulence (Schwenn & Marsch 1991; Horbury 1999).

The heliosphere at both low and high latitudes has been covered between about 1.3 and 5.4 AU by Ulysses, launched in 1990. South and North polar passes in 1994 and 95 preceded solar minimum, while the 2000 and 2001 polar passes will cover solar maximum. Ulysses is the first mission with a real 3D coverage of the inner heliosphere. The first *fast latitude scan* from 1994 to 95 provided a snapshot of the latitudinal structure at a time when temporal changes in the heliosphere were relatively slow. The next similar snapshot is expected to provide information on a more dynamical 3D structure of the heliosphere near solar maximum.

3. Large-scale heliospheric structure

The core of the heliosphere is the supersonic SW bubble emanating from the rotating solar corona. Frozen-in Archimedean spiral magnetic field lines thread the bubble, mapping out the polarity of the radial field components from the 'source surface' of the SW (at about 3 solar radii, so that field lines are mostly open) to the whole bubble and also to the inner, subsonic heliosheath. The superexpansion of the fast polar wind extends the latitudinal spread of unipolar coronal hole fields, leaving but a relatively narrow ecliptic latitude bin with alternating field directions at solar minima. Solar wind speed in that 'streamer belt' region is about a factor of 2 lower than at high latitudes. Opposite polarities are separated by a wavy current sheet that has a simple geometry at solar minima, but becomes more tilted and topologically complex at solar maxima. In the streamer belt, alternating slow and fast SW streams form corotating inward and outward propagating shocks.

The distant heliosphere and its boundary region remind of the terrestrial magnetosphere and its upstream and downstream extension: the bow shock, the magnetosheath and the magnetotail. Analogous structures are, however, scaled up by a factor of about 10^5. There are also several important differences. The SW streams past the magnetosphere much faster than the LISM does past the heliosphere, and there is no terrestrial analogue of the supersonic SW bubble surrounding the Sun. The SW is fully ionized, while the LISM is only partially ionized. The terrestrial magnetic field is much more regular, giving rise to radiation belts.

The heliocentric distance to the TS in the upstream direction is expected to be between 80 and 100 AU. So far, none of the distant heliospheric probes has crossed that boundary. The solar wind plasma is separated from the ionized component of the streaming interstellar medium by the heliopause. From considerations of pressure equilibrium with the ionized component of the LISM, the heliosphere is expected to extend to 100–130 AU in the upstream (nose) direction. Its downstream extension, the heliotail, is probably thousands of AU in length (which is still only about 1 per cent of the distance to the nearest star). The heliosphere is surrounded by the heliosheath (or outer heliosheath), the interstellar plasma streaming past the heliopause, diverted by the SW plasma and magnetic field pressure. The fairly weak bow shock is expected to be strongest in the direction of the nose of the heliosphere.

The LISM feeds neutral gas into the heliosphere, while the ionized component provides external pressure for confinement. The heliosphere is embedded in a warm interstellar cloudlet called the local cloud or 'local fluff'. It extends to no more than a few pc, and may be an evaporative extension of the 'squall line', a structure of denser clouds in the direction of the galactic centre. Gas in the anticentre direction is more dilute and more uniform. For a detailed review of our interstellar environment see Frisch (1995).

Magnetic reconnection on the heliopause may arise both with the interstellar field and between alternate stripes of oppositely directed magnetic fields, 'painted' onto the heliopause by the expansion of the substagnation region upstream of the termination shock. As the interstellar flow happens to be close to the ecliptic, convected 'streamer belt' solar fields should change sign at least twice per solar rotation in that region. Unipolar northern and southern fields are mapped into deeper layers, with reversal of the field only once per solar cycle.

4. Cyclicity of fields and particles

Solar-heliospheric magnetic fields have a 22-year periodicity. For many solar and heliospheric phenomena the sign of the field is of secondary importance, but that is not the case for the heliospheric access of predominantly positively charged particles arriving from the galaxy. Drifts due to density gradients and field line curvature reverse their direction for opposite field polarity. When northern solar polarity is outward (such as in the 90's), CR protons drift in from the poles toward the HCS, while for opposite fields the inward drift is mainly along the HCS. Diffusion, convection and adiabatic energy losses in the expanding SW all reduce CR intensity with decreasing solar distance, but, except for solar maximum periods, the large-scale pattern is largely determined by drift effects. This is particularly so in the distant heliosphere.

Recent IMP-8 and Voyager observations revealed that while low-energy (10 to 200 MeV) CR and ACR intensity at Earth almost completely recovered to the 1987 levels by the 1996 activity minimum, outer heliospheric fluxes remained much lower. The difference probably comes from the drift effect at the Voyagers, while at Earth the other modulation effects predominate. Near solar maxima, fields are more disordered and drift effects less important. Shielding by turbulent magnetic shells arising from particularly intense sequences of CMEs then causes long-lasting intensity decreases. In the inner heliosphere, CIRs also contribute both to the modulation (reduction) of CR and ACR fluxes, and to the acceleration of low-energy (MeV) fluxes. For more detail, see several contributions in two proceedings of recent ISSI workshops (ed. By Fisk *et al.* 1998 and by Balogh *et al.* 1999).

At 1 AU, most of the low-energy (< 10–20 MeV) protons are of solar-heliospheric origin. Their hourly (or daily) mean fluxes vary by several orders of magnitude, even at solar minima. Medians of the daily flux distributions increase by about a factor of 40 to 50 from the 1975–77 solar minimum to the 1979–81 maximum, and by 80 to

100 from 1985–87 to 1989–91. Median fluxes are more or less in phase with solar activity, while CR fluxes are in counterphase.

Very low-level fluxes at about 1 MeV proton energies are only seen around solar activity minima. Transition periods between their presence and absence are fairly sharp. The lowest levels measured are sometimes determined by 'instrumental background' caused e.g. by inefficient active shielding of the detectors. It appears, however, that a genuine energy-dependent baseline of those low-level fluxes exists, which is different for each cycle. The level at about 1 MeV was lowest around the 1986 solar minimum, and considerably higher around 1976. The 1996 level is in between. The baseline flux level increases with decreasing energy, opposite to what would be expected from CRs or ACRs adiabatically decelerated in the expanding SW. A solar and/or CIR origin is more likely to explain this observation.

5. Long-term effects

Energy releases in large solar events give rise to huge shocks and radiation increases in interplanetary space. Such events may endanger human life and technology in space, but indirectly may also damage power lines and oil pipelines. It is an important question whether much more powerful solar events occur often enough on geological time scales to affect atmospheric and biospheric processes, and be competitive with meteor impacts and sudden changes in the interstellar environment of the solar system (e.g. with nearby supernova explosions).

Wdowczyk & Wolfendale (1977) called attention to the dangers inherent in the flat integral spectra of solar energy releases observed over about 20 years. The logarithmic slope was estimated to be around –0.5. If that slope continued, several dramatic solar energy releases should be expected on geologically short time scales. In fact, for 10 times longer observation time the largest event would then be about 100 times more energetic, thus long-term mean fluences would be dominated by the largest events.

Luckily, better statistics and additional information available today provide a more optimistic forecast. A power-law function with exponential steepening was recently found by Nymmik (1999), making large events even rarer than predicted by the log-normal model of Feynman *et al.* (1993). Radiation history of lunar regolith (e.g. Reedy 1996), influenced by solar particle fluences over the last 1 Myr, as well as meteoritic and other samples provide now a strong argument against the predominance of very large solar events.

6. Conclusions

Our Sun’s environment is but one of the billions of stellar environments in our galaxy. Some of them might be quite similar to ours, some others very different. Ours is, however, the only one we have direct access to. We hope it reflects universal processes as a droplet of water reflects the sea. It is amazing how much of its complexities have already been uncovered, and how many secrets it still holds. The quest is endless. One may recall Mahatma Gandhi's words as given in N. K. Bose’s book (1948): “The goal ever recedes from us. The greater the progress the greater the recognition of our unworthiness. Satisfaction lies in the effort, not in the attainment.”

Acknowledgements

The organizers are gratefully thanked for their help and hospitality, and IAU for financial support. Travel support of Hungarian national grant *OTKA-T-030078* is acknowledged. The International Space Science Institute (ISSI) in Bern is thanked for supporting a project related to the present research.

References

Balogh, A. *et al.* (eds.) 1999, *Corotating Interaction Regions,* (Kluwer Academic Publishers: Dordrecht); Also *Space Science Reviews,* **89.**

Bose, N. K., 1948, *Selections from Gandhi,* (Navajivan Publishing House: Ahmedabad).

Feynman, J. G. *et al.* 1993, *J. Geophys. Res.,* **98**, 13281.

Fisk, L. A. *et al.* (eds.) 1998, *Cosmic Rays in the Heliosphere,* (Kluwer Academic Publishers: Dordrecht); Also *Space Science Reviews,* **83**.

Frisch, P. C. 1995, *Space Sci. Rev.,* **72**, 499.

Horbury, T. S. 1999, in *Plasma Turbulence and Energetic Particles in Astrophysics,* (eds.) M. Ostrowski & R. Schlickeiser, (Cracow) 115.

Nymmik, R. A. 1999, in *Proceedings of the 26th International Cosmic Ray Conf,* **6**, (eds.) D. Kieda *et al.,* (Salt Lake City, USA) 268.

Paularena, K. I., King, J. H. 1999, in *Interball in the ISTP Program,* (eds.) D. G. Sibeck & K. Kudela, (Kluwer Acad. Publishers: Dordrecht) 145.

Reedy, R. 1996, in *Solar Drivers of Interplanetary and Terrestrial Disturbances, Astron. Soc. Pacific Conf. Series,***95**,(San Francisco) 429.

Schwenn, R., Marsch, E. (eds.) 1991, *Physics of the Inner Heliosphere II — Particles, Waves and Turbulence,* (Springer: Berlin).

Simpson, J. A. 1985, in *Early History of Cosmic Ray Studies,* (eds.) I. Sekido & H. Elliot, (Reidel Publishing Company) 385.

Wdowczyk, J., Wolfendale, A. W. 1977, *Nature,* **268**, 510.

J. Astrophys. Astr. (2000) **21**, 439–444

Remote Sensing of the Heliospheric Solar Wind using Radio Astronomy Methods and Numerical Simulations

S. Ananthakrishnan, *National Center for Radio Astrophysics, Tata Institute of Fundamental Research, Pune, India*

Abstract. The ground-based radio astronomy method of interplanetary scintillations (IPS) and spacecraft observations have shown, in the past 25 years, that while coronal holes give rise to stable, reclining high speed solar wind streams during the minimum of the solar activity cycle, the slow speed wind seen more during the solar maximum activity is better associated with the closed field regions, which also give rise to solar flares and coronal mass ejections (CME's). The latter events increase significantly, as the cycle maximum takes place. We have recently shown that in the case of energetic flares one may be able to track the associated disturbances almost on a one to one basis from a distance of 0.2 to 1 AU using IPS methods. Time dependent 3D MHD models which are constrained by IPS observations are being developed. These models are able to simulate general features of the solar-generated disturbances. Advances in this direction may lead to prediction of heliospheric propagation of these disturbances throughout the solar system.

Key words. Sun—heliosphere, solar wind.

1. Introduction

More than 20 years ago we made a detailed analysis of interplanetary scintillation (IPS) data from the 3 station radio observatory in San Diego and showed how the solar wind changes with the solar cycle (Coles *et al.* 1980). In particular we noted that solar phenomena are 'intimately linked to the solar magnetic fields, which exhibit complex but systematic variations'. It was also noted that 'the dominance of the high speed streams during the declining phase of the solar cycle is the most obvious change in the ecliptic wind'. Observations since then, by both ground based IPS and *in situ* spacecraft, including the out-of-the-ecliptic mission by Ulysses spacecraft in 1995 have confirmed these amply. The polar solar wind is dominated by coronal holes. Apart from flares and coronal holes, coronal mass ejections (CMEs) are also an important component of solar activity and all these give rise to phenomena that may be studied by ground based IPS.

IPS arises when the scattered wavefront from a distant quasar gives rise to intensity fluctuations, which as they drift past the observer on a multi-telescope system at the prevailing solar wind speed, produce fluctuations that are correlated with a time lag. Knowledge of the baseline geometry and the time lag enables one to estimate the solar wind speed.

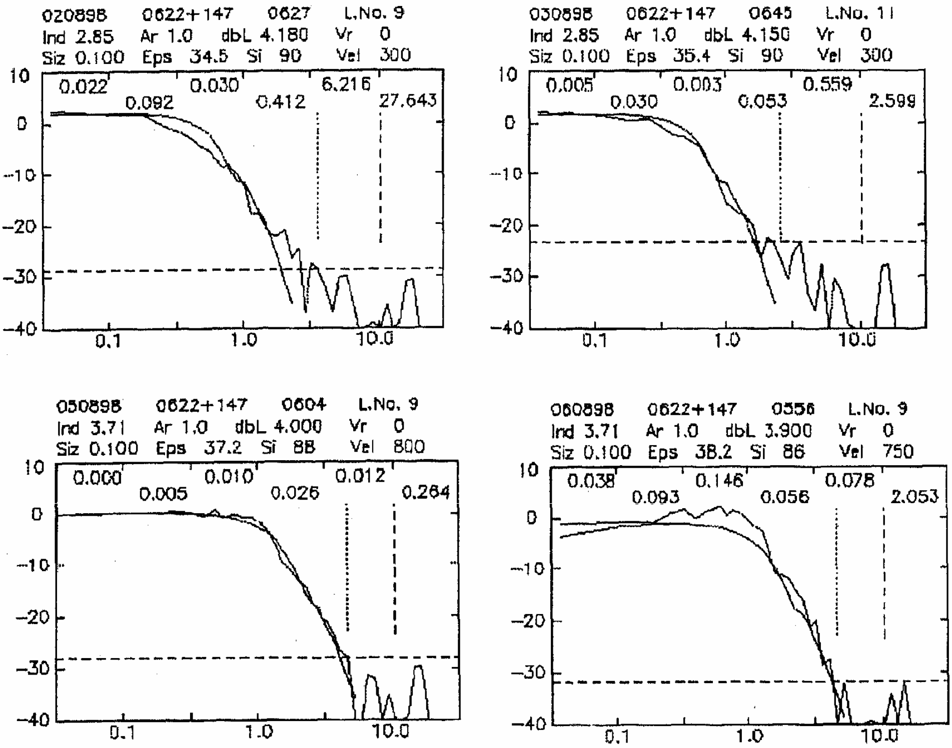

Figure 1. Temporal spectra of compact radio sources 0622 + 147 on four days in August 1998. The captions show the date, source name and time of observation in the first line, the fitted spectral index (Ind), axial ratio (AR), power level (dbl), random velocity (Vr) in the second line and size of the source (siz), solar elongation during observation (Eps), the fitted inner scale of the irregularities (Si) and the best fitted value for the solar wind velocity in the third line. The Y coordinate shows relative power in log scale and X-coordinate gives temporal frequencies in Hz. The observed temporal spectrum shown by the fluctuating line is overplotted with the smooth fitted model spectrum.

It is also possible to find a reasonable estimate of the solar wind speed based on the temporal spectra recorded in a single station, provided one has observations with good signal to noise ratio. While this was initially shown by Scott, Coles & Bourgois (1984), Manoharan & Ananthakrishnan (1990) developed this for systematically estimating the solar wind velocity by observing daily a large number of compact radio sources at 327 MHz using the large collecting area of the Ooty Radio Telescope.

A number of temporal spectra (Fig. 1) are shown on a compact radio source 0622 + 147 observed using the Ooty telescope for several days which show how the solar wind velocity changes from day to day (Balasubramanian *et al.* 2000). If one uses reasonable model parameters for the temporal spectral index, angular size of the compact component in the radio source and the axial ratio of the irregularities and estimate the solar wind velocity, the values are found to be in good agreement with three or more station velocities (Manoharan *et al.* 1995).

Further, as the Sun's apparent position changes in the sky, the elongation angle formed by the Sun-Earth-Source line keeps changing. This leads to a change in the scattering/scintillation strength for the same source. Hence, if one plots the scintillation vs elongation curve, one sees a systematic variation (Manoharan *et al.* 1995). The resulting plot is known as the m-p curve, '*m*' denoting the scintillation index (rms fluctuation normalised by the mean source intensity) and '*p*', the sine of the elongation angle.

Instead of using the scintillation index, Gapper *et al.* (1982) preferred to use a scintillation enhancement factor '*g*'. The *g* value is defined as the ratio of the scintillation index of the date normalized by the averaged scintillation index at that elongation. When the solar wind is quiet, the value of *g* is around unity. Thus, one may use both the estimated velocity, V and the scintillation enhancement factor, g to study the heliospheric solar wind.

2. Observations

During the past several years we have used the Ooty telescope to observe a number of solar transient events which show a significant increase in velocity as well as enhanced g. While tracing their origin back to the Sun, we find that a majority of them appear to be associated with energetic flares accompanied by Type II/IV radio bursts. A few of them could also be associated with CME's and a fewer with transient coronal holes. Many of these events are discussed in Janardhan *et al.* (1996) and Ananthakrishnan *et al.* (1999). We term these transient events as inter planetary disturbances (IPD's). In this brief review we refer to only the recent global campaign in August 1998 called the whole sun month (WSM II) campaign, in which IPS observations were also made using the Ooty telescope (Balasubramanian *et al.* 2000). Several IPD's were tracked during WSM II. The most interesting period during the campaign was, when an energetic flare event occurred on August 24th, 1998 with a maximum at 2204 UT in the active region AR 8307 at N35E09. Moreton waves were reported by MLSO from a nearby region. The most impulsive Type II during this period also occurred at 2207 UT on the same day. Shock speeds of 1300 km/s were reported by Culgoora radio observatory. This solar event was seen as a clear IPD in our IPS observations. The IPD propagated over a range of heliographic latitude and radial distance from 0.2 AU onwards to 1 AU (Fig. 2). This IPD was also detected by the ACE spacecraft at L1 at 0620 UT on August 26th, 1998. A geo-effective ssc was observed at the earth at 0651 UT on the same day. The shock speed derived by estimating the time interval between the flare maximum time and the ssc seen on the earth is in good agreement with the IPS velocities as well as the enhancement seen in g values, the details of which are given in Balasubramanian *et al.* (2000). Near simultaneous observations were also made by the Toyokawa four station IPS observatory and are reported in Tokumaru *et al.* (2000). IPS observations are therefore seen to be a useful tool for the remote sensing of heliospheric space weather. Currently, efforts are being made to predict the propagation of such IPDs and also model them using simulations.

3. Discussions

Energetic flare timings appear to be good markers for the beginning of a disturbance. In the last few years, we have shown that based on a simple shock time of arrival

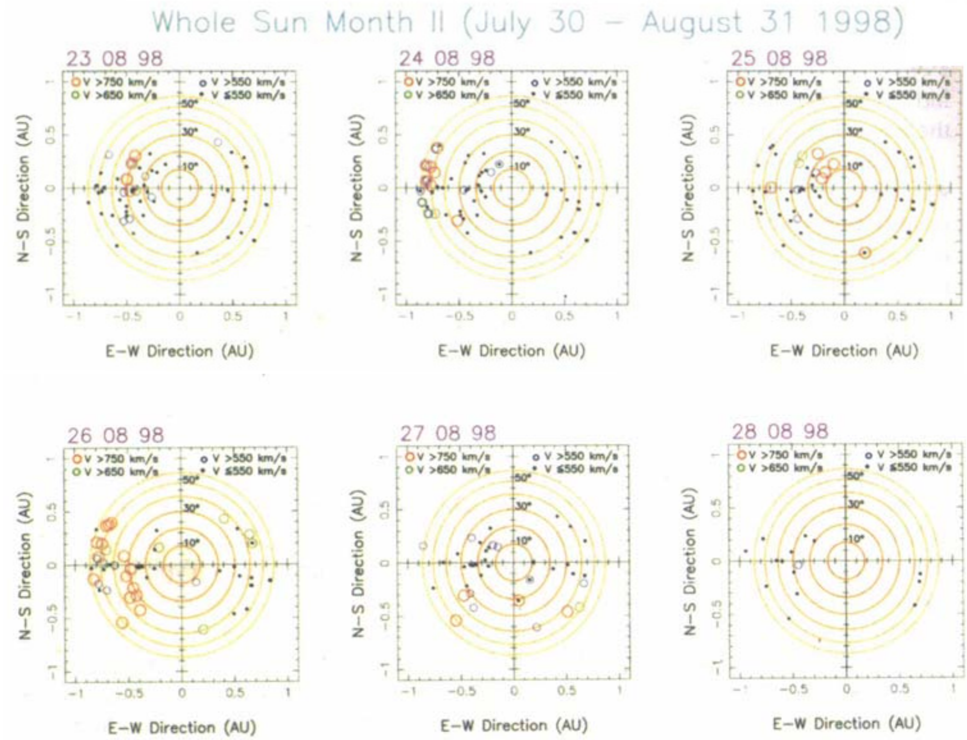

Figure 2. Plots show the velocity distribution in a polar plot for six days during August 23-28, 1998, as a function of distance from the Sun in AU. The inside elongation circles are in the interval of 10°. The diameters of the small circles are in proportion to the estimated velocity, as shown in the inset. During August 23–24 and August 25–26, one can clearly see the propagation of high velocity transients from close to the Sun towards 1 AU.

(STOA) model and knowing the flare position and flaring time, it is possible to predict the general direction of propagation and look for enhancement in the turbulence of scintillating sources. It has also been possible to track the disturbances and find that the initial high velocities at close radial distances from the Sun decelerate in a predictable way, as they propagate (Ananthakrishnan *et al.* 1999, Ananthakrishnan *et al.* 2000). While the STOA model has not been fully vindicated due to the smallness of the available event samples, Smith *et al.* (2000) have recently shown that 'the percentage of successful predictions to within an accuracy of 12 hours of shocks for the STOA is 53%'. Reliable use of the STOA model for the purpose of predicting IPD propagation on a routine basis requires many such studies.

However, in order to be make more reliable predictions, it is valuable to do 3D MHD modelling. At present these models do not cover the full range of heliocentric distances from Sun to Earth. Detman *et al.* (2000) are currently developing a hybrid heliospheric modeling system (HHMS), which uses the potential field source surface model of Wang & Sheeley (1990) and produces a model for the solar corona to a surface that is at a distance of 2.5 solar radii. Empirical models are being developed that extrapolate the solar wind parameters from 2.5 to 21 R⊙. An interplanetary global model 3D has been developed (Detman *et al.* 2000), which is a full 3D time

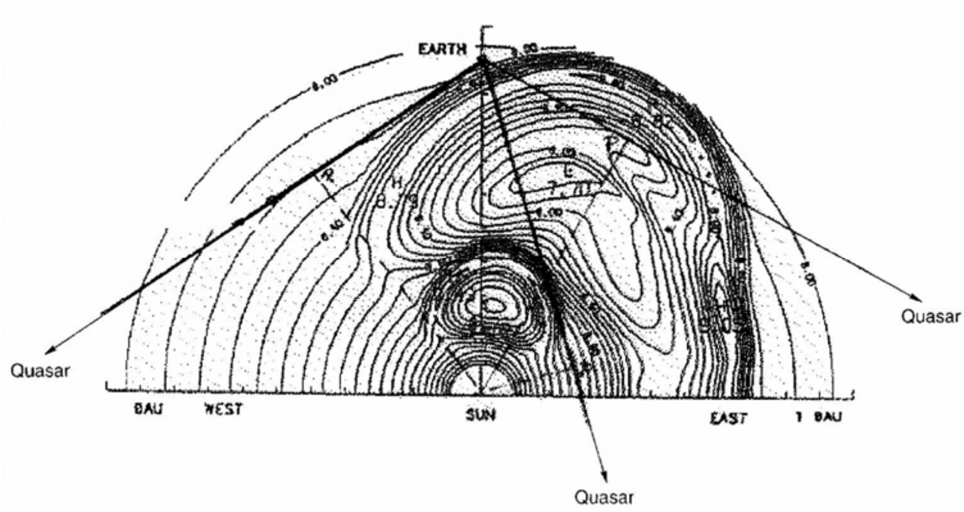

Figure 3. 3D MHD simulation showing the outward propagation of a disturbance. The straight lines are towards three quasars observed from the Earth by IPS, data from which could be used to constrain the model.

dependent MHD solar wind model for extrapolating the solar wind parameters from 21 $R_\odot$ to 214 $R_\odot$ .The time series of solar wind parameters thus developed are to be constrained by the IPS time series observations principally using Ooty and Nagoya data. As shown in Fig. 3, IPS observations can be made in many different directions and the estimated model parameters in those directions can be compared with the observations. Such modeling is currently underway.

4. Conclusion

Based on a recent IPS observing campaign during August 1998 as well as on observations over the past several years using Ooty and Nagoya radio telescopes it is shown that propagating interplanetary disturbances which appear to originate from solar events like flares, CME's and transient coronal holes can be studied in the heliospheric distance range of 0.2 to 1.0 AU, by the simple, yet powerful method of IPS. This is of considerable value for space weather predictions. While the initial observing predictions used a simple shock-time-of-arrival model, preliminary work has been done to make 3D MHD model simulations which are constrained by parameters derived from IPS observations.

Acknowledgements

I thank my principal collaborator Dr. V. Balasubramanian, RAC, Ooty for providing extensive data and figures before publication. I also want to thank our other collaborators, Dr. P. Janardhan of the PRL, Ahmedabad, and Drs. T. Detman and M. Dryer of the Space Environmental Centre, Boulder, Colorado, USA and M. Tokumaru of STE Lab., Toyokawa, Japan for help in the preparation of this presentation.

References

Ananthakrishnan, S. *et al.* 1999, *Solar Wind Nine,* CP471, 321.
Ananthakrishnan, S. *et al.* 2000, *Adv. Space Res.,* in press.
Balasubramanian, V. *et al.* 2000, in preparation.
Coles, W. A. *et al.* 1980, *Nature,* **286**, 239.
Detman, T. *et al.* 2000, in preparation.
Gapper, G. R., Hewish, A., Purvis, A., Duffett-Smith, P. J. 1982, *Nature,* **296**, 633.
Janardhan, P. *et al.* 1996, *Sol. Phys.,* **166**, 379.
Manoharan, P. K., Ananthakrishnan, S. 1990, *MNRAS,* **244**, 691.
Manoharan, P. K. *et al.* 1995, *Sol. Phys.,* **156**, 377.
Scott, S. L., Coles, W. A., Bourgois, G. 1984, *Astr. Astrophys.,* **123**, 207.
Smith, Z., *et al,* 2000, *Jour. Atm. Sol. Terr. Phys.,* in press.
Tokumaru, M. *et al.* 2000, *JGR,* **105**, 10435.
Wang, Y.-M., Sheeley, Jr. 1990, *JGR,* **355**, 726.

J. Astrophys. Astr. (2000) **21**, 445–446

Tomography of the Solar Wind using Interplanetary Scintillation

Divya Oberoi[1,2*] & A. Pramesh Rao,[1†]

[1]*National Centre for Radio Astrophysics, Tata Institute of Fundamental Research, Pune 411 007.*
[2]*Indian Institute of Science, Bangalore 560 012.*
**e-mail: div@ncra.tifr.res.in*
[†]*e-mail: pramesh@ncra.tifr.res.in*

Key words. Tomography—solar wind—interplanetary scintillation.

Extended abstract

Interplanetary scintillation (IPS) measurements are sensitive to a weighted sum of the properties of solar wind (SW) along the line-of-sight (*los*) to a distant compact radio source. Mapping a *los* back to the surface of the Sun provides information of the sites of origin of the SW sampled by the *los*. By observing different sources, lines-of-sight can be so chosen that they sample overlapping regions of Solar surface. In addition, the rotation of the Sun causes the long lived features in the SW to co-rotate, much like the twirling skirt of a ballerina, presenting different perspective views to the Earth based observers. These properties raise the possibility that systematic IPS observations can be inverted to give the maps of density and the velocity of the SW in the inner heliosphere, using techniques similar to tomography.

This technique has not been used extensively, mainly because of lack of availability of suitable datasets and the inherent complexity of the problem (Jackson *et al.* 1998). In order to investigate the feasibility of inverting IPS data to get distributions of velocity (v) and strength of scattering (C_n^2) on the solar surface, a series of simulations were undertaken. These simulations also explored the validity of the assumptions necessary for a tomographic reconstruction using IPS data. A distribution of the SW υ and C_n^2 was assumed at some fiducial surface. This distribution was propagated to fill the entire inner heliosphere accessible to IPS. The velocities were assumed to be purely radial and interaction between the fast and the slow moving SW was ignored. Lines-of-sight to radio sources were traced through the inner heliosphere and power spectra of intensity fluctuations, the primary IPS observable, constructed using the distribution of properties of the SW along the *los*. υ and C_n^2 were estimated for each of the lines-of-sight using a featureless SW model. A distribution of properties of SW at the fiducial surface was obtained by projecting the SW parameters estimated for all the lines-of-sight observed in one solar rotation on the fiducial surface. This distribution formed the initial guess for a χ^2 minimisation process, the surface distribution of the SW properties formed the degrees of freedom and the power spectra along individual lines-of-sight the constraints.

The preliminary results from simulations are presented in the form of Carrington maps of υ and C_n^2 for a solar rotation in Fig. 1. The features in the SW model, used to

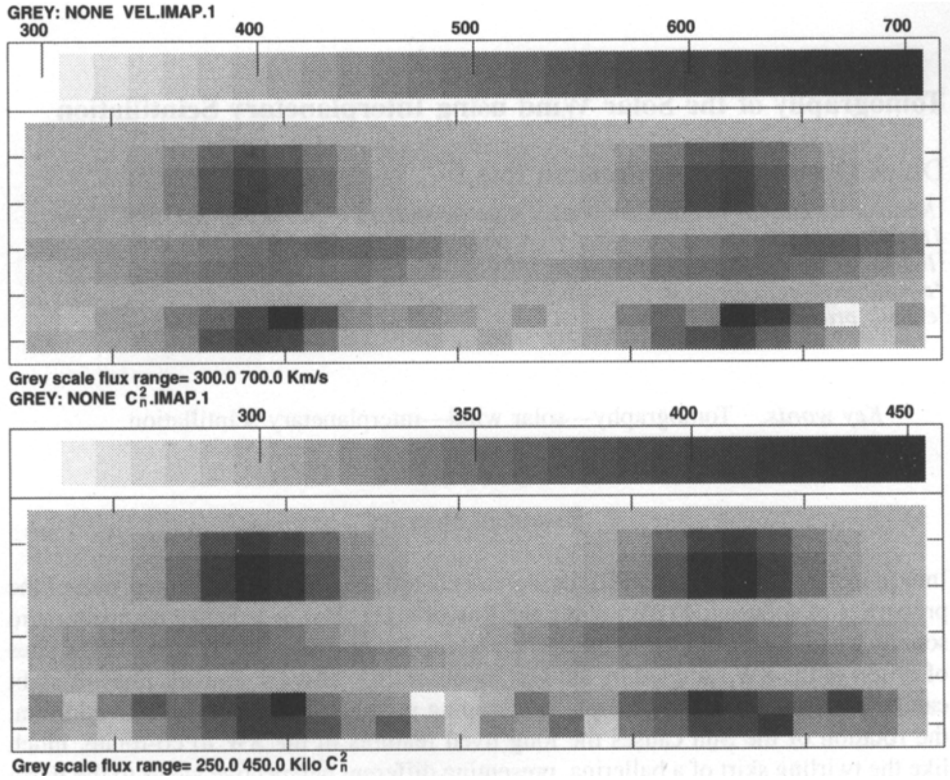

Figure 1. Velocity and C_n^2 maps– In the top figure, the first panel shows the input model which was used to simulate the IPS data, the second panel the initial guess which was computed from the simulated data and was used as input for the reconstruction procedure and the third panel shows the final reconstructed model for velocity of the SW. The bottom figure shows the same set of plots for C_n^2 (in arbitrary units). The first panel shows a heliographic range of [+10°, 20°] and the second and the third panels that of [+12°, –20°]. The pixel size in the reconstructed surface distribution is 13.3° in longitude and 16° in latitude.

generate the IPS data, were represented quite well in the reconstruction. The formal errors in the reconstruction were estimated using *Monte Carlo* methods and independently under the small error approximation. The two error estimates match well. The errors in ν range from ~ 5% –13% and those in C_n^2 from ~ 8% – 20%.

References

Jackson, B. V. *et. al* 1998, *J. Geophys Res.,* **103**, **A6**, 12049–12067.

J. Astrophys. Astr. (2000) **21**, 447–450

Ulysses Observations of Nonlinear Wave-wave Interactions in the Source Regions of Type III Solar Radio Bursts

G. Thejappa[1]* & R. J. MacDowall[2]
[1]*Department of Astronomy, University of Maryland, College Park, MD 20742.*
[2]*NASA, Goddard Space Flight Center, Greenbelt, MD 20771.*
**e-mail: golla@urap.gsfc.nasa.gov*

Abstract. The Ulysses Unified Radio and Plasma Wave Experiment (URAP) has observed Langmuir, ion-acoustic and associated solar type III radio emissions in the interplanetary medium. Bursts of 50–300 Hz (in the spacecraft frame) electric field signals, corresponding to long-wavelength ion-acoustic waves are often observed coincident in time with the most intense Langmuir wave spikes, providing evidence for the electrostatic decay instability. Langmuir waves often occur as envelope solitons, suggesting that strong turbulence processes, such as modulational instability and soliton formation, often coexist with weak turbulence processes, such as electrostatic decay, in a few type III burst source regions.

Key words. Type HI bursts—electrostatic decay—modulational instability.

1. Introduction

Solar and interplanetary type III radio bursts, which occur at the fundamental and the second harmonic of the electron plasma frequency, (f_{pe}), are due to Langmuir waves excited by the outward propagating electron beams in the solar atmosphere. Several non-linear processes are believed to be involved in the excitation of Langmuir waves, the stabilization of electron beams so that they can travel several Astronomical Units (AU) in the solar atmosphere and conversion of Langmuir waves into electromagnetic radiation at f_{pe} and $2f_{pe}$. The Unified Radio and Plasma Wave Experiment (URAP) on the Ulysses spacecraft with its broad frequency coverage from ~ 0 Hz to ~ 1 MHz and its high time resolution ~ 1 ms is well suited for studies of these nonlinear processes. Several local type III interplanetary radio bursts, when the spacecraft was located inside the source regions have been identified in the URAP data (Reiner *et al.* 1992; Thejappa *et al.* 1993; Thejappa & MacDowall 1998).

2. Observations

In Fig. 1, we present the dynamic spectrum of one of the local type III radio bursts and its associated *in situ* waves. The fast drifting emission feature extending from 48.5 kHz down to local electron plasma frequency, $f_{pe} \sim 10.2$ kHz is the type III burst. The intense emission at the plasma line at $\sim f_{pe}$ corresponds to Langmuir waves, as

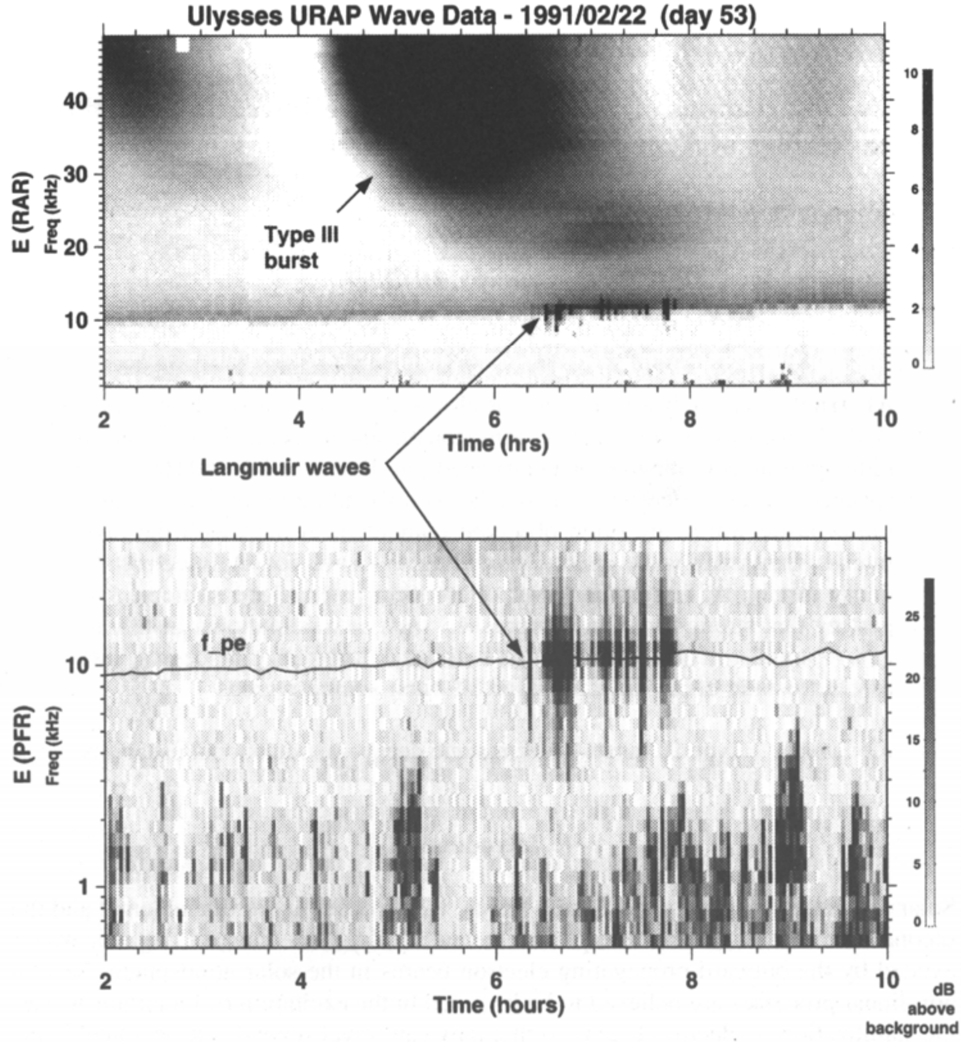

Figure 1. Dynamic spectrum of the local type III radio burst of February 22nd, 1991 and its associated *in situ* waves. The fast drifting emission feature from 48.5 kHz down to local electron plasma frequency, $f_{Pe} \sim 10.2$ kHz is the local type IΠ burst.

seen in the top as well as bottom panels. The random noise below ~ 5 kHz is due to high frequency ion-acoustic-like waves. The *in situ* wave data associated with these events have been extensively used for the purpose of verifying the emission mechanisms at f_{pe} (Thejappa *et al.* 1993), and at $2f_{pe}$ (Thejappa *et al.* 1996), where the observed brightness temperatures were shown to agree very well with the values predicted by the strong turbulence emission mechanisms. The fast envelope sampler (FES) of URAP, which is capable of resolving the field structures with time scales as small as one millisecond has provided several high time resolution snapshots of the Langmuir wave electric field envelopes associated with the local type III bursts. Fig. 2(a) presents one such event, corresponding to the Langmuir waves of the type III

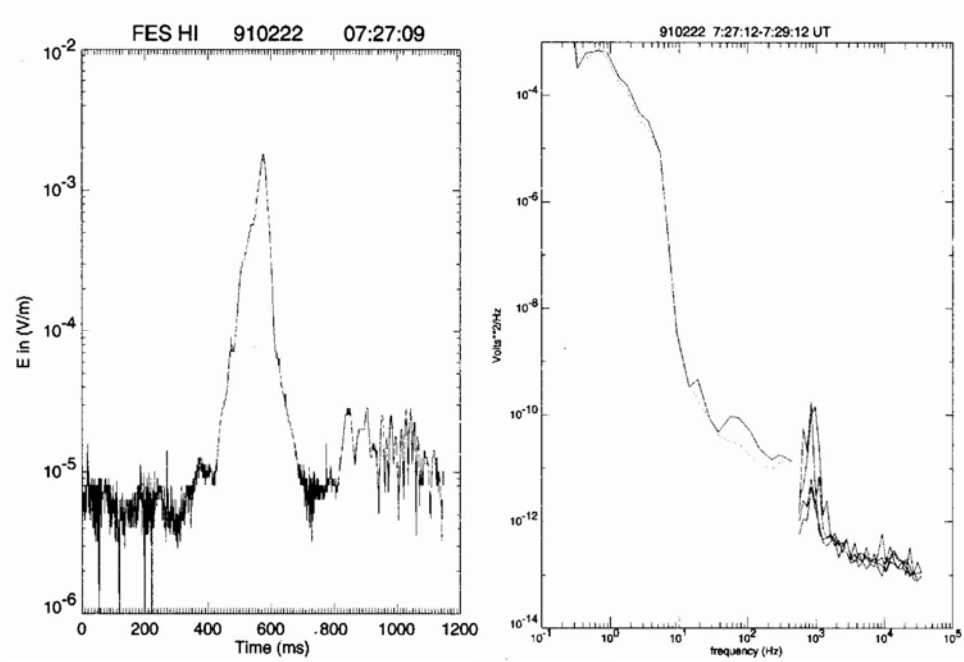

Figure 2. (a): Langrauir envelope soliton, (**b**): the spectral plots of wave electric fields during the Langmuir envelope soliton.

burst presented in Fig. 1. The prominent broad field structures in these FES events have the properties expected of Langmuir envelope solitons, namely the normalized peak energy densities, $W_L/n_eT_e \sim 10^{-5}$, are well above the modulational instability threshold; the spatial scales L, which range from 1 to 5 Langmuir wavelengths, show a high degree of inverse correlation with $(W_L/n_eT_e)^{1/2}$; and the observed widths of these broad peaks agree well with the predicted widths of envelope solitons (Thejappa *et al.* 1999). Sometimes, enhanced low frequency electric field signals around 50–300 Hz are observed in close association with these modulationally unstable Langmuir waves. For example, in Fig. 2(b), we plot the low frequency electric field spectra observed by the Ulysses Wave Form Analyzer (WFA) in the frequency range 0–448 Hz, as well as the high frequency electric field spectra observed by the Ulysses Plasma Frequency Receiver (PFR) (0.57–35kHz) during the 2 minute interval containing the time of the Langmuir envelope soliton of Fig. 2(a). Here, the dotted line corresponds to the instrumental background level. The prominent spectral peak at ~ 10 kHz is due to Langmuir waves, whereas, the spectral enhancement seen at ~ 100 Hz is most probably due to long wavelength ion-acoustic waves.

3. Discussion and conclusions

The simultaneous occurrence of Langmuir and ion-acoustic waves is indicative of the decay of beam excited Langmuir waves into daughter Langmuir and ion-acoustic waves. This interpretation is supported by the observations that: (1) the peak Langmuir wave intensity is well above the threshold for electrostatic decay, and (2) the observed frequency and intensity of ~ 100 Hz electric field signals agree very well with the values expected by the electrostatic decay instability. The occurrence of ion-acoustic waves in close association with the modulationally unstable Langmuir waves is good evidence that the strong and weak turbulence processes are not mutually exclusive in the source regions of the type III radio bursts; rather they coexist. One of the main roles of nonlinear processes is to remove the Langmuir waves from the spectral regions of resonance with the electron beam, i.e., to inhibit quasi-linear relaxation. The observed coexistence of weak and strong turbulence processes suggests that in some cases, the electrostatic decay instability (decay of the beam excited Langmuir wave into a daughter Langmuir wave and an ion-acoustic wave) appears to remove the Langmuir waves from the resonance with the beam. This leads to the accumulation of Langmuir waves at long wavelengths, forming the so-called weak turbulence Langmuir condensate, which eventually becomes modulationally unstable by getting absorbed by the ambient electrons through Langmuir collapse and other non-linear processes. The Langmuir waves undergoing electrostatic decay interact very weakly with the coherent field structures formed due to strong turbulence processes because of the large differences in their spatial scales. Therefore, these processes sometimes operate simultaneously. The coexistence is possible even in the presence of weak damping (γ_0), either due to collisions, or due to power-law type energetic electrons present in the solar wind plasmas, provided it is less than the Langmuir wave growth rate γ_b due to beam plasma instability by an order of magnitude.

Acknowledgements

The research of GT is supported by the NASA grants NAG57145, NCC5-372, and NAG56059.

References

Reiner, M. J., Feinberg, J., Stone, R. J. 1992, *Astrophy. J.,* **394**, 340.

Thejappa, G., Lengyel-Frey, D., Stone, R. G., Goldstein, M. L. 1993, *Astrophys. J.,* **416**, 831.

Thejappa, G., Stone, R. G., Goldstein, M. L. 1996, *Astrophys. and Space Sci,* **243**, 195.

Thejappa, G., MacDowall, 1998, *Astrophys. J.,* **498** 465.

Thejappa, G.. Goldstein, M. L., MacDowall, R. J., Papadopoulos, K., Stone, R. G. 1999, *J. Geophys. Res.,* **104**, 28279.

J. Astrophys. Astr. (2000) **21**, 451–457

Summary Lecture

J. O. Stenflo, *Institute of Astronomy, ETH Zentrum, CH-8092 Zurich, Switzerland. email: stenflo@astro.phys.ethz. ch*

Abstract. This summary lecture makes no attempt to summarize what was actually said at the meeting, since this is well covered by the other contributors. Instead I have structured my presentation in three parts: First I try to demonstrate why the Sun is unique by comparing it with laboratory plasmas. This is followed by some personal reminiscences that go back a significant fraction of the century. I conclude in the form of a poem about this memorable conference in honor of the centennial anniversary of the Kodaikanal Observatory.

Key words. Sun—plasma physics—history of science.

1. The Sun – a unique physics laboratory

The solar plasma, from the solar core to the corona and solar flares, occupies similar locations in a temperature-density diagram as laser plasmas, Tokamak plasmas, and gas discharge plasmas (Petrasso 1990). This may convey the erroneous impression that these various plasmas are in fact similar, and that the local conditions on the Sun may be simulated in the laboratory. Solar and laboratory plasmas are however fundamentally different because of the vastly different scales involved. To make the comparison more meaningful we need to rescale the solar dimensions to laboratory dimensions. The length scales however cannot be rescaled alone without affecting the other physical parameters of the system. If we impose the condition that all the energies within the system should be left unchanged by the scaling, we obtain the so-called "similarity transformations" (Alfvén & Fälthammar 1963).

Let us assume that the linear scale is changed by a factor γ. Then Maxwell's equations demand that the time scale is also changed by the same factor. The condition that the energies are left unchanged requires that $\vec{E}\ell$ should not change, where $\vec{E}$ is the electric field, and ℓ is a length. Since ℓ scales with γ, it follows that $\vec{E}$ must scale with γ^{-1}. Then Maxwell's equations demand that the magnetic field $\vec{B} \sim \gamma^{-1}$ and the electric current density $\vec{j} \sim \gamma^{-2}$, while the electrical conductivity $\sigma \sim \gamma^{-1}$ according to Ohm's equation. To conserve the number of energy-exchanging collisions per particle, the density times the mean free path should be left invariant, but since the latter scales with γ, the density ρ should scale as γ^{-1} . These various scalings have the consequence that the magnetic Reynolds number remains invariant.

Let us now apply these scaling laws to magnetic flux tubes in the network of the quiet Sun. There the typical parameter values are ℓ = 100 km, B= 1 kG, time t= 1000 s, and particle density N= 10^{17} cm^{-3}. Assuming a laboratory scale $\ell_{\rm lab}$ = 1 m, we have $\gamma = 10^{-5}$. Then $B_{\rm lab} = 10^8$ G, $t_{\rm lab}$ = 10ms, and $N_{\rm lab} = 10^{22}$ cm^{-3}.

As the next example we scale the solar cycle, for which the typical parameters are $\ell \approx 10^6$ km, $B \approx 10$ G, t= 22 yr. Again assuming a laboratory scale $\ell_{\rm lab} = 1$ m, we have $\gamma = 10^{-9}$. Then $B_{\rm lab} = 10^{10}$ G and $t_{\rm lab} \approx 1$ s.

As an amusing curiosity, for whatever it may mean, let us use this scaling to compare us with the Sun. The scale of humans is on the order of 1 m (here we are not concerned with factors of two), and our pulse has a period of about 1 s. Scaring the spatial dimension to that of the Sun, our pulse period scales to something quite close to 22 yr. In this sense we can consider the Sun's magnetic cycle as the "pulse of the Sun". The ratio between the cycle period and 1 s is also of the same order of magnitude as the ratio between the orbital period of the Sun around the center of our galaxy and the orbital period of the Earth around the Sun. The life span of the Sun in units of galactic orbital periods is about the same as the life span of human beings in units of orbital periods of the Earth.

Turning our attention back to plasma physics, the above examples of similarity transformations lead us to conclude that the laboratory analogs of solar and other cosmic plasmas are transient, high-density plasmas with superstrong electric and magnetic fields, which are far out of reach of current technology. The Sun is really a unique physical system, where a domain of physics can be explored that is not accessible by other means.

2. Personal reminiscences of solar "gurus"

The concept of attaining spiritual enlightenment or profound learning from a great teacher, a "guru", is generally associated with Indian life and philosophy. However, also in the West, in particular in the scientific enterprise, great personalities often serve as a kind of gurus forming various "schools" of thought. Our achievements are possible because we "stand on the shoulders of giants" of previous generations.

The Kodaikanal Observatory celebrates its centennial anniversary, and I have myself reached an age that allows me to look back and reminisce over a significant fraction of the century. One of my "gurus", who attracted me to work on solar magnetic fields and to focus my attention on the small-scale, intermittent nature of the field, was Hannes Alfven. In Fig. 1 we see him sitting cross-legged, in "guru position", together with his wife outside their home in La Jolla, California. The picture was taken when I visited him there in the summer of 1968, shortly after I had received my PhD (in Lund, Sweden) on the thesis "The Sun's Magnetic Field", and 2½ years before he received the Nobel Prize in physics for his discovery of magnetohydrodynamic waves. This discovery was presented in a short note to the journal *Nature* in 1942, the year I was born (Alfven 1942). The whole paper is reproduced in Fig. 2.

It is interesting to note in his *Nature* paper that what Alfvén really was after was an explanation for the origin of sunspots. His discovery of magnetohydrodynamic waves was a byproduct of his efforts to find a solution to a problem in solar physics. While his explanation of sunspots did not get very far, his discovery of MHD waves has had a profound influence on much of the later development of solar physics in general. This demonstrates that the byproducts of your efforts may often be of much greater importance than the main work that you are trying to do!

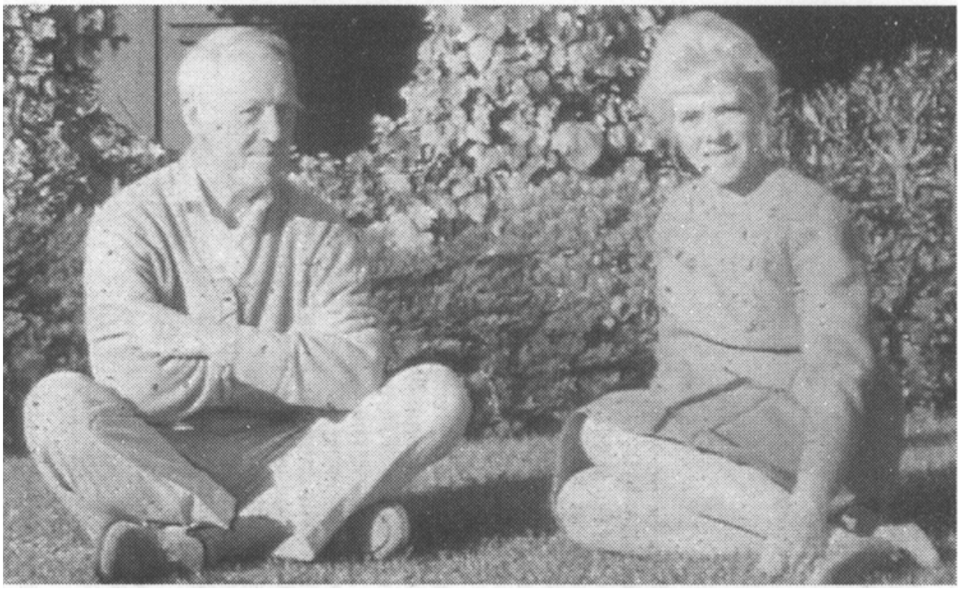

Figure 1. Hannes Alfven with his wife outside their home in La Jolla, in the summer of 1968.

In 1965 when I was 22, Alfven sent me over to Crimea to explore the fine structure of the Sun's magnetic field with Severny's magnetograph. Alfven and Sevemy came up with the idea for this project during a NATO meeting in 1964 in Newcastle on "Magnetism and the Cosmos" (Hindmarsh *et al.* 1967). They were the only participants at that meeting who were not from any NATO country. Their idea had the consequence that I did all the observational work for my PhD thesis during extended visits to the USSR.

A few years later Alfvén brought me in contact with another "guru" of sorts, Max Steenbeck in Jena, DDR, who is the father of $\alpha - \omega$ dynamo theory and mean-field magnetohydrodynamics, and who formed a successful school of prominent dynamo theorists. My first visit to Jena was in 1969, shortly before they published their main, ground-breaking paper on $\alpha - \omega$ dynamo theory (Steenbeck & Krause 1969). The day I arrived, Steenbeck was eager to describe to me on the blackboard in his office the principles of the new dynamo theory, while his young collaborators Fritz Krause and Karl-Heinz Radler were quietly listening in. (A slide I showed at the conference of Steenbeck in his office is of too poor quality to be reproduced here.) It was a strange world with the iron curtain dividing Germany and Europe, but having neutral Sweden as my base I could rather easily collaborate with scientists on both sides. Regardless of the political systems, it was and continues to be natural for scientists to strive for an open world free from secrecy, barriers, and national or political boundaries.

In the area of magnetohydrodynamics, Great Britain had a "guru" in the form of T. G. Cowling from Leeds, who is much known for his anti-dynamo theorem, but who can also be considered as the father of the new generations of eminent MHD theorists in the UK. Figure 3 shows a picture of Cowling (right) from 1971, in conversation with Robert Howard (middle) and Vaclav Bumba. When I began my work on solar magnetic fields I was greatly impressed and influenced by the seminal work of Bumba

Existence of Electromagnetic-Hydrodynamic Waves

If a conducting liquid is placed in a constant magnetic field, every motion of the liquid gives rise to an E.M.F. which produces electric currents. Owing to the magnetic field, these currents give mechanical forces which change the state of motion of the liquid. Thus a kind of combined electromagnetic-hydrodynamic wave is produced which, so far as I know, has as yet attracted no attention.

The phenomenon may be described by the electrodynamic equations

$$\mathrm{rot}\ H = \frac{4\pi}{c} i$$

$$\mathrm{rot}\ E = -\frac{1}{c}\frac{dB}{dt}$$

$$B = \mu H$$

$$i = \sigma\left(E + \frac{v}{c} \times B\right);$$

together with the hydrodynamic equation

$$\partial \frac{dv}{dt} = \frac{1}{c}(i \times B) - \mathrm{grad}\ p,$$

where σ is the electric conductivity, μ the permeability, ∂ the mass density of the liquid, i the electric current, v the velocity of the liquid, and p the pressure.

Consider the simple case when $\sigma = \infty$, $\mu = 1$ and the imposed constant magnetic field H_0 is homogeneous and parallel to the z-axis. In order to study a plane wave we assume that all variables depend upon the time t and z only. If the velocity v is parallel to the x-axis, the current i is parallel to the y-axis, and produces a variable magnetic field H' in the x-direction. By elementary calculation we obtain

$$\frac{d^2H'}{dz^2} = \frac{4\pi\partial}{H_0^2}\frac{d^2H'}{dt^2},$$

which means a wave in the direction of the z-axis with the velocity

$$V = \frac{H_0}{\sqrt{4\pi\partial}},$$

Waves of this sort may be of importance in solar physics. As the sun has a general magnetic field, and as solar matter is a good conductor, the conditions for the existence of electromagnetic-hydrodynamic waves are satisfied. If in a region of the sun we have $H_0 = 15$ gauss and $\partial = 0{\cdot}005$ gm. cm.$^{-3}$, the velocity of the waves amounts to

$$V \sim 60 \text{ cm. sec.}^{-1}.$$

This is about the velocity with which the sunspot zone moves towards the equator during the sunspot cycle. The above values of H_0 and ∂ refer to a distance of about 10^{10} cm. below the solar surface where the original cause of the sunspots may be found. Thus it is possible that the sunspots are associated with a magnetic and mechanical disturbance proceeding as an electromagnetic-hydrodynamic wave.

The matter is further discussed in a paper which will appear in *Arkiv för matematik, astronomi och fysik*.

H. Alfvén.

Kgl. Tekniska Högskolan,
Stockholm.
Aug. 24.

Figure 2. Alfvén's *Nature* paper from 1942, in which he announced his discovery of magnetohydrodynamic waves, awarded with the Nobel Prize in 1970.

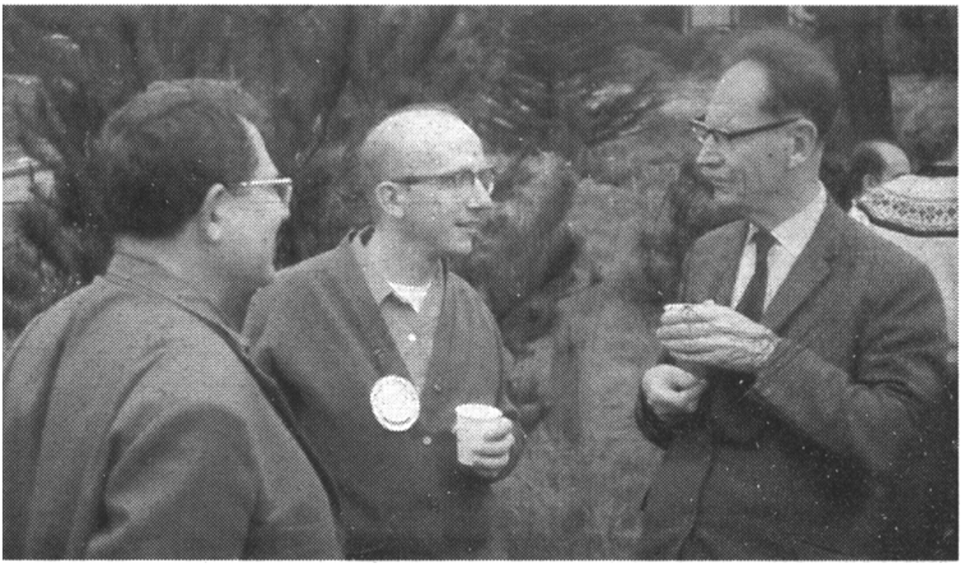

Figure 3. From right to left: T. G. Cowling, R. F. Howard, and V. Bumba, during a coffee break at the Solar Wind conference in Asilomar, California, in 1971.

and Howard in 1965 on the large-scale structure and evolution of the magnetic field (Bumba & Howard 1965), and in 1968 I spent 7 months with Bob Howard in Pasadena and at Mt Wilson. Most of the time in Pasadena I shared office with Arvind Bhatnagar, who later founded and directed the Udaipur Solar Observatory, which has evolved into a major center for solar physics in India.

In the US, the towering figure and “guru” for theoretical solar physics and magnetohydrodynamics has of course been Eugene Parker, a scientific giant who has dominated the field for many decades and has his former students in eminent positions all over the world. In the photo of Fig. 4, from the COSPAR meeting in Tokyo in May 1968, we see him to the left in the second row. Beside him is John Wilcox, who founded and directed the Wilcox Solar Observatory (named after him after his untimely death in the early 1980s), which has been a major center for solar-cycle studies. In the same row follow Howard, Bumba, and myself. I am 25 years old in this picture, taken only a few weeks after I completed, my PhD. In the first row, in front of Bumba, is David Rust, who at that time was working on solar magnetic fields at the Sacramento Peak Observatory. We notice how well and formally dressed all the conference participants were at that meeting! Times have changed, but I. appreciate the more informal atmosphere that we now have.

At the Kodaikanal meeting I had the opportunity of showing many more old slides from about three decades ago, showing other key personalities in solar physics, but due to space limitations I have here only sampled a few glimpses from that era.

3. Poetic conclusion

At this centennial Kodaikanal anniversary at the end of the millennium we are enjoying a very special occasion at an unusual place and time. The meeting therefore

Figure 4. From theCOSPAR meeting in Tokyo, May 1968. In the second row, from left to right: E. N. Parker, J. M. Wilcox, R. F. Howard, V. Bumba, J. O. Stenflo. In the first row in front of Bumba: D. M. Rust.

deserves a somewhat unusual conclusion, which has prompted me to round off my presentation with a poem written for the occasion. You need to keep in mind that I have not been trained for something like this, but at least I have tried my best, and here it is:

It is good to meet so many friends, both old and new,
as we have gathered here under the umbrella of the IAU.

Thanks to the organizers all has been fine.
It has been a memorable Colloquium 179,

I will now make some remarks on the meeting,
but excuse me if my comments are too sweeping.

The fits between theory and observations can be fantastic
with a model that has free parameters and is kinematic.

Instead of using superficial dermatology,
we now need to diagnose the Sun with helioseismology.

To be doing work on solar tomography
can at least be good for your own bibliography.

Bright new ideas on the evolution of helicity
may not be successful in terms of publicity.

Prominences have remained quiet until this time,
when they erupted into a new paradigm.

Some people have a strange attraction
to numerical simulations of magnetoconvection.

When the Sun increases its luminosity,
it is not an expression of animosity.

It is rather the preponderance of faculae over sunspots,
as has been demonstrated to us with novel and fun plots.

For all of us this centennial celebration has been a most fitting way
to end the century before facing Y2K.

To our Indian hosts we say thanks and cheers,
and best wishes to all of you for the next 100 years !

References

Alfvén, H. 1942, *Nature,* **150**, 405–406.
Alfvén, H., Fälthammar, C.-G. 1963, *Cosmical Electrodynamics – Fundamental Principles,* 2nd ed., (Oxford: Oxford Univ. Press), 137.
Bumba, V., Howard, R. 1965, *Astrophys. J.,* **141**, 1502.
Hindmarsh, W. R., Lowes, F. J., Roberts, P. H. 1967, Runcorn, S. K. (ed.) *Magnetism and the Cosmos,* (Edinburgh/London: Oliver & Boyd).
Petrasso, R. D. 1990, *Nature,* **343**, 21–22.
Steenbeck, M., Krause, F. 1969, *Astron. Nachr.,* **291**, 49.